Mechanistic Investigations and Search Directions for Catalyst Discovery

By

Saurabh Bhandari

A dissertation submitted in partial fulfillment of

the requirements for the degree of

Doctor of Philosophy

(Chemical Engineering)

at the

UNIVERSITY OF WISCONSIN-MADISON

2020

Date of final oral examination: 08/13/2020

The dissertation is approved by the following members of the Final Oral Committee:

Manos Mavrikakis, Professor, Chemical & Biological Engineering
George W. Huber, Professor, Chemical & Biological Engineering
Matthew Gebbie, Assistant Professor, Chemical & Biological Engineering
Michael S. Arnold, Professor, Materials Science & Engineering

ABSTRACT

The transition towards a sustainable energy future hinges strongly on the effective deployment of renewable energy carriers. Wide-scale adoption of sustainable technologies requires major innovation in the development of storage materials that exhibit high energy density and of catalytic materials, that help facilitate the relevant chemical transformations to release the stored energy, in an efficient and cost-effective manner. Fundamental investigations aimed at elucidating detailed mechanistic understanding of such chemistries could greatly accelerate the discovery of favorable energy-storage and catalytic materials.

In this dissertation, we utilize a combination of first-principles density functional theory (DFT) calculations, reaction kinetics experimentation, and coverage self-consistent mean-field microkinetic modeling to elucidate detailed atomistic-scale insights for the heterogeneously catalyzed chemistries. We emphasize on the importance of formulating computational models that closely-replicate the surface environment present on the catalyst under reaction conditions, an aspect which is oft-ignored in conventional investigations. Consideration of spectator induced coverage-effects were found to not only influence the energetics of the reaction network through lateral adsorbate-adsorbate repulsions, but more importantly alter the reaction pathway itself, by participating in the reaction mechanism.

Our multi-faceted methodology yields an unbiased understanding of the reaction mechanism and enables us to develop a comprehensive picture of the *in situ* active site. In a broader context, our algorithmic approach provides a systematic framework for elucidating novel descriptions for the nature of the active site as well as reaction mechanisms, consequently providing a more rigorous basis for computational prediction of improved catalytic materials.

ACKNOWLEDGMENTS

First and foremost, I would like to express my most sincere gratitude to my advisor, Professor Manos Mavrikakis. His scientific rigor, creative approach toward scientific problem solving, relentless work ethic, and professionalism have been a constant source of motivation for me and will continue to inspire me in my scientific career. I have benefited tremendously from his mentorship and cannot imagine having made all the progress without his guidance and support. I feel absolutely blessed to have had an opportunity to work with him over the past 5 years and will strive to exemplify and pass on all that I have learned from him.

I am also deeply grateful to Professor James A. Dumesic for guiding me on the experimental portion of my projects. The numerous discussions that I have had with him over the course of my graduate studies have enabled me to better appreciate reaction engineering from an experimental perspective, which has in turn provided me with a holistic view of heterogeneous catalysis. I would like to thank Professor George W. Huber for serving on my thesis committees over the past 5 years, Professor Christos T. Maravelias for serving preliminary exam committee, as well as, Professor Matthew Gebbie and Professor Michael S. Arnold for serving on my defense committee.

I would like to thank our collaborators – Dr. Stacey I. Zones (Chevron), Professor Lars Grabow (University of Houston), and Professor Konstantinos Goulas (Oregon State University). I feel fortunate to have worked alongside them and learn from their scientific expertise.

I am grateful to all the current and former group members of the Computational Surface Science and Catalysis group. It was a privilege to work alongside such talented and hard-working researchers. In particular – Professor Srinivas Rangarajan – for helping me decide to join the group, for mentoring me in my first year, and for collaborating on numerous projects throughout the entirety of my time at UW. I would also like to thank – Dr. Lang Xu, Dr. Benjamin W. J. Chen, Dr. Thomas Kropp, Dr. Roberto Schimmenti, Dr. Florian Goeltl, Dr. Sean A. Tacey, and Michael Rebarchik – for our fruitful collaborations. I would like to acknowledge – Dr. Tibor Szilvasi, Dr. Anthony Plauck, Dr. Ahmed Elnabawy, Dr. Duygu Gerceker, Jake I. Gold, Ellen A. Murray, Trent Wolter, and Lisa Je – for our productive discussions and for maintaining a positive work-environment in the group. I am also grateful to the members from Professor Dumesic's group, particularly – Dr. Madelyn Ball, Dr. Ali Hussain Motagamwala, Keishla Rivera-Dones, Benginur Demir, and Lifeng Zhang – for their insight and help with the experimental portions of my projects.

I would like to thank the staff at the Chemical & Biological Engineering (CBE) department – Kate Fanis, Oscar Garcia-Romero, Theresa R. Neisius, Russ Poyner, Beth Brandl, Michelle Kirch, Kathy Heinzen, Mary Heimbecker, Christi Levenson, Susanne Ely – for their technical and administrative support during my graduate studies.

I would also like to acknowledge financial support from the U.S. Department of Energy – Office of Basic Energy Sciences (DOE-BES) and the National Science Foundation for supporting our catalysis projects, as well as the Donald A. Baldovin Graduate Fellowship for the partial financial support during the first year of my graduate studies.

I am also grateful to some of my closest friends in the CBE department – Roberto Schimmenti, Jing-Yao (Sandy) Chen, Ranjeet Kumar, Apoorva Sampat, Ashwin Shekhar, and Benginur Demir – for being there during the challenging times and for making my stay in Madison a delightful experience.

Finally, I would like to thank my brother, Shubham Bhandari, and my parents Sunil and Neeru Bhandari, for their unconditional love and support – I owe them everything.

TABLE OF CONTENTS

ABSTRACT ..... **I**

ACKNOWLEDGMENTS ..... **II**

TABLE OF CONTENTS ..... **V**

LIST OF TABLES ..... **XII**

LIST OF FIGURES ..... **XXII**

CHAPTER 1 INTRODUCTION **1**

1.1 Heterogeneous Catalysis for Sustainable and Environmentally Benign Technologies 1

1.2 First-principles Investigation of Catalytic Chemistries and Rational Design of Catalysts 2

1.3 Scope of Dissertation 5

CHAPTER 2 METHODS **8**

2.1 Introduction 8

2.2 Density Functional Theory 8

2.2.1 The Schrödinger Equation 8

2.2.2 Application of DFT in Heterogeneous Catalysis 12

2.3 Reaction Kinetics Experimentation 18

2.4 Microkinetic Modeling 20

CHAPTER 3 REACTION MECHANISM OF VAPOR-PHASE FORMIC ACID DECOMPOSITION OVER PLATINUM CATALYSTS: DFT, REACTION KINETICS EXPERIMENTS, AND MICROKINETIC MODELING **23**

3.1 Introduction 23

3.2 Methods 26

3.2.1 Computational Methods 26

3.2.2 Experimental Methods 28

3.2.3 Microkinetic Modeling 30

3.3 Results and Discussion 34

3.3.1 DFT Study 34

3.3.2 Experimental Kinetics 54

3.3.3 Microkinetic Modeling 56

3.4 Active Site for Vapor-Phase Decomposition of Formic Acid on Pt/C 75
3.5 Conclusions 77
CHAPTER 4 A COVERAGE SELF-CONSISTENT MICROKINETIC MODEL FOR VAPOR-PHASE FORMIC ACID DECOMPOSITION ON PD/C CATALYSTS 80
4.1 Introduction 80
4.2 Methods 83
4.2.1 Experimental Section 83
4.2.2 Microkinetic Modeling 85
4.3 Results and Discussion 89
4.3.1 Reaction Kinetics Experiments 89
4.3.2 Microkinetic Modeling Results 90
4.3.3 CO* Coverage-Cognizant Pd(111) Model 102
4.4 Active Site for Vapor-Phase Decomposition of FA on Pd/C 109
4.5 Conclusions 111
CHAPTER 5 ROLE OF HYDROGEN-BONDED BIMOLECULAR FORMIC ACID-FORMATE COMPLEXES FOR FORMIC ACID DECOMPOSITION ON CU(111): A FIRST-PRINCIPLES DFT AND MICROKINETIC MODELING STUDY 114
5.1 Introduction 114
5.2 Methods 116
5.2.1 Density Functional Theory Calculations 116
5.2.2 Search for Low Energy Configurations 118
5.2.3 Microkinetic Models 119
5.3 Results 122
5.3.1 Density Functional Theory Results 123
5.3.2 Microkinetic Modeling Results 132
5.3.3 Coverage Self-Consistent 0.375 ML $HCOO_{BX}$ Model 138
5.4 Discussion 141
5.5 Conclusions 143
CHAPTER 6 COMBINING COMPUTATIONAL MODELING WITH REACTION KINETICS EXPERIMENTS FOR ELUCIDATING THE *IN SITU* NATURE OF THE ACTIVE SITE IN CATALYSIS 145

6.1 Introduction 145
6.2 Going Beyond the State-of-the-Art 147
6.3 FA Decomposition on Supported Gold Catalysts 150
6.3.1 Elucidating the Active Site for FA Decomposition on Au/SiC 151
6.3.2 Experimental Insight on the Active Site for FA Decomposition on Au/SiC 153
6.3.3 FA decomposition on Unsupported Au Clusters 154
6.4 FA Decomposition on Supported Platinum Catalysts 157
6.4.1 Iterative Approach for Elucidating the Active Site for FA Decomposition on Pt/C . 157
6.4.2 Modeling CO* Spectator-induced Coverage-effects 159
6.5 An Algorithm to Identify the Active Site and Reaction Mechanism 162
6.6 Parameter Estimation 164
6.7 Outlook 165
6.8 Summary 167
CHAPTER 7 TOWARDS EXPERIMENT CALIBRATED COVERAGE-COGNIZANT VOLCANO PLOTS: FORMIC ACID DECOMPOSITION REACTION 169
7.1 Introduction 169
7.2 Methods 171
7.2.1 Computational Methods 171
7.2.2 Model Formulation 174
7.2.3 Reaction Network 176
7.3 Results and Discussion 178
7.3.1 Conventional Reactivity Maps 178
7.3.2 Experiment-Calibrated Coverage-Cognizant Reactivity Maps 180
7.3.3 Design of Improved Intermetallic Binary Alloy Catalysts 183
7.3.4 Scope for Improvement 185
7.4 Conclusions 188
CHAPTER 8 HOW NON-INNOCENT SPECTATOR SPECIES IMPROVE THE OXYGEN REDUCTION ACTIVITY OF SINGLE-ATOM CATALYSTS: MICROKINETIC MODELS FROM FIRST-PRINCIPLES CALCULATIONS 190
8.1 Introduction 190

8.2 Computational Details 192
8.2.1 DFT Calculations 192
8.2.2 Microkinetic Modeling 193
8.3 Results and Discussion 196
8.4 Conclusions 204
CHAPTER 9 AMMONIA ELECTRO-OXIDATION REACTION ON PT(111): THE EFFECT OF NITROGEN COVERAGE 206
9.1 Introduction 206
9.2 Computational Methods 210
9.3 Results and Discussion 213
9.4 Conclusions 222
CHAPTER 10 CONCLUSIONS AND FUTURE DIRECTIONS 223
10.1 Conclusions 223
10.2 Future Work 226
10.2.1 Discovery of Novel Reaction Mechanisms and the Role of Spectators 226
10.2.2 Design of Experiments 228
10.2.3 Coverage Self-consistent Solutions for Electrocatalytic Reactions 230
10.2.4 Detailed Investigations over Intermetallic Binary-alloy Catalysts 231
10.2.5 Implications of Coverage-cognizant Volcano Plots for Materials Discovery 233
APPENDIX A CHLOROFORM HYDRODECHLORINATION ON PALLADIUM SURFACES: A COMPARATIVE DFT STUDY ON PD(111), PD(100), AND PD(211) 235
A.1 Introduction 235
A.2 Methods 237
A.3 Results and Discussion 240
A.3.1 Adsorption of Reaction Intermediates 241
A.3.2 Reaction Energies and Activation Energy Barriers 245
A.3.3 Analysis of Reaction Network and Potential Energy Diagram (PED) 261
A.4 Analysis of Site-Blocking Species 263
A.5 Conclusions 268

APPENDIX B A THERMODYNAMIC PERSPECTIVE ON THE STEPWISE CONVERSION OF METHANE TO METHANOL OVER CU-EXCHANGED SSZ-13 270

B.1 Introduction 270

B.2 The Stepwise Conversion of Methane to Methanol 273

B.3 Computational Methods 275

B.4 The Thermodynamic Model 277

B.4.1 Included Structures 277

B.4.2 Constructing a Model 283

B.5 Activation 285

B.5.1 Phase Diagrams 285

B.5.2 Comparison to experimental data 290

B.6 Methane activation and methanol extraction 292

B.7 Discussion 299

B.8 Conclusions 302

B.9 Supporting Information 303

B.9.1 Reaction Conditions Along the Stepwise Conversion of Methane to Methanol 303

B.9.2 Spin States of Cu Dimers and Trimers 303

B.9.3 The Impact of Unit-Cell Size on Dimer Stability 304

B.9.4 Legend for the Phase Diagrams 307

B.9.5 T/P(O_2) phase diagrams for 2Al-B through 2Al-E 308

B.9.6 Relative Stability of Dimers and Trimers 310

B.9.7 P(H_2O)/T Phase Diagram for 2Al-A 311

B.9.8 Cu-X Distances for Non-stabilized Dimers, Trimers and Dehydrated Monomers 312

B.9.9 T/P(CH_4) Phase Diagrams for 2Al-B through 2Al-E 314

APPENDIX C SUPPORTING INFORMATION FOR CHAPTER 3:REACTION MECHANISM OF VAPOR-PHASE FORMIC ACID DECOMPOSITION OVER PLATINUM CATALYSTS: DFT, REACTION KINETICS EXPERIMENTS, AND MICROKINETIC MODELING 318

C.1 Supplementary Tables for the 4/9 ML CO*-Covered Pt(111) Model 318

C.2 Corrections Predicted by Parameter Estimation vs. DFT Intrinsic Errors 325

C.3 Catalyst Characterization 327

C.4 PFR Simulation: Optimized CO*-coverage Dependent Energetics Pt(111) 328

APPENDIX D SUPPORTING INFORMATION FOR CHAPTER 4: A COVERAGE SELF-CONSISTENT MICROKINETIC MODEL FOR VAPOR-PHASE FORMIC ACID DECOMPOSITION ON PD/C CATALYSTS 329

D.1 Experimental 330

D.1.1 Reaction Kinetics Experiments 330

D.1.2 Catalyst Characterization 331

D.1.3 Operando FTIR Spectroscopy 332

D.2 Model Formulation 333

D.2.1 Coverage Dependent Thermochemical Parameters 334

D.2.2 Coverage Dependent Kinetic Parameters 336

D.2.3 Reaction Energetics on 5/9ML CO*-covered Pd(111) and Pd(100) Facets 338

D.3 Comparison of PW91-GGA Derived Binding energies with Single Crystal Adsorption Calorimetry (SCAC) 343

D.4 PFR Simulation: Optimized CO* Coverage-dependent Energetics Pd(111) 344

APPENDIX E SUPPORTING INFORMATION FOR CHAPTER 5: ROLE OF HYDROGEN-BONDED BIMOLECULAR FORMIC ACID-FORMATE COMPLEXES FOR FORMIC ACID DECOMPOSITION ON CU(111): A FIRST-PRINCIPLES DFT AND MICROKINETIC MODELING STUDY 345

E.1 Coverage Self-Consistent Microkinetic Modeling 345

E.1.1 Clean Cu(111) Model – Reduced Reaction Network 346

E.1.2 0.625 ML $HCOO_B$-covered Cu(111) Model – Reduced Reaction Network 349

E.1.3 Clean Cu(111) Model – Full Reaction Network 353

E.1.4 0.625 ML $HCOO_B$-covered Cu(111) Model – Full Reaction Network 356

E.1.5 0.375 ML $HCOO_{BX}$-covered Cu(111) Model – Full Reaction Network 360

E.2 Supplementary Figures 363

APPENDIX F SUPPORTING INFORMATION FOR CHAPTER 7: TOWARDS EXPERIMENT CALIBRATED COVERAGE-COGNIZANT VOLCANO PLOTS: FORMIC ACID DECOMPOSITION REACTION 367

F.1 Reaction Thermochemistry 367

F.2 Unadjusted DFT Energetics on Clean Pd(111) 368

F.3 Optimized DFT Energetics for CO*-coverage Cognizant Model on Pd(111) 369

F.4 CO and HCOO Coverage-dependent Energetics 370
F.5 Optimized Structures of the Reaction Intermediates 372
F.6 Optimized Lattice-constants for Intermetallic Binary Alloys 376
APPENDIX G SUPPORTING INFORMATION FOR CHAPTER 8: HOW NON-INNOCENT SPECTATOR SPECIES IMPROVE THE OXYGEN REDUCTION ACTIVITY OF SINGLE-ATOM CATALYSTS: MICROKINETIC MODELS FROM FIRST-PRINCIPLES CALCULATIONS 377
G.1 Gibbs Free Reaction Energies 378
G.2 Scaling Relations 380
G.3 Microkinetic Modeling 381
G.4 Electronic Structure of ORR Intermediates 386
APPENDIX H SUPPORTING INFORMATION FOR CHAPTER 9: AMMONIA ELECTRO-OXIDATION REACTION ON PT(111): THE EFFECT OF NITROGEN COVERAGE 387
H.1 Impact of the Functional Choice on the Onset Potential 387
H.2 N*-coverage Estimation from Previous Experimental Studies 390
H.3 Optimized geometries of AOR reaction intermediates at different N* coverages 391
APPENDIX I BIBLIOGRAPHY 398

LIST OF TABLES

Table 3.1 Calculated binding energies (BE) of reactants, products, and reaction intermediates at their preferred adsorption structures on Pt(111) and Pt(100). 36

Table 3.2 Calculated activation energy barriers (EA) and reaction energies (ΔH) for the elementary steps considered in the HCOOH decomposition reaction network on clean Pt(111) and Pt(100). All the values are relative to the best initial/final states and infinite separation (*except #22 for Pt(111) and #24 for Pt(100), which are reported with respect to the co-adsorbed initial states, since the coadsorbed states are stabilized through hydrogen bonding) 37

Table 3.3 Calculated binding energies (BE) at their preferred adsorption configuration on 4/9 ML CO*-covered Pt(111) and Pt(100). 45

Table 3.4 Calculated activation energy barriers (E_A) and reaction energies (ΔH) for the elementary steps considered in the HCOOH decomposition reaction network on 4/9 ML CO*-covered Pt(111) and Pt(100). All the values are relative to the best initial/final states and infinite separation. The spectator CO* is indicated in bold in relevant elementary steps. 46

Table 3.5 Reaction rates obtained from kinetics experiments on Pt/C catalyst. The inlet feed flowrate reported here has been normalized by the number of sites for Pt/C used in the reactor. 55

Table 3.6 Corrections to the DFT-derived binding energy of the intermediates for the clean Pt(100) model obtained from parameter estimation. 58

Table 3.7 Corrections to the DFT-derived activation energy barrier of the elementary steps for the clean Pt(100) model obtained from parameter estimation. 58

Table 3.8 Corrections to the DFT-derived binding energy of the intermediates for the clean Pt(111) model obtained from parameter estimation. 60

Table 3.9 Corrections to the DFT-derived activation energy barrier of the elementary steps for the clean Pt(111) model obtained from parameter estimation. 60

Table 3.10 Corrections to the DFT-derived binding energy of the intermediates for the 4/9 ML CO*-covered Pt(100) model-I obtained from parameter estimation. 63

Table 3.11 Corrections to the DFT-derived activation energy barrier of the elementary steps for the 4/9 ML CO*-covered Pt(100) model-I obtained from parameter estimation. 64

Table 3.12 Comparison of experimentally measured and model predicted apparent activation energy and reaction orders with respect to the partial pressure of HCOOH, H_2O, H_2, CO_2 and CO for the dehydrogenation ($HCOOH \rightarrow CO_2 + H_2$) and dehydration pathway ($HCOOH \rightarrow CO + H_2O$), for the optimized 4/9 ML CO*-covered Pt(100) model-I. †The dehydration reaction order for the CO cofeed experiments could not be accurately measured because of small selectivity of the catalyst toward CO formation. 65

Table 3.13 Corrections to the DFT-derived binding energy of the intermediates for the 4/9 ML CO*-covered Pt(100) model-II obtained from parameter estimation. 67

Table 3.14 Corrections to the DFT-derived activation energy barrier of the elementary steps for the 4/9 ML CO*-covered Pt(100) model-II obtained from parameter estimation. 68

Table 3.15 Comparison of experimentally measured and model predicted apparent activation energy and reaction orders with respect to the partial pressure of HCOOH, H_2O, H_2, CO_2 and CO for the dehydrogenation ($HCOOH \rightarrow CO_2 + H_2$) and dehydration pathway ($HCOOH \rightarrow CO + H_2O$), for the optimized 4/9 ML CO*-covered Pt(100) model-II. †The dehydration reaction order for the CO cofeed experiments could not be accurately measured because of small selectivity of the catalyst toward CO formation. 69

Table 3.16 Corrections to the DFT-derived binding energy of the intermediates for the 4/9 ML CO*-covered Pt(111) model, as obtained from parameter estimation. 71

Table 3.17 Corrections to the DFT-derived activation energy barrier of the elementary steps on the 4/9 ML CO*-covered Pt(111) model, as obtained from parameter estimation. 71

Table 3.18 Comparison of experimentally measured and model predicted apparent activation energy barriers and reaction orders with respect to the partial pressure of HCOOH, H_2O, H_2, CO_2, and CO for the dehydrogenation ($HCOOH \rightarrow CO_2 + H_2$) and dehydration pathway ($HCOOH \rightarrow CO + H_2O$), for the optimized 4/9 ML CO*-covered Pt(111) model. †The dehydration reaction order for the CO cofeed experiments could not be accurately measured because of small selectivity of the catalyst toward CO formation. 74

Table 4.1 Corrections to the DFT-derived binding energy of the reaction intermediates and activation energy of the elementary steps for the clean Pd(100) model, as obtained from parameter estimation. †For CO*, the number outside the parenthesis refers to the correction in the energy of CO* as predicted from parameter estimation, while the number within the parenthesis ([•]) represents the 'overall' correction in the binding energy of CO*, including the adjustment to the CO(g) gas-phase energy by -0.60 eV (see Model Formulation). 92

Table 4.2 Corrections to the DFT-derived binding energy of the reaction intermediates and activation energy of the elementary steps for the clean Pd(111) model, as obtained from parameter estimation. †For CO*, the number outside the parenthesis refers to the correction in the energy of CO* as predicted from parameter estimation, while the number within the parenthesis ([•]) represents the 'overall' correction in the binding energy of CO*, including the adjustment to the CO(g) gas-phase energy by -0.60 eV (see Model Formulation). 95

Table 4.3 Corrections to the DFT-derived binding energy of the reaction intermediates and activation energy of the elementary steps for the CO* coverage-cognizant Pd(100) model, as obtained from parameter estimation. †For CO*, the number outside the parenthesis refers to the correction in the energy of CO* as predicted from parameter estimation, while the number within the parenthesis ([•]) represents the 'overall' correction in the binding energy of CO*, which also includes the adjustment to the CO(g) gas-phase energy by -0.60 eV (see Model Formulation). 100

Table 4.4 Corrections to the DFT-derived binding energy of the reaction intermediates and activation energy of the elementary steps for the CO* coverage-cognizant Pd(111) model, as obtained from parameter estimation. †For CO*, the number outside the parenthesis refers to the correction in the energy of CO* as predicted from parameter estimation, while the number within

the parenthesis ([•]) represents the 'overall' correction in the binding energy of CO*, which also includes the adjustment to the CO(g) gas-phase energy by -0.60 eV (see Model Formulation). 104

Table 4.5 Comparison of experimentally determined and model-predicted apparent activation energy barrier and reaction orders with respect to the partial pressure of HCOOH, H_2O, H_2, CO_2 and CO for the dehydrogenation ($HCOOH \rightarrow CO_2 + H_2$) and dehydration pathway ($HCOOH \rightarrow CO + H_2O$). †The dehydration reaction order for the CO cofeed experiments could not be accurately quantified due to small selectivity of Pd/C towards CO formation..... 108

Table 5.1 Results from optimized, parameter-adjusted models for formic acid (FA) decomposition over Cu(111). Maximum absolute corrections for the binding energy (max $|\Delta BE|$) and activation energy barriers (max $|\Delta E_A|$), most abundant surface intermediate (MASI) coverages (averaged across the considered experimental temperature and pressure range), the FA apparent reaction order (at 373 K in a partial pressure range of 2.5–10%), and the apparent activation energy (E_{app}) (10% FA in a temperature range of 368–383 K) are reported. Under similar reaction conditions, the experimentally measured FA reaction order and E_{app} on Cu/Al_2O_3 are 0.0 and 95-100 kJ/mol, respectively.[223] The final coverage self-consistent model that matches the experimental observations is marked in bold. Subscripts B and M refer to the bidentate and monodentate configurations of HCOO, respectively. Subscript X refers to complexation of HCOO with HCOOH (i.e. FA-HCOO complexes). 134

Table 5.2 Corrections to the DFT-derived binding energies (ΔBE) and activation energy barriers (ΔE_A) for the 0.375 ML $HCOO_{BX}$ covered Cu(111) model obtained from parameter estimation for the full reaction mechanism. Note that at a coverage of 0.375 ML $HCOO_{BX}$, HCOOH complexes with the uncoordinated O atom of a spectator $HCOO_{BX}$ (Figure 5.5). Negative (positive) corrections denote stabilization (destabilization). Intermediates and elementary steps not listed have no corrections from their initial DFT energetics. Subscripts B and M refer to the bidentate and monodentate configurations of HCOO, respectively. Subscript X refers to complexation of HCOO with HCOOH (i.e. FA-HCOO complexes). 137

Table 5.3 Campbell's kinetic degrees of rate control (X_{RC})[245] for elementary steps in our 0.375 $HCOO_{BX}$ covered Cu(111) model. The degrees of rate control are calculated at our defined home conditions (10% FA, 373 K, balance He). Subscripts B and M refer to the bidentate and monodentate configurations of HCOO, respectively. Subscript X refers to complexation of HCOO with HCOOH (i.e. FA-HCOO complexes). 140

Table A.1 Binding energies of reactants and reaction intermediates at their preferred adsorption sites on Pd(111) (data reproduced from Xu *et al.*),[376] Pd(100), and Pd(211). Zero of binding energy corresponds to infinite separation between adsorbate in the gas phase and clean slab. 243

Table A.2 Diffusion barriers and paths of Cl* and C* on Pd(111), Pd(100), and Pd(211). 265

Table B.1 Numerical values for the reaction conditions at each point during the stepwise conversion of methane to methanol. The temperature is given in K and the pressures are given with respect to a reference pressure P_0 of 1 bar. 303

Table B.2 Modeled spin states and their relative stability of all dimers and trimers included in this study. Energy differences (ΔE) are given in kJ/mol and with respect to the most stable spin state for each dimer/trimer. 303

Table B.3 Energy difference (ΔE) and difference in chemical potential ($\Delta\mu^{Cu}$) for Cu dimers anchored in Al-configuration C modeled in a single primitive unit cell (single u.c.) or double primitive unit cell (double u.c.). Numerical values are given in kJ/mol..... 306

Table C.1 Optimized Shomate parameters (A to H) for the adsorbate binding energies (in kJ/mol) in reaction network in T-range: 300 – 1200 K evaluated on the 4/9ML CO*-covered Pt(111). 319

Table C.2 Optimized Shomate parameters (A to H) for the transition-state energies (in kJ/mol) in the reaction network in T-range: 300 – 1200 K evaluated on the 4/9ML CO*-covered Pt(111)320

Table C.3 Pre-exponential factors for the adsorption steps on 4/9ML CO*-covered Pt(111), where, per collision theory, rate constant $k = AT^{-0.5}$ (where, k is in s^{-1})..... 320

Table C.4 Coefficients for the polynomial expression (ΔBE (in kJ/mol) $= \alpha_0 + \alpha_1\theta + \alpha_2\theta^2 + \alpha_3\theta^3$) employed to update the binding energy of the adsorbates with surface coverage of CO*, from the values calculated on the 4/9 ML CO*-covered Pt(111) facet, where θ is the surface coverage of CO (in ML) calculated by the mean-field microkinetic model during a forward simulation. Value of α_1 was set to zero to ensure that the energy minimum for each species was at clean surface level (no coadsorbed CO*).The parameters α_0, α_2, and α_3 are fit using unadjusted DFT energies calculated at varying coadsorbed CO*-coverages, as described in the main text. 321

Table C.5 Coefficients for the polynomial expression (ΔE_{TS} (in kJ/mol) $= \alpha_0 + \alpha_1\theta + \alpha_2\theta^2 + \alpha_3\theta^3$) employed to update the transition-state energies for the elementary steps with surface coverage of CO*, from the values calculated on the 4/9 ML CO*-covered Pt(111) facet, where θ is the surface coverage of CO (in ML) calculated by the mean-field microkinetic model during a forward simulation. Value of α_1 was set to zero to ensure that the energy minimum for each transition-state was at clean surface level (no coadsorbed CO*). The parameters α_0, α_2, and α_3 are fit using unadjusted DFT energies calculated at varying coadsorbed CO*-coverages, as described in the main text..... 322

Table C.6 Degree of rate control (X_{RC}) and enthalpies (H), wrt. HCOOH(g), CO(g), and H_2(g), for reaction intermediates and elementary steps in FA dehydrogenation pathway on the CO* coverage-cognizant Pt(111) microkinetic model, at home conditions (2.6% FA, balance He, 373K). 323

Table C.7 Degree of rate control (X_{RC}) for the relevant elementary steps toward the decomposition of FA, obtained by keeping the (a) direct COOH* dehydrogenation, (b) CO* assisted COOH* mechanisms active, one at a time. The energetics were maintained at the steady-state CO* coverages corresponding to home conditions (2.6% FA, balance He, 373K), by co-feeding appropriate amounts of CO(g) in the feed. 324

Table C.8 Comparison of PW91-evaluated binding energy of formic acid with the enthalpy for adsorption of formic acid obtained from experimental values in the literature.[146] Negative Δ implies under prediction of binding energy by PW91-DFT (at FA coverage of 1/9 ML on clean Pt(111)). All values are in eV. 326

Table C.9 Comparison of PW91-evaluated binding energy of CO with the enthalpy for adsorption of CO obtained from experimental values in the literature.[115] Positive Δ implies over prediction of binding energy by PW91-DFT (at CO* coverage of 1/9 ML on clean Pt(111)). All values are in eV. 326

Table C.10 Comparison of PW91-evaluated reaction energy for dissociative adsorption of H_2 with that from experimental values in the literature.[143] Numbers in square brackets ([ ]) represents DFT H* binding energy values (at H* coverage of 1/9 ML on Pt(111)), referenced to atomic H(g) in the gas phase, which were used to calculate the reaction energies. The PW91-gas phase bond energy for H_2 is 4.55 eV, whereas that value is 4.52 eV per experiment. Positive Δ implies over prediction of dissociative adsorption energy by PW91-DFT. The entries in the last column: ΔBE (H*) = Δ/2, indicates over-prediction in the H* binding energy by DFT. All values are in eV. 326

Table D.1 Reaction rates obtained from kinetics experiments on Pd/C at 1 atm. The inlet feed flowrates have been normalized by the number of surface sites for Pd/C used in the reactor. .. 330

Table D.2 Comparison of CO coverages on Pd/SiO_2 catalyst through *operando* FTIR. Sample were reduced under 25% H_2/He at 573K for 4h before the first and the second exposure. 333

Table D.3 Coefficients for the polynomial expression (ΔBE (in kJ/mol) = $\alpha_0 + \alpha_1\theta + \alpha_2\theta^2 + \alpha_3\theta^3$) employed to update the binding energy of the adsorbates with surface coverage of CO*, from the values calculated on 5/9 ML CO*-covered Pd(111), where θ is the surface coverage of CO (in ML) calculated by the mean-field microkinetic model during the simulation. Value of α_1 was set to zero to ensure that the energy minimum for each species was at clean surface level (no coadsorbed CO*). The parameters α_0, α_2, and α_3 are fit using unadjusted DFT energies calculated at varying coadsorbed CO*-coverages, as described in the main text. 334

Table D.4 Coefficients for the polynomial expression (ΔBE (in kJ/mol) = $\alpha_0 + \alpha_1\theta + \alpha_2\theta^2 + \alpha_3\theta^3$) employed to update the binding energy of the adsorbates with surface coverage of CO*, from the values calculated on the 5/9 ML CO*-covered Pd(100) facet, where θ is the surface coverage of CO (in ML) calculated by the mean-field microkinetic model during the simulation. Value of α_1 was set to zero to ensure that the energy minimum for each species was at clean surface level (no coadsorbed CO*).The parameters α_0, α_2, and α_3 are fit using unadjusted DFT energies calculated at varying coadsorbed CO*-coverages, as described in the main text. 335

Table D.5 Coefficients for the polynomial expression (ΔE_{TS} (in kJ/mol) = $\alpha_0 + \alpha_1\theta + \alpha_2\theta^2 + \alpha_3\theta^3$) employed to update the transition state energies of the elementary steps with surface coverage of CO*, from the values calculated on the 5/9 ML CO*-covered Pd(111) facet, where θ is the surface coverage of CO (in ML) calculated by the mean-field microkinetic model during the simulation. Value of α_1 was set to zero to ensure that the energy minimum for each transition-state was at clean surface level (no coadsorbed CO*).The parameters α_0, α_2, and α_3 are fit using unadjusted DFT energies calculated at varying coadsorbed CO*-coverages, as described in the main text. 336

Table D.6 Coefficients for the polynomial expression (ΔE_{TS} (in kJ/mol) = $\alpha_0 + \alpha_1\theta + \alpha_2\theta^2 + \alpha_3\theta^3$) employed to update the transition state energies of the elementary steps with surface coverage of CO*, from the values calculated on the 5/9 ML CO*-covered Pd(100) facet, where θ is the surface coverage of CO (in ML) calculated by the mean-field microkinetic model during the simulation. Value of α_1 was set to zero to ensure that the energy minimum for each transition-state was at clean

surface level (no coadsorbed CO*).The parameters α_0, α_2, and α_3 are fit using unadjusted DFT energies calculated at varying coadsorbed CO*-coverages, as described in the main text. 337

Table D.7 Optimized Shomate parameters (A to G) for the gas-phase species and reaction intermediates in reaction network evaluated on 5/9 ML CO* covered Pd(111) facet..... 338

Table D.8 Pre-exponential factors for the adsorption steps on 5/9 ML CO* covered Pd(111), where, per collision theory, rate constant $k = AT^{-0.5}$ (where, k is in s^{-1})..... 338

Table D.9 Optimized Shomate parameters (A to G) for the transition-state energies of the elementary steps (in kJ/mol) in reaction network evaluated on the 5/9 ML CO* covered Pd(111) facet..... 339

Table D.10 Optimized Shomate parameters (A to G) for the gas-phase species and reaction intermediates in reaction network evaluated on 5/9 ML CO* covered Pd(100) facet..... 340

Table D.11 Pre-exponential factors for the adsorption steps on 5/9ML CO* covered Pd(100), where, per collision theory, rate constant $k = AT^{-0.5}$ (where, k is in s^{-1})..... 340

Table D.12 Optimized Shomate parameters (A to G) for the transition-state energies of the elementary steps considered in the reaction network evaluated on 5/9ML CO* covered Pd(100) facet..... 341

Table D.13 Degree of rate control (X_{RC}) for the relevant elementary steps toward the decomposition of FA, obtained by keeping the (a) direct COOH* dehydrogenation and (b) CO* assisted COOH* dehydrogenation mechanisms active, one at a time. The energetics were maintained at values corresponding to the steady-state CO* coverage at home conditions (2.6% FA, balance He, 373K), by co-feeding appropriate amounts of CO(g) in the feed. 342

Table D.14 Comparison of PW91-DFT-evaluated binding energy of formic acid (FA) with the enthalpy for adsorption of FA obtained from experimental values in the literature. Negative Δ implies under prediction of binding energy by PW91-DFT (at FA coverage of 1/9 ML on clean Pd(111)). All values are in eV. 343

Table D.15 Comparison of PW91-DFT-evaluated binding energy of CO* with the reaction enthalpy for adsorption of CO* obtained from experimental values in the literature. Positive Δ implies over prediction of binding energy by PW91-DFT (at CO coverage of 1/9 ML on clean Pd(111)). All values are in eV. 343

Table D.16 Comparison of PW91-DFT-evaluated reaction energy for dissociative adsorption of H2 with that from experimental values in the literature. Numbers in the square parentheses ([]) represents the DFT – binding energy for H*, which were used to calculate the reaction energies. The PW91-gas phase bond energy for H_2 is 4.56 eV, whereas that value is 4.52 eV per experiment. Positive Δ implies over prediction of dissociative adsorption energy by PW91-DFT (at H coverage of 1/9 ML on clean Pd(111)). All values are in eV. 343

Table E.1 Optimized Shomate parameters (A to H, temperature range: 300–1200 K) for energies of gas-phase species, reaction intermediates and transition-states (in kJ/mol) for the clean Cu(111) model with the reduced reaction network. For adsorption of HCOOH(g), the rate constant (k) is

calculated using collision theory, where $k = AT^{-0.5}$ (where, k is in s^{-1}) and pre-factor (A) is included in the table. 347

Table E.2 Corrections for the DFT-derived binding energies (ΔBE) and activation energy barriers (ΔE_A) for the clean Cu(111) model with the reduced reaction network, as determined from parameter estimation. Negative (positive) corrections denote stabilization (destabilization). Intermediates and elementary steps not listed required no corrections from their initial DFT energetics. 348

Table E.3 Coefficients for the quadratic expression employed to update the energies of intermediates and transition states with surface coverage of $HCOO_B$ ($\Delta E(\theta)$ (in kJ/mol) = $\alpha_0 + \alpha_1\theta + \alpha_2\theta^2$), using DFT energetics calculated on clean and 0.625 ML $HCOO_B$ covered Cu(111), where θ is the surface coverage of $HCOO_B$ (in ML) calculated by the mean-field microkinetic model. We set α_1 as zero to ensure zero slope for the functions at clean surface (θ = 0). 350

Table E.4 Optimized Shomate parameters (A to H, temperature range: 300–1200 K) for energies of gas-phase species, reaction intermediates and transition-states (in kJ/mol) for the 0.625 ML $HCOO_B$ covered Cu(111) model with the reduced reaction network. For adsorption of HCOOH(g), the rate constant (k) is calculated using collision theory, where $k = AT^{-0.5}$ (where, k is in s^{-1}) and pre-factor (A) is included in the table. 351

Table E.5 Corrections for the DFT-derived binding energies (ΔBE) and activation energy barriers (ΔE_A) for the 0.625 ML $HCOO_B$ covered Cu(111) model with the reduced reaction network, as determined from parameter estimation. Negative (positive) corrections denote stabilization (destabilization). Intermediates and elementary steps not listed required no corrections from their initial DFT energetics. 352

Table E.6 Optimized Shomate parameters (A to H, temperature range: 300–1200 K) for energies of gas-phase species, reaction intermediates and transition-states (in kJ/mol) for the clean Cu(111) model with the full reaction network. For adsorption of HCOOH(g), the rate constant (k) is calculated using collision theory, where $k = AT^{-0.5}$ (where, k is in s^{-1}) and pre-factor (A) is included in the table. 354

Table E.7 Corrections for the DFT-derived binding energies (ΔBE) and activation energy barriers (ΔE_A) for the clean Cu(111) model with the full reaction network, as determined from parameter estimation. Negative (positive) corrections denote stabilization (destabilization). Intermediates and elementary steps not listed required no corrections from their initial DFT energetics. 355

Table E.8 Coefficients for the quadratic expression employed to update the energies of intermediates and transition states with surface coverage of $HCOO_B$ ($\Delta E(\theta)$ (in kJ/mol) = $\alpha_0 + \alpha_1\theta + \alpha_2\theta^2$), using DFT energetics calculated on clean and 0.625 ML $HCOO_B$ covered Cu(111), where θ is the surface coverage of $HCOO_B$ (in ML) calculated by the mean-field microkinetic model. We set α_1 as zero to ensure zero slope for the functions at clean surface (θ = 0). 357

Table E.9 Optimized Shomate parameters (A to H, temperature range: 300–1200 K) for energies of gas-phase species, reaction intermediates and transition-states (in kJ/mol) for the 0.625 ML $HCOO_B$ covered Cu(111) model with the full reaction network. For adsorption of HCOOH(g), the

rate constant (k) is calculated using collision theory, where $k = AT^{-0.5}$ (where, k is in s^{-1}) and pre-factor (A) is included in the table. 358

Table E.10 Corrections for the DFT-derived binding energies (ΔBE) and activation energy barriers (ΔE_A) for the 0.625 ML $HCOO_B$ covered Cu(111) model with the full reaction network, as determined from parameter estimation. Negative (positive) corrections denote stabilization (destabilization)..... 359

Table E.11 Coefficients for the quadratic expression employed to update the energies of intermediates and transition states with surface coverage of $HCOO_{BX}$ ($\Delta E(\theta)$ (in kJ/mol) = $\alpha_0 + \alpha_1\theta + \alpha_2\theta^2$), using DFT energetics calculated on clean and 0.375 ML $HCOO_{BX}$ covered Cu(111), where θ is the surface coverage of $HCOO_{BX}$ (in ML) calculated by the mean-field microkinetic model. We fit the coefficients to ensure zero slope for the functions at $HCOO_{BX}$ coverage of 0.375 ML since the interaction energies are stabilizing below 0.375 ML and destabilizing at coverages above 0.375 ML. 361

Table E.12 Optimized Shomate parameters (A to H, temperature range: 300–1200 K) for energies of *gas-phase species,* reaction intermediates and transition-state*s* (in kJ/mol) for the 0.375 ML $HCOO_{BX}$ covered Cu(111) model with the full reaction network. For adsorption of HCOOH(g), the rate constant (*k*) is calculated using collision theory, where $k = AT^{-0.5}$ (where, *k* is in s^{-1}) and pre-factor (*A*) is included in the table. 362

Table F.1 Binding energy of reaction intermediates on close-packed (111) facets of Ag, Au, Cu, Ir, Ni, Pd, Pt, and Rh. The energies are referenced wrt. the corresponding gas-phase energy of the reaction intermediate. All energies are in eV..... 367

Table F.2 Shomate parameters (A to H) for gas-phase species and adsorbed reaction intermediates (in kJ/mol) in reaction network in T-range: 300 – 1200 K. The energetics of the reaction intermediates were evaluated on clean Pd(111)..... 368

Table F.3 Shomate parameters (A to H) for transition-state energies (in kJ/mol) for the elementary steps in reaction network in T-range: 300 – 1200 K evaluated on clean Pd(111). 368

Table F.4 Pre-exponential factors for the adsorption steps on clean Pd(111), where, per collision theory, rate constant $k = AT^{-0.5}$ (where, k is in s^{-1})..... 368

Table F.5 Shomate parameters (A to H) for gas-phase species and adsorbed reaction intermediates (in kJ/mol) in reaction network in T-range: 300 – 1200 K. The energetics of the reaction intermediates were evaluated on 5/9 ML CO*-covered Pd(111). 369

Table F.6 Shomate parameters (A to H) for transition-state energies (in kJ/mol) for the elementary steps in reaction network in T-range: 300 – 1200 K evaluated on 5/9 ML CO*-covered Pd(111). 369

Table F.7 Coefficients for the polynomial expression (ΔBE (in kJ/mol) = $\alpha_0 + \alpha_1\theta + \alpha_2\theta^2 + \alpha_3\theta^3$) employed to update the binding energy of the adsorbates with surface coverage of CO*, from the values calculated on 5/9 ML CO*-covered Pd(111), where θ is the surface coverage of CO* (in ML) calculated by the mean-field microkinetic model during a forward simulation. Value of α_1 was set to zero to ensure that the energy minimum for each species was at clean surface level (no

coadsorbed CO*).The parameters α_0, α_2, and α_3 are fit using unadjusted DFT energies calculated at varying coadsorbed CO*-coverages. 370

Table F.8 Coefficients for the polynomial expression (ΔBE (in kJ/mol) = $\alpha_0 + \alpha_1\theta + \alpha_2\theta^2 + \alpha_3\theta^3$) employed to update the transition-state energies of the elementary steps with surface coverage of CO*, from the values calculated on 5/9 ML CO*-covered Pd(111), where θ is the surface coverage of CO* (in ML) calculated by the mean-field microkinetic model during a forward simulation. Value of α_1 was set to zero to ensure that the energy minimum for each species was at clean surface level (no coadsorbed CO*).The parameters α_0, α_2, and α_3 are fit using unadjusted DFT energies calculated at varying coadsorbed CO*-coverages. 370

Table F.9 Coefficients for the polynomial expression (ΔBE (in kJ/mol) = $\alpha_0 + \alpha_1\theta + \alpha_2\theta^2$) employed to update the binding energy of the adsorbates with surface coverage of HCOO*, from the values calculated on Cu(111), where θ is the surface coverage of HCOO* (in ML, not accounting for denticity) calculated by the mean-field microkinetic model during a forward simulation. Value of α_0 was set to zero to ensure that the energy minimum for each species was at clean surface level (no coadsorbed HCOO*). The parameters α_0, α_1, and α_2 are fit using unadjusted DFT energies calculated at varying coadsorbed HCOO*-coverages. 371

Table F.10 Coefficients for the polynomial expression (ΔBE (in kJ/mol) = $\alpha_0 + \alpha_1\theta + \alpha_2\theta^2$) employed to update the transition-state energy of the reaction intermediates with surface coverage of HCOO*, from the values calculated on Cu(111), where θ is the surface coverage of HCOO* (in ML, not accounting for denticity) calculated by the mean-field microkinetic model during a forward simulation. The values are approximated based on the expressions derived for the reaction intermediates assuming the same changes to the transition-state energy as the initial state. 371

Table F.11 Optimized lattice-constants for intermetallic binary alloy catalysts with an fcc crystal structure (PW91-GGA, DACAPO). 376

Table G.1 Binding energies (BE) of O relative to ½ gas phase O_2 (r_{O-O} = 122 pm) and of water on the single-atom catalysts considered in this work (values in parentheses refer to binding energies in the presence of co-adsorbed water) as well as Gibbs free binding energies for O_mH_n at 298 K and 0.1 MPa relative to gas phase H_2 and O_2; the corresponding atomization energies amount to 2.27 eV (½ $H_2 \rightarrow$ H) and 3.04 eV (½ $O_2 \rightarrow$ O). ΔG_{sel} is the decomposition energy of H_2O_2 ($H_2O_2 + * \rightarrow O* + H_2O$), which indicates whether the $2e^-$ or $4e^-$ pathway is preferred (positive or negative values, respectively). All values are in eV..... 378

Table G.2 Binding energies (BE) of H_2O and O_mH_n intermediates on metal centers of the single-atom catalysts studied in this work relative to gas phase H_2 and O_2; the corresponding atomization energies amount to 2.27 eV (½ $H_2 \rightarrow$ H) and 3.04 eV (½ $O_2 \rightarrow$ O). Values in parentheses refer to the presence of co-adsorbed H_2O. All values are in eV..... 379

Table G.3 Calculated ORR onset potential for $\mathbf{M_{clean}}$ on [Fe] as a function of the H-transfer barrier. 384

Table G.4 Magnetic moments on the metal ions (μ_B) for each ORR intermediate considered herein. 386

Table G.5 Bader charges of metal ions (Q_{Me}) for ORR intermediates on Fe and Ru catalysts. 386

Table H.1 Deprotonation free energies (PW91-GGA, in eV) for NHx and HxNNHy species at 0V on Pt(111), at different N* coverages. 389

Table H.2 Free energy of Reaction (PW91-GGA, in eV) for N–N bond making steps, at different N* coverages. 389

Table H.3 Activation energy barriers (PW91-GGA, in eV) for N–N bond making steps on a clean and in presence of 1/2 ML of N*. 389

LIST OF FIGURES

Figure 2.1 Schematic showing the close-packed (111) and open (100) facets of a metal nanoparticle. CN refers to coordination number of surface atoms. 13

Figure 2.2 Atomistic representation of the p(6x5) unit-cell employed for modeling graphene-supported transition-metal atom (M) based single-atom catalysts embedded in a four-fold N substituted double C-vacancy (M/GN_4-V_{2C}). 14

Figure 2.3 A schematic of the reactor setup utilized for performing kinetics experiments for the formic acid (FA) decomposition chemistry. 20

Figure 3.1 Side and top views of the most stable structures of reaction intermediates on clean Pt(111). Platinum, carbon, hydrogen, and oxygen atoms are shown as silver, black, white, and red spheres, respectively. 35

Figure 3.2 Side and top views of the most stable structures of reaction intermediates on clean Pt(100). Platinum, carbon, hydrogen, and oxygen atoms are shown as silver, black, white, and red spheres, respectively. 35

Figure 3.3 Potential Energy Diagram of FA decomposition on clean Pt(111). The HCOO*-pathway and COOH*-pathway leading to CO_2+H_2, and the COOH*-pathway leading to CO+H_2O are represented with red, green, and blue lines, respectively. Energy zero corresponds to gas phase FA and clean Pt(111) slab at infinite separation. All the transition states (TS) for the HCOO*-pathway to form CO_2+H_2 and the COOH*-pathway to form CO_2+H_2 and CO+H_2O are marked with TS. Along the minimum energy paths, the highest TS energy values in both the HCOO*- and COOH*-paths are given by the green/red numbers (in eV). Structures of the TS's are shown in the insets, are marked with 'TS', and the corresponding bond-breaking step is given by the text nearby (e.g., HCOO-H indicates the TS for O-H bond breaking step in HCOOH). Color code for structures presented in the inset: White - H, Red - O, Dark Gray - C, Silver - Pt. 38

Figure 3.4 Potential Energy Diagram of FA decomposition on clean Pt(100). The HCOO*-pathway and COOH*-pathway leading to CO_2+H_2, and the COOH*-pathway leading to CO+H_2O are represented with red, green, and blue lines, respectively. Energy zero corresponds to gas phase FA and clean Pt(100) slab at infinite separation. All the transition states (TS) for the HCOO*-pathway to form CO_2+H_2 and the COOH*-pathway to form CO_2+H_2 and CO+H_2O are marked with TS. Along the minimum energy paths, the highest TS energy values in both the HCOO*- and COOH*-paths are given by the green/red numbers (in eV). Structures of the TS's are shown in the insets, are marked with 'TS', and the corresponding bond-breaking step is given by the text nearby. (e.g., HCOO-H indicates the TS for O-H bond breaking step in HCOOH). Color code for structures presented in the inset: White - H, Red - O, Dark Gray - C, Silver - Pt. 39

Figure 3.5 Side and top views of the most stable structures of intermediates on the 4/9 ML CO*-covered Pt(111). Platinum, carbon, hydrogen, and oxygen atoms are indicated by silver, black, white, and red, respectively. 44

Figure 3.6 Side and top views of the most stable structures of reaction intermediates on the 4/9 ML CO*-covered Pt(100). Platinum, carbon, hydrogen, and oxygen atoms are indicated by silver, black, white, and red, respectively. 44

Figure 3.7 Potential Energy Diagram of FA decomposition on 4/9 ML CO*-covered Pt(111). The HCOO*-pathway and COOH*-pathway leading to CO_2+H_2, and the COOH*-pathway leading to CO+H_2O are represented with red, green, and blue lines, respectively. Energy zero corresponds to gas phase FA and 4/9 ML CO*-covered Pt(111) slab at infinite separation. All the transition states (TS) for the HCOO*-pathway to form CO_2+H_2 and the COOH*-pathway to form CO_2+H_2 and CO+H_2O are marked with TS. Along the minimum energy paths, the highest TS energy values in both the HCOO*- and COOH*-paths are given by the green/red numbers (in eV). Structures of the TS's are shown in the insets, are marked with 'TS', and the corresponding bond-breaking step is given by the text nearby (e.g., HCOO-H indicates the TS for O-H bond breaking step in HCOOH). Color code for structures presented in the inset: White - H, Red - O, Dark Gray - C, Silver - Pt.49

Figure 3.8 Potential Energy Diagram of FA decomposition through COOH* mediated pathways on 4/9 ML CO*-covered Pt(111) surface. Comparison for direct COOH* (mechanism 1), CO* spectator-assisted COOH* decomposition through COH* (mechanism 2a: COOH* (+**CO***) → CO_2* + **CO**H* → CO_2* + H* (+**CO***)) and COH→HCO* (mechanism 2b: COOH* (+**2CO***) → CO_2* + **CO**H* (+**CO***) → CO_2* + H**CO*** + **CO*** → CO_2* + H* (+**2CO***)) pathways are shown with green, brown, and pink lines, respectively. The spectator CO* molecules are indicated in bold in the scheme above. Energy zero corresponds to gas phase FA and 4/9 ML CO*-covered Pt(111) slab at infinite separation. All the transition states (TS) for the COOH*-pathway to form CO_2+H_2 are marked with TS. The TS energies corresponding to the highest point for COOH* dehydrogenation routes are reported by the numbers (in eV) in the figure. Structures of the TS's are shown in the insets, are marked with 'TS', and the corresponding bond-breaking step is given by the text nearby. Color code for structures presented in the inset: White - H, Red - O, Dark Gray - C, Silver - Pt. 51

Figure 3.9: Potential Energy Diagram of FA decomposition on 4/9 ML CO*-covered Pt(100). The HCOO*-pathway and COOH*-pathway leading to CO_2+H_2, and the COOH*-pathway leading to CO+H_2O are represented with red, green, and blue lines, respectively. Energy zero corresponds to gas phase FA and 4/9 ML CO*-covered Pt(100) slab at infinite separation. All the transition states (TS) for the HCOO*-pathway to form CO_2+H_2 and the COOH*-pathway to form CO_2+H_2 and CO+H_2O are marked with TS. Along the minimum energy paths, the highest TS energy values in both the HCOO*- and COOH*-paths are given by the green/red numbers (in eV). Structures of the TS's are shown in the insets, are marked with 'TS', and the corresponding bond-breaking step is given by the text nearby (e.g., HCOO-H indicates the TS for O-H bond breaking step in HCOOH). Color code for structures presented in the inset: White - H, Red - O, Dark Gray - C, Silver - Pt.53

Figure 3.10 Parity plot of clean Pt(100) model predicted versus experimental TOFs (s^{-1}) for (a) Dehydrogenation: HCOOH → CO_2 + H_2; inset shows the parity at low TOFs corresponding to the CO-cofeed data, (b) Dehydration: HCOOH → CO + H_2O. MAPE: mean absolute percentage error. 57

Figure 3.11 Parity plot of clean Pt(111) model predicted versus experimental TOFs (s^{-1}) for (a) Dehydrogenation: HCOOH → CO_2 + H_2; inset shows the parity at low TOFs corresponding to the

CO-cofeed data, (b) Dehydration: HCOOH → CO + H_2O. MAPE: mean absolute percentage error. 59

Figure 3.12 Parity plots of coverage-cognizant Pt(100) model-I predicted versus experimental TOFs (s^{-1}) for: (a) Dehydrogenation: HCOOH → CO_2 + H_2 (R^2=0.98); inset shows the parity at low TOFs corresponding to the CO-cofeed data, (b) Dehydration: HCOOH → CO + H_2O (R^2=0.99). MAPE: mean absolute percentage error. 63

Figure 3.13 Parity plot of coverage-cognizant Pt(100) model-II predicted versus experimental TOFs (s^{-1}) for: (a) Dehydrogenation: HCOOH → CO_2 + H_2 (R^2=0.97); inset shows the parity at low TOFs corresponding to the CO-cofeed data, (b) Dehydration: HCOOH → CO + H_2O (R^2=0.99). MAPE: mean absolute percentage error. 66

Figure 3.14 Parity plot of coverage-cognizant Pt(111) model predicted versus experimental TOFs (s^{-1}) for: (a) Dehydrogenation: HCOOH → CO_2 + H_2; inset shows the parity at low TOFs corresponding to the CO-cofeed data (R^2=0.97), (b) Dehydration: HCOOH → CO + H_2O (R^2=0.99). MAPE: mean absolute percentage error. 70

F**igure 3.15** Simplified reaction network (not showing the isomerization steps) indicating the flux carrying pathways for the FA decomposition on the 4/9 ML CO*-covered Pt(111), as predicted by the optimized microkinetic model. The step with +/- CO* indicates H-transfer with the participation of a spectator CO* molecule. The percentage flux contribution for the dehydrogenation pathway (indicated by the green box) by the various mechanisms, under our defined home conditions (2.6% FA, balance He, 373K) and CO-cofeed conditions (averaged) (2.6% FA, 0.025 – 0.1% CO, balance He, 373K), are indicated in red and purple, respectively. The dehydration pathway (indicated by the blue box, shaded out) proceeds through the COOH* dehydroxylation, under all conditions..... 73

Figure 4.1 Arrhenius plot for FA dehydrogenation: HCOOH → CO_2 + H_2 (green) and dehydration: HCOOH → CO + H_2O (red) on Pd/C at 1 atm. The dashed lines represent the fit to the experimentally determined TOFs. 89

Figure 4.2 Parity plot of clean Pd(100) model predicted vs. experimental TOFs (s^{-1}) for (a) Dehydrogenation: HCOOH → CO_2 + H_2; inset shows the parity at low TOFs (corresponding to CO co-feed experiments), (b) Dehydration: HCOOH → CO + H_2O. 91

Figure 4.3 Surface coverages predicted by the optimized clean Pd(100) model under various experimental conditions. Going from left to right, the shaded regions correspond to different experimental conditions (eg. variation in temperature, variation in the partial pressure of reactant/product, etc.). The experimental data points for various shaded regions, are listed in Table D.1: Variation in Temperature (#1-5), P(HCOOH) (#6-8), P(H_2O) (#9-12), P(H_2) (#13-15), P(CO_2) (#16-19) and P(CO) (#20-22). In each shaded region, going left to right indicates the increase in the value of the corresponding experimental parameter (i.e., temperature or partial pressure of the indicated gas-phase species), e.g. for the section labeled 'Temperature variation' moving left to right, i.e. #1-5 (Table D.1), indicates increase in temperature, with other experimental parameters held constant. 93

Figure 4.4 Parity plot of clean Pd(111) model predicted vs. experimental TOFs (s^{-1}) for (a) Dehydrogenation: HCOOH → CO_2 + H_2; inset shows the parity at low TOFs (corresponding to CO co-feed experiments), (b) Dehydration: HCOOH → CO + H_2O. 94

Figure 4.5 Surface coverages predicted by the optimized clean Pd(111) model under various experimental conditions. Going from left to right, the shaded regions correspond to different experimental conditions (eg. variation in temperature, variation in the partial pressure of reactant/product, etc.). The experimental data points for various shaded regions, are listed in Table D.1: Variation in Temperature (#1-5), P(HCOOH) (#6-8), P(H_2O) (#9-12), P(H_2) (#13-15), P(CO_2) (#16-19) and P(CO) (#20-22). In each shaded region, going left to right indicates the increase in the value of the corresponding experimental parameter (i.e., temperature or partial pressure of the indicated gas-phase species), e.g. for the section labeled 'Temperature variation' moving left to right, i.e. #1-5 (Table D.1), indicates increase in temperature, with other experimental parameters held constant. 96

Figure 4.6 Parity plot of CO*-coverage cognizant Pd(100) model predicted vs. experimental TOFs (s^{-1}) for (a) Dehydrogenation: HCOOH → CO_2 + H_2; inset shows the parity at low TOFs (corresponding to CO co-feed experiments), (b) Dehydration: HCOOH → CO + H_2O. 99

Figure 4.7 Coverages of relevant reaction intermediates under various experimental conditions, as predicted by the optimized CO* coverage-cognizant Pd(100) model. Going from left to right, the shaded regions correspond to different experimental conditions (eg. variation in temperature, variation in the partial pressure of reactant/product, etc.). The experimental data points for various shaded regions, are listed in Table D.1: Variation in Temperature (#1-5), P(HCOOH) (#6-8), P(H_2O) (#9-12), P(H_2) (#13-15), P(CO_2) (#16-19) and P(CO) (#20-22). In each shaded region, going left to right indicates the increase in the value of the corresponding experimental parameter (i.e., temperature or partial pressure of the indicated gas-phase species), e.g. for the section labeled 'Temperature variation' moving left to right, i.e. #1-5 (Table D.1), indicates increase in temperature, with other experimental parameters held constant. 101

Figure 4.8 Parity plot of CO*-coverage cognizant Pd(111) model predicted vs. experimental TOFs (s^{-1}) for (a) Dehydrogenation: HCOOH → CO_2 + H_2; inset shows the parity at low TOFs (corresponding to CO co-feed experiments), (b) Dehydration: HCOOH → CO + H_2O. 102

Figure 4.9 Simplified reaction mechanism for FA decomposition determined by the optimized CO*-coverage cognizant Pd(111) model (isomerization steps are not explicitly shown). The green and red arrows correspond to the elementary steps in the dehydrogenation (green arrows) and dehydration (red arrows) pathways, respectively. Elementary steps with participation of a spectator CO* are denoted by ±*CO** next to the arrows. 105

Figure 4.10 Coverages of relevant reaction intermediates under various experimental conditions, as predicted by the optimized CO* coverage-cognizant Pd(111) model. Going from left to right, the shaded regions correspond to different experimental conditions (eg. variation in temperature, variation in the partial pressure of reactant/product, etc.). The experimental data points for various shaded regions, are listed in Table D.1: Variation in Temperature (#1-5), P(HCOOH) (#6-8), P(H_2O) (#9-12), P(H_2) (#13-15), P(CO_2) (#16-19) and P(CO) (#20-22). In each shaded region, going left to right indicates the increase in the value of the corresponding experimental parameter

(i.e., temperature or partial pressure of the indicated gas-phase species), e.g. for the section labeled 'Temperature variation' moving left to right, i.e. #1-5 (Table D.1), indicates increase in temperature, with other experimental parameters held constant. 107

Figure 4.11 Potential descriptions for the Pd/C nanoparticles under FA decomposition reaction conditions: (a) Single-site model – partially (~0.3 ML) CO*-covered Pd(111) facet serving as the active site and partially (0.4-0.5 ML) CO*-covered Pd(100) poisoned under reaction conditions, (b) Dual-site model – both partially CO*-covered (~0.3 ML) Pd(111) and (~0.4-0.5 ML) Pd(100) active towards FA decomposition, with the later facet active only for FA dehydrogenation. Nature of the reactive-intermediate carrying the reaction flux, as determined from the optimized microkinetic models, is indicated next to the facets. Color codes for atoms: white – H, red – O, dark gray – C, and blue – Pd. 111

Figure 5.1 Schematic representation of the implementation of coverage-dependent energetics in our mean-field microkinetic models. Binding and transition-state energies were computed using DFT at different coverages of most abundant surface intermediate (MASI) and were fitted to polynomial functions dependent on the coverage of MASI. These polynomial functions are self-consistently incorporated in our models to calculate and adjust the energetics (and equivalently, the rate parameters dependent on these energetics) on-the-fly to account for the lateral adsorbate-adsorbate interactions due to the coverage of MASI, thus realizing a coverage-cognizant microkinetic model. Here, x is the set of flow-rate of gas-phase species and surface coverages of reaction intermediates; k is the set of rate constants; u is the set of input conditions consisting of (F_{in} – input flow rates, P_{tot} – total pressure, T – temperature); y – is the linearly transformed solution of x at steady-state; B is a transformation matrix relating x to y; θ is the surface coverage of MASI. 120

Figure 5.2 Optimized structures of intermediates involved in formic acid decomposition on clean Cu(111). Panels above and below are top and side views, respectively. Energies are with respect to gas-phase H_2 and CO_2. Color code: light grey – Cu, dark grey – C, red – O, blue – H, yellow – H from complexed HCOOH. Subscripts B and M refer to the bidentate and monodentate configurations of HCOO, respectively. Subscript X refers to complexation of HCOO with HCOOH (i.e. FA-HCOO complexes). 123

Figure 5.3 Pathways for HCOO decomposition to CO_2(g) + H. Colored arrows mark different decomposition pathways. Dotted lines represent hydrogen bonds. Dark yellow and teal colored H atoms denote H atoms from the complexed FA and the decomposing HCOO species respectively. Subscripts B and M refer to the bidentate and monodentate configurations of HCOO, respectively. Subscript X refers to complexation of HCOO with HCOOH (i.e. FA-HCOO complexes). 124

Figure 5.4 Potential energy diagrams (PEDs) for HCOO decomposition on clean Cu(111). Bold and thin lines indicate intermediate and transition states respectively. '|' indicates infinite separation. Colors of the pathways are identical to those in Figure 5.3. All states are labeled by their energies, which are with respect to the initial state to compare the pathways on an equal energetic footing; intermediate states are additionally labeled with names of the adsorbates. Teal colored H atoms denote H atoms from the decomposing HCOO species. Subscripts B and M refer to the bidentate and monodentate configurations of HCOO, respectively. Subscript X refers to complexation of HCOO with HCOOH (i.e. FA-HCOO complexes). 125

Figure 5.5 Optimized structures of intermediates involved in formic acid decomposition on 0.375 ML $HCOO_{BX}$ covered Cu(111). Panels show top views. Black dashed lines mark the unit cell. Energies are with respect to gas-phase H_2 and CO_2. Subscripts B and M refer to the bidentate and monodentate configurations of HCOO, respectively. Subscript X refers to complexation of HCOO with HCOOH (i.e. FA-HCOO complexes). Color code: light grey – Cu, dark grey – C, red – O, blue – H of spectator species, teal – H of species of interest, yellow – H from complexed HCOOH. 128

Figure 5.6 Coverage effects on the energetics of species involved in formic acid decomposition on Cu(111). (a) Intermediates. (b) Transition states (TSs). Energies are with respect to gas-phase H_2, CO_2, and the clean slab. ΔEs given below the bars denote the energy differences between the clean and 0.375 ML $HCOO_{BX}$ models. Negative ΔE values indicate stabilization of the species at higher coverage. Subscripts B and M refer to the bidentate and monodentate configurations of HCOO, respectively. Subscript X refers to complexation of HCOO with HCOOH (i.e. FA-HCOO complexes) 129

Figure 5.7 Potential energy diagrams (PEDs) for HCOO decomposition on 0.375 ML $HCOO_{BX}$ covered Cu(111). Bold and thin lines indicate intermediate and transition states respectively. '|' indicates infinite separation. Colors of the pathways are identical to those in Figure 5.3. All states are labeled by their energies, which are with respect to the initial state to compare the pathways on an equal energetic footing; intermediate states are additionally labeled with names of the adsorbates. Teal colored H atoms denote H atoms from the decomposing HCOO species. Subscripts B and M refer to the bidentate and monodentate configurations of HCOO, respectively. Subscript X refers to complexation of HCOO with HCOOH (i.e. FA-HCOO complexes). 131

Figure 5.8 Surface coverages, reaction fluxes, and species fluxes predicted by the optimized 0.375 ML $HCOO_{BX}$ Cu(111) model with the full reaction network. (a-b) Adsorbate coverages and complexed vs. uncomplexed reaction fluxes under varying (a) FA partial pressure (2.5–10%, balance He) at 373 K, and (b) temperature (368-383 K) at a FA partial pressure of 10 mol %, balance He. Coverages account for species denticities. Dashed lines represent linear trend lines. (c) Reaction fluxes (purple numbers) at our defined home conditions (10% FA, balance He, 373 K). Dark yellow and teal colored H atoms denote H atoms from the complexed FA and the decomposing HCOO species respectively. Note that with 0.375 ML $HCOO_{BX}$ spectators, HCOOH binds to/complexes with the uncoordinated O atom of a spectator $HCOO_{BX}$ (Figure 5.5). Subscripts B and M refer to the bidentate and monodentate configurations of HCOO, respectively. Subscript X refers to complexation of HCOO with HCOOH (i.e. FA-HCOO complexes). 138

Figure 6.1 Schematic representation of the typical workflow adopted in a microkinetic-modeling (MKM)-based analysis for heterogeneous catalysis. '*A'*, *'B'/'C'*, and 'X_i's refer to reactant, products, and reaction intermediates, respectively. PED refers to potential energy diagram. Reactor balance equations (system of differential-algebraic equations) solved in a MKM are shown in the third panel. 148

Figure 6.2 An iterative approach for elucidating the structure of the active site for FA decomposition on Au/SiC.[42] Feedback from parameter adjustment, required to fit the experiments (steady-state, <20% conversion, 1-4% FA, 0-6% H_2/CO_2, 343-383K), is used to continually revise the hypothesis for the active site: Au(111)→Au(100)→Au(211). To fit the reaction kinetics

experimental measurements, for all three facets (shown in the potential energy diagram (PED)), large parameter adjustments were necessary, indicating that the active site is more undercoordinated than Au(211). CN refers to surface coordination number. Vertical dashed black-line in the inset for Au(211) marks the step edge. 152

Figure 6.3 Elucidating the active site for FA decomposition on unsupported subnanometric Au clusters.[43] Most stable geometries of Au_n (n=2-25) clusters (<0.85nm) obtained from *ab initio* molecular dynamics (AIMD) are shown. Combination of DFT-derived mean-field MKMs and reaction kinetics experiments on Au/SiC, led to the conclusion that Au_{18} might resemble the active site the best. Kinetic Monte Carlo (KMC) study on Au_{18} revealed that a pair of adjacent Au_3 ensembles (coordination number (CN) of 5), can be the active site for FA decomposition on Au/SiC.[44] 155

Figure 6.4 Workflow for developing a coverage self-consistent description of the active site for FA decomposition on Pt/C.[45] Mean-field MKMs formulated using DFT energetics on clean Pt(100) and Pt(111) were found to poorly describe the active site. Feedback from the parameter adjustment procedure is used to iteratively update the hypothesis for the nature of the active site. 159

Figure 6.5 Results from the MKM on a 4/9 ML CO*-covered Pt(111)[45] :(a) Reaction mechanism for FA decomposition on Pt/C. Formate-mediated pathways were considered, but did not contribute significantly to FA decomposition. Flux contributions for the various pathways at 2.6% FA, balance He (1 atm, 373K) are indicated, (b) Parity plots comparing model-predicted and experimental turnover frequencies (TOFs). 161

Figure 6.6 Proposed algorithmic scheme for elucidating the nature of the catalytic active site and the reaction mechanism, using a combination of DFT, reaction kinetics experiments, and microkinetic modeling. 163

Figure 7.1 Schematic representation of the workflow to formulate the experiment-calibrated coverage-cognizant volcano plots. CS-MKM refers to coverage self-consistent microkinetic modeling. The text in red refers to the steps in the workflow that are proposed as an improvement over the conventional methodology. 176

Figure 7.2 Calculated reactivity maps formulated using the conventional methodology, showing (a) Activity and (b) Selectivity maps, for 2.6% FA, balance He, 373 K. TOF refers to the turnover frequency (s^{-1}). 178

Figure 7.3 Calculated coverage maps for the most-abundant reaction intermediates in the descriptor space determined using the model formulated using the conventional methodology for 2.6% FA, balance He, 373 K. 179

Figure 7.4 Experiment-calibrated coverage-cognizant reactivity maps, showing: (a) Activity and (b) Selectivity maps, for 2.6% FA, balance He, 373 K. TOF refers to the turnover frequency (s^{-1}). Coverage-dependent energetics for CO and HCOO were incorporated on-the-fly across the descriptor space. 181

Figure 7.5 Calculated coverage maps for the most-abundant reaction intermediates in the descriptor space determined using the experiment-calibrated coverage-cognizant methodology, for

2.6% FA, balance He, 373 K. Coverage-dependent energetics for CO and HCOO were incorporated on-the-fly across the descriptor space..... 183

Figure 7.6 High-throughput screening of intermetallic binary alloy catalysts through Experiment-calibrated coverage-cognizant model, showing: (a) activity map ,(b) selectivity map, and (c) bar-plot comparing the activity (wrt. Pd) and selectivity of various intermetallic binary alloy catalysts, for 2.6% FA, balance He, 373 K. TOF refers to the turnover frequency (s^{-1}). Coverage-dependent energetics for CO and HCOO were incorporated on-the-fly across the descriptor space. 185

Figure 8.1 Full ORR mechanism considered in this work. While previous studies only considered $\mathbf{M_{clean}}$, $\mathbf{M_O}$, and $\mathbf{M_{OH}}$ individually, we study the full interlinked mechanism herein..... 195

Figure 8.2 ORR mechanism on Fe atoms embedded in fourfold N-substituted double vacancies in graphene at low coverage ($\mathbf{M_{clean}}$) and in the presence of an OH spectator species ($\mathbf{M_{OH}}$). At U_{RHE} > 0.57 V, an O_2-assisted pathway ($\mathbf{M_{O2\text{-}ast}}$) was found to be dominant. (a) Optimized reaction intermediates are shown as side views. (b) Gibbs free energies profiles are shown for each pathway using the same color code as in (a) starting with the OH* intermediate that is common to all three pathways. 196

Figure 8.3 Current density (normalized to the diffusion-limited current) and coverage from microkinetic analysis of ORR on Co, Fe, and Ru single-atom catalysts. The color code provided in the panel for Co applies to all metals. Coverage profiles for only the relevant states are shown in the respective panel for each metal and those not explicitly shown indicate zero coverage, e.g., coverages of [Co](O)-OH and [Co](O)=O are zero in the investigated potential range and are therefore not shown in the corresponding panel for Co. Cation charges (Me^{N+}) represent formal oxidation states; calculated Bader charges are provided in Table G.5. The arrows over the top panels (in silver; pointing towards left) qualitatively represent the over-potential for the corresponding metal (shorter arrows represent lower over-potentials). 199

Figure 8.4 Potential-dependent flux along $\mathbf{M_{clean}}$, $\mathbf{M_{OH}}$, and $\mathbf{M_{O2\text{-}ast}}$ (the overall flux is shown as a gray area) as well as the degree of rate control for each elementary step on Co, Fe, and Ru atoms embedded in fourfold N-substituted double vacancies of graphene. Unless specified otherwise, labels refer to elementary steps via $\mathbf{M_{clean}}$. 200

Figure 8.5 ORR onset potentials from thermodynamic analysis[321] (black squares; linear fit shown as black line) and from microkinetic analysis (red and blue circles for $\mathbf{M_{clean}}$ and $\mathbf{M_{O2\text{-}ast}}$, respectively; lines refer to values obtained using linear scaling relations shown in Appendix G). Differences in the onset potentials predicted from thermodynamic and microkinetic analysis (ΔU_{ORR} = UORRmk − UORRtd) are shown above: positive (negative) values correspond to an increase (decrease) in onset potential due to the microkinetic analysis..... 202

Figure 9.1 Free energy diagram (FED) for AOR on Pt(111) at 0 V vs. RHE. (a) FED on a clean Pt(111) surface. The inset reports an enlarged view of the FED, showing the $2NH_2^* \rightarrow NH^*+NH_2^* \rightarrow 2NH^*$ molecular steps. (b) FED on a surface pre-covered by 1/2 ML of N*. The inset reports an enlarged view of the FED, showing the energy difference between the NNH_2^* and HNNH* states. Red lines indicate the Oswin-Salomon (OS) AOR mechanism; blue lines indicate the Gerischer-Mauerer (GM) AOR mechanism. Dashed red and purple lines indicate N–N bond formation steps of the OS and GM mechanisms, respectively. For each step, stoichiometry is

balanced with OH^-, H_2O and e^- and not explicitly shown. All energies are reported considering adsorbates at infinite separation. 214

Figure 9.2 Optimized geometries for the dimeric (H_xNNH_y) species of the GM mechanism of AOR on a 1/2 ML N*-covered Pt(111) surface. N, H, and Pt atoms are represented with blue, white, and silver spheres, respectively. Side and top views are reported in the top and bottom panel, respectively. Dashed black lines delineate the unit cell lattice vectors. 216

Figure 9.3 Onset potential of AOR as a function of N* coverage on Pt(111). Points are colored according to the identity of the potential determining step at a given coverage (red, hydrazine deprotonation; black, ammonia deprotonation). The dashed line is intended to be a guide for eyes. 218

Figure 9.4 Reaction mechanism for trimeric species formation at 1/2 ML N* coverage, starting from HNNH* and NNH*. The optimized structures of transition states (TS) are shown inside boxes. For the sake of clarity, only the top two Pt layers are shown in the insets. Solid arrows indicate thermal steps. Dashed arrows indicate electrochemical steps (proton-electron transfers). The black and green color code and reaction intermediates and TS nomenclature refers to the free energy diagram (FED) presented in Figure 9.5. 220

Figure 9.5 Free energy diagram (FED) for the formation of trimeric NHNNH* and NNNH* from dimeric HNNH* and NNH* species on 1/2 ML N*-covered Pt(111). Green lines indicate a pathway starting from HNNH* and involving a *trans* → *cis* isomerization step (TS_6 to $HNNH_r$*). Black lines indicate the pathway proceeding through NNH* formation. N atoms indicated in cyan refer to N* spectators, which are added to the existing HNNH* or NNH* moieties. For each step, stoichiometry is balanced with OH^-, H_2O, H^+ and e^-. All energies are reported considering adsorbates at infinite separation. 221

Figure A.1 Site nomenclature for the Pd(211) slab. (a) Top and (b) side views of the Pd(211) surface are shown. Grey spheres indicate the protruding row of the surface Pd atoms representing the step edge atoms; purple spheres indicate the other (terrace) Pd atoms. Green dash lines indicate the unit cell. 240

Figure A.2 Chloroform hydrodechlorination reaction network. Orange arrows indicate dechlorination steps; black arrows indicate hydrogenation steps; pink arrows indicate the dehydrogenation steps. Dashed arrows denote those dehydrogenation steps that are later shown as energetically unfavorable against competing steps. Red: reactant ($CHCl_3$); blue: product (CH_4); green: by-products (CH_2Cl_2 and CH_3Cl). 241

Figure A.3 Minimum energy structures of reactants, products, and reaction intermediates on Pd(111), Pd(100), and Pd(211). The structures on Pd(111) were reproduced from Xu *et al.*;[376] Color code: Grey – step-edge Pd; pink – other Pd; black – C; yellow – H; green – Cl. 244

Figure A.4 Activation energy barriers (numbers outside the parentheses) and reaction energies (numbers inside the parentheses) of surface elementary reaction steps (red: Pd(111) (data reproduced from Xu *et al.*);[376] green: Pd(100); purple: Pd(211)). Orange arrows indicate dechlorination steps; black solid arrows indicate hydrogenation steps; pink arrows indicate the dehydrogenation steps. Dashed arrows denote those dehydrogenation steps that are energetically unfavorable against competing steps. 'X' denotes a step for which we were unable to determine

any feasible reaction path from NEB calculations, and another elementary step would always occur ahead of this step..... 246

Figure A.5 Top views of the initial-state (IS), transition-state (TS) and final-state (FS) structures of each surface elementary reaction step on Pd(111), Pd(100), and Pd(211). The structures on Pd(111) were reproduced from Xu *et al.*[376] Color code: Grey – step-edge Pd; pink – other Pd; black – C; yellow – H; green – Cl. 'X' denotes a step for which we were unable to determine any feasible reaction path from NEB calculations, and another elementary step would always occur ahead of this step. Several images for the structures on Pd(211) are rotated by 90° so that all the reactive species can be captured in these images..... 247

Figure A.6 Potential energy diagram for methane formation from chloroform hydrodechlorination through the proposed reaction pathway on Pd(111) (red lines), Pd(100) (green lines), and Pd(211) (purple lines). Dash lines indicate the formation of C* through CH* dissociation. The inset indicates the comparison between the chloroform first dechlorination barrier and the chloroform desorption barrier. '*' denotes adsorbed species. '|' indicates infinite separation with each surface species at 1/9 ML coverage. '-' denotes the bond made/broken in a transition state. 263

Figure A.7 Potential energy diagram for diffusion of (a) atomic chlorine and (b) atomic carbon on Pd(211). The insets illustrate the side and top views of the stable binding structures and transition states. In each diagram, the energy zero is chosen as the energy of the preferred adsorption structure (b1 and h5 for Cl* and C*, respectively). The arrows and numbers (in eV) denote the activation energy barriers for diffusion from the preferred adsorption structure. Color code: Grey – step-edge Pd; pink – other Pd; black – C; green – Cl. 265

Figure B.1 A representation of the conditions during the stepwise conversion of methane to methanol. The temperature (black line) is given in Kelvin and gas-phase pressure of various participating species (red, green, and blue lines) are given as natural logarithms with respect to a reference pressure P_0 of 1 bar. The temperature and partial pressure profiles of various components correspond to the left and right y-axis, respectively. Shaded regions correspond to catalyst activation (red), methane exposure (green) and methanol extraction (blue), respectively. 275

Figure B.2 (a): The primitive unit cell of the purely siliceous SSZ-13 framework. (b): Schematic representation of the various local Al configurations for Cu_1 exchange studied in a single unit cell. Si(Al)-O-Si bonds in the six O-rings are shown as black lines, Al positions are marked by red circles. (c): Extended structure of SSZ-13 zeolite, with highlighted Cu_1 exchange positions in the six O-ring (6R) and eight O-ring (8R). Highlighted structures, displayed using a ball and stick model, while the remaining framework is displayed using a stick representation, are linked to framework models using dashed lines. In the atomistic representation, Si is shown as yellow spheres and O as red spheres. 278

Figure B.3 (a) Schematic representation of local Al configurations for dimer/trimer anchoring. Si(Al)-O-Si bonds are shown as black lines, the Al positions are marked by red circles. (b) Extended structure of SSZ-13 zeolite, with highlighted dimer exchange sites in the eight O-ring (8R) and bridging a six O-ring and an eight O-ring (6R/8R). Highlighted structures, displayed using a ball and stick model, while the remaining framework is displayed using a stick representation, are linked to framework models using dashed lines. In the atomistic representation, Si is shown as yellow spheres and O as red spheres..... 281

Figure B.4 A graphical representation of dimer and trimer structures included in the thermodynamic model. On top the Al configuration for the studied exchange sites is shown and on the left the studied stoichiometries are given. Atomistic pictures show the optimized structures. In atomistic pictures red atoms correspond to O, yellow atoms to Si, blue atoms to Cu, white atoms to H and blue-grey atoms to Al. As described in the caption of Figure B.2 and Figure B.3, in the schematic representations black lines show Si-O-Si bonds and red circles indicate the position of Al. The presence of a third Al atom in atomistic structures of Al configuration D-C is an artifact of the periodic boundary conditions chosen in this work. A detailed discussion is given in the Section B.9. 282

Figure B.5 T/PO2 phase diagrams for different Al configurations (a) Cu_1 anchored in a 1Al configuration or (b) the 2Al-A configuration. The temperature is given in K and PO2 is given with respect to a reference pressure of one bar. The thermodynamically preferred sites are indicated by regions of identical color and the site type is indicated by the labels. The included Al configurations are indicated by schematic representations on the right side of the phase diagrams, which correspond to Figure B.2(b) and Figure B.3(a). Green crosses indicate Al configurations not included in the phase diagrams. Marked points correspond to specific points in the stepwise methane to methanol conversion displayed in Figure B.1. A detailed legend is given in Figure B.11. 287

Figure B.6 Bond distances calculated for sites predicted to be stable in Cu-SSZ-13. Red symbols indicate distances between Cu and O in the dimers, green symbols distances between Cu and O in the framework, yellow signals Cu-Al distances and blue symbols shown Cu-Cu distances. X-axis labels correspond to the local Al configurations and columns marked by dashed lines for each Al configurations indicate (from left to right) Cu_2OH (D-A through D-D) and $Cu_2O_2H_2$ (D-A and D-B) (see Figure B.4). Black lines indicate literature values for bond distances measured using EXAFS[408] and grey shaded areas mark the experimentally reported error bars. 292

Figure B.7 A graphical representation of all stable sites after exposure to methane and formation of methanol (MeOH). On top the different local Al configurations of the exchange sites are given (see Figure B.3(a)) and on the left the stoichiometries of the different Cu structures are listed. The color code corresponds to Figure B.4 and C atoms are displayed in brown. MeOH is used as shorthand notation for methanol. 293

Figure B.8 T/PCH4 phase diagrams for different Al configurations and (a) Cu monomers anchored in a 1Al configuration or (b) the 2Al-A configuration. The temperature is given in K and PCH4 is given with respect to a reference pressure of one bar. Regions of identical color indicate the thermodynamically preferred sites and the site type is indicated by the labels. The included Al configurations are indicated by schematic representations on the right side of the phase diagrams, which correspond to Figure B.2(b) and Figure B.3(a). Green crosses indicate Al configurations not included in the phase diagrams. Marked points correspond to labels in Figure B.1. A detailed legend is given in Figure B.11. 296

Figure B.9 T/PH2O phase diagrams for different Al configurations and (a) Cu monomers anchored in a 1Al configuration or (b) the 2Al-A configuration in the presence of CH_4. The temperature is given in K and PH2O is given with respect to a reference pressure of one bar. The thermodynamically preferred sites are indicated by regions of identical color and the site type is

indicated by the labels. The included Al configurations are indicated by schematic representations on the right side of the phase diagrams, which correspond to Figure B.2(b) and Figure B.3(a). Green crosses indicate Al configurations not included in the phase diagrams. Marked points correspond to labels in Figure B.1. A detailed legend is given in Figure B.11. 298

Figure B.10 Structures of C-Cu_2O modeled in a single (A) and a double (B) primitive unit cell. Structures are very similar, but for the single unit cell twice as many Cu atoms are present and a second Al atom is located in the six O-ring. The color code in atomistic pictures corresponds to Figure B.4. 305

Figure B.11 Detailed legend for the phase diagrams shown in Figure B.5, Figure B.8, Figure B.9, Figure B.12, Figure B.13, Figure B.14, Figure B.16, and Figure B.17. On the top the legend for each individual phase diagram is shown and on the bottom the arrangement of panels for the figures noted above. 307

Figure B.12 T/PO2 phase diagrams for different Al configurations and (a) Cu monomers anchored in a 2Al-B configuration or (b) the 2Al-C configuration, (c) the 2Al-D configuration and (d) the 2Al-E configuration. The temperature is given in K and PO2 is given with respect to a reference pressure of one bar. The thermodynamically preferred sites are indicated by regions of identical color and the site type is indicated by the labels. The included Al configurations are indicated by schematic representations on the right side of the phase diagrams, which correspond to Figure B.2(b) and Figure B.3(a). Green crosses indicate Al configurations not included in the phase diagrams. Marked points correspond to specific points in the stepwise methane to methanol conversion displayed in Figure B.1. A detailed legend is given in Figure B.11. 309

Figure B.13 T/PO2 phase diagrams including multiple Al configurations for dimer sites and Cu_1 in the 1Al configuration. Subsequently the most stable sites are removed, which allows to establish an order of thermodynamic stability. The temperature is given in K and PO2 is given with respect to a reference pressure of one bar. The thermodynamically preferred sites are indicated by regions of identical color and the site type is indicated by the labels. The included Al configurations are indicated by schematic representations on the right side of the phase diagrams, which correspond to Figure B.2(b) and Figure B.3(a). Green crosses indicate Al configurations not included in the phase diagrams. A detailed legend is given in Figure B.11. 310

Figure B.14 T/PH2O phase diagram for Al configuration d-A and Cu_1 stabilized in the 2Al-A Al configuration. The temperature is given in K and PH2O is given with respect to a reference pressure of one bar. Regions of identical color indicate the thermodynamically preferred sites and the site type is indicated by the labels. The included Al configurations are indicated by schematic representations on the right side of the phase diagrams, which correspond to Figure B.2(b) and Figure B.3(a). Green crosses indicate Al configurations not included in the phase diagrams. A detailed legend is given in Figure B.11. 311

Figure B.15 Bond distances calculated for (a) dimer sites predicted to not be stable in Cu-SSZ13, (b) trimer sites and (c) non-hydrated Cu_1(II) sites. Red symbols indicate distances between Cu and O in the dimers, green symbols distances between Cu and O in the framework, yellow signals Cu-Al distances and blue symbols shown Cu-Cu distances. X-axis labels correspond to the local Al configurations and columns highlighted by dashed lines for each Al configuration indicate (from

left to right) in (a) Cu_2O, Cu_2O_2, Cu_2O_2H (Al configurations D-A through D-D) and $Cu_2O_2H_2$ (Al configurations D-C and D-D) and in (b) Cu_3O_3, Cu_3O_3H, $Cu_3O_3H_2$ and $Cu_3O_3H_3$ Black lines indicate literature values for bond distances measured using EXAFS and grey shaded areas mark the experimentally reported error bars. 313

Figure B.16 T/PCH4phase diagrams for different Al configurations and (a) Cu monomers anchored in a 2Al-B configuration or (b) the 2Al-C configuration, (c) the 2Al-C configuration and (d) the 2Al-E configuration. The temperature is given in K and PCH4 is given with respect to a reference pressure of one bar. The thermodynamically preferred sites are indicated by regions of identical color and the site type is indicated by the labels. The included Al configurations are indicated by schematic representations on the right side of the phase diagrams, which correspond to Figure B.2(b) and Figure B.3(a). Green crosses indicate Al configurations not included in the phase diagrams. Marked points correspond to specific points in the stepwise methane to methanol conversion displayed in Figure B.1. A detailed legend is given in Figure B.11. 315

Figure B.17 T/PH2Ophase diagrams for different Al configurations and (a) Cu monomers anchored in a 2Al-B configuration or (b) the 2Al-C configuration, (c) the 2Al-D configuration and (d) the 2Al-E configuration in the presence of CH_4. The temperature is given in K and PH2O is given with respect to a reference pressure of one bar. The thermodynamically preferred sites are indicated by regions of identical color and the site type is indicated by the labels. The included Al configurations are indicated by schematic representations on the right side of the phase diagrams, which correspond to Figure B.2(b) and Figure B.3(a). Green crosses indicate Al configurations not included in the phase diagrams. Marked points correspond to specific points in the stepwise methane to methanol conversion displayed in Figure B.1. A detailed legend is given in Figure B.11. 317

Figure C.1 Particle size distribution of Pt/C catalyst (Average particle size: 2.16 ± 0.65 nm, by analyzing ~2000 particles) as determined by STEM (FEI-Titan). Inset displays an STEM image. The images were collected in high-angle annular dark field (HAADF) mode with a probe current of approximately 25 pA, probe convergence angle of 24.5 mrad, and detector angle ranging from 54 to 270 mrad. 327

Figure C.2 CO* coverage profile as predicted from a PFR simulation (shown in blue) using the optimized CO* coverage dependent energetics, at the home conditions (2.6% FA, balance He, 373 K). The corresponding CO* coverage predicted by the CSTR model is indicated by the dashed line, along with ±10% error bars. 328

Figure D.1 Particle size distribution of Pd/C catalyst. Average particle size is: 2.47 ± 0.94 nm. Inset displays an STEM image of the catalyst, captured in the high-angle annular dark field (HAADF) mode (probe current: ~25 pA, probe convergence angle: 24.5 mrad, detector angle: 54 to 270 mrad). 331

Figure D.2 FTIR spectra comparing the CO* bond-stretching peak under reaction conditions with CO* saturation. The '*h*' values reported in the inset correspond to the peak intensity at respective feed condition. 332

Figure D.3 CO* coverage profile as predicted from a PFR simulation (shown in blue) using the optimized CO* coverage dependent energetics, at the home conditions (2.6% FA, balance He, 373

K). The corresponding CO* coverage predicted by the CSTR model is indicated in black, along with ±10% bars. 344

Figure E.1 Surface coverages predicted by the optimized clean Cu(111) model with the reduced reaction network, under varying (a) FA partial pressure (2.5-10%) at 373 K, (b) Temperature (368-383 K) at 10% FA. The reported coverages account for the denticity of the reaction intermediates. Dashed lines are linear trend lines. 348

Figure E.2 Surface coverages predicted by the optimized 0.625 ML $HCOO_B$ covered Cu(111) model with the reduced reaction network, under varying (a) FA partial pressure (2.5-10%) at 373 K, (b) Temperature (368-383 K) at 10% FA. The reported coverages account for the denticity of the reaction intermediates. Dashed lines are linear trend lines. 352

Figure E.3 Surface coverages predicted by the optimized clean Cu(111) model with the full reaction network, under varying (a) FA partial pressure (2.5-10%) at 373 K, (b) Temperature (368-383 K) at 10% FA. The reported coverages account for the denticity of the reaction intermediates. Dashed lines are linear trend lines. 355

Figure E.4 Surface coverages predicted by the optimized 0.625 ML $HCOO_B$ Cu(111) model with the full reaction network, under varying (a) FA partial pressure (2.5-10%) at 373 K, (b) Temperature (368-383 K) at 10% FA. The reported coverages account for the denticity of the reaction intermediates. Dashed lines are linear trend lines. 360

Figure E.5 Optimized structures of transition states involved in formic acid decomposition on clean Cu(111). Panels above and below are top and side views, respectively. Energies are with respect to gas-phase H_2 and CO_2. Color code: light grey – Cu, dark grey – C, red – O, blue – H, yellow – H from complexed HCOOH. Subscripts B and M refer to the bidentate and monodentate configurations of HCOO, respectively. Subscript X refers to complexation of HCOO with HCOOH (i.e. FA-HCOO complexes). 363

Figure E.6 Optimized structures of transition-states involved in formic acid decomposition on 0.375 ML $HCOO_{BX}$ covered Cu(111). Panels show top views. Black dashed lines mark the unit cell. Energies are with respect to gas-phase H_2 and CO_2. Color code: light grey – Cu, dark grey – C, red – O, blue – H of spectator species, cyan – H of species of interest, yellow – H from complexed HCOOH. Some H atoms are hidden behind other atoms; these atoms are outlined in dotted lines. 364

Figure E.7 Effect of coverage (clean Cu(111) vs. 0.375 ML $HCOO_{BX}$ models; ΔE) on the energetics of species involved in formic acid decomposition on Cu(111) evaluated with the PBE and PBE+D3 functionals. PBE energies were calculated with single-point calculations on the PBE+D3 geometries; PBE+D3 energies were calculated self-consistently with PBE+D3 geometries. Energies are with respect to gas-phase H_2, CO_2, and the clean slab. $\Delta\Delta E$s given below the bars denote the differences in coverage effects between the two functionals. Negative ΔE values indicate that PBE+D3 predicts greater stabilization of species higher coverage than PBE. 365

Figure E.8 Side-by-side comparison of potential energy diagrams (PEDs) for $HCOO_B$ decomposition on clean Cu(111) and 0.375 ML $HCOO_{BX}$ covered Cu(111). Bold and thin lines indicate intermediate and transition states respectively. '|' indicates infinite separation. Colors of

the pathways are identical to those in Figure 2 in the main text. All states are labeled by their energies, which are with respect to the initial state to compare the pathways on an equal energetic footing; intermediate states are additionally labeled with names of the adsorbates. Teal colored H atoms denote H atoms from the decomposing HCOO species. Subscripts B and M refer to the bidentate and monodentate configurations of HCOO, respectively. Subscript X refers to complexation of HCOO with HCOOH (i.e. FA-HCOO complexes). 366

Figure F.1 Side and top views of the most stable structures of CO on clean close-packed (111) facets of: Ag (silver), Au (gold), Cu (brown), Ir (pink), Ni (green), Pd (blue), Pt (purple), and Rh (orange). Carbon and oxygen are shown in gray and red, respectively. 372

Figure F.2 Side and top views of the most stable structures of COH on clean close-packed (111) facets of: Ag (silver), Au (gold), Cu (brown), Ir (pink), Ni (green), Pd (blue), Pt (purple), and Rh (orange). Carbon, oxygen, and hydrogen are shown in gray, red, and white, respectively. 372

Figure F.3 Side and top views of the most stable structures of COOH on clean close-packed (111) facets of: Ag (silver), Au (gold), Cu (brown), Ir (pink), Ni (green), Pd (blue), Pt (purple), and Rh (orange). Carbon, oxygen, and hydrogen are shown in gray, red, and white, respectively. 373

Figure F.4 Side and top views of the most stable structures of H on clean close-packed (111) facets of: Ag (silver), Au (gold), Cu (brown), Ir (pink), Ni (green), Pd (blue), Pt (purple), and Rh (orange). Hydrogen is shown in white. 373

Figure F.5 Side and top views of the most stable structures of OH on clean close-packed (111) facets of: Ag (silver), Au (gold), Cu (brown), Ir (pink), Ni (green), Pd (blue), Pt (purple), and Rh (orange). Oxygen and hydrogen are shown in red, and white, respectively. 373

Figure F.6 Side and top views of the most stable structures of HCOO on clean close-packed (111) facets of: Ag (silver), Au (gold), Cu (brown), Ir (pink), Ni (green), Pd (blue), Pt (purple), and Rh (orange). Carbon, oxygen, and hydrogen are shown in gray, red, and white, respectively. 374

Figure F.7 Side and top views of the most stable structures of H_2O on clean close-packed (111) facets of: Ag (silver), Au (gold), Cu (brown), Ir (pink), Ni (green), Pd (blue), Pt (purple), and Rh (orange). Oxygen and hydrogen are shown in red, and white, respectively. 374

Figure F.8 Side and top views of the most stable structures of CO_2 on clean close-packed (111) facets of: Ag (silver), Au (gold), Cu (brown), Ir (pink), Ni (green), Pd (blue), Pt (purple), and Rh (orange). Carbon and oxygen are shown in gray and red, respectively. 374

Figure F.9 Side and top views of the most stable structures of HCO on clean close-packed (111) facets of: Ag (silver), Au (gold), Cu (brown), Ir (pink), Ni (green), Pd (blue), Pt (purple), and Rh (orange). Carbon, oxygen, and hydrogen are shown in gray, red, and white, respectively. 375

Figure F.10 Side and top views of the most stable structures of HCOOH on clean close-packed (111) facets of: Ag (silver), Au (gold), Cu (brown), Ir (pink), Ni (green), Pd (blue), Pt (purple), and Rh (orange). Carbon, oxygen, and hydrogen are shown in gray, red, and white, respectively. 375

Figure G.1 Gibbs free binding energies of O_mH_n on pristine metal sites (Table G.1) are plotted against BE_O at the same site. R^2 is the coefficient of determination, and MAE denotes the mean absolute error of the fits. 380

Figure G.2 Gibbs free adsorption energies of co-adsorbed O_2 and OH (i.e., [Me] + 1.5 O_2 + 0.5 H_2 → [Me](OH)-O_2) as a function of BE_O at the pristine metal site. R^2 is the coefficient of determination, and MAE denotes the mean absolute error of the fit. 381

Figure H.1 Parity plot of reaction free energies (in eV) calculated with the PW91 and RPBE functionals. N–N bond formation and deprotonation reaction steps are represented by black circles and red triangles, respectively. Data for 0, 1/12, 1/6, 1/3, and 1/2 ML N* coverages are presented. The dashed line is a linear fit according to the equation shown. 388

Figure H.2 NH_3 adsorption free energy (PW91-GGA) as function of N* coverage. The dashed line is intended to be a guide for eyes. 388

Figure H.3 Optimized structures of the AOR intermediates, with the general formula NHx with x=0−3, on a clean Pt(111) surface. N, H, and Pt are represented with blue, white, and silver spheres, respectively. Top and side views are provided in the bottom and upper panel, respectively. An enlarged prospective of a single unit cell is shown in the top view. Dashed black lines delineate the unit cell lattice vectors. 391

Figure H.4 Optimized structures of the AOR intermediates, with the general formula NHxNHy with x, y =0−2, on a clean Pt(111) surface. N, H, and Pt are represented with blue, white, and silver spheres, respectively. Top and side views are provided in the bottom and upper panel, respectively. An enlarged prospective of a single unit cell is shown in the top view. Dashed black lines delineate the unit cell lattice vectors. 391

Figure H.5 Optimized structures of the AOR intermediates, with the general formula NHx with x=0−3, on a Pt(111) surface covered by 1/12 ML of spectator N* adatoms. N, H, and Pt are represented with blue, white, and silver spheres, respectively. Top and side views are provided in the bottom and upper panel, respectively. An enlarged prospective of a single unit cell is shown in the top view. Dashed black lines delineate the unit cell lattice vectors. 392

Figure H.6 Optimized structures of the AOR intermediates, with the general formula NH_xNH_y with x, y =0−2, on a Pt(111) surface covered by 1/12 ML of spectator N* adatoms. N, H, and Pt are represented with blue, white, and silver spheres, respectively. Top and side views are provided in the bottom and upper panel, respectively. An enlarged prospective of a single unit cell is shown in the top view. Dashed black lines delineate the unit cell lattice vectors. 392

Figure H.7 Optimized structures of the AOR intermediates, with the general formula NH_x with x=0−3, on a Pt(111) surface covered by 1/6 ML N* of spectator adatoms. N, H, and Pt are represented with blue, white, and silver spheres, respectively. Top and side views are provided in the bottom and upper panel, respectively. An enlarged prospective of a single unit cell is shown in the top view. Dashed black lines delineate the unit cell lattice vectors. 393

Figure H.8 Optimized structures of the AOR intermediates, with the general formula NH_xNH_y with x, y =0−2, on a Pt(111) surface covered by 1/6 ML of spectator N* adatoms. N, H, and Pt are represented with blue, white, and silver spheres, respectively. Top and side views are provided in

the bottom and upper panel, respectively. An enlarged prospective of a single unit cell is shown in the top view. Dashed black lines delineate the unit cell lattice vectors. 393

Figure H.9 Optimized structures of the AOR intermediates, with the general formula NH_x with x=0−3, on a Pt(111) surface covered by 1/4 ML of spectator N* adatoms. N, H, and Pt are represented with blue, white, and silver spheres, respectively. Top and side views are provided in the bottom and upper panel, respectively. An enlarged prospective of a single unit cell is shown in the top view. Dashed black lines delineate the unit cell lattice vectors. 394

Figure H.10 Optimized structures of the AOR intermediates, with the general formula NH_xNH_y with x, y =0−2, on a Pt(111) surface covered by 1/4 ML of spectator N* adatoms. N, H, and Pt are represented with blue, white, and silver spheres, respectively. Top and side views are provided in the bottom and upper panel, respectively. An enlarged prospective of a single unit cell is shown in the top view. Dashed black lines delineate the unit cell lattice vectors. 394

Figure H.11 Optimized structures of the AOR intermediates, with the general formula NH_x with x=0−3, on a Pt(111) surface covered by 1/3 ML of spectator N* adatoms. N, H, and Pt are represented with blue, white, and silver spheres, respectively. Top and side views are provided in the bottom and upper panel, respectively. An enlarged prospective of a single unit cell is shown in the top view. Dashed black lines delineate the unit cell lattice vectors. 395

Figure H.12 Optimized structures of the AOR intermediates, with the general formula NH_xNH_y with x, y =0−2, on a Pt(111) surface covered by 1/3 ML of spectator N* adatoms. N, H, and Pt are represented with blue, white, and silver spheres, respectively. Top and side views are provided in the bottom and upper panel, respectively. An enlarged prospective of a single unit cell is shown in the top view. Dashed black lines delineate the unit cell lattice vectors. 395

Figure H.13 Optimized structures of the AOR intermediates, with the general formula NH_x with x=0−3, on a Pt(111) surface covered by 1/2 ML of spectator N* adatoms. N, H, and Pt are represented with blue, white, and silver spheres, respectively. Top and side views are provided in the bottom and upper panel, respectively. An enlarged prospective of a single unit cell is shown in the top view. Dashed black lines delineate the unit cell lattice vectors. 396

Figure H.14 Optimized structures of the AOR intermediates, with the general formula NH_xNH_y with x, y =0−2, on a Pt(111) surface covered by 1/2 ML of spectator N* adatoms. N, H, and Pt are represented with blue, white, and silver spheres, respectively. Top and side views are provided in the bottom and upper panel, respectively. An enlarged prospective of a single unit cell is shown in the top view. Dashed black lines delineate the unit cell lattice vectors. 396

Figure H.15 Optimized structures of the AOR intermediates, with the general formula NH_x with x=0−3, on a Pt(111) surface covered by 3/4 ML N* of spectator adatoms. N, H, and Pt are represented with blue, white, and silver spheres, respectively. Top and side views are provided in the bottom and upper panel, respectively. An enlarged prospective of a single unit cell is shown in the top view. Dashed black lines delineate the unit cell lattice vectors. 397

Figure H.16 Optimized structures of the AOR intermediates, with the general formula NH_xNH_y with x, y =0−2, on a Pt(111) surface covered by 3/4 ML of spectator N* adatoms. N, H, and Pt are represented with blue, white, and silver spheres, respectively. Top and side views are provided in

the bottom and upper panel, respectively. An enlarged prospective of a single unit cell is shown in the top view. Dashed black lines delineate the unit cell lattice vectors. 397

CHAPTER 1

INTRODUCTION

1.1 Heterogeneous Catalysis for Sustainable and Environmentally Benign Technologies

The growing demand for energy coupled with the rapidly deteriorating environmental outlook, necessitates substantial innovation in our energy infrastructure as well as in environmental remediation approaches. Addressing these challenges in a meaningful manner would require development of: (1) sustainable energy technologies for facilitating effective utilization of renewable energy carriers and (2) energy- and cost-efficient processes for selectively transforming chemical feedstocks to the desired products, e.g., conversion to high-value commodity chemicals, energy generation, or environmental remediation, with minimal concomitant generation of undesired byproducts.

Heterogeneous catalysis is well-positioned to make a global impact by enabling the transition towards a sustainable energy future. Not only does it facilitates lower energy pathways for the transformation of reactants to products, but also provides a multitude of tunable parameters, which can be utilized to optimize a given process in terms of the reaction rates, selectivity towards desired products, stability under reaction conditions, alleviating catalyst deactivation, etc. A first-

principles atomic-scale understanding of the catalytic processes and the reaction phenomena is therefore critical for obtaining a handle on these tunable parameters and for rationally designing catalysts that are well-tailored for their desired application.

Fundamental studies have yielded unprecedented mechanistic insights for a wide-range of catalytic chemistries, for both thermally- and electrochemically-catalyzed reactions, such as the oxygen reduction/evolution reaction,[1–6] water-gas shift reaction,[7–9] ammonia synthesis,[10,11] methanol synthesis,[12–14] synthesis-gas conversion,[15–17] hydrogen evolution reaction,[18,19] alkane dehydrogenation,[20–22] preferential oxidation of CO,[23,24] to name a few instances. More importantly, these detailed insights have enabled the formulation of rational catalyst design strategies[25–32] that utilize a first-principles methodology rather than relying on the conventional experimental approach involving trial-and-error which is both time and resource intensive.

1.2 First-principles Investigation of Catalytic Chemistries and Rational Design of Catalysts

Recent breakthroughs in theoretical methods, in particularly for density functional theory (DFT), together with the ever-increasing availability of computational power, now allow for the investigation of catalytic reactions at an atomic scale. Implemented in highly parallelized codes, these methods provide first-principles derived thermodynamic and kinetic information regarding the reaction network, in terms of favorable adsorption sites, optimized gas-phase and adsorbate geometries, binding energies, minimum energy pathways for various bond-breaking/bond-formation events, diffusion barriers, etc., enabling a systematic elucidation of the catalyst reactivity.

DFT investigations provide insight into plausible reaction pathways, reaction rates, selectivity towards various products, rate-/potential-determining steps, surface environment under reaction conditions, etc, allowing a qualitative reactivity comparison across catalytic materials. These energetics, however, present a picture that is representative of experiments performed at 0 K and under ultra-high vacuum (UHV) conditions, which are substantially different compared with the typical reaction conditions. By combining with statistical mechanics, it is possible to bridge the temperature and pressure gap and obtain the energetic landscape that more accurately portrays the phenomena occurring under realistic reaction conditions.[12]

To connect the nanoscale phenomena captured by DFT calculations, with the macroscopic observables determined during reaction kinetics experiments, one can perform microkinetic modeling which provides a rigorous mathematical basis for bridging atomic-scale information with macroscopic information, enabling quantitative insights.[33–36] Insights into the catalytic systems, in terms of *in situ* surface environment, active reaction pathways, rate- and selectivity-determining steps, which cannot be directly obtained from either DFT or the reaction kinetics experiments, can be derived from microkinetic modeling.[37,38] DFT-derived energetics can be utilized to calculate the thermochemical and kinetic parameters for the various bond-breaking/bond-formation as well as the adsorption/desorption steps, which can be incorporated to formulate the rate expressions, subject to the reactor balance equations.

In conventional microkinetic modeling approaches, the model predicted reaction rates differ substantially compared with those determined during the experiments.[8,39–41] Even so, the microkinetic models can serve to provide valuable activity and selectivity trends across the host of potential catalysts as well as help in the identification of optimal operating conditions. However,

importantly, this lack of model-experiment parity can also be utilized to refine the catalyst model, i.e., by bridging the materials gap, and to derive a detailed atomic-scale picture of the active site.[42–45] Since, the DFT-energetics that govern the model-predicted reaction rates, are a strong function of the catalyst model at which these energetics were calculated at, the mismatch between the model and the experimental reaction rates, can be used to iteratively update the catalyst model, in terms of the geometric model of the catalyst, decoration with spectator species, and consideration of additional mechanisms. Thus combining computational methods with reaction kinetics experiments, can yield rich mechanistic insights regarding the catalytic chemistry.

In addition to deriving fundamental insights, computational methods can greatly accelerate the design and discovery of catalytic materials that are specifically tailored for a given catalytic chemistry.[8,39–41] In contrast with conventional time-consuming trial-and-error strategy for discovering improved catalytic materials, first-principles DFT based approach allows for formulating rational catalyst design strategies. By studying the reaction thermochemistry and kinetics on a host of catalyst surfaces, it is possible to derive Linear-Scaling[46] and Brønsted–Evans–Polanyi (BEP)[47] correlations, which allow for correlation of binding energy for the reaction intermediates and transition-state energies for the elementary steps, respectively, on carefully determined energetic descriptors. These descriptors are typically thermochemical entities, such as the binding energy of select reaction intermediates, which facilitate the dimensionality-reduction of the reaction network. Once the theoretical correlations are formulated, it is possible to efficiently determine the energetics of the entire reaction network over a new catalyst candidate by simply evaluating these energetic descriptors and extrapolating the energetics on the basis of the Linear-Scaling and BEP correlations. In conjunction with microkinetic modeling, this approach can be

utilized to make quantitative predictions regarding the activity and selectivity of the catalyst candidates, enabling high-throughput screening of catalysts. In the recent years, this methodology has greatly accelerated the discovery of improved catalysts for several chemistries.

By utilizing an integrated approach involving first principles DFT-calculations, reaction kinetics experiments, and microkinetic modeling, we strive to obtain detailed mechanistic understanding of the catalytic chemistries, formulate quantitatively accurate kinetic models, and extend our understanding for designing improved catalytic materials for the chemistries of our interest.

1.3 Scope of Dissertation

In this dissertation, we investigate both thermal- and electro-catalytic chemistries, finding application in sustainable energy production and environmental remediation applications. Through a combination of computational modeling, in particular, first-principles DFT calculations and microkinetic modeling, together with reaction kinetics experimentation (for thermal catalysis, in particular), we seek to elucidate detailed atomic scale understanding of the catalytic chemistry, in terms of the reaction mechanism, the nature of the active site, the surface environment under reaction conditions, and the rate-/selectivity-controlling steps. We believe that fundamental atomistic-scale insights derived from these studies would help guide the rational design of improved catalytic materials.

The dissertation is structured as follows: In Chapter 2, we present a concise overview of the computational and experimental methods which provide the foundational basis for our investigations. A major portion of the dissertation focusses on elucidating the vapor-phase FA decomposition chemistry on supported monometallic powder catalysts. In Chapter 3, we present

our iterative methodology involving DFT calculations, reaction kinetics experiments, and microkinetic modeling to systematically develop a *coverage self-consistent* picture for the *in situ* nature of the active site of FA decomposition on Pt/C catalysts. In Chapters 4 & 5, we extend this approach to investigate the FA decomposition reaction on Pd/C and Cu/Al_2O_3 catalysts, respectively. In Chapter 6, we formalize our iterative methodology to propose a refined generalized-algorithm for elucidating the nature of the active site in metal catalysis. In Chapter 7, we utilize our fundamental understanding of the FA decomposition chemistry to formulate *experiment-calibrated coverage-cognizant* volcano plots and perform high-throughput descriptor-based screening to computationally predict bimetallic catalysts exhibiting improved activity and/or selectivity toward FA dehydrogenation. In the next two chapters, we translate our rigorous methodology of treating realistic adsorbate coverages, developed by investigating thermal catalysis, to now model electrocatalytic reactions. In Chapter 8, we utilize a combination of DFT and microkinetic modeling to study the oxygen reduction reaction on graphene-supported transition-metal single atom catalysts (SACs). In Chapter 9, we study the ammonia electrooxidation reaction at incremental coverages of N* species on Pt(111) and elucidate the deactivation mechanism for this chemistry. Finally, in Chapter 10, we briefly summarize our key findings and propose potential avenues for future investigations.

The chapters presented in this dissertation are interlinked with a consistent theme of developing more accurate computational models by investigating chemistries under realistic surface environment and explicitly elucidating adsorbate induced coverage-effects. In Appendix A and B, we present detailed computational studies aimed at elucidating the chloroform hydro-dechlorination chemistry over clean Pd surfaces and the methane-to-methanol conversion over Cu-

SSZ-13 catalysts, respectively, which follow the broader theme of this dissertation aimed at elucidating detailed atomistic-scale understanding of chemistries relevant for sustainable energy production and environmental remediation processes.

CHAPTER 2

METHODS

2.1 Introduction

In this chapter, we present a brief overview of the computational and experimental methods used in our studies, namely, density functional theory (DFT), reaction kinetics experimentation, and mean-field microkinetic modeling. The description presented here is intended to the provide the reader with a general introduction of the methods utilized in this dissertation.

2.2 Density Functional Theory

2.2.1 The Schrödinger Equation

Determining of the energetics of a physical system involving an ensemble of atoms and molecules, as a function of their spatial arrangement, serves as the foundational basis for atomistic simulations. Obtaining this information from first-principles quantum mechanics involves solving the time-independent Schrödinger Equation (TISE):

$$\hat{H}\psi = E\psi \tag{2.1}$$

where, $\widehat{H}$ is the Hamiltonian operator, ψ is the set of wavefunctions describing the eigenstates or the stationary states, and E is the total ground-state energy of the system, i.e., the eigenvalue. The definition of the Hamiltonian operator, $\widehat{H}$, depends on the physical system being described by the TISE. For select systems, e.g., particle in a box, the Harmonic oscillator, the hydrogen atom, etc., the Hamiltonian operator takes a simple form, which allows for an exact solution of the TISE. However, for atomistic systems relevant in heterogeneous catalytic applications, which typically involve several atoms (i.e., multiple nuclei and electrons), the complexity of the problem compounds rapidly. For such a system, the Hamiltonian operator can be expressed as follow:

$$\widehat{H} = \hat{T} + \hat{V} + \hat{U} \tag{2.2}$$

where, the three terms describe the kinetic energy of the electrons ($\hat{T}$), the interaction of the electrons with the nuclei ($\hat{V}$), the interactions between the electrons ($\hat{U}$). For a system comprising of N electrons, the above equation can be expressed as:

$$\widehat{H} = \sum_{i=1}^{N} -\frac{\hbar^2}{2m}\nabla_i^2 + \sum_{i=1}^{N} V(\boldsymbol{r_i}) + \sum_{i=1}^{N}\sum_{j>i}^{N} U(\boldsymbol{r_i}, \boldsymbol{r_j}) \tag{2.3}$$

where, $\hbar$ is the Planck's constant, m is the mass of an electron, r_i is the spatial coordinates of the electron i, $V(\boldsymbol{r_i})$ is the interaction between the nuclei and the electron i, and $U(\boldsymbol{r_i}, \boldsymbol{r_j})$ is the interaction between electrons i and j. Per the Born-Oppenheimer approximation, due to mass difference between the nuclei and the electrons, the nuclei are assumed to be fixed exerting a potential V, while the electrons are allowed to move. The challenge in solving this equation arises from the electron-electron interaction term, $U(\boldsymbol{r_i}, \boldsymbol{r_j})$, which is a many-body problem and thus rapidly compounds with increasing number of electrons in the system. Over the years, several methods such as Hartree-Fock (HF), Coupled Cluster (CC), Møller-Plesset perturbation theory

(MP), and density functional theory (DFT), have been developed to obtain solutions to this challenging problem.[48] In this dissertation, we restrict our scope to discussing DFT.

Due to its relatively reduced computational expense (~$O(N^3)$), DFT-based methods have become one of the most widely adopted solution schemes for tackling this challenging problem. DFT was proposed by W. Kohn, P. Hohenberg, and L. J. Sham in the 1960's. The formulation is based on the pioneering approach which proposed dealing with electron-density, a 3-dimensional variable, instead of wavefunctions, a 3N-dimensional variable. Further, the founders prove that the true functional form of the electron density would correspond to the electron density that minimizes the energy of the system under consideration. These concepts, formalized as the following two theorems, serves as the foundational basis for DFT:

Theorem 1: The ground-state energy from the Schrödinger Equation is a unique functional of the electron density $\rho(\boldsymbol{r})$.

Theorem 2: The electron density that minimizes the energy of the overall functional is the true form of the electron density corresponding to the full solution of the Schrödinger Equation.

The electron density, $\rho(\boldsymbol{r})$, referred to above, can be determined from the individual electron wavefunctions, $\psi_i(\boldsymbol{r_i})$, as follows:

$$\rho(\boldsymbol{r}) = 2\sum_{i=1}^{N} \psi_i^*(\boldsymbol{r_i})\psi_i(\boldsymbol{r_i}) \tag{2.4}$$

where, $\psi_i^*(\boldsymbol{r_i})$ denotes the complex conjugate of wavefunction $\psi_i(\boldsymbol{r_i})$. Further, Kohn and Sham demonstrated that one can determine the electron density by solving a set of equations involving only single electron wavefunctions:

$$\left[-\frac{\hbar}{2m}\nabla^2 + V(\boldsymbol{r}) + V_H(\boldsymbol{r}) + V_{XC}(\boldsymbol{r})\right]\psi_i(\boldsymbol{r}) = E_i\psi_i(\boldsymbol{r}) \tag{2.5}$$

where, $-\frac{\hbar}{2m}\nabla^2$ corresponds to the kinetic energy, $V(\boldsymbol{r})$ corresponds to the electron-nuclei interaction, $V_H(\boldsymbol{r})$ corresponds to the Hartree potential, representing the Coulombic repulsions between the electron and the total electron density, and $V_{XC}(\boldsymbol{r})$ corresponds to the exchange-correlation potential, essentially a heuristic approach to lump all quantum mechanical effects not considered in other terms. The Hartree potential, consisting of an unphysical self-interaction term and eventually corrected in the exchange-correlation term, can be represented as:

$$V_H(\boldsymbol{r}) = e^2 \int \frac{\rho(\boldsymbol{r}')}{|\boldsymbol{r} - \boldsymbol{r}'|} d^3\boldsymbol{r}' \tag{2.6}$$

The exchange-correlation term, $V_{XC}(\boldsymbol{r})$, is defined as the functional derivative of the exchange-correlation energy $(E_{XC}(\boldsymbol{r}))$:

$$V_{XC}(\boldsymbol{r}) = \frac{\delta E_{XC}(\boldsymbol{r})}{\delta \rho(\boldsymbol{r})} \tag{2.7}$$

The detailed functional form of the exchange-correlation energy, $E_{XC}(\boldsymbol{r})$, is known only for uniform electron gas, thus $V_{XC}(\boldsymbol{r})$ can be derived analytically only for that case. Typically, for applications of our interest, there exist two major class of solution methods: (1) Local-density approximation (LDA)[49,50] and (2) Generalized-gradient approximation (GGA).[51] In this dissertation, we utilize the Perdew-Wang 1991 (PW91)[52] and the Perdew-Burke-Ernzerhof (PBE) functional.[53] The Kohn-Sham equation is solved iteratively, per the following algorithm: (1) Define an initial guess for the electron density, (2) Solve the Kohn-Sham equation using the initial guess of the electron density and determine the single-electron wave-functions, (3) Calculate a new electron density using the wave-functions determined in step 2, (4) Compare the new electron density with that used to initialize the procedure and update the electron density until a self-consistent solution is determined. In this dissertation, we utilize two DFT-total energy codes,

namely, the Vienna *ab initio* Simulation Package (VASP)[54,55] and DACAPO[56,57] to obtain approximate solutions to the Schrödinger Equation.

2.2.2 Application of DFT in Heterogeneous Catalysis

In this dissertation, we use DFT to determine physical properties of atomistic-nanostructures and systematically approach problems in heterogenous catalysis via first-principles calculations, e.g., lattice constants, optimized geometries of gas-phase and adsorbed species, binding energies for reaction intermediates, activation energy barriers for elementary steps, etc. Such calculations typically involve providing an initial guess for the atomic scale architectures which are optimized to their lowest energy arrangement by DFT codes. By calculating the energetics of gas-phase reactants and productions, reaction intermediates involved in various reaction pathways, and transition-states for the various bond-breaking and bond formation steps, one can systematically determine the energetic landscape for the transformation of reactants to products.

2.2.2.1 Catalyst Models

Heterogeneous catalysts typically utilized in reaction kinetics studies, such as those discussed subsequently in this dissertation, comprise of supported metal-nanoparticles, containing hundreds or thousands of atoms. Although, given the recent advances in computing capabilities, simulating these systems in their full-complexity is starting to become increasingly more feasible, the computational costs, however, still remain exorbitantly high for catalytic chemistries with medium-to-large sized reaction networks, that are of interest to us. To this end, we adopt two approximations to keep the computational costs tractable: (1) *Lack of consideration of support effects* – For inert support materials, e.g. carbon (verified experimentally for the chemistries reported in this dissertation) and for transition-metal based nanometer-sized catalysts, it is

reasonable to omit support-metal interactions from further consideration. (2) *Deconvoluting nanoparticle to extended surfaces* – A catalyst nanoparticle can be approximated as an ensemble of low-miller index facets, which are exposed by the nanoparticles under reaction conditions. This approach allows for the decomposition of complexity involved in treating an entire nanoparticle to instead individually consider dominant surfaces that are presented in a supported nanoparticle, which can be efficiently handled with periodically repeated plane-wave DFT codes. The shape of the nanoparticle is essentially an optimization problem, wherein the surface energy of the nanoparticle is minimized. Thus depending on the size of the nanoparticle, one can estimate the fraction of the closed-packed (111) facet, the more open (100) facet, and steps/kinks, modeled by the (211) facet. Considering the size of nanoparticles used in our reaction kinetics studies, representing the nanoparticle with the (111) and (100) surfaces served as a sound approximation (Figure 2.1).

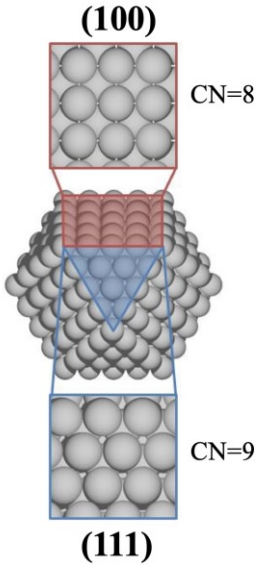


Figure 2.1 Schematic showing the close-packed (111) and open (100) facets of a metal nanoparticle. CN refers to coordination number of surface atoms.

We note that for a more novel class of materials, i.e. single-atom catalysts – also investigated in this dissertation, which present the maximum limit in terms of atomic efficiency, one cannot utilize the two approximations listed above. In that instance, we model a 2-D surface, comprising of a single metal-atom embedded in the support, representing the single-atom catalysts (Figure 2.2). A more detailed description of the model, in terms of the unit-cell composition, nature of the defective site, coordination/substitution around to the metal site, etc., is provided in the computational methods section for the corresponding Chapter.

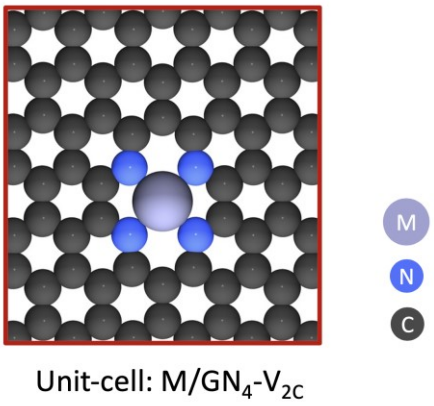


Figure 2.2 Atomistic representation of the p(6x5) unit-cell employed for modeling graphene-supported transition-metal atom (M) based single-atom catalysts embedded in a four-fold N substituted double C-vacancy (M/GN_4-V_{2C}).

2.2.2.2 Reaction Thermochemistry: Binding Energy and Reaction Energy

For heterogeneously catalyzed reactions, the first step involves adsorption of the reactant(s) onto the surface of the catalyst. Once adsorbed, the reactant can then undergo various bond-breaking/bond-formation steps to achieve the desired chemical transformations to form the final products. Thus, the interaction energy of various species appearing in the reaction network with the surface of the catalyst, defined as the binding energy, plays a critical role in determining the

reaction rate and the selectivity of a given catalyst. The binding energy of an adsorbate X, can be defined as:

$$BE_{X^*} = E_{slab+X^*} - E_{slab} - E_{X(gas)} \tag{2.8}$$

where, the subscript * denotes the reaction intermediate being adsorbed to the catalyst surface, E_{slab+X^*} denotes the total energy of the system comprising of the adsorbed species and the slab, E_{slab} denotes the total energy of the slab, and $E_{X(gas)}$ denotes the energy of the species X in the gas-phase. A more negative values of the binding energy indicates stronger interaction of the adsorbate with the catalyst surface, i.e., stronger binding, while a less negative value indicates weaker interaction of the adsorbate with the catalyst surface. Typically, several potential binding configurations and high-symmetry binding sites are explicitly elucidated using DFT to determine the most favorable binding configuration of the reaction intermediates on the catalyst surface.

The binding energy of reaction intermediates can also be used to calculated the reaction energetics of the elementary steps, ΔH_{rxn}, using the following:

$$\Delta H_{rxn} = \sum_{i \in products} BE_{i^*} + E_{i(gas)} - \sum_{j \in reactants} BE_{j^*} + E_{j(gas)} \tag{2.9}$$

here, a negative value of ΔH_{rxn} would indicate an exothermic reaction, while a positive value would indicate an endothermic reaction.

2.2.2.3 Reaction Kinetics: Transition-State Energy and Activation Energy Barrier

The chemical transformations of reactants going to products involve undergoing various bond-breaking/bond-formation steps. This transformation entails going from the initial state to the final state of the elementary step, via a transition-state. A transition-state is essentially a saddle point on

the potential energy surface, wherein, it corresponds to the highest point along the reaction coordinate and the local minimum along all other plausible degrees of freedom.

In this dissertation, we utilize the climbing-image nudged elastic band method (CI-NEB)[58] for determining the transition-states for all elementary steps. This method involves defining the initial and final states involved in an elementary step, followed by discretizing along the reaction coordinate to obtain a set of intermediate images. Typically, a set of seven interpolated intermediate images are utilized to initialize the procedure. Each intermediate image is connected with the corresponding adjacent images through "elastic bands" with defined spring constants. The images are then simultaneously optimized and the forces acting parallel and perpendicular to the bands are evaluated. The calculation is said to converge once all perpendicular forces are below the convergence criteria of the calculation. The images corresponding to the highest energy corresponds to the transition state for the elementary step. The transition-state is confirmed by performing vibrational frequency calculation, yielding a single imaginary frequency along the reaction coordinate. Using the transition-state energy, one can the determine the activation energy barrier, E_a, for a given step:

$$E_a = E_{TS+slab} - E_{slab} \sum_{j \in reactants} BE_{j^*} + E_{j(gas)} \tag{2.10}$$

where, $E_{TS+slab}$ corresponds to the total energy of the image corresponding to the transition state including the slab. Using reaction thermochemistry and reaction kinetics, one can formulate potential energy diagrams (PEDs) and systematically elucidate the energetics of various plausible competing mechanisms that could play a role in the transformation of reactants to the products.

2.2.2.4 Vibrational Frequency

DFT-derived vibrational frequencies provide valuable information that could facilitate a one-to-one comparison with values determined experimentally using spectroscopic techniques, in particular, regarding the nature of the reaction intermediates participating under realistic catalytic conditions. The harmonic vibrational frequencies are calculated by diagonalizing the mass-weighted Hessian matrix, yielding the frequencies and normal modes. The second derivatives are derived by displacing the position of the atoms by a small step-size and determining the energy of the thus obtained structure.

The vibrational modes can also be used to calculate the zero-point energy (ZPE) of the system and the vibrational component for the finite temperature corrections ($\Delta E_{vib}^{T_{corr}}$). The ZPE and $\Delta E_{vib}^{T_{corr}}$ can be calculated using the following:

$$ZPE = \frac{h}{2}\sum_{i=1}^{n} \nu_i \tag{2.11}$$

$$\Delta E_{vib}^{T_{corr}} = RT \sum_{i} \frac{h\nu_i}{k_B T}\left[\frac{e^{-\frac{h\nu_i}{k_B T}}}{1 - e^{-\frac{h\nu_i}{k_B T}}}\right] \tag{2.12}$$

where, h is the Planck's constant, n is the number of vibrational modes, and ν_i is the i^{th} frequency. Together with statistical mechanics, the vibrational frequencies can be used to calculate the entropy of the adsorbed reaction intermediates and the gas-phase species, which enables the determination of Gibbs-free energies and helps bridge the temperature and pressure gap for DFT-derived energetics. For gas-phase species, the entropy, S_{tot}^{gas}, comprises of three terms:

$$S_{tot}^{gas} = S_{trans}^{3D} + S_{rot} + S_{vib} \tag{2.13}$$

where, S_{trans}^{3D}, S_{rot}, and S_{vib} refer to the 3-D translational, rotational, and vibrational contributions, respectively, defined as follows:

$$S_{trans}^{3D} = R\left\{ln\left[\left(\frac{2\pi m k_B T}{h^2}\right)^{1.5}\frac{k_B T}{P}\right] + 2.5\right\} \quad (2.14)$$

$$S_{rot}^{lin} = R\left[\ln\left(\frac{8\pi^2 I k_B T}{\sigma h^2}\right) + 1\right];\ S_{rot}^{non-lin} = R\left[\ln\left(\frac{k_B T}{h}\right) - \ln(\sigma) - 0.5\ln\left(\frac{I}{\pi}\right) + 1.5\right] \quad (2.15)$$

$$S_{vib} = R\sum_i\left[ln\left(1 - e^{-\frac{h\nu_i}{k_B T}}\right)\right] + R\sum_i \frac{h\nu_i}{k_B T}\left[\frac{e^{-\frac{h\nu_i}{k_B T}}}{1 - e^{-\frac{h\nu_i}{k_B T}}}\right] \quad (2.16)$$

where, m is the molecular mass of the gas-phase species, k_B is the Boltzmann's constant, h is the Planck's constant, T is the temperature, P is the pressure, R is the gas-constant, I is the moment of inertia, and σ is the symmetry factor for the gas-phase species.

On the other hand, the translational and rotational modes for the adsorbed species are replaced by frustrated models, separated before diagonalizing the Hessian matrix, but still treated as vibrational models in entropy calculations.[12,59]

2.3 Reaction Kinetics Experimentation

Reaction kinetics experiments provide valuable insight into the performance of a catalyst, as a function of reactor temperature, pressure, space-velocity and feed composition, and inform the activity and selectivity for a given catalytic chemistry. By modulating the reactor conditions, one can determine experimental metrics, such as the apparent activation energy barriers and the apparent reaction orders wrt. reactants and products. These then allow for comparison of the catalyst performance with other potential candidate materials, as well as serve as targets for

subsequent modeling efforts. For the purposes of extracting only kinetically relevant information, it is critical to ensure that no thermal or mass-transfer gradients exist within the reactor.

For the experiments reported in this dissertation, a fixed-bed tubular reactor was utilized for studying gas-phase catalytic chemistries over transition-metal based catalysts. The details regarding the experimental setup used in various studies is provided in the methods section of the corresponding chapters. However, briefly, the catalyst was packed using quartz-wool plugs and was held in place using silica-chips. The experimental conditions were selected in a manner to ensure that the kinetics data is collected in a low conversion regime (typically, <10%). The flow-rate of various gas-phase species were controlled at the reaction inlet using calibrated mass-flow controllers. Liquid reactants were vaporized at the reactor inlet and carried through the reactor by an inert carrier-gas (e.g., He, N_2, etc) or gas-phase reactants. A schematic for the reactor setup utilized to the study the formic acid (FA) decomposition chemistry is shown in Figure 2.3. To quantify the composition of the products, we typically utilized a gas chromatograph with a thermal-conductivity detector (GC-TCD), gas chromatograph with a flame-ionization detector (GC-FID), and/or a mass-spectrometer (MS). To determine the number of exposed surface sites for a given catalyst, the catalysts were characterized using microscopy and chemisorption techniques, which was then utilized to obtain turnover frequencies (TOFs) for various reaction pathways. The thus obtained TOFs as a function of experimental conditions served as the kinetic dataset utilized subsequently in the microkinetic modeling portion of our studies.

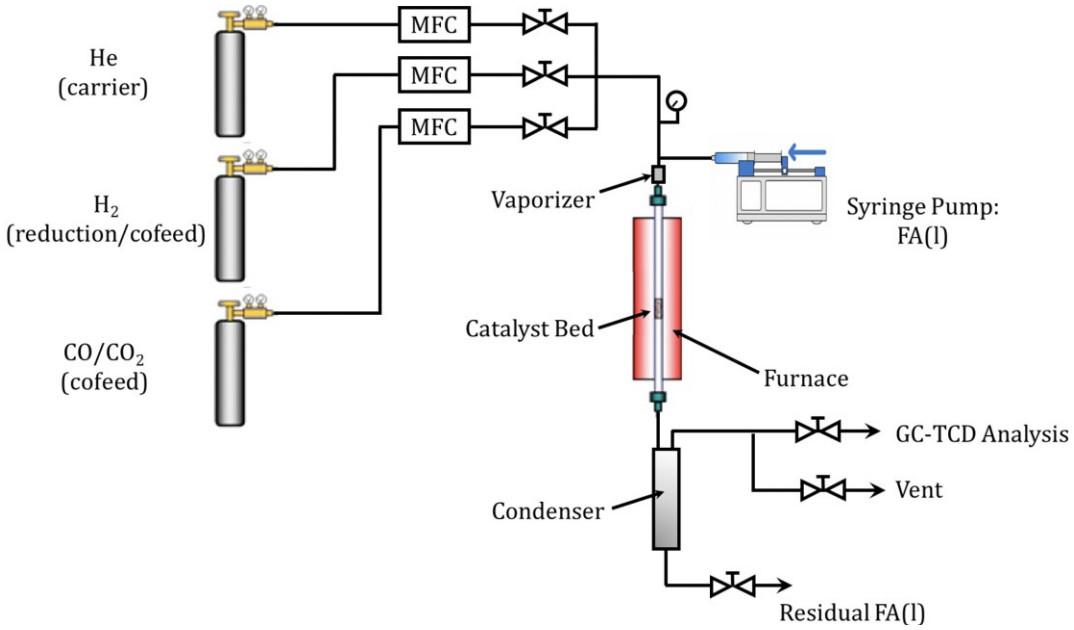


Figure 2.3 A schematic of the reactor setup utilized for performing kinetics experiments for the formic acid (FA) decomposition chemistry.

2.4 Microkinetic Modeling

Microkinetic modeling provides a rigorous mathematical basis for bridging atomistic-scale information derived from DFT with the macroscopic observables determined from reaction kinetics experiments.[33] It provides valuable mechanistic details for the catalytic chemistry in terms of flux contribution from various reaction paths, surface coverages as a function of experimental conditions, rate-controlling steps,[60,61] etc., which are otherwise not directly achievable from either DFT or reaction kinetics experiments.

Throughout this dissertation, we use a controlled-stirred tank reactor (CSTR) model, which has been demonstrated to serve well for modeling the kinetics of experiments with low per-pass conversion.[41] A CSTR model can be expressed using the following set of differential algebraic equations (DAEs):

$$\frac{dF_i}{dt} = F_{i,in} - F_i + \sum_{j \in reactions} \nu_{ij} r_j \tag{2.18}$$

$$\frac{d\theta_k}{dt} = \sum_{j \in reactions} \nu_{kj} r_j \tag{2.19}$$

$$\theta_* + \sum_{j \in adsorbates} \theta_k = 1 \tag{2.20}$$

where, F_i corresponds to the molar flow-rate of gas-phase species i, ν_{ij} is the stoichiometric coefficient of gas-phase species i in the elementary step j, ν_{kj} is the stoichiometric coefficient of adsorbed species k in the elementary step j, r_j is the reaction rate for step j, θ_k is the surface coverage of species k, subscript * denotes vacant sites, and indices i, j, and k, correspond to the gas-phase species, elementary steps, and surface intermediates, respectively. The rate constants for the bond-breaking/formation steps are calculated using the transition-state theory, whereas those for the adsorption/desorption steps are calculated using the collision theory, per the following:

$$k_{surf-steps} = \frac{k_B T}{h} \exp\left(\frac{\Delta S^{\ddagger}}{R}\right) exp\left(\frac{-\Delta H^{\ddagger}}{RT}\right) \tag{2.21}$$

$$k_{ads} = \frac{\sigma^o(T)}{\sqrt{2\pi m k_B T}} \, exp\left(\frac{-\Delta H^{\ddagger}}{RT}\right) \tag{2.22}$$

where, the superscript ‡ indicates the entropy (S)/enthalpy (H) difference between the transition-state and the reactants appearing in the elementary step and σ^o is the sticking coefficient. Shomate parameters were used to incorporate temperature and ZPE corrected DFT-energetics in our microkinetic models.[62] The DFT-energetics were utilized as initial estimates for the kinetic and thermodynamic parameters, which were adjusted to achieve parity with the reaction kinetics

experiments. To perform parameter estimation, we used the generic sequential optimization framework, proposed by our group, which utilizes a Latin-hypercube based multi-start approach.[41] As discussed in subsequent chapters, we adopt this combined computational and experimental methodology, involving DFT calculations, reaction kinetics experimentation, and microkinetic modeling to systematically elucidate the nature of the active site and the reaction mechanism for heterogeneously-catalyzed chemistries.

CHAPTER 3

REACTION MECHANISM OF VAPOR-PHASE FORMIC ACID DECOMPOSITION OVER PLATINUM CATALYSTS: DFT, REACTION KINETICS EXPERIMENTS, AND MICROKINETIC MODELING[⊥]

3.1 Introduction

Integration of molecular hydrogen generated from renewable sources into our energy infrastructure, especially for transportation applications, is crucial for the transition toward a sustainable energy future.[63] Obtained as a by-product in biomass reforming,[64–69] formic acid (FA, HCOOH) has recently attracted widespread attention for hydrogen storage and on-demand hydrogen production[70–79], including for fuel cell applications. The low toxicity and flammability, high hydrogen content (53.4 g-H_2/l; 4.4 wt.%), and its liquid nature at ambient conditions allow FA to be readily integrated into existing liquid fuel infrastructure. In addition, FA decomposition

[⊥]Adapted from – Bhandari, S.; Rangarajan, S.; Maravelias, C.T.; Dumesic, J.A.; Mavrikakis, M. Reaction Mechanism of Vapor-Phase Formic Acid Decomposition over Platinum Catalysts: DFT, Reaction Kinetics Experiments, and Microkinetic Modeling. *ACS Catalysis* **2020**, 10 (7) 4112-4126 – https://doi.org/10.1021/acscatal.9b05424

has been extensively utilized to probe catalytic activity of various materials including metals,[80–83] metal-oxides,[84–88] metal-carbides,[89–92] and zeolite-based catalysts.[93–98]

FA can decompose through either dehydrogenation to H_2 and CO_2 (ΔH^o = -14.9 kJ/mol) or dehydration to CO and H_2O (ΔH^o = 26.2 kJ/mol), the latter being the undesired pathway, as CO binds strongly to most transition metals rendering inactive a good fraction of the catalyst's surface. In the 1960s, Sachtler and Fahrenfort presented a volcano plot correlating FA decomposition activity of monometallic catalysts with the bulk metal formate formation energy and found Pt-group metals (Pt, Pd, and Ir) to be at the activity peak.[99] More recently, Wachs and coworkers revisited this reaction using unsupported metal powder catalysts and concluded Pt to be the most active metal.[100] Similar conclusions were obtained in the comparative study by Solymosi and coworkers for carbon-supported Pt-group metals.[101] Bulushev *et al.* reported a promotional effect of N-doped carbon nanofibers on Pt-catalysts, resulting in improved activity and selectivity, along with enhanced CO tolerance.[102] These authors also reported a variation in the experimentally measured apparent activation energy with the particle size: 51 kJ/mol and 64 kJ/mol for catalysts with average particle-size of 1.3 nm and 2.3 nm, respectively. Yoo *et al.* proposed theoretical activity and selectivity volcano plots for vapor-phase FA decomposition, and suggested a Cu-Pt bimetallic catalyst for improved activity and selectivity.[103]

FA has been widely studied in the context of vapor-phase decomposition,[42,83,102,104–108] as well as electrochemical oxidation.[109–111] Despite several studies, however, the detailed reaction mechanism, the identity of active intermediates and the nature of the active site under reaction conditions, all remain under debate. Under certain experimental conditions, formate (HCOO*) has been identified spectroscopically on Pt catalysts. [101] However, CO(g) formation determined

experimentally for FA decomposition over Pt catalysts, suggests that part of the reaction proceeds through the spectroscopically elusive carboxyl (COOH) intermediate, the key precursor to CO formation.[108] COOH* is also known to play a critical role in the water-gas-shift reaction (WGSR).[8] Therefore, a comprehensive mechanistic model capable of capturing experimental observables over a wide range of conditions might be able to resolve contradictory proposals pertaining to the reaction mechanism and the nature of the active site while the reaction is taking place.

Further, CO* poisoning of Pt-based catalysts has been well established.[101,102,112,113] In particular, Thiel and coworkers have suggested that under Ultra High Vacuum conditions, the presence of CO* on the Pt surface can modify the reaction mechanism and promote additional pathways for FA decomposition.[113,114] However, the role of spectator CO* species under atmospheric reaction conditions in determining reactive intermediates and the reaction mechanism has not been elucidated. At room temperature and low CO partial pressures, the CO* saturation coverage on Pt(111) has been reported to be in the range of 0.4-0.5 monolayer (ML).[115–118] An even higher CO* saturation coverage (>0.70 ML) has been reported on the Pt(100) surface.[119–121] To facilitate a more direct comparison between the two facets, and to assess the CO*-spectators effect on the reaction mechanism, we chose to study this reaction on both the clean and a 4/9 ML CO*-covered version of the Pt(111) and Pt(100) facets.

In this study, we aim to achieve a comprehensive understanding of the vapor-phase FA decomposition on carbon-supported Pt-catalysts. We perform first-principles density functional theory (DFT) calculations to parameterize mean-field microkinetic models and fit reaction kinetics experimental data. Through this combination, we iteratively develop a coverage-self-consistent description for the nature of the active site. Often, there exists a discrepancy between the coverages

predicted by the microkinetic models and the catalyst models employed during DFT calculations.[122] We show that performing calculations under relevant coverages of surface intermediates (such as CO*) is key to obtaining accurate initial estimates of kinetic and thermodynamic parameters and to achieving a quantitative agreement with the experiments. Further, we demonstrate that the inclusion of adsorbate-induced coverage effects can also modify the reaction mechanism by allowing for spectator-assisted pathways, which were found to be critical for accurately modeling the experiment. Our results provide important insights into the nature of the active site, the detailed reaction mechanism, the rate-controlling steps, and the environment of the active site under reaction conditions.

3.2 Methods

3.2.1 Computational Methods

Periodic DFT calculations were performed using the Vienna *ab initio* Simulation Package (VASP),[54,55] a plane-wave total energy code. The exchange-correlation functional was described within the generalized gradient approximation (GGA-PW91)[52], and the electron-ion interactions were described by projector augmented wave (PAW) potentials.[123,124] The electronic wave functions were expanded using plane-waves with an energy cutoff of 400 eV. We calculated the lattice constant for bulk Pt to be 3.986 Å, in good agreement with the experimental value of 3.912 Å.[125] Both the Pt(111) and Pt(100) surfaces were modeled by four-atomic-layer slabs using a (3 × 3) unit cell. Successive slabs were separated in the z-direction by a vacuum space of 15 Å. The bottom two layers of the slab were fixed at their bulk-optimized lattice positions, whereas the top two layers of the slab, as well as all the adsorbates, were allowed to fully relax. The adsorbates

were allowed to bind on only one side of the slab, and the electrostatic potential was adjusted accordingly.[126,127] The first Brillouin zone was sampled with a (4×4×1) Monkhorst-Pack k-point mesh.[128] Convergence of the total energy was confirmed with respect to the k-point mesh, energy cutoff, and the number of metal atom layers included in the slab.

Binding energies (BE) are reported with respect to the gas-phase adsorbate and the slab decorated with the relevant spectator CO* coverage. BE of species 'i' at a spectator CO* coverage of θ was calculated as:

$$BE_{i^*(\theta_{CO})} = E_{i^*(\theta_{CO})} - E_{(\theta_{CO})} - E_{i(gas)} \quad (3.1)$$

Where, the terms on the right-hand side of the equation represent total energy of the system with adsorbed species 'i' and a CO* spectator coverage of θ ($E_{i^*(\theta_{CO})}$), total energy of the slab with CO* coverage of θ ($E_{(\theta_{CO})}$), and the total energy of species 'i' in the gas phase ($E_{i(gas)}$). We report the binding energy of CO* consistent with the definition above, i.e., its binding energy is reported under the presence of spectator CO* coverage of θ. While discussing *clean surface* energetics, we imply the absence of coadsorbed CO* species, whereas for the *CO*-covered surface*, the energetics are evaluated in the presence of relevant coverage of CO* adsorbed spectator molecules. The activation energy barrier for each elementary step is evaluated by using the climbing image nudged elastic band (CI–NEB) method[129] with seven interpolated images between the initial and final states. The structures were relaxed until the maximum force on each interpolated image is smaller than 0.05 eV $Å^{-1}$. The transition states (TS) were verified by performing vibrational frequency calculations yielding a single imaginary frequency along the reaction coordinate. The harmonic vibrational frequencies were determined from the diagonalization of the mass-weighted

Hessian matrix. In the discussion of the DFT results, we referred to electronic energy values neglecting zero-point energy (ZPE).

3.2.2 Experimental Methods

3.2.2.1 Reaction Kinetics Experiments

The experimental setup was similar to the one employed in our previous studies.[42] We used a stainless-steel reactor with an OD of 1/4" operated in a fixed-bed down-flow configuration. Carbon-supported Pt catalyst (1 wt.%) obtained from Sigma-Aldrich was used for performing the reaction kinetics experiments. Typically, ca. 100 mg (dry weight) of 1 wt.% Pt/C catalyst was loaded into the reactor and packed in place using silica chips at both ends. The catalyst was reduced *in situ* at 623 K, ramped up at a rate of 1 K min^{-1} under 10% H_2/He flow (80 cm^3 min^{-1} at standard temperature and pressure) for 4h, and cooled down to the reaction temperature under He flow.

The experiments were performed at atmospheric pressure. Gas flowrates were regulated at the reactor inlet with calibrated mass flow controllers. FA, introduced using a syringe pump (Chemyx Inc.) as a liquid, was vaporized at the inlet of the reactor, and carried by He. The reactor temperature was measured using a K-type thermocouple and regulated by a furnace connected using a temperature controller.

The residual FA was condensed by passing the reactor effluent gas stream through a condenser. At steady state, the composition of CO and CO_2 in the effluent stream was used to determine the reaction rate for the dehydration and dehydrogenation pathways, respectively. The carbon balance was satisfied within 99-99.5% by measuring the decomposition products CO/CO_2 and the condensed residual FA. A gas chromatograph with a thermal conductivity detector (GC-TCD) was employed to quantify the concentration of the decomposition products. The conversion was

calculated based on the moles of reactant FA converted to the decomposition products CO and CO_2, and was maintained below 10% for all experiments in order to collect data in the kinetically limited regime. Further, we used the GradientCheck[130] tool to ensure the absence of thermal gradients and diffusion limitations in our reactor setup.

To determine the apparent activation energy barrier for the dehydrogenation and dehydration pathways, the reaction temperature was varied between 358 and 378 K. To determine the apparent reaction orders with respect to the reactant (HCOOH) and products (CO, CO_2, H_2, H_2O), the partial pressures were varied between 1-5% for FA, 0-10% for the dehydrogenation products (H_2 and CO_2), and 0-0.1% for the dehydration products (H_2O and CO), with He as the balance gas.

3.2.2.2 Catalyst Characterization

The Pt/C catalyst was characterized using CEOS (Corrected Electron Optical Systems) probe aberration corrected-scanning transmission electron microscopy (FEI-Titan STEM) with a spatial resolution of <0.1 nm, operated at 200 kV. The images were collected in high-angle annular dark field (HAADF) mode with a probe current of approximately 25 pA, probe convergence angle of 24.5 mrad, and detector angle ranging from 54 to 270 mrad. The samples were suspended in ethanol, deposited on holey carbon Cu grid, and plasma cleaned before loading into the microscope. Approximately, 2000 particles were analyzed from different regions in the catalyst sample, using the ImageJ software for determining the particle size distribution. The reported average particle size was calculated by sum normalizing the particle diameters of the Pt nanoparticles (Average particle size: 2.16 ± 0.65 nm – Figure C.1)

The surface site density for the catalyst sample was determined by performing CO chemisorption at 298 K using the Micromoretics ASAP 2020C. The catalyst sample was reduced *in situ* using the procedure described earlier for the reaction kinetics experiments. We assume the adsorption stoichiometry between CO and Pt to be 1:1, as reported previously.[131,132]

3.2.3 Microkinetic Modeling

We modeled the reactor as a continuous stirred tank reactor (CSTR), given the low per pass conversion (<10%) for our experimental dataset. In addition, to verify the applicability of a CSTR model, we used the optimized CO*-coverage dependent energetics and also simulated a plug flow reactor (PFR). Results from the PFR model demonstrate that the coverage profiles stabilize to within 10% of the coverages predicted by the CSTR model, in the initial portion (~3%) of the PFR's length (Appendix C). Therefore, we conclude that CSTR offers a good approximation for modeling the kinetics of FA decomposition on Pt catalysts.

To account for temperature corrections on the energetics of the reaction network, ideally *ab initio* molecular dynamics (AIMD) simulations would be desirable. However, given the impractical computational cost of such calculations and the complexity of the reaction network, we here calculate the energetics using static DFT calculations, and then introduce temperature corrections to gas phase species, adsorbed species and transition states by performing vibrational frequency calculations. ZPE-corrected energetics (thermochemistry and kinetics) were used to parameterize the microkinetic models presented in this study. The model formulation procedure was similar to that employed in our previous studies.[41] To incorporate temperature dependent energetics, Shomate parameters fit using the vibrational frequency calculations together with statistical mechanical equations,[12] were used in our models. The decomposition reaction (dehydrogenation

and dehydration) energies and entropy values of the gas-phase species, as calculated from Shomate parameters, were compared with the values from NIST.[12,14,133,134] By adjusting the enthalpy of CO(g) and HCOOH(g) by -0.28 eV and 0.06 eV, respectively, we are able to achieve good agreement with the values corresponding to the FA dehydrogenation and dehydration reaction energies. Further, the entropy values of CO(g) and HCOOH(g) also required adjustment by -22.3 J/mol/K and -28.5 J/mol/K, respectively, to obtain agreement with the NIST values. The optimized gas-phase energetics were used to perform parameter estimation. The reported corrections correspond to the changes after the gas-phase energy adjustments, unless explicitly specified.

In our models, we considered a reaction network comprising of 6 gas-phase species, 14 surface species and ~25 elementary steps (some steps were omitted on the 4/9 ML CO*-covered facets, because they had high activation energy barrier on the clean surface). DFT was used to derive thermochemistry and kinetic rate constant parameters (both – activation energy and pre-exponential) for these elementary steps on Pt(100) and Pt(111). Since models formulated using the unadjusted DFT-derived energetics did not fit the experimental kinetics dataset, parameter estimation was performed using the sequential optimization framework developed by Rangarajan et al.[41] The objective function ($Z_{Param,Est}$) comprised of normalized squared residuals corresponding to the model-experiment mismatch, summed over all experimental conditions 'c', and a term penalizing the corrections from DFT-derived energetics ($\pi - \pi_{DFT}$) , i.e., the binding and transition-state energies, so that the optimizer only allows as few parameters to have non-zero values as necessary. Parameter (δ) is a constant, prechosen at 0.05 in our study, and which modulates the contribution of the corrections to the objective function. The DFT-derived binding and transition-state energies (π-π_{DFT}) were allowed to deviate in a ±0.6 eV range during the

parameter estimation procedure. By minimizing the objective function, we search for a set of corrections from the DFT energetics, that would yield agreement of the model predicted turnover frequencies (TOF), for the dehydrogenation and dehydration pathways, '$\overline{y}$' with the experiment 'y', while allowing for correction of only the sensitive energetic parameters from their nominal values.

$$\mathrm{Z}_{Param.Est} = Min \sum_{c \in C} \left(1 - \frac{\overline{y_c}}{y_c}\right)^T \left(1 - \frac{\overline{y_c}}{y_c}\right) + \delta(\pi - \pi_{DFT})^T(\pi - \pi_{DFT}) \qquad (3.2)$$

We employed a multi-start approach through Latin Hypercube sampling,[135,136] with ~500 randomized initial guesses for corrections to the DFT parameters to comprehensively sample multiple local minima and thereby identify plausible alternate solutions. For models, where we find multiple solutions that can explain the experiments, we explicitly mention the number of unique solutions determined using the Latin-hypercube sampling based multi-start approach and discuss each of the solutions separately.

Rate constants for surface reaction steps were derived from transition-state theory, whereas that for the adsorption/desorption steps were calculated using collision theory. The sticking coefficients for these steps were varied in a range of 0.01-1 and were found to have no effect on the model predicted fluxes. The adsorption and desorption steps were, therefore, assumed to be quasi-equilibrated. In the results and discussion section, negative and positive corrections to the binding energy of adsorbates are often referred to as stabilization and destabilization, respectively. For the elementary steps, we report the net corrections in the activation energy barriers by considering the changes in the transition state energies as well as binding of the corresponding adsorbates involved in the initial state, as required by our parameter estimation procedure. While looking for favorable solutions, we examined the models by ranking them based on objective function values to ensure

model-experiment parity. For the promising solutions, we then checked, if the corrections for net changes in activation energy barriers are within the typically accepted ± 0.2 eV error bars[42,122,137–139] and if the resulting coverages are consistent with the environment of the active site as represented in the DFT calculations the parameters had been derived for.

The partially CO*-covered facet models were formulated using the Shomate parameters derived on Pt(100) and Pt(111) covered with 4/9 ML of spectator CO*. For these models, wherein we explicitly account for the effect of 4/9 ML of CO* spectators, we formulate our models using energetics of the most stable adsorption configuration for all reaction intermediates and the lowest transition state energy for all elementary steps. These models are labeled as 4/9 ML CO*-covered Pt(111)/Pt(100) in our study. In addition, the variation of the lateral adsorbate-adsorbate interactions due to CO* coverage levels on the thermochemistry and kinetics were explicitly included as polynomial-functions dependent on CO* coverage (Table C.4 and Table C.5). These functions ensured that the calculated binding energy of the respective species on the clean slab (no coadsorbed CO*) was captured correctly. To obtain these polynomial expressions, we performed DFT calculations at varying CO* coverage levels. We evaluated the binding energy of all the adsorbates on the clean surface (i.e., no coadsorbed CO*), as well as in the presence of 3/9, 4/9, and 5/9 ML of coadsorbed CO* spectator species, to capture changes in stability of the intermediates as a function of CO* coverage. The transition-state energies for elementary steps were calculated on the clean surface and on a 4/9 ML CO*-covered surface to determine the effect of CO* coverage on the activation energy barriers. The obtained polynomial expressions (for binding energies and transition-state energies) were incorporated into our microkinetic model, to update the energetics, per the model predicted CO* coverage during the simulations and in order

to use energetics consistent with the CO* coverage predicted by the model. For the presented microkinetic models, we examined the model predicted reaction pathways under our defined *home* conditions (2.6% FA, balance He, 373K), as well as under the CO-cofeed conditions (2.6% FA, 0.025 – 0.1% CO, balance He, 373K). These models speak clearly to the importance of explicitly including: (i) coverage effects on energetics and (ii) spectator-mediated elementary reaction steps.

3.3 Results and Discussion

3.3.1 DFT Study

We first discuss the reaction network on clean Pt(111) and Pt(100) surfaces, followed by a discussion of the respective results on a 4/9 ML CO*-covered Pt surfaces, which we determined better represented the surface of the catalyst under reaction conditions.

3.3.1.1 Clean Pt(111) and Pt(100)

The most stable binding configurations of all relevant species on the clean Pt(111) and Pt(100) surfaces are presented in Figure 3.1 and Figure 3.2, respectively, with the corresponding BE values and most-stable adsorption site reported in Table 3.1. Starting from FA, we studied the reaction network by considering the O-H and C-H bond breaking, to form the isomers HCOO* and trans-COOH* (referred to as COOH* for brevity), respectively, and the C-O bond breaking to form the formyl (HCO*) intermediate. The calculated energetics for the entire reaction network, comprised of 27 elementary steps, is provided in Table 3.2 and the potential energy diagrams (PEDs) for the entire catalytic cycle accounting for both dehydrogenation (CO_2+H_2) and dehydration (CO+H_2O) pathways on clean Pt(111) and Pt(100) surfaces are provided in Figure 3.3 and Figure 3.4, respectively.

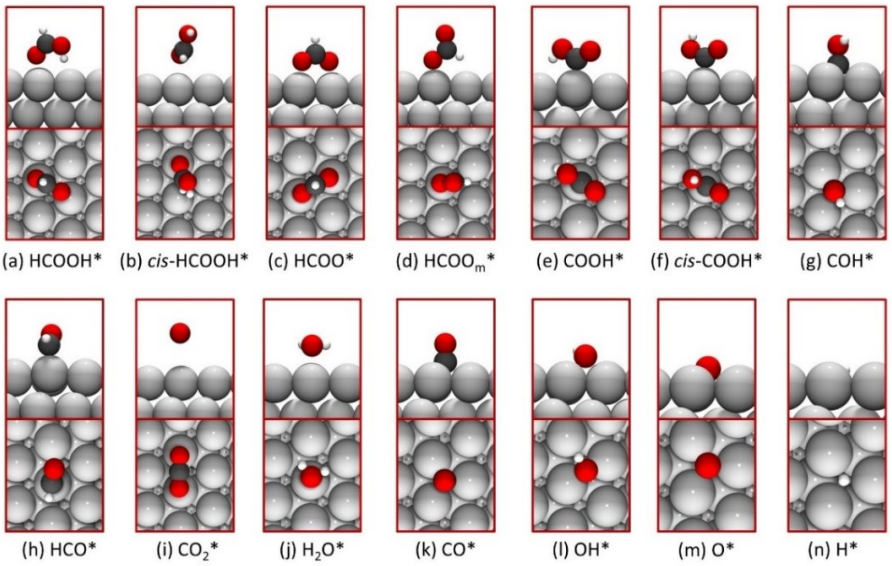


Figure 3.1 Side and top views of the most stable structures of reaction intermediates on clean Pt(111). Platinum, carbon, hydrogen, and oxygen atoms are shown as silver, black, white, and red spheres, respectively.

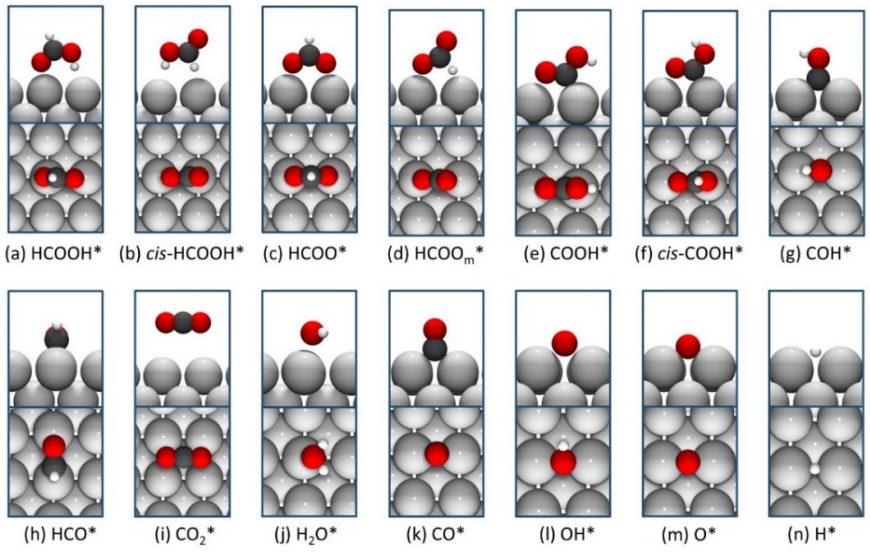


Figure 3.2 Side and top views of the most stable structures of reaction intermediates on clean Pt(100). Platinum, carbon, hydrogen, and oxygen atoms are shown as silver, black, white, and red spheres, respectively.

Table 3.1 Calculated binding energies (BE) of reactants, products, and reaction intermediates at their preferred adsorption structures on Pt(111) and Pt(100).

Species	Pt(111)		Pt(100)	
	adsorption site	BE / eV	adsorption site	BE / eV
HCOOH*	top-top	-0.34	top-top	-0.50
cis-HCOOH*	top-top	0.01	top-top	-0.04
HCOO*	top-top	-2.28	top-top	-2.58
$HCOO_m$*	top	-1.47	top-top	-1.85
COOH*	top-top	-2.37	top-top	-2.71
cis-COOH*	top	-2.26	top-top	-2.61
COH*	fcc	-4.73	bridge	-4.75
HCO*	top	-2.44	top-top	-2.69
CO_2*	physisorbed	-0.04	physisorbed	-0.04
H_2O*	top	-0.25	top	-0.31
CO*	fcc	-1.80	bridge	-2.07
OH*	bridge	-2.32	bridge	-2.96
O*	fcc	-4.29	bridge	-4.35
H*	fcc	-2.78	bridge	-2.89

Table 3.2 Calculated activation energy barriers (EA) and reaction energies (ΔH) for the elementary steps considered in the HCOOH decomposition reaction network on clean Pt(111) and Pt(100). All the values are relative to the best initial/final states and infinite separation (*except #22 for Pt(111) and #24 for Pt(100), which are reported with respect to the co-adsorbed initial states, since the coadsorbed states are stabilized through hydrogen bonding)

	Elementary Step	Pt(111)		Pt(100)	
		E_A / eV	ΔH / eV	E_A / eV	ΔH / eV
1	HCOOH(g) + * ↔ HCOOH*	0.00	-0.34	0.00	-0.49
2	CO_2(g) + * ↔ CO_2*	0.00	-0.04	0.00	-0.04
3	CO(g) + * ↔ CO*	0.00	-1.80	0.00	-2.07
4	H_2O(g) + * ↔ H_2O *	0.00	-0.25	0.00	-0.31
5	HCOOH* + 2* ↔ HCOO* + H*	0.59	-0.03	0.51	-0.29
6	HCOO* ↔ $HCOO_m$* + *	1.06	0.81	1.13	0.73
7	$HCOO_m$* + * ↔ CO_2* + H*	0.00	-1.30	0.00	-1.04
8	HCOOH* ↔ *cis*-HCOOH*	0.75	0.35	0.75	0.45
9	*cis*-HCOOH* ↔ COOH* + H*	0.36	-0.77	0.12	-1.19
10	COOH* + * ↔ CO_2* + H*	0.73	-0.10	0.96	0.13
11	COOH* ↔ *cis*-COOH*	0.47	0.11	0.49	0.10
12	*cis*-COOH* ↔ CO* + OH*	0.61	0.12	0.57	-0.44
13	*cis*-HCOOH* ↔ HCO* + OH*	0.73	0.44	0.21	-0.41
14	H* +H* ↔ H_2(g) + 2*	1.02	1.00	1.23	1.23
15	OH* + H* ↔ H_2O* + *	0.94	0.61	0.78	-0.08
16	COOH* + CO* ↔ COH* + CO_2*	0.65	0.45	1.25	1.06
17	COH* + * ↔ CO* + H*	0.93	-0.55	0.91	-0.93
18	COH* + CO* ↔ HCO* + CO*	1.22	0.43	1.17	0.19
19	HCO* + * ↔ CO* + H*	0.32	-0.98	0.38	-1.12
20	CO* + O* ↔ CO_2* + *	1.18	-0.32	0.75	0.01
21	OH* + * ↔ O* + H*	1.04	0.00	0.98	0.47
22	OH* + OH* ↔ H_2O* + O*	0.02*	-0.61	0.23	0.54
23	HCOO* + * ↔ HCO* + O*	1.85	0.82	--	0.80
24	HCOO* + CO* ↔ HCOOCO*	1.23	1.22	--	--
25	HCOOCO* ↔ HCO* + CO_2*	0.32	-0.73	--	--
26	COOH* + O* ↔ CO_2* + OH*	0.36	-0.10	0.02*	-0.33
27	COOH* + CO* ↔ CO_2* + HCO*	0.65	0.89	--	1.25

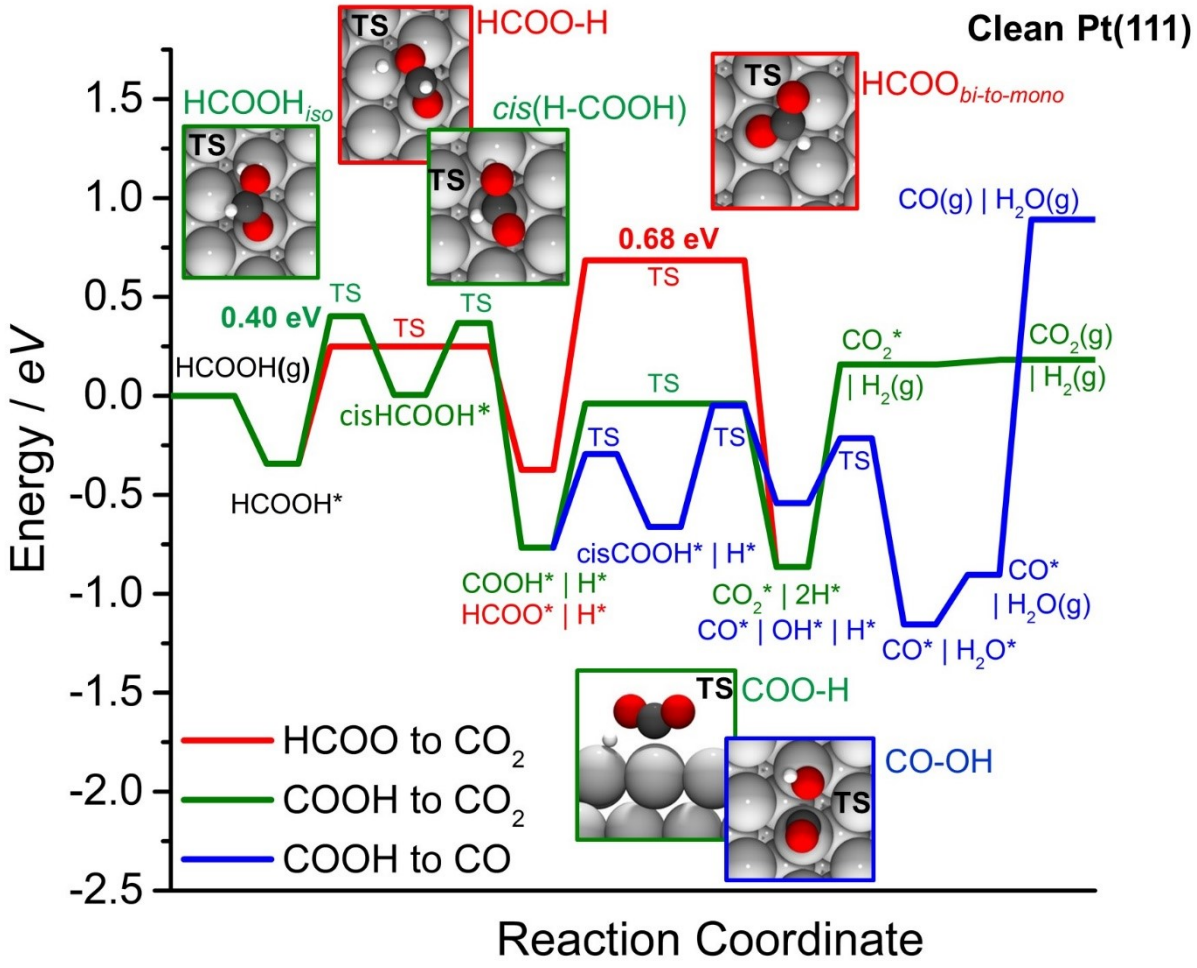


Figure 3.3 Potential Energy Diagram of FA decomposition on clean Pt(111). The HCOO*-pathway and COOH*-pathway leading to CO_2+H_2, and the COOH*-pathway leading to CO+H_2O are represented with red, green, and blue lines, respectively. Energy zero corresponds to gas phase FA and clean Pt(111) slab at infinite separation. All the transition states (TS) for the HCOO*-pathway to form CO_2+H_2 and the COOH*-pathway to form CO_2+H_2 and CO+H_2O are marked with TS. Along the minimum energy paths, the highest TS energy values in both the HCOO*- and COOH*-paths are given by the green/red numbers (in eV). Structures of the TS's are shown in the insets, are marked with 'TS', and the corresponding bond-breaking step is given by the text nearby (e.g., HCOO-H indicates the TS for O-H bond breaking step in HCOOH). Color code for structures presented in the inset: White - H, Red - O, Dark Gray - C, Silver - Pt.

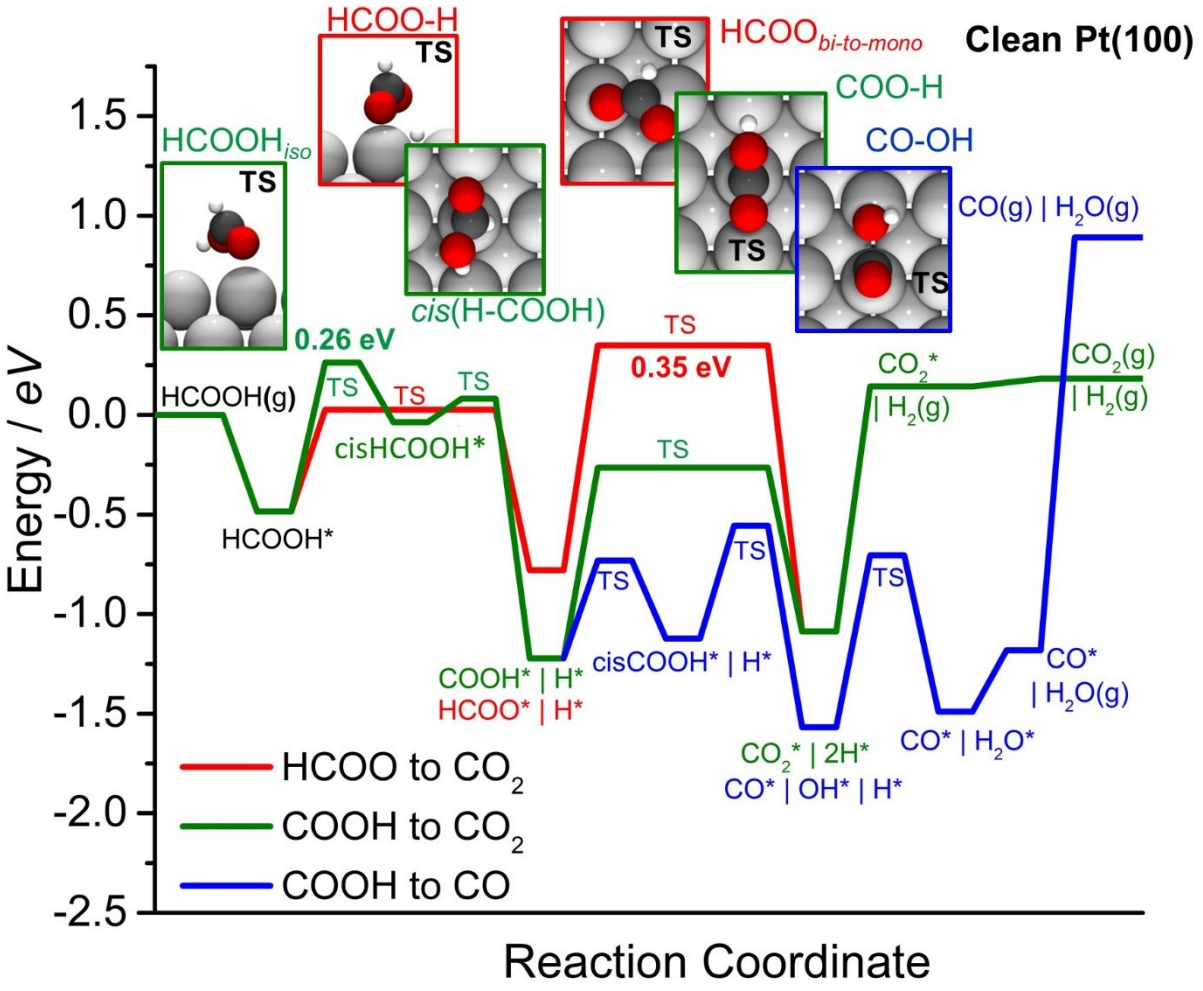


Figure 3.4 Potential Energy Diagram of FA decomposition on clean Pt(100). The HCOO*-pathway and COOH*-pathway leading to CO_2+H_2, and the COOH*-pathway leading to CO+H_2O are represented with red, green, and blue lines, respectively. Energy zero corresponds to gas phase FA and clean Pt(100) slab at infinite separation. All the transition states (TS) for the HCOO*-pathway to form CO_2+H_2 and the COOH*-pathway to form CO_2+H_2 and CO+H_2O are marked with TS. Along the minimum energy paths, the highest TS energy values in both the HCOO*- and COOH*-paths are given by the green/red numbers (in eV). Structures of the TS's are shown in the insets, are marked with 'TS', and the corresponding bond-breaking step is given by the text nearby. (e.g., HCOO-H indicates the TS for O-H bond breaking step in HCOOH). Color code for structures presented in the inset: White - H, Red - O, Dark Gray - C, Silver - Pt.

FA (*trans*-HCOOH*, referred to as HCOOH* for brevity) binds to the clean Pt(111) surface in a perpendicular configuration with a BE of -0.34 eV. The molecule sits on two adjacent Pt atoms with the carbonyl O and O-H pointing towards the surface. FA binds to the clean Pt(100) in a similar configuration but the interaction is stronger (BE = -0.50 eV). Starting with these configurations, the O-H bond breaks to form formate (HCOO*) with an activation energy barrier of 0.59 eV for the (111) and 0.51 eV for the (100) facet. The respective reaction energy is -0.03 eV and -0.29 eV, respectively. Formate binds on two adjacent Pt atoms in a bidentate configuration, with BE of -2.28 eV and -2.58 eV on Pt(111) and Pt(100), respectively. Subsequent decomposition of the formate intermediate involves its reorientation from the bidentate to a monodentate configuration ($HCOO_m$*), which binds through one O atom and the C-H bond pointing toward the surface. This intermediate has been identified spectroscopically.[112,140,141] The rotation from bi- to mono-dentate formate is activated with a barrier of 1.06 eV and 1.13 eV, on the Pt(111) and Pt(100), respectively. This elementary step is endothermic by 0.81 and 0.73 eV, on (111) and (100) respectively, and its transition state is the highest point on the PED for the HCOO*-pathway (Figure 3.3 and Figure 3.4 - red lines). On both surfaces, $HCOO_m$* undergoes spontaneous dehydrogenation to form CO_2*.

Formation of carboxyl (COOH*) from FA has been suggested to occur through the *cis*-HCOOH* isomer of FA, formed upon the rotation of the O-H bond.[106,107] This isomerization step of adsorbed FA (HCOOH*) is endothermic on the (111) and (100) facets by 0.35 and 0.45 eV, respectively, and is characterized by an activation energy barrier of 0.75 eV on both the facets. On both surfaces, the isomerization step possessed the highest transition state energy in the entire PED for the COOH*-pathway (Figure 3.3 and Figure 3.4). The *cis*-HCOOH* interacts weakly with the Pt

surface, with a BE of 0.01 eV on (111) and -0.04 eV on (100). Breaking the C-H bond in *cis*-HCOOH*, has an activation energy barrier of 0.36 and 0.12 eV on (111) and (100), respectively, and leads to adsorbed carboxyl (COOH*). The COOH* intermediate then undergoes a dehydrogenation step to form CO_2* + H*, with an activation energy barrier of 0.73 eV and 0.96 eV, on (111) and (100), respectively. Alternatively, the COOH* intermediate can first isomerize to *cis*-COOH* and then lose its OH to form CO*. The isomerization and dehydroxylation steps have an activation energy barrier of 0.47 eV and 0.61 eV, respectively, on Pt(111), and 0.49 eV and 0.57 eV, respectively, on Pt(100).

Next, we compare the HCOO*- and COOH*-pathways as illustrated in Figure 3.3 and Figure 3.4. On both Pt(111) and Pt(100) surfaces, the formation of HCOO* is kinetically less activated than the formation of its isomer (COOH*) by 0.16 eV and 0.24 eV, respectively. On Pt(111) and Pt(100), carboxyl (COOH*) is more stable than formate (HCOO*) by 0.38 eV and 0.45 eV, respectively. The dehydrogenation of COOH* is, however, energetically much easier than that of HCOO* on both surfaces. Based on the highest point on the PED for the dehydrogenation route, the COOH*-pathway is favored by 0.28 eV and 0.09 eV on the (111) and (100) facet, respectively, compared with the HCOO*-pathway. Given a smaller energetic difference (within the DFT error) on Pt(100), we would expect both format- and carboxyl-mediated pathways to be contributing toward the dehydrogenation reaction. Comparing the PED on Pt(111) and Pt(100), for the most stable dehydrogenation route (COOH*→CO_2*, on both facets), Pt(100) is characterized by more stable energetics (since, the highest point in the PED for (100) lies below that for (111)) and thus would be predicted to be more active than Pt(111), based on a PED analysis alone.

We then turn our attention to reaction selectivity. Based on PEDs alone, on Pt(100), the COOH* intermediate prefers to decompose to CO*, whereas on Pt(111), COOH* is equally likely to decompose to CO* or CO_2*. Further, given the large desorption barrier of CO*, one can expect its buildup on both the surfaces, which is consistent with experimental findings.[118,120,121]

Thus, based on our DFT results on clean Pt(111) and Pt(100), we arrive at the following conclusions: (1) On both facets, formation of COOH* is more activated than formation of HCOO*; however, COOH* decomposition to CO_2 is energetically favorable. (2) On both facets, transformation of HCOOH* to *cis*-HCOOH* and HCOO* to monodentate $HCOO_m$* serve as the highest point in the PED for the COOH*- and HCOO*-pathways, respectively. (3) For the dehydrogenation reaction, the COOH*-pathway is more favorable than the HCOO*-pathway on both facets. (4) On Pt(111), COOH* is equally likely to decompose to CO* and CO_2, whereas COOH* preferentially decomposes to CO* on Pt(100). (5) Although Pt(100) is expected to be more reactive than Pt(111), it is also more prone to CO* poisoning due to: (i) preferential decomposition of COOH* to CO* and (ii) higher desorption barrier of CO* compared to that on Pt(111).

3.3.1.2 4/9 ML CO-Covered Pt(111) and Pt(100)*

Determining the most-stable arrangement of reaction intermediates in the presence of spectator CO* species is a high dimensionality search problem. To tackle this challenge, we developed an algorithm and the associated in-house code to automatically generate and rigorously sample configurations of reaction intermediates in the presence of spectator species. For each unique adsorption structure of the reaction intermediate, we initialize the position of the spectator CO* species using Latin-hypercube sampling. The structures are then examined to ensure that there is

no overlap of atoms with their periodically repeated images. The spectators are then moved to their nearest high-symmetry positions (top, bridge, fcc, or hcp sites for (111) and top, bridge, or four-fold hollow sites for (100)) and coarsely optimized in the z-direction. Each generated structure is then assigned a set of three geometric descriptors: (1) site-occupancy of the spectator species ('top', 'fcc', etc), (2) spectator-spectator distances, and (3) spectator-reaction intermediate distances. These descriptors are then used to eliminate repeated structures. To ensure that all possible unique structures are generated, we incrementally increase the number of structures to be generated, until no new unique configurations are identified. Each of these unique structures are then optimized using DFT to elucidate most stable adsorption configuration of the reaction intermediate in the presence of CO* spectators. Post optimization, we sort all these structures in decreasing order of their stability. To determine the lowest energy transition-state, we then perform nudged elastic band (NEB) calculations starting from all structures, which are within ~0.3 eV of the most stable adsorption configuration. Typically, to determine the most stable adsorption and transition-state configurations, at every coverage level of CO*, we elucidate hundreds of adsorption configurations for each reaction intermediate and perform ~4-7 NEB calculations for each elementary step.

The most stable adsorption configurations of the intermediates on 4/9 ML CO*-covered Pt(111) and Pt(100) surfaces are shown in Figure 3.5 and Figure 3.6, respectively, and the corresponding BEs are summarized in Table 3.3. The presence of coadsorbed 4/9 ML CO*-spectator species destabilizes the binding of key reactive intermediates.

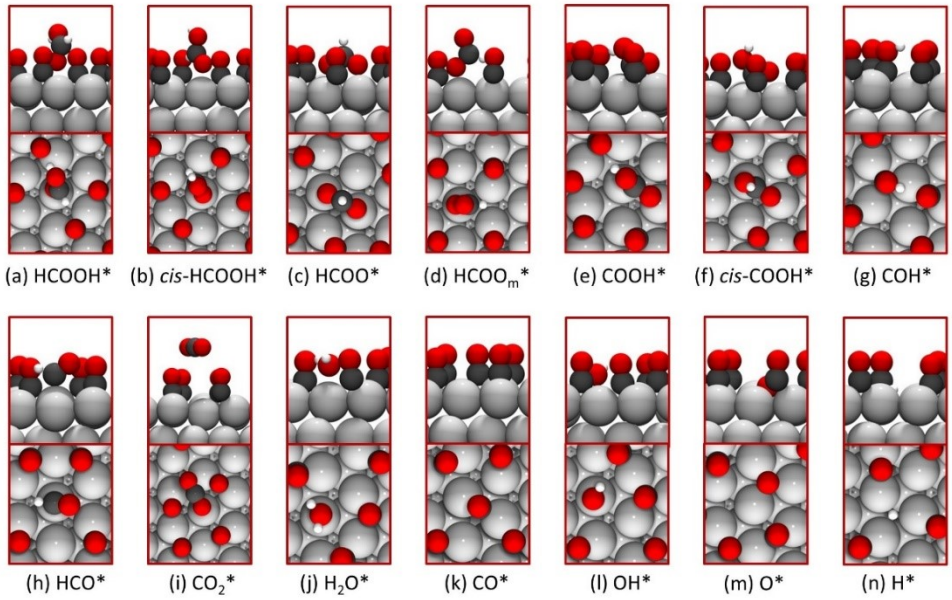


Figure 3.5 Side and top views of the most stable structures of intermediates on the 4/9 ML CO*-covered Pt(111). Platinum, carbon, hydrogen, and oxygen atoms are indicated by silver, black, white, and red, respectively.

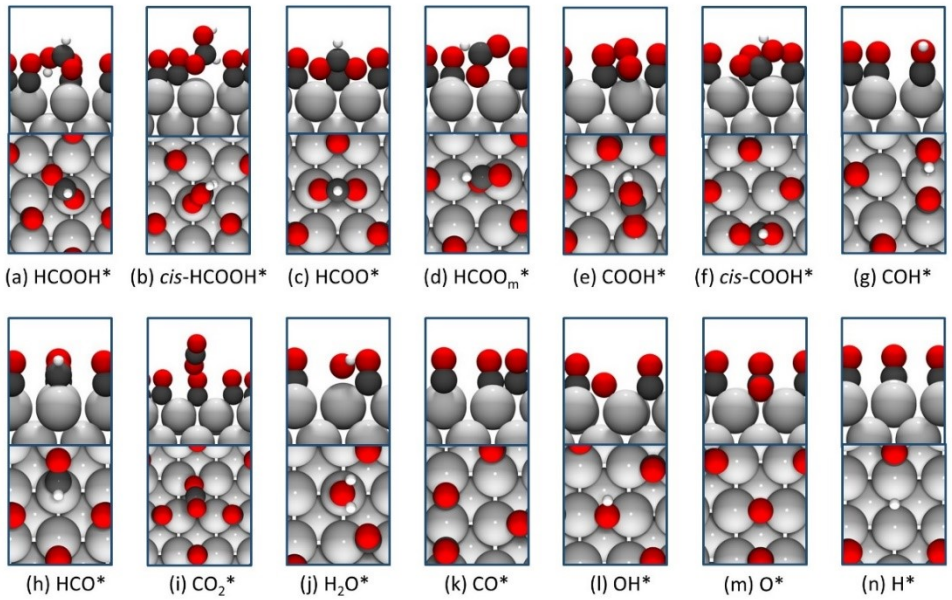


Figure 3.6 Side and top views of the most stable structures of reaction intermediates on the 4/9 ML CO*-covered Pt(100). Platinum, carbon, hydrogen, and oxygen atoms are indicated by silver, black, white, and red, respectively.

Table 3.3 Calculated binding energies (BE) at their preferred adsorption configuration on 4/9 ML CO*-covered Pt(111) and Pt(100).

Species	4/9 ML CO* Pt(111)		4/9 ML CO* Pt(100)	
	adsorption site	BE / eV	adsorption site	BE / eV
HCOOH*	top	-0.16	top-top	-0.35
cis-HCOOH*	top	-0.01	top-hollow	-0.02
HCOO*	top-top	-1.92	top-top	-2.24
$HCOO_m$*	top	-1.07	top	-1.54
COOH*	top-top	-1.92	top-top	-2.34
cis-COOH*	top-top	-1.82	top-top	-2.27
COH*	fcc	-4.25	bridge	-4.57
HCO*	top	-2.03	top-top	-2.23
CO_2*	physisorbed	-0.03	physisorbed	0.05
H_2O*	top	-0.32	top	-0.45
CO*	bridge	-1.20	bridge	-1.70
OH*	top	-2.01	bridge	-2.63
O*	fcc	-3.77	bridge	-4.00
H*	fcc	-2.63	bridge	-2.76

Table 3.4 Calculated activation energy barriers (E_A) and reaction energies (ΔH) for the elementary steps considered in the HCOOH decomposition reaction network on 4/9 ML CO*-covered Pt(111) and Pt(100). All the values are relative to the best initial/final states and infinite separation. The spectator CO* is indicated in bold in relevant elementary steps.

	Elementary Step	4/9 ML CO* Pt(111)		4/9 ML CO* Pt(100)	
		E_A /	ΔH / eV	E_A / eV	ΔH / eV
1	$HCOOH(g) + * \leftrightarrow HCOOH*$	0.00	-0.16	0.00	-0.35
2	$CO_2(g) + * \leftrightarrow CO_2*$	0.00	-0.03	0.00	0.00
3	$CO(g) + * \leftrightarrow CO*$	0.00	-1.20	0.00	-1.70
4	$H_2O(g) + * \leftrightarrow H_2O*$	0.00	-0.32	0.00	-0.45
5	$HCOOH* + 2* \leftrightarrow HCOO* + H*$	0.92	0.90	0.74	0.04
6	$HCOO* \leftrightarrow HCOO_m* + *$	1.49	0.44	0.86	0.71
7	$HCOO_m* + * \leftrightarrow CO_2* + H*$	0.00	-1.14	0.00	-1.13
8	$HCOOH* \leftrightarrow$ *cis*-$HCOOH*$	0.49	0.15	0.54	0.34
9	*cis*-$HCOOH* \leftrightarrow COOH* + H*$	1.16	-0.15	0.52	-0.71
10	$COOH* + * \leftrightarrow CO_2* + H*$	0.96	-0.39	1.18	-0.01
11	$COOH* \leftrightarrow$ *cis*-$COOH*$	0.45	0.10	0.44	0.07
12	*cis*-$COOH* \leftrightarrow CO* + OH*$	0.73	0.57	0.72	-0.44
13	$H* + H* \leftrightarrow H_2(g) + 2*$	1.14	0.70	1.06	0.97
14	$OH* + H* \leftrightarrow H_2O* + *$	1.52	1.14	1.21	0.53
15	$COOH* + \mathbf{CO}* \leftrightarrow COH* + CO_2*$	0.63	-0.10	1.22	0.59
16	$COH* + * \leftrightarrow \mathbf{CO}* + H*$	1.51	-0.29	1.20	-0.60
17	$COH* + \mathbf{CO}* \leftrightarrow HCO* + \mathbf{CO}*$	1.02	0.35	0.91	0.47
18	$HCO* + * \leftrightarrow CO* + H*$	0.56	-0.64	0.51	-1.07
19	$CO* + O* \leftrightarrow CO_2* + *$	1.14	-1.42	0.79	-0.62
20	$OH* + * \leftrightarrow O* + H*$	1.47	0.36	1.23	0.62
21	$COOH* + O* \leftrightarrow CO_2* + OH*$	0.74	-0.75	0.92	-0.63
22	$OH* + \mathbf{CO}* \leftrightarrow HCO* + O*$	1.50	1.01	1.84	1.69
23	$OH* + \mathbf{CO}* \leftrightarrow COH* + O*$	1.14	0.65	1.86	1.21
24	$HCOO* + OH* \leftrightarrow HCOO_m* + OH* + *$	0.80	0.67	-	-
25	$HCOO* + H_2O* \leftrightarrow HCOO_m* + H_2O* + *$	0.83	0.53	-	-

Similar to the clean Pt surfaces discussed in the previous section, the *trans*-FA configuration (HCOOH*) is more stable than its *cis*-HCOOH* on both (111) and (100), with BEs of -0.16 eV and -0.35 eV, respectively. On 4/9 ML CO*-covered facets, *cis*-HCOOH* interacts weakly with a BE of -0.01 eV on Pt(111) and -0.02 eV on Pt(100), binding through the O-atom at the top-site with the C-H bond pointing downward toward the surface. On the 4/9 ML CO*-covered Pt(111), both the HCOO* and COOH* species bind with a BE of -1.92 eV. However, COOH* is more stable than its isomer HCOO* by 0.31 eV. The HCOO* intermediate binds through its two O atoms in a bidentate configuration, while COOH* interacts through the C and the O atoms on adjacent top-sites with the O-H bond pointing toward the O atom of a spectator CO* molecule. The *cis*-COOH* intermediate, however, binds through its C and O atoms to adjacent top-sites with the O-H bond pointing away from the surface, though weaker by 0.1 eV than its *trans*-isomer (COOH*). The hydroxymethylidyne intermediate (COH*) binds on a fcc-site through its C atom with a BE of -4.25 eV, with the O-H bond pointing toward a nearby spectator CO* molecule. The isomer formyl (HCO*) prefers a top site with a BE -2.03 eV.

In the presence of 4/9 ML CO* coverage, intermediates bind consistently more strongly to Pt(100) than to Pt(111). On the 4/9 ML CO*-covered Pt(100), COOH* binds through its C and O atoms on two adjacent top sites with a BE of -2.34 eV, whereas its isomer HCOO* binds in a bidentate configuration with a BE of -2.24 eV. In terms of total energy, however, COOH* is more stable than HCOO* by 0.40 eV in this environment. Similar to the *trans*-configuration (COOH*), *cis*-COOH* binds on two adjacent top sites through its C and O atoms, with a BE of -2.27 eV. The isomers COH* and HCO* prefer to bind to bridge (BE = -4.57 eV) and top-sites (BE = -2.23 eV) respectively.

At CO* coverage of 4/9 ML, we considered a slightly reduced subset of the reaction network that we studied on the clean surface. We specifically did not include some of the elementary steps that required a high activation energy barrier on the clean surface (eg. steps 23-25 and 27 in Table 3.4). Instead, some additional steps which include the participation of CO* spectators were considered at the 4/9 ML CO* coverage models (eg. steps 22-23 in Table 3.4). The calculated activation energy barriers and reaction energies for all the elementary steps considered at the 4/9 ML CO*-covered Pt(111) and Pt(100) surfaces are presented in Table 3.4. Typically, the presence of spectator CO* species tends to destabilize the transition state energy of elementary steps.

Similar to the clean Pt(111), on the 4/9 ML CO*-covered Pt(111) formation of HCOO* is easier than that of COOH* (Figure 3.7). However, subsequent dehydrogenation of HCOO* is energetically much more unfavorable than dehydrogenation of COOH*, to form CO_2* and H*. Starting from HCOOH*, breaking the O-H bond to form formate (HCOO*) requires an activation energy barrier of 0.92 eV. Further dehydrogenation involves the rotation of the HCOO* species from bidentate to monodentate, which is the highest point in the PED (Figure 3.7, red lines), and requires an activation energy barrier of 1.49 eV. Formation of COOH* involves isomerization of HCOOH* to *cis*-HCOOH*, followed by the C-H bond breaking, which require an activation energy barrier of 0.49 eV and 1.16 eV, respectively, the latter step involving the highest point in the PED for the COOH*-pathway (Figure 3.7, green lines). Subsequent decomposition of COOH* to form CO_2* requires an activation energy barrier of 0.96 eV. The COOH* intermediate can alternatively decompose to CO* and OH*, after COOH* isomerizes to *cis*-COOH*. Although decomposition of COOH* to CO* and OH* is thermochemically favored, we note that the TS for the reaction between H* and OH* to form H_2O*, needed to complete the catalytic cycle, lies above

the TS for COOH*-dehydrogenation (Figure 3.7). The CO* desorption barrier on a 4/9 ML CO*-covered Pt(111) is reduced significantly to 1.20 eV (clean surface value 1.80 eV).

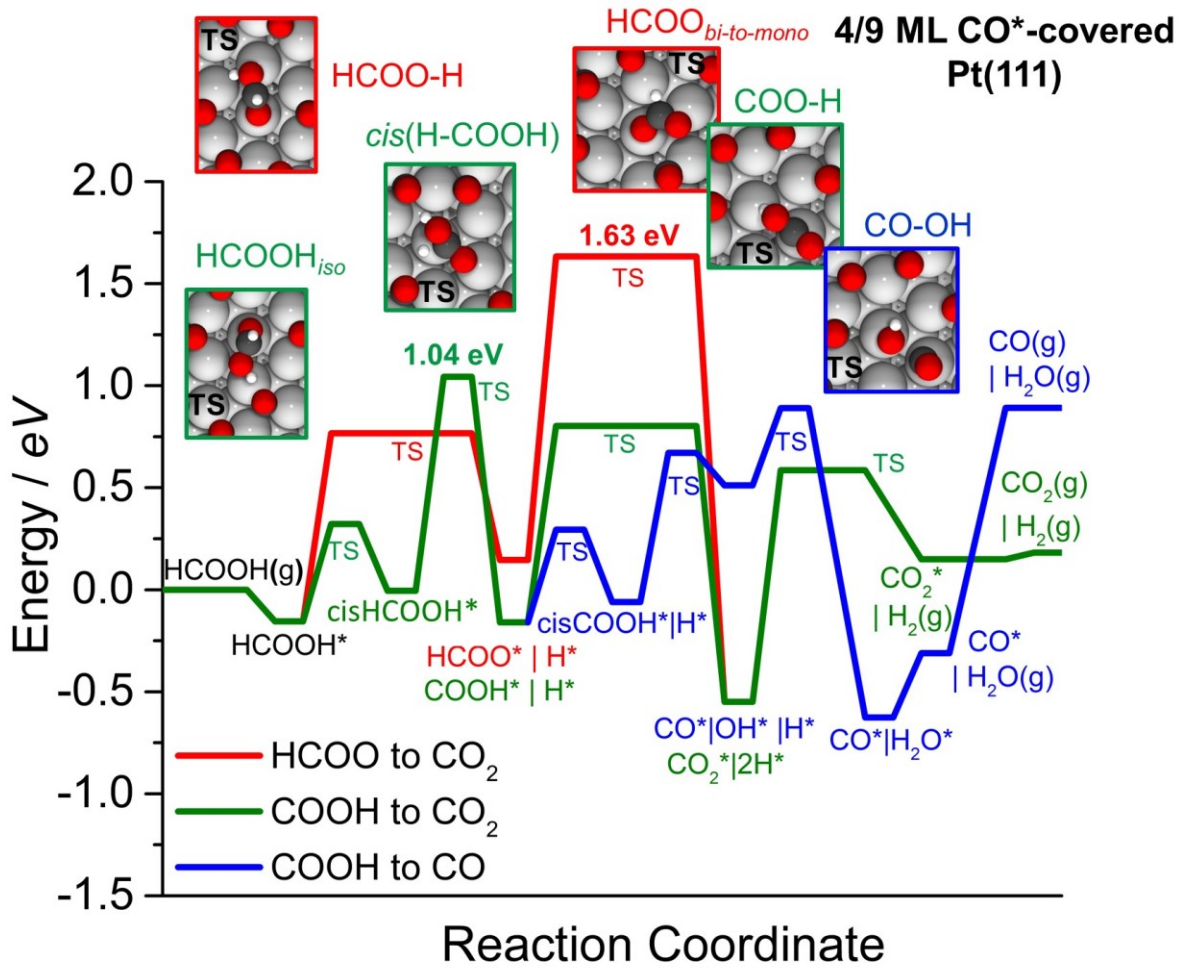


Figure 3.7 Potential Energy Diagram of FA decomposition on 4/9 ML CO*-covered Pt(111). The HCOO*-pathway and COOH*-pathway leading to CO_2+H_2, and the COOH*-pathway leading to CO+H_2O are represented with red, green, and blue lines, respectively. Energy zero corresponds to gas phase FA and 4/9 ML CO*-covered Pt(111) slab at infinite separation. All the transition states (TS) for the HCOO*-pathway to form CO_2+H_2 and the COOH*-pathway to form CO_2+H_2 and CO+H_2O are marked with TS. Along the minimum energy paths, the highest TS energy values in both the HCOO*- and COOH*-paths are given by the green/red numbers (in eV). Structures of the TS's are shown in the insets, are marked with 'TS', and the corresponding bond-breaking step is given by the text nearby (e.g., HCOO-H indicates the TS for O-H bond breaking step in HCOOH). Color code for structures presented in the inset: White - H, Red - O, Dark Gray - C, Silver - Pt.

On the 4/9 ML CO*-covered Pt(111), the dehydrogenation of COOH* by H-transfer to a spectator CO* molecule to form CO_2* and COH* has an activation energy barrier that is 0.33eV lower than the respective barrier for the direct decomposition of COOH* to CO_2* and H* (mechanism 1) (Figure 3.8). The COH* intermediate can then decompose to form H* and CO* (mechanism 2a) with an activation energy barrier of 1.51 eV, thus regenerating the spectator CO* molecule. Alternatively, the COH* can also decompose with the assistance of another spectator CO* molecule to form the HCO* intermediate, followed by its decomposition to form CO* and H* (mechanism 2b). As shown in the PED at 4/9 ML CO*-coverage (Figure 3.8) the decomposition of COOH* through this mechanism (COOH* + **2CO*** → CO_2* + COH* + **CO*** → CO_2* + CO* + H**CO*** → CO_2* + **2CO*** + H*, spectator CO* molecules indicated in bold) is energetically favored over the direct COOH* (COOH* → CO_2* + H*) or single CO*-assisted COOH* mechanism through COH* decomposition (COOH* + **CO*** → CO_2* + COH* → CO_2* + H* + **CO***). Since the TS energies of the highest point in each of these three pathways (Figure 3.8) is within DFT (GGA-PW91) error, we expect that all three decomposition routes (mechanisms 1, 2a, and 2b) may contribute under reaction conditions, with the exact flux varying, based on the CO* coverage and the experimental conditions.

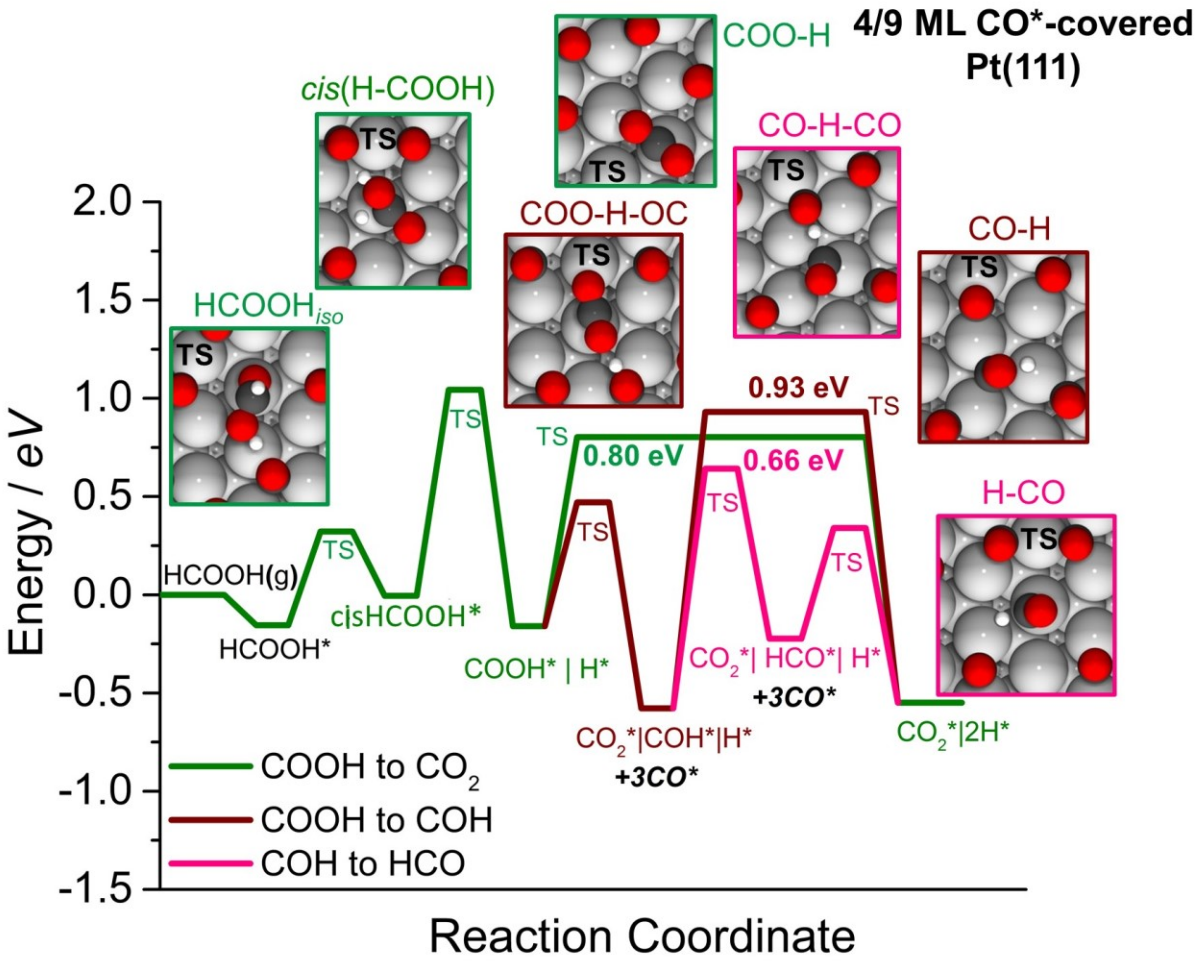


Figure 3.8 Potential Energy Diagram of FA decomposition through COOH* mediated pathways on 4/9 ML CO*-covered Pt(111) surface. Comparison for direct COOH* (mechanism 1), CO* spectator-assisted COOH* decomposition through COH* (mechanism 2a: COOH* (+**CO***) → CO_2* + **CO**H* → CO_2* + H* (+**CO***)) and COH→HCO* (mechanism 2b: COOH* (+**2CO***) → CO_2* + **CO**H* (+**CO***) → CO_2* + H**CO*** + **CO*** → CO_2* + H* (+**2CO***)) pathways are shown with green, brown, and pink lines, respectively. The spectator CO* molecules are indicated in bold in the scheme above. Energy zero corresponds to gas phase FA and 4/9 ML CO*-covered Pt(111) slab at infinite separation. All the transition states (TS) for the COOH*-pathway to form CO_2+H_2 are marked with TS. The TS energies corresponding to the highest point for COOH* dehydrogenation routes are reported by the numbers (in eV) in the figure. Structures of the TS's are shown in the insets, are marked with 'TS', and the corresponding bond-breaking step is given by the text nearby. Color code for structures presented in the inset: White - H, Red - O, Dark Gray - C, Silver - Pt.

On the 4/9 ML CO*-covered Pt(100), dehydrogenation through both HCOO*- and COOH*-mediated pathways is competitive (Figure 3.9). The highest point in the PED for the HCOO-pathway corresponds to the HCOO* transformation from the bidentate to the monodentate state (TS energy 0.55 eV). The highest point in the PED for the COOH-pathway corresponds to the TS for the formation of COOH* from *cis*-HCOOH* (TS energy 0.50 eV). Given such a small difference, we cannot rule out contribution from either path, and, therefore, HCOOH dehydrogenation through both pathways is likely. Regarding the selectivity between dehydrogenation and dehydration reactions on the 4/9 ML CO*-covered Pt(100): the COOH* intermediate will preferentially decompose to the dehydration product CO after transforming to *cis*-COOH* (Figure 3.9). The CO* desorption barrier from the 4/9 ML CO*-covered Pt(100) is 1.70 eV, implying significant CO* buildup on the surface at lower reaction temperatures.

CO* spectator-assisted decomposition of COOH* to form COH* + CO_2* has an activation energy barrier of 1.22 eV, and a reaction energy of 0.58 eV. Subsequently, COH* decomposes to CO* + H* with an activation energy barrier of 1.20 eV. Alternatively, COH* can also react with another CO* on the surface to form HCO* which then decomposes to CO* and H*, with activation energy barriers of 0.91 eV and 0.51 eV, respectively. Considering the endothermicity of H-transfer from COOH* to a spectator CO* and the large activation energy barrier (Table 3.4) associated with the subsequent spectator-assisted steps, we expect spectator-assisted mechanisms to be less favorable than the direct COOH*/HCOO* decomposition on the 4/9 ML CO*-covered Pt(100) surface.

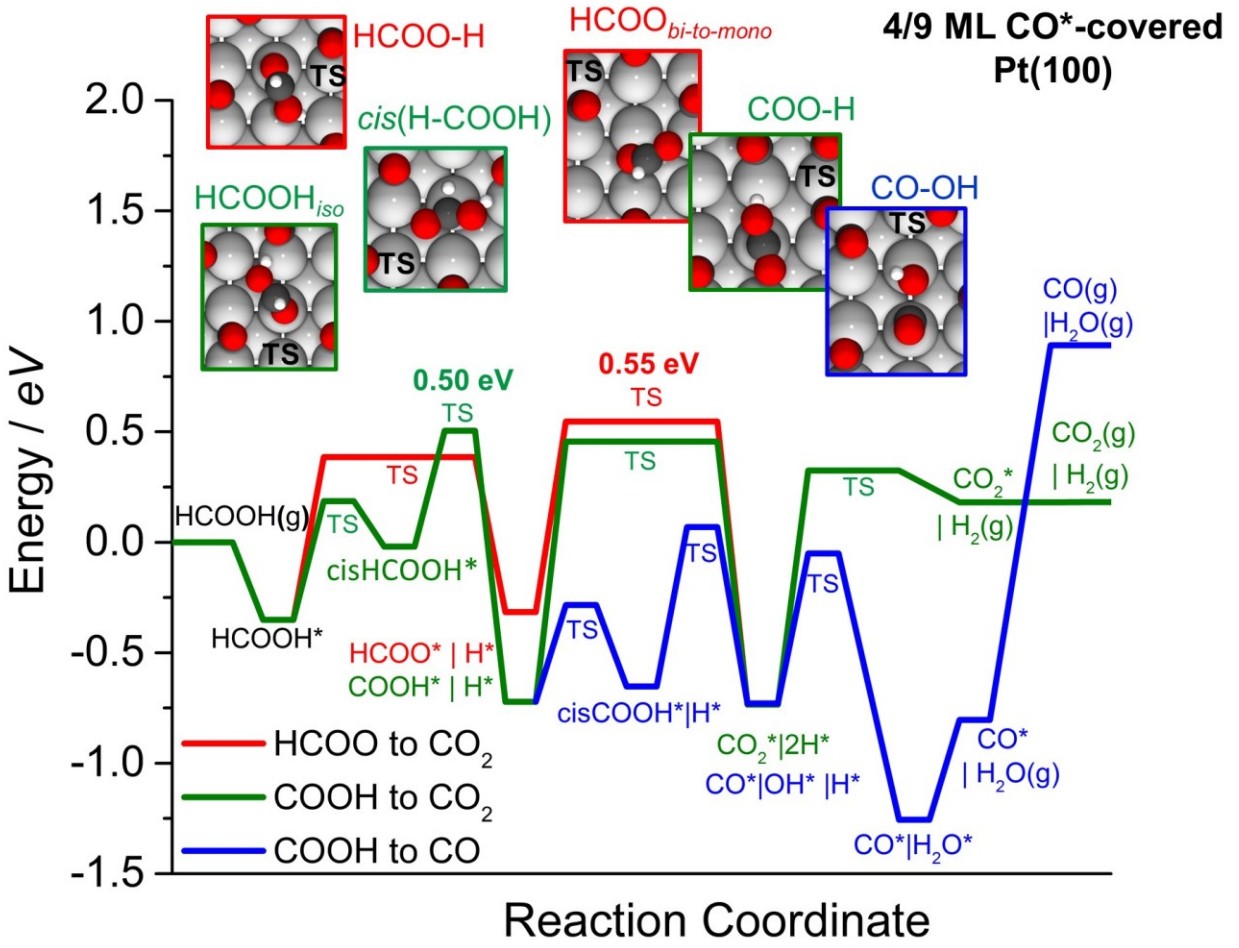


Figure 3.9: Potential Energy Diagram of FA decomposition on 4/9 ML CO*-covered Pt(100). The HCOO*-pathway and COOH*-pathway leading to CO_2+H_2, and the COOH*-pathway leading to CO+H_2O are represented with red, green, and blue lines, respectively. Energy zero corresponds to gas phase FA and 4/9 ML CO*-covered Pt(100) slab at infinite separation. All the transition states (TS) for the HCOO*-pathway to form CO_2+H_2 and the COOH*-pathway to form CO_2+H_2 and CO+H_2O are marked with TS. Along the minimum energy paths, the highest TS energy values in both the HCOO*- and COOH*-paths are given by the green/red numbers (in eV). Structures of the TS's are shown in the insets, are marked with 'TS', and the corresponding bond-breaking step is given by the text nearby (e.g., HCOO-H indicates the TS for O-H bond breaking step in HCOOH). Color code for structures presented in the inset: White - H, Red - O, Dark Gray - C, Silver - Pt.

Based on our DFT results on 4/9 ML CO*-covered Pt(111) and 4/9 ML CO*-covered Pt(100), we conclude the following: (1) Formation of HCOO* is easier than COOH*; however, dehydrogenation of the COOH* is energetically more favorable on both facets. (2) For the

dehydrogenation route, the highest point in the PED for the HCOO*-pathway corresponds to the rotation from the bidentate to the monodentate HCOO*, whereas the highest point in the PED for COOH*-mediated pathway is COOH* formation from *cis*-HCOOH*, on both facets. (3) For the dehydrogenation route, COOH*-pathway is energetically more favorable than the HCOO*-pathway on the 4/9 ML CO*-covered Pt(111). The two mechanisms are energetically more comparable on the 4/9 ML CO*-covered Pt(100). (4) CO* spectator-assisted dehydrogenation steps are energetically more favorable than the direct surface dehydrogenation of COOH*/HCOO* on the 4/9 ML CO*-covered Pt(111) surface, but not on the 4/9 ML CO*-covered Pt(100) surface. (5) For the dehydrogenation pathway, the highest point in the PED for the 4/9 ML CO*-covered Pt(100) lies below that for the 4/9 ML CO*-covered Pt(111), indicating potentially higher activity on the (100) facet. However, similar to what we found the clean surface, preferential decomposition of COOH* to CO* and higher desorption barrier of CO* on the 4/9 ML CO*-covered Pt(100), could lead to greater CO* poisoning of Pt(100), which may point to Pt(100) being less active than Pt(111) for FA decomposition.

3.3.2 Experimental Kinetics

The experimental kinetics data obtained using the Pt/C catalyst is reported in (Table 3.5). The apparent activation energy barriers for the dehydrogenation and dehydration pathway were determined in a temperature range of 358-378 K. For the dehydrogenation pathway, the apparent activation energy barrier was determined to be 66.1 kJ/mol, in close agreement with the previously reported values of ~65-70 kJ/mol.[83,101,102] The reaction was found to be 0.8-1.2% selective toward the dehydration pathway across the range of experimental conditions, with an apparent activation energy barrier of 75.4 kJ/mol.

Table 3.5 Reaction rates obtained from kinetics experiments on Pt/C catalyst. The inlet feed flowrate reported here has been normalized by the number of sites for Pt/C used in the reactor.

			Inlet Feed (1/s)						Experimental Rates	
#	Temperature (K)	Pressure (atm)	FA	CO	CO_2	H_2	H_2O	He	$TOF_{CO2(H2)}$ (s^{-1})	$TOF_{CO(H2O)}$ x10^2 (s^{-1})
1	358	1	1.74	0.00	0.00	0.00	0.00	64.97	0.057	0.047
2	363	1	1.74	0.00	0.00	0.00	0.00	64.97	0.088	0.076
3	368	1	1.74	0.00	0.00	0.00	0.00	64.97	0.109	0.101
4	373	1	1.74	0.00	0.00	0.00	0.00	64.97	0.149	0.141
5	378	1	1.74	0.00	0.00	0.00	0.00	64.97	0.191	0.186
6	373	1	0.87	0.00	0.00	0.00	0.00	65.84	0.144	0.141
7	373	1	2.61	0.00	0.00	0.00	0.00	64.10	0.151	0.153
8	373	1	3.49	0.00	0.00	0.00	0.00	63.23	0.158	0.163
9	373	1	1.74	0.00	0.00	1.67	0.00	63.30	0.121	0.134
10	373	1	1.74	0.00	0.00	3.34	0.00	61.63	0.115	0.129
11	373	1	1.74	0.00	0.00	6.67	0.00	58.30	0.106	0.125
12	373	1	1.74	0.00	1.67	0.00	0.00	63.30	0.153	0.138
13	373	1	1.74	0.00	3.34	0.00	0.00	61.63	0.149	0.135
14	373	1	1.74	0.00	6.67	0.00	0.00	58.30	0.151	0.142
15	373	1	1.74	0.02	0.00	0.00	0.00	64.95	0.022	-[a]
16	373	1	1.74	0.03	0.00	0.00	0.00	64.94	0.015	-[a]
17	373	1	1.74	0.07	0.00	0.00	0.00	64.90	0.009	-[a]
18	373	1	1.74	0.00	0.00	0.00	0.02	64.95	0.149	0.138
19	373	1	1.74	0.00	0.00	0.00	0.03	64.94	0.152	0.133
20	373	1	1.74	0.00	0.00	0.00	0.07	64.90	0.149	0.144

[a]The dehydration turnover frequency for the CO co-feed experiments, which corresponds to #15-#17, could not be accurately measured because of small selectivity of the catalyst toward CO formation.

In a FA partial pressure range of 1-5%, we measured apparent reaction orders of 0.06 and 0.09 with respect to FA for the dehydrogenation and dehydration pathways, respectively. These are consistent with previously reported zero-order kinetics with respect to FA in a similar partial pressure range.[83,101] Experiments with H_2-cofeed demonstrated an apparent reaction order of -0.10 and -0.05, respectively. Co-feeding of CO had a strong inhibiting effect on the FA decomposition reaction. CO partial pressure of 0.03% led to a factor of 7 decrease in the dehydrogenation TOF, from 0.141 to 0.022 s^{-1}, at 373K. We determined the apparent reaction order with respect to CO to be -0.63 for the dehydrogenation pathway. CO* based poisoning on Pt-catalysts has been well established in the literature and has been reported observed also in the context of FA decomposition.[102,113,142] The reaction was found to have zero-reaction orders with respect to co-feed of CO_2 and H_2O for both the dehydrogenation and dehydration pathways.

3.3.3 Microkinetic Modeling

Microkinetic models formulated using energetics calculated on clean Pt(100) and Pt(111) facets, predicted reaction rates that were several orders of magnitude lower than observed experimentally. Since the unadjusted rate parameters derived on the clean Pt surfaces failed to rationalize experimental data, parameter estimation was performed to identify the corrections in the DFT energetics that would explain the experimental data. Results from parameter estimation for both the clean Pt(100) and clean Pt(111) models are discussed below:

3.3.3.1 Clean Pt(100) Model

Upon parameter estimation, the Pt(100) model yielded an improved fit with the experiment. The model predicted the experimentally measured dehydrogenation and dehydration TOFs, with a mean absolute percentage error (MAPE) of 9.2% and 7.5%, respectively (Figure 3.10). However,

the CO-cofeed subset of the dehydrogenation TOFs were significantly underpredicted by this model (Figure 3.10 (a) – inset).

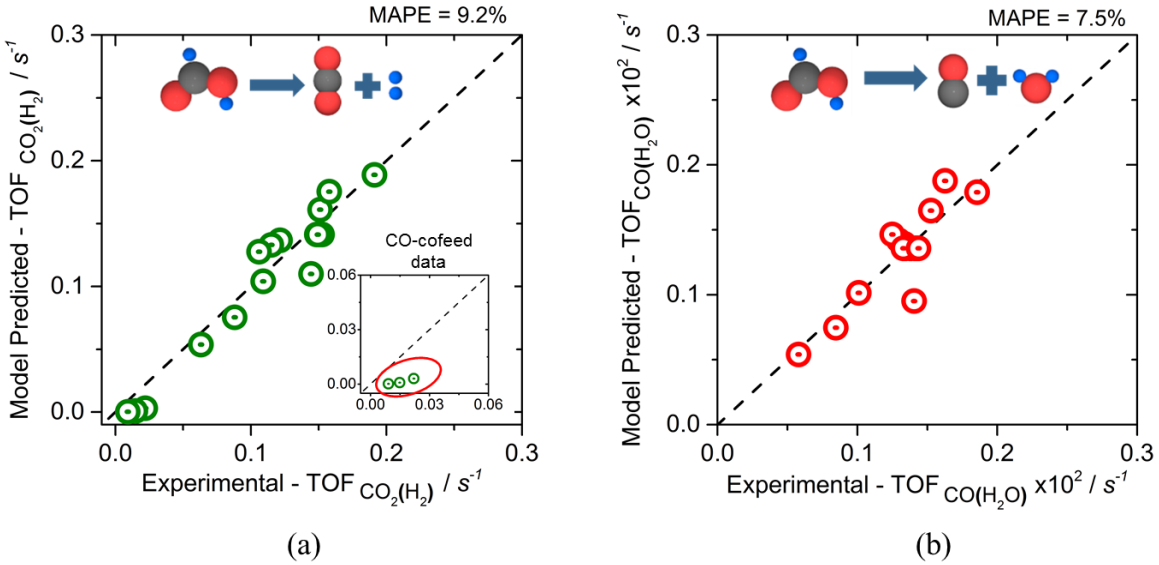


Figure 3.10 Parity plot of clean Pt(100) model predicted versus experimental TOFs (s^{-1}) for (a) Dehydrogenation: HCOOH → CO_2 + H_2; inset shows the parity at low TOFs corresponding to the CO-cofeed data, (b) Dehydration: HCOOH → CO + H_2O. MAPE: mean absolute percentage error.

The model required stabilization to the binding energy of *cis*-HCOOH* and COOH* by 0.16 eV and 0.21 eV, respectively (Table 3.6). The BE of CO* and H*, required destabilization by 0.36 eV and 0.16 eV, respectively. The model also required two significantly large corrections to the DFT activation energy barriers (Table 3.7): Both the COOH* dehydrogenation step and H_2O* formation step required lowering of the activation energy barrier by 0.31 eV. The isomerization step for HCOOH* to form *cis*-HCOOH* and the subsequent dehydrogenation to COOH* required corrections of -0.19 eV and -0.11 eV, respectively.

Table 3.6 Corrections to the DFT-derived binding energy of the intermediates for the clean Pt(100) model obtained from parameter estimation.

Clean Pt(100) model	ΔBE (eV)
cis-HCOOH*	-0.16
COOH*	-0.21
CO*	0.36
H*	0.16

Table 3.7 Corrections to the DFT-derived activation energy barrier of the elementary steps for the clean Pt(100) model obtained from parameter estimation.

Clean Pt(100) model	ΔE_A (eV)
HCOOH* ↔ *cis*-HCOOH*	-0.19
cis-HCOOH* + * ↔ COOH* + H*	-0.11
COOH* + * ↔ CO_2* + H*	-0.31
H* + OH* ↔ H_2O* + *	-0.31

The model predicts the reaction to proceed through the COOH* pathway. While the dehydration flux was always predicted to occur through the *cis*-carboxyl dehydroxylation (HCOOH* → *cis*-HCOOH* → COOH* + H* → *cis*-COOH* + H* → CO* + H* + OH* → CO + H_2O), the dehydrogenation reaction occurred through COOH* dehydrogenation (HCOOH* → *cis*-HCOOH* → COOH* + H* → CO_2* + 2H* → CO_2 + H_2). When averaged over all experimental conditions, the optimized model predicts the surface to be nearly fully covered by CO* (0.93 ML), 0.02 ML by H* with the remaining 0.05 ML of the sites vacant.

3.3.3.2 Clean Pt(111) Model

Similar to the clean Pt(100) model, the Pt(111) model demonstrated improved fit with the experimental dataset upon parameter estimation. The model agrees with the experimentally measured dehydrogenation and dehydration TOFs, with a MAPE of 9.5% and 11.1%, respectively (Figure 3.11). However, the (111) model failed to accurately fit the dehydrogenation TOFs corresponding to the CO cofeed subset of the experimental kinetics dataset (Figure 3.11 (a) – inset).

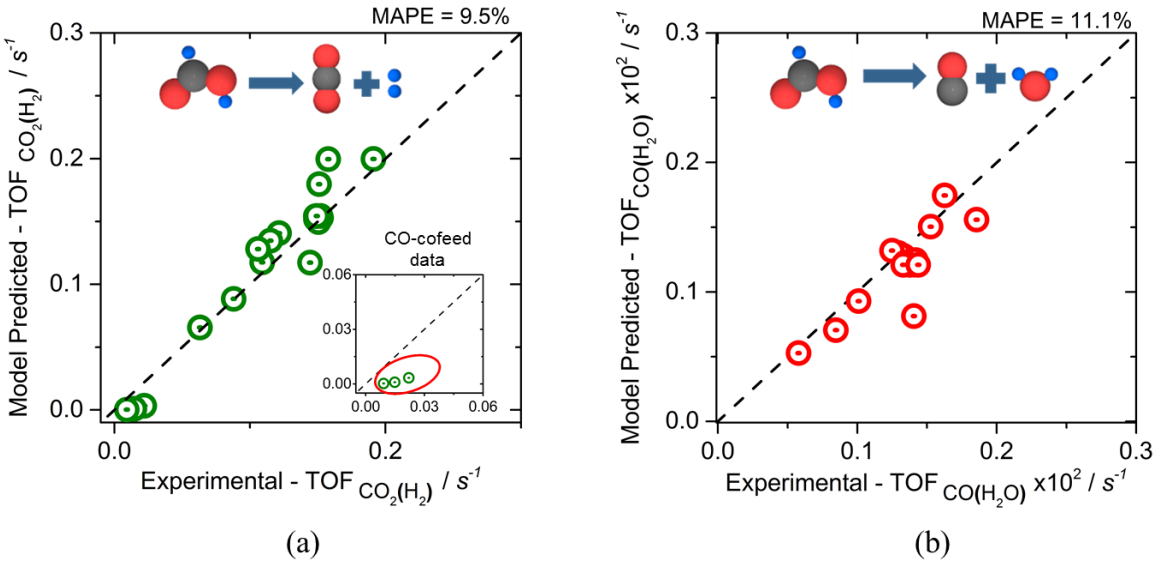


Figure 3.11 Parity plot of clean Pt(111) model predicted versus experimental TOFs (s^{-1}) for (a) Dehydrogenation: HCOOH → CO_2 + H_2; inset shows the parity at low TOFs corresponding to the CO-cofeed data, (b) Dehydration: HCOOH → CO + H_2O. MAPE: mean absolute percentage error.

The model required several corrections to the DFT-derived thermochemistry parameters, i.e., the BE of the intermediate species (Table 3.8). The BE of HCOOH* and the isomer *cis*-HCOOH*, required stabilization by 0.13 eV and 0.10 eV, respectively. The model predicted the BE of CO* and H* to be destabilized by 0.31 eV and 0.19 eV, respectively.

Table 3.8 Corrections to the DFT-derived binding energy of the intermediates for the clean Pt(111) model obtained from parameter estimation.

Clean Pt(111) model	ΔBE (eV)
HCOOH*	-0.13
cis-HCOOH*	-0.10
H_2O*	-0.14
CO*	0.31
OH*	-0.22
H*	0.19

The model also required several large corrections to the activation energy barriers calculated on the clean Pt(111) (Table 3.9). In particular, the model required corrections to activation energy barriers for: the COOH* dehydrogenation step (-0.34 eV), *cis*-COOH* dehydroxylation step (-0.29 eV), and H_2O* formation step (-0.23 eV), which were outside of the typically accepted 0.2 eV error bars for the DFT calculations.

Table 3.9 Corrections to the DFT-derived activation energy barrier of the elementary steps for the clean Pt(111) model obtained from parameter estimation.

Clean Pt(111) model	ΔE_A (eV)
HCOOH* ↔ *cis*-HCOOH*	-0.08
cis-HCOOH* + * ↔ COOH* + H*	-0.14
COOH* + * ↔ CO_2* + H*	-0.34
COOH* ↔ *cis*-COOH*	-0.07
cis-COOH* + * ↔ CO + OH*	-0.29
H* + OH* ↔ H_2O* + *	-0.23
2H* ↔ $H_{2(g)}$ + 2*	-0.15

The model predicted the reaction to occur through the COOH* pathway. When averaged over all experimental conditions, Pt(111) was predicted to be covered with: 0.92 ML of CO*, 0.05 ML of H*, and the remaining sites vacant.

Upon adjustment of the energies, both the clean surface Pt(100) and Pt(111) models demonstrated better agreement with the experiments. However, both models significantly underpredicted the dehydrogenation TOFs for the subset of the reaction kinetics data treating CO co-feed experiments (inset – Figure 3.10 (a) for Pt(100) and Figure 3.11 (a) for Pt(111)). Further, both models predicted a high coverage of CO* (0.93 and 0.92 ML for the (100) and (111) models, respectively, when averaged over all experimental conditions) which is inconsistent with the model at which the DFT energetics were calculated (i.e., clean surfaces). These models, therefore, fail to provide a coverage self-consistent description of this chemistry. Furthermore, the parameter estimation, described earlier, predicted large corrections to the activation energy barriers (up to 0.36 eV) (Table 3.7 for Pt(100) and Table 3.9 for Pt(111)). We therefore conclude that clean Pt(100) and Pt(111) surface models do not accurately represent the nature of the active site for the vapor-phase formic acid decomposition, while the reaction is taking place.

Inspired by the evidence of CO* on the surface of the catalyst,[101,102,113,142] together with the results obtained from the clean-surface microkinetic models, we reformulated the microkinetic models using the energetics derived on the 4/9 ML CO*-covered Pt(100) and Pt(111) surfaces. Dependence of the binding and transition state energies on the coverage of spectator CO* species was explicitly included in our models as polynomial expressions, to ensure the utilization of CO* coverage-cognizant energetics. These CO*-spectator informed models, when used with the unadjusted DFT-derived rate parameters, yielded reaction rates that were several orders of magnitude smaller than the experimentally measured values. Subsequently, parameter estimation was performed with these coverage-dependent DFT-derived rate parameters as initial guesses to achieve quantitative agreement with the experiment. We start with the results on 4/9 ML CO*-

covered Pt(100) facet, since based on PEDs alone, that facet would be expected to be more active than the 4/9ML CO*-covered Pt(111) facet.

3.3.3.3 4/9 ML CO-Covered Pt(100) Model*

Using the multi-start approach, we determined two parameter sets, which can explain the experimental kinetics data well. For both solutions, the dehydration reaction was found to occur through the COOH*-pathway, through the following sequence of elementary transformations: HCOOH* $\rightarrow$ *cis*-HCOOH* $\rightarrow$ COOH* + H* $\rightarrow$ *cis*-COOH* + H* $\rightarrow$ CO* + H* + OH* $\rightarrow$ CO + H_2O). The two solutions, however, differ in their predictions for the pathway carrying the flux for the dehydrogenation reaction. In particular, the first solution (model-I) points to dehydrogenation through the COOH*-pathway, whereas the second solution (model-II) points to contributions from both the COOH*- and HCOO*-pathways, with the latter mechanism (HCOO*-pathway) playing the dominant role in model-II. Further, unlike the models formulated using clean-surface DFT energetics, these solutions were able to accurately describe the CO-cofeed subset of the experimental dataset. We present the findings from the two solutions in the following:

4/9 ML CO*-covered Pt(100) Model-I: After parameter estimation, the optimized model demonstrated a good agreement with the experimental kinetics dataset. Both the dehydrogenation and dehydration TOFs were predicted accurately, with a mean absolute percentage error (MAPE) of 3.7% ($R^2 = 0.98$) and 4.7% ($R^2 = 0.99$), respectively. Parity plots comparing the model predicted TOFs for the dehydrogenation and dehydration pathways with the experimentally measured values are presented in Figure 3.12.

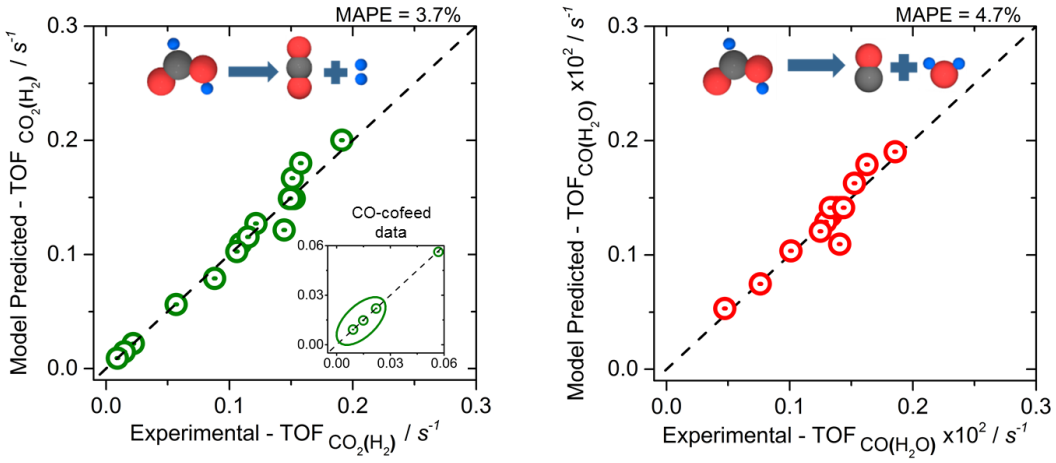


Figure 3.12 Parity plots of coverage-cognizant Pt(100) model-I predicted versus experimental TOFs (s^{-1}) for: (a) Dehydrogenation: HCOOH → CO_2 + H_2 (R^2=0.98); inset shows the parity at low TOFs corresponding to the CO-cofeed data, (b) Dehydration: HCOOH → CO + H_2O (R^2=0.99). MAPE: mean absolute percentage error.

Parameter estimation required stabilization to the binding energy of HCOOH* and the isomer *cis*-HCOOH*, by 0.26 and 0.21 eV, respectively. Dispersion interactions, which can contribute significantly to the binding energy of closed-shell species, were not explicitly accounted for by the functional (PW91) employed in our calculations.[12,143,144] The magnitude of the stabilization is consistent with the lack of inclusion of dispersion interactions in our theoretical treatment. The binding energy of CO* and H* required destabilization by 0.21 and 0.20 eV, respectively (Table 3.10).

Table 3.10 Corrections to the DFT-derived binding energy of the intermediates for the 4/9 ML CO*-covered Pt(100) model-I obtained from parameter estimation.

4/9ML CO Pt(100) model-I	**ΔBE (eV)**
HCOOH*	-0.26
cis-HCOOH*	-0.21
CO*	0.21
H*	0.20

The DFT activation energy barriers corresponding to the dehydrogenation steps starting from the *cis*-HCOOH* leading to the formation of COOH*, as well as the decomposition of the COOH* to form CO_2, required corrections of -0.19 and -0.34 eV, respectively (Table 3.11). The activation energy barrier for dehydroxylation of *cis*-COOH*, leading to the formation of CO*, required an increase by 0.07 eV, whereas the H-H recombinative desorption required its activation energy barrier to be lowered -0.06 eV. The model also required a large stabilization of 0.38 eV to the activation energy barrier for to the H-transfer step from COOH* to a spectator CO*, leading to the formation of COH* (Table 3.11).

Table 3.11 Corrections to the DFT-derived activation energy barrier of the elementary steps for the 4/9 ML CO*-covered Pt(100) model-I obtained from parameter estimation.

4/9ML CO Pt(100) model-I	**ΔE_A (eV)**
cis-HCOOH* + * ↔ COOH* + H*	-0.19
COOH* + * ↔ CO_2* + H*	-0.34
cis-COOH* + * ↔ CO + OH*	0.07
2H* ↔ $H_{2(g)}$ + 2*	-0.06
COOH* + CO* ↔ COH* + CO_2*	-0.38

When averaged over all experimental conditions, this solution predicted surface coverages of 0.49 ML CO*, 0.14 ML H*, and 0.37 ML vacant sites. Since the CO* coverage prediction (~0.49ML) is close to the CO* coverage used in the DFT calculations (4/9 ML CO*) for deriving the energetics implemented in the microkinetic model, we find the model to be coverage self-consistent. On the 4/9 ML CO*-covered model-I, the flux goes entirely though the COOH*-pathway. In particular, the dehydration flux was predicted to occur through the *cis*-COOH* dehydroxylation. Importantly, the dehydrogenation flux was carried out by two parallel pathways: (i) direct COOH* decomposition (HCOOH* → *cis*-HCOOH* → COOH* + H* → CO_2* + 2H* → CO_2 + H_2), and (ii) CO*-assisted COOH* decomposition involving formation of COH* and its

decomposition through its isomerization to formyl (HCO*) (i.e., HCOOH* (+**2CO***) → *cis*-HCOOH* (+**2CO***) → COOH* + H* (+**2CO***)) → CO_2*+ COH* + H* (+**CO***) → CO_2*+ HCO* + H* (+**CO***) → CO_2*+ 2H* (+2**CO***) → CO_2 + H_2 (+2**CO***)). Under our defined home conditions (2.6% FA, balance He, 373K), the direct decomposition of COOH* contributed ~85% of the observed dehydrogenation flux, with the remainder contributed by the CO*-assisted pathway. However, under CO-cofeed conditions (2.6% FA, 0.025 – 0.1% CO, balance He, 373K), almost all of (~98%) the observed dehydrogenation flux went through the CO*-assisted COOH* mechanism. Notably, these results indicate that at experimental conditions where higher surface CO* coverage is expected, practically all FA decomposition to CO_2 and H_2 goes through the spectator CO*-assisted mechanism. Comparison of the model predicted apparent activation energy barriers and apparent reaction orders for the dehydrogenation and dehydration pathways with the experiments is presented in Table 3.12.

Table 3.12 Comparison of experimentally measured and model predicted apparent activation energy and reaction orders with respect to the partial pressure of HCOOH, H_2O, H_2, CO_2 and CO for the dehydrogenation (HCOOH → CO_2 + H_2) and dehydration pathway (HCOOH → CO + H_2O), for the optimized 4/9 ML CO*-covered Pt(100) model-I. †The dehydration reaction order for the CO cofeed experiments could not be accurately measured because of small selectivity of the catalyst toward CO formation.

4/9ML CO Pt(100) model-I	**Dehydrogenation**		**Dehydration**	
	Expt	**Model**	**Expt**	**Model**
E_A (kJ/mol)	66.1 ± 3.7	72.4	75.4 ± 4.0	71.8
HCOOH	0.06 ± 0.01	0.15	0.10 ± 0.04	0.34
H_2O	0.00 ±0.02	0.00	0.03 ± 0.05	0.00
H_2	-0.10 ± 0.01	-0.16	-0.05 ± 0.04	-0.08
CO_2	-0.01 ± 0.02	0.01	0.02 ± 0.03	0.00
CO	-0.63 ± 0.04	-0.63	--†	--†

In summary, the 4/9 ML CO*-covered Pt(100) model-I was able to fit the experimental kinetics dataset accurately, with the decomposition flux predicted to occur through the COOH*

intermediate. Both, the direct decomposition and CO*-assisted decomposition of COOH* mechanisms were found to contribute to the dehydrogenation flux. Since, the model predicted CO* coverages were consistent with the 4/9 ML CO*-covered Pt(100) surface where the initial DFT energetics were derived on, the model was coverage self-consistent. However, in order to fit the experimental dataset, the model required two large corrections in the activation energy barriers (Table 3.11), outside of the typically accepted error for DFT calculations. We therefore, believe that 4/9 ML CO*-covered Pt(100) model-I falls short of representing the true nature of the active site for the FA decomposition reaction on Pt-catalysts.

4/9 ML CO*-covered Pt(100) Model-II: The second optimized solution obtained from parameter estimation yielded good agreement with the experiments (Figure 3.13), with a MAPE of 4.2% (R^2 = 0.97) and 4.4% (R^2 = 0.99), for the dehydrogenation and dehydration TOFs, respectively.

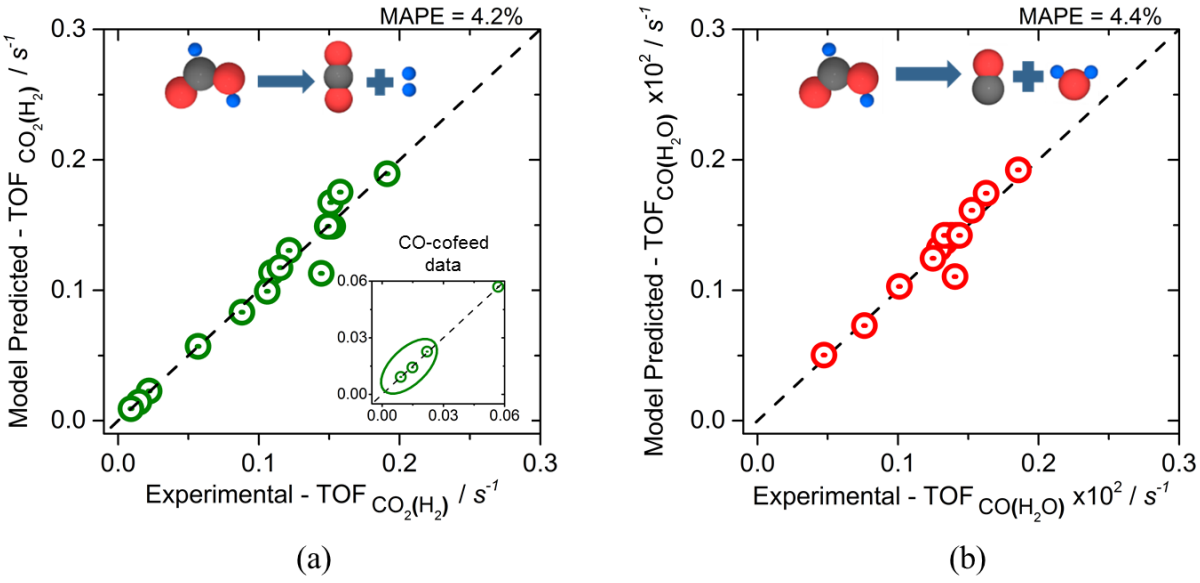


Figure 3.13 Parity plot of coverage-cognizant Pt(100) model-II predicted versus experimental TOFs (s^{-1}) for: (a) Dehydrogenation: HCOOH → CO_2 + H_2 (R^2=0.97); inset shows the parity at low TOFs corresponding to the CO-cofeed data, (b) Dehydration: HCOOH → CO + H_2O (R^2=0.99). MAPE: mean absolute percentage error.

Similar to the 4/9 ML CO*-covered Pt(100) model-I, the binding of HCOOH* and *cis*-HCOOH* required stabilization by 0.31 and 0.21 eV, respectively. The model predicted the binding energy of HCOO* to be stabilized by 0.21 eV. On the other hand, CO* and H* binding required destabilization by 0.21 and 0.22 eV, respectively (Table 3.13).

Table 3.13 Corrections to the DFT-derived binding energy of the intermediates for the 4/9 ML CO*-covered Pt(100) model-II obtained from parameter estimation.

4/9ML CO* Pt(100) model-II	**ΔBE (eV)**
HCOOH*	-0.31
cis-HCOOH*	-0.21
HCOO*	-0.21
CO*	0.21
H*	0.22

Several corrections to the DFT-derived activation energy barriers were required in this model solution in order to fit the experimental dataset. The activation energy barrier for the first dehydrogenation step starting from HCOOH* to form HCOO* required destabilization by 0.15 eV (Table 3.14). The activation energy barrier for dehydrogenation of HCOO* required stabilization by 0.25eV. The activation energy barrier for the COOH* formation step had to be lowered by 0.19 eV. The activation energy barrier for the H-transfer step from COOH* to a spectator CO* molecule to form COH* required a large correction (-0.34 eV). The H-H recombinative desorption and COH* decomposition steps required their activation energy barrier to be lowered by 0.12 and 0.11 eV, respectively.

Table 3.14 Corrections to the DFT-derived activation energy barrier of the elementary steps for the 4/9 ML CO*-covered Pt(100) model-II obtained from parameter estimation.

4/9ML CO* Pt(100) model-II	**ΔE_A (eV)**
HCOOH* + 2* ↔ HCOO* + H*	0.15
HCOO* ↔ CO_2* + H*	-0.25
cis-HCOOH* + * ↔ COOH* + H*	-0.19
cis-COOH* + * ↔ CO + OH*	0.07
2H* ↔ $H_{2(g)}$ + 2*	-0.12
COOH* + CO* ↔ COH* + CO_2*	-0.34
COH* + * ↔ CO* + H*	-0.11

Averaged over all experimental conditions, this solution predicted an average CO*-coverage of 0.49 ML, along with ~0.08 ML COH*, 0.06 ML H*, with the balance of 0.37 ML sites remaining vacant. Importantly, the 4/9 ML CO*-covered Pt(100) model-II predicted both the HCOO*- and COOH*-mediated pathways to be active under our experimental conditions. At our defined home conditions (2.6% FA, balance He, 373K), the direct HCOO*-mediated decomposition mechanism (HCOOH* → HCOO* + H* → CO_2* + 2H* → CO_2 + H_2) played the dominant role (97%) in dehydrogenation. The CO*-assisted COOH* decomposition, through the COH* intermediate (HCOOH* (+**CO***) → *cis*-HCOOH* (+**CO***) → COOH* + H* (+**CO***) → CO_2*+ H* + **CO**H* → CO_2*+ 2H* (+**CO***) → CO_2 + H_2 (+**CO***)) accounted for the remainder dehydrogenation. Under CO-cofeed conditions (2.6% FA, 0.025 – 0.1% CO, balance He, 373K), the direct HCOO* decomposition carried ~70% of the dehydrogenation flux, with the balance contributed by the CO*-assisted COOH* decomposition mechanism. Comparison of the model predicted apparent activation energy barriers and apparent reaction orders for the dehydrogenation and dehydration pathways with the experiments is presented in Table 3.15.

Table 3.15 Comparison of experimentally measured and model predicted apparent activation energy and reaction orders with respect to the partial pressure of HCOOH, H_2O, H_2, CO_2 and CO for the dehydrogenation ($HCOOH \rightarrow CO_2 + H_2$) and dehydration pathway ($HCOOH \rightarrow CO + H_2O$), for the optimized 4/9 ML CO*-covered Pt(100) model-II. †The dehydration reaction order for the CO cofeed experiments could not be accurately measured because of small selectivity of the catalyst toward CO formation.

4/9ML CO Pt(100) model-I	**Dehydrogenation**		**Dehydration**	
	Expt	**Model**	**Expt**	**Model**
E_A (kJ/mol)	66.1 ± 3.7	67.2	75.4 ± 4.0	75.3
HCOOH	0.06 ± 0.01	0.14	0.10 ± 0.04	0.32
H_2O	0.00 ±0.02	0.00	0.03 ± 0.05	0.00
H_2	-0.10 ± 0.01	-0.20	-0.05 ± 0.04	-0.07
CO_2	-0.01 ± 0.02	-0.00	0.02 ± 0.03	0.00
CO	-0.63 ± 0.04	-0.65	--†	--†

To summarize, the optimized 4/9 ML CO*-covered Pt(100) model-II explained the experimental dataset accurately, while being CO* coverage self-consistent. The model predicted both the HCOO- and COOH-mediated pathways to be active under our experimental conditions, with the former dominating across all but CO-cofeed conditions. The optimized model, however, required two large corrections to the DFT-derived activation energy barriers (see Table 3.14), which were outside of standard DFT error. We therefore, suggest that the 4/9 ML CO*-covered Pt(100) model-II does not represent the nature of the active site for FA decomposition on Pt/C catalysts.

Since, both the solutions obtained from the model formulated using the 4/9 ML CO*-covered Pt(100) energetics required large corrections (>0.20 eV) to the DFT-derived activation energy barriers, we conclude that a partially CO*-covered Pt(100) model fails to accurately represent the active site for FA decomposition on Pt/C catalysts.

3.3.3.4 4/9 ML CO-Covered Pt(111) Model*

For the model formulated using DFT energetic parameters derived on the 4/9 ML CO*-covered Pt(111), parameter estimation yielded one solution explaining the experimental dataset accurately. The optimized solution was able to fit the experimentally measured dehydrogenation and dehydration TOFs, with a MAPE of 5.1% (R^2 = 0.97) and 4.1% (R^2 = 0.99), respectively. The parity plots comparing the model-predicted TOFs with the experimental values are presented in Figure 3.14.

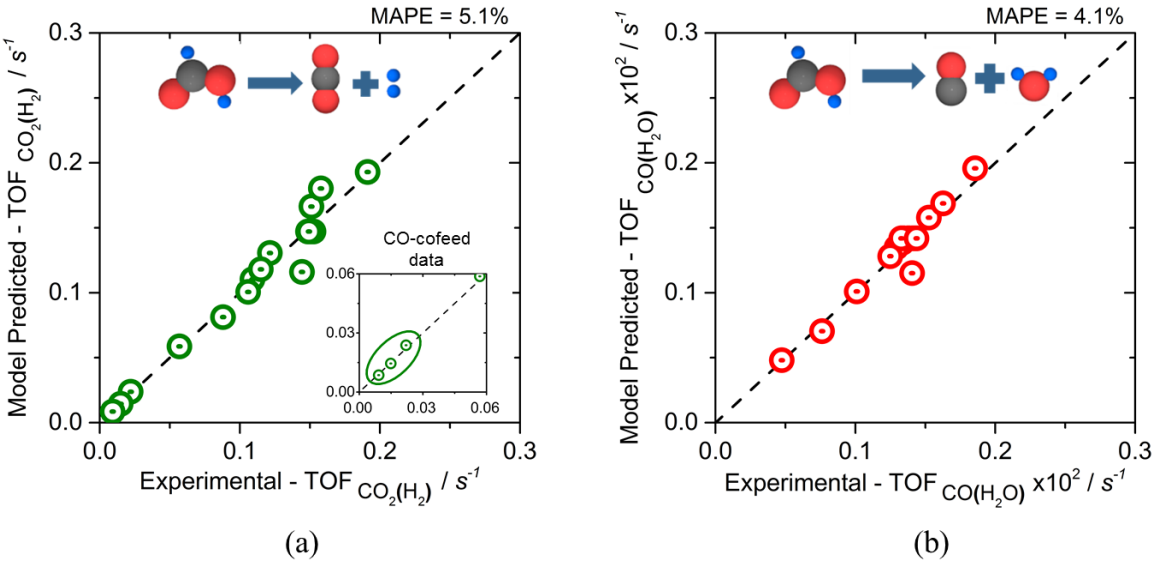


Figure 3.14 Parity plot of coverage-cognizant Pt(111) model predicted versus experimental TOFs (s^{-1}) for: (a) Dehydrogenation: HCOOH → CO_2 + H_2; inset shows the parity at low TOFs corresponding to the CO-cofeed data (R^2=0.97), (b) Dehydration: HCOOH → CO + H_2O (R^2=0.99). MAPE: mean absolute percentage error.

To fit the experimental dataset, parameter estimation led to a stabilization in the binding energies of HCOOH* and *cis*-HCOOH*, by 0.26 and 0.20 eV, respectively (Table 3.16). Dispersion interactions which can dominate the binding energy of closed-shell species to surfaces,[12,143,145]

were not explicitly accounted for by the functional (PW91) used in our study. Thus, these two corrections required by the parameter estimation procedure can be justified by the lack of inclusion of such interactions in our theoretical treatment. In addition, our parameter estimation for this solution led to: (i) a stabilization of the COH* binding by 0.09 eV, and (ii) a destabilization of CO* and H* binding, by 0.10 eV and 0.17 eV, respectively. All these corrections to the binding energies are within the error of PW91-GGA DFT (Appendix C). In terms of activation energy barriers, the parameter estimation procedure led to only minor corrections (+/-0.09 eV), except for the activation energy barrier for COOH* formation (*cis*-HCOOH*→COOH*+H), which needed to be lowered by 0.20 eV (Table 3.17).

Table 3.16 Corrections to the DFT-derived binding energy of the intermediates for the 4/9 ML CO*-covered Pt(111) model, as obtained from parameter estimation.

4/9ML CO* Pt(111) model	**ΔBE (eV)**
HCOOH*	-0.26
cis-HCOOH*	-0.20
COH*	-0.09
CO*	0.10
H*	0.17

Table 3.17 Corrections to the DFT-derived activation energy barrier of the elementary steps on the 4/9 ML CO*-covered Pt(111) model, as obtained from parameter estimation.

4/9ML CO* Pt(111) model	**ΔE_A (eV)**
cis-HCOOH* + * ↔ COOH* + H*	-0.20
COOH* + * ↔ CO_2* + H*	-0.04
H* + OH* ↔ H_2O* + *	0.06
2H* ↔ $H_{2(g)}$ + 2*	-0.09
COOH* + CO* ↔ COH* + CO_2*	0.08

For this solution, the reaction flux was predicted to go entirely through the COOH*-pathway. The dehydration reaction was found to occur through dehydroxylation of *cis*-COOH* (HCOOH* →

cis-HCOOH* → COOH* + H* → *cis*-COOH* + H* → CO* + OH* + H* → CO + H_2O). The dehydrogenation reaction, however, was accounted for by: (1) direct COOH* decomposition (HCOOH* → *cis*-HCOOH* → COOH* + H* → CO_2*+ 2H* → CO_2 + H_2), (2) CO*-assisted COOH* decomposition through the COH* intermediate (HCOOH* (+**CO***) → *cis*-HCOOH* (+**CO***) → COOH* + H* (+**CO***) → CO_2*+ H* + COH*) (Figure 3.15). The flux through the CO*-assisted pathway further bifurcates into two sub-mechanisms, through either the direct COH* decomposition to replenish the previously consumed CO* spectator molecule (mechanism 2a: COH* → **CO*** + H*), or through the formation of a formyl (HCO*) intermediate involving participation of another CO* spectator molecule (mechanism 2b: COH* (+**CO***) → H**CO*** (+CO*) → **CO*** + H* (+CO*)) (Figure 3.15). The mechanism (2b) essentially involves H-transfer from the COH* species to a spectator CO* molecule to form HCO*, followed by dehydrogenation of HCO*.

At our defined home conditions (2.6% FA, balance He, 373K), our model predicts mechanisms (1) and (2a) to be dominant, contributing about equally to the dehydrogenation flux, with only a very minor contribution (~1%) from mechanism (2b). However, under the CO-cofeed conditions (2.6% FA, 0.025 – 0.1% CO, balance He, 373K), we find a significant drop in the contribution of the direct dehydrogenation mechanism (1), with the CO*-assisted pathways contributing ~95% of the observed dehydrogenation flux (~35% and 60%, for mechanisms (2a) and (2b), respectively) (Figure 3.15). This suggests that an increase in the CO-partial pressure leads to a decrease in the dehydrogenation flux through mechanisms (1) and (2a), accompanied by an increased contribution of mechanism (2b).

At the home conditions, and for the entire reaction network, including both dehydrogenation and dehydration reactions, the direct COOH* decomposition carries the highest degree of rate control (X_{RC}=0.36),[60] followed by the CO*-assisted COOH* decomposition to form COH* (X_{RC}=0.24), and H-H recombinative desorption (X_{RC}=0.27). The X_{RC} values for all the relevant surface intermediates and elementary steps for the dehydrogenation pathway are provided in Appendix C.[61] Further, X_{RC} values for the relevant elementary steps for FA decomposition, obtained by keeping the (a) direct COOH* dehydrogenation, (b) CO* assisted COOH* mechanisms active, one at a time are provided in Appendix C.

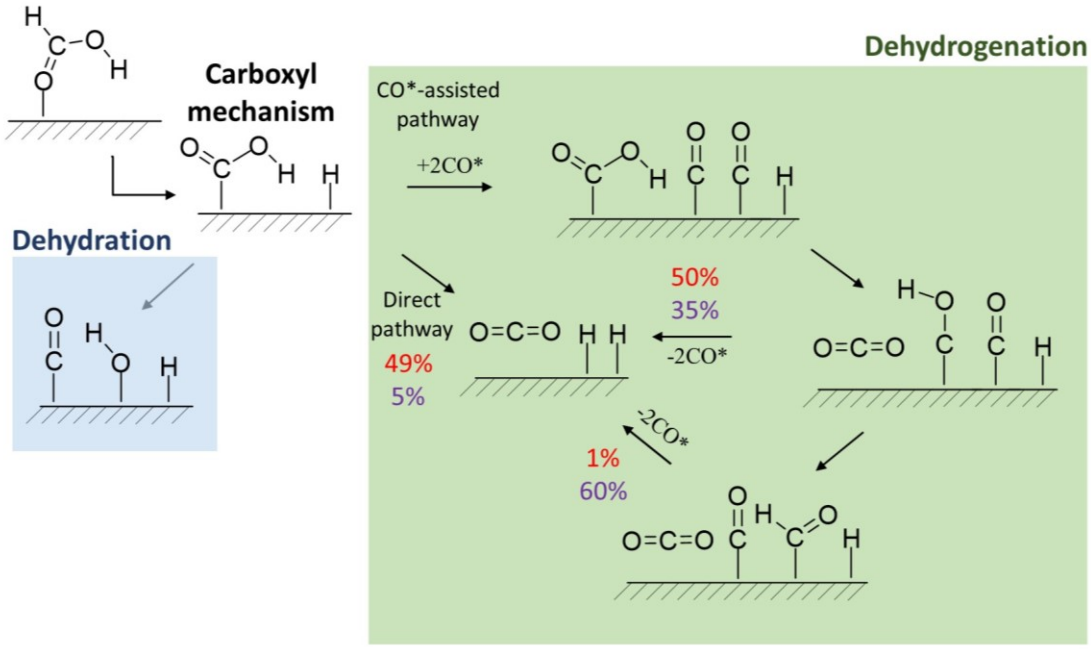


Figure 3.15 Simplified reaction network (not showing the isomerization steps) indicating the flux carrying pathways for the FA decomposition on the 4/9 ML CO*-covered Pt(111), as predicted by the optimized microkinetic model. The step with +/- CO* indicates H-transfer with the participation of a spectator CO* molecule. The percentage flux contribution for the dehydrogenation pathway (indicated by the green box) by the various mechanisms, under our defined home conditions (2.6% FA, balance He, 373K) and CO-cofeed conditions (averaged) (2.6% FA, 0.025 – 0.1% CO, balance He, 373K), are indicated in red and purple, respectively. The dehydration pathway (indicated by the blue box, shaded out) proceeds through the COOH* dehydroxylation, under all conditions.

Averaged over all experimental conditions, our model predicts surface coverage of 0.30 ML CO*, 0.12 ML H*, and 0.10 ML COH*, with the remaining sites (0.48 ML) vacant. Although the predicted coverages were ~1/9 ML lower than the CO* coverage explicitly accounted for in our DFT calculations, inclusion of CO* coverage dependent binding and transition state energies as polynomial-type corrections enabled the use of CO* coverage-cognizant energetics in the vicinity of 4/9 ML CO* coverage and ensured coverage self-consistency in our microkinetic models. Importantly, this solution also provides close agreement with the experimentally determined apparent activation energy barriers and reaction orders (Table 3.18).

Table 3.18 Comparison of experimentally measured and model predicted apparent activation energy barriers and reaction orders with respect to the partial pressure of HCOOH, H_2O, H_2, CO_2, and CO for the dehydrogenation ($HCOOH \rightarrow CO_2 + H_2$) and dehydration pathway ($HCOOH \rightarrow CO + H_2O$), for the optimized 4/9 ML CO*-covered Pt(111) model. †The dehydration reaction order for the CO cofeed experiments could not be accurately measured because of small selectivity of the catalyst toward CO formation.

4/9ML CO Pt(111) model	**Dehydrogenation**		**Dehydration**	
	Expt	**Model**	**Expt**	**Model**
E_A (kJ/mol)	66.1 ± 3.7	66.9	75.4 ± 4.0	79.0
HCOOH	0.06 ± 0.01	0.11	0.10 ± 0.04	0.27
H_2O	0.00 ±0.02	0.00	0.03 ± 0.05	0.00
H_2	-0.10 ± 0.01	-0.19	-0.05 ± 0.04	-0.06
CO_2	-0.01 ± 0.02	0.00	0.02 ± 0.03	0.00
CO	-0.63 ± 0.04	-0.73	--†	-- †

In summary, the optimized 4/9 ML CO*-covered Pt(111) solution was able to capture the experimental dataset accurately, with corrections to the DFT-derived activation energy barriers within the error of GGA-PW91. We found that both the dehydration and dehydrogenation reaction proceed through the COOH*-mediated pathway. Both the direct and CO*-assisted mechanisms contributed toward the experimentally observed TOFs, with the latter becoming more relevant at higher CO* coverages.

3.4 Active Site for Vapor-Phase Decomposition of Formic Acid on Pt/C

The 4/9 ML CO*-covered Pt(100) models (I and II), both required significant corrections to the DFT activation energy barriers derived explicitly at 4/9ML CO* coverage. The model predicted average CO* coverage was found to be ~0.50 ML for both the Pt(100) solutions obtained. These large corrections suggest that even the ~50% CO*-covered Pt(100) is not a good representation of the active site in Pt/C catalysis during FA decomposition. Constraining the corrections during the parameter estimation procedure to the ± 0.2 eV error bars for the activation energy barriers, significantly reduced the activity toward the decomposition reaction and rendered the (100) facet inactive. On the other hand, the 4/9 ML CO*-covered Pt(111) model was able to represent the experimental kinetics dataset, requiring corrections of energetics within the standard DFT error bars. When averaged over all experimental conditions, this model predicted ~1/3 of the Pt(111) sites to be covered by CO*.

Furthermore, to capture the experimental results, parameter estimation required larger destabilization to the CO* binding on Pt(100) (0.21 eV) compared that on Pt(111) (0.10 eV). This may suggest a higher probability for Pt(100) to be poisoned by CO*, perhaps beyond the coverages of ~0.50 ML currently predicted by our microkinetic models. Increase in CO* surface coverage would likely further reduce the activity of Pt(100) through destabilization of the energetics and site-blocking. Therefore, based on our study, we expect the Pt(100) facet to be largely poisoned by CO*, practically not contributing to FA decomposition. Instead, a partially CO*-covered Pt(111) emerges as a better representation for the active site of FA decomposition on Pt/C catalysts, capable of explaining both activity and selectivity determined in experiments.

We note here that based on DFT-derived PEDs alone, even when including 4/9 ML of CO* in the calculations, one would have predicted that Pt(100) is more active than Pt(111). Yet, the microkinetic modeling analysis revealed that under experimental conditions, the reaction flux is carried through the partially CO*-covered Pt(111) facet. This highlights the importance of performing coverage self-consistent microkinetic modeling of experimental reactivity measurements, to derive a deeper understanding of the nature of the active site while the reaction is taking place.

Contrary to common belief for formic acid decomposition on transition metals, our study finds that carboxyl (COOH*), not formate (HCOO*), is the reactive intermediate, turning reactants to products on Pt/C catalysts. Due to the high activation energy barrier for transformation of formate (HCOO*) from the bidentate to the monodentate configuration, our results predict no flux through the formate pathway. Low temperature single crystal absorption calorimetry (SCAC) studies in conjunction with DFT studies, have demonstrated that the presence of coadsorbed OH* and H_2O* can reduce the activation energy barrier for the bidentate to monodentate transformation of formate via H-bonding interactions.[141,146–148] However, under our experimental conditions, the optimized 4/9 ML CO*-covered Pt(111) model predicts a coverage of $<10^{-8}$ ML for both OH* and H_2O*. Our microkinetic modeling results predict no flux through these OH*/H_2O* assisted pathways and thus suggest that H-bonding interactions arising from co-adsorbed OH*/H_2O* species do not contribute towards the reaction flux under steady-state catalytic FA decomposition conditions. HCOO* is a spectator species, at least under the experimental conditions considered in this study. All models presented here predicted HCOO* coverages in the range of 10^{-8} ML, demonstrating no significant site-blocking of Pt by that intermediate. For the optimized 4/9 ML CO*-covered

Pt(111) model, which we are argue likely represents the active site while the reaction is taking place on Pt/C catalysts, since HCOO* was not involved as a reactive intermediate, the corresponding energetic parameters were found statistically insignificant and could not be verified with our kinetics dataset. Interestingly, for the less significant 4/9 ML CO*-covered Pt(100) model-II, the formate (HCOO*) pathway carried the majority of the flux from reactants to products, even though the HCOO* coverage remained very low at ~10^{-8} ML.

In our study, we utilized a mean field representation of kinetics, which assumes perfect mixing of the adsorbates. Spatial distributions of adsorbates can be described more accurately with stochastic kinetic modeling (e.g.: kinetic Monte Carlo (kMC)).[149–154] Cluster expansion (CE) Hamiltonians, trained using DFT calculations, can be introduced to determine energetics that are cognizant with the spatial distribution of adsorbates.[155–157] However, given the large computational cost required to parameterize and solve these models, in context of kinetics studies, their implementation is typically limited to chemistries with smaller reaction networks (eg. CO, NO, HCl oxidation). Coverage cognizant mean-field microkinetic models with energetics depending on coverage explicitly included, serve as a reasonable compromise between the CE-informed kMC models and the conventional mean-field approach (which includes no coverage effects), enabling modeling of realistic coverage effects for much larger reaction networks. [8,34,138,158–161]

3.5 Conclusions

A combination of DFT calculations, experimental kinetics, and microkinetic modeling was used to derive mechanistic insights for the vapor-phase decomposition of formic acid on a Pt/C catalyst. Initial estimates of kinetic and thermodynamic parameters obtained from DFT on clean Pt(100)

and Pt(111) facets were used to formulate mean-field microkinetic models. After parameter estimation, and inconsistent with the assumption of a clean surface used in the DFT calculations, these models predicted high CO* surface coverage (~0.92 ML) under reaction conditions. To remedy this inconsistency, we derived the energetics of the reaction mechanism with DFT calculations on 4/9 ML CO*-covered Pt(111) and Pt(100) surfaces. Accordingly, we incorporated CO* coverage-cognizant energetics in our models, by evaluating the thermochemistry and kinetics at varying levels of CO* coverage. Both the 4/9 ML CO*-covered Pt(100) and Pt(111) models were able to reproduce the experimental kinetics dataset, including the CO-cofeed subset, which was previously not captured by the clean Pt(111) and Pt(100) models. These optimized microkinetic models predicted a CO* coverage, consistent with the 4/9 ML CO*-covered DFT models, where the DFT calculations performed to derive the energetics used in these microkinetic models. Therefore, the 4/9 ML CO*-covered Pt(100) and Pt(111) models were shown to be CO*-coverage consistent. Rigorous parameter estimation of these models suggests that a partially CO*-covered Pt(111) surface (~1/3 ML) captures experimental activity and selective trends, and therefore is an accurate representation of the active site, whereas Pt(100) is largely poisoned by CO* (~1/2 ML) and does not contribute to the reactants to products flux in any significant way. The reaction occurs through the COOH*-mediated paths, through both the direct and the CO* spectator-assisted mechanisms, with relative contributions depending on reaction conditions. When CO is co-fed with FA, the CO*-spectator-assisted mechanisms play a dominant role in FA decomposition.

Fundamental mechanistic insights derived in this work might be useful for designing improved catalysts for efficient H_2 production from FA, and for further advancing the utilization of FA as a

hydrogen storage medium. More broadly, for elucidating the nature of the catalytic active site while the reaction is taking place, this work elucidated the importance of explicitly including spectator-coverage effects for obtaining better initial estimates of the thermochemical and kinetic DFT parameters used in coverage-cognizant microkinetic models. Importantly, we demonstrated that spectator-assisted elementary reaction steps can play a central role in complex catalytic reaction mechanisms.

CHAPTER 4

A COVERAGE SELF-CONSISTENT MICROKINETIC MODEL FOR VAPOR-PHASE FORMIC ACID DECOMPOSITION ON PD/C CATALYSTS

4.1 Introduction

Transition towards a sustainable energy future hinges strongly on the effective deployment of renewable energy carriers. Obtained as a byproduct during biomass reforming,[64–66] formic acid (HCOOH, FA) has been widely considered as one of the most promising hydrogen storage vectors.[75–79,162,163] Its high volumetric capacity (53.4 g-H_2/l), low toxicity, and low flammability, makes FA a promising carbon-neutral hydrogen carrier for transportation applications. FA can be used as a fuel in direct formic acid fuel cells (DFAFCs)[164–169] or alternatively, it can be decomposed to generate on-board hydrogen for powering hydrogen fuel cells, a technology which is in more advanced stages. Importantly, FA has also been explored as an *in situ* hydrogen source for hydrogenation reactions.[170–179] Due to its potential as a hydrogen storage material, FA decomposition has been widely investigated in the heterogeneous catalysis literature on a variety of catalysts including metals[81,82,114,180], metal oxides[85–87,181], and metal carbides.[89,182]

FA decomposition can occur through the dehydrogenation reaction to form CO_2 and H_2 (ΔH^o = -14.9 kJ/mol) and through the dehydration reaction to form CO and H_2O (ΔH^o = 26.2 kJ/mol), the two routes coupled together through the water gas shift reaction (WGSR). Pt-group metals, especially Pd and Pt, have been reported to be the most promising monometallic catalysts in terms of FA decomposition activity and selectivity towards H_2 (>95%).[104,183] In the 1960s, Sachtler and Fahrenfort proposed a volcano-type relationship correlating the FA decomposition temperature at fixed conversion with the heat of formation of bulk metal formate and identified Pt-group metals near the peak.[99] Recent experimental studies by Tang *et al.*[100] on unsupported metal powder catalysts (turnover frequency trend: Pt > Cu > Pd > Rh > Ni) and by Solymosi *et al.*[101] on carbon-supported metal catalysts (specific activity trend: Ir ~ Pt ~ Pd > Ru > Rh), have also demonstrated Pd as one of the most active monometallic catalysts for FA decomposition.

Despite numerous experimental and theoretical studies involving Pd-based catalysts, detailed mechanistic understanding of the reaction mechanism, dominant reaction pathways, surface intermediate(s), and the active site(s) remains largely unsettled due to conflicting hypotheses regarding this chemistry. Li *et al.*[184] reported that the apparent activation energy barrier for FA decomposition is independent of the particle size of Pd/C and suggested the reaction to be structure insensitive. The authors also report an inverse dependence of the turnover frequency (TOF) on the size of the catalyst nanoparticles. These observations are in disagreement with a previous study by Garcia *et al.* who report a volcano-type dependence of the TOF with the particle size and instead suggest the reaction to be structure sensitive.[185] Additionally, the nature of reactive intermediate is still under debate. While certain *in situ* spectroscopic studies have corroborated the presence of formate (HCOO*) on Pd catalyst, the experimental selectivity of FA towards CO suggests the

participation of the spectroscopically elusive carboxyl (COOH*) species in the reaction mechanism.[7–9] Thus, a mechanistic model that comprehensively captures experimental kinetics, over a wide range of experimental conditions, would contribute to resolving conflicting hypotheses and would enable elucidation of the reaction mechanism and of the active site for FA decomposition on Pd catalysts.

In this study, we utilize density functional theory (DFT) derived microkinetic modeling and reaction kinetics experiments to iteratively develop a coverage self-consistent description of the active site for FA decomposition on Pd/C. Our goal of coverage self-consistency emanates from the criterion that the coverages of surface intermediates as predicted by the microkinetic model should be in agreement with those utilized during DFT calculations,[42,45,122,186] which is oft-ignored in typical microkinetic modeling based analyses. Upon parameter estimation to fit with reaction kinetics experiments, the microkinetic models for clean Pd(111) and Pd(100) indicated a high coverage of CO* (~0.90 ML and ~0.99 ML for Pd(111) and Pd(100), respectively) under reaction conditions. These coverages were inconsistent with the starting assumption of a clean surface on which the energetics (or equivalently, the rate-parameters) for the clean Pd(111) and Pd(100) models were calculated upon. *Operando* Fourier Transformed Infrared Spectroscopy (FTIR) studies corroborated the presence of CO* under FA decomposition reaction conditions on Pd catalysts. Therefore, subsequent microkinetic models were parameterized with DFT energetics calculated on partially (5/9 ML) CO*-covered Pd surfaces, with explicit dependence of the thermochemistry and kinetics of the reaction network on the CO* coverage. The resultant "*CO* coverage-cognizant*" microkinetic models in addition to being self-consistent in CO* coverage, also provided quantitative agreement with the reaction kinetics experiments. Our results highlight

the importance of investigating reaction networks under realistic catalytic surface environment, in terms of the coverages of spectator species, for obtaining accurate initial estimates of the kinetic and thermodynamic rate-parameters. In addition, we also demonstrate that presence of spectator species can alter the reaction mechanism by enabling spectator-assisted reaction pathways to play a crucial role under reaction conditions. Our results provide detailed insights on the reaction mechanism, the nature of the active site, the rate-controlling steps, as well as the catalytic surface environment under reaction conditions.

4.2 Methods

4.2.1 Experimental Section

4.2.1.1 Reaction Kinetics Experiments

The reactor setup and experimental protocols were similar to those used in our previous studies.[42,45] The reaction kinetics experiments were performed using a 12.7 mm (outer diameter) stainless steel reactor, operated in a fixed-bed down-flow configuration. In a typical experiment, ca. 60 mg (dry weight) of 1 wt.% Pd/C catalyst (Sigma Aldrich) was charged into the reactor and packed in place using silica chips. The temperature of the reactor was measured using a K-type thermocouple and was modulated by a furnace connected to a variable autotransformer. Prior to the reactivity measurements, the catalyst was reduced *in situ* at 573 K (ramp rate of 1 K min^{-1}) under 25% H_2/He (60 cm^3 min^{-1}) for 4h and cooled down to the reaction temperature under He flow.

The experiments were performed at a total pressure of 1 atm. The partial pressures of gases were controlled at the reactor inlet using calibrated mass flow controllers. The partial pressures were maintained between 1-5% for FA, 0-10% for dehydrogenation products (H_2 and CO_2), and 0-0.1%

for dehydration products (H_2O and CO), with He as the balance gas. FA was introduced in the reactor system as a liquid using a syringe pump (Chemyx Inc.), evaporated at the reactor inlet and was carried through the reactor with He flow. The reactor effluent was passed through a condenser to remove the unconverted FA from the gas stream. The composition of the residual effluent stream was analyzed through a gas chromatograph with a thermal conductivity detector (GC-TCD, Shimadzu). At the steady-state, the composition of decomposition products – CO_2 and CO was used to determine the reaction rate corresponding to FA dehydrogenation and dehydration, respectively. The carbon balance was verified by measuring the condensed FA and the decomposition products CO/CO_2 and was determined to be within 99-99.5%. The conversion was calculated based on the number of moles of FA converted to the decomposition products (CO_2 + H_2 and CO + H_2O). To gather experimental data in a kinetically limited regime, the reactor was operated at differential conversion (below 10% conversion, for all but one data point) (Table D.1). The apparent activation energy barriers for the dehydrogenation and dehydration pathways were measured by varying the temperature from 353 to 393 K. The apparent reaction orders for dehydrogenation and dehydration pathways wrt. to the reactant – FA, dehydrogenation products – CO_2 and H_2, and dehydration products – CO and H_2O, were determined by varying the partial pressure of the respective component in the feed stream, at a total pressure of 1 atm and reaction temperature of 373 K.

4.2.1.2 Catalyst Characterization

The surface site density for the catalyst sample was determined by performing CO chemisorption at 298 K.[187] Prior to CO chemisorption, the catalyst sample was reduced using the same protocols followed during the reaction kinetics experiments, as described above. The Pd surface site density

was obtained using a surface stoichiometry of 3:2 for surface Pd atom:CO.[122,188] The TOFs for the dehydrogenation and dehydration pathways are reported with respect to the surface site-density of the Pd/C catalyst.

The morphology of the supported Pd/C catalyst was characterized using scanning transmission electron microscopy (FEI-Titan STEM) instrument with aberration correction (spatial resolution of <0.1 nm), operated at 200 kV. The images were collected in high-angle annular dark field (HAADF) mode with detector angle ranging from 54 to 270 mrad, probe convergence angle of 24.5 mrad, and probe current of approximately 25 pA. The samples were charged into the microscope through a procedure described previously.[45] The particle size distribution was determined by analyzing the STEM micrographs using the ImageJ software. The average particle size was determined by sum normalizing the particle diameters of the analyzed Pd/C catalyst (Figure D.1). Approximately 1400 particles, from different regions in the catalyst sample, were analyzed to determine the particle size distribution.

4.2.2 Microkinetic Modeling

4.2.2.1 Reaction Network

Our reaction network comprised of 5 gas-phase species, 13 surface species, and 28 elementary steps (Scheme 4.1). The elementary steps 1-5 represent the adsorption and desorption of the reactant and products, respectively. Steps 6-7 and 8-10 represent the formation of dehydrogenation product – CO_2 – through the direct decomposition of formate (HCOO*) and carboxyl (COOH*), respectively. The formation of dehydration product, CO, through the dehydroxylation of COOH* is indicated by steps 11-13. Steps 14-16 describe the reactions common with the redox mechanism

in the WGSR. Elementary reactions involving CO-/OH-/O-assisted decomposition routes are described by steps 17-28.

We calculate the energetics of the reaction network using DFT (GGA-PW91[189]; DACAPO[56,57]) on clean and on partially CO*-covered version of Pd(100) and Pd(111) (Appendix D). In this work, we utilize DFT energetics to obtain initial estimates of the thermodynamic and kinetic rate parameters and formulate mean-field microkinetic models.

Reaction Network for Formic Acid (FA) Decomposition

Adsorption/Desorption

1. $HCOOH(g) + * \leftrightarrow HCOOH*$
2. $CO_2* \leftrightarrow CO_2(g) + *$
3. $CO* \leftrightarrow CO(g) + *$
4. $H_2O* \leftrightarrow H_2O(g) + *$
5. $2H* \leftrightarrow H_2(g) + 2*$

Dehydrogenation

6. $HCOOH* + 2* \leftrightarrow HCOO* + H*$
7. $HCOO* \leftrightarrow CO_2* + H*$
8. $HCOOH* \leftrightarrow HCOOHpa*$
9. $HCOOHpa* + * \leftrightarrow COOH* + H*$
10. $COOH* + * \leftrightarrow CO_2* + H*$

Dehydration

11. $COOH* \leftrightarrow cis\text{-}COOH*$
12. $cis\text{-}COOH* + * \leftrightarrow CO* + OH*$
13. $OH* + H* \leftrightarrow H_2O* + *$

Redox

14. $2OH* + * \leftrightarrow H_2O* + O*$
15. $OH* + * \leftrightarrow O* + H*$
16. $CO* + O* \leftrightarrow CO_2* + *$

Spectator-Assisted

17. $HCOOH* + CO* + * \leftrightarrow HCOO* + COH*$
18. $HCOO* + CO* \leftrightarrow CO_2* + COH* + *$
19. $COOH* + CO* \leftrightarrow CO_2* + COH*$
20. $COH* + CO* \leftrightarrow CO* + HCO*$
21. $COH* \leftrightarrow CO* + H*$
22. $HCO* \leftrightarrow CO* + H*$
23. $HCO* + O* \leftrightarrow CO* + OH*$
24. $COH* + O* \leftrightarrow CO* + OH*$
25. $COH* + H* \leftrightarrow HCOH*$
26. $HCO* + H* \leftrightarrow HCOH*$
27. $HCOO* + OH* \leftrightarrow CO_2* + H* + OH*$
28. $HCOO* + H_2O* \leftrightarrow CO_2* + H* + H_2O*$

Scheme 4.1 Reaction network for the formic acid (FA) decomposition reaction considered in this study. Surface sites are denoted by '*'; adsorbed reaction intermediates are denoted by a subscript '*' (e.g., HCOOH*, HCOO*, COOH*, etc.).

4.2.2.2 Model Formulation

Given the low per pass conversion in our reaction kinetics experiments (<10%, for all but one data point), we modeled the reactor as a continuous stirred tank reactor (CSTR).[45] Entropy values corresponding to the adsorbed intermediates and transition states were calculated using the DFT-derived vibrational frequencies. Shomate parameters were fit using DFT-derived vibrational frequency calculations and statistical mechanics,[12] which were used to incorporate zero-point energy (ZPE) corrected and temperature-dependent thermochemistry and kinetics in our models. Parameter estimation was performed using the generic sequential optimization framework developed by Rangarajan et al.[41] The optimization objective (Equation 4.1) consisted of a least-squares representation of model-experiment mismatch corresponding to dehydrogenation and dehydration TOFs for all experimental conditions 'c', along with a term penalizing (δ = 0.05) the corrections from the DFT-derived energetics to obtain sparse solutions. By minimizing the objective function value (Equation 4.1), we search for corrections (π-π_{DFT}) in sensitive parameters that are required to fit model-predictions (y) with the experimental measured dehydrogenation and dehydration TOFs ($\overline{y}$).

$$Z_{Param.Est} = Min \sum_{c \in C} \left(1 - \frac{\overline{y_c}}{y_c}\right)^T \left(1 - \frac{\overline{y_c}}{y_c}\right) + \delta(\pi - \pi_{DFT})^T(\pi - \pi_{DFT}) \qquad (4.1)$$

To elucidate plausible alternate solutions, we employed a multi-start approach using Latin hypercube sampling to randomly initialize the starting values of the corrections to the DFT parameters (binding and transition state energies) from which the optimization is initiated. We searched for favorable solutions in a ±0.6 eV range from the DFT-derived binding and transition-state energy values.

Gas-phase reaction energetics were calculated using Shomate parameters for both dehydrogenation and dehydration pathways and were compared with the corresponding values obtained from NIST.[190] By adjusting the CO(g) gas-phase energy by -0.60 eV, we were able to achieve good agreement with the NIST reaction energetics. The adjusted CO(g) gas-phase energies is used in our microkinetic models. While discussing the corrections for adsorbed CO*, we explicitly specify if: (1) the correction refers to that determined using parameter estimation (i.e, correction in the energy of adsorbed CO* only) or (2) the correction refers to the 'overall' correction in the *binding* energy of CO* (i.e., considering the corrections for both adsorbed CO* and gas-phase CO(g)). The kinetic and thermochemistry parameters used in our models are included in Appendix D.

We utilized a mean-field implementation to account for spectator CO* coverage-effects.[8,45,158] By investigating the reaction network at varying levels of CO* coverage, we derived the polynomial functions for the binding energies (BE) and transition-state (TS) energies dependent on surface coverage of CO*. The binding energy of reaction intermediates were evaluated at different levels of spectator CO* coverages, varying from clean surface (i.e., no coadsorbed CO*) to 5/9 ML of spectator CO* in increments of 1/9 ML. The transition state energies were evaluated on clean and 5/9 ML CO* covered facets. The energetics used in the microkinetic models were updated on-the-fly per the CO* coverages determined during the model simulation, thereby ensuring the use of CO* coverage-cognizant energetics.[45]

Further, we used the optimized CO* coverage-dependent energetics to simulate a plug-flow reactor (PFR) and verified the applicability of a controlled-stirred tank reactor (CSTR) model. The results from the PFR simulation demonstrated that CO* coverages saturate rapidly (to within 10% of

steady-state CSTR coverages) in the initial portion of the reactor (~2% of normalized bed-length), which reinforces the choice of CSTR for performing parameter estimation and for modeling the kinetics of FA decomposition on Pd/C (Appendix D).

4.3 Results and Discussion

4.3.1 Reaction Kinetics Experiments

The apparent activation barriers for the dehydrogenation and dehydration pathways were measured in a temperature range of 353-393K. The activation energy barrier for the dehydrogenation pathway was determined as 69.0 kJ/mol (Figure 4.1), which were in agreement with the values (65-67 kJ/mol) reported in the literature for Pd/C catalysts. [104,180] The apparent activation energy barrier for the dehydration pathway was determined as 82.9 kJ/mol (Figure 4.1). The selectivity towards dehydrogenation pathway had a moderate temperature dependence, decreasing from 99.5% at 353 K to 98.9% at 393 K.

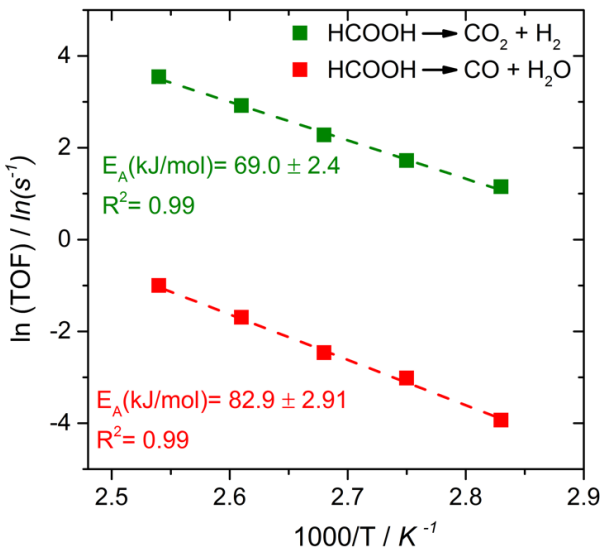


Figure 4.1 Arrhenius plot for FA dehydrogenation: HCOOH → CO_2 + H_2 (green) and dehydration: HCOOH → CO + H_2O (red) on Pd/C at 1 atm. The dashed lines represent the fit to the experimentally determined TOFs.

In a FA partial pressure range of 1-5%, we determined reaction orders with respect to FA of -0.03 and 0.08 for dehydrogenation and dehydration, respectively. Co-feeding the dehydration product CO had a strong poisoning effect on the FA decomposition reaction. Severe deactivation of Pd catalysts due to CO site blocking is well known and has been observed for both vapor- and liquid-phase FA decomposition. [82,104,180,191,192] CO partial pressure of 0.02% at 373 K, led to a 4-fold decrease in the dehydrogenation TOF compared with when no CO was co-fed (from 0.16 s^{-1} to 0.04 s^{-1}) (Table D.1). The reaction order with respect to CO was determined as -0.58 for the dehydrogenation pathway.

The reaction order with respect to H_2 was determined as -0.26 for the dehydrogenation reaction pathway and 0.02 for the dehydration pathway. The partial pressure of decomposition product CO_2 incurred no appreciable change in the TOFs of either reaction pathway. We observed a zero-reaction order with respect to CO_2 for the dehydrogenation pathway and a small positive order (0.11) for the dehydration reaction.

We observed a zero-reaction order with respect to H_2O for both dehydrogenation (0.02) and dehydration (0.04). Negligible improvement towards the dehydrogenation selectivity indicates absence of water-gas shift reaction under our experimental conditions, which is in agreement with previous experimental studies on Pd/C catalysts.[180]

4.3.2 Microkinetic Modeling Results

The models formulated using DFT energetics calculated on clean Pd(100) and Pd(111) predicted reaction rates that were several orders of magnitude smaller than the experimentally determined rates. We therefore performed parameter estimation to identify the corrections to the DFT

energetics that would yield quantitative agreement with the experimentally determined TOFs. The results from clean surface models are discussed in further detail below:

4.3.2.1 Clean Pd(100) model

Upon parameter estimation, the clean Pd(100) solution demonstrated an improved fit with the reaction kinetics experiments. The model predicted the experimental dehydrogenation and dehydration TOFs with a mean absolute percentage error (MAPE) of 13.1% (R^2 = 0.96) and 7.7% (R^2 = 0.98), respectively (Figure 4.2). However, the model was unable to fit the subset of experiments with cofeed of CO (Figure 4.2(a) - inset).

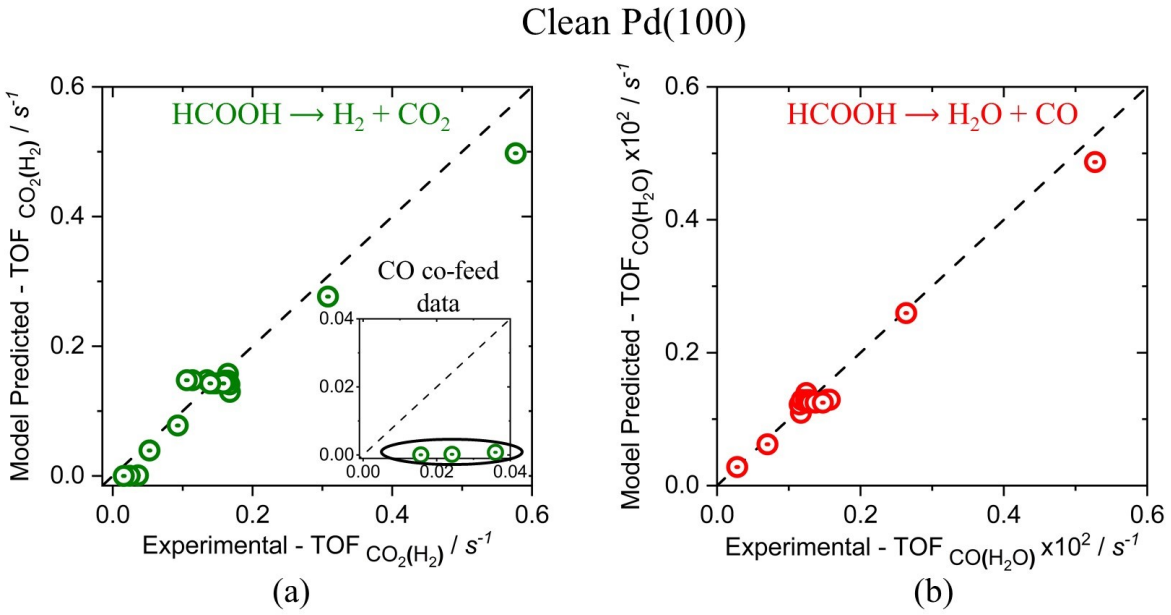


Figure 4.2 Parity plot of clean Pd(100) model predicted vs. experimental TOFs (s^{-1}) for (a) Dehydrogenation: HCOOH ⟶ CO_2 + H_2; inset shows the parity at low TOFs (corresponding to CO co-feed experiments), (b) Dehydration: HCOOH ⟶ CO + H_2O.

To achieve this parity with the experiments, parameter estimation required several large corrections to the DFT-derived binding energies and activation energy barriers (Table 4.1). The binding energy of HCOOH*pa** required a correction of -0.36 eV. The binding energy of CO* and

H* required destabilization by 0.67 eV and 0.26 eV, respectively. In terms of activation energy barriers, the COOH* formation (HCOOH*pa** → COOH* + H*) and COOH* dehydrogenation (COOH* → CO_2* + H*) required lowering of activation energy barriers by 0.26 eV and 0.37 eV, respectively. Recombinative desorption of H_2 required lowering of activation energy barrier by 0.80 eV, largely due to significant destabilization of the initial state involving 2H* (each H* required a destabilization of 0.26 eV). The large corrections in the binding energies and activation energy barriers to improve parity with the experiments suggests that the clean Pd(100) surface is not a good representation for the active site of FA decomposition on Pd/C.

Table 4.1 Corrections to the DFT-derived binding energy of the reaction intermediates and activation energy of the elementary steps for the clean Pd(100) model, as obtained from parameter estimation. †For CO*, the number outside the parenthesis refers to the correction in the energy of CO* as predicted from parameter estimation, while the number within the parenthesis ([•]) represents the 'overall' correction in the binding energy of CO*, including the adjustment to the CO(g) gas-phase energy by -0.60 eV (see Model Formulation).

Clean Pd(100)	*Corrections / eV*
Intermediate	*ΔBE*
HCOOH*pa**	-0.36
CO*	0.07 [0.67]†
H*	0.26
Elementary Step	ΔE_A
HCOOH* ↔ HCOOH*pa**	-0.26
COOH* + * ↔ CO_2* + H*	-0.37
COOH* + * ↔ CO* + OH*	-0.16
2H* ↔ H_2(g) + 2*	-0.80

The optimized model predicted the reaction to occur through the carboxyl (COOH*) pathway. The dehydrogenation reaction occurred through direct decomposition of COOH* (HCOOH* → HCOOH*pa** → COOH* + H* → CO_2* + 2H* → CO_2 + H_2). While the dehydration reaction occurred through dehydroxylation of COOH* (HCOOH* → HCOOH*pa** → COOH* + H* → CO* + OH* + H* → CO + H_2O). Under all experimental conditions, the clean Pd(100) model was

predicted to be almost entirely covered by CO* (~0.99 ML) (Figure 4.3). The high-coverage of CO* and large corrections in the binding energies and activation energy barriers to fit the experiments suggests that the clean Pd(100) surface is not a good representation for the active site of FA decomposition on Pd/C.

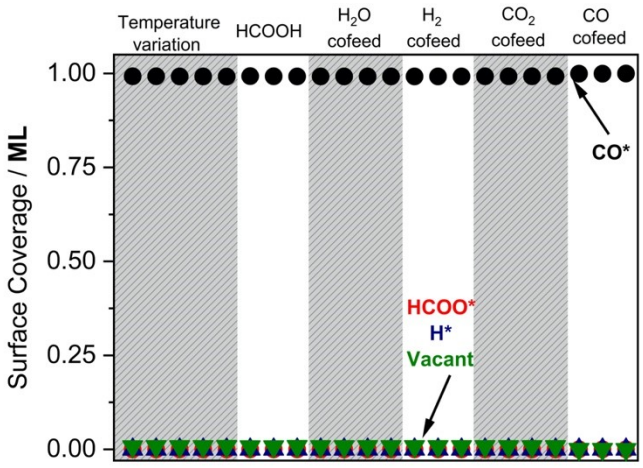


Figure 4.3 Surface coverages predicted by the optimized clean Pd(100) model under various experimental conditions. Going from left to right, the shaded regions correspond to different experimental conditions (eg. variation in temperature, variation in the partial pressure of reactant/product, etc.). The experimental data points for various shaded regions, are listed in Table D.1: Variation in Temperature (#1-5), P(HCOOH) (#6-8), P(H_2O) (#9-12), P(H_2) (#13-15), P(CO_2) (#16-19) and P(CO) (#20-22). In each shaded region, going left to right indicates the increase in the value of the corresponding experimental parameter (i.e., temperature or partial pressure of the indicated gas-phase species), e.g. for the section labeled 'Temperature variation' moving left to right, i.e. #1-5 (Table D.1), indicates increase in temperature, with other experimental parameters held constant.

In summary, the clean Pd(100) model: (1) failed to explain the entire kinetic dataset, since it did not capture the CO cofeed experiments accurately, (2) required several large corrections of the DFT-derived binding energies and activation energy barriers, and (3) predicted ~0.99 ML of CO* (under all experimental conditions), which was inconsistent with the starting assumption of a clean surface at which the DFT energetics were calculated. The clean Pd(100) model therefore, failed to accurately represent the nature of the active site for FA decomposition on Pd/C.

4.3.2.2 Clean Pd(111) model

Similar to the clean Pd(100) model, upon parameter estimation, the clean Pd(111) model demonstrated an improved fit with the reaction kinetics experiments. The model reproduced the experimental dehydrogenation and dehydration TOFs with a MAPE of 11.1% (R^2 = 0.91) and 8.6% (R^2 = 0.98), respectively (Figure 4.4). However, the model significantly under-predicted the dehydrogenation TOFs for the CO-cofeed subset of the experiments (Figure 4.4(a) – inset).

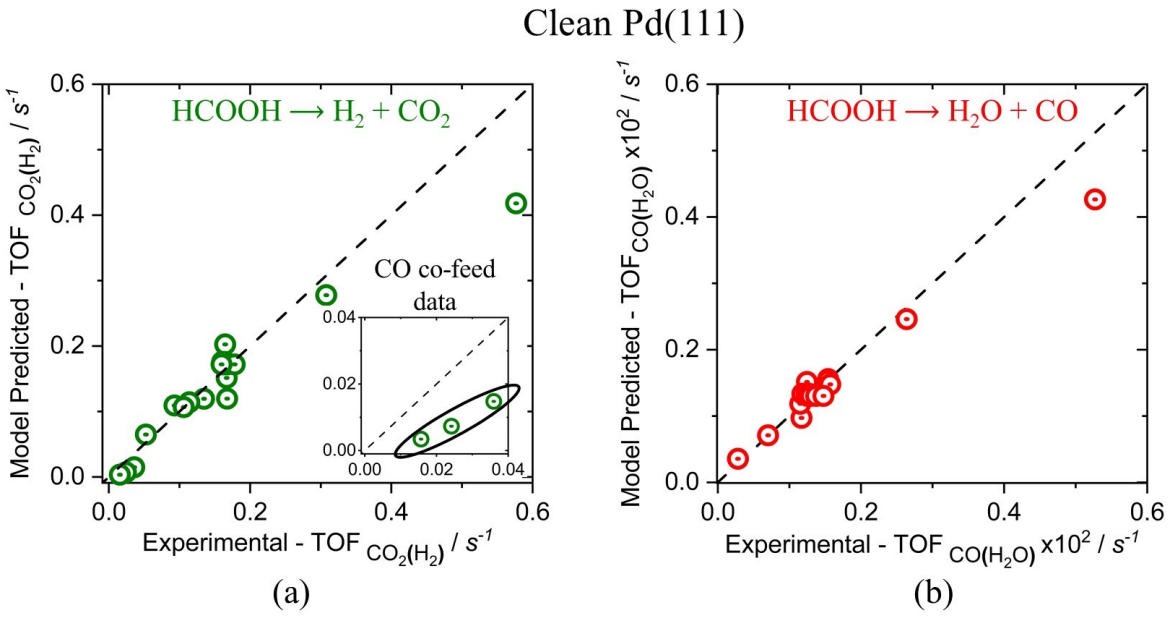


Figure 4.4 Parity plot of clean Pd(111) model predicted vs. experimental TOFs (s^{-1}) for (a) Dehydrogenation: HCOOH → CO_2 + H_2; inset shows the parity at low TOFs (corresponding to CO co-feed experiments), (b) Dehydration: HCOOH → CO + H_2O.

To achieve this fit with the reaction kinetics experiments, the model required a large correction to the binding energy of CO* by 0.88 eV (Table 4.2). The binding energy of H* required a correction of 0.16 eV. Additionally, the activation energy barrier for the FA isomerization step (HCOOH* → HCOOH*pa**) required a correction of +0.29 eV. The activation energy barriers for the COOH* formation (HCOOHpa* → COOH* + H*) and dehydrogenation (COOH* → CO_2* + H*) required

corrections of -0.12 eV and -0.13 eV, both of which are within the DFT (PW91-GGA) error. The activation energy barrier for dehydroxylation of COOH* (COOH* → CO* + OH*) and formation of water (H* + OH* → H_2O*) required corrections of -0.26 eV and -0.29 eV, respectively.

Table 4.2 Corrections to the DFT-derived binding energy of the reaction intermediates and activation energy of the elementary steps for the clean Pd(111) model, as obtained from parameter estimation. †For CO*, the number outside the parenthesis refers to the correction in the energy of CO* as predicted from parameter estimation, while the number within the parenthesis ([•]) represents the 'overall' correction in the binding energy of CO*, including the adjustment to the CO(g) gas-phase energy by -0.60 eV (see Model Formulation).

Clean Pd(111)	*Corrections / eV*
Intermediate	*ΔBE*
HCOOH*	-0.21
HCOOH*pa**	-0.19
CO*	0.28 [0.88]†
H*	0.16
Elementary Step	ΔE_A
HCOOH* ↔ HCOOH*pa**	0.29
HCOOH*pa** + * ↔ COOH* + H*	-0.12
COOH* + * ↔ CO_2* + H*	-0.14
COOH* + * ↔ CO* + OH*	-0.26
H_2O* + * ↔ H* + OH*	-0.29

Similar to the clean Pd(100) model, the clean Pd(111) model predicted the reaction to occur through the carboxyl (COOH*) pathway. The dehydrogenation and dehydration reactions occurred through the COOH*-dehydrogenation (HCOOH* → HCOOH*pa** → COOH* + H* → CO_2* + 2H* → CO_2 + H_2) and COOH*-dehydroxylation mechanisms (HCOOH* → HCOOH*pa** → COOH* + H* → CO* + OH* + H* → CO + H_2O), respectively. Averaged over the experimental conditions, the model predicted surface coverage of 0.88 ML CO*, 0.09 ML H*, and 0.02 ML vacant sites (Figure 4.5).

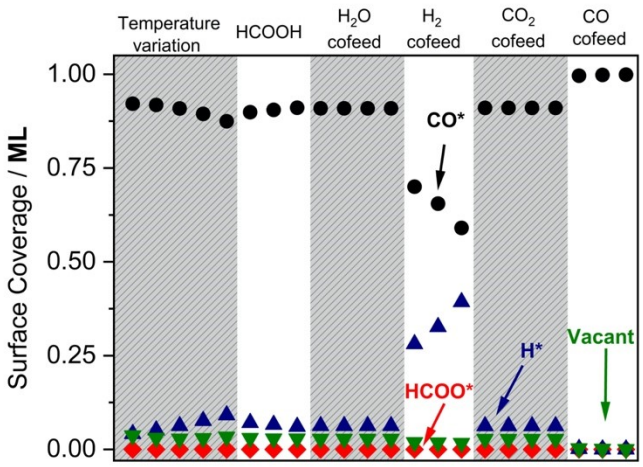


Figure 4.5 Surface coverages predicted by the optimized clean Pd(111) model under various experimental conditions. Going from left to right, the shaded regions correspond to different experimental conditions (eg. variation in temperature, variation in the partial pressure of reactant/product, etc.). The experimental data points for various shaded regions, are listed in Table D.1: Variation in Temperature (#1-5), P(HCOOH) (#6-8), P(H_2O) (#9-12), P(H_2) (#13-15), P(CO_2) (#16-19) and P(CO) (#20-22). In each shaded region, going left to right indicates the increase in the value of the corresponding experimental parameter (i.e., temperature or partial pressure of the indicated gas-phase species), e.g. for the section labeled 'Temperature variation' moving left to right, i.e. #1-5 (Table D.1), indicates increase in temperature, with other experimental parameters held constant.

In summary, the clean Pd(111) model: (1) was unable to capture the CO-cofeed subset of the reaction kinetics experiments, (2) required several large corrections of the DFT-derived binding energies and activation energy barriers, and (3) predicted ~0.90 ML of CO* (averaged over all experimental conditions), which was inconsistent with the starting assumption of a clean surface. The clean Pd(111) model, therefore, does not accurately represent the nature of the active site for FA decomposition on Pd/C.

The results obtained from the optimized (i.e., parameter-adjusted) clean Pd(100) and clean Pd(111) solutions were as follows: (1) Both models failed to accurately predict the dehydrogenation reaction rates for the CO co-feed subset (0.02-0.1% CO, 2.6% FA, 373 K) of the experimental dataset. Under these conditions, both models significantly underpredicted the dehydrogenation

TOFs compared with those determined experimentally. (2) Both models required large corrections of >0.3 eV for several parameters, which were outside of the DFT error of ~0.2 eV for PW91-GGA.[138,143] (3) Averaged over the experimental conditions, both models predicted high surface coverage of CO* (~0.99 ML and ~0.90 ML for Pd(100) and Pd(111), respectively) which was inconsistent with the assumption of a clean surface at which the DFT energetics for these models were calculated upon. The models were therefore inconsistent in terms of the surface coverages. Since the clean Pd(100) and clean Pd(111) solutions failed on the three counts noted above, we conclude that these models do not accurately capture the nature of the active site and its surface environment under reaction conditions.

We performed *operando* FTIR studies to directly probe the nature of surface species and obtain an estimate for the surface coverage of the reaction intermediates under FA decomposition reaction conditions (Appendix D). By comparing the spectra (Figure D.2) under reaction conditions with that obtained under CO/He feed (at the same temperature), we determined a significant coverage of adsorbed CO* species on the surface of the catalyst. The peak height was determined to be ~75% that of the saturation coverage, as obtained under a CO-only feed. The saturation coverage on Pd(111) and Pd(100) is reported between 0.5-0.7 ML,[116,193–199] under low CO partial pressure. Our results therefore suggest a CO* coverage of ~0.3 ML on Pd(111) and ~0.5 ML on Pd(100), under experimental conditions, which is in agreement with the observations made by Wachs and Madix (Appendix D).[200]

Using the experimentally determined estimate for the *in situ* coverage of CO*, we reperformed the DFT calculations on (5/9 ML) CO*-covered Pd(100) and Pd(111). Subsequently, CO* coverage-cognizant microkinetic models were formulated for both Pd(100) and Pd(111), with explicit

consideration of the variation in binding and transition-state energies on the CO* coverage. Both models predicted reaction rates that were several orders of magnitude smaller than the experimentally observed rates. We therefore performed parameter estimation to adjust the energetics and improve parity with the experiments. We note that the CO*-spectator coverage of 5/9 ML, informed by the *operando FTIR* studies, was used only as an initial estimate of the *in situ* CO* coverage. In case the microkinetic model predictions for the surface coverages were drastically different from those utilized herein, we would have re-evaluated the reaction network under the presence of suitable coverages of the relevant reaction intermediate(s). The solutions from parameter estimation for the CO* coverage-cognizant Pd(100) and Pd(111) models are presented below:

4.3.2.3 CO Coverage-Cognizant Pd(100) Model*

The microkinetic model formulated using DFT energetics derived on 5/9 ML CO*-covered Pd(100) failed to fit our experimental dataset satisfactorily. First, the Pd(100) solution was completely selective towards dehydrogenation; i.e., the model failed to predict any flux through the dehydration pathway (Figure 4.6 (b)). This was in contrast with our experimental measurements, wherein we determined both dehydrogenation and dehydration to be active on Pd/C, with ~99% selectivity towards dehydrogenation. Second, under CO co-feed conditions (0.02-0.1% CO, 2.6 % FA, 373 K), the model predicted a complete shutdown of the dehydrogenation reaction (Figure 4.6 (a) – inset), whereas experimentally we determined the reaction to be active, although the TOFs were reduced by factor of 4-10, compared with those under home conditions (2.6% FA, 373 K).

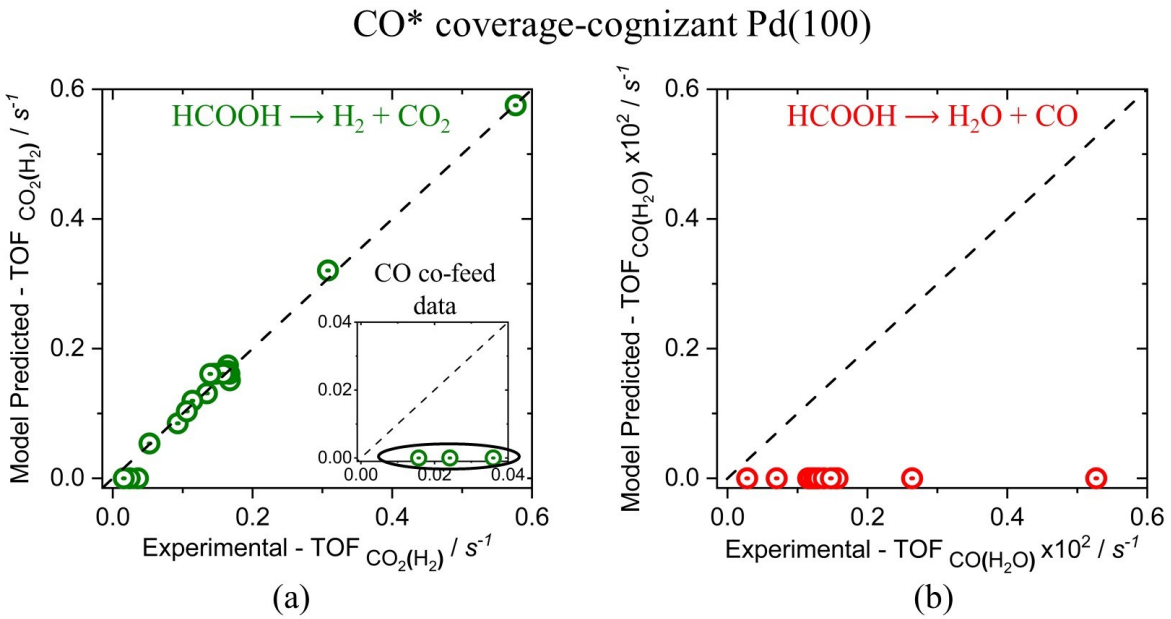


Figure 4.6 Parity plot of CO*-coverage cognizant Pd(100) model predicted vs. experimental TOFs (s^{-1}) for (a) Dehydrogenation: HCOOH → CO_2 + H_2; inset shows the parity at low TOFs (corresponding to CO co-feed experiments), (b) Dehydration: HCOOH → CO + H_2O.

On Pd(100), the reaction occurs through the formate mechanism (HCOOH* → HCOO* + H* → CO_2* + 2H* → CO_2 + H_2). Our model predicted no flux through the carboxyl (COOH*) mechanism under our reaction conditions. Since carboxyl is a precursor for CO formation, the lack of carboxyl participation in the reaction mechanism under steady-state catalytic conditions, resulted in no reaction flux going through dehydration pathway on partially CO*-covered Pd(100). Parameter estimation led to a stabilization in the BE of HCOO* by 0.16 eV (Table 4.3). The BE of H* and CO* required corrections of 0.16 eV and 0.19 eV, respectively. Parameter estimation required three corrections to the activation energy barriers, all of which were within the PW91-GGA error. The activation energy barriers for HCOO* formation (HCOOH* + 2* → HCOO* + H*) and HCOO* decomposition (HCOO* → CO_2* + H*) steps required corrections of –0.08 eV

and –0.10 eV, respectively. The H-H recombinative desorption step to form H_2(g) required a correction of +0.14 eV.

Table 4.3 Corrections to the DFT-derived binding energy of the reaction intermediates and activation energy of the elementary steps for the CO* coverage-cognizant Pd(100) model, as obtained from parameter estimation. †For CO*, the number outside the parenthesis refers to the correction in the energy of CO* as predicted from parameter estimation, while the number within the parenthesis ([•]) represents the 'overall' correction in the binding energy of CO*, which also includes the adjustment to the CO(g) gas-phase energy by -0.60 eV (see Model Formulation).

5/9 ML CO-covered Pd(100)*	*Corrections / eV*
Intermediate	ΔBE
HCOO*	-0.16
CO*	-0.41 [0.19]†
H*	0.16
Elementary Step	ΔE_A
HCOOH* + 2* ↔ HCOO* + H*	-0.08
HCOO* ↔ CO_2* + H*	-0.10
2H* ↔ H_2(g) + 2*	0.14

Averaged over the experimental conditions, the model predicted surface coverages of 0.44 ML CO*, 0.06 ML H*, and 0.50 ML vacant sites (Figure 4.7). Consistent with the assumption of a 5/9 ML CO*-covered Pd(100) at which DFT energetics were calculated, this model predicts a high CO* coverage under reaction conditions. The model is therefore self-consistent in CO* coverage. Averaged over the experimental conditions, the model also predicts ~10^{-3} ML HCOO*, which has been suggested as a reaction intermediate by FTIR studies in context of FA decomposition on Pd catalysts.[101,201–207]

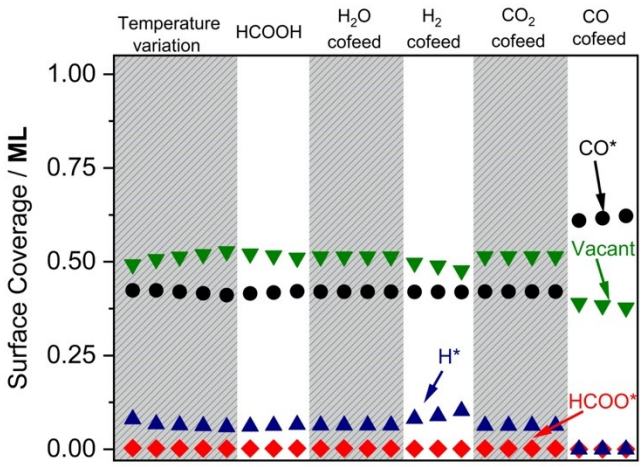


Figure 4.7 Coverages of relevant reaction intermediates under various experimental conditions, as predicted by the optimized CO* coverage-cognizant Pd(100) model. Going from left to right, the shaded regions correspond to different experimental conditions (eg. variation in temperature, variation in the partial pressure of reactant/product, etc.). The experimental data points for various shaded regions, are listed in Table D.1: Variation in Temperature (#1-5), P(HCOOH) (#6-8), P(H_2O) (#9-12), P(H_2) (#13-15), P(CO_2) (#16-19) and P(CO) (#20-22). In each shaded region, going left to right indicates the increase in the value of the corresponding experimental parameter (i.e., temperature or partial pressure of the indicated gas-phase species), e.g. for the section labeled 'Temperature variation' moving left to right, i.e. #1-5 (Table D.1), indicates increase in temperature, with other experimental parameters held constant.

In summary, our results suggest that the FA decomposition reaction occurs through the HCOO* mechanism on Pd(100). Under the examined conditions, we determine CO* as the most abundant surface intermediate with a coverage of ~4/9 ML. The optimized CO*-coverage cognizant Pd(100) model failed to accurately rationalize the experimentally determined dehydration selectivity on Pd/C. Contrary to the experiments, the model was found to be completely selective towards FA dehydrogenation and predicted no flux through dehydration pathway. In addition, the model was unable to capture the FA dehydrogenation TOFs under CO-cofeed conditions. We therefore conclude that Pd(100), by itself, fails to capture the active site for FA decomposition on Pd/C. However, since the model required small corrections to the DFT energetics to explain the dehydrogenation subset of the reaction kinetics experiments, we do not disqualify the possibility

that the Pd(100) facet could potentially contribute towards a portion of the dehydrogenation flux, under certain reaction conditions.

4.3.3 CO* Coverage-Cognizant Pd(111) Model

Upon parameter estimation, the model formulated using DFT energetics derived on the 5/9 ML CO*-covered Pd(111) yielded one solution that was able to rationalize the reaction kinetics experiments. The parity plots comparing the model-predicted TOFs with the experimental values (Figure 4.8) demonstrate a good fit with a mean absolute percentage error of 3.7% ($R^2 = 0.94$) and mean relative percentage error of 7.3% ($R^2 = 0.96$) for the dehydrogenation and dehydration pathways, respectively. Importantly, the model was able to capture the CO co-feed subset of the experimental dataset which was not captured satisfactorily by the clean Pd(100) model, the clean Pd(111) model, or the CO* coverage-cognizant Pd(100) model.

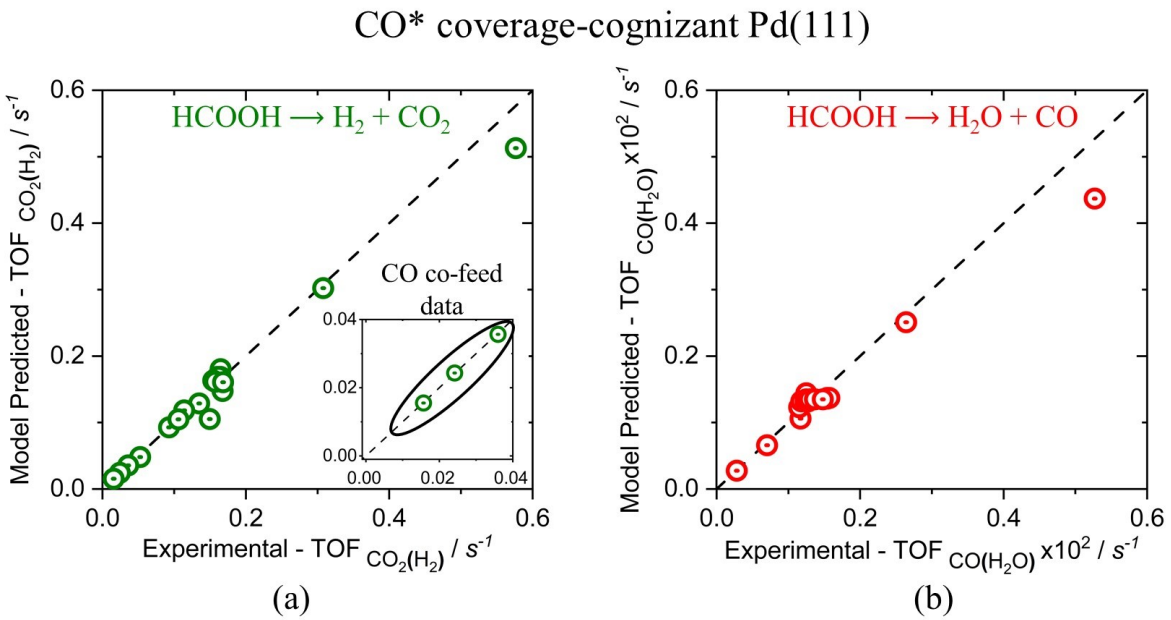


Figure 4.8 Parity plot of CO*-coverage cognizant Pd(111) model predicted vs. experimental TOFs (s^{-1}) for (a) Dehydrogenation: HCOOH ⟶ CO_2 + H_2; inset shows the parity at low TOFs (corresponding to CO co-feed experiments), (b) Dehydration: HCOOH ⟶ CO + H_2O.

To fit the experimental kinetics dataset, parameter estimation required stabilizing the binding energy of closed-shell intermediates, HCOOH* and HCOOH*pa**, by 0.27 and 0.16 eV, respectively (Table 4.4). Since standard DFT functionals (in particular PW91-GGA utilized here) fail to account for long-range dispersion interactions,[143,145] these corrections suggested by parameter estimation can be attributed to the lack of consideration of these effects in our theoretical treatment (PW91-GGA). To the best our knowledge there are no studies reporting the experimentally determined binding energy of HCOOH* on Pd(111) which could facilitate a direct comparison vis-à-vis the DFT computed binding energy. However, by comparing with the experimentally (single crystal adsorption calorimetry (SCAC)) reported binding energy of HCOOH* at low-coverage level (1/4ML) on Pt(111) (BE = –0.37 eV)[146] and on Ni(111) (BE = –0.32 eV)[208], we determined that PW91-GGA, using a computational setup consistent with that used this study,[108] systematically underpredicts the BE of HCOOH* by ~0.2-0.3 eV (Appendix D); this is similar in magnitude to the stabilization for HCOOH* predicted by our parameter estimation procedure. Parameter estimation requires stabilization of *cis*-COOH* by 0.09 eV, which is within the error of PW91-GGA. The binding energy of H* and CO* required destabilization by 0.15 and 0.34 eV (overall correction for CO*; including the correction of CO(g) energy of -0.60 eV), respectively. Benchmarking study by Wellendorff *et al.*, which compared the SCAC adsorption energies of chemisorbed species with that obtained using DFT, revealed systematic over-binding of such species with the PW91-GGA functional.[143] Binding of CO* on clean Pd(111) required a destabilization of ~0.47 eV to match the SCAC values measured at low adsorbate coverages (1/4 ML).[195] Similarly, the reaction energy for dissociative adsorption of H_2 on Pd(111) was calculated as -1.19 eV compared to experimentally measured value of -0.91 eV[143] for 1/4 ML of adsorbed

H*, which translates to PW91-GGA overpredicting the binding of H* by 0.14 eV. Thus, the corrections to the adsorbate binding energies, predicted by parameter estimation, are consistent with the intrinsic errors of PW91-GGA DFT calculations (Appendix D). In addition, this solution required three corrections for the activation energy barriers. The activation energy barrier for (1) dehydrogenation of HCOOH*pa** to form COOH* + H* required a correction of -0.19 eV, (2) H-H recombination to form H_2(g) required a correction of -0.20 eV, and (3) dehydrogenation of COH* to form CO* + H* required a correction of 0.08 eV, all of these are within the typical errors of ~0.2 eV for PW91-GGA functional.

Table 4.4 Corrections to the DFT-derived binding energy of the reaction intermediates and activation energy of the elementary steps for the CO* coverage-cognizant Pd(111) model, as obtained from parameter estimation. †For CO*, the number outside the parenthesis refers to the correction in the energy of CO* as predicted from parameter estimation, while the number within the parenthesis ([•]) represents the 'overall' correction in the binding energy of CO*, which also includes the adjustment to the CO(g) gas-phase energy by -0.60 eV (see Model Formulation).

5/9 ML CO-covered Pd(111)*	*Corrections / eV*
Intermediate	ΔBE
HCOOH*	-0.27
HCOOH*pa**	-0.16
cis-COOH*	0.09
CO*	-0.26 [0.34]†
H*	0.15
Elementary Step	ΔE_A
HCOOH*pa** + * ↔ COOH* + H*	-0.19
2H* ↔ H_2(g) + 2*	-0.20
COH* + * ↔ CO* + H*	0.08

For the optimized CO*-coverage cognizant Pd(111) solution, the flux goes entirely through the carboxyl (COOH*) mechanism (Figure 4.9). Under all experimental conditions, the dehydration reaction goes through the dehydroxylation of *cis*-COOH* (HCOOH* → HCOOH*pa** → COOH* + H* → *cis*-COOH* + H* → CO* + OH* + H* → CO + H_2O). While, the dehydrogenation

reaction occurs via two sub-mechanisms: (1) direct decomposition of COOH* (HCOOH* → HCOOH*pa** → COOH* + H* → CO_2* + 2H* → CO_2 + H_2) and (2) CO*-assisted decomposition of COOH* (HCOOH* (+**CO***) → HCOOH*pa** (+**CO***) → COOH* + H* (+**CO***) → CO_2* + H* + **CO**H* → CO_2* + 2H* (+**CO***) → CO_2 + H_2 (+**CO***); spectator CO* are denoted by (+**CO***)). In the CO*-assisted mechanism, COOH* donates the H to a spectator CO* to form COH*, which then dehydrogenates to release H* and regenerate the spectator CO*. At our home conditions (2.6% FA, 373 K), the CO*-assisted COOH* mechanism contributes ~40% of the dehydrogenation flux, with the remainder accounted for by the direct COOH* mechanism. Interestingly, we find that under CO co-feed condition (0.02-0.1% CO, 2.6% FA, 373 K) the direct COOH* mechanism becomes inactive and only the CO*-assisted COOH* mechanism contributes towards the observed dehydrogenation flux.

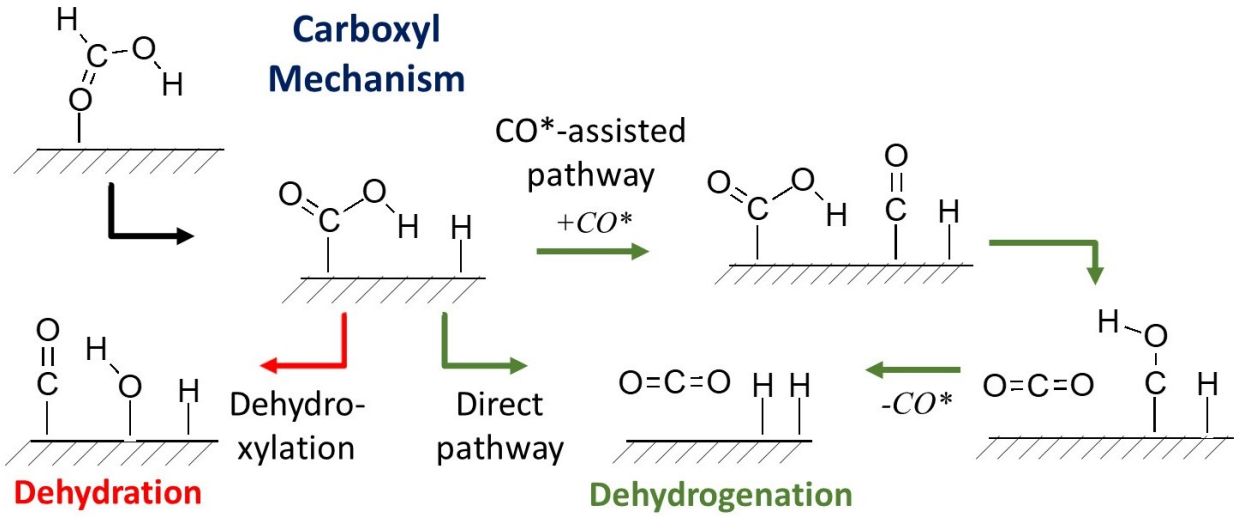


Figure 4.9 Simplified reaction mechanism for FA decomposition determined by the optimized CO*-coverage cognizant Pd(111) model (isomerization steps are not explicitly shown). The green and red arrows correspond to the elementary steps in the dehydrogenation (green arrows) and dehydration (red arrows) pathways, respectively. Elementary steps with participation of a spectator CO* are denoted by ±*CO** next to the arrows.

At the home conditions (2.6% FA, 373 K) and considering the entire reaction network (both dehydrogenation and dehydration), the degree of rate control[60] (X_{RC}) for the dehydrogenation pathway was distributed over three elementary steps: (1) COOH* $\rightarrow$ CO_2* + H* (X_{RC} = 0.25), (2) COH* $\rightarrow$ CO* + H* (X_{RC} = 0.24), and (3) H* + H* $\rightarrow$ H_2(g) (X_{RC} = 0.23). Further, X_{RC} values determined by considering: (1) direct COOH* mechanism and (2) CO*-assisted COOH* mechanism, one-at-a-time are provided in the Table D.13 (Appendix D). Averaged over all experimental conditions, the optimized CO*-coverage cognizant Pd(111) model predicts surface coverages of 0.34 ML CO*, 0.05 ML COH*, 0.02 ML H*, and 0.59 ML vacant sites (Figure 4.10). Consistent with the assumption of a partially CO*-covered Pd(111) surface at which the energetics for this model were derived, the optimized model suggests CO* as the most abundant surface intermediate. Although the model predicted CO* coverages were ~2/9 ML lower than the coverage of 5/9 ML that was explicitly considered in our DFT calculations, the inclusion of CO*-coverage dependent thermochemistry and kinetics ensured the use of energetics that were consistent with the CO* coverages predicted by microkinetic models.

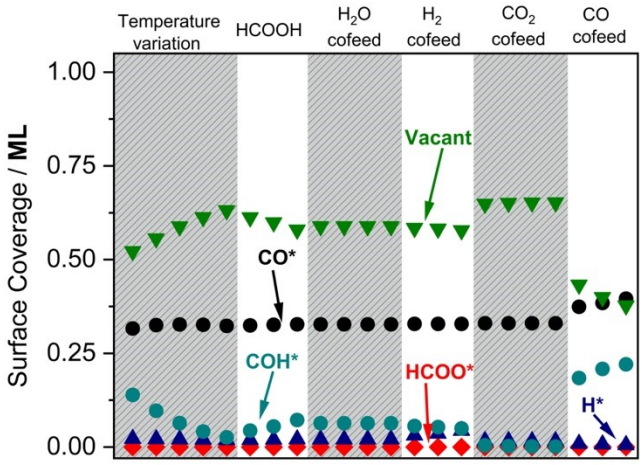


Figure 4.10 Coverages of relevant reaction intermediates under various experimental conditions, as predicted by the optimized CO* coverage-cognizant Pd(111) model. Going from left to right, the shaded regions correspond to different experimental conditions (eg. variation in temperature, variation in the partial pressure of reactant/product, etc.). The experimental data points for various shaded regions, are listed in Table D.1: Variation in Temperature (#1-5), P(HCOOH) (#6-8), P(H_2O) (#9-12), P(H_2) (#13-15), P(CO_2) (#16-19) and P(CO) (#20-22). In each shaded region, going left to right indicates the increase in the value of the corresponding experimental parameter (i.e., temperature or partial pressure of the indicated gas-phase species), e.g. for the section labeled 'Temperature variation' moving left to right, i.e. #1-5 (Table D.1), indicates increase in temperature, with other experimental parameters held constant.

Inclusion of CO* coverage-dependent energetics and of spectator CO*-assisted mechanisms were found crucial in explaining the experiments, especially for the CO-cofeed subset of the experimental dataset (0.02-0.1% CO, 2.6% FA, 373 K). Under these conditions, our models suggest that the coverage of CO* increased to ~0.4 ML compared with ~0.32 ML of CO* under the home conditions (2.6% FA, 373 K). This increase in CO* coverage destabilizes the energetics for the direct COOH* mechanism, through lateral adsorbate-adsorbate interactions, and renders the direct COOH* mechanism inactive under the CO-cofeed conditions. The increased CO* coverage, however, enables the spectator CO*-assisted COOH* decomposition routes to contribute towards the dehydrogenation flux under CO-cofeed conditions. Our results therefore suggest that inclusion of coverage effects, in particular the use of energetics cognizant with

coverages of spectator species, and consideration of spectator-assisted mechanisms were critical for accurately capturing reaction kinetics experiments, especially when surface coverages are expected to change across the various experimental conditions. Further, the model demonstrated close agreement with the experimentally determined apparent activation energy barriers and reaction orders, for both the dehydrogenation and dehydration pathways (Table 4.5).

Table 4.5 Comparison of experimentally determined and model-predicted apparent activation energy barrier and reaction orders with respect to the partial pressure of HCOOH, H_2O, H_2, CO_2 and CO for the dehydrogenation (HCOOH → CO_2 + H_2) and dehydration pathway (HCOOH → CO + H_2O). †The dehydration reaction order for the CO cofeed experiments could not be accurately quantified due to small selectivity of Pd/C towards CO formation.

CO(111) model	**Dehydrogenation**		**Dehydration**	
	Expt	**Model**	**Expt**	**Model**
E_A (kJ/mol)	69.0	68.2	82.9	79.4
HCOOH	-0.03	0.22	0.08	0.34
H_2O	-0.02	0.00	0.04	0.00
H_2	-0.26	-0.23	0.02	0.00
CO_2	-0.00	-0.02	0.11	0.00
CO	-0.58	-0.58	--†	--†

In summary, the optimized CO*-coverage cognizant Pd(111) model was able to accurately capture our reaction kinetics experiments. The corrections to the DFT-derived activation energy barriers were within the DFT error of ~0.2 eV, typically ascribed to GGA-based functionals.[138,143] Averaged over the experimental conditions, the model predicted CO* coverage of ~3/9 ML which was consistent with assumption of a partially CO*-covered Pd(111), at which DFT energetics for this model were calculated upon. The model is therefore, self-consistent with respect to the surface coverages of CO*. The reaction flux for both the dehydrogenation and dehydration pathways goes through the COOH* mechanism. Finally, our results suggest that CO* spectator-assisted COOH*

mechanism plays a critical role in rationalizing the experimentally observed reaction fluxes, especially for the CO-cofeed experiments.

4.4 Active Site for Vapor-Phase Decomposition of FA on Pd/C

The optimized CO*-coverage cognizant Pd(100) model failed to serve as an accurate model for the active site of FA decomposition on Pd/C. Although the model was self-consistent in terms of the CO* coverage and the corrections to the energetics were within the DFT error, it was unable to rationalize the experimental dataset, specifically on the following two counts: (1) Contrary to the experimentally determined selectivity of ~1% towards FA dehydration, the model predicted no flux through the dehydration pathway, under any experimental condition. The Pd(100) model therefore failed to capture the selectivity towards dehydration reaction. (2) The Pd(100) model failed to capture the dehydrogenation TOFs for the CO-cofeed conditions. Contrary to the reaction kinetics experiments, the model predicted a complete shutdown of the dehydrogenation reaction under CO-cofeed conditions.

On the other hand, the optimized CO*-coverage cognizant Pd(111) model was able to fit the entire experimental kinetics dataset (both the dehydrogenation and dehydration TOFs), and required corrections to the DT energetics that were within the error of PW91-GGA functional. Averaged over the experimental conditions, the model predicted coverage of ~1/3 ML CO* was consistent with the assumption of a partially CO*-covered surface at which the DFT energetics for this model were calculated upon.

From our results, we believe that the following two descriptions are plausible for the Pd/C nanoparticles, under the considered reaction conditions (Figure 4.11). (1) **Single-site model**:

Wherein the Pd(111) facets of the nanoparticle are partially covered with CO* (~0.3 ML) and serve as the active site for FA decomposition, converting FA to H_2+CO_2 and H_2O+CO via the dehydrogenation and dehydration pathways, respectively. While the Pd(100) facets are largely poisoned by CO* (0.4-0.5 ML) and do not contribute towards the FA decomposition reactivity (Figure 4.11 (a)). (2) **Dual-site model**: Since, the corrections for both partially CO*-covered Pd(111) and Pd(100) models were found to be within the DFT error – we cannot exclude the possibility that both these facets contribute towards the FA decomposition reactivity (Figure 4.11 (b)). In such a scenario, both Pd(100) and Pd(111) facets contribute towards the dehydrogenation flux. However, since our results suggest that Pd(100) preferentially decomposes FA to H_2, only the Pd(111) facets would account for the dehydration flux. Importantly, under CO-cofeed conditions, since Pd(100) was determined to be poisoned by CO* and was rendered inactive, only Pd(111) would contribute toward the dehydrogenation flux.

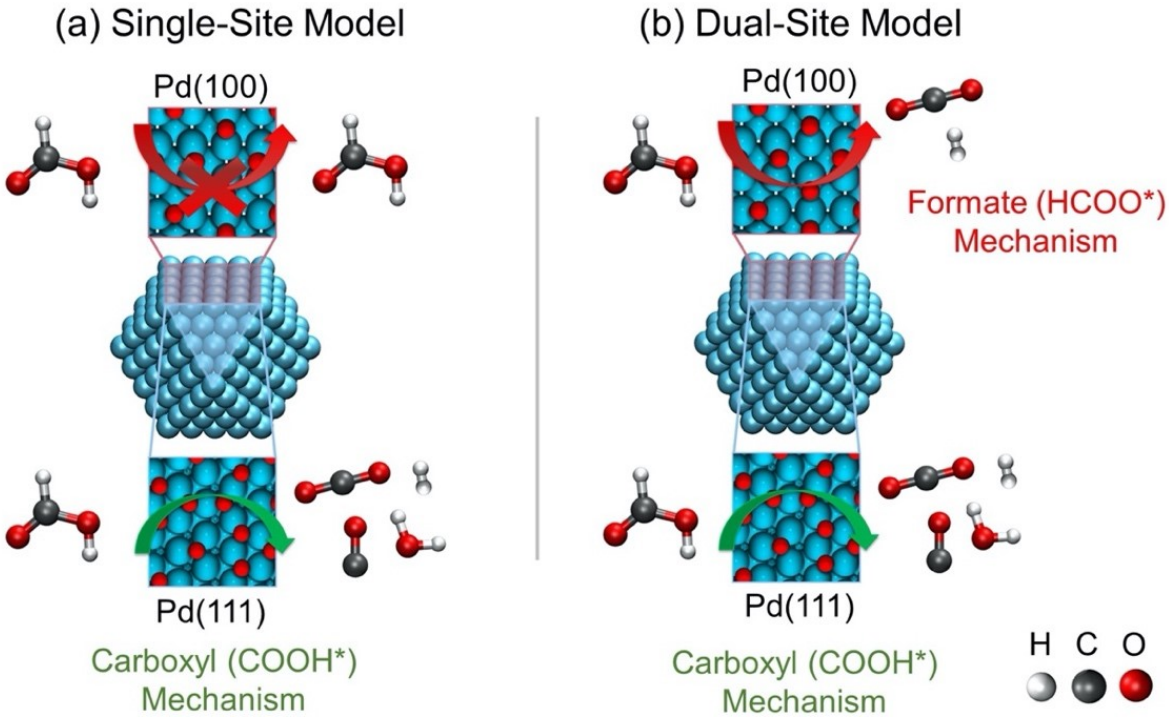


Figure 4.11 Potential descriptions for the Pd/C nanoparticles under FA decomposition reaction conditions: (a) Single-site model – partially (~0.3 ML) CO*-covered Pd(111) facet serving as the active site and partially (0.4-0.5 ML) CO*-covered Pd(100) poisoned under reaction conditions, (b) Dual-site model – both partially CO*-covered (~0.3 ML) Pd(111) and (~0.4-0.5 ML) Pd(100) active towards FA decomposition, with the later facet active only for FA dehydrogenation. Nature of the reactive-intermediate carrying the reaction flux, as determined from the optimized microkinetic models, is indicated next to the facets. Color codes for atoms: white – H, red – O, dark gray – C, and blue – Pd.

4.5 Conclusions

A combination of DFT-derived mean-field microkinetic modeling and reaction kinetics experiments were utilized to gain an in-depth understanding of the FA decomposition reaction on Pd/C. Upon parameter estimation, the microkinetic models formulated using DFT energetics on clean Pd(100) and Pd(111) required large corrections of the DFT energetics and were unable to rationalize the entire experimental dataset. Inconsistent with the assumption of clean surface used in the DFT calculations, these models predicted high CO* coverage (~0.99 ML and ~0.90 ML for

Pd(100) and Pd(111), respectively). *Operando* FTIR studies revealed the presence of ~0.3-0.5 ML CO* on the surface of the catalyst under our experimental conditions. We therefore, reformulated microkinetic models using DFT energetics that were calculated on partially (5/9 ML) CO*-covered Pd(100) and Pd(111) facets, which explicitly account for the presence of CO* on the catalyst surface. CO* coverage-dependent energetics were incorporated in our models, which were derived by calculating the reaction thermochemistry and kinetics at varying coverages of CO* spectators. Upon rigorous parameter estimation, these revised models predicted surface coverages that were consistent with the coverage of CO* at which DFT calculations were performed, i.e., the models were CO* coverage self-consistent. The partially (~0.4 ML) CO*-covered Pd(100) model was able to rationalize only a subset of the dehydrogenation TOFs, and was unable to explain the experimentally observed selectivity towards the dehydration reaction. Whereas a partially (~0.3 ML) CO*-covered Pd(111) was able to explain the entire experimental dataset (both dehydrogenation and dehydration TOFs), including the CO-cofeed subset which was unexplained by the other models. The reaction occurs through the carboxyl (COOH*) mechanism, with both the direct and CO*-assisted COOH* mechanisms contributing towards FA dehydrogenation. Importantly, CO*-assisted COOH* mechanism plays a critical in rationalizing the dehydrogenation TOFs, especially under the CO-cofeed conditions.

Our results demonstrate that a partially CO*-covered Pd(111) model is capable of rationalizing the experimental activity and selectivity, and can therefore, by itself, serve as an accurate description for the active site of FA decomposition on Pd/C. However, since the optimized CO*-coverage cognizant Pd(100) model (requiring small corrections) is able to fit the dehydrogenation TOFs for all but CO-cofeed conditions, we cannot exclude the possibility that Pd(100) might contribute

towards a portion of the dehydrogenation flux under conditions for all but the CO cofeed conditions.

Our study demonstrates the complexity of deciphering the *in situ* nature of the active site for heterogeneously catalyzed chemistries and the importance of computationally modeling a more realistic description of the active site, i.e., including spectator coverage effects and spectator-assisted mechanisms, for accurately modeling experimental observations. Detailed atomic-scale mechanistic insights derived from this work could be valuable for design of improved catalytic materials that are more active and selective than the monometallic catalysts and thus advance the consideration of FA as a promising hydrogen storage material.

CHAPTER 5

ROLE OF HYDROGEN-BONDED BIMOLECULAR FORMIC ACID-FORMATE COMPLEXES FOR FORMIC ACID DECOMPOSITION ON CU(111): A FIRST-PRINCIPLES DFT AND MICROKINETIC MODELING STUDY

5.1 Introduction

Ubiquitous and strong, hydrogen bonding interactions significantly influence chemical reactivity.[209–211] Despite this, the effects of hydrogen bonding on many chemistries remain unexplored. One chemistry for which hydrogen bonding potentially plays a large role in is in the reactions of formic acid (FA, chemical formula: HCOOH), which is both a strong hydrogen bond donor and acceptor; FA even forms hydrogen-bonded dimers with itself in the gas-phase.[212] FA has been intensely studied because of its promising characteristics as an energy-dense hydrogen storage material (4.4 wt. %, 53.4 g-H_2/l).[81,108,148,213–219] It is non-toxic, non-flammable, and liquid at ambient conditions, allowing the reuse of existing liquid fuel infrastructure with minimal modifications.[220] However, to enable the commercialization of FA as a viable hydrogen storage

vector, it is necessary to develop catalysts that decompose FA efficiently under mild conditions to release the stored hydrogen. A deeper understanding of the nanoscale reaction mechanisms for FA decomposition is crucial for the rational design of such catalysts.

Although there have been several theoretical studies of FA decomposition on Cu(111)[105,221,222], the effects of hydrogen bonding have not been explicitly addressed in most studies. This is despite the wealth of experimental evidence suggesting that hydrogen bonding significantly affects FA decomposition chemistry. For example, reaction kinetics experiments by Iglesia and Boudart[223], as well as by high resolution electron energy loss spectroscopy (HREELS) studies by Dubois *et al*.[224], suggest that hydrogen-bonded complexes of HCOO with FA (FA-HCOO complexes) are responsible for the differences in the reaction kinetics of catalytic FA decomposition versus temperature programmed desorption (TPD) of HCOO. Additionally, infrared[224,225] and X-ray photoelectron spectroscopy (XPS)[226] experiments indicate that HCOO species adsorbed on Cu surfaces possess two chemically distinct O atoms, suggested to be because FA breaks the symmetry of HCOO by complexing to one oxygen atom of HCOO. Hydrogen bonding has also shown to lead self-assembly of polymeric HCOOH chains on Cu(111).[227,228] Despite these experimental indications, the exact nature of these hydrogen-bonded complexes and the role they play in FA decomposition remains to be elucidated.

In this work, we determine how hydrogen bonding affects the kinetics of FA decomposition on Cu(111) by using density functional theory (DFT) calculations and coverage self-consistent microkinetic modeling. Specifically, we probe the energetics of hydrogen bonding of FA with HCOO and how the resulting bimolecular FA-HCOO complexes enable new nanoscale reaction pathways for the decomposition of HCOOH. We account for the lateral interactions caused by

high adsorbate coverages by explicitly including coadsorbates and searching for the minimum energy configurations at each considered coverage, allowing us to realistically recreate experimental reaction conditions. Finally, we feed these energetics into a microkinetic model and compare the predicted apparent activation energy barrier and FA reaction order with that reported in the experimental literature by means of rigorous parameter estimation. Our results reveal that on Cu(111), bimolecular FA-HCOO complexes present a high coverage on the surface of the catalyst under reaction conditions and play significant roles by lowering the overall barriers for decomposing HCOO. Importantly, pathways involving FA-HCOO complexes also carry majority of the reaction flux under most considered reaction conditions.

5.2 Methods

5.2.1 Density Functional Theory Calculations

First-principles density functional theory (DFT) calculations were performed using the Vienna *ab initio* Simulation Package (VASP).[54,55] Core states were represented by projector augmented-wave (PAW) pseudopotentials and valence states were expanded in terms of a plane-wave basis set with an energy cutoff of 400 eV.[123,124] We used the Perdew-Burke-Ernzerhof (PBE) exchange-correlation functional[229], together with Grimme's D3 method to account for dispersion corrections.[230]

In this study, we employ the kinetics data from the FA decomposition experiments reported by Iglesia and Boudart[223], which were performed using Cu/Al_2O_3 with average size of > 5 nm. Given the large size of the catalyst nanoparticles evaluated experimentally in this study, we believe that close-packed (111) facet—which has been reported to be the preferentially exposed facet for

supported Cu catalysts using transmission electron microscopy (TEM)[231]—accurately represents the surface of the catalyst.

We modeled the Cu(111) surface as a 4 × 4 slab with 5 layers, where the top 3 layers were relaxed and the bottom two layers were kept fixed at their optimized bulk lattice constants (calculated: 3.56 Å, experimental[232]: 3.61 Å). Structures were considered converged when the maximum forces on all atoms were below 0.02 eV/Å. The Brillouin zone was sampled with a 4 × 4 × 1 Monkhorst-Pack k-point mesh[128] centered on the gamma point. The periodic images were separated by ~15 Å of vacuum in the *z*-direction to avoid spurious interactions between them. Adsorbates were placed on one side of the slab only; dipole corrections[126,233] were applied in the *z*-direction to correct for electrostatic interactions between the periodic images. The Fermi surface was treated with second-order Methfessel-Paxton smearing[234] with a smearing width of 0.2 eV to accelerate electronic convergence. Final energies were obtained by extrapolating the energies to a Fermi temperature of 0 K.

Transition states were located with the climbing-image nudged elastic band (CI-NEB) method.[58] We used a minimum of seven images for each calculation, excluding the initial and final states. The transition states were similarly optimized until the forces on all atoms were below than 0.02 eV $Å^{-1}$ and were confirmed using vibrational analysis by the presence of a single imaginary mode. Harmonic vibrational frequencies were obtained by first building up the Hessian by a finite-differences approach with a step size of 0.007 Å and then diagonalizing the mass-weighted Hessian to obtain the normal mode frequencies.

All DFT energies reported are electronic energies without zero-point energy (ZPE) and finite-temperature corrections unless stated otherwise. The energies are referenced to H_2(g), CO_2(g), and the clean Cu(111) slab. The energy of a slab+adsorbate system, E, is thus:

$$E = E_{\text{tot}} - E_{\text{slab}} - nE_{H_2(g)} - mE_{CO_2(g)} \tag{5.1}$$

where E_{tot} is the total energy of the system, E_{slab} is the total energy of the clean slab, $E_{\text{H2(g)}}$ is the total energy of H_2 in the gas-phase, $E_{\text{CO2(g)}}$ is the total energy of CO_2 in the gas-phase, and $\underline{n}$ and m are the number of H_2 and CO_2 molecules required to form the adsorbate. For example, for HCOO, $n = 0.5$ and $m = 1$.

5.2.2 Search for Low Energy Configurations

Locating low energy, high-coverage adsorbate configurations is a high-dimensional search problem. In our approach to this problem, we used an in-house methodology, described in our previous work[45], which thoroughly samples configurations of reaction intermediates (referred here as "probe molecules") co-adsorbed with spectator species. Per this methodology, the spectator species were initialized within the unit cell using Latin-hypercube sampling (LHS)[135,136] for each unique adsorption configuration of the probe molecule. The adsorbates were then adjusted to their closest high-symmetry positions and optimized appropriately in the z-direction as informed by clean surface (i.e., no spectators) calculations. The structures were analyzed to prevent overlap of atoms within the unit cell as well as its periodically repeated images. Lastly, each structure was fingerprinted by a set of geometric descriptors: *i)* the site-occupancy (top, bridge, fcc, hcp, etc) of the spectators, *ii)* spectator-spectator distances, and *iii)* spectator-probe molecule distances, which enabled us to eliminate repeated structures.

To ensure rigorous sampling of the coadsorbed configurations, we incrementally increased the number of generated structures until no new unique structures were identified. Typically, hundreds of configurations were ultimately generated. All structures were then optimized using DFT calculations. Using this approach, we thus elucidate the most stable adsorption structures for the probe molecules under the presence of spectator species.

5.2.3 Microkinetic Models

To develop a coverage self-consistent description of the active site for the FA decomposition reaction on Cu(111), we use mean-field microkinetic models, which assume perfect mixing of the adsorbates. The models were initialized using DFT-derived energetics evaluated on various hypothesized active site models. The microkinetic models were then calibrated via parameter estimation to match the experimentally reported apparent activation energy and FA reaction order measured on Cu/Al_2O_3.[223] Using the insights gained from our fitting procedure, as detailed below, we iteratively refine our hypothesis to identify a coverage self-consistent description of the active sites.

We modeled the kinetics of the FA decomposition reaction on Cu catalyst using a continuous stirred tank reactor (CSTR), which has been shown to accurately capture the kinetics for low conversion reaction kinetics experiments.[41,45] Shomate parameters fitted from vibrational frequency calculations were used to determine ZPE-corrected and temperature dependent energetics, [62] which were used as initial estimates for the kinetic and thermodynamic parameters in our microkinetic models.

We additionally implemented coverage effects within the mean-field representation, enabling a *coverage-cognizant* mean-field microkinetic model, which has been shown to accurately capture

lateral adsorbate-adsorbate interactions for large nanoparticles.[45,158,159] Specifically, we calculate DFT binding and transition state energies at varying spectator coverages and fitted them to polynomial functions dependent on the spectator coverages. These polynomial functions for binding and transition state energies are self-consistently incorporated in our models; they are calculated and applied on-the-fly based on the adsorbate coverages at each time step in order to self-consistently account for the effect of lateral adsorbate-adsorbate interactions (due to MASI coverages) on the thermodynamics and kinetics Figure 5.1.

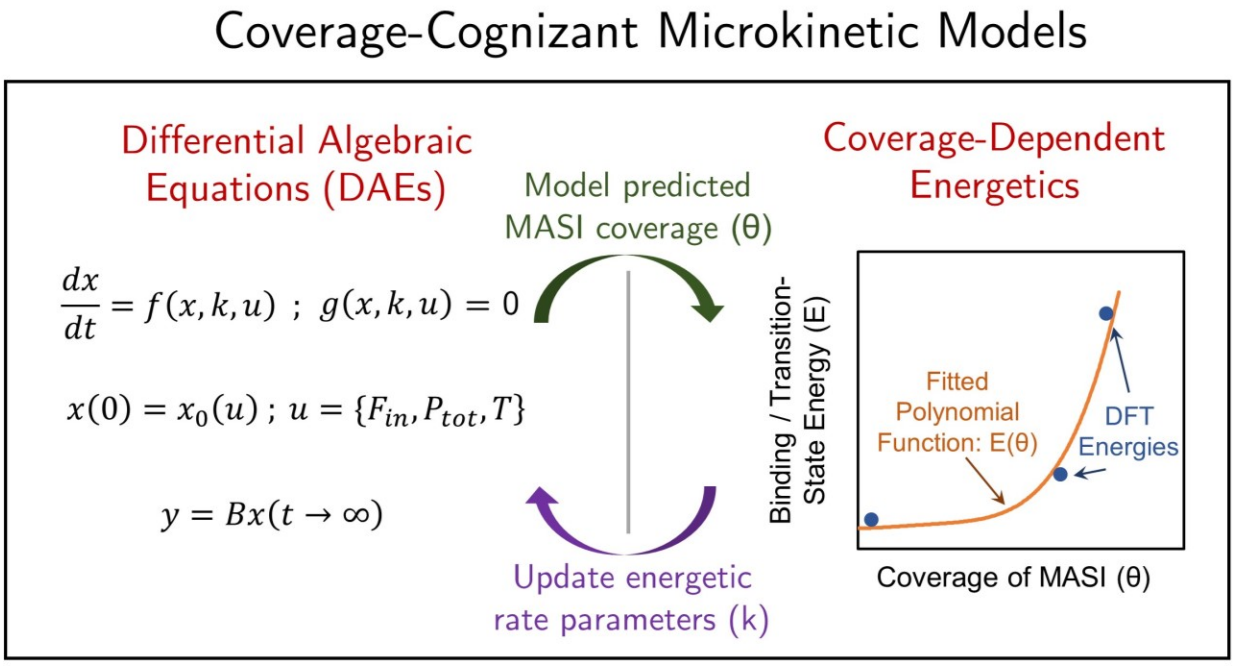


Figure 5.1 Schematic representation of the implementation of coverage-dependent energetics in our mean-field microkinetic models. Binding and transition-state energies were computed using DFT at different coverages of most abundant surface intermediate (MASI) and were fitted to polynomial functions dependent on the coverage of MASI. These polynomial functions are self-consistently incorporated in our models to calculate and adjust the energetics (and equivalently, the rate parameters dependent on these energetics) on-the-fly to account for the lateral adsorbate-adsorbate interactions due to the coverage of MASI, thus realizing a coverage-cognizant microkinetic model. Here, x is the set of flow-rate of gas-phase species and surface coverages of reaction intermediates; k is the set of rate constants; u is the set of input conditions consisting of (F_{in} – input flow rates, P_{tot} – total pressure, T – temperature); y – is the linearly transformed solution of x at steady-state; B is a transformation matrix relating x to y; θ is the surface coverage of MASI.

We perform parameter estimation using the sequential optimization framework proposed by Rangarajan *et al*.[41] to determine the corrections to the initial DFT energetics for reproducing the experimentally-determined apparent activation energy and FA reaction order. Since this is a non-linear optimization problem, we employ a multi-start approach based on LHS to randomly initialize the corrections to the DFT-derived binding and activation energies. All corrections were limited to ±0.6 eV. The multi-start approach enables convergence to multiple-local minima and allows us to identify plausible alternate solutions.

The optimized solutions were ranked based on the quality of the fit with the experimental apparent activation energies and FA reaction order. Promising solutions were further analyzed to determine: *i)* if the energetic corrections required for achieving parity with the experimental metrics were within the statistical DFT error of approximately 0.2 eV (for generalized gradient approximation (GGA) functionals),[139,143]and *ii)* if the model predicted coverages were consistent (within ~0.1 ML) with the active site model used in the DFT calculations (i.e. coverage self-consistency).

If both the above criteria are satisfied, we have identified the most plausible active site for FA decomposition on Cu/Al_2O_3 catalysts. In our study, it was easy to fit the experimental apparent activation energy barrier and FA reaction order for most models by adjusting the DFT energetics within the errors of DFT calculations. However, coverage self-consistency was often not satisfied. In such scenarios, we revise our active site model and recalculate the energetics in the presence of coverages of spectator species determined by the previous iteration, as close as allowable by the size our of unit cell. We then create a new microkinetic model with these energetics, perform parameter estimation, and re-evaluate our model to determine if it meets the above criteria. This process is repeated until we converge at a coverage self-consistent model for the active site.

5.3 Results

Creating a coverage self-consistent atomistic model for FA decomposition over Cu(111) is an iterative process involving several intermediate models. More information about this iterative process can be found in the Methods Section and details of the intermediate models can be found in Appendix E. In this manuscript, we focus on two models: *i)* the final coverage self-consistent model, which we believe best replicates the experimental coverages; and *ii)* the clean surface model, which serves to facilitate introduction of the FA decomposition pathways.

In Section 5.3.1, we present our DFT results. We first introduce the various intermediates and pathways involved in HCOO decomposition on clean Cu(111). We then discuss the potential energy diagrams (PEDs) of each pathway to understand their reactivity. Finally, we discuss the effects of coverage on the energetics of the intermediates and transition states. In Section 5.3.2, we present our microkinetic modeling results. We demonstrate our iterative approach of developing a coverage self-consistent description of the catalytic active site, briefly describing the intermediate models that we evaluated in the process. We then present results from our coverage self-consistent model in terms of surface coverages, dominant reaction pathways, and rate-controlling steps.

5.3.1 Density Functional Theory Results

5.3.1.1 Formic Acid Decomposition Pathways—Clean Cu(111)

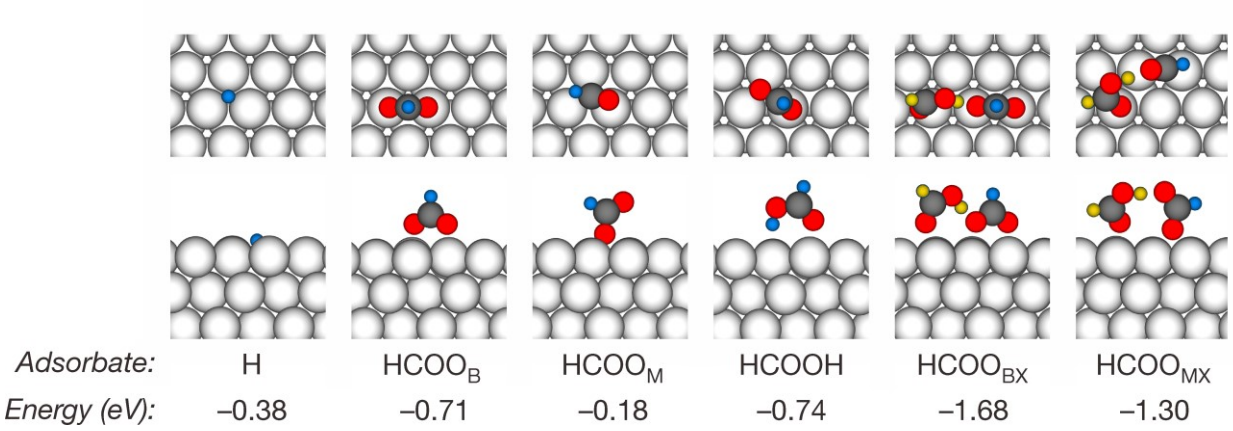


Figure 5.2 Optimized structures of intermediates involved in formic acid decomposition on clean Cu(111). Panels above and below are top and side views, respectively. Energies are with respect to gas-phase H_2 and CO_2. Color code: light grey – Cu, dark grey – C, red – O, blue – H, yellow – H from complexed HCOOH. Subscripts B and M refer to the bidentate and monodentate configurations of HCOO, respectively. Subscript X refers to complexation of HCOO with HCOOH (i.e. FA-HCOO complexes).

FA decomposes via two intermediates: *i)* the formate (HCOO) intermediate, formed by breaking the HCOO–H bond; and *ii)* the carboxyl (COOH) intermediate, formed by breaking the H–COOH bond. Since the barrier of forming COOH is much higher than that of forming HCOO on Cu(111),[105] we will not consider COOH in this work.

Formate (HCOO) exists in two main configurations (Figure 5.2): a bidentate configuration with both O atoms bound to the surface ($HCOO_B$), and a monodentate configuration with one O atom bound to the surface ($HCOO_M$) and the other pointing away from the surface—a dangling bond. Due to this unsaturated dangling bond, the monodentate configuration is 0.53 eV less stable than the bidentate configuration on a clean Cu(111) surface.

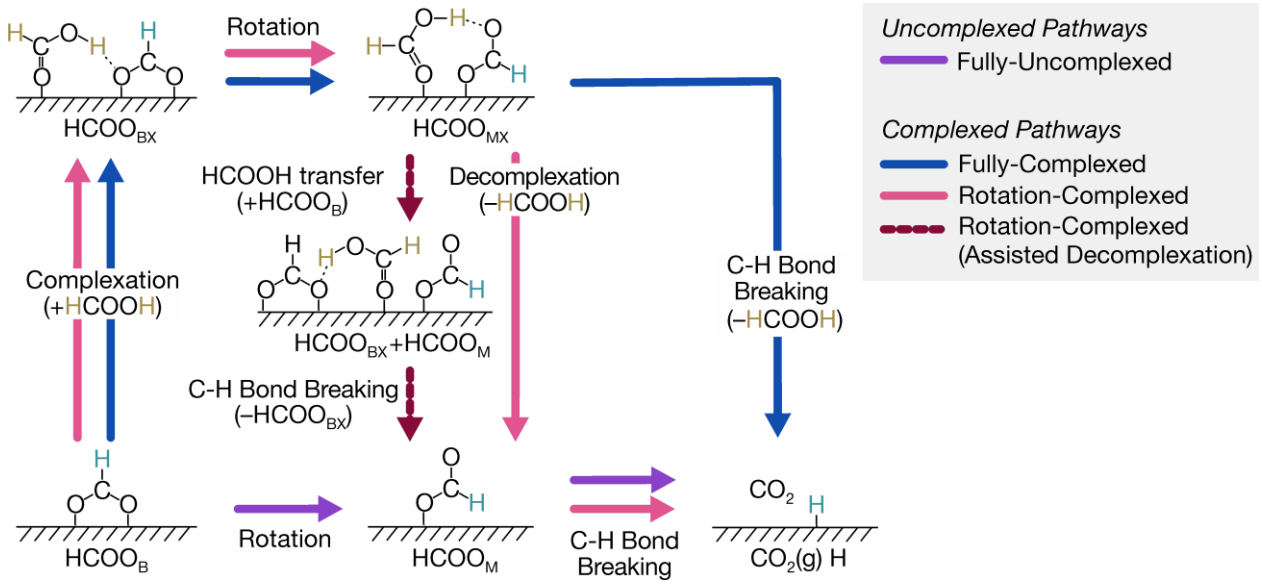


Figure 5.3 Pathways for HCOO decomposition to CO_2(g) + H. Colored arrows mark different decomposition pathways. Dotted lines represent hydrogen bonds. Dark yellow and teal colored H atoms denote H atoms from the complexed FA and the decomposing HCOO species respectively. Subscripts B and M refer to the bidentate and monodentate configurations of HCOO, respectively. Subscript X refers to complexation of HCOO with HCOOH (i.e. FA-HCOO complexes).

Both HCOO configurations can be complexed by HCOOH, forming bimolecular FA-HCOO complexes. In this process, the O–H group of HCOOH forms a hydrogen bond with one of the O atoms of HCOO. We term these complexed intermediates $HCOO_{BX}$ and $HCOO_{MX}$ (Figure 5.2), where the subscript "X" stands for "complex". On clean Cu(111), this is an exothermic process—complexation of $HCOO_B$ and $HCOO_M$ releases 0.23 eV and 0.38 eV, respectively—hinting that these complexes are relevant in realistic reaction environments. Note that $HCOO_M$ is stabilized more than $HCOO_B$ as the unsaturated dangling bond forms a stronger hydrogen bond with HCOOH. This closes the energetic gap $HCOO_B$ and $HCOO_M$, which plays an important role in the kinetics of HCOO decomposition, as discussed later.

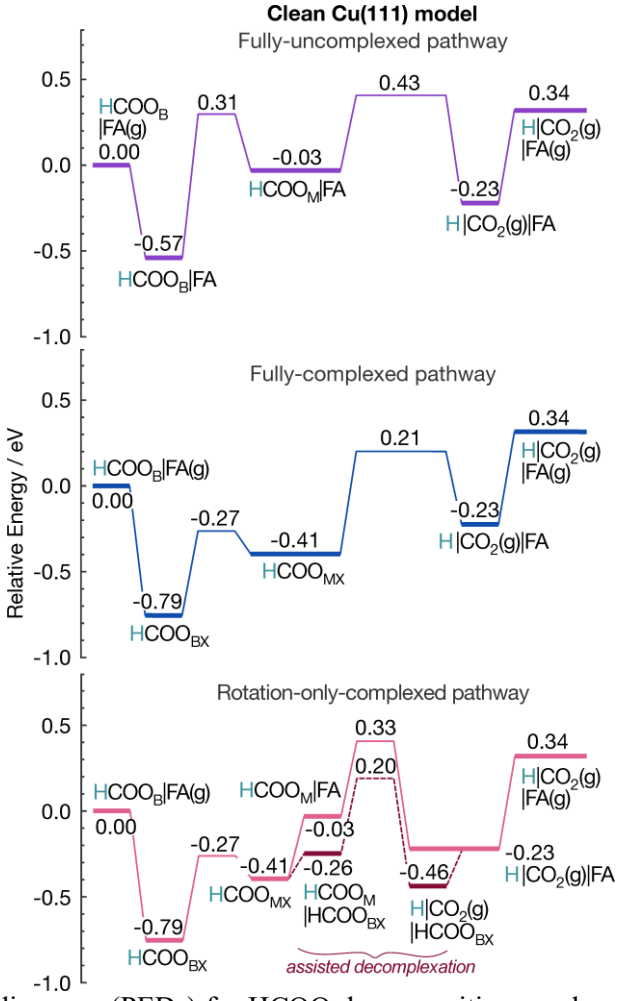


Figure 5.4 Potential energy diagrams (PEDs) for HCOO decomposition on clean Cu(111). Bold and thin lines indicate intermediate and transition states respectively. '|' indicates infinite separation. Colors of the pathways are identical to those in Figure 5.3. All states are labeled by their energies, which are with respect to the initial state to compare the pathways on an equal energetic footing; intermediate states are additionally labeled with names of the adsorbates. Teal colored H atoms denote H atoms from the decomposing HCOO species. Subscripts B and M refer to the bidentate and monodentate configurations of HCOO, respectively. Subscript X refers to complexation of HCOO with HCOOH (i.e. FA-HCOO complexes).

In catalytic heterogeneous FA decomposition, decomposition of HCOO is often suggested by both theory and experiments to be rate limiting.[105,223] Our mechanistic understanding of FA decomposition can thus be enhanced by elucidating the most favorable pathways by which HCOO may decompose. Schematics of the pathways we considered are shown in Figure 5.3, and their corresponding PEDs, evaluated on clean Cu(111), are shown in Figure 5.4. To simplify these

pathways, we excluded the elementary steps for HCOOH decomposition (HCOOH → HCOO + H) and H_2 recombination (H + H → H_2(g)), which have activation energies of 0.58 and 0.98 eV, respectively, since they are identical for all pathways. All pathways begin from $HCOO_B$ since it is the more stable HCOO configuration. Illustrations of the transition state structures for all elementary steps are shown in Figure E.5 (Appendix E).

In the *fully-uncomplexed* pathway—which is also the conventionally-considered HCOO pathway[105] (Figure 5.3, purple arrows)—$HCOO_B$ begins its decomposition by first rotating to $HCOO_M$. This is an endothermic process with a reaction energy of 0.54 eV and a high barrier of 0.88 eV (Figure 5.4, purple lines; $HCOO_B$|FA → $HCOO_M$|FA; '|' indicates infinitely-separated intermediates). In the monodentate form, the C–H bond of $HCOO_M$ points towards the surface and is primed to break to form CO_2 + H; this step occurs with a barrier of 0.46 eV (Figure 5.4, purple lines; $HCOO_M$|FA → CO_2(g)|H|FA). Since this transition state has the highest energy along the reaction pathway of 0.43 eV, 0.12 eV higher than the rotation barrier, decomposition of $HCOO_M$ is likely the rate determining step. Note that at typical reaction temperatures of ~400 K, a difference in the barrier by 0.08 eV corresponds to a change in the reaction rate by one order of magnitude.

In the *fully-complexed* and the *rotation-only-complexed* pathways—our two newly considered pathways involving the FA-HCOO complexes (Figure 5.3, blue and red arrows)—$HCOO_{BX}$ first rotates to $HCOO_{MX}$. This has a barrier of just 0.52 eV (Figure 5.4, blue and red lines; $HCOO_{BX}$ → $HCOO_{MX}$), 0.36 eV less than that of rotation of $HCOO_B$ to $HCOO_M$. This reduced barrier is because complexation helps reduce the energy differences between the monodentate and bidentate configurations of HCOO, making rotation less endothermic: $HCOO_{MX}$ is just 0.38 eV less stable than $HCOO_{BX}$ whereas $HCOO_M$ is 0.54 eV less stable than $HCOO_B$.

The two pathways split after rotation to $HCOO_{MX}$: in the fully-complexed pathway (Figure 5.3, blue arrows), $HCOO_{MX}$ decomposes by breaking of the C–H bond. This entails a barrier of 0.62 eV (Figure 5.4, blue lines; $HCOO_{MX} \rightarrow CO_2(g)|H|FA$), 0.16 eV higher than that of the breaking of the C–H bond of $HCOO_M$ because $HCOO_{MX}$ is more stable than $HCOO_M$. Despite this, the transition state for $HCOO_{MX}$ decomposition has an energy of just 0.21 eV, thus the fully-complexed pathway is more favorable than the uncomplexed pathway, where the highest transition state had an energy of 0.43 eV.

In the *rotation-only-complexed pathway* (Figure 5.3, red arrows), however, we can try to circumvent the energetically difficult decomposition of $HCOO_{MX}$ by first decomplexing—releasing $HCOO_M$ from FA—and then allowing $HCOO_M$ to decompose on its own. The overall barrier of this pathway is 0.43 eV, identical to that of the uncomplexed pathway (Figure 5.4, red lines). Alternatively, if the coverage of $HCOO_B$ is high enough—a reasonable assumption given that most studies proposed $HCOO_B$ to be the most abundant surface intermediate (MASI)[100,105,224]—the decomplexation may occur in a concerted process where the decomplexed FA is simultaneously transferred to a nearby spectator $HCOO_B$ (Figure 5.3, dark red arrows). Complexing of FA with the $HCOO_B$ spectator is exothermic and therefore partially offsets the energetic cost of $HCOO_{MX}$ decomplexation. The rotation-only complexed pathway with assisted decomplexation thus has the lowest overall barrier out of all the considered pathways of 0.20 eV (Figure 5.4, dark red lines).

5.3.1.2 Coverage Effects on Energetics

Our results until now focused on the clean Cu(111) surface. Yet, as we will see in the next section, our final coverage-self-consistent microkinetic model predicts that 0.45 ML of $HCOO_{BX}$ covers

the surface under reaction conditions. Since coadsorbates significantly impact the binding energies of intermediates[235–241], the clean DFT energetics presented above are inconsistent with our microkinetic modeling results. To resolve this discrepancy, we thus sought to determine the energetics of the system at coverages similar to that suggested by our microkinetic model.

Using Latin-hypercube sampling,[135,136] we rigorously sampled the large space of possible adsorbate configurations and ultimately determined the most stable structures of each intermediate adsorbed with 0.375 ML of $HCOO_{BX}$ spectator species, corresponding to 2 $HCOO_{BX}$ spectators—each occupying 3 surface sites since HCOO is a bidentate species and complexed HCOOH is a monodentate species(Figure 5.2)—in a 4 × 4 unit cell (Figure 5.5). Starting from these structures, we also determined the high coverage transition states for all reactions (

Figure E**.6** – Appendix E). These intermediates and transition states make up the 0.375 ML $HCOO_{BX}$ model.

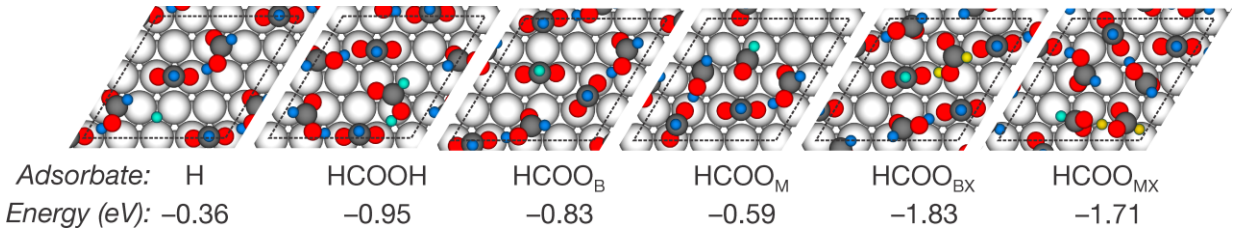


Figure 5.5 Optimized structures of intermediates involved in formic acid decomposition on 0.375 ML $HCOO_{BX}$ covered Cu(111). Panels show top views. Black dashed lines mark the unit cell. Energies are with respect to gas-phase H_2 and CO_2. Subscripts B and M refer to the bidentate and monodentate configurations of HCOO, respectively. Subscript X refers to complexation of HCOO with HCOOH (i.e. FA-HCOO complexes). Color code: light grey – Cu, dark grey – C, red – O, blue – H of spectator species, teal – H of species of interest, yellow – H from complexed HCOOH.

Even at the high coverage of 0.375 ML $HCOO_{BX}$, the structures of all intermediates remained unchanged from their clean surface structures, except for that of HCOOH (Figure 5.5). Whereas the O–H group of HCOOH binds to the surface via the H atom at low coverages (Figure 5.2), there is no space for HCOOH to bind freely at high coverages. Instead, the O–H group binds to the free O atom of one of the spectator $HCOO_{BX}$ species, creating a doubly-complexed $HCOO_B$ species.

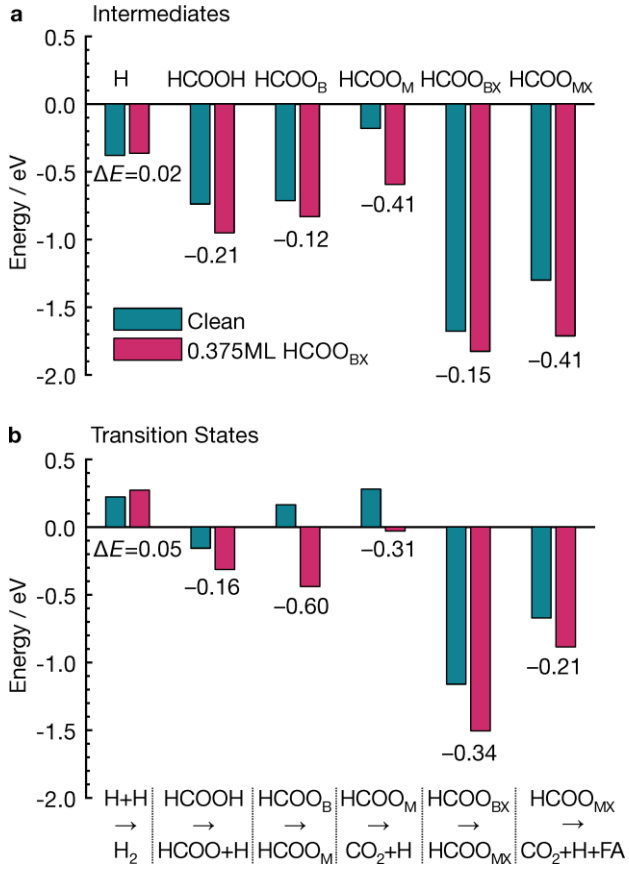


Figure 5.6 Coverage effects on the energetics of species involved in formic acid decomposition on Cu(111). (a) Intermediates. (b) Transition states (TSs). Energies are with respect to gas-phase H_2, CO_2, and the clean slab. ΔEs given below the bars denote the energy differences between the clean and 0.375 ML $HCOO_{BX}$ models. Negative ΔE values indicate stabilization of the species at higher coverage. Subscripts B and M refer to the bidentate and monodentate configurations of HCOO, respectively. Subscript X refers to complexation of HCOO with HCOOH (i.e. FA-HCOO complexes)

Comparing the energetics of the intermediates and transition states in our 0.375 ML $HCOO_{BX}$ model versus our clean Cu(111) model (Figure 5.6), we find that all carbon-containing intermediates and transition states were stabilized at high coverage. The $HCOO_B \rightarrow HCOO_M$ transition state was stabilized the most, by 0.60 eV. This is surprising as lateral interactions between small atomic and molecular adsorbates are usually destabilizing. Part of the stabilization for HCOOH could be because of its hydrogen bonding to one of the spectator $HCOO_{BX}$ species. There are, however, no obvious hydrogen bonding interactions for the other intermediates. The stabilization of these species is likely due to van der Waals interactions between the intermediates and the coadsorbed $HCOO_{BX}$ species as single-point calculations with the PBE functional (i.e. without D3 dispersion corrections) show significantly (~0.2 eV) less stabilization (Figure E.7). This also explains why atomic H and the transition state for H_2 recombination were not stabilized (Figure 5.6)—they are not strongly affected by van der Waals interactions.

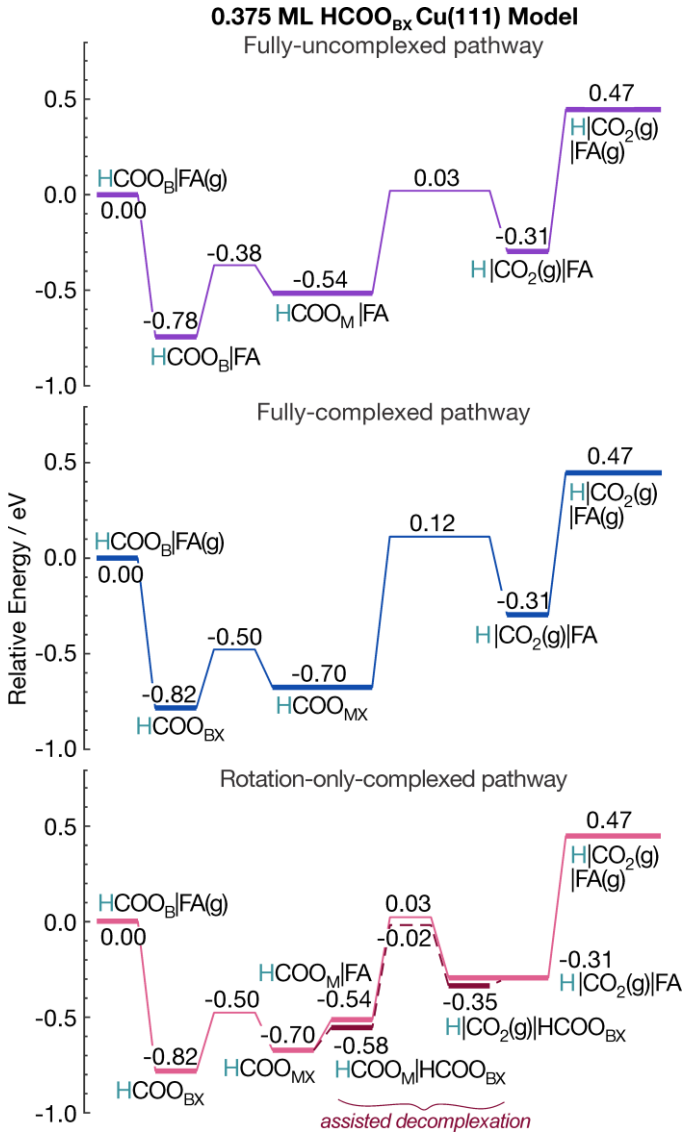


Figure 5.7 Potential energy diagrams (PEDs) for HCOO decomposition on 0.375 ML $HCOO_{BX}$ covered Cu(111). Bold and thin lines indicate intermediate and transition states respectively. '|' indicates infinite separation. Colors of the pathways are identical to those in Figure 5.3. All states are labeled by their energies, which are with respect to the initial state to compare the pathways on an equal energetic footing; intermediate states are additionally labeled with names of the adsorbates. Teal colored H atoms denote H atoms from the decomposing HCOO species. Subscripts B and M refer to the bidentate and monodentate configurations of HCOO, respectively. Subscript X refers to complexation of HCOO with HCOOH (i.e. FA-HCOO complexes).

The resulting PEDs for the 0.375 ML $HCOO_{BX}$ model are shown in Figure 5.7; a side-by-side comparison of PEDs for the clean and the 0.375 ML $HCOO_{BX}$ models are shown in Figure E.8. The stabilization observed for most species at high coverage translates to a downshift of the PEDs for all pathways. This downshift is greater for the uncomplexed pathway (Figure 5.7; purple lines) than the complexed pathways (Figure 5.7; blue and red lines). This is because both FA and the $HCOO_B \rightarrow HCOO_M$ transition state are stabilized greatly at high coverages (Figure 5.6). Consequently, the fully-uncomplexed pathway is now more favorable than the fully-complexed pathway at higher coverages although it was less favorable at lower coverages. The rotation-only-complexed pathway is, however, still the most favorable if $HCOO_B$ spectator species can assist in the $HCOO_{MX}$ decomplexation, albeit by only 0.05 eV (Figure 5.7; dark red lines).

In our 0.375 ML $HCOO_{BX}$ model, the highest energy transition states for all pathways are all within ~0.1 eV of each other (Figure 5.7). Based on energetics alone, the pathways are highly competitive with each other. To determine which of these pathways contribute to the reaction flux under experimental conditions, it is necessary to employ microkinetic modeling, which accounts not only for energetics but also for adsorbate coverages; this is discussed in the next section.

5.3.2 Microkinetic Modeling Results

To evaluate the catalytic relevance of the various HCOO decomposition pathways, we performed microkinetic modeling using our DFT-calculated energies as initial inputs. Besides DFT energetics, our microkinetic models also account for ZPE-corrections, finite-temperature energy corrections, and entropic effects, thus bridging the temperature and pressure gap between our calculations and experiments. Importantly, the effects of adsorbate coverage on both binding and transition state energies are explicitly accounted for via parameterized polynomial-type functions,

which allows us to adjust the reaction energetics on-the-fly according to the predicted coverages at any time step.

Using DFT energetics without any adjustments, our models predicted reaction kinetics that were inconsistent with experiment. For example, the unadjusted clean Cu(111) model, using a reduced reaction network without complexed pathways, predicts a FA apparent reaction order of 0.31 (2.5–10% FA partial pressure, 373 K, total pressure of 1 atm) and an apparent activation energy (E_{app}) of 59.1 kJ/mol (10% FA, 368–383 K, total pressure of 1 atm). This disagrees with the experimentally measured reaction order of zero with respect to FA and E_{app} of 95–100 kJ/mol under similar experimental conditions.[223] Such discrepancies could be due to multiple factors such as intrinsic errors in the DFT calculations[143,242]; an incorrect description of the active site; or an incomplete reaction mechanism.

Therefore, the first step for all models is to perform parameter estimation to calibrate the DFT energetics so that the models are consistent with the experimental zero reaction order wrt. FA and E_{app} of 95–100 kJ/mol. The models capable of reproducing the experimental metrics are evaluated on the following two criteria. First, for judging how well these optimized models reproduce the catalytic active site is the magnitude of the required corrections to the energetics: models that require larger corrections are less likely to represent the active site. Second, whether not the optimized model predicts adsorbate coverages that are consistent with the coverages at which its initial DFT energetics were calculated, that is, coverage self-consistency.[45]

Throughout the iterative process of arriving at a coverage self-consistent model, we studied a total of five models, differing by the reaction pathways that were included and the adsorbate coverages

at which the DFT energies were calculated (Table 5.1). All results presented here refer to results obtained with the optimized, parameter-adjusted models unless otherwise stated.

Table 5.1 Results from optimized, parameter-adjusted models for formic acid (FA) decomposition over Cu(111). Maximum absolute corrections for the binding energy (max |ΔBE|) and activation energy barriers (max $|\Delta E_A|$), most abundant surface intermediate (MASI) coverages (averaged across the considered experimental temperature and pressure range), the FA apparent reaction order (at 373 K in a partial pressure range of 2.5–10%), and the apparent activation energy (E_{app}) (10% FA in a temperature range of 368–383 K) are reported. Under similar reaction conditions, the experimentally measured FA reaction order and E_{app} on Cu/Al_2O_3 are 0.0 and 95-100 kJ/mol, respectively.[223] The final coverage self-consistent model that matches the experimental observations is marked in bold. Subscripts B and M refer to the bidentate and monodentate configurations of HCOO, respectively. Subscript X refers to complexation of HCOO with HCOOH (i.e. FA-HCOO complexes).

Model	Reaction Quantities		| Maximum Corrections | (eV)		MASI Coverages (ML)
	FA Order	E_{app} (kJ/mol)	Max | BE |	Max | E_A |	
Reduced Reaction Mechanism					
Clean	0.04	95.5	0.15	0.16	0.89 $HCOO_B$
0.625 ML $HCOO_B$	0.36	81.1	0.57	0.30	0.67 $HCOO_B$
Full Reaction Mechanism					
Clean	-0.01	97.9	0.14	0.16	0.65 $HCOO_B$
0.625 ML $HCOO_B$	-0.05	93.9	0.16	0.11	0.43 $HCOO_{BX}$
0.375 ML $HCOO_{BX}$	**-0.03**	**93.7**	**0.13**	**0.17**	**0.45 $HCOO_{BX}$**

5.3.2.1 Models with Reduced Reaction Mechanism: Uncomplexed Pathways Only

In our first self-consistent iteration, we considered a reduced reaction mechanism that is typically considered in studies of FA decomposition on Cu catalysts. This includes HCOOH adsorption and desorption, HCOOH dehydrogenation (HCOOH → HCOO + H), the elementary steps in the uncomplexed HCOO decomposition pathway (Figure 5.3, purple lines), and H_2 recombinative desorption (H + H → H_2(g)). For this iteration, we explicitly excluded our newly discovered complexed HCOO decomposition pathways from the reaction mechanism to determine if arriving at a coverage self-consistent model was possible without such pathways.

The first model in this iteration used DFT energetics evaluated on clean Cu(111). Upon parameter estimation, the model yielded good agreement with the experimentally measured FA reaction order and E_{app}. However, the model predicted a high coverage of 0.89 ML $HCOO_B$ averaged over the experimental conditions, inconsistent with our starting assumption of a clean Cu(111) surface.

For the second model in the iteration, we therefore sought to create a model with high $HCOO_B$ coverage. Even though the first model predicted a coverage of 0.89 ML $HCOO_B$, this is unrealistically high; therefore, for this second model we used 0.625 ML $HCOO_B$ covered Cu(111) as a first estimate to check if Cu(111) can indeed support such high $HCOO_B$ coverages. After parameter estimation, the optimized model predicted a surface coverage of 0.67 ML $HCOO_B$, consistent with our initial assumption of 0.625 ML $HCOO_B$. However, the model failed to reproduce both the experimental FA reaction order (model: 0.36, experiment: 0) and E_{app} (model: 81.1 kJ/mol, experiment: 95-100 kJ/mol). It also required large corrections (0.57 eV) to the energy of $HCOO_B$.

Although we were able to obtain a coverage self-consistent model by considering just the reduced reaction mechanism, the model was not able to reproduce the experimental observations even with large corrections to the DFT energies. This highlights the shortcomings of the conventionally-considered reduced (uncomplexed) decomposition pathway and suggests that alternative reaction mechanisms must be included to reproduce the experimental data.

5.3.2.2 Models with Full Reaction Mechanism: Both Complexed and Uncomplexed Pathways

In this new self-consistent iteration, we considered a full reaction mechanism where we augment the reduced reaction mechanism with the complexed pathways (blue, pink, and red pathways in Figure 5.3) to determine if including complexed pathways could enable us to reproduce the experimental observations.

We first used DFT energetics evaluated on clean Cu(111). Upon parameter estimation, this model predicted a high coverage of 0.65 ML $HCOO_B$ averaged over the experimental conditions, which is inconsistent with the starting assumption of clean Cu(111). Therefore, we created a second microkinetic model using DFT energetics evaluated on 0.625 ML $HCOO_B$ covered Cu(111). This new model was able to fit the experiments but suggested a 0.43 ML coverage of $HCOO_{BX}$ (averaged over the experimental conditions), which is again inconsistent with our assumption of a 0.625 ML $HCOO_B$ covered surface.

In our third model, we created a microkinetic model using DFT energetics evaluated on 0.375 ML $HCOO_{BX}$ covered Cu(111). Upon parameter estimation, this model fits the experimental data and predicts a coverage of 0.45 ML $HCOO_{BX}$, which is close to the coverage used in our DFT calculations (0.375 ML $HCOO_{BX}$). We have thus arrived at a coverage self-consistent model. The largest corrections to the binding energies of intermediates and transition states were 0.13 and 0.17 eV, respectively, which is within the DFT error (Table 5.2).

Table 5.2 Corrections to the DFT-derived binding energies (ΔBE) and activation energy barriers (ΔE_A) for the 0.375 ML $HCOO_{BX}$ covered Cu(111) model obtained from parameter estimation for the full reaction mechanism. Note that at a coverage of 0.375 ML $HCOO_{BX}$, HCOOH complexes with the uncoordinated O atom of a spectator $HCOO_{BX}$ (Figure 5.5). Negative (positive) corrections denote stabilization (destabilization). Intermediates and elementary steps not listed have no corrections from their initial DFT energetics. Subscripts B and M refer to the bidentate and monodentate configurations of HCOO, respectively. Subscript X refers to complexation of HCOO with HCOOH (i.e. FA-HCOO complexes).

0.375 ML $HCOO_{BX}$ Cu(111)*	*Corrections / eV*
Intermediate	ΔBE
H	0.12
$HCOO_B$	0.10
$HCOO_{BX}$	-0.13
HCOOH	-0.09
Elementary Step	ΔE_A
$HCOO_M \leftrightarrow CO_2(g) + H$	0.08
$HCOO_{MX} \leftrightarrow H + CO_2(g) + HCOOH$	-0.17

Overall, the models with a reduced reaction mechanism, containing only uncomplexed HCOO decomposition pathways, could not fit the experimental data. However, the models with full reaction mechanisms, which were augmented with complexed HCOO decomposition pathways, allowed us to reach a coverage self-consistent model that required only minimal corrections to the DFT-calculated binding energies and activation energies to reproduce experimental observations. This strongly indicates that complexed pathways are a vital part of the reaction mechanism for FA decomposition over Cu(111).

5.3.3 Coverage Self-Consistent 0.375 ML $HCOO_{BX}$ Model

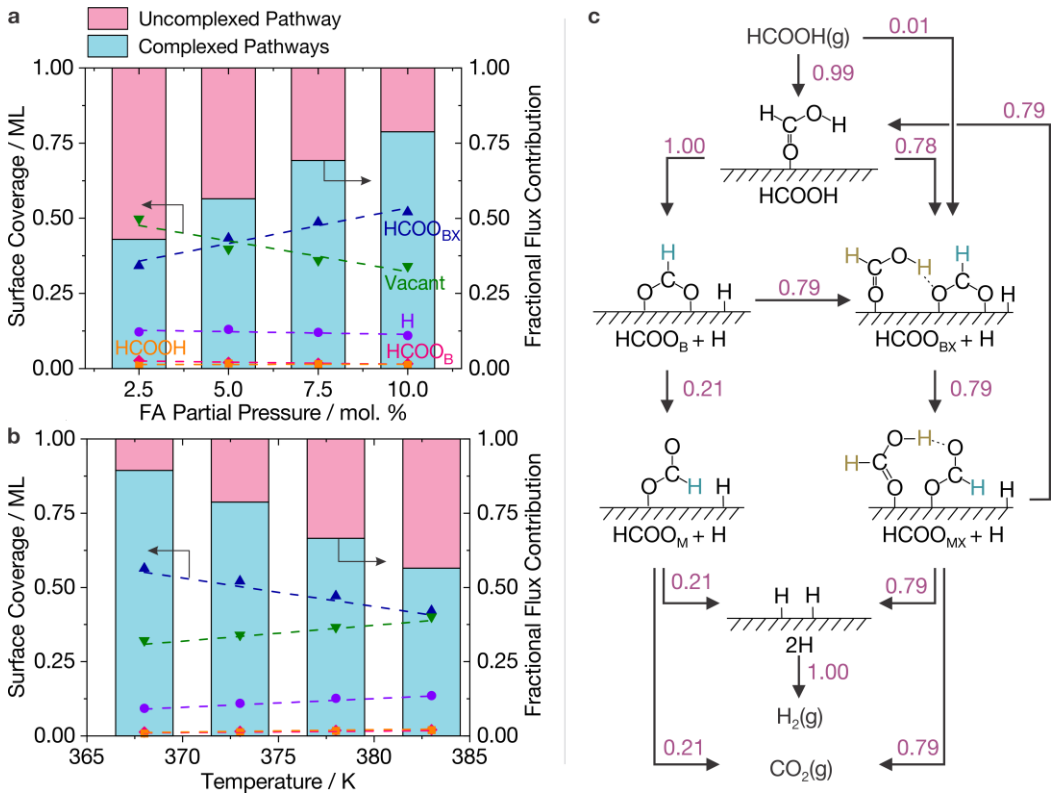


Figure 5.8 Surface coverages, reaction fluxes, and species fluxes predicted by the optimized 0.375 ML $HCOO_{BX}$ Cu(111) model with the full reaction network. (a-b) Adsorbate coverages and complexed vs. uncomplexed reaction fluxes under varying (a) FA partial pressure (2.5–10%, balance He) at 373 K, and (b) temperature (368-383 K) at a FA partial pressure of 10 mol %, balance He. Coverages account for species denticities. Dashed lines represent linear trend lines. (c) Reaction fluxes (purple numbers) at our defined home conditions (10% FA, balance He, 373 K). Dark yellow and teal colored H atoms denote H atoms from the complexed FA and the decomposing HCOO species respectively. Note that with 0.375 ML $HCOO_{BX}$ spectators, HCOOH binds to/complexes with the uncoordinated O atom of a spectator $HCOO_{BX}$ (Figure 5.5). Subscripts B and M refer to the bidentate and monodentate configurations of HCOO, respectively. Subscript X refers to complexation of HCOO with HCOOH (i.e. FA-HCOO complexes).

Having established that complexed pathways are an essential part of the FA decomposition reaction mechanism, we discuss in detail the 0.375 ML $HCOO_{BX}$ Cu(111) model (Table 5.1; last

row). This model best represents the active site for FA decomposition on Cu because it is coverage self-consistent and required only small corrections (<0.18 eV) to the DFT calculated binding energies and activation energy barriers to obtain good agreement with experimental observables. Averaged over all experimental conditions (differing in FA partial pressure and temperature, as shown in Figure 5.8 a and Figure 5.8 b, respectively), the optimized model predicts surface coverages of 0.45 ML $HCOO_{BX}$, 0.12 ML H, 0.02 ML HCOOH, 0.02 ML $HCOO_B$, and 0.39 ML vacant sites. Although the literature often proposes $HCOO_B$ to be as the most abundant surface intermediate (MASI) in context of FA decomposition on Cu catalysts[105,224,243], our model finds relatively low coverages of $HCOO_B$. The MASI is its complexed form, $HCOO_{BX}$, instead.

Analyzing the species fluxes from our microkinetic model (Figure 5.8 c), the reaction proceeds predominantly via the fully-complexed pathway. Adsorbed FA undergoes the first dehydrogenation step via O-H bond cleavage to form $HCOO_B$. $HCOO_B$ then decomposes by either undergoing *A)* uncomplexed rotation and dehydrogenation ($HCOO_B \rightarrow HCOO_M \rightarrow CO_2(g) + H$), or *B)* complexation by FA to form $HCOO_{BX}$, followed by complexed rotation and dehydrogenation ($HCOO_B + HCOOH \rightarrow HCOO_{BX} \rightarrow HCOO_{MX} \rightarrow CO_2(g) + H + HCOOH$). Lastly, H_2 recombinative desorption completes the catalytic cycle.

At our defined home conditions (10% FA, 373 K), our model predicts that complexed mechanism (*A*) contributes ~80% of the reaction flux, with the remaining ~20% going through the uncomplexed mechanism (*B*) (Figure 5.8 c). The reaction flux via complexed pathways is positively correlated with FA pressure and inversely correlated with temperature (Figure 5.8 a and b), both of which factors increase $HCOO_{BX}$ coverage and in turn the flux via complexed pathways: higher FA pressures and lower temperatures increase the gas-phase FA chemical potential such

that it is more favorable for FA to complex with $HCOO_B$. The reaction flux contributions via uncomplexed pathways, however, decreases due to the decreasing $HCOO_B$ coverage. Interestingly, it is this compensation between the different flux contributions that leads to an overall zero FA reaction order even though the surface is not saturated. This is consistent with experiments that show constant FA decomposition rates on Cu catalysts with increasing total surface coverage.[244] Our microkinetic model prediction that the reaction proceeds predominantly via the fully-complexed pathway differs from our DFT prediction that the reaction should proceed via the rotation-only-complexed pathway, which has a lower overall reaction barrier. There are two main reasons for this. Firstly, the microkinetic model accounts for coverage. Since the coverage of $HCOO_B$ is low, $HCOO_B$ is unable to assist in the decomplexation of $HCOO_{MX}$—the crucial step in the rotation-only-complexed pathway. In models with high $HCOO_B$ coverages, such as the 0.625 ML $HCOO_B$ covered Cu(111) model (Appendix E), the rotation-only-complexed pathway does indeed contribute significantly to the flux. Secondly, our parameter-estimation procedure revealed that an increase the energy of the $HCOO_M \rightarrow CO_2(g) + H$ transition state and a decrease in the energy of the $HCOO_{MX} \rightarrow CO_2(g) + H + HCOOH$ transition state was required to match experimental data; these corrections favor the fully-complexed pathway.

Table 5.3 Campbell's kinetic degrees of rate control (X_{RC})[245] for elementary steps in our 0.375 $HCOO_{BX}$ covered Cu(111) model. The degrees of rate control are calculated at our defined home conditions (10% FA, 373 K, balance He). Subscripts B and M refer to the bidentate and monodentate configurations of HCOO, respectively. Subscript X refers to complexation of HCOO with HCOOH (i.e. FA-HCOO complexes).

Transition State	X_{RC}
$HCOOH + * \leftrightarrow HCOO + H$	0.24
$HCOO_B \leftrightarrow HCOO_M + *$	0.00
$HCOO_M \leftrightarrow CO_2(g) + H$	0.20
$HCOO_{BX} \leftrightarrow HCOO_{MX} + *$	0.00
$HCOO_{MX} \leftrightarrow CO_2(g) + H + HCOOH$	0.42
$H + H \leftrightarrow H_2(g) + 2*$	0.14

The kinetic degrees of rate control for the 0.375 ML $HCOO_{BX}$ covered Cu(111) model are distributed across four elementary steps (Table 5.3). Dehydrogenation of $HCOO_{MX}$ ($HCOO_{MX} \rightarrow CO_2 + H + HCOOH$) has the highest degree of rate control ($X_{RC} = 0.42$) in our reaction network, with the rest of the rate control spread out over dehydrogenation of HCOOH (HCOOH → HCOO + H), dehydrogenation of $HCOO_M$ ($HCOO_M \rightarrow CO_2(g) + H$) and recombinative desorption of H_2 ($H + H \rightarrow H_2(g)$). This is consistent with the rate determining step being the decomposition of HCOO species, as described in the literature[105,246], as well as with our DFT energetics showing that the breaking of the C-H bond in this step is the highest energy point in the PEDs. Note that the rotation of $HCOO_B$ to $HCOO_M$, and analogously the rotation of $HCOO_{BX}$ to $HCOO_{MX}$, does not possess any degree of rate control. This suggests that $HCOO_{MX}$ is too stable on Cu(111). Thus, although rotation of $HCOO_{MX}$ is very facile (E_A = 0.32 eV; 0.375 ML $HCOO_{BX}$ model), decomposition of $HCOO_{MX}$ is inhibited (E_A = 0.82 eV; 0.375 ML $HCOO_{BX}$ model). Improved catalysts would need to bind $HCOO_{MX}$ less strongly so that the C-H bond breaking step in the decomposition of $HCOO_{MX}$ can be catalyzed easier.

5.4 Discussion

The results from our combined DFT and microkinetic modeling study demonstrate that bimolecular, hydrogen-bonded FA-HCOO complexes ($HCOO_{BX}$ and $HCOO_{MX}$) play a critical role in FA decomposition on Cu(111). By complexing with FA, the barriers for rotation of bidentate to monodentate HCOO are significantly lowered. Accordingly, our coverage self-consistent microkinetic model (0.375 ML $HCOO_{BX}$ covered Cu(111)) shows that majority of the FA decomposition flux moves through complexed pathways, whereas only a small portion of the flux

goes through the uncomplexed pathway. The uncomplexed pathway is, however, frequently the only considered pathway in mechanistic studies of FA decomposition over Cu catalysts.[105,228] Additionally, our results indicate that the MASI is $HCOO_{BX}$ instead of the often proposed uncomplexed $HCOO_B$[105,224,243], which we find has low coverage under reaction conditions. Because hydrogen bonding with FA is exothermic, we expect $HCOO_B$ to be largely complexed under reaction conditions with one FA molecule (to form $HCOO_{BX}$) and to a smaller extent with even two FA molecules; at high $HCOO_{BX}$ coverages for example, we found that HCOOH binds on the uncoordinated O-atom of $HCOO_{BX}$ (Figure 5.5).

Our results demonstrate the importance of FA-HCOO complexes for understanding how FA decomposes over Cu(111). Although proposed in the literature as early as the 1960s by Hirota *et al*.[247], these bimolecular complexes were until now neglected in most mechanistic analyses. Our findings are consistent with these literature reports, one of the most relevant of which is a study by Iglesia and Boudart.[223] With kinetics experiments, they determined that catalytic FA decomposition had a lower apparent activation energy and smaller pre-exponential factor than that of decomposition of HCOO via temperature programmed desorption (TPD).[223] They attributed this to a bimolecular mechanism whereby FA assists in the decomposition of HCOO intermediates.

Additionally, although FA binds weakly to surfaces, XPS and TPD experiments on Cu(110) by Yao and Zaera[226] reveal that when coadsorbed with HCOO, FA surprisingly remains adsorbed up to temperatures of ~420 K. Tellingly, FA desorbs as soon as HCOO decomposes to CO_2(g) + H. Together with infrared[224,225] and XPS[226] data suggesting that the two O atoms of HCOO are chemically distinct, these findings strongly suggest that bimolecular FA-HCOO complexes, previously misassigned as tilted HCOO species due to their asymmetry[225,248], exist on Cu surfaces.

Our work provides a rich and detailed understanding of the nanoscale mechanisms and the importance of hydrogen-bonded intermediates for FA decomposition on Cu(111). These results may guide the study of vapor-phase FA decomposition on other metal surfaces, especially at low temperatures and high FA pressures where we find increased flux via complexed pathways. These conclusions may also be applicable in condensed-phase systems, such as under aqueous conditions, where we expect H_2O molecules to play roles similar to those of HCOOH since it is also a strong hydrogen bond donor. Under such conditions, it may also be necessary to study in further detail how multiple hydrogen bonds—like how multiple HCOOH molecules complex with HCOO at higher coverages—affect the energetics of the FA decomposition pathways. More broadly, we demonstrate that by utilizing experimental kinetics to ensure model-experiment parity via rigorous parameter estimation, one can iteratively determine a coverage self-consistent picture of the active site.

Ultimately, we believe that our results will inform the design of catalysts that optimize the hydrogen-bonded pathways we discovered in this work. For example, zeolites[249] or metal organic frameworks[250] decorated with hydrogen bond donors may be able to intrinsically accelerate the rotation of $HCOO_B$ and, therefore, bypass the need for complexation with HCOOH, which is prone to desorb at higher reaction temperatures.

5.5 Conclusions

By combining first-principles DFT calculations and coverage self-consistent microkinetic modeling, we have elucidated the nanoscale mechanisms for FA decomposition on Cu(111). These mechanisms demonstrate that hydrogen bonded bimolecular complexes of HCOOH with HCOO,

never before considered in theoretical analyses of FA decomposition, are highly relevant for FA decomposition on Cu(111). Importantly, they facilitate the rotation of bidentate HCOO to monodentate HCOO by reducing the energy differences between these intermediates and stabilizing the transition states for their interconversion.

Under catalytic conditions, the active site is a surface covered by ~0.4 ML of these complexes, which has an interesting effect of strongly stabilizing coadsorbed species via van der Waals interactions: this underscores the importance of modeling lateral adsorbate-adsorbate interactions for deriving an accurate picture for the nature of the active-site under reaction conditions. Our proposed reaction mechanism and model of the active site reproduce the experimental observations of a FA reaction order of zero and an apparent activation energy of 95–100 kJ/mol closely. On the contrary, models with incomplete reaction mechanisms lacking such complexes cannot reproduce the experimental data even with large corrections to the DFT calculated energetics, further reinforcing the pivotal role of these complexes. A compensation effect, whereby flux via complexed pathways increases with FA partial pressure but flux via the uncomplexed pathway instead decreases, is responsible for the experimentally observed FA reaction order of 0.

Our work sheds light into the fundamental role hydrogen bonding plays in heterogeneously catalyzed reactions under realistic reaction conditions. By harnessing these interactions, researchers may be able to develop improved active and selective catalysts not just for FA decomposition but also for the multitude of chemistries that involve adsorbates capable of accepting and donating hydrogen bonds.

CHAPTER 6

COMBINING COMPUTATIONAL MODELING WITH REACTION KINETICS EXPERIMENTS FOR ELUCIDATING THE *IN SITU* NATURE OF THE ACTIVE SITE IN CATALYSIS[⊥]

6.1 Introduction

Microkinetic modeling based on density functional theory (DFT) derived energetics is important for addressing fundamental questions in catalysis. The quantitative fidelity of microkinetic models (MKMs), however, is often insufficient to conclusively infer the mechanistic details of a specific catalytic system. This can be attributed to a number of factors such as an incorrect model of the active site for which DFT calculations are performed, deficiencies in the hypothesized reaction mechanism, inadequate consideration of the surface environment under reaction conditions, and the intrinsic errors in the DFT exchange-correlation functional. Despite these limitations, we aim at developing a rigorous understanding of the reaction mechanism and of the nature of the active

[⊥] Adapted from – Bhandari, S.; Rangarajan, S.; Mavrikakis, M. Combining Computational Modeling with Reaction Kinetics Experiments for Elucidating the *In Situ* Nature of the Active Site in Catalysis. *In Press 2020* – https://dx.doi.org/10.1021/acs.accounts.0c00340

site for heterogeneous catalytic chemistries under reaction conditions. By achieving parity between reaction kinetics experimental outcomes and modeling outcomes through robust parameter estimation and by ensuring coverage-consistency between DFT calculations and MKM predictions, it is possible to systematically refine the mechanistic model and, thereby, our understanding of the catalytic active site *in situ*.

Our general approach consists of developing *ab initio*-informed MKM for a given active site and then re-estimating the energies of the transition and intermediate states so that the model predictions match quantities measured in reaction kinetics experiments. If: (i) model-experiment parity is high, (ii) the adjustments to the DFT-derived energetics for a given model of the active site are rationalized within the standard errors of DFT, and (iii) the resultant MKM predicts surface coverages that are consistent with those assumed in the DFT calculations used to initialize the MKM, we conclude that we have correctly identified the active site and the reaction mechanism. If one or more of these requirements are not met, we iteratively refine our model by updating our hypothesis for the structure of the active site and/or by incorporating coverage effects, until we obtain a high-fidelity coverage-self-consistent MKM whose final kinetic and thermodynamic parameters are within error of the values derived from DFT.

Using the catalytic reaction of formic acid (FA) decomposition over transition-metal catalysts as an example, here we provide an account of how we applied this algorithm to study this chemistry on powder Au/SiC and Pt/C catalysts. For the case of Au catalysts, our approach was used to iteratively refine the model starting from the (111) facet until we found that specific ensembles of Au atoms present in sub-nanometer clusters can describe the active site for this catalysis. For the case of Pt catalysts, our approach identified that a partially CO*-covered (111) surface serves as

the active site and that CO*-assisted steps contributed substantially to the overall FA dehydrogenation activity. Finally, we suggest that once the active site and the mechanism are conclusively identified, the model can subsequently serve as a high-quality basis for designing specific goal-oriented experiments and improved catalysts.

6.2 Going Beyond the State-of-the-Art

MKMs formulated using energetics derived from DFT calculations are frequently employed to elucidate the underlying reaction mechanism of heterogeneously catalyzed reactions. Figure 6.1 shows a schematic for an algorithm reflecting the state-of-the-art for microkinetic modeling analysis that is employed in the catalysis literature, viz. – (i) enumerating the elementary steps in the reaction mechanism, (ii) using DFT to evaluate binding energies for each intermediate and transition-state energies for each elementary step, on an hypothesized structure of the catalytically-active site, (iii) formulating a MKM, which is a system of differential-algebraic equations within the mean-field approximation, with DFT computed parameters for kinetics (activation energies and pre-exponential factors) and thermochemistry, and (iv) solving the model to obtain information on the catalytic chemistry, including reaction rates, flux-carrying pathways, selectivity, apparent activation energy barriers, reaction orders, and rate-/selectivity-determining steps.

Being entirely *ab initio*, these models are in principle predictive and serve to bridge the gap between atomic-scale information (i.e., energies corresponding to most stable structures of intermediates and transition-states on a certain structure of the active site) and macroscopic observables (e.g., conversion and selectivity).[33–36] MKMs have often complemented experiments

(microscopy, spectroscopy, and reaction kinetics experiments) to offer comprehensive insights into the reaction mechanism over a wide range of experimental conditions.[37,38] These insights can then serve as the basis for identifying new material compositions and atomic-scale architectures with improved catalytic activity and/or selectivity.[29,251,252]

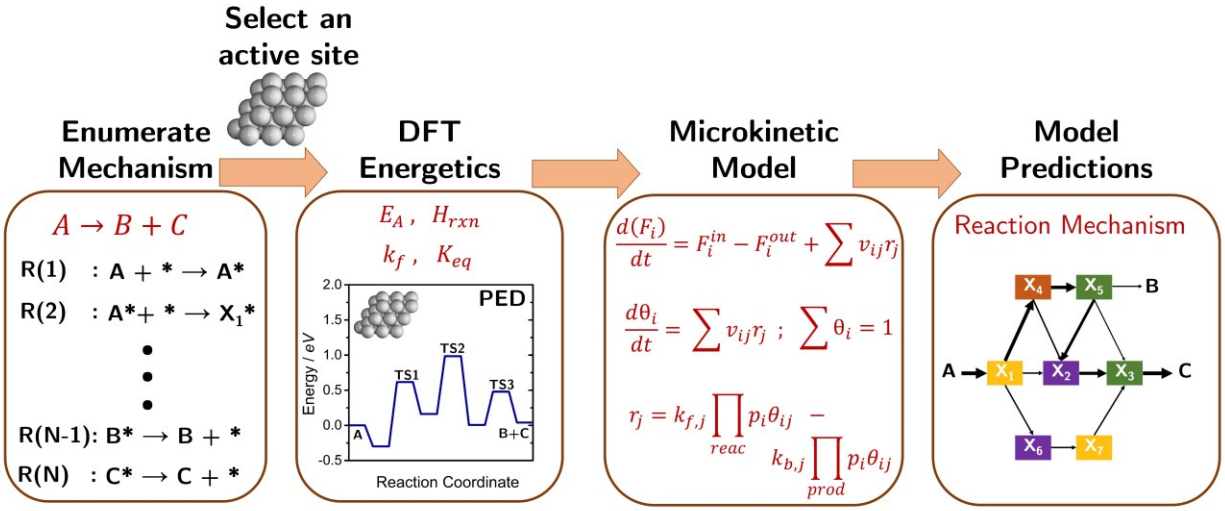


Figure 6.1 Schematic representation of the typical workflow adopted in a microkinetic-modeling (MKM)-based analysis for heterogeneous catalysis. '*A*', '*B*'/'*C*', and 'X_i's refer to reactant, products, and reaction intermediates, respectively. PED refers to potential energy diagram. Reactor balance equations (system of differential-algebraic equations) solved in a MKM are shown in the third panel.

A major caveat of the current approach (Figure 6.1) is that while these models often capture qualitative reactivity trends across experimental conditions and catalytic materials,[34,103,253,254] their quantitative accuracy vis-à-vis reaction kinetics experiments is often lacking. Indeed, the mismatch in reaction rates between model predictions and experiments can be several orders in magnitude and could stem from a number of factors,[42,255] such as : (1) an incomplete/incorrect reaction mechanism, (2) an active site model for which DFT energies are calculated, which is not dominating the catalytic action, (3) lack of consideration of surface environment effects, i.e., adsorbate-induced coverage-effects (clean-surface vs. a surface partially covered by

spectators/reactants/products), and (4) the intrinsic limitations of standard DFT exchange-correlation functionals which are used to calculate the energetics. A pertinent question arises: *Given this lack of fidelity, how can we identify active sites and reaction mechanism with a high degree of confidence?* To address this question, it is common to simply adjust the kinetic and thermochemical parameters, to achieve model-experiment parity.[8,39–41] This parameter adjustment is often rationalized based on qualitative intuition such as: (i) the idealized models may not fully capture the complexity of the real catalyst, (ii) standard DFT functionals (PBE/PW91) overpredict the binding of covalently-bound small intermediates, whereas they underpredict the binding of larger intermediates (due to inadequate treatment of dispersive interactions),[56,143,256] and (iii) most common functionals perform poorly in predicting gas-phase energetics.[12,134,143] We have performed such adjustments through parameter estimation previously, however, we suggest that this approach represents only a partial solution to the problem of parity between measured and model predicted rates. While the resulting model might offer good predictive power, it does not necessarily provide a conclusive picture of the underlying reaction mechanism and of the nature of the active site. This is because: (i) there may be multiple solutions to the parameter estimation problem, (ii) the adjustments to the DFT-derived parameters may be too large to be easily rationalized, i.e., larger than the statistical-error of ~0.2 eV for the common DFT-GGA functionals (eg. PBE/PW91),[137–139,143] and (iii) the predicted surface coverage of various species could be dramatically different from the coverage assumed to compute the DFT energetics.

Here, we provide an account of the methodology developed in our group for formulating high-fidelity MKMs.[7,41–45,59,257–259] Specifically, we present our algorithmic approach for identifying active sites and reaction mechanisms in the context of the formic acid (FA) decomposition reaction

(Scheme 6.1) – a chemistry which we have studied extensively, both computationally and experimentally – on supported Au[42–44] and Pt[45] catalysts. Through these examples, we strive to convey the advantages of a systematic and integrated approach of combining DFT calculations, reaction kinetics experiments, and microkinetic modeling to iteratively refine the atomic-scale picture of the active site and the reaction mechanism.

$$HCOOH \rightarrow H_2 + CO_2 \quad \text{(Dehydrogenation)} \quad ; \quad \Delta G\ (298\ K) = -43.5\ kJ/mol$$

$$HCOOH \rightarrow H_2O + CO \quad \text{(Dehydration)} \quad ; \quad \Delta G\ (298\ K) = -14.8\ kJ/mol$$

Scheme 6.1 Formic acid (FA, HCOOH) decomposition reactions. Gibbs free energies (ΔG) are calculated using the NIST thermochemistry database.[260]

6.3 FA Decomposition on Supported Gold Catalysts

Ojeda and Iglesia reported that finely-dispersed Au/Al_2O_3 catalysts decompose FA to H_2 selectively and exhibit higher activities compared to Pt catalysts,[83] one of the most active monometallic catalysts for FA decomposition.[99–101] These authors proposed that small Au clusters on Al_2O_3, undetected by transmission electron microscopy (TEM), were likely responsible for the exceptional catalytic activity.[83] Others have since corroborated that well-dispersed Au catalysts on a host of supports (SiC,[42] SiO_2,[261] ZrO_2,[80,262] CeO_2,[80,263] and TiO_2[264]) also exhibit high activity and high H_2 selectivity for FA decomposition. Although there is a consensus among these experimental studies that smaller Au nanoparticles or clusters are responsible for the remarkable FA decomposition reactivity of Au catalysts, the precise nature of the active site remained unknown. In the following, we describe our efforts to identify the nature of the active site for FA decomposition on Au/SiC using an algorithm that significantly expands on the approach outlined in Figure 6.1.

6.3.1 Elucidating the Active Site for FA Decomposition on Au/SiC

We started with studying this catalysis by combining DFT, microkinetic modeling, and reaction kinetics experiments over Au/SiC.[42] Specifically, we proposed an algorithmic workflow, wherein we take input from reaction kinetics experiments and iteratively refine our computational models to identify the nature of the active site (Figure 6.2). Accordingly, we initialized this procedure by hypothesizing a model for the active site, followed by: (i) evaluating DFT energetics to formulate a mean-field MKM, (ii) utilizing reaction kinetics experiments to systematically adjust DFT energetics to minimize model-experiment mismatch, (iii) evaluating if the parameter adjustments are rationalized within DFT error; if yes, we conclude that our hypothesis is correct, else, we utilize the insights gained from the parameter adjustment procedure to refine our hypothesis for the nature of the active site and re-perform this analysis iteratively until adjustments to DFT energetics are within the standard DFT error. It is only then that we conclude that we have developed a reasonable vision for the nature of the active site.

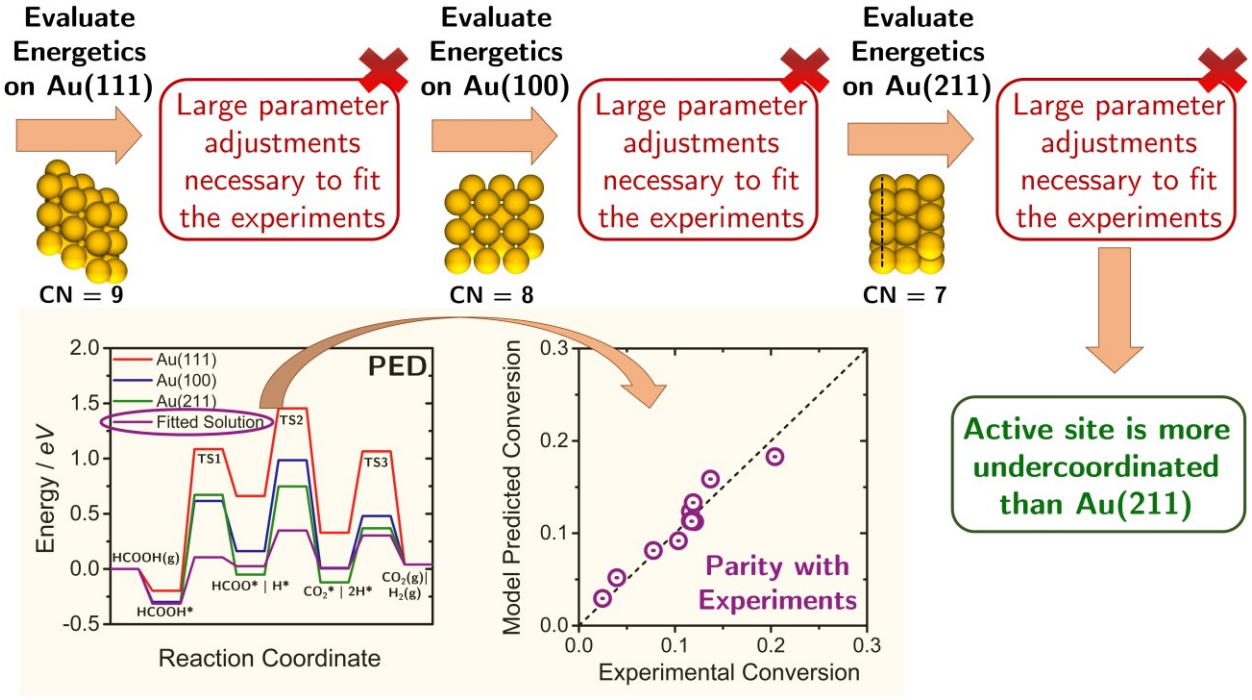


Figure 6.2 An iterative approach for elucidating the structure of the active site for FA decomposition on Au/SiC.[42] Feedback from parameter adjustment, required to fit the experiments (steady-state, <20% conversion, 1-4% FA, 0-6% H_2/CO_2, 343-383K), is used to continually revise the hypothesis for the active site: Au(111)→Au(100)→Au(211). To fit the reaction kinetics experimental measurements, for all three facets (shown in the potential energy diagram (PED)), large parameter adjustments were necessary, indicating that the active site is more undercoordinated than Au(211). CN refers to surface coordination number. Vertical dashed black-line in the inset for Au(211) marks the step edge.

We started by considering the close-packed Au(111) facet (surface coordination number (CN) of 9) as the hypothesized model for the active site (Figure 6.2) and evaluated the energetics of a comprehensive reaction network comprising of 17 reaction steps and 15 distinct species, using plane-wave periodic DFT (PW91-GGA). We used zero-point energy (ZPE) corrected energetics to obtain initial estimates for the rate parameters used in the MKMs. However, the model significantly underpredicted the reaction rates compared to our experimental measurements. To fit the model-predicted rates with experimental rates, the energies of the transition-states and reaction intermediates had to be substantially modified (by as large as 1 eV). Such adjustments cannot be

justified on the basis of DFT errors alone, and since a detailed reaction mechanism was modeled, we concluded that Au(111) cannot represent the active site for this chemistry. Nevertheless, the parameter adjustments needed for the MKM on Au(111) to capture the experimental data provided valuable guidance in searching for an alternative model for the active site. We noted that all the intermediates and transition-states had to be stabilized, suggesting that a more under-coordinated model site would potentially represent the active site better. Algorithmically (Figure 6.2), this led us to evaluate Au(100) (CN=8) and then Au(211) (CN=7) as plausible active sites. However, since large parameter adjustments were necessary on these two facets as well, we concluded that none of the facets explored yet were a good representation of the active site on Au/SiC.

The results showed that upon going from Au(111)→Au(100)→Au(211), the magnitude of the parameter adjustments progressively decreased, but all states still had to be further stabilized to rationalize the experimental reaction rates. These observations suggest that the active site might be more undercoordinated than Au(211) (CN<7), which would potentially stabilize the energetics for the intermediates and transition-states to an even greater extent, compared to Au(111), Au(100), and Au(211). Additionally, for all three models, >0.95 ML of the sites were predicted to be vacant under all reaction conditions, which precludes any potential stabilizations stemming from adsorbate-adsorbate interactions.

6.3.2 Experimental Insight on the Active Site for FA Decomposition on Au/SiC

To further explore the role of undercoordinated Au sites, we synthesized Au catalysts with varying dispersion (average particle size ranging from 2.5-10.7 nm) and evaluated those through reaction kinetics experiments.[42] The results indicated that the turnover frequency (TOF) decreased with increasing average particle size, demonstrating the structure sensitivity of FA decomposition on

Au/SiC. Subsequently, we estimated the fraction of various surface sites (corner, perimeter, terrace) as a function of particle size,[265–268] and concluded that the reaction rate correlated well with the number of corner sites. This conclusion based on experiments is in agreement with the insight gained from DFT-derived MKMs suggesting that indeed low-coordinated Au sites are playing a key role in FA decomposition.

6.3.3 FA decomposition on Unsupported Au Clusters

Motivated by this conclusion, we studied the role of low-coordinated sites in catalytically relevant sub-nanometric regimes. Specifically, we analyzed FA decomposition reaction paths on unsupported subnanometric Au clusters (up to Au_{25}~0.85nm), identified using *ab initio* molecular dynamics simulations.[43] To select the clusters characterized by energetics that could rationalize the experimental reaction rates, we used the activation energy barrier for the first FA dehydrogenation step (HCOOH* $\leftrightarrow$ HCOO*+H*) as a screening criterion (Figure 6.3). As Au(211), the most reactive of the three extended surfaces considered, predicted reaction rates that were 5-6 orders of magnitude smaller than the experimental reaction rates, the active clusters in the Au/SiC catalysts used in experiments should at least have a smaller activation energy barrier for FA dehydrogenation compared to that on Au(211).

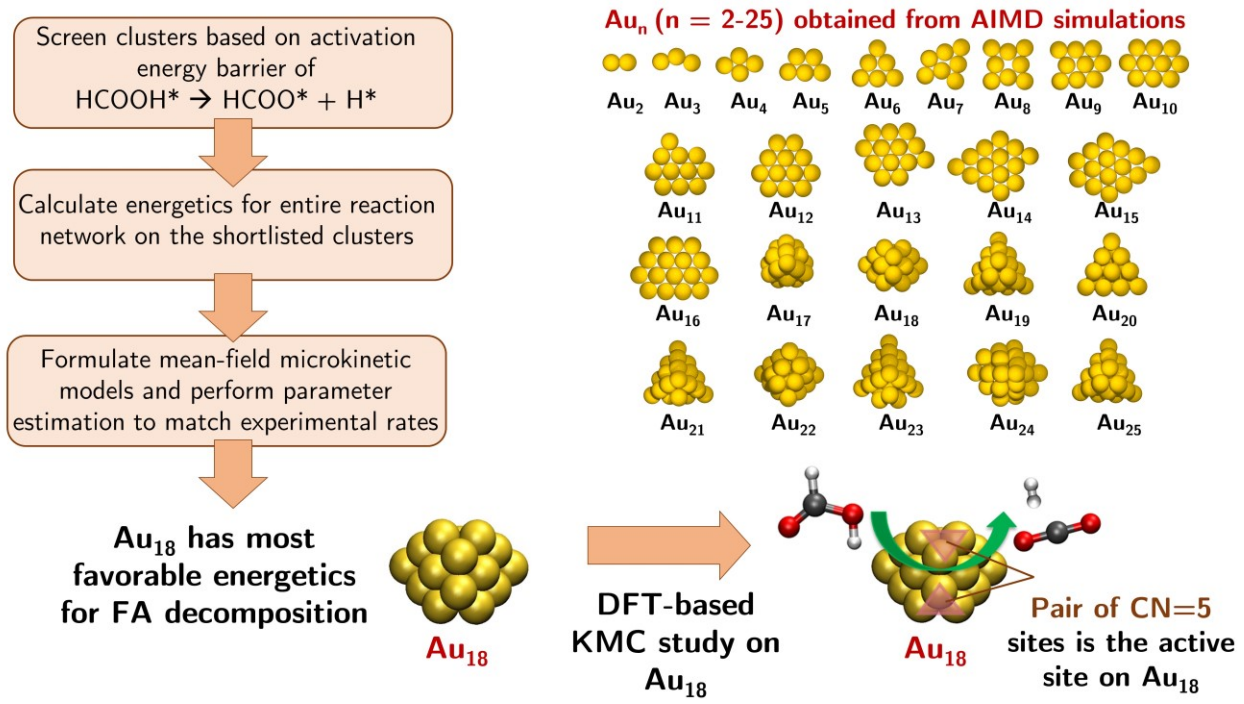


Figure 6.3 Elucidating the active site for FA decomposition on unsupported subnanometric Au clusters.[43] Most stable geometries of Au_n (n=2-25) clusters (<0.85nm) obtained from *ab initio* molecular dynamics (AIMD) are shown. Combination of DFT-derived mean-field MKMs and reaction kinetics experiments on Au/SiC, led to the conclusion that Au_{18} might resemble the active site the best. Kinetic Monte Carlo (KMC) study on Au_{18} revealed that a pair of adjacent Au_3 ensembles (coordination number (CN) of 5), can be the active site for FA decomposition on Au/SiC.[44]

Consequently, we performed detailed reaction pathway studies on the shortlisted subset of clusters (Au_4, Au_5, Au_7, Au_{17}, Au_{18}, and Au_{19}), which were identified as potential candidates for representing the active site on Au/SiC. Mean-field MKMs were then developed using the DFT energetics calculated for these clusters and were subsequently fit to the experimental data through parameter adjustment. This entire process (Figure 6.3) identified the Au_{18} cluster to possess the most favorable energetics, requiring only minimal parameters adjustments to fit the experimental data.

Although, mean-field MKMs provide valuable information to guide the search of active site geometry, subnanometric clusters such as the catalytically active Au_{18}: (i) offer a spatially

inhomogeneous surface, (ii) present discrete adsorbate coverages, and (iii) lead to strong adsorbate interactions due to quantum-size effects and superatomic nature of the clusters.[44,269] These properties mandate the use of methods that better capture local effects. In a recent study,[44] we combined DFT calculations with cluster-expansion[270,271] and on-lattice kinetic Monte Carlo (KMC) simulations[154,272] to derive a rigorous mechanistic description for the FA decomposition on Au_{18} clusters. The results suggest that a pair of adjacent Au_3 triangular ensembles (CN=5) is likely the active site for FA decomposition on Au_{18} clusters. Dissociation of a single FA molecule, leads to the simultaneous occupation of each of these triangular-sites by HCOO* and H*, which in turn results into a strong stabilization of the Au_{18} cluster. This stabilization prevents dehydrogenation of a second FA molecule, until the first molecule is fully decomposed to CO_2(g) and H_2(g). In other words, Au_{18} processes one FA molecule at a time, thereby explaining the kinetic isolation of decomposition events associated with the exclusive HD production observed in experiments with half-deuterated FA molecules over Au/Al_2O_3.[83] The reaction occurs through the HCOO*-mediated pathway ($HCOOH^* \leftrightarrow HCOO^*+H^* \leftrightarrow CO_2^*+2H^* \leftrightarrow CO_2+H_2$) with complete selectivity towards H_2, which rationalizes the experimentally observed selectivity towards dehydrogenation on Au/SiC. Dehydrogenation of HCOO* carries the highest degree of rate control for all conditions and is therefore the rate-determining step.

In the case of FA decomposition over Au/SiC, we clearly showed that the mechanism and active site (pair of Au_3 sites on Au_{18}) could not have been identified following the approach described in Figure 6.1. Further, we demonstrated that finding an accurate active site model alone through parameter adjustments, is insufficient. Only an active site model that yields a high degree of parity with experimental measurements and whose parameter adjustments are within the DFT error,

offers a desirable stopping point for the active site identification algorithm. It is only at that point we can extract reliable mechanistic insights.

6.4 FA Decomposition on Supported Platinum Catalysts

Experimental studies demonstrate Pt as one of the most active monometallic catalysts for FA decomposition.[99–102] Unlike Au catalysts which selectively dehydrogenates FA, both the dehydrogenation (CO_2+H_2) and dehydration (CO+H_2O) pathways are active on Pt, with >95% selectivity towards dehydrogenation.[101,102] Additionally, formation of CO as one of the decomposition products implies the presence of adsorbed CO (CO*) on the catalyst surface, leading to the well-known problem of CO*-poisoning of Pt catalysts.[101,112,113] Despite numerous computational and experimental studies of this reaction, the nature of surface reaction intermediates along with their abundance, the reaction mechanism, and the nature of the active site as a function of reaction conditions, have not been elucidated. Herein, we discuss our algorithmic approach for addressing these fundamental questions for FA decomposition on Pt/C (Figure 6.4).[45]

6.4.1 Iterative Approach for Elucidating the Active Site for FA Decomposition on Pt/C

We started by considering extended clean Pt(100) and Pt(111) surfaces as the active site model and calculated the energetics (DFT-PW91-GGA) for a comprehensive reaction network involving 25 elementary steps and 20 distinct species. To incorporate ZPE and temperature–corrected DFT energetics in our mean-field MKMs, we derived Shomate parameters,[260] using vibrational frequency calculations and statistical mechanics. Both clean (111) and (100) models, however, predicted reaction rates that were several orders of magnitude lower than our experimental rates (steady-state, <10% conversion, 1-5% FA, 0-10% H_2/CO_2, 0-0.1% H_2O/CO, 358-378 K). Next,

we performed parameter estimation to determine the adjustments on the two model surfaces that would yield quantitative agreement with our experimental data.

Post parameter adjustments, both clean Pt(111) and Pt(100) demonstrated improved agreement with experimental measurements. However, these models were found to be inadequate representations of the active site on Pt/C, since they: (i) failed to reproduce rates when CO was co-fed in the reactor, (ii) predicted high coverage of CO* (>0.90 ML, averaged over all experiments), inconsistent with the clean-surface assumption at which the DFT energetics were calculated, and (iii) required large adjustments to the DFT-derived activation energy barriers for several elementary steps, well beyond the typical DFT errors (Figure 6.4). Although these models fell short in explaining the experiments, their analysis provided useful insights regarding the nature of the most abundant surface intermediate (MASI) under experimental conditions, viz. CO*. In principle, one could also validate this model prediction using *operando* spectroscopy. Indeed, there is ample spectroscopic evidence (*in situ* Fourier-transform infrared spectroscopy (FTIR)) for partial CO*-poisoning of supported Pt catalysts, under typical FA decomposition conditions.[101,102,113] Motivated by these insights, we updated our hypothesis for the active site model and, in the next step, considered partially CO*-covered (111) and (100) facets (Figure 6.4), thereby explicitly accounting for CO* coverage-effects.

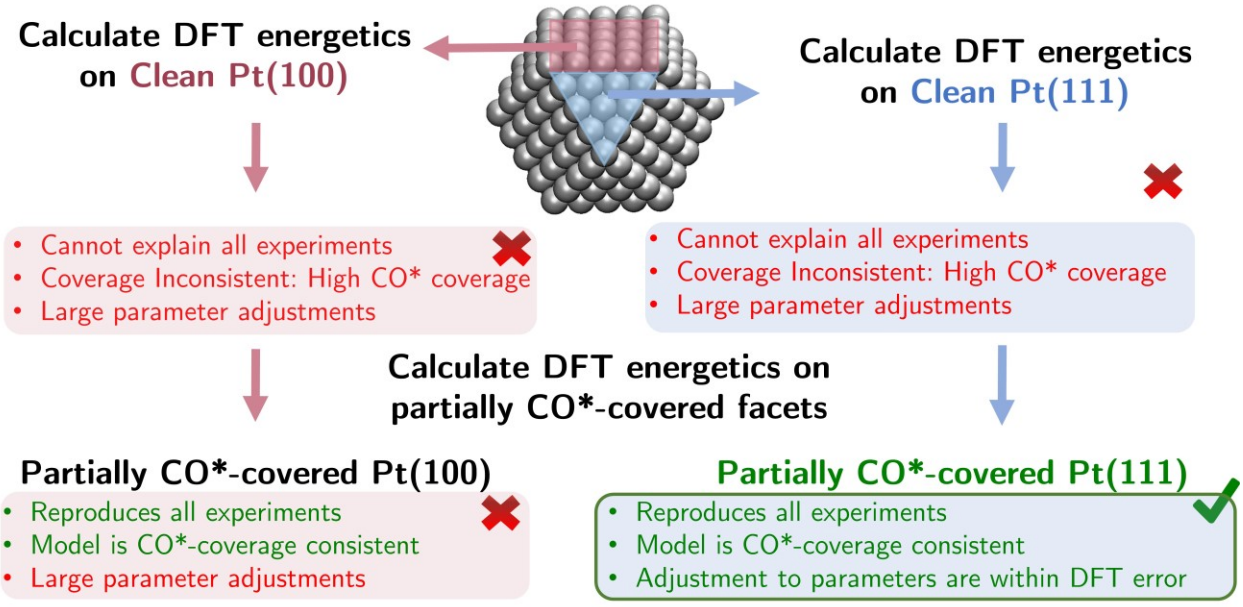


Figure 6.4 Workflow for developing a coverage self-consistent description of the active site for FA decomposition on Pt/C.[45] Mean-field MKMs formulated using DFT energetics on clean Pt(100) and Pt(111) were found to poorly describe the active site. Feedback from the parameter adjustment procedure is used to iteratively update the hypothesis for the nature of the active site.

6.4.2 Modeling CO* Spectator-induced Coverage-effects

Consequently, using DFT, we reinvestigated the entire reaction network on partially (4/9 ML) CO*-covered Pt(100) and Pt(111) surfaces. The choice of 4/9 ML CO*, used as an initial estimate of the *in situ* coverage, was motivated by previous experimental determination of CO*-saturation coverages on Pt surfaces under low CO partial pressures, which is similar to that experienced by Pt/C under FA decomposition reaction conditions.[121] The presence of CO* on the catalyst surface opened new pathways, including CO*-assisted dehydrogenation steps, which were now included in the refined reaction network. In addition, we evaluated the reaction energetics (binding/transition-state energies) at varying CO*-coverage levels to determine the variation of the energetics as polynomial-functions of CO* coverage. The resultant polynomial-functions were

incorporated in our MKMs, thereby enabling CO* coverage-dependent energetics for the new models.

After parameter adjustments, both the *CO* coverage-cognizant* Pt(100) and Pt(111) models were able to accurately describe the experimental data, including the subset of the experiments with CO-co-feed, which were not well reproduced by our clean-surface parameter-adjusted models. Furthermore, these MKMs predicted CO* coverages (~4/9 ML CO* on Pt(100); ~3/9 ML on Pt(111)) which were consistent with coverages of 4/9 ML CO* spectators used in the catalyst model for DFT calculations. Both these MKMs were therefore CO*-coverage *self-consistent*. Analysis of the parameter adjustments revealed that Pt(100) required large changes to the DFT calculated activation energy barriers (Figure 6.4). By constraining the adjustments to the typical DFT (PW91-GGA) error of ±0.2 eV,[122,137–139,143,273] we found that Pt(100) was largely poisoned by CO* (~0.5 ML) and was rendered inactive under our reaction conditions. On the other hand, parameter adjustments required for the partially CO*-covered Pt(111) model were within DFT error. We therefore concluded that a partially CO*-covered Pt(111) accurately represents the active site for FA decomposition on Pt/C.

The MKM analysis revealed that on the partially CO*-covered Pt(111), the reaction proceeds through the COOH* mechanism (Figure 6.6). Both the direct COOH* dehydrogenation (COOH* $\leftrightarrow$ CO_2*+H*) and the CO*-spectator assisted dehydrogenation (COOH*+**<u>CO</u>*** $\leftrightarrow$ CO_2*+**<u>CO</u>**H***;*** CO*-spectators are denoted by **<u>CO</u>***) pathways contributed to the dehydrogenation reaction flux. These CO* spectator-assisted pathways were found to be essential for accurately reproducing the experimentally measured apparent activation energy barriers and reaction orders.

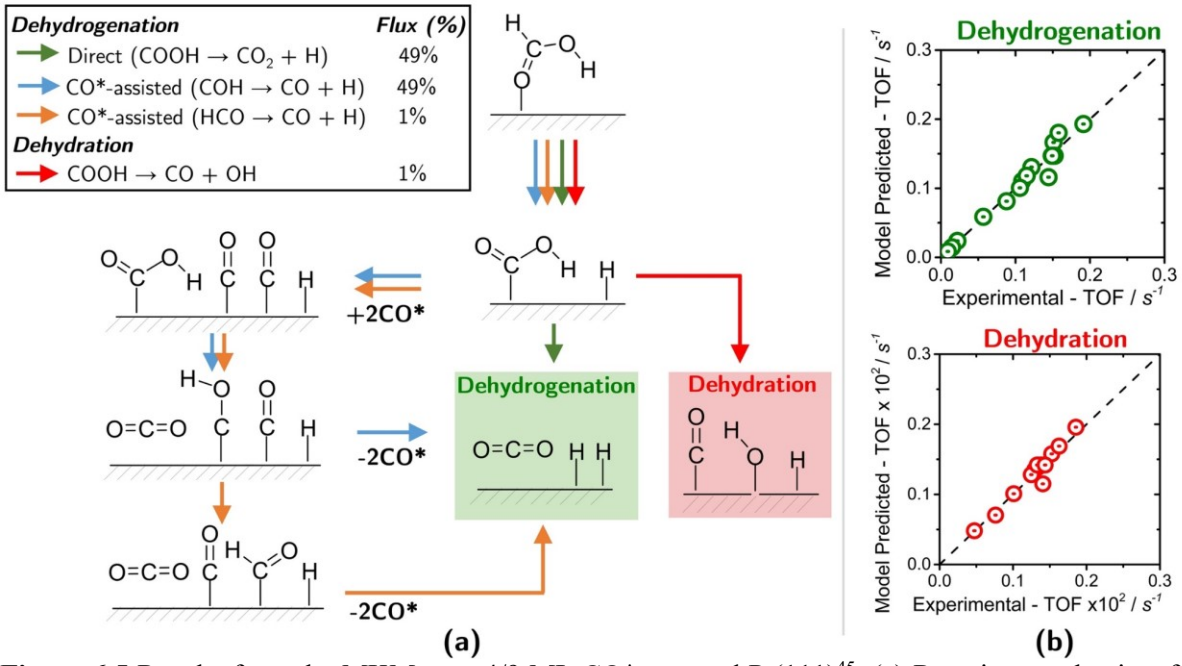


Figure 6.5 Results from the MKM on a 4/9 ML CO*-covered Pt(111)[45] :(a) Reaction mechanism for FA decomposition on Pt/C. Formate-mediated pathways were considered, but did not contribute significantly to FA decomposition. Flux contributions for the various pathways at 2.6% FA, balance He (1 atm, 373K) are indicated, (b) Parity plots comparing model-predicted and experimental turnover frequencies (TOFs).

This example speaks to the importance of practicing coverage self-consistent microkinetic modeling and of combining it with experimental data for elucidating the nature of active site and the reaction mechanism. Modeling CO* coverage-effects for this chemistry: (1) yielded improved initial estimates for the energetics used in the MKM, since these parameters required minimal adjustments to quantitatively fit with the experiments and (2) inspired the consideration of CO* spectator-assisted pathways, which were essential in reproducing the experimental data. The traditional approach (Figure 6.1) was again insufficient ; our iterative approach, however, revealed that accounting for CO* coverage was essential in determining both the active site and the reaction mechanism.

6.5 An Algorithm to Identify the Active Site and Reaction Mechanism

The process of iterative model refinement, employed in both examples, can be formalized as a general algorithm (Figure 6.6), which substantially expands on the state-of-the-art shown in Figure 6.1. We initialize the algorithm with a hypothesized active site model, perform detailed reaction pathway studies using DFT, and formulate a MKM. We then incorporate data from reaction kinetics experiments and perform parameter estimation to achieve parity with the experiments. The optimized model is evaluated on the following three criteria: *(i) Can the model accurately reproduce the experimental data?, (ii) Are the parameter adjustments needed to capture the experiments within DFT error?, (iii) Is the model-predicted surface-environment consistent with the coverages at which the DFT energetics were calculated?* If the optimized model satisfies all three criteria, we conclude that the hypothesized model for the active site accurately describes the nature of the active site. However, if even one of these criteria is not satisfied, we use insights gained from our parameter adjustment procedure to revise our hypothesis for the active site (i.e., active site geometric model, reaction mechanism, site's environment including decoration by adsorbates), and reiterate all steps in the algorithm until all three criteria are met. The resultant high-fidelity model can then be used to perform well-educated reaction engineering tasks, such as to: (i) predict behavior of the catalyst with quantitative accuracy (i.e., activity, selectivity, surface coverages, reaction mechanism, etc.), under other experimental conditions, (ii) perform experimental design with specific goals in mind: to identify experimental conditions for optimizing yield of product(s) or surface concentration of reaction intermediate(s), which, in turn, could enable spectroscopic identification of elusive reaction intermediates, and (iii) investigate related chemistries (e.g., the reverse reaction).

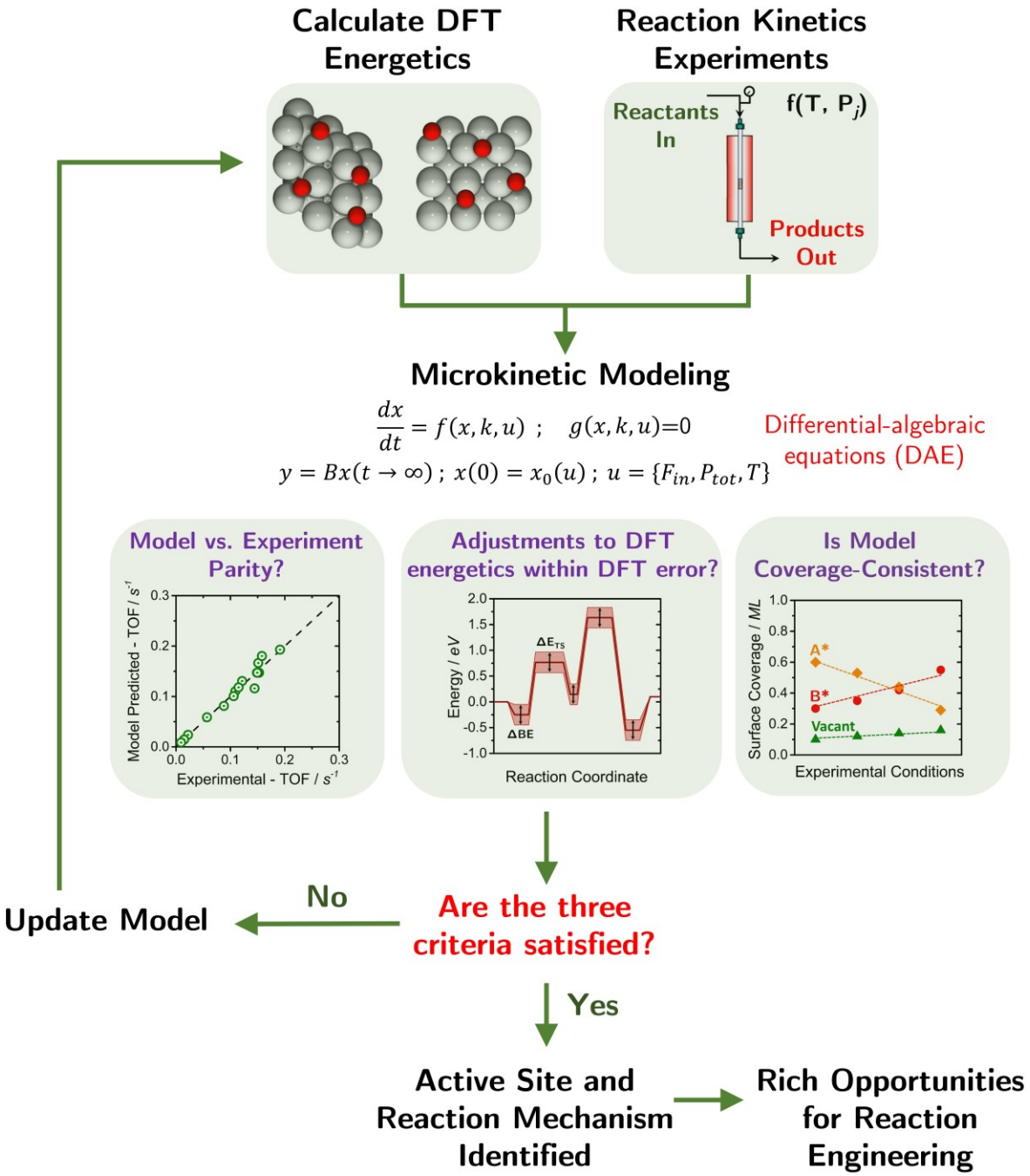


Figure 6.6 Proposed algorithmic scheme for elucidating the nature of the catalytic active site and the reaction mechanism, using a combination of DFT, reaction kinetics experiments, and microkinetic modeling.

6.6 Parameter Estimation

A critical part of the algorithm is parameter estimation where we minimize the model-experiment mismatch (of TOFs) by adjusting the energetics of surface intermediates and transition-states from their respective DFT-values. Mathematically, this is a nonlinear optimization problem with the MKM (at different experimental conditions) as constraints. Solving this problem is challenging because: (i) the optimization problem is highly nonlinear due to the numerical stiffness of the MKM, (ii) we seek solutions where the insensitive parameters are automatically identified and set to zero (i.e., energy is set to the respective DFT value) to avoid having too many parameters and too little data, (iii) we require alternative solutions (minima) to compare potentially competing models. Accordingly, we have developed efficient solution strategies for solving this problem.

Nonlinear optimization problems with embedded differential-algebraic equations (DAEs) can be solved (i) "sequentially",[274–276] where the DAEs (i.e., MKM) are solved at each step of optimization and the predictions/sensitivities are passed on to a gradient-based optimizer, or (ii) "simultaneously",[277–279] wherein the DAEs are reformulated as a set of nonlinear equality constraints, thereby allowing the use of automatic differentiation to compute the gradients. We developed and applied both types of solution methods to these kinds of problems. Specifically, we developed a generic sequential-optimization framework[41] which utilizes state-of-the-art gradient and Hessian-based inter-point optimizer[280], a backward-difference algorithm based DAE solver[281], and a linear-algebra based sensitivity analysis module to provide a fast and robust solution scheme. We further developed an alternative and substantially faster simultaneous-optimization approach,[258] where the MKM at steady state is reformulated as a system of nonlinear equations and solved as a nonlinear programming problem (NLP)[277–279,282] within GAMS. In both methods,

we apply (i) a ridge (or L_2) regularization and (ii) a multi-start scheme enabling the uniform sampling of the parameter space (Latin-hypercube sampling[135,136]), and simultaneously elucidate plausible local minima. The regularization term, a penalty added to the objective of the optimization problem, forces insensitive parameters to zero, thereby providing a *sparse* solution. The multi-start scheme identifies multiple solutions which can then be compared to each other. These methods are mathematically rigorous and identify a comprehensive set of solutions meeting the convergence criteria of our algorithm.

6.7 Outlook

Figure 6.6 describes the current state-of-art in terms of algorithm combining DFT, reaction kinetics experiments, and MKM for determining: (i) the nature of the active site in catalysis while the reaction is taking place and (ii) the detailed reaction mechanism for small-to-medium sized chemistries (~50 elementary steps). Selected opportunities for further methodological development are summarized here:

- *Errors in entropy*: In the parameter adjustment step of the algorithm, we have implicitly assumed that the errors arise in energies; not in entropy. While this assumption is reasonable when the intermediates are strongly bound (as in the examples discussed here), using standard quantum-harmonic approximations to estimate the partition function may grossly under-predict the entropy of weakly bound intermediates. Therefore, appropriate care must be taken when calculating entropy for such cases.[283–285] Further, inclusion of surface configurational entropy, associated with compensation effects in heterogeneous catalysis,[286–288] could also help

improve the description of the active site. How these corrections/contributions can be included in our algorithm remains to be assessed.

- *Beyond monometallic catalysts*: While our iterative algorithm is catalyst agnostic, its application to metal alloys, metal-support interfaces, oxide/sulfide-based catalysts, and materials with intrinsically isolated sites (e.g., zeolites, single-atom catalysts) has not yet been explored.
- *Size-scalability:* Intrinsically complex reaction networks (comprising of hundreds of intermediates and thousands of reaction steps) routinely arise in catalysis (e.g., alkane reforming, hydrotreating, biomass upgrading, etc.); how this approach scales to such large reaction networks remains to be studied.
- *Assessing and improving the accuracy of first-principles calculations*: Given the inadequacies of standard exchange-correlation functionals used in DFT calculations, a number of recent studies have proposed systematic frameworks to analyze error propagation and to assess the uncertainty associated with MKM predictions.[137,289–291] Given their exorbitant computational cost, more accurate methods such as coupled cluster calculations, random-phase approximations, quantum Monte Carlo methods, etc. cannot yet be routinely applied in conjunction with MKM. However, advances in computing power and the recent development of approaches such as hybrid multi-level calculations[292] or quantum-mechanical embedding techniques[293,294] now allow for accurate calculation of a relatively small set of energies. The feasibility of infusing, perhaps selectively, such calculations to improve the model fidelity, represents an interesting research direction.

Finally, we propose that our mathematically rigorous approach may have important implications for enhancing the fidelity of computational catalyst discovery approaches such as descriptor-based catalyst screening via higher-dimensional volcano plots. Conventionally this procedure entails: (i) evaluating the energetics of the reaction network on a 'reference' monometallic catalyst, (ii) extrapolating reaction energetics using the linear scaling[46] and Brønsted-Evans-Polanyi (BEP)[47] relationships, and (iii) elucidating reactivity trends across the descriptor space and identifying catalysts with optimal descriptor characteristics. While this established approach certainly has *qualitative* merit, its inherent shortcomings (i.e., assumed active site for the reference catalysts, assumed reaction mechanism, intrinsic-errors of DFT functionals, neglect/inadequate treatment of coverage-effects) could potentially lead to predictions that are not *quantitatively* accurate. We propose that: (i) introducing experimental kinetics data to derive the true active site and energetics of the reference catalyst and (ii) using coverage-dependent energetics,[8,157,160] to formulate *experiment-calibrated coverage-cognizant* volcano plots, could help the community move closer to quantitative accuracy in computational catalyst discovery approaches.

6.8 Summary

In this Account, we described an optimization-based mathematically rigorous approach to elucidate the nature of the active site and the reaction mechanism while the catalysis is taking place. We formulate quantitatively accurate MKMs by introducing experimental reaction kinetics data and discussed this methodology for FA decomposition reaction on Au/SiC and Pt/C catalysts. We demonstrated how this approach can be employed to develop high-fidelity MKMs, which can predict the behavior of a catalyst at any experimental condition with quantitative accuracy. Finally,

we highlighted some opportunities for improvement and potential implications of this methodology for computational catalyst discovery.

CHAPTER 7

TOWARDS EXPERIMENT CALIBRATED COVERAGE-COGNIZANT VOLCANO PLOTS: FORMIC ACID DECOMPOSITION REACTION

7.1 Introduction

Wide-scale integration of sustainable technologies into our energy infrastructure hinges strongly on carbon-neutral energy storage and generation systems. Generated as a byproduct in biomass reforming, formic acid (HCOOH, FA) has recently attracted widespread attention as a promising carbon-neutral hydrogen storage vector.[68,81,148,213,214,216–219] FA has a high hydrogen content (53.4 g-H_2/l; 4.4 wt.%), is non-flammable, and is liquid at ambient conditions, making it a promising energy-storage material for mobile applications, which is also compatible with our current liquid-fuel infrastructure. The success of FA-based technologies is contingent on discovery of catalysts that can selectively decompose FA via the dehydrogenation path, at near ambient conditions, without concomitant production of CO through the dehydration path.

Computational descriptor-based catalyst screening methodologies have greatly accelerated the discovery of improved catalytic materials. Typically, this approach involves: (1) elucidating the energetics of the reaction network on an active site model for a said reference monometallic

catalyst, (2) calculating reaction thermochemistry and kinetics on a host of monometallic catalysts to identify reactivity descriptors and derive linear-scaling and Brønsted–Evans–Polanyi (BEP) correlations, (3) extrapolating the energetics of the reaction network across the material space to derive reactivity maps dependent on the energetics of the chosen descriptors, and (4) comparing the reactivity trends for the monometallic catalyst and identifying improved catalyst formulations via high-throughput descriptor based screening.

While this approach has qualitative merit, the quantitative fidelity of these prediction in terms of activity and selectivity vis-à-vis the experiments if often lacking. This discrepancy can be attributed to: (1) an arbitrarily chosen model for the catalytic active site of the reference catalyst, (2) incorrect presumption of the reaction mechanism, (3) lack of consideration of coverage-effects stemming due to the presence of spectator species for the reference catalyst and also across the descriptor space, and (4) intrinsic errors of standard DFT functionals.

To address these potential sources of errors and improve the quantitative predictability of computational materials discovery approach, in this study we suggest the following: (1) Utilizing experimental kinetics data to determine the correct model of the active site and the reaction mechanism on the reference catalyst. By concurrently ensuring model-experiment parity, through rigorous parameter estimation, one can experimentally-calibrate the energetics of the reference catalyst and address systematic intrinsic errors of standard DFT functionals. (2) Starting with the calibrated model for the reference catalyst, one can then utilize linear-scaling and BEP correlations to extrapolate the energetics across the descriptor space, followed by the use of coverage-dependent energetics to account for spectator coverage-effects on-the-fly, within the mean-field approximation.[34] We discuss our methodology in context of the FA decomposition reaction. We

determine that experimental-calibration of the reference catalyst and inclusion of spectator coverage effects, to formulate experiment-calibrated coverage-cognizant models, can greatly influence the nature of the reactivity (activity and selectivity) maps, compared with that obtained from the conventional methodology, thereby impacting the predicted reactivity trends for the monometallic catalysts. Further, we determine that formulation of experiment-calibrated coverage-cognizant volcano plots can also drastically modify the shape, height, and location of the activity volcano map and thus have significant implications for computational descriptor-based screening methodologies.

7.2 Methods

7.2.1 Computational Methods

Periodic self-consistent DFT calculations were performed with the PW91-GGA functional[189] using DACAPO,[56,57] a total energy code. The calculation setup for the monometallic systems was consistent with our previous study.[108] The catalyst surfaces were modeled with the close-packed (111) facet of face-centered cubic (fcc) metals: Ag, Au, Cu, Ir, Ni, Pd, Pt, and Rh. The optimized bulk lattice constants were found to be in close-agreement with the experimentally reported values[125] (in parentheses): Ag 4.14 Å (4.09 Å), Au 4.18 Å (4.08 Å), Cu 3.67 Å (3.62 Å), Ir 3.86 Å (3.83 Å), Ni 3.52 Å (3.52 Å), Pd 3.99 Å (3.89 Å), Pt 4.00 Å (3.92 Å), and Rh 3.83 Å (3.80 Å). The (111) surfaces were modeled by periodically repeated (3x3) unit-cells, with three atomic-layers. All slab atoms were fixed at their bulk-truncated positions, as our tests indicated a negligible effect (in terms of adsorbate binding energies) due to surface relaxation for the close-packed (111) facets of monometallic systems.[108] Successive slabs were separated by a vacuum of

at least five-atomic layers. The core-electron interaction were described with Ultrasoft Vanderbilt pseudopotentials[295] and the Kohn-Sham one-electron states were expanded using plane-waves with an energy cutoff of 25 Ry. Adsorption of reaction intermediates was allowed on only one of the exposed surfaces and the dipole monument was adjusted accordingly.[126,127] The surface Brillouin zone was sampled at 6 special Chadi-Cohen k-points for Ir, Ni, Pd, Pt, and Rh, and 18 special k-points for Au, Ag, and Cu.[296] Spin-polarized calculations were performed for Ni. Convergence of the computed binding energies (BEs) with respect to computational parameters has been verified previously.[108]

The BE of an adsorbate '*i*', on clean surfaces (adsorbate coverage of 1/9 ML) were calculated using the following:

$$BE_i = E_{total} - E_{slab} - E_{i,gas} \tag{7.1}$$

where, E_{total} is the total energy of the slab/adsorbate system, E_{slab} is the total energy of the clean slab, and $E_{i,gas}$ is the energy of the adsorbate '*i*' in the gas-phase.

The transition states (TS) were determined using the climbing images nudged elastic band (CI-NEB) method.[129,297,298] The minimum energy path for each elementary step was determined by interpolating seven intermediate images between the initial- and the final-states. The structures were relaxed until the forces for all images were <0.1 eV/Å. TS was verified by performing vibrational-frequency calculation yielding an imaginary frequency along the reaction coordinate.

The linear-scaling and BEP correlations were formulated using BE of CO and HCOO as independent energetic descriptors representing C- and O-bound reaction intermediates, respectively. The choice of these two adsorbates as descriptors was motivated by the fact that: (1) both CO and HCOO are key reaction intermediates in the FA decomposition reaction network and

(2) CO and HCOO are commonly proposed as most abundant surface intermediates (MASIs), qualitatively speaking, for the regions in the descriptor space with strong binding of C-bound species (e.g., Pd, Pt)[45,101,299] and strong O-bound species (e.g., Cu)[100,105,224], respectively. The energetics of the reaction network were evaluated on the (111) facet of eight transition metal surfaces: Ag, Au, Cu, Ir, Ni, Pd, Pt, and Rh Appendix F.

To account for the coverage-effects due to the presence of spectator CO and HCOO species, we utilized the mean-field implementation of coverage effects.[34,45] The thermochemistry and kinetics of the reaction network were derived under varying coverages of spectator CO and HCOO, to derive polynomial-functions representing binding and transition-state energies as a function of the coverage of spectator species. To accurately capture the variation in the thermochemistry and kinetics due to the presence of spectator species, in the respective regions in the descriptor-space, coverage effects for CO were determined on Pd(111) (representing the stronger C-binding region on the descriptor space) and for HCOO on Cu(111) (representing the stronger O-binding region on the descriptor space). In particular, to derive CO coverage-effects, the binding energy for all reaction intermediates were calculated on clean Pd(111), and on 1/9 to 5/9 ML spectator CO-covered versions of Pd(111) (in increments of 1/9 ML). Owing to substantial computational expense, the transition-state energies for the elementary steps were derived on clean and on 5/9 ML CO*-covered Pd(111). For HCOO coverage effects, the binding energy for all reaction intermediates was determined on clean and on 2/9 to 6/9 ML spectator HCOO-covered Cu(111) (in increments of 2/9 ML, since HCOO is a bidentate species; 1 spectator HCOO corresponds to a 2/9 ML coverage in a (3x3) unit-cell), while the effect of HCOO-coverage on the kinetics was adjusted using indications from the thermochemistry, as an approximation.

In the catalyst screening portion of the study, we narrowed our scope to consider ordered stoichiometric intermetallic binary alloys with an fcc crystal-structure. The optimized lattice-constants are reported in Appendix F. The alloy surfaces were modeled using a (4x4) unit cell with 4 atomic-layers; the bottom two layers were truncated at their bulk-positions, while the top two layers were allowed to relax. The surface Brillouin zone was sampled using a 4x4x1 Monkhorst-Pack k-point mesh.[128] The BE of descriptors CO and HCOO were calculated at the dilute-limit (clean surfaces), corresponding to a coverage of 1/16 ML for CO and 2/16 ML for HCOO (i.e., 1 HCOO in a (4x4) unit-cell). Spin polarized calculations were performed for Ni-based alloys.

7.2.2 Model Formulation

To formulate the volcano plots, we utilized the generic microkinetic modeling framework developed in our group.[41] To incorporate zero-point energy (ZPE) corrected and temperature-dependent energetics in our models, Shomate parameters were derived using vibrational frequency DFT-calculations, through a procedure outlined previously.[12] The rate-constants for the adsorption and desorption steps were calculated using the collision theory, while those for the bond-breaking/bond-formation steps were calculated using the transition-state theory. We define Pd(111) as the reference catalyst, which we have previously determined to serve as the active site for FA decomposition on Pd/C catalysts.[299]

In this study, we formulate two sets of volcano plots, namely: (1) *Conventional volcano plots* and (2) *Experiment-Calibrated Coverage-Cognizant* volcano plots. For the conventional volcano plots, we used the '*unadjusted'* DFT-derived energetics on clean Pd(111) as the energetics for the reference catalyst. We utilized the linear-scaling and BEP correlations derived on clean surfaces to extrapolate across the descriptor space. Importantly, for the conventional volcano plots, we do

not consider the effect of spectator coverages on the reaction thermochemistry and kinetics. For the experiment-calibrated coverage-cognizant volcano plots, we utilize the CO*-coverage cognizant description of Pd(111) as the reference catalyst, which we had previously determined via rigorous parameter-estimation to be capable of quantitatively reproducing the reaction kinetics experiments on Pd/C.[299] Further, the adjustments to the energetics for this model were rationalized within intrinsic-errors of PW91-GGA functional used in the calculation setup. Similar to the conventional volcano plots, we utilized the linear-scaling and BEP correlations (derived on clean surfaces) to extrapolate the energetics across the descriptor space. However, for the experiment-calibrated coverage-cognizant volcano plots, we self-consistently incorporated the effect of spectator coverages on the thermochemistry and kinetics of the FA decomposition reaction network (Figure 7.1). In essence, we utilize *clean* surface energetics of the reference catalyst, and extrapolate using linear-scaling and BEP correlations to determine the *clean* surface energetics across the descriptor space, and calculate *on-the-fly* and within the mean-field implementation, the adjustments to the energetics (thermochemistry and kinetics – Appendix F) due to the relevant MASIs, so as to obtain a coverage-cognizant depiction of the descriptor space. In particular, we considered the coverage effects due to the presence of CO and HCOO, which were determined to be the MASIs in our conventional volcano plots (discussed subsequently in Results and Discussion) and have also been reported in the literature in context of the FA decomposition chemistry. Coverage effects for both CO and HCOO were applied across the entire descriptor space and were calculated *on-the-fly.* The reactivity maps were generated at 2.6% FA, balance He, at 373 K and 1 atm, defined as '*home-conditions'* in our previous studies.[45,299] The conversions were maintained below 10% across all points in the descriptor space.

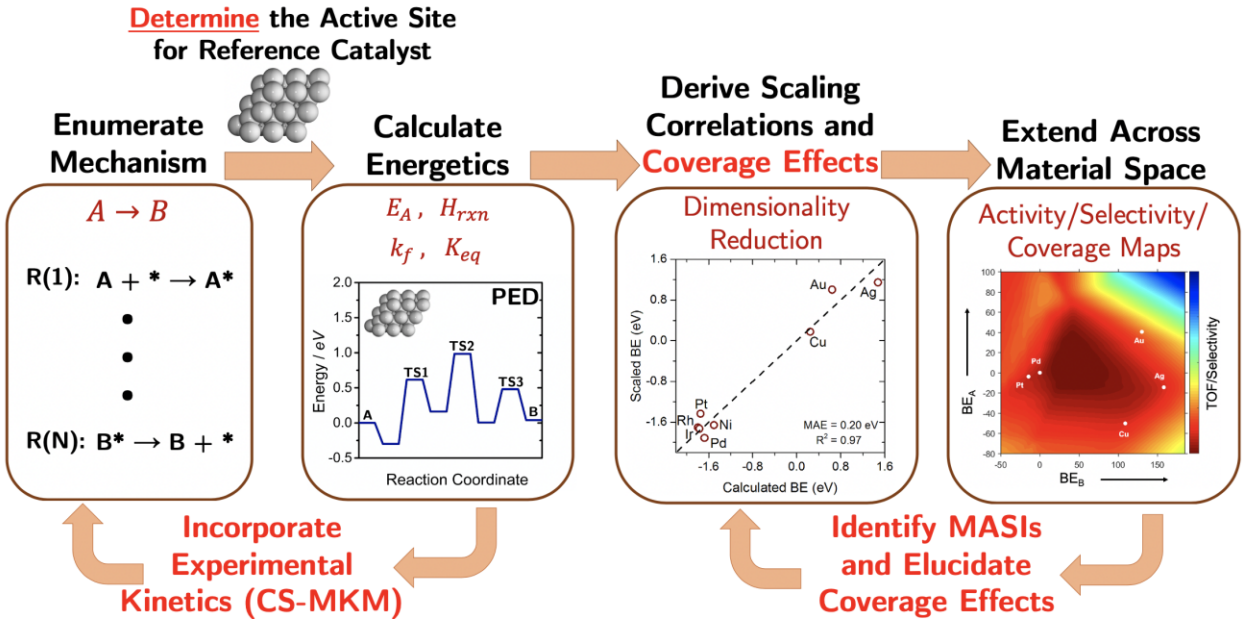


Figure 7.1 Schematic representation of the workflow to formulate the experiment-calibrated coverage-cognizant volcano plots. CS-MKM refers to coverage self-consistent microkinetic modeling. The text in red refers to the steps in the workflow that are proposed as an improvement over the conventional methodology.

7.2.3 Reaction Network

In this study, we utilize a reaction network involving 5 gas-phase species, 10 surface species and 15 elementary steps. As shown in Scheme 7.1, steps 1-5 indicate the adsorption and desorption of gas-phase species. The HCOO dehydrogenation pathway, which proceeds by the breaking of O-H bond in FA, is denoted by steps 6-7. In our reaction network, HCOO was modeled as a bidentate species, while all the other reaction intermediates were treated as monodentate species. The COOH dehydrogenation pathway, which occurs through the breaking of C-H bond, is indicated by steps 8-9, while the dehydration pathway, occurring through COOH dehydroxylation is shown by steps 10-11. Consistent with the previous studies investigating the reactivity maps for FA decomposition chemistry, we considered a reaction network comprising of steps 1-11 for the maps generated

using the conventional approach.[103,300] However, for the experiment-calibrated coverage-cognizant models, in addition to the elementary steps indicated above, we also included CO-spectator assisted steps, occurring through the formation of COH and HCO species, shown in steps 12-15, which we have previously determined to be active under typical reaction conditions on Pd and Pt catalysts.[45,299]

Reaction Network for Formic Acid (FA) Decomposition

Adsorption/Desorption

1. $HCOOH(g) + * \leftrightarrow HCOOH*$
2. $CO_2* \leftrightarrow CO_2(g) + *$
3. $CO* \leftrightarrow CO(g) + *$
4. $H_2O* \leftrightarrow H_2O(g) + *$
5. $2H* \leftrightarrow H_2(g) + 2*$

Dehydrogenation

6. $HCOOH* + 2* \leftrightarrow HCOO* + H*$
7. $HCOO* \leftrightarrow CO_2* + H*$
8. $HCOOH* + * \leftrightarrow COOH* + H*$
9. $COOH* + * \leftrightarrow CO_2* + H*$

Dehydration

10. $COOH* + * \leftrightarrow CO* + OH*$
11. $OH* + H* \leftrightarrow H_2O* + *$

Spectator-Assisted

12. $COOH* + CO* \leftrightarrow CO_2* + COH*$
13. $COH* + CO* \leftrightarrow CO* + HCO*$
14. $COH* \leftrightarrow CO* + H*$
15. $HCO* \leftrightarrow CO* + H*$

5 gas-phase species
10 surface species
15 elementary steps

Scheme 7.1 Reaction network for the FA decomposition considered in this study. Steps 1-11 were considered as the reaction network for the reactivity maps formulated using the conventional methodology. Steps 12-15 were additionally included in the refined reaction network considered for the experimentally-calibrated coverage-cognizant maps.

7.3 Results and Discussion

7.3.1 Conventional Reactivity Maps

We first present the activity and selectivity maps that were formulated using the conventional approach (at 2.6% FA, 373 K, balance He), wherein we chose clean Pd(111) as our reference catalyst and utilized the linear-scaling and BEP correlations to extrapolate the energetics across the descriptor space. A negative (positive) value of $\Delta BE_{CO,vs.Pd(111)}$ $\left(BE_{CO} - BE_{CO,Pd(111)}\right)$ and $\Delta BE_{HCOO,vs.Pd(111)}$ $\left(BE_{HCOO} - BE_{HCOO,Pd(111)}\right)$ indicates stronger (weaker) binding of CO and HCOO, respectively, compared with that on clean Pd(111).

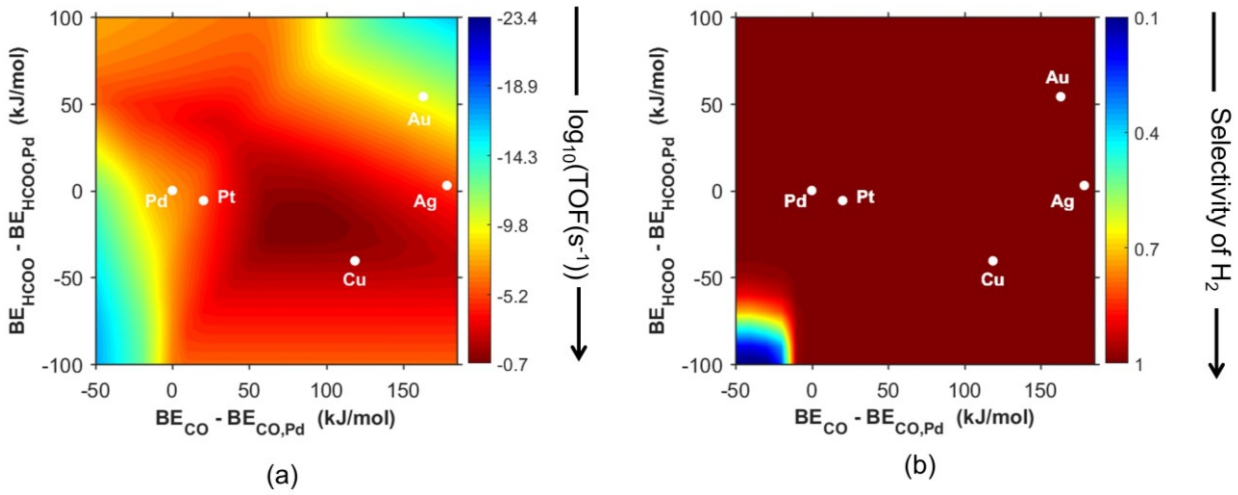


Figure 7.2 Calculated reactivity maps formulated using the conventional methodology, showing (a) Activity and (b) Selectivity maps, for 2.6% FA, balance He, 373 K. TOF refers to the turnover frequency (s^{-1}).

The maps formulated using the conventional approach suggest the reactivity trend (log(TOF(s^{-1})) shown in the brackets) as: Au (-10.0) < Pd (-6.8) < Pt (-5.3) < Ag (-4.9) < Cu (-1.8), indicating Cu as the most active monometallic catalyst (Figure 7.2). All monometallic systems appear to be

selective towards dehydrogenation pathway (log(selectivity(CO)) < -4.3). The results suggest that the optimal catalyst would destabilize CO by 86.4 kJ/mol and stabilize HCOO by 19.3 kJ/mol, compared with clean Pd(111). At the examined conditions of 2.6% FA, 373 K (balance He) the optimal catalyst is predicted to be 4 orders of magnitude more active than Pd(111), while being highly selective towards FA dehydrogenation (log(selectivity(CO)) = – 7.1).

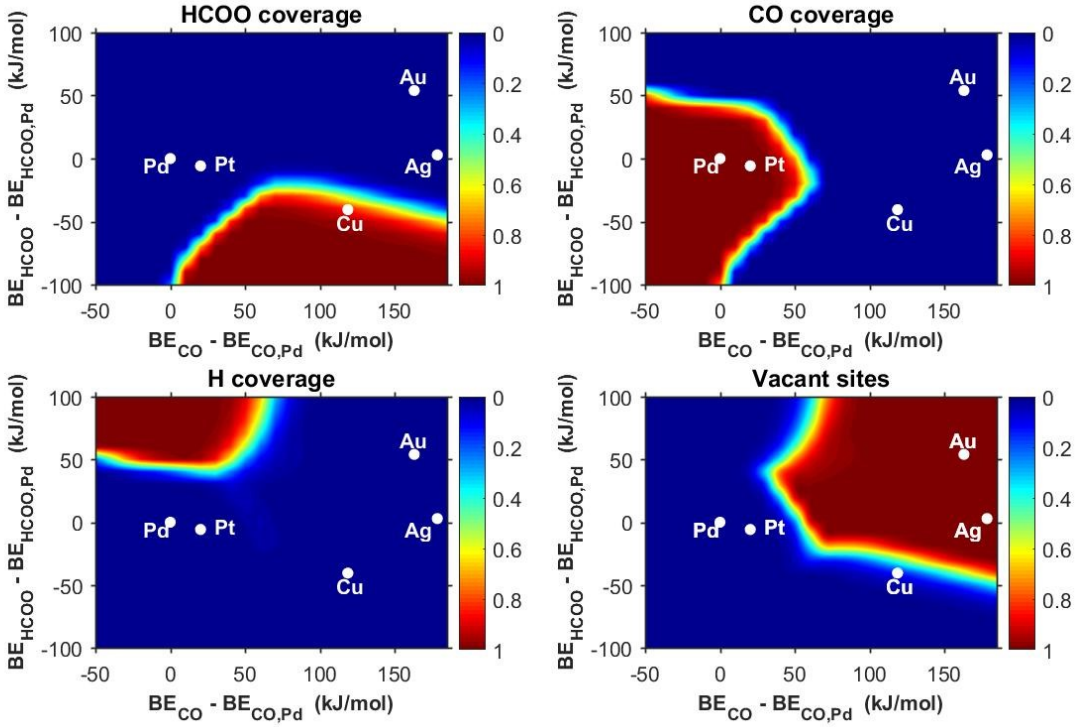


Figure 7.3 Calculated coverage maps for the most-abundant reaction intermediates in the descriptor space determined using the model formulated using the conventional methodology for 2.6% FA, balance He, 373 K.

In Figure 7.3, we show the coverage profiles of the MASIs over the descriptor space. Our results indicate that for the catalysts appearing in the stronger CO binding region of the descriptor space (e.g., Pt and Pd), the surface is completely occupied by CO, whereas, for the catalysts in the

stronger HCOO region (e.g., Cu), the surface is completely covered by HCOO. For the catalysts in the top-right quadrant of the maps (e.g., Au and Ag), which bind weakly with both CO and HCOO, the surface is completely vacant under the examined reaction conditions. Interestingly, the results indicate very sharp transitions in the surface environment as we move around the descriptor space.

The results obtained using the conventional approach: (1) fail to yield quantitative parity for the reference catalyst, as the TOFs were several orders of magnitude lower compared with the experimentally determined values, (2) predict incorrect CO selectivity for Pt and Pd, which are experimentally reported to be active for FA dehydration under the considered experimental conditions (log(selectivity(CO)) = -2 to -1), and (3) predict unrealistically high coverages of MASIs (e.g., CO and HCOO), indicating the unsuitability of the energetics to be able to reproduce experimental TOFs for the reference catalysts and the inadequate treatment of lateral adsorbate-adsorbate interactions. To address these discrepancies, in the next section, we utilize the experiment-calibrated coverage-cognizant Pd(111) model as the model for the reference catalyst, which is capable of quantitatively reproducing the experimental TOFs on Pd/C. In addition, as informed by the results from the conventional approach, we also incorporate on-the-fly the effect of spectator-coverages, stemming from the presence of CO and HCOO species, on the reaction thermochemistry and kinetics.

7.3.2 Experiment-Calibrated Coverage-Cognizant Reactivity Maps

The activity and selectivity maps derived from the experiment-calibrated coverage-cognizant volcano plots are show in Figure 7.4. Qualitatively, it can be observed that utilizing an experiment-calibrated model for the reference catalyst and consideration of spectator induced coverage-effects

greatly influences the activity and selectivity landscape over the descriptor space, compared with that obtained using the conventional approach (Figure 7.2). The results suggest the activity trend (log(TOF(s^{-1})) are shown in the brackets) as: Au (-11.6) < Ag (-6.5) < Cu (-2.2) < Pd (-1.1) < Pt (-0.6), indicating Pt as the most active monometallic catalyst. The CO selectivity trend was determined as (log(selectivity(CO)) shown in brackets): Au (-20.1) < Ag (-19.7) < Cu (-11.8) < Pd (-1.6) < Pt (-1.3). Thus the results suggest that experimental calibration of the reference catalyst and modeling of adsorbate coverage-effects can greatly alter the activity and reactivity trends, compared with those predicted by the conventional approach.

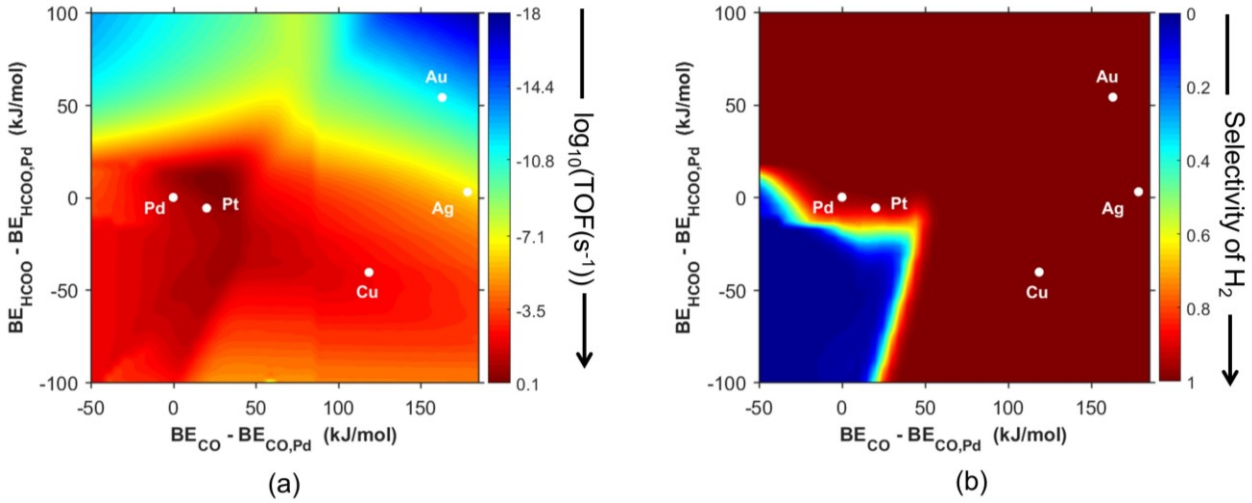


Figure 7.4 Experiment-calibrated coverage-cognizant reactivity maps, showing: (a) Activity and (b) Selectivity maps, for 2.6% FA, balance He, 373 K. TOF refers to the turnover frequency (s^{-1}). Coverage-dependent energetics for CO and HCOO were incorporated on-the-fly across the descriptor space.

The results suggest that the optimal catalyst would destabilize CO by 28.5 kJ/mol and HCOO by 4.8 kJ/mol, compared with that on clean Pd(111). Importantly, at the examined conditions of 2.6% FA, 373 K (balance He) the optimal catalyst is predicted to be a factor of 11 more active than Pd(111), exhibiting a selectivity of 98.5% towards FA dehydrogenation (log(selectivity(CO)) = –

7.1), suggesting a substantial change in the location, height, and shape of the volcano peak compared with that determined from the conventional approach.

In Figure 7.5, we show the coverage profiles of the MASIs over the descriptor space. Our results indicate that inclusion of lateral adsorbate-adsorbate interactions significantly flattens the coverage profiles for both CO and HCOO. Similar to the results predicted by the conventional approach, for the catalysts appearing in the stronger CO binding region of the descriptor space (e.g., Pt and Pd), CO appears as the MASI. However, the CO coverage seem to be substantially reduced: 0.3 ML for Pd(111) and 0.26 ML for Pt(111), compared with ~1 ML for both these surfaces, predicted by the conventional approach. Similarly, for the catalysts in the stronger HCOO region (e.g., Cu), the coverages were reduced substantially: 0.4 ML for Cu(111) compared with ~1 ML predicted by the conventional approach. For the catalysts in the top-right quadrant of the maps (e.g., Au and Ag), which bind weakly with both CO and HCOO, the surface is completely vacant under the examined reaction conditions and thus the CO/HCOO coverage effects are not expected to influence the energetics of the reaction network.

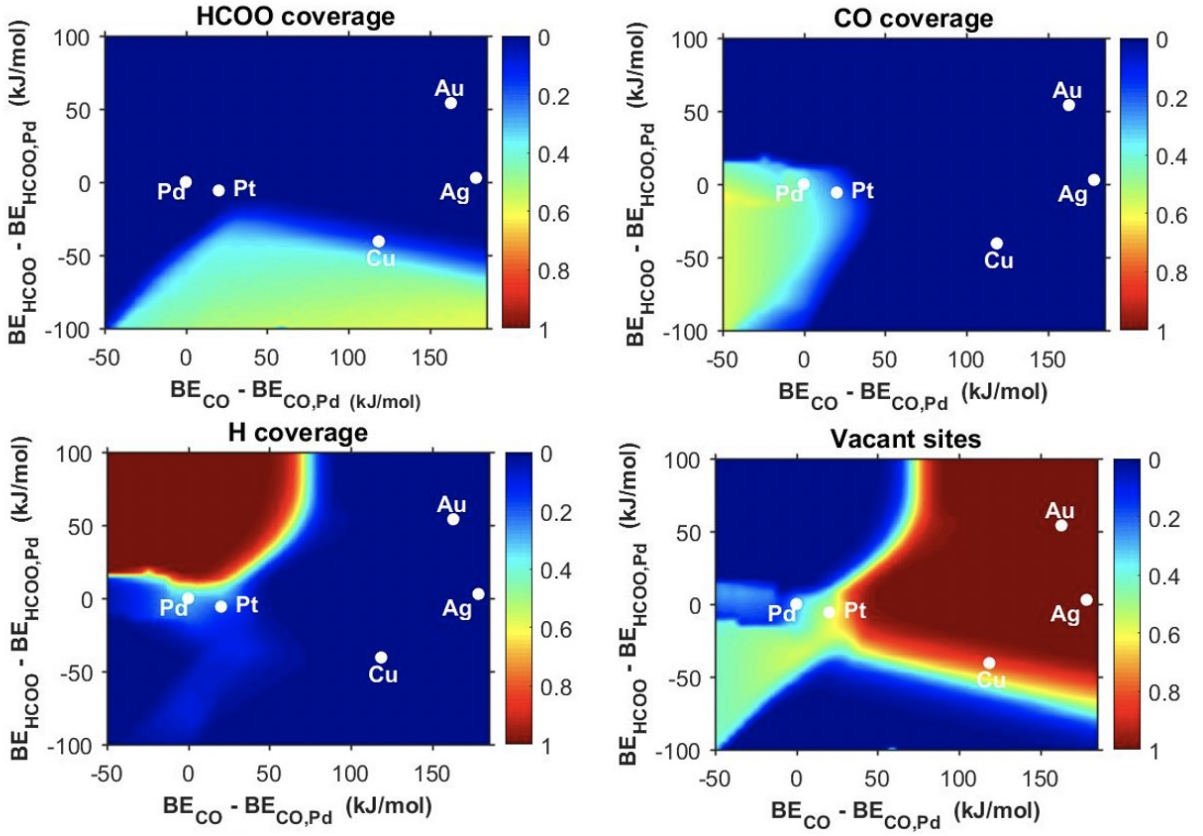


Figure 7.5 Calculated coverage maps for the most-abundant reaction intermediates in the descriptor space determined using the experiment-calibrated coverage-cognizant methodology, for 2.6% FA, balance He, 373 K. Coverage-dependent energetics for CO and HCOO were incorporated on-the-fly across the descriptor space.

7.3.3 Design of Improved Intermetallic Binary Alloy Catalysts

Our results revealed that addressing the systematic intrinsic errors of typical DFT functionals, by utilizing reaction kinetics experiments to adjust the energetics of the reference catalyst, and consideration of spectator coverage-effects can greatly influence the nature of the obtained reactivity maps. Formulation of experiment-calibrated coverage-cognizant maps can greatly alter the shape, height, and location for the peak of the reactivity volcano maps and also modify the selectivity landscape across the descriptor space, impacting not only the quantitative reactivity

predictions, but also qualitative activity and selectivity trends. Consequently, our methodology can have significant implications for computational catalyst discovery approaches, performed typically via descriptor-based high-throughput screening.

In Figure 7.6, we present the results from our descriptor-based screening of intermetallic binary alloy catalysts. As described in the methods section, in this study, we constrain our scope to consider only thermally stable stoichiometric intermetallic binary alloy catalysts. Qualitatively, catalysts with $\Delta BE_{CO,vs.Pd(111)} < 0$ kJ/mol and $\Delta BE_{CO,vs.Pd(111)} < 40$ kJ/mol are largely selective towards the undesired dehydration reaction (indicated by blue regions in Figure 7.6b), e.g., Ni_3Pt, Pt_3Y, Pd_3Y, Pt_3Sc, Pd_3Sc, $PtRh_3$, and $PtRh_3$. We determined several intermetallic alloys that were on the selectivity boundary separating dehydrogenation from dehydration, which were nearly as active as monometallic Pd but comparatively less selective towards the FA dehydrogenation, e.g., Pt_3Zn, Pt_3Sn, Cu_3Pt, Pd_3Sn, Pt_3Cd, and Pd_3Pb. Among the considered candidates, we identified two compositions, Cu_3Pd and Ag_3Pd, that were predicted to be slightly inferior in terms of catalyst activity but completely selective towards FA dehydrogenation. Importantly, we identified three compositions that were both more active as well as more selective towards FA dehydrogenation, compared with monometallic Pd, namely, $AuPd_3$, Pd_3Cd, and Pt_3Pb.

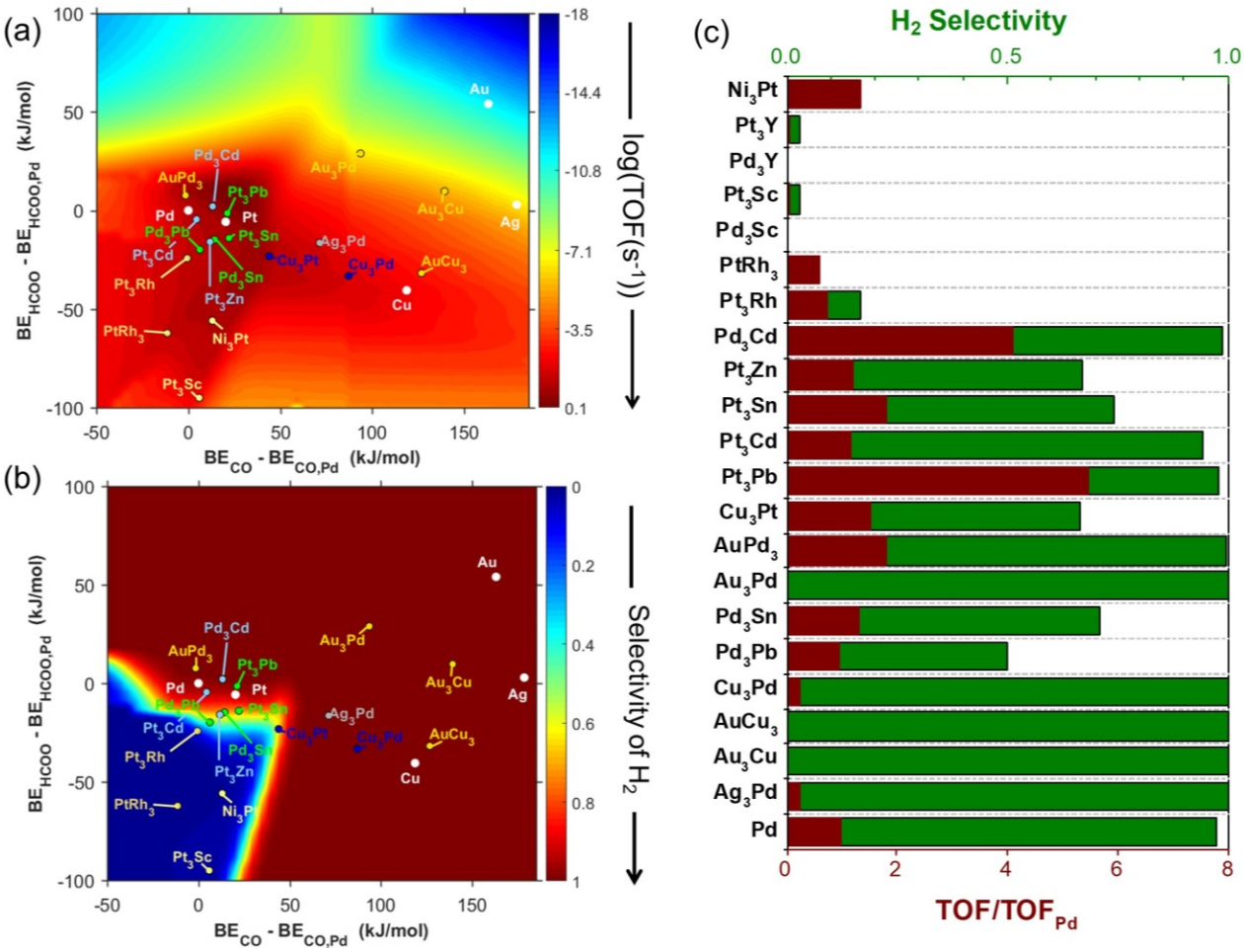


Figure 7.6 High-throughput screening of intermetallic binary alloy catalysts through Experiment-calibrated coverage-cognizant model, showing: (a) activity map ,(b) selectivity map, and (c) bar-plot comparing the activity (wrt. Pd) and selectivity of various intermetallic binary alloy catalysts, for 2.6% FA, balance He, 373 K. TOF refers to the turnover frequency (s^{-1}). Coverage-dependent energetics for CO and HCOO were incorporated on-the-fly across the descriptor space.

7.3.4 Scope for Improvement

In the preceding sections, we discussed the impact of experimentally calibrating the reference catalyst and modeling spectator coverage-effects on the predictability of descriptor-based methodologies compared with that typically practiced in the literature. Although, in our study we attempt to address the typical sources of errors in conventional computational catalyst discovery

approaches, we believe that there are additional avenues for methodological improvement that can further improve the quantitative predictability of these models, as discussed below.

Incorporating experimental kinetics and performing parameter estimation to achieve quantitative agreement enables adjustment of the energetics for the thermochemistry and kinetic parameters for the subset of the reaction network involved in the mechanism for the reference catalyst, e.g., performing parameter estimation using kinetic experiments for Pd/C, enabled adjustment of the energetic parameters that were involved in the COOH mechanism, determined to be relevant on Pd/C. However, the energetic parameters corresponding to elementary steps in the HCOO mechanism, which were found to be inactive on Pd(111) but could potentially contribute to the reaction flux in a different region of the descriptor space (e.g., on Cu(111)), were not adjusted and could not be statistically evaluated. Additionally, quantitatively fitting with the experiments for the reference catalyst, via rigorous parameter estimation can also lead to the discovery of novel reaction mechanisms that have not been considered previously, e.g., CO-assisted mechanisms for the case of Pd and Pt catalysts. However, it is indeed possible that there are similar spectator assisted mechanisms, which might be contributing to the reaction flux on catalysts appearing in other regions of the descriptor spaces.

These adjustments for mechanisms other than those active on the reference catalysts and additional novel-mechanisms for catalysts other than the reference catalyst, cannot be envisioned purely on the basis of the calibration from a single reference catalyst alone. While these aspects would likely not influence the reactivity landscape in the vicinity of the reference catalyst, it might incur changes in the activity and selectivity maps, in regions of the descriptor space, where mechanisms different than that for the reference catalyst, might be at play. Thus, formulating parameter adjusted

(i.e., experimentally calibrated) models for multiple monometallic catalysts, lying in different regions of the descriptor space, could help calibrate the energetics of reaction mechanisms, in addition to those relevant for the reference catalyst, while also ensuring the consideration of an even more rigorous reaction network.

The reactivity maps presented in our study were formulated for the closed-packed (111) facet, which was determined to serve as the active site for FA decomposition on Pd/C. However, this assumes that the (111) facet on a nanoparticle, would be the dominant contributor to the catalytic activity throughout the entire descriptor space. It is indeed possible that for various regions in the descriptor space, other facets on the nanoparticle, e.g., the more open (100) facet or the step-edge (211) model, might be more catalytically active compared with the (111) model chosen herein, determined as the active site for Pd/C, which was the reference catalyst. Thus, detailed analysis of monometallic catalysts in different regions in the descriptor space, could help in the identification of other facets, that might be catalytically relevant and consequently enable their experimental calibration to formulate reactivity maps.

In our study, we emphasize on the need for including spectator coverage-effects on the reaction thermochemistry and kinetics. To model the coverage effects stemming from MASIs that were found relevant in context of FA decomposition, we utilized polynomial functions for the BEs and transition-state energies dependent on the coverage of CO and HCOO, derived on Pd(111) and Cu(111), respectively. The adjustment for the reaction energetics due to the presence of MASIs under reaction conditions were estimated based on the binding energy values of the descriptors on a clean surface. Since, the functional form of the coverage effects were assumed to be the same for the all monometallic systems, and more importantly for bimetallics, it essentially implied same

adjustments to the energetics for all systems, for a given coverage of CO and/or HCOO. While, this might be a reasonable first approximation, it is important to note that the given the heterogeneity of the sites exposed by bimetallic catalysts, the spatial arrangement of spectators might be different on bimetallic catalysts, compared with those observed on monometallic catalysts. Therefore, the polynomial dependence of the energetics might be markedly different compared on bimetallic catalysts, making if challenging to generalize coverage-effects for computational high-throughput screening approaches. We posit that this methodology can be utilized to perform a first-pass screening of bimetallic catalysts, which upon experimental validation, might warrant an in-depth analysis.

7.4 Conclusions

We present a refined methodology aimed at improving the quantitative accuracy in computational catalyst discovery approaches. By formulating experiment-calibrated coverage-cognizant volcano maps we seek to elucidate the effect of experimental calibration of the reference catalyst and of inclusion of coverage-dependent energetics on the reactivity landscape for the FA decomposition reaction. We demonstrate that calibration of the reference catalyst can serve to alleviate the systematic errors associated with the choice of the chosen exchange-correlation functional and inform the consideration of additional mechanisms, viz., CO spectator-assisted pathways, that might be missed in conventional analyses. Our results suggest that formulating experimental-calibrated coverage-cognizant maps modify the reactivity landscape, influencing not only the quantitative reactivity predictions, but could also the qualitative activity and selectivity trends, compared with the predictions from the conventional methodology. Further, following our refined

approach greatly influenced the shape, height, and location of the activity volcano peak. Our methodology can have major implications for computational catalyst discovery approaches and thus calls for careful consideration of the considered reaction network, of the intrinsic DFT errors and of spectator induced coverage-effects for improving the quantitative accuracy of these predictive models.

CHAPTER 8

HOW NON-INNOCENT SPECTATOR SPECIES IMPROVE THE OXYGEN REDUCTION ACTIVITY OF SINGLE-ATOM CATALYSTS: MICROKINETIC MODELS FROM FIRST-PRINCIPLES CALCULATIONS[⊥]

8.1 Introduction

Due to the lower material cost, atomically dispersed transition metals on graphene have become promising alternatives to platinum catalysts for fuel cell applications.[301–303] For the oxygen reduction reaction (ORR), experimental onset potentials on chromium,[304] cobalt,[305–307] iron,[308–310] magnesium,[311] and ruthenium[312] atoms embedded in N-doped graphene are similar to or even superior to those on commercial platinum catalysts. However, these single-atom catalysts are currently limited by their durability in harsh electrolyte environments and by a lack of fundamental understanding of the active site under reaction conditions.[313–315] More research is needed to improve our fundamental mechanistic understanding, catalyst stability, and the metal loading.

[⊥] Adapted from – Rebarchik, M.†; Bhandari, S.†; Kropp, T.; Mavrikakis, M. († - Equal Contribution) How Non-innocent Spectator Species Improve the Oxygen Reduction Activity of Single-atom Catalysts: Microkinetic Models from First-principles Calculations. *ACS Catalysis* **2020** (*In Press*) – https://doi.org/10.1021/acscatal.0c01642

To identify the most active metals for graphene-based catalysts, density functional theory (DFT) has been used to screen a large number of single-atom catalysts for fuel cell applications.[316–321] In these studies, onset potentials are typically estimated by calculating the lowest potential required to make each electrochemical reduction step exergonic. However, onset potentials obtained through such thermodynamic analysis deviate substantially from experimental values, a discrepancy that has been attributed to shortcomings of the computational methods.[318,319] Other studies suggest that O* spectator species affect ORR onset potentials on Fe[310] and Ru[312] atoms embedded in N-doped graphene, but a recent microkinetic model suggests that both metals are actually decorated by OH* under experimental conditions.[322] Importantly, this model assumes that co-adsorbed OH* species do not participate in the reaction, which may not be the case given their proton affinity. Overall, a more rigorous computational treatment is needed to improve the agreement between computational and experimental work.

To gain further insight into the ORR activity of graphene-based catalysts in acidic electrolytes, we model the reaction on Au, Co, Cr, Cu, Fe, Ir, Mn, Ni, Pd, Pt, Rh, and Ru, which form stable single-atom catalysts inside fourfold N-substituted double vacancies in graphene.[323] Within the approximations of the computational hydrogen electrode,[324] onset potentials, potential-dependent coverage, the dominant reaction mechanism, and degrees of rate control[245] are determined from DFT results via microkinetic analysis.[33] Compared to a previous study,[322] we consider a more complete ORR network, wherein O_2 adsorption and reduction steps may occur on both faces of the catalyst.

We find that onset potentials predicted from our microkinetic models improve by up to 0.5 V compared to values predicted by purely thermodynamic models, indicating that kinetic effects have

a significant impact and should not be neglected. We also find that the ORR activity of more oxophilic metals (Cr, Fe, Mn, and Ru) increases in the presence of co-adsorbed O_mH_n intermediates, which lower the oxophilicity of the bare active site. While these findings agree qualitatively with an earlier microkinetic analysis,[322] we find that the reaction follows an O_2-assisted mechanism that was not considered previously.

8.2 Computational Details

8.2.1 DFT Calculations

Spin-polarized calculations were performed using the projector augmented wave (PAW) method[123,124] as implemented in the Vienna *ab initio* simulation package (VASP).[54,55] Exchange–correlation energies were obtained using the functional by Perdew, Burke, and Ernzerhof (PBE)[53] with a plane wave cutoff of 600 eV. While previous studies[318,319] argue that this functional significantly underestimates ORR onset potentials, we show that the agreement between computational and experimental values improves substantially once kinetic effects and co-adsorbed species are considered. Structure optimizations were performed until total energies were converged to 10^{-6} eV, and forces acting on the relaxed ions were below 0.02 eV/Å. Structures were proven to be minima by the absence of imaginary frequencies. Metal centers were initialized in high-spin configuration and allowed to relax; the resulting magnetic moments are compiled in Table G.4. Spin crossing events were not considered.

Gibbs free energies (Equation 8.1) were obtained by adding electronic energies (E_{elec}), zero-point vibrational energies (E_{ZPVE}), and entropy contributions (TS) at 298 K and 0.1 MPa; E_{ZPVE} and S are calculated from harmonic frequencies that were obtained by diagonalizing a partial, mass-

weighted matrix of second derivatives with respect to the three Cartesian degrees of freedom of each atom of the O_mH_n species. Reaction energies were calculated within the approximation of the computational hydrogen electrode introduced by Nørskov and coworkers.[324]

$$G = E_{elec} + E_{ZVPE} - TS \tag{8.1}$$

Graphene films ($r_{C–C}$ = 142 pm) were modeled using a *p*(6×5) supercell with a vacuum layer of 15 Å. The Brillouin zone was sampled using a 4 × 4 × 1 Monkhorst–Pack *k* point mesh. Gas phase molecules were calculated inside a 12 × 12 × 12 $Å^3$ box, using only the Γ point for Brillouin zone integration.

8.2.2 Microkinetic Modeling

Since O_2 dissociation is prohibitively endothermic on these catalysts,[322,323] ORR (Equation 8.2) is predicted to follow the associative pathway in acidic electrolytes involving (i) O_2 adsorption, (ii) OOH* formation, (iii) O* formation accompanied by water desorption, (iv) OH* formation, and (v) water formation from OH*. The formation of H_2O_2 is less favorable than reduction to H_2O catalytically relevant metals (negative ΔG_{sel} values in Table G.1) and therefore not included in our microkinetic model. This is in agreement with experimental work that shows high selectivity (>96%) toward the 4-electron pathway.[309,311]

$$4(H^+ + e^-) + O_2 \rightarrow 2H_2O \tag{8.2}$$

To evaluate the impact of co-adsorbed species, we formulate a microkinetic model for the oxygen reduction reaction on transition metal atoms embedded in N-doped graphene from DFT-derived energetics (Table G.1) using a similar approach as Nørskov and coworkers.[325] Previous studies only considered subsets of the set of elementary steps comprising the full reaction mechanism by assuming that co-adsorbed O_mH_n species are chemically inert.[310,312,322] As shown in Figure 8.1, we

allow for adsorption and electrochemical reduction events on both sides of the metal-doped graphene film at any stage in the reaction network. This *interlinked* mechanism enables a more dynamic treatment of co-adsorbed species. For example, Wang *et al.*[322] only considered oxygen reduction at clean and OH-decorated sites (i.e., $\mathbf{M}_{\mathbf{clean}}$ and $\mathbf{M}_{\mathbf{OH}}$ in Figure 8.1, respectively), but our model takes into account that both pathways are connected through the shared OH* intermediate. Note that both sides of the graphene film are symmetrically equivalent, which is why A*/B* and B*/A* are identical. Further details regarding elementary steps and the values of rate constants are included in Appendix G.

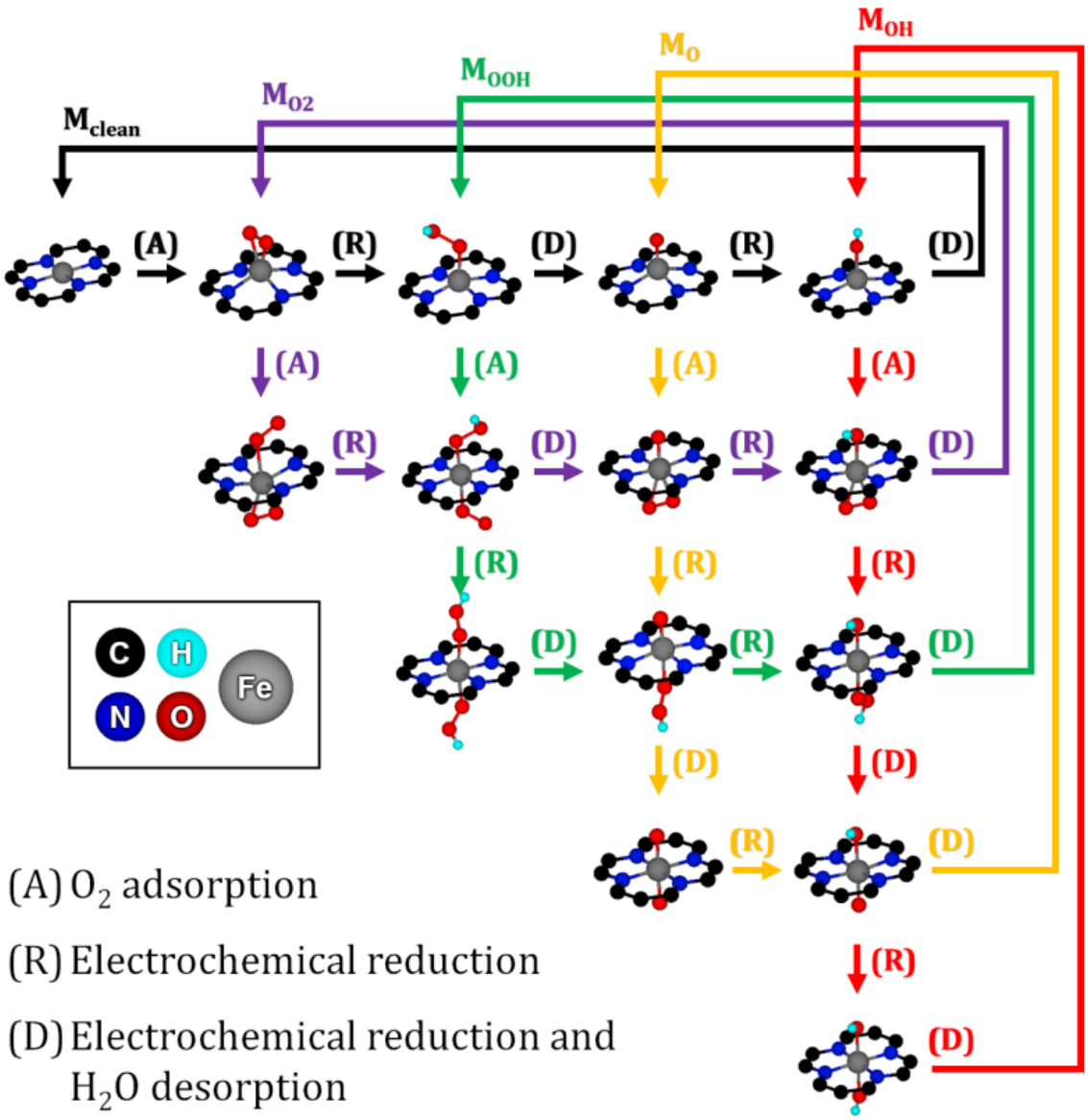


Figure 8.1 Full ORR mechanism considered in this work. While previous studies only considered $\mathbf{M_{clean}}$, $\mathbf{M_O}$, and $\mathbf{M_{OH}}$ individually, we study the full interlinked mechanism herein.

8.3 Results and Discussion

We first discuss Fe single-atom catalysts, which are predicted to be the most active ORR catalysts in computational studies.[315,317] High ORR activity on Fe catalysts has been confirmed experimentally with onset potential between 0.86–0.96 V_{RHE}.[308–310,312] While Figure 8.1 shows the full ORR mechanism considered herein, Figure 8.2a shows only the most preferable pathways identified by our microkinetic analysis. Figure 8.2b shows the corresponding energy profiles, and reaction energies for all elementary reactions are compiled in Table G.1. In the absence of co-adsorbed species ($\mathbf{M_{clean}}$), water formation from OH* is the least exergonic step (ΔG = -0.48 eV at 0 V_{RHE}). Based on thermodynamic analysis, one would expect an onset potential of 0.48 V_{RHE}, which is significantly lower than the experimental value. This discrepancy has been attributed to shortcomings of GGA-type density functionals such as PBE.[318,319] While PBE does underestimate the equilibrium potential by 0.16 V (U_{PBE} = 1.07 V_{RHE} compared to U_{exp} = 1.23 V_{RHE}[260]), recent computational work indicates that the reaction may actually follow a different mechanism.[322]

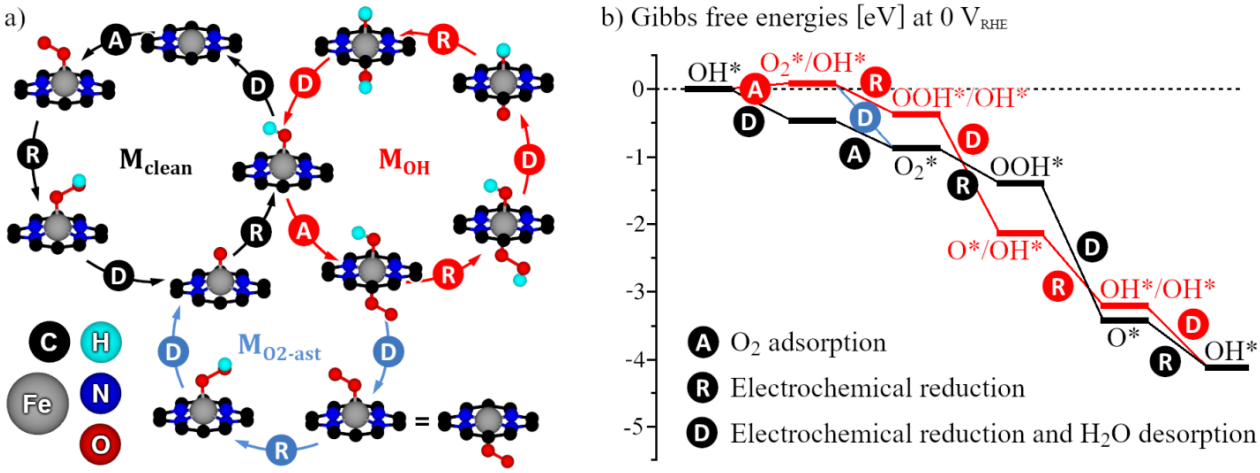


Figure 8.2 ORR mechanism on Fe atoms embedded in fourfold N-substituted double vacancies in graphene at low coverage ($\mathbf{M_{clean}}$) and in the presence of an OH spectator species ($\mathbf{M_{OH}}$). At U_{RHE} > 0.57 V, an O_2-assisted pathway ($\mathbf{M_{O2\text{-}ast}}$) was found to be dominant. (a) Optimized reaction intermediates are shown as side views. (b) Gibbs free energies profiles are shown for each pathway using the same color code as in (a) starting with the OH* intermediate that is common to all three pathways.

While the adsorption energy of oxygen is not significantly affected by the half-cell potential, electrochemical reduction steps become less exergonic with increasing values of U_{RHE}. As a result, O_2 adsorption at the OH-decorated site becomes more exergonic than the electrochemical reduction of OH* for $U_{RHE} > 0.57$ V. Thus, oxygen reduction may occur on the other side of the Fe atom in the presence of co-adsorbed OH* (**M_{OH}**). Along this pathway (red in Figure 8.1 and Figure 8.2), OOH* formation is the least exergonic reduction step (ΔG = -0.52 eV at 0 V_{RHE}). Based on thermodynamic analysis, one would therefore expect an onset potential of 0.52 V_{RHE} for **M_{OH}**, which is slightly higher than the value for **M_{clean}** (0.48 V_{RHE}). A similar increase has been reported for co-adsorbed O atoms.[310] To verify that this shift is not an artifact of neglecting the solvent, we also considered co-adsorbed water. Water adsorption at the active site is only mildly exothermic and changes reaction energies by less than 0.2 eV (Table G.2), which is much lower than the impact of co-adsorbed O* and OH*. Since water is readily replaced by more strongly binding species, this is not expected to affect the conclusions of our work.

These findings agree with a recent microkinetic analysis.[322] However, the authors show that co-adsorbed OH* increases the ORR onset potential on Fe catalysts by assuming that OH* is an innocent spectator species. In contrast, we allow for adsorbates on both sides of the metal-doped graphene film to react. For example, when O_2 and OH are co-adsorbed on an Fe site (i.e., [Fe](OH)–O_2) protonation of both adsorbates may occur competitively. In that particular case, protonation of OH* (blue in Figure 8.2) is actually 0.50 eV more exergonic than the protonation of O_2 since OH^- is the stronger base. This pathway, henceforth referred to as O_2-assisted ORR mechanism (**$M_{O2\text{-}ast}$**), has not yet been reported.

To determine the predominant mechanism and the preferred oxidation state of the metal under experimental conditions, we perform a microkinetic analysis using our DFT data, and following an approach similar to that of Nørskov and coworkers.[325] The rate for electrochemical reduction steps is calculated assuming an activation energy of 0.26 eV for proton transfers between O ions in aqueous solution as previously suggested;[326] this value is in good agreement with experimental proton transfer barriers (e.g., 0.18 eV for $H_2O + OH^- \rightarrow OH^- + H_2O$).[327] Bao and coworkers report H transfer barriers of up to 0.4 eV for the ORR on doped graphene in alkaline solution.[328] However, this is expected to be an upper limit for the barriers in acidic solution as H_3O^+ is a stronger proton donor than H_2O. Importantly, we find that onset potentials are not significantly affected by variations in the barrier below 0.4 eV. For example, changing the barrier by ±0.1 eV affects onset potentials on the Fe catalyst by less than 5 mV (Table G.3). We therefore do not calculate specific barriers for each H transfer step.

Figure 8.3 shows the current density predicted by our microkinetic model for the Fe single-atom catalyst. The onset potential for the low-coverage mechanism $\mathbf{M_{clean}}$ (black line) is calculated as the intersection of the tangent at the inflection point with zero current (U_{ORR} = 0.65 V_{RHE}). At the onset potential predicted by our thermodynamic model (0.48 V_{RHE}), the reaction is already diffusion-limited. Including the full mechanism ($\mathbf{M_{full}}$) increases the onset potential to 0.74 V_{RHE} (red line in Figure 8.3). The remaining deviation (0.2 V) is close to the margin by which PBE underestimates the equilibrium potential (ΔU_{eq} = 0.16 V). Correspondingly, the predicted overpotential (η_{PBE} = 0.33 V) is now within the range of experimental values (0.27–0.37 V in refs).

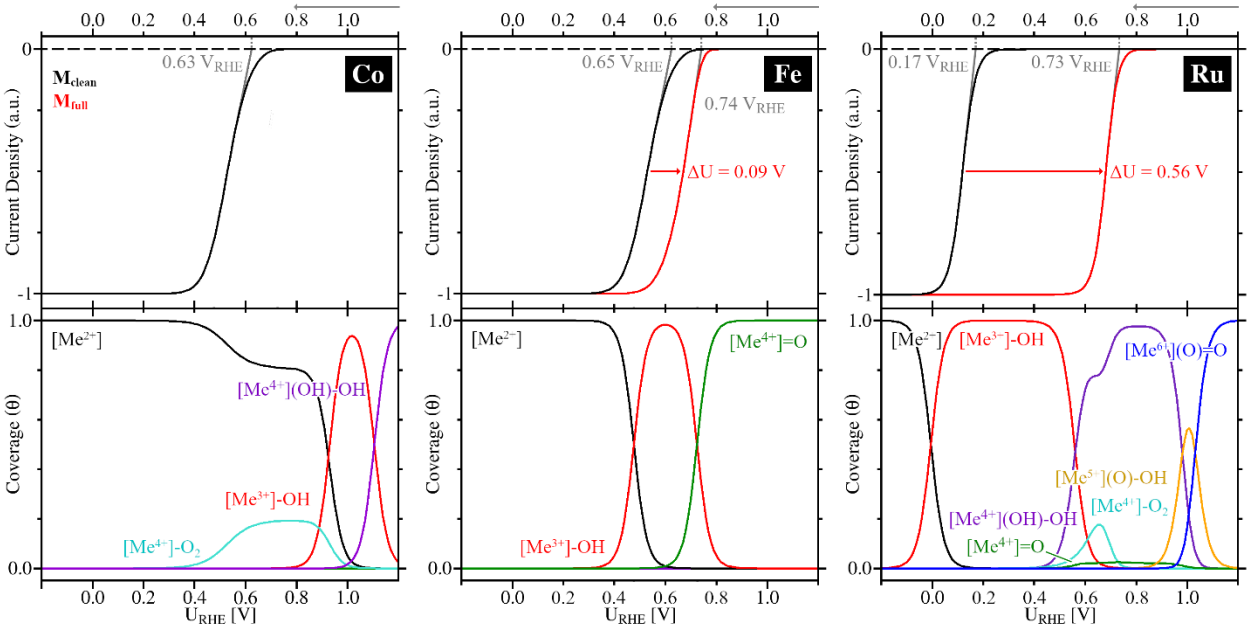


Figure 8.3 Current density (normalized to the diffusion-limited current) and coverage from microkinetic analysis of ORR on Co, Fe, and Ru single-atom catalysts. The color code provided in the panel for Co applies to all metals. Coverage profiles for only the relevant states are shown in the respective panel for each metal and those not explicitly shown indicate zero coverage, e.g., coverages of [Co](O)-OH and [Co](O)=O are zero in the investigated potential range and are therefore not shown in the corresponding panel for Co. Cation charges (Me^{N+}) represent formal oxidation states; calculated Bader charges are provided in Table G.5. The arrows over the top panels (in silver; pointing towards left) qualitatively represent the over-potential for the corresponding metal (shorter arrows represent lower over-potentials).

In agreement with a recent study,[322] we find that [Fe]–OH is the most abundant species within 0.48 $V_{RHE} < U_{ORR} < 0.73$ V_{RHE}. Based on Bader charge analysis, the OH-decorated site is more oxidized than the pristine catalyst corresponding to an oxidation state of +3; without adsorbates, this porphyrin-like environment stabilizes cations in the +2 oxidation state. However, we predict that for $U_{ORR} > 0.64$ V_{RHE} oxygen reduction proceeds exclusively through the O_2-assisted pathway (**$M_{O2\text{-}ast}$**), with the hydrogenation of [Fe](OH)–O_2 (H transfer to OH*) being rate-limiting (blue line in Figure 8.4). Thus, OH* is not an innocent spectator. At lower half-cell potentials, **M_{clean}** becomes dominant with O_2 diffusion being rate-limiting (black line in Figure 8.4). The O_2-assisted pathway was not considered previously, and **M_{OH}** was identified as the dominant pathway instead. We do not obtain flux through **M_{OH}** for the Fe catalyst, though onset potentials for **M_{OH}** and **$M_{O2\text{-}ast}$** are identical (0.74 V_{RHE}).

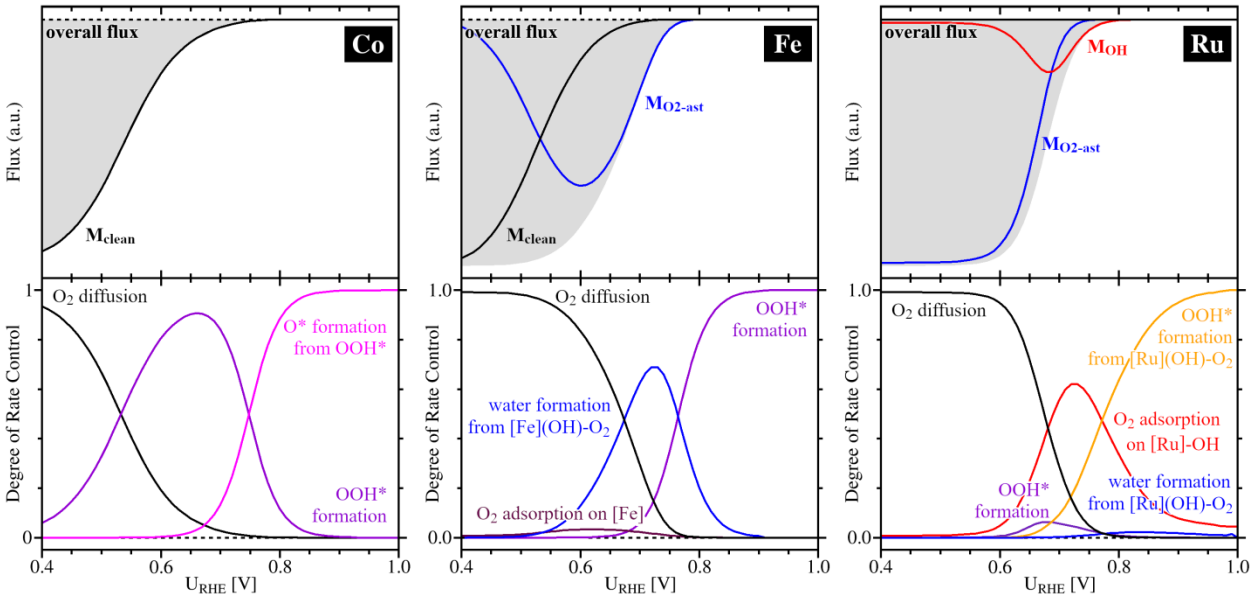


Figure 8.4 Potential-dependent flux along **M_{clean}**, **M_{OH}**, and **$M_{O2\text{-}ast}$** (the overall flux is shown as a gray area) as well as the degree of rate control for each elementary step on Co, Fe, and Ru atoms embedded in fourfold N-substituted double vacancies of graphene. Unless specified otherwise, labels refer to elementary steps via **M_{clean}**.

Co-adsorbed O* species were also suggested to improve the ORR[312] and OER[38] activity of Ru catalysts. Figure 8.3 shows that, on the Ru catalyst, the ORR onset potential on the Ru catalyst increases from 0.17 V_{RHE} for $\mathbf{M_{clean}}$ to 0.73 V_{RHE} for the full mechanism, which is within 0.15 V of the experimental value (0.88 V_{RHE} in ref). Around the onset potential, O_2 adsorption at [Ru]–OH has the highest degree of rate control (red line in Figure 8.4), but O_2 diffusion becomes rate-limiting below 0.68 V_{RHE} (black line in Figure 8.4).Our analysis also shows that the more oxophilic Ru is more oxidized than Fe at a given half-cell potential, lowering the oxophilicity of Ru under reaction conditions (Table G.1). Thus, ORR onset potentials on Fe and Ru do not follow the activity trend predicted by the oxophilicity of the clean catalysts. Since dissociative water adsorption on [Ru]=O is exergonic, [Ru](OH)–OH (purple line in Figure 8.3) is predicted to be the most abundant species around the onset potential. This leads to some flux through the $\mathbf{M_{OH}}$ pathway (red line in Figure 8.4c), even though $\mathbf{M_{O2\text{-}ast}}$ is energetically more favorable.

For Co catalysts, experimental ORR onset potentials (0.93 and 0.96 V_{RHE})[305,306] are similar to those on Fe and Ru catalysts. Again, thermodynamic analysis significantly underestimates the onset potential (0.22 V_{RHE}). Microkinetic analysis based on the full mechanism described above yields a much higher onset potential (0.64 V_{RHE}) in agreement with previous findings.[322] While the onset potential on the Co catalyst is similar to the values on Fe (0.74 V_{RHE}) and Ru (0.73 V_{RHE}), the reaction follows a different mechanism ($\mathbf{M_{clean}}$) with OOH* formation being rate-limiting at the onset potential (Figure 8.4). Furthermore, since the majority of sites are vacant around the onset potential, we determine that the active site for Co is not oxidized under ORR conditions (Figure 8.3).

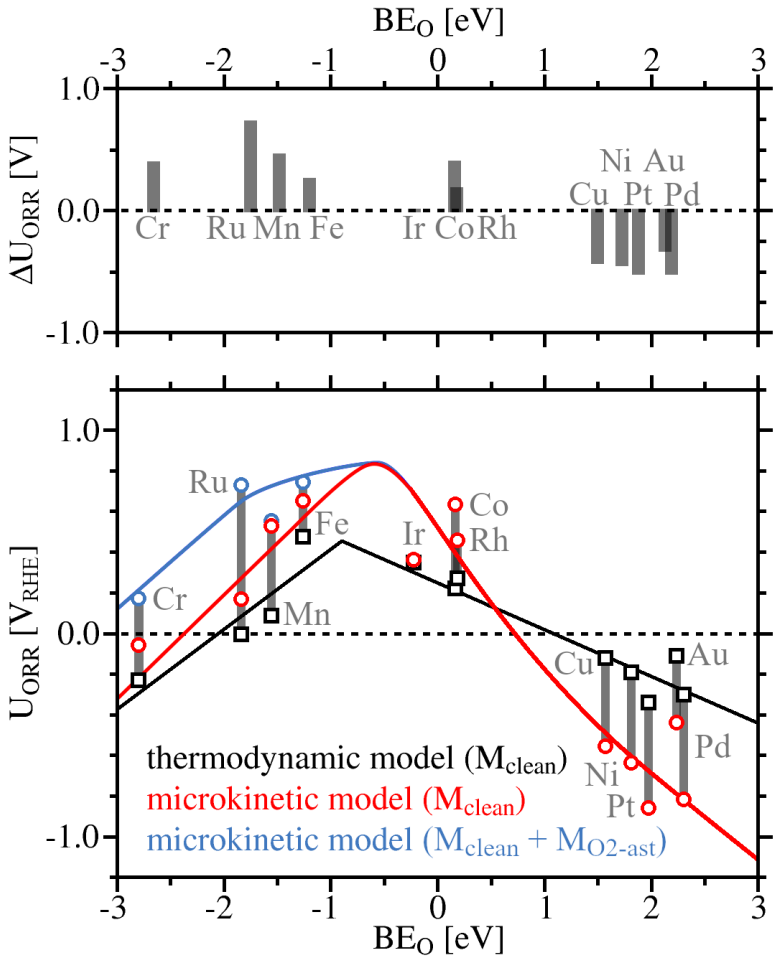


Figure 8.5 ORR onset potentials from thermodynamic analysis[321] (black squares; linear fit shown as black line) and from microkinetic analysis (red and blue circles for $\mathbf{M_{clean}}$ and $\mathbf{M_{O2\text{-}ast}}$, respectively; lines refer to values obtained using linear scaling relations shown in Appendix G). Differences in the onset potentials predicted from thermodynamic and microkinetic analysis ($\Delta U_{ORR} = U_{ORR}^{mk} - U_{ORR}^{td}$) are shown above: positive (negative) values correspond to an increase (decrease) in onset potential due to the microkinetic analysis.

Figure 8.5 shows the ORR onset potential for all transition metal atoms considered in this work as a function of the electronic binding energy of atomic O (BE_O) relative to gas phase O_2 at the pristine catalyst (Equation 8.3). Based on our thermodynamic analysis (black squares in Figure 8.5), Fe is predicted to be the most active transition metal, as its oxygen affinity (BE_O = -1.20 eV) is closest to the ideal value (-0.80 eV) for our linear fit (R^2 = 0.88, MAE = 0.14 V). However, this

thermodynamic analysis disagrees qualitatively with experimental results: While experimental onset potentials for Co,[305,306] Fe,[308–310,312] and Ru[312] catalysts are within 0.8–1.0 V_{RHE}, our purely thermodynamic data would predict an increase in ORR activity following Ru (0.00 V_{RHE}) < Co (0.22 V_{RHE}) < Fe (0.48 V_{RHE}).

$$[Me] + \frac{1}{2}O_2 \rightarrow [Me] = O \tag{8.3}$$

Compared to values obtained via microkinetic analysis (red circles in Figure 8.5), thermodynamic analysis of the same mechanism (M_{clean}) underestimates ORR onset potentials on earlier transition metals (Co, Cr, Fe, Ir, Mn, Rh, and Ru) by up to 0.44 V due to temperature effects: At the onset potential obtained from microkinetic analysis, the least exergonic step is up to 0.43 eV endergonic, while the overall reaction is still exergonic. This 'barrier' can be readily overcome at 298 K, and the reaction occurs at much higher half-cell potentials. Coverage effects further increase the onset potentials of the most oxophilic metals (Cr, Fe, Mn, and Ru) by up to 0.56 V. After including these effects, computational onset potentials for Co (0.64 V_{RHE}), Fe (0.74 V_{RHE}), and Ru (0.73 V_{RHE}) are all within 0.1 V, which is in qualitative agreement with experimental results.

For late transition metals (Au, Cu, Ni, Pd, and Pt) thermodynamic analysis overestimates onset potentials by up to 0.52 V, since the potential-limiting O_2 adsorption is not included in the analysis. This shift does not improve the agreement between computational and experimental ORR onset potentials: while experimental onset potentials of 0.87 and 0.85 V_{RHE} have been reported for Cu[329] and Pt[330] single-atom catalysts, respectively, both computational models predict negligible ORR activity for the late transition metals at these potentials. However, metal atoms embedded in partially N-substituted double vacancies bind oxygen more strongly than the fully N-substituted sites examined in our study,[311,321] thereby shifting the late transition metals closer to the peak of

the volcano. It is therefore important to keep in mind that the catalytic activity depends on the identity of the transition metal atom and its coordination environment.

Lastly, we develop scaling relations to express Gibbs free reaction energies as a function of BE_O (Figure G.1 and Figure G.2), which were then used to calculate ORR onset potentials from a single descriptor. The low coverage mechanism M_{clean} (black line in Figure 8.5) has a broad maximum at -0.8 eV. Since the O_2-assisted reduction mechanism was found to be dominant at higher half-cell potentials on earlier transition metals, we only include scaling relations for $\mathbf{M_{O2\text{-}ast}}$ to incorporate coverage effects. This leads to additional broadening of the volcano peak (blue line in Figure 8.5). A similar behavior was reported for thermal CO oxidation on extended transition metal surfaces, where increasing degrees of surface oxidation lead to an increase in oxidation activity by destabilizing surface O.[34]

8.4 Conclusions

We find that purely thermodynamic models systematically underestimate onset potentials for the more oxophilic metal (Cr, Fe, Mn, and Ru) by assuming that all elementary steps have to be exergonic. However, an overall exergonic reaction can occur even if one step is endergonic, as long as the activation energy can be overcome at room temperature. For the ORR on weakly oxophilic transition metals embedded in graphene, O_2 adsorption is kinetically relevant and should, therefore, be considered explicitly when discussing catalytic activity. We also find that more oxophilic metals (Cr, Fe, Mn, and Ru) are oxidized under reaction conditions, leading to an increase in activity compared to their reduced state. Thus, deviations between experimental onset potentials and values obtained from thermodynamic analysis of DFT data cannot be solely

attributed to shortcomings of the electronic structure methods. When plotted against O binding energies of the clean active sites, ORR onset potentials have a broad maximum due to differences in the oxidation states under reaction conditions. This could explain why experimental onset potentials for single-atom electrocatalysts embedded in N-substituted graphene di-vacancies appear to be largely independent from the identity of the transition metal.

CHAPTER 9

AMMONIA ELECTRO-OXIDATION REACTION ON PT(111): THE EFFECT OF NITROGEN COVERAGE

9.1 Introduction

We report a computational, Density Functional Theory (DFT) investigation aimed at understanding the effect of N* coverage on the electrocatalytic oxidation of ammonia (AOR) on Pt(111). We study the reaction network on clean and on 1/2 ML N*-covered Pt(111), determined experimentally for AOR in the potential range between 0.6 and 0.8V vs. the reversible hydrogen electrode (RHE). We comment on the effect of spectator N* species on the reaction mechanism, and on the nature of potential determining step. By using a more realistic description of the catalytic active site, our results provide mechanistic insights on possible catalyst deactivation routes. We conclude that N* coverage on Pt(111) causes an increase of the onset potential of the reaction, going from ~0.5 V vs. RHE on clean Pt(111), to ~1.6 V vs. RHE on 1/2 ML N*-covered Pt(111). At the same time, activation energy barriers associated with N–N bond formation steps decrease on 1/2 ML N*-covered Pt(111) compared with the corresponding values on clean Pt(111). Contrary to the commonly proposed hypothesis that sluggish N–N bond formation steps are the

potential source of deactivation for AOR, our results suggest that at higher coverage of spectator N* species, N–N bond formation steps become energetically more favorable than on a clean surface, while deprotonation of NH_3(g) limits the reaction flux. In addition, we also elucidate possible mechanisms leading to the formation of spectroscopically elusive trimeric nitrogen species in the AOR. These insights can be used to achieve a comprehensive understanding of electrocatalytic processes and of deactivation mechanisms under realistic *in situ* surface environment, which could be utilized to design improved catalysts for AOR.

The efficient utilization of ammonia (NH_3) is fundamentally important in development of environmentally beneficial processes, such as for bio-remediation applications and substantiable energy production.[331–333] To this end, electrocatalytic oxidation of NH_3 (AOR) plays a pivotal role. Indeed, the use of NH_3 as fuel in direct ammonia fuel cells (DAFC) has been largely investigated in the literature owing to several advantages with respect to hydrogen-based fuel cell technologies.[334] For example, NH_3 has a higher energy density with respect to H_2, and does not present transportation and storage limitations.[335] Equally importantly, NH_3 is a carbon-free feedstock and thus DAFCs anode electrocatalysts do not suffer from severe CO poisoning,[336,337] which is common to hydrogen fuel cells and direct formic acid fuel cells.

Motivated by these advantages of using NH_3 as an electrochemical fuel, many experimental and computational studies have aimed at elucidating the AOR mechanism on transition metal electrocatalysts. Recently, Song et al.[338] studied the AOR on polycrystalline Pt, Ir and PtIr electrocatalysts and determined that the reaction mechanism proceeds via NH_2* dimerization, following the mechanism previously proposed by Gerischer and Mauerer [339] (GM mechanism, Scheme 9.1). Similar results were obtained by Rosca and Koper on single-crystal Pt(111)

electrodes.[340] They reported that the electrocatalyst can operate in a narrow range of potential, 0.5 V – 0.65 V vs. the reversible hydrogen electrode (RHE), after which deactivation occurs due to N* accumulation on the surface. In support of the GM mechanism, Matsui et al. were able to individuate hydrazine (H_2NNH_2) as a reactive intermediate of AOR on Pt(111) through attenuated total reflection infrared (ATR-IR) spectroscopy.[341] Despite the general consensus on the plausibility of the GM mechanism for AOR, several discrepancies exist on the operating potential interval of Pt(111) and on the role of co-adsorbed species present on the electrocatalyst under reaction conditions. An early study of Gootzen et al.[342] report the onset potential for AOR of ~0.45 V on Pt(111), registering a maximum current density achieved around 0.7 V and complete deactivation occurring at 1.0 V. By using differential electrochemical mass spectroscopy (DEMS), at 0.6 V vs RHE, they estimated a N* coverage of approximately 0.6 ML.[342] These N* atoms are generally considered strong inhibitors of AOR on Pt(111).[339,340,343,344] More recent studies ascribe the inhibiting effect to oxygen-containing species.[341] De Vooys et al., estimated a maximum coverage of 1/2 ML N* on Pt(111) in the potential range between 0.6 and 0.8V vs. RHE.[345] Moreover, they postulated the existence of electrochemical steps involving the assistance of co-adsorbed N* species (e.g., $NH^* + N^* \rightarrow N_2(g) + H^+ + e^-$). Vidal-Iglesias et al.[346] hypothesized that azide (N_3^-) ion, spectroscopically determined through surface-enhanced Raman spectroscopy (SERS), could also form from the reaction of NH_3 with pre-existing dimeric species on the surface. However, N_3^- remained an elusive reaction intermediate in more recent studies using ATR-IR spectroscopy.[341]

To shed light on the processes underlying deactivation of Pt(111) in the AOR and the formation of N_3^-, it is fundamentally important to assess the role of co-adsorbates in the AOR. To this end,

resolutive atomistic insights on the catalyst active site under reaction conditions are needed. We have previously studied the AOR mechanism on the (111) facet of 12 late transition metal surfaces at the dilute limit (1/9 ML coverage of reaction intermediates).[343] On a clean Pt(111) model surface, we demonstrated that the GM mechanism is more favored than the Oswin-Salomon[347] mechanism, proceeding through complete NH_3 dehydrogenation (OS mechanism, Scheme 9.1), and we attributed the catalyst deactivation to the high activation energy barriers required for the N* recombinative desorption step.

To model a more realistic *in situ* catalytic surface environment, in this contribution, we investigate the role of N* co-adsorption, which is frequently proposed as a dominant reaction intermediate for AOR on Pt(111).[342,345] Specifically, we address the following linked questions: i. *What is the nature of the potential- and rate-determining steps of AOR in presence of co-adsorbed N*?*; ii. *Does N* play a role in the deactivation mechanism of AOR on Pt(111)?*; iii. *What are the potential pathways leading to the formation of spectroscopically elusive trimeric species?*. In this study, we aim to gain atomistic and mechanistic insights on the AOR mechanism under relevant coverage conditions for Pt(111) surface.

We performed periodic Density Functional Theory (DFT) calculations, using the Vienna *ab initio* Simulation Package (VASP)[54,348] using the PW91 exchange-correlation functional[349] in conjunction with the computational hydrogen electrode formalism[324]. To determine the most stable adsorption configurations of the reaction intermediates in the presence of N* adatoms, we used a methodology[350] to automatically generate and thoroughly sample co-adsorption configurations of the AOR reaction intermediates and N* adatoms at selected coverages: 1/12, 1/6, 1/4, 1/3, 1/2, and 3/4 ML (a $2\sqrt{3}\times2\sqrt{3}$ unit cell was used). We investigated the thermochemistry of the full AOR

reaction network at these varying coverages of spectator N* species. The case of clean and 1/2 ML N*-covered Pt(111) is analyzed in detail, as the latter coverage was previously reported experimentally as the maximum N* coverage in context of this chemistry, in a potential range of 0.6 and 0.8V, where deactivation occurs.[345]

Ammonia Electrooxidation Reaction

$$NH_3(g) + OH^-(aq) + * \rightarrow NH_2* + H_2O(l) + e^-$$

$$NH_2* + OH^-(aq) \rightarrow NH* + H_2O(l) + e^-$$

$$NH* + OH^-(aq) \rightarrow N* + H_2O(l) + e^-$$

Gerischer-Mauerer (GM) ***Oswin-Salomon (OS)***

$$NH_x* + NH_y* \rightarrow H_xNNH_y* + * \qquad N* + N* \rightarrow N_2(g) + 2*$$

$$H_xNNH_y* + (x+y)OH^-(aq) \rightarrow N_2(g) + (x+y)H_2O(l) + (x+y)e^- + *$$

Scheme 9.1 Ammonia electrooxidation reaction (AOR) mechanism. The first three deprotonation steps leading to the formation of NH* are common to both Gerischer-Mauerer (GM) and Oswin-Salomon (OS) mechanisms. In the GM mechanism, x and y can vary in the range 0-2. The superscript * denotes an adsorbed species on the surface. * denotes a vacant surface site.

9.2 Computational Methods

Periodic density functional theory (DFT) calculations were performed using the Vienna Ab initio Simulation Package (VASP).[54,348] Projector augmented wave (PAW) potentials were used to describe the core electron interactions. A plane wave basis set with a kinetic energy cutoff of 400 eV was used to expand the electronic wave function of the valence electrons. The PW91[349] exchange-correlation functional was employed. The calculated Pt bulk lattice constant calculated with these settings is 3.986 Å, which compares well with the experimental value of 3.912 Å.[351]

Periodic 2√3×2√3 supercells, comprising 4 Pt layers, and exposing the Pt(111) facet were used to model the electrocatalyst surface. The bottom two layers were kept fixed at their bulk positions. In order to avoid artifacts in the surface calculations arising from the interactions of periodic replicas in the *z* direction, we provided for at least 15 Å of vacuum layers in the supercell. The top two layers, and all the structures of AOR reaction intermediates and co-adsorbed N* adatoms were allowed to fully relax until the Hellman-Feynman forces on each atom were less than 0.01 eV $Å^{-1}$. Activation energy barriers for N–N bond formation steps were calculated using the climbing image nudged elastic band method (CI-NEB)[58], using seven images in addition to the initial and final states. A convergence criterion of 0.05 eV $Å^{-1}$ was used for the maximum force. The structures of the located transition states were successively refined using the dimer method,[352,353] until the forces acting on each atom were less than 0.01 eV $Å^{-1}$. A 4×4×1 G-centered Monkhorst-Pack[354] *k*-point sampling was used for all the calculations. The Gibbs free energy (G) of adsorbed and gas-phase species was calculated as:

$$G = E_{Tot} + ZPE - TS \tag{9.1}$$

where E_{Tot} is the total energy of the system calculated from DFT, ZPE is the calculated zero-point energy, S is the calculated entropy, and T is the standard temperature of 298.15K.

The computational hydrogen electrode (CHE) formalism[324] was employed to treat the electrochemical steps. In this context, activation energy barriers for N–N bond making steps are assumed to not depend from the applied bias. All potentials are relative to the reversible hydrogen electrode (RHE). In the calculation of the free-energy change of elementary steps we include the half-cell potential of the reaction OH^- + (1/2) H_2 → H_2O + e^-, tabulated as 0.83 V versus the standard hydrogen electrode. The DFT-calculated free energy of deprotonation reactions was

corrected for the pH, employing the expression $G(pH) = - k_B T \ln[H^+]$, and assuming pH = 14. A correction of +0.16 eV was applied to the gas-phase energy of NH_3 (g). To obtain this value, we compared the enthalpy of adsorption of NH_3 obtained with our computational setting on a Cu (100) 2×2 supercell (corresponding to 1/4 ML coverage), with 4 Cu layers, and the enthalpy of adsorption experimentally determined by Wu et al.[355] at the same coverage. With this correction, the equilibrium potential obtained for AOR is 0.047 eV, in good agreement with the theoretical equilibrium potential of 0.057 V vs RHE.

The free energy change of a proton-electron transfer step is calculated as:

$$\Delta G = \Delta E + \Delta ZPE - T\Delta S - |e|U \tag{9.2}$$

where U is the applied bias. This methodology is consistent with our previous work.[343]

To determine the most stable adsorption structures of reaction intermediates in presence of coadsorbed N*, we use methodology[350] to automatically generate and rigorously sample all plausible co-adsorption configurations. For each unique adsorption configuration of the reaction intermediate, we initialize the position of the N* spectators using Latin-hypercube sampling. The spectators are then moved to their nearest high symmetry site (top, bridge, fcc, hcp) as well as coarsely optimized in the z-direction. Structures are analyzed to avoid overlapping of adsorbed species within the unit-cell as well as their periodically repeated images. Each generated structure is then assigned a set of three descriptors: (1) site-occupancy of the spectator species (top, bridge, fcc, hcp), (2) distance of the reaction intermediate and the spectators, and (3) distance between the spectators, which is used to eliminate repeated structures. All generated structures are optimized using DFT to elucidate the most stable arrangement for every reaction intermediate in the presence of N* spectators. The N* adatom morphologies on Pt(111) obtained through our methodology are

in agreement with previous experimental scanning tunneling microscopy (STM) evidences, reporting the surface structure of Pt(111) pre-covered by 1/4 and 1/3 ML of N*.[356]

9.3 Results and Discussion

On clean Pt(111) (Figure 9.1(a)), the formation of H_2NNH_2* starting from NH_2* has the lowest among the activation energy barriers for N−N bond making steps (E_a = 1.22 eV, TS_1 in Figure 9.1(a)), suggesting that the GM mechanism is energetically preferred, in agreement with our previous work.[343] However, this high activation energy barrier is indicative of the low electrocatalytic activity of Pt(111). Indeed, previous experimental studies have determined Pt(100) to be highly active compared with Pt(111).[340,357] A computational study by Katsounaros et al. reported that on a clean Pt(100) model surface the reaction occurs via NH* dimerization to form NHNH*, with an activation energy barrier of approximately 0.5 eV.[358] At room temperature (298 K), a difference of 0.06 eV in terms of activation energy barrier could lead to an order of magnitude difference in reactivity.

Following the GM mechanism on the clean Pt(111) surface, the most difficult electrochemical step is hydrazine deprotonation, associated with a free energy of reaction of 0.47 eV. We therefore predict that the onset potential for the AOR is 0.47 V, in agreement with previous experiments reporting onset potentials varying between ~0.4 and ~0.5V.[340,342] In this potential range, low N* coverage is expected.[345]

Interestingly, at the experimentally determined 1/2 ML N* coverage (Figure 9.1(b)), the activation energy barriers for N−N bond formation steps are considerably lower than on the clean surface

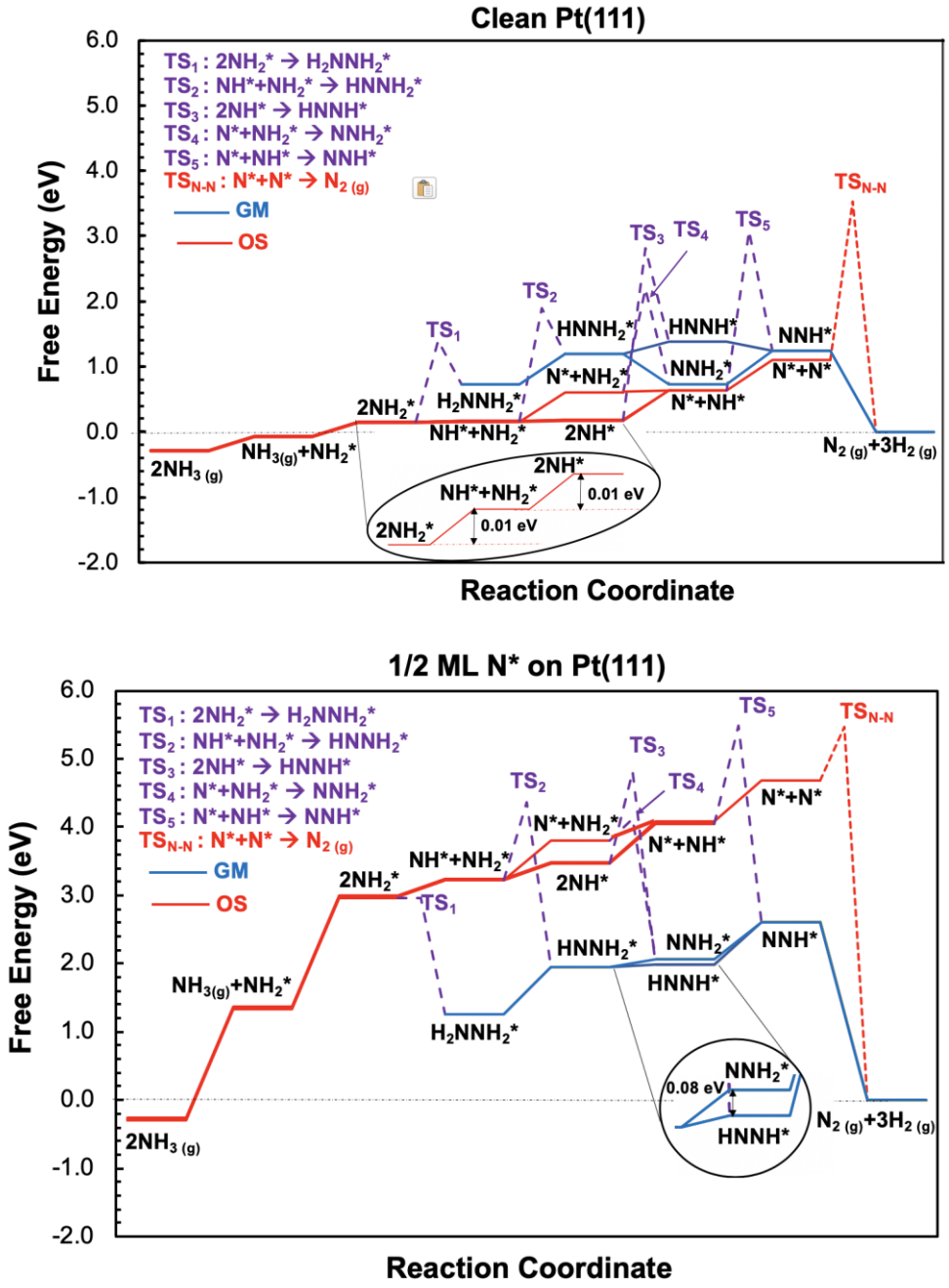


Figure 9.1 Free energy diagram (FED) for AOR on Pt(111) at 0 V vs. RHE. (a) FED on a clean Pt(111) surface. The inset reports an enlarged view of the FED, showing the $2NH_2^* \rightarrow NH^*+NH_2^* \rightarrow 2NH^*$ molecular steps. (b) FED on a surface pre-covered by 1/2 ML of N*. The inset reports an enlarged view of the FED, showing the energy difference between the NNH_2^* and HNNH* states. Red lines indicate the Oswin-Salomon (OS) AOR mechanism; blue lines indicate the Gerischer-Mauerer (GM) AOR mechanism. Dashed red and purple lines indicate N–N bond formation steps of the OS and GM mechanisms, respectively. For each step, stoichiometry is balanced with OH^-, H_2O and e^- and not explicitly shown. All energies are reported considering adsorbates at infinite separation.

Therefore, the commonly accepted mechanism of deactivation of Pt(111) catalysts, associated with the sluggish $N_2(g)$ recombinative desorption[340,343] is valid only at the low coverage limit. Accordingly, on a clean Pt(111) surface, the OS pathway (red line, Figure 9.1(a)) leading to the formation of N*, is thermodynamically preferred, and recombinative desorption of $N_2(g)$ is the rate determining step. Instead, our computational work demonstrates that at 1/2 ML N* coverage (Figure 9.1(b)) AOR is inhibited by the high free energy barrier (1.63 eV) required for the potential-determining $NH_3(g)$ deprotonation step: $NH_3(g) + OH^-(aq) \rightarrow NH_2* + H_2O(l)$.

The presence 1/2 ML of co-adsorbed N* (Figure 9.1(b)) has two major effects on the AOR mechanism. (i) The OS pathway is considerably destabilized, due to the repulsive interactions between N* and the adsorbates. (ii) The NH_2* recombination step of the GM pathway becomes now almost barrierless (E_a = 0.01 eV, TS_1 in Figure 9.1(b)). Furthermore, the repulsion between N* and the H_xNNH_y species seems to be counterbalanced by the formation of hydrogen bonds, as it can be noticed from Figure 9.2, especially in the case of H_2NNH_2*, $NHNH_2^*$, and NNH_2^* (the optimized geometry of all the AOR reaction intermediates at the investigated coverages is reported in Appendix H)

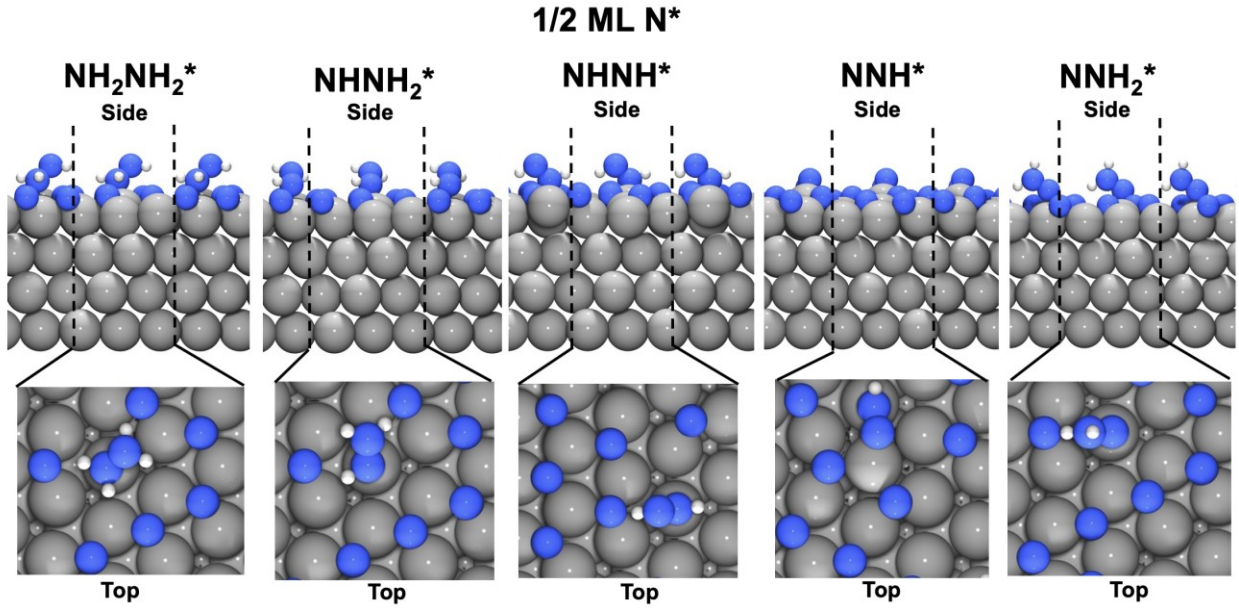


Figure 9.2 Optimized geometries for the dimeric (H_xNNH_y) species of the GM mechanism of AOR on a 1/2 ML N*-covered Pt(111) surface. N, H, and Pt atoms are represented with blue, white, and silver spheres, respectively. Side and top views are reported in the top and bottom panel, respectively. Dashed black lines delineate the unit cell lattice vectors.

The high onset potential of 1.63 V vs RHE predicted for the AOR on a 1/2 ML of N* covered Pt(111) surface suggests that in the operating range of the electrocatalyst Pt(111) would not be active, even if the kinetic barriers for H_2NNH_2* formation (E_a = 0.01 eV) or N_2 recombinative desorption (E_a = 0.80 eV) are actually lower than on a clean surface (E_a = 1.22 eV and 2.43 eV, for H_2NNH_2* formation and N_2 recombinative desorption, respectively). This means that that the presence of N* considerably increase the onset potential of the reaction, but does not inhibit the N–N bond formation steps in AOR.

Previous experimental determinations of N* coverage on Pt(111) suggest that 1/2 ML can be considered the maximum coverage under operating conditions between 0.6 and 0.8 V, but N* coverages may be lower at lower potentials.[345] To model the gradual accumulation of N* and

assess the effect of lower N* coverages, we have performed calculations on Pt(111) pre-covered by 1/12, 1/6, 1/4, and 1/3 ML of N*. The predicted AOR onset potential at increasing coverage conditions is reported in Figure 9.3. The onset potential slowly increases (from 0.47 V to 0.70 V) until 1/4 ML of N* is adsorbed. For N* coverages higher than this value, the onset potential for AOR sharply increases. While at the low coverage limit hydrazine deprotonation is the potential determining step (PDS), at higher coverages deprotonation of NH_3(g) (NH_3(g) + OH^-(aq) → NH_2* + H_2O(l)) becomes potential-determining. At N* coverages of 1/6 ML and 1/4 ML on Pt(111), the reaction is not limited by NH_3 adsorption, but from the destabilization of NH_2*. Indeed, the adsorption of NH_3(g) on a clean Pt(111) surface, on a surface pre-covered by 1/6 ML and by 1/4 ML of N* is nearly isoenergetic. For these three cases, the free energies of adsorption of NH_3(g) (reported in Appendix H), are -0.51, -0.51, and -0.55 eV, in order of increasing coverage. Instead, after N* coverage of 1/3 ML, both the difficult adsorption NH_3(g) and destabilization of NH_2^* determine the nature of the PDS.

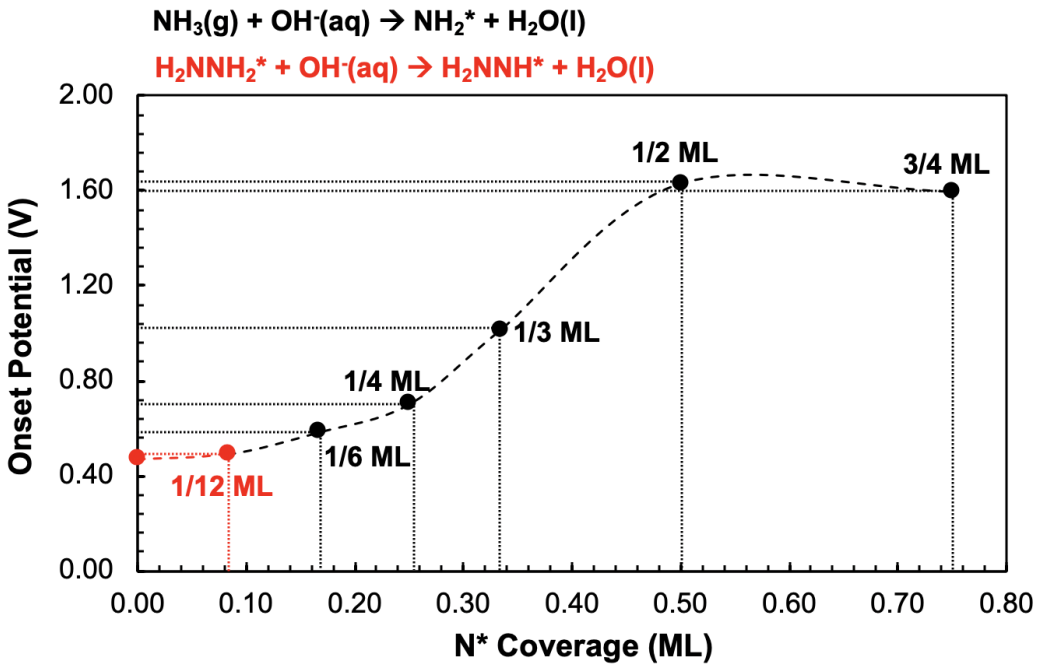


Figure 9.3 Onset potential of AOR as a function of N* coverage on Pt(111). Points are colored according to the identity of the potential determining step at a given coverage (red, hydrazine deprotonation; black, ammonia deprotonation). The dashed line is intended to be a guide for eyes.

The deactivation of Pt(111) is generally ascribed to the accumulation of N* and their kinetically difficult recombinative desorption from the surface.[339,342,345] Instead, we have demonstrated that the presence of N* does not inhibit N–N bond formation on Pt(111), but instead it can inhibit activity of AOR by increasing the free energy barrier of the first deprotonation step ($NH_3(g) + OH^-(aq) \rightarrow NH_2^* + H_2O(l)$). At N* coverages of <1/4 ML, the catalyst should be active towards AOR. After this limiting coverage value, the onset potential would become prohibitively high, well beyond the operating reaction conditions. This interpretation is in qualitative agreement with the results of de Vooys et al., who performed reductive stripping of the AOR reaction intermediates produced in the potential window between 0.36 and 0.85 V on a Pt polycrystalline electrode.[345] In the potential window between 0.4 and 0.6 V, where AOR occurs without deactivation, they

determined a gradual increase in the number of electrons transferred per surface Pt atom (from ~0.2 to ~1.2), indicative of increasing coverage. Assuming that the surface is covered by N* only, one can estimate that the coverage may vary from approximately 0.06 ML (at ~0.4 V) to 0.36 ML (at ~ 0.6 V), which is in line with our proposed interval of activity (see Appendix H) . Instead, in the region after 0.6 V, the number of electrons transferred per surface Pt atom is constant (1.63), corresponding to a N* coverage of 1/2 ML.[342,345] As a consequence, for potentials >0.6 V, the catalysts deactivates, which is in agreement with our computational predictions.

Finally, we want to shed light on the formation of trimeric species on catalyst surface. Intuitively, the formation of trimeric species ($NH_xNH_yNH_z$, with x-y-z=0-2) would be more relevant at high coverage, where coupling of multiple monomeric and dimeric species can occur. We studied two possible reaction pathways for the formation of NNHNH*, starting from HNNH* and NNH* and assisted by N*. The reaction mechanism is reported in Figure 9.4, and the associated Free energy diagram for these N*-assisted pathway is reported in Figure 9.5.

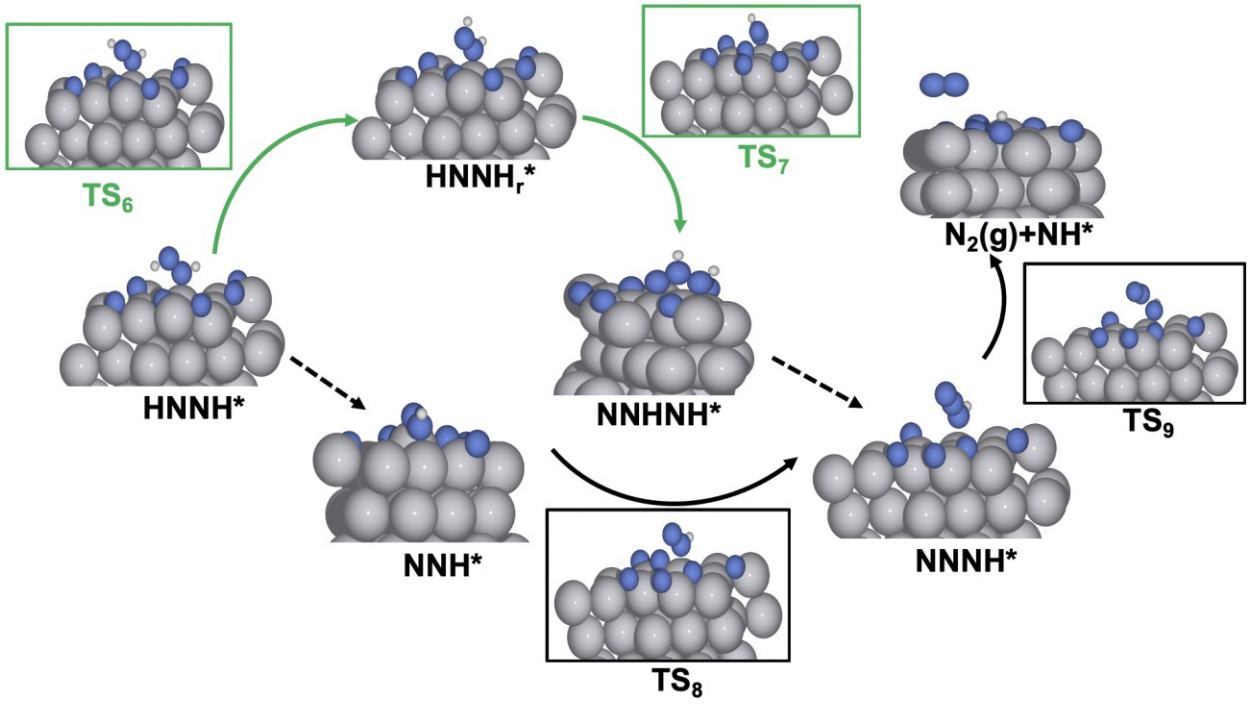


Figure 9.4 Reaction mechanism for trimeric species formation at 1/2 ML N* coverage, starting from HNNH* and NNH*. The optimized structures of transition states (TS) are shown inside boxes. For the sake of clarity, only the top two Pt layers are shown in the insets. Solid arrows indicate thermal steps. Dashed arrows indicate electrochemical steps (proton-electron transfers). The black and green color code and reaction intermediates and TS nomenclature refers to the free energy diagram (FED) presented in Figure 9.5.

The activation energy barriers for NNNH* formation from NNH* (0.86 eV, TS_8 in Figure 9.5) and for NHNNH* formation from the *trans*-isomer of HNNH* (1.00 eV, TS_7 in Figure 9.5) are prohibitively high to expect significant reaction flux through these pathways at room temperature. The direct deprotonation of NNH* to N_2(g), which is exothermic by 2.66 eV, would be energetically more favorable. For this reason, our results do not suggest trimeric species to be a possible source of deactivation of the catalyst, even at high coverage. At the same time, the high activation energy barriers corresponding to the formation of trimeric species might rationalize their elusive nature.

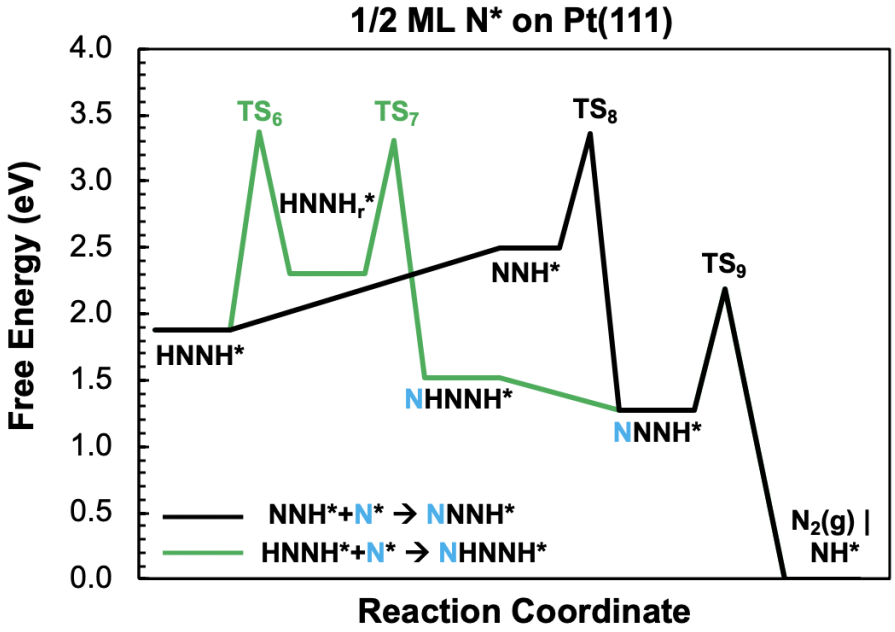


Figure 9.5 Free energy diagram (FED) for the formation of trimeric NHNNH* and NNNH* from dimeric HNNH* and NNH* species on 1/2 ML N*-covered Pt(111). Green lines indicate a pathway starting from HNNH* and involving a *trans* → *cis* isomerization step (TS_6 to $HNNH_r$*). Black lines indicate the pathway proceeding through NNH* formation. N atoms indicated in cyan refer to N* spectators, which are added to the existing HNNH* or NNH* moieties. For each step, stoichiometry is balanced with OH^-, H_2O, H^+ and e^-. All energies are reported considering adsorbates at infinite separation.

9.4 Conclusions

In summary, our computational investigation provides new insights on the mechanism of Pt(111) deactivation. We determined that it exists a critical N* coverage (1/4 ML) after which Pt(111) deactivates, due to the high potential associated with the first NH_3(g) deprotonation step. However, we demonstrated that N* adatoms decrease the activation energy barriers associated to N-N bond-making steps. These evidences suggest that under realistic coverage conditions N* adatoms do not inhibit AOR on Pt(111) because of their difficult recombinative desorption, but because of the difficult NH_3(g) deprotonation. Furthermore, we demonstrate that even at high N* coverage conditions, the formation of trimeric species, leading to the formation of N_3^- is not favored at room temperature. By utilizing coverage-cognizant microkinetic modeling one could obtain concrete insights on the reaction mechanism, on the exact coverages of reaction intermediates, and on the PDS as a function of applied potential and reaction conditions.[359,360] These results could inform the design of improved AOR electrocatalysts that are able to operate at optimal N* coverages regimes and in a wide potential window.

CHAPTER 10

CONCLUSIONS AND FUTURE DIRECTIONS

10.1 Conclusions

In this dissertation, we have utilized an integrated approach involving first-principles density functional theory (DFT) calculations, reaction kinetics experiments, and mean-field microkinetic modeling to elucidate atomistic-scale understanding of the catalytic chemistry. By concurrently ensuring model experiment parity, we seek iteratively refine our understanding of the nature of the active site and elucidate the reaction mechanism. We establish that by striving for coverage self-consistency during the parameter estimation procedure, one can systematically evaluate potential active sites models and identify the *in situ* description that quantitatively captures the macroscopic observables determined from reaction kinetics experiments.

We demonstrate that consideration of spectator-induced coverage effects, an aspect which is frequently missed in conventional investigations, influenced the reaction network via: (1) lateral adsorbate-adsorbate interactions – impacting the energetics of the reaction thermochemistry and kinetics, and (2) spectator-assisted mechanisms – leading to novel reaction pathways contributing actively towards the flux, under realistic reaction conditions. Inclusion of spectator coverage-

effects were found essential for quantitatively explaining the experimental observations. Our investigations revealed that spectator species do not merely appear as innocent bystanders in the catalytic mechanism, as typically assumed, but instead actively participate in the reaction network, thereby, altering the reaction mechanism. Importantly, our algorithmic approach provides a systematic framework for the identification of novel spectator-assisted mechanisms and decorations of the active site, typically missed in the literature.

Specifically, in Chapter 3, we determined that clean Pt(100) and clean Pt(111) were not accurate representations for the active site for the FA decomposition reaction over Pt/C. Although these models fell short in capturing the reaction kinetics experiments, requiring large corrections of the DFT parameters, and yielded a coverage-inconsistent solution, they indicated high coverages of adsorbed CO*, under reaction conditions, which informed us to pursue partially CO*-covered Pt facets as potential active site models. Consequently, investigation of the reaction network on partially CO*-covered models: (1) yielded improved estimates for the DFT-derived rate-parameters and (2) led to the identification of CO*-assisted hydrogen-transfer mechanisms, not previously considered in the literature; both proving essential for accurately representing the *in situ* nature of the active site. In Chapter 4, we extended our methodology to investigate the chemistry on Pd/C and arrived at similar observations, wherein consideration of CO*-induced coverage effects and of CO*-spectator assisted mechanisms were found critical for reproducing experimental observations. In Chapter 5, we studied this chemistry of Cu catalysts, wherein our methodology led us to first go from clean Cu(111) to partially HCOO*-covered Cu(111). However, investigation of the reaction network on partially HCOO*-covered Cu(111) led to the discovery of stable FA-HCOO complexes, speculated previously in experimental studies, which

when included in the next iteration of the algorithm replaced HCOO* as the most abundant surface intermediate and also served to catalyze the FA decomposition reaction. Inclusion of this novel-intermediate as well as the related mechanisms served to rationalize the previously conceived bimolecular mechanism in context of the FA decomposition chemistry on Cu catalysts.

In Chapter 6, we condense the insights gained from our fundamental investigations for the FA decomposition chemistry and formalize our methodology to propose a generic algorithm, which can be utilized to parameterize high-fidelity microkinetic models and extract detailed mechanistic insights. In Chapter 7, we extend our fundamental understanding for the FA decomposition to computationally propose binary-intermetallic catalysts that are expected to be more active and/or selective towards the desired decomposition pathway.

In Chapters 8 and 9, we utilize our methodology of treating spectator coverage-effects, to investigate electro-catalyzed reactions. In Chapter 8, our integrated approach involving DFT calculations and microkinetic modeling revealed the importance of dynamically treating coverage effects for accurately modeling the ORR chemistry on transition metal based single-atom catalysts supported on graphene, which led a novel reaction mechanism not previously considered in the context of this chemistry. In Chapter 9, we study the ammonia electrooxidation reaction on clean and partially N*-covered Pt(111), the latter more relevant under typical operating conditions, and elucidated the deactivation mechanism for this chemistry.

Through the studies presented in this dissertation, we demonstrate the necessity and the complexity associated with modeling the *in situ* nature of the active site, in terms of both the geometric model for the active site as well as its decoration by reaction intermediates. Careful consideration of spectator-induced coverage effects in the computational models resulted in better estimates for the

rate-parameters and led to the discovery of novel catalytic mechanisms, allowing us to formulate high-fidelity kinetic models, capable of quantitatively capturing experimental kinetics. These models can then serve as the foundational basis for optimizing existing industrial processes and for the discovery of improved catalytic materials that facilitate efficient transformation of molecules.

10.2 Future Work

10.2.1 Discovery of Novel Reaction Mechanisms and the Role of Spectators

Spectator-induced coverage-effects are frequently ignored in conventional DFT and microkinetic modeling studies. As demonstrated in Chapter 3, 4, and 5, careful consideration of spectator coverage-effects can greatly influence the energetics of the reaction network via lateral adsorbate-adsorbate interactions or through the electronic structure modification of the catalytic site induced by spectator coverages. At coverages relevant in FA decomposition catalysis, for CO spectators (on Pt and Pd catalysts), these interactions were found to be largely repulsive in nature, whereas, for spectators with a larger footprint (e.g., $HCOO_{BX}$ formed upon complexation of FA and bidentate HCOO on Cu), coverage effects served to stabilize the reaction thermochemistry and kinetics via stabilizing van der Waals interactions. However, more importantly treatment of spectator coverage effects led to the discovery novel reaction mechanisms, e.g. the CO spectator assisted H-transfer steps and FA-assisted isomerization of HCOO from bidentate to monodentate configuration, which were not previously considered for FA decomposition chemistry. Specifically, comparing with the reaction kinetics experiments and following the algorithmic approach presented in Chapter 6, first informed us of the nature of the MASI, led us to investigate

the reaction network on the spectator-decorated versions of the catalyst surfaces. A closer-look at the optimized geometries of reaction intermediates on the spectator-decorated surfaces, together with shortcomings of the reaction network, which surfaced during subsequent iterations our algorithm (i.e., lack of parity with experiments), informed us to investigate these additional spectator-assisted mechanisms. When included in the reaction network, these newly considered mechanisms were found to carry a significant amount of reaction flux, under conditions, and were ultimately determined to be essential in rationalizing the experiments.

These novel spectator-assisted mechanisms are non-trivial to envision solely on the basis of clean surface calculations, due to the large number of combinatorial possibilities involving the species involved in the reaction network and the changes in adsorption configurations of reaction intermediates on high-coverage surfaces vs. that on clean surface. However, comparing with experiments quantitatively (as demonstrated in Chapter 3 and 4) or even semi-quantitatively (fitting reaction orders and apparent activation energy barriers – as shown in Chapter 5), via rigorous parameter estimation, could help identify the nature of MASI, which in conjunction with our algorithm could ultimately serve to inform these additional reaction mechanisms. In the broader context, our studies demonstrate that for the examined catalytic systems, the spectator species are not innocent bystanders in the reaction network, which serve to only influence the energetics of the reaction thermochemistry and kinetics, but more importantly actively participate in the reaction network by enabling the transformation of reaction intermediates. We therefore believe that utilizing our algorithmic approach provides rich opportunities for discovery of novel reaction mechanisms, for a wide-range of chemistries, such as Fischer-Tropsch synthesis,

ammonia synthesis, hydrodesulphurization, hydrodechlorination, (de)hydrodeoxygenation, NO_x reduction, etc., which are typically characterized by highly covered surfaces.

10.2.2 Design of Experiments

In Chapters 3, 4, and 5, we present our integrated approach for formulating high fidelity microkinetic models, in the context of FA decomposition over Pt/C, Pd/C, and Cu/Al_2O_3. As briefly discussed in Chapter 6, the *experimentally-calibrated* microkinetic models obtained via parameter-estimation now provide a high-quality basis for the design of experiments. The microkinetic model, capable of quantitatively explaining the experiments over a wide range of reaction conditions, can be used to formulate optimized processes and to predict the behavior of the catalyst under conditions different from that used in the parameter estimation procedure. Further, the model can be used to investigate related chemistries, such as the reverse reaction, which in the case of our example would be CO_2 reduction to FA, a first step towards CO_2 chemical capture.

In addition, one can start with the optimized microkinetic model and use it to optimize the yield of products(s) and or the concentration of specific surface intermediates. By posing this as an optimization problem, one can widely sample the experimental space and determine the conditions that would maximize or minimize the yield of certain products or the coverage of surface species. In particular, this approach can be utilized for *in situ* detection of spectroscopically elusive species, providing experimentalists a set of conditions: temperature, pressure, flow-rate of reactants, etc., wherein the surface coverage of the species of interest is maximized, thereby facilitating the identification of elusive intermediates. More broadly, it will also provide a methodology to achieve precise atomic-scale control over the *in situ* surface environment.

Although not discussed in this dissertation in detail, we have implemented this methodology within the generic microkinetic modeling framework developed in our group.[41] The model formulation is similar to that used for the parameter estimation module, wherein a given objective function (Z) is optimized subject to the reactor balance equations and the constraints (π) are defined per the specifications of the reactor system:

$$Z = \ max/min(\theta_k) \tag{10.1}$$

$$\frac{dF_i}{dt} = F_{i,in} - \ F_{i,out} + \sum_{j \in J} v_{ij} r_j \ ; \quad i \ \in I^{Gaseous-species} \tag{10.2}$$

$$\frac{d\theta_i}{dt} = \sum_{j \in J} v_{ij} r_j \ ; \quad = f(k, K, \theta, F) \quad ; \quad j \in I^{Reactions} \tag{10.3}$$

$$\sum_{i \in I^s} \theta_i = 1; \quad i \ \in I^{Surface-species} \tag{10.4}$$

$$\pi \in F_i, P, T; \qquad \pi_L \leq \pi \leq \pi_U; \quad i \ \in I^{Gas-species} \tag{10.5}$$

The solution procedure involves an iterative sequence of forward integration of the system of differential algebraic equations (DAEs), sensitivity calculations and gradient based non-linear optimization, similar to the scheme adopted by Rangarajan et al. for parameter estimation.[41] State-of-the-art open source codes such as, SUNDIALS[281] for solving the system of DAEs, EIGEN[361] for evaluation of sensitivities and IPOPT[282] for optimization, were utilized to implement the solution procedure. Each sequential optimization iteration involves evaluation of steady-state solution for the system of DAEs and calculation of sensitivities based on the value of the decision variables at that iteration. The calculated objective function and sensitivities values are supplied to the optimizer, which determines the values for the decision variables for the next iteration, until convergence. The optimized values of the decision variables represent the optimized experimental

conditions (temperature, pressure, flow-rate of reactants), which would guide the experimental detection of elusive species. To elucidate multiple local minima, given the non-linearity associated with this formulation, we adopt a multi-start approach using Latin-hypercube sampling.[135,136] Consideration of coverage-cognizant energetics for all dominant reaction intermediates, would be critical in utilizing this formulation in a meaningful way. During optimization to maximize/minimize the concentration of a reaction intermediate, it is possible that the nature and coverages of reaction intermediates predicted at the determined optimal conditions, would be substantially different than those encountered for the reaction kinetics experiments utilized in parameter estimation. This can lead to reaction intermediates, not previously considered as MASIs, to become dominant on the surface, and require modeling of their coverage-effects. Thus, the determination and utilization of coverage-cognizant energetics will be critical to enable sound predictions. In conjunction with *in situ* spectroscopic techniques, this methodology can be employed to first optimize the surface concentration of known reaction intermediates, which can be more readily detected, and for small reaction networks, wherein the coverage dependent energetics can be easily calculated for all the plausible MASIs, followed by incrementally adding complexity and extending to intermediates that remain elusive.

10.2.3 Coverage Self-consistent Solutions for Electrocatalytic Reactions

While microkinetic modeling is now frequently employed to elucidate fundamental mechanistic understanding of vapor-phase catalysis, first principles studies of electrocatalytic chemistries are still largely based on thermochemical arguments, subject to the computational hydrogen electrode (CHE) formalism.[324] For the recent studies that do utilize microkinetic modeling analyses for

electrocatalysis, similar to the conventional investigations in vapor-phase catalysis, the energetics are typically calculated on clean surfaces.

We propose extending our generalized algorithm, presented in Chapter 6, to also study electrocatalytic reactions. Using the microkinetic models, one can then simulate the kinetics, typically determined experimentally, on the rotating-disc electrodes to formulate voltammograms, Tafel plots, and cyclic-voltammograms, etc., to facilitate a one-to-one comparison with the experiments. It is well known that the surface environment of the electrocatalysts changes drastically as a function of applied potential, in terms of both the coverage of reaction intermediates as well as the nature of the most abundant surface intermediate. To address the changes in surface environment, our strategy of utilizing coverage-dependent energetics can be directly extended to update on-the-fly the rate-parameters for electrochemical steps, for accurately simulating different potential regimes. In addition, as we have demonstrated for the case of vapor-phase FA decomposition reaction, careful consideration of the surface environment could also inform the additional spectator-assisted mechanisms that might not been considered for electrocatalytic systems yet.

10.2.4 Detailed Investigations over Intermetallic Binary-alloy Catalysts

In Chapter 7, we presented our approach for formulating experiment-calibrated coverage-cognizant volcano plots for the formic acid decomposition reaction and proposed a number of promising candidates that were computationally predicted to be more active and/or selective compared with the monometallic Pd/C, which was chosen as the reference catalyst. By enlisting the help of inorganic synthesis experts, it will be important to synthesize, characterize and

experimentally evaluate the reactivity of these proposed intermetallic-alloys, and thus ultimately gauge the quantitative fidelity of the coverage-cognizant volcano plots.

Additionally, detailed computational studies over bimetallic catalysts, will be essential in identifying potential avenues for improving the quantitative accuracy of these predictive models. In particular, detailed reactivity studies will inform the applicability and the accuracy of linear scaling/BEP correlations and of coverage-dependent energetics, in extrapolating and describing the energetics landscape of intermetallic binary alloy catalysts. Further, our models do not yet account for the adsorbate-induced segregation effects that might be induced in the presence of reaction intermediates, viz., CO and HCOO, under reaction conditions. In our descriptor-based high-throughput screening work, to first evaluate the quantitative accuracy of the reactivity predictions for the bimetallic catalysts and to avoid complications arising from surface-induced segregation, we only considered stable intermetallic-binary alloy compositions, which are marked by long-range ordering and are less prone to segregation. However, detailed computational studies and careful *in situ* characterization will be critical in establishing if adsorbate-induced segregation effects are indeed absent from these systems. As demonstrated in Chapters 3, 4, and 5, and formalized as an algorithm in Chapter 6, one can use our iterative methodology, involving DFT calculations, reaction kinetics experiments, and microkinetic modeling to start to systematically determine a coverage self-consistent description for the *in situ* catalytic active site.

Further, once a favorable alloy candidate identified, which is more active and/or selective compared with the monometallic reference catalyst, one can leverage catalyst composition as a tunable parameter and experimentally determine the composition that optimizes the catalyst activity and selectivity. We thus propose utilizing our approach for performing a rigorous

screening to propose a shortlisted set of intermetallic-alloy formulations, which can be utilized as a starting point by the experimentalists to further optimize the catalyst composition. Importantly, from a methodological standpoint, our investigations showcase the complexity involved in computational catalyst discovery approaches, often largely ignored by conventional studies in the literature.

10.2.5 Implications of Coverage-cognizant Volcano Plots for Materials Discovery

In Chapter 7, we demonstrated the impact of the intrinsic errors of DFT functionals and of spectator induced coverage-effects on the quantitative fidelity of microkinetic models for computational catalyst discovery. Specifically, we show that experimental calibration of the model for the reference catalyst can greatly impact the reactivity landscape across the descriptor space, both in terms of proposing qualitative trends, as well as making quantitative predictions. For our study, we have used Pd/C as the reference catalyst, from which the energetics are extrapolated across the descriptor space, as discussed in Chapter 4. Our results demonstrate that the reaction occurs via the COOH* mechanism on a partially CO*-covered Pd(111), which serves as the active site for this chemistry. Thus, in our parameter-adjustment procedure, only the systematic DFT errors for the thermochemistry and kinetic parameters appearing in the COOH* mechanism were corrected, while those appearing in competing mechanisms, e.g. HCOO mechanism, could not be statistically evaluated. Although, this aspect is not expected to impact the energetic landscape near the reference catalyst, i.e., in terms of the descriptor space, it might have an impact on catalyst candidates that are predicted to be far from the reference catalyst. To address this, for a given catalytic chemistry, we propose utilizing our iterative methodology developed in Chapters 3, 4, and 5, to first investigate the reaction on monometallic catalysts that are qualitatively different

from each other, in terms of the binding energy of descriptors, expected MASIs, reaction mechanisms, and reactivity (both activity and selectivity). These models will then allow for more accurate extrapolation of the energetics across the material space, while addressing the intrinsic errors in the thermochemistry and kinetic parameters of various competing mechanisms.

APPENDIX A

CHLOROFORM HYDRODECHLORINATION ON PALLADIUM SURFACES: A COMPARATIVE DFT STUDY ON PD(111), PD(100), AND PD(211)[⊥]

A.1 Introduction

Chlorinated hydrocarbon compounds are common soil and groundwater contaminants, which pose serious environmental hazards. These species can affect human health adversely due to their high toxicity and carcinogenicity.[362–364] The catalytic hydrodechlorination process has been proposed as a promising treatment method for chlorinated hydrocarbon wastes.[365] Among these chemical compounds, the hydrodechlorination of chloroform ($CHCl_3 + 3H_2 \rightarrow CH_4 + 3HCl$, $\Delta G°(298K)$ = 267.0 kJ/mol[260]) has been extensively studied in the literature.[366,367,376,368–375] Chloroform is commonly used in the chemical industry as the precursor for the large-scale production of polytetrafluoroethylene (PTFE) and as a solvent for other organic compounds. Therefore, effective treatment for chloroform wastes from industrial effluent streams through hydrodechlorination is

[⊥]Adapted from – Xu, L.; Bhandari, S.; Chen, J.; Glasgow, J; Mavrikakis, M. Chloroform Hydrodechlorination on Palladium Surfaces: A Comparative DFT Study on Pd(111), Pd(100), and Pd(211). *Topics in Catalysis* **2020**, 1-15 – https://doi.org/10.1007/s11244-019-01218-6

highly desired. Due to its relatively simple molecular structure, chloroform may also serve as a surrogate molecule for mechanistic studies of chlorinated hydrocarbon compounds with longer carbon chains.

Late transition metals are the most widely used catalysts for the hydrodechlorination reaction. Several of these metals have been evaluated experimentally for chloroform hydrodechlorination, including Fe,[366,367] Ni,[368,369] Pt,[369,370] and Pd.[369,371–374] Pd is proposed as the best-performing monometallic catalyst due to its superior activity and stability; it has been shown to catalyze chloroform hydrodechlorination reactions effectively even at ambient temperature and pressure.[375] Velázquez et al. reported that a Pd-Au bimetallic catalyst, synthesized by dispersing Pd onto an Au/Al_2O_3 support, is even more active than pure Pd catalysts.[375] Theoretical mechanistic studies are rare for this chemistry. To our knowledge, Chen et al. performed the only theoretical study for Pd-catalyzed chloroform hydrodechlorination; that work was focused on the Pd(110) surface and used density functional theory (DFT).[374] To probe the promotional role of Au in Pd hydrodechlorination catalysts, we previously performed a comparative DFT study on Pd(111) and PdML/Au(111) surfaces.[376] However, this study was limited to the (111) close-packed facet. Catalyst particles synthesized through conventional preparation methods without shape control are known to expose different facets, including the more open (100) facet as well as step edges and kinks. To our knowledge, no evidence for structure dependence of this reaction has been provided in the experimental literature. In order to advance the fundamental understanding of chloroform hydrodechlorination, particularly its structure sensitivity on Pd surfaces, more detailed theoretical investigations on different Pd facets are desired.

Here, we present a systematic DFT study for this chemistry on three representative facets of Pd: Pd(111), the most stable, close-packed facet; Pd(100), a more open facet; and Pd(211), a surface model for the step edges in a typical Pd nanoparticle. Using DFT calculations, we first examined the preferred binding structures and corresponding binding energies of all the reaction intermediates on these three Pd facets. Then, we identified the transition state of each elementary step in the chloroform hydrodechlorination reaction network and evaluated the reaction energies and activation energy barriers. Finally, based on the DFT-derived reaction energetics, we proposed a reaction pathway for chloroform hydrodechlorination on Pd catalysts and constructed the reaction potential energy diagram on all three facets of Pd. Our DFT study offers valuable insights into the chloroform hydrodechlorination reaction mechanism on Pd catalysts. Moreover, through a comparative study on different facets of the Pd metal, we provide evidence for the structure dependence of the activity of Pd catalysts, which should be beneficial for future catalyst design and performance improvements.

A.2 Methods

All the DFT calculations were performed using the Vienna *ab-initio* Simulation Package (VASP),[54,55] a plane-wave total-energy code. The electron-ion interactions were described by the projector augmented-wave (PAW) potentials,[123,124] and the exchange-correlation functional was described using the generalized gradient approximation (GGA–PW91).[52] The electronic wave functions were expanded using plane waves with an energy cutoff of 400 eV. The energy of each gas-phase species was evaluated in a (14 Å × 15 Å × 16 Å) unit cell, with the first Brillouin zone sampled at the gamma point. Convergence of the gas-phase energies with respect to the unit cell

size is observed. The calculated standard Gibbs free energy at 298 K for the gas-phase chloroform hydrodechlorination reaction ($CHCl_3 + 3H_2 \rightarrow CH_4 + 3HCl$) is 276.5 kJ/mol, in reasonable agreement with the handbook value of 267.0 kJ/mol.[260]

The Pd(111) and Pd(100) surfaces were all modeled by periodically repeated (3 × 3) unit cells; each slab consists of four Pd atomic layers; the bottom two layers were fixed at their bulk lattice positions while the top two layers, as well as the adsorbates, were allowed to relax fully. The Pd(211) stepped surface was modeled by a slab of 12 atomic layers in a (1 × 3) unit cell (Figure A.1), with the bottom six layers fixed at their bulk lattice positions. Successive slabs were separated in the z-direction by a vacuum layer of at least 12 Å. The calculated Pd lattice constant is 3.957 Å based on bulk Pd calculations, in reasonable agreement with the experimental value of 3.890 Å.[125] Adsorption was allowed on only one side of the slab, and the electrostatic potential was adjusted accordingly.[126,127] The site nomenclature for the Pd(211) surface is graphically illustrated in Figure A.1 and used consistently throughout this work. The first Brillouin zone was sampled with a (4×4×1) gamma-centered Monkhorst-Pack k-point mesh.[128] Convergence of the total energy with respect to the k-point set, energy cutoff and the number of metal layers included was confirmed to 0.01 eV.

The activation energy barriers of all the elementary steps were evaluated using the climbing image nudged elastic band (CI-NEB) method[129] with seven interpolated images in addition to the initial and final states. The structures were relaxed until the maximum force on all images is smaller than 0.1 eV/Å. For the hydrogen activation step ($H_2 + 2* \rightarrow 2H*$; * denotes an empty site or an adsorbed species), a tighter convergence criterion (0.05 eV/Å) was employed. The transition state was confirmed by vibrational frequency calculations, yielding a single imaginary frequency along the

reaction coordinate. The binding energies of all the surface adsorbates were calculated with respect to their gas phase energy using:

$$BE = E_{tot} - E_{slab} - E_{gas} \quad (A.1)$$

where BE denotes the binding energy of the adsorbate, E_{tot} denotes the total energy of the adsorbed species and the slab together, E_{slab} denotes the total energy of the clean slab alone, and E_{gas} denotes the total energy of the adsorbate alone in the gas phase.

The reaction energies and activation energy barriers were evaluated with respect to the energies of the best (i.e., lowest-energy) initial and final states as defined:

$$\Delta E = E_{BFS} - E_{BIS} \quad (A.2)$$

$$E_a = E_{TS} - E_{BIS} \quad (A.3)$$

where ΔE denotes the reaction energy, E_a denotes the activation energy barrier, E_{BIS} and E_{BFS} denote the energies of the best initial and final states, respectively, and E_{TS} denotes the energy of the transition state. When two species are involved in an initial/final state, the best state is defined as the one in which the two species are adsorbed at infinite separation, each at its preferred adsorption site.

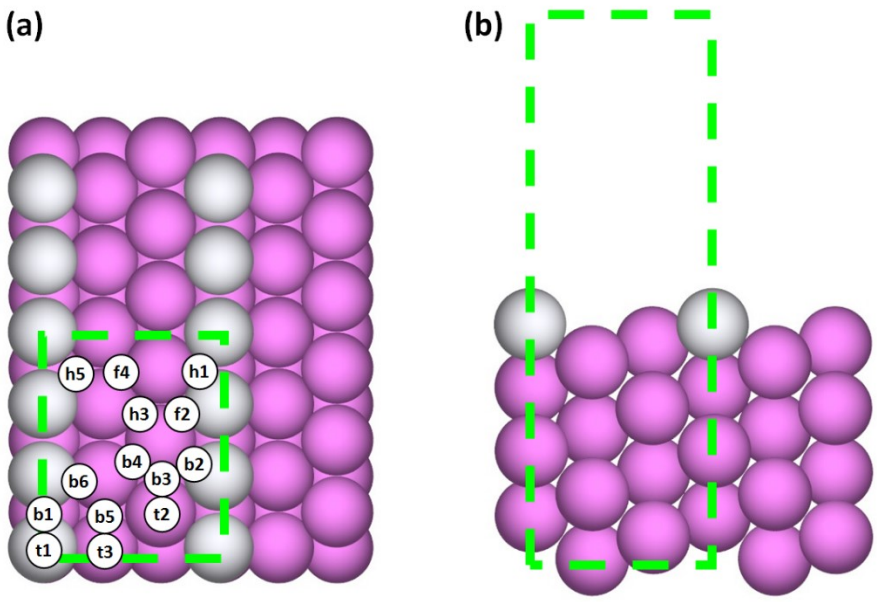


Figure A.1 Site nomenclature for the Pd(211) slab. (a) Top and (b) side views of the Pd(211) surface are shown. Grey spheres indicate the protruding row of the surface Pd atoms representing the step edge atoms; purple spheres indicate the other (terrace) Pd atoms. Green dash lines indicate the unit cell.

A.3 Results and Discussion

The reaction network for the chloroform hydrodechlorination reaction is illustrated in Figure A.2, where all possible dechlorination and hydrogenation steps after breaking the first C-Cl bond in $CHCl_3$ are taken into consideration. We also include the CH dissociation step (pink solid arrow in Figure A.2) to form atomic hydrogen and carbon in order to probe potential routes towards coke formation. We will show towards the subsequent sections that the H removal steps from $CHCl_3$, $CHCl_2$, and CHCl (pink dashed arrows in Figure A.2) are not competing effectively with Cl removal and H addition steps; therefore, no subsequent reaction steps following these dehydrogenation steps are included in our proposed reaction network. Based on this reaction network, the adsorption of reaction intermediates, the energetics of elementary steps, and the

overall reaction potential energy diagrams are presented in the following subsections. The DFT results on the Pd(111) surface were already presented in our previous publication.[376] These results are discussed alongside those on Pd(100) and Pd(211) in each subsection for better comparison.

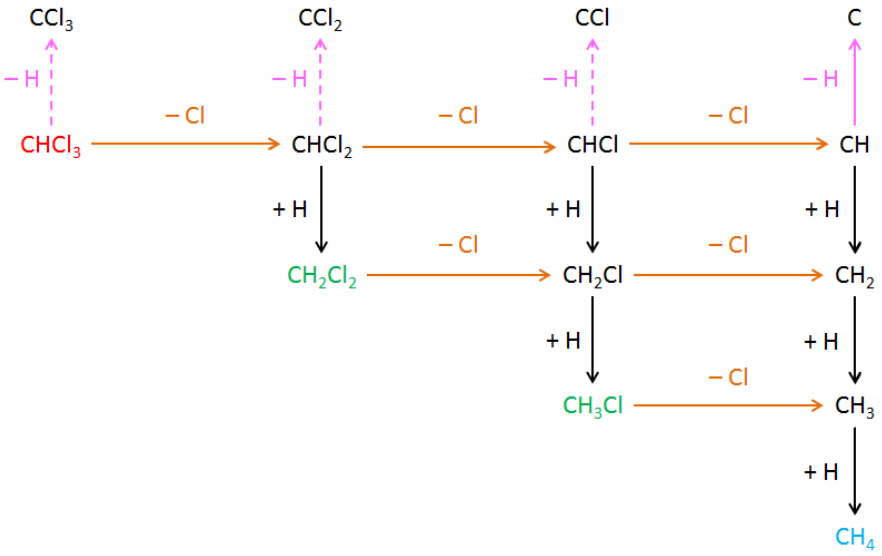


Figure A.2 Chloroform hydrodechlorination reaction network. Orange arrows indicate dechlorination steps; black arrows indicate hydrogenation steps; pink arrows indicate the dehydrogenation steps. Dashed arrows denote those dehydrogenation steps that are later shown as energetically unfavorable against competing steps. Red: reactant ($CHCl_3$); blue: product (CH_4); green: by-products (CH_2Cl_2 and CH_3Cl).

A.3.1 Adsorption of Reaction Intermediates

The calculated binding energies of all reaction intermediates on their preferred binding sites are summarized in Table A.1, and the graphical illustrations of the minimum energy structures at the preferred binding mode are shown in Figure A.3. We did not observe stable binding structures for H_2 on any of the three Pd facets; H_2 always dissociates spontaneously to adsorbed hydrogen (H*) atoms. On the other hand, CH_4 barely interacts with each Pd surface through physisorption (almost zero binding energy). Therefore, these two species are not listed in Table A.1 and Figure A.3.

As shown in Table A.1, we observe a strong correlation between the binding-site preference of the carbonaceous intermediates and the number of valence electrons on the C atom available for carbon-surface binding. All the closed-shell species ($CHCl_3$, CH_2Cl_2, and CH_3Cl) cannot bind to the Pd surfaces through the C atom. Instead, they tend to bind to the surface through one or more Cl and/or H atoms. The binding strengths of these species are also much weaker compared to the other carbonaceous species. For the open-shell CH_xCl_y intermediates, CH_3, CH_2Cl, and $CHCl_2$ tend to bind the strongest to the top site; CH_2 and CHCl prefer to bind to the bridge site; CH prefers to bind to the three- or four-fold hollow site. The only exception is CH_3 on Pd(211), which prefers to bind on the b1 site on the step edge.

Table A.1 Binding energies of reactants and reaction intermediates at their preferred adsorption sites on Pd(111) (data reproduced from Xu *et al.*),[376] Pd(100), and Pd(211). Zero of binding energy corresponds to infinite separation between adsorbate in the gas phase and clean slab.

Species	**Pd(111)**		**Pd(100)**		**Pd(211)**	
	Binding Site[a]	BE (eV)	Binding Site[a]	BE (eV)	Binding Site[a]	BE (eV)
$CHCl_3$	t_H-t_{Cl}	-0.20	t_{Cl}-t_{Cl}-t_{Cl}	-0.27	$t1_{Cl}$-$t1_{Cl}$	-0.50
CH_2Cl_2	t_H-t_{Cl}-t_{Cl}	-0.23	t_{Cl}-t_{Cl}-b_H	-0.31	$t1_{Cl}$-$t1_{Cl}$	-0.48
CH_3Cl	t_H-t_H-t_{Cl}	-0.24	t_H-t_H-t_{Cl}	-0.26	$t1_{Cl}$	-0.41
$CHCl_2$	top	-1.79	Top	-1.95	t1	-2.03
CH_2Cl	top	-1.92	Top	-1.97	t1	-2.15
CH_3	top	-1.85	Top	-1.82	b1	-1.96
CHCl	bridge	-3.88	Bridge	-4.08	b1	-4.05
CH_2	bridge (tilted)	-4.00	Bridge	-4.00	b1	-4.14
CH	fcc	-6.54	Hollow	-6.59	h5	-6.40
HCl	t_H-b-t_{Cl}	-0.23	t_H-b-t_{Cl}	-0.32	$t1_H$-b-$t1_{Cl}$	-0.21
H	fcc	-2.93	bridge	-2.73	h1	-2.83
Cl	fcc	-3.18	hollow	-3.33	b1	-3.34
C	fcc	-6.86	hollow	-7.88	h5	-7.72

[a] t and b denote the top and bridge sites, respectively. The subscripts denote the atom(s) through which the adsorbate binds. All the open-shell CH_xCl_y species prefer to bind through the carbon atom.

The results in Table A.1 also allow us to compare the binding energies on different Pd facets. For all the carbonaceous species, we observe that the binding strength generally increases in the following order: Pd(111) < Pd(100) < Pd(211). On Pd(211), it is observed that the reaction intermediates almost always prefer to bind on the step-edge sites (t1 and b1). These observations are consistent with the general expectation that the adsorption strength of a surface should increase with decreasing coordination number of the surface atoms.[265,377] A notable exception is CH, which binds the weakest on Pd(211). This is likely due to the strong binding preference of CH to three-fold hollow sites, which is not present on the step edge of Pd(211).

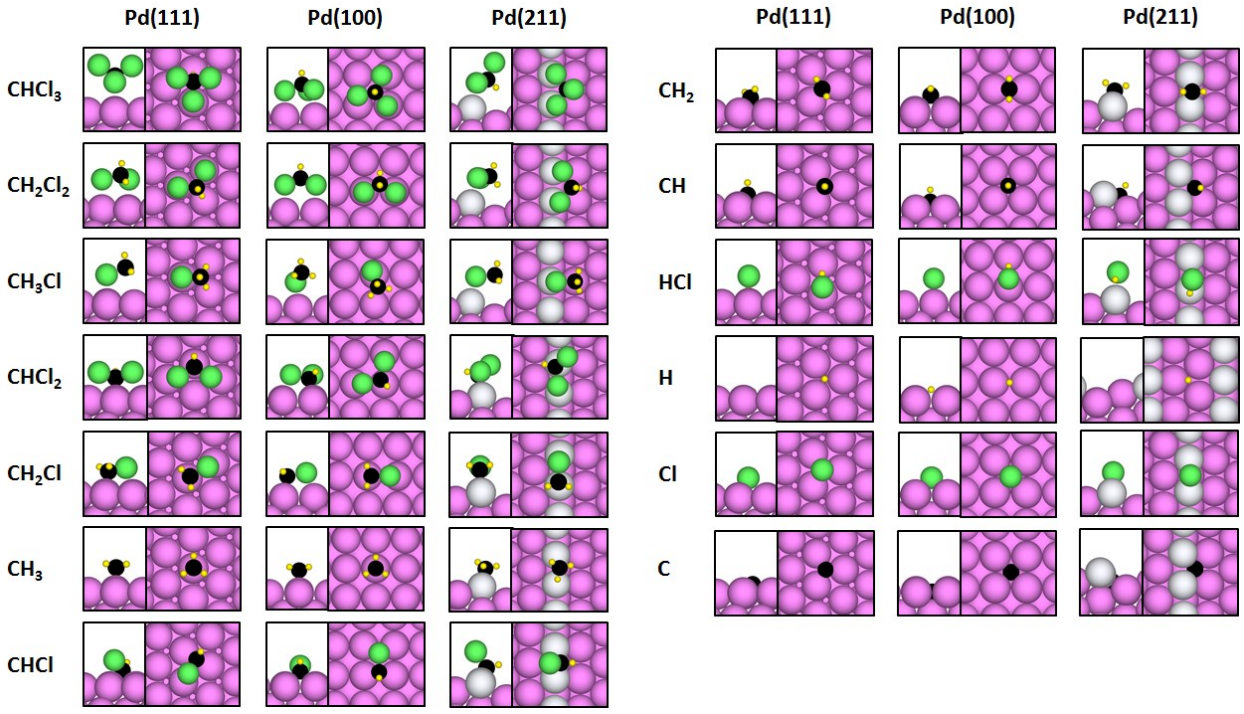


Figure A.3 Minimum energy structures of reactants, products, and reaction intermediates on Pd(111), Pd(100), and Pd(211). The structures on Pd(111) were reproduced from Xu *et al.*;[376] Color code: Grey – step-edge Pd; pink – other Pd; black – C; yellow – H; green – Cl.

A.3.2 Reaction Energies and Activation Energy Barriers

The calculated reaction energies (ΔE) and activation energy barriers (E_a) for all the elementary steps listed in Figure A.2 on all three Pd facets are summarized in Figure A.4. The initial, final, and transition states of the lowest-energy path for each elementary step are summarized in Figure A.5. Here, we briefly discuss the other two elementary steps not shown in Figure A.5: the dissociative adsorption of H_2 ($H_2 + 2* \rightarrow 2H*$) and the formation of HCl ($H* + Cl* \rightarrow HCl + 2*$). On all three facets, we observed zero activation energy barrier for the dissociative adsorption of H_2; the reaction energies of this step are -1.31 eV, -0.90 eV, and -1.11 eV on Pd(111), Pd(100), and Pd(211), respectively. The reverse reaction of the HCl formation step, i.e., the dissociative adsorption of HCl ($HCl + 2* \rightarrow H* + Cl*$), is also barrierless on all three Pd facets. The calculated reaction energies for the HCl formation step are 1.45 eV, 1.39 eV, and 1.51 eV on Pd(111), Pd(100), and Pd(211), respectively. The detailed reaction paths for the other elementary steps are discussed below.

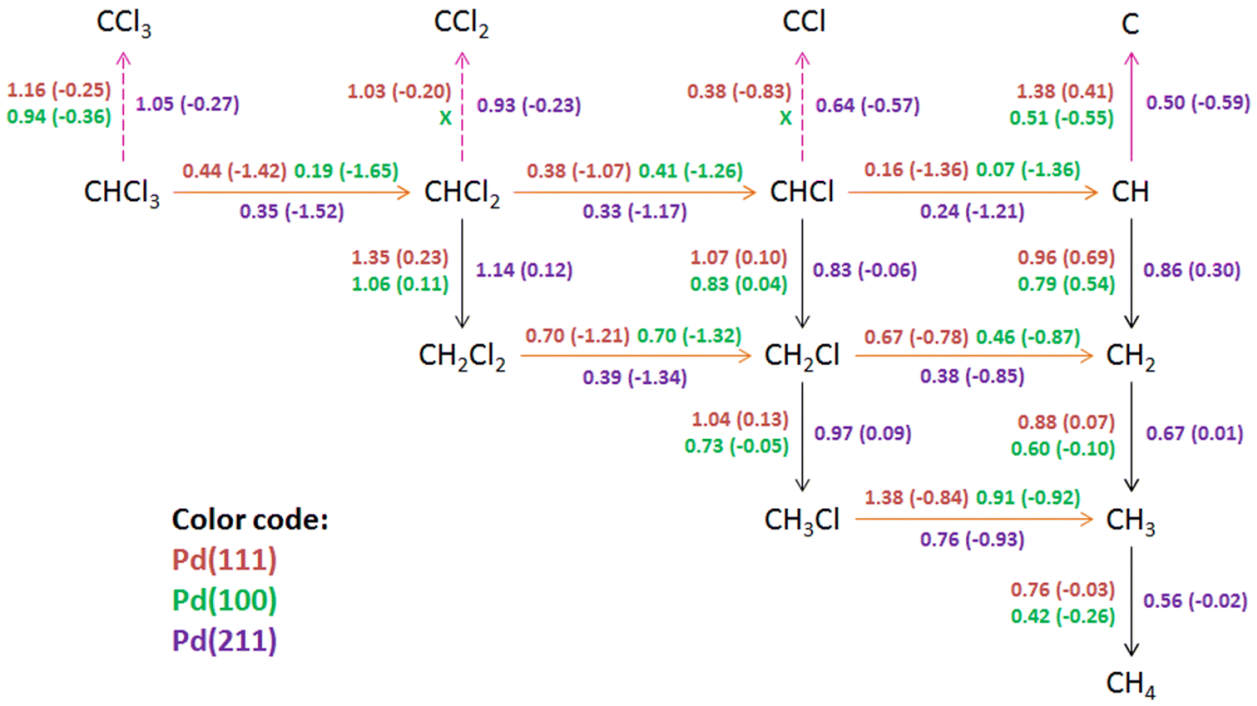


Figure A.4 Activation energy barriers (numbers outside the parentheses) and reaction energies (numbers inside the parentheses) of surface elementary reaction steps (red: Pd(111) (data reproduced from Xu *et al.*);[376] green: Pd(100); purple: Pd(211)). Orange arrows indicate dechlorination steps; black solid arrows indicate hydrogenation steps; pink arrows indicate the dehydrogenation steps. Dashed arrows denote those dehydrogenation steps that are energetically unfavorable against competing steps. 'X' denotes a step for which we were unable to determine any feasible reaction path from NEB calculations, and another elementary step would always occur ahead of this step.

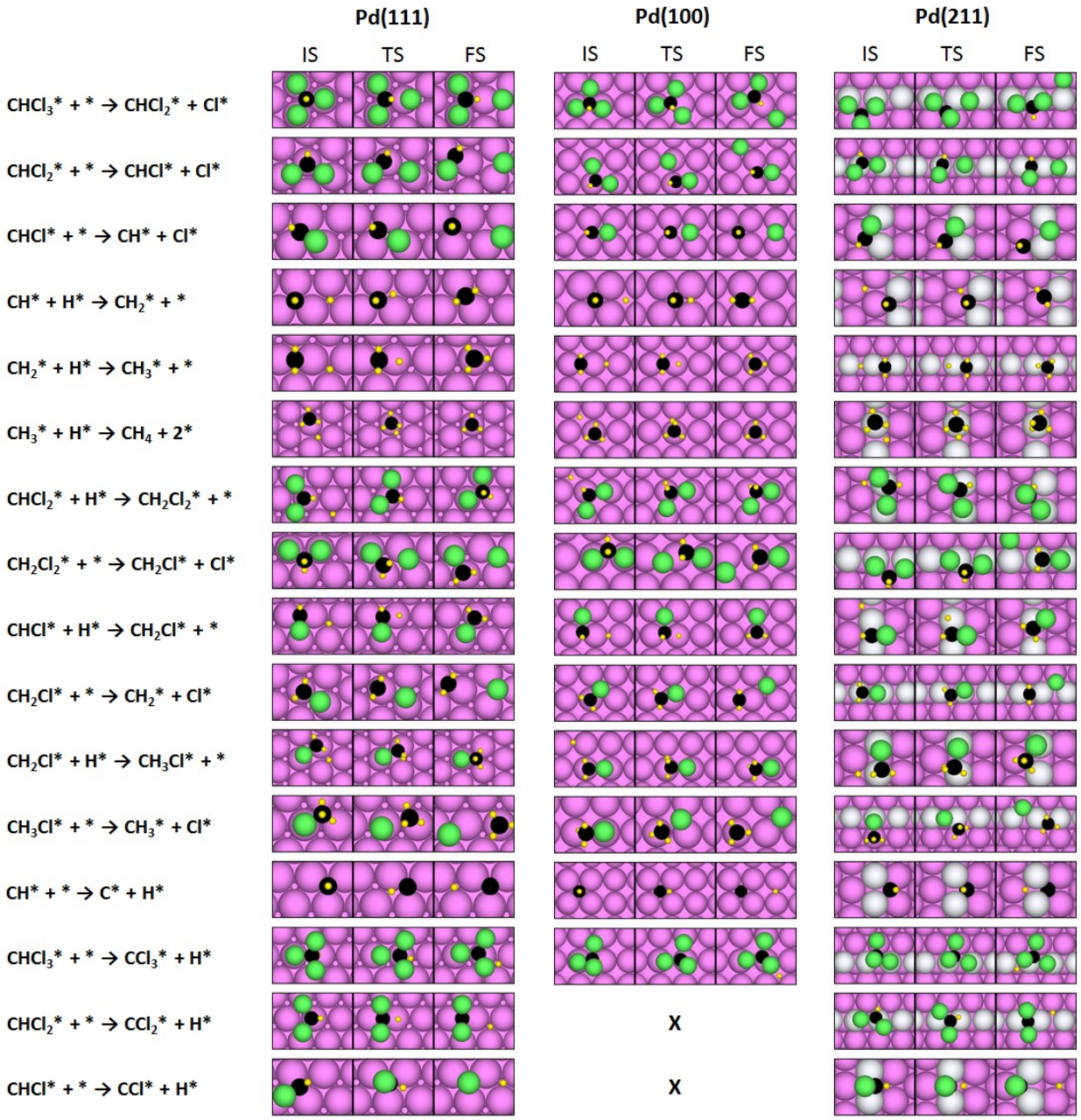


Figure A.5 Top views of the initial-state (IS), transition-state (TS) and final-state (FS) structures of each surface elementary reaction step on Pd(111), Pd(100), and Pd(211). The structures on Pd(111) were reproduced from Xu *et al.*[376] Color code: Grey – step-edge Pd; pink – other Pd; black – C; yellow – H; green – Cl. 'X' denotes a step for which we were unable to determine any feasible reaction path from NEB calculations, and another elementary step would always occur ahead of this step. Several images for the structures on Pd(211) are rotated by 90° so that all the reactive species can be captured in these images.

A.3.2.1 $CHCl_3$ + * → $CHCl_2$* + Cl**

The first dechlorination step is highly exothermic on all three Pd facets; the reaction energies of this step are -1.42 eV, -1.65 eV, and -1.52 eV on Pd(111), Pd(100), and Pd(211), respectively. On Pd(111), this step initiates with the chloroform molecule adsorbed to the surface through all three of its Cl atoms; the center of the molecule sits on top of an hcp site. This structure is merely 0.01 eV less stable than the preferred configuration on Pd(111) binding through one H and one Cl (Figure A.3). As the reaction step proceeds through the reaction coordinate, one of the C-Cl bonds starts to stretch, until it reaches a bond length of 2.63 Å at the transition state. The calculated activation energy barrier to reach this transition state on Pd(111) is 0.44 eV. Once the C-Cl bond is broken, the Cl* atom moves to a nearby fcc site, while the $CHCl_2$* fragment binds to the surface through two Cl atoms instead of its C atom, a metastable binding structure 1.36 eV less stable than the optimal binding structure of $CHCl_2$*, where $CHCl_2$* binds through its C atom.

On Pd(100), the dechlorination of $CHCl_3$* occurs through a similar path to that on Pd(111). In the initial state, the adsorption of $CHCl_3$* is characterized by two Cl atoms binding to two adjacent top sites, with the third Cl atom siting near a bridge site; this is a slightly rotated structure from its preferred binding structure shown in Figure A.3. During the reaction, one of the top-site Cl atoms is broken away from the chloroform molecule. At the transition state, the C-Cl bond is stretched to a length of 2.38 Å. In the final state, the $CHCl_2$* fragment binds through a metastable state with two Cl atoms binding to the surface, similar to that on Pd(111). The activation energy barrier of this step is 0.19 eV on Pd(100), the lowest among all three Pd facets. We examined the reorientation of $CHCl_2$* from the metastable final states to its preferred binding structures on both Pd(111) and Pd(100). This step is highly exothermic and much less activated (barriers less than

0.10 eV) than the bond-breaking event. Therefore, this reorientation process is not considered as a rate-limiting factor in the dechlorination step.

On Pd(211), the activation energy barrier of the initial dechlorination step of $CHCl_3$* is 0.35 eV, 0.09 eV lower than that on Pd(111), yet 0.16 eV higher than that on Pd(100). This step occurs on the step edge of the Pd(211) surface. In the initial state, $CHCl_3$* sits on its preferred binding site with two of its Cl atoms on top of two adjacent t1 sites on the step edge. One of these two Cl atoms moves away from the molecule as the reaction step proceeds. When the transition state is reached, the C-Cl bond length is stretched to 2.83 Å. Unlike the paths on Pd(111) and Pd(100), the final state of this step on Pd(211) does not involve a metastable adsorption state of $CHCl_2$*. Rather, $CHCl_2$ binds to its preferred t1 site on the step edge, with one Cl atom tilting towards an adjacent t1 site. The Cl* atom broken away from the chloroform molecule sits on a nearby f2 site, which is a three-fold hollow site right next to the step edge, in the final state.

A.3.2.2 $CHCl_2^* + * \rightarrow CHCl^* + Cl^*$

The dechlorination of $CHCl_2$*, formed from the first dechlorination step of chloroform, is exothermic by 1.07 eV, 1.26 eV, and 1.17 eV on Pd(111), Pd(100), and Pd(211), respectively. On all three Pd facets, this elementary step initiates with the $CHCl_2$* species adsorbed to its preferred adsorption sites. It then proceeds with the elongation of one of the C-Cl bonds. The transition-state bond lengths for the C-Cl bond being broken during this process are 2.60 Å, 2.59 Å, and 2.69 Å on Pd(111), Pd(100), and Pd(211), respectively. On Pd(111), this step is characterized by an energy barrier of 0.38 eV; in the final state, CHCl* is adsorbed on its preferred bridge site through the C atom, and Cl* binds on a nearby fcc site. On Pd(100), the activation energy barrier of this step is 0.41 eV; the process is completed with CHCl* on the preferred bridge site and Cl* on a hollow

site. On Pd(211), the final state of this elementary step consists of both the CHCl* and Cl* species on two adjacent b1 sites over the step edge; the activation energy barrier on Pd(211) is 0.33 eV.

A.3.2.3 $CHCl^* + * \rightarrow CH^* + Cl^*$

Like the previous two dechlorination steps, the dechlorination of CHCl* to form CH* and Cl* is also exothermic on all three Pd facets. The reaction energies for this step are -1.36 eV, -1.36 eV, and -1.21 eV on Pd(111), Pd(100), and Pd(211), respectively. On Pd(111) and Pd(100), this reaction step starts with CHCl* on its preferred binding site. The C-Cl bond is stretched until it reaches 2.15 Å and 1.99 Å at the transition state on Pd(111) and Pd(100), respectively. After the C-Cl bond is fully broken, CH* binds on an hcp site, and the Cl* atom binds on an fcc site on Pd(111). In the final state on Pd(100), CH* binds on a hollow site while Cl* binds on a nearby bridge site. The initial state of this step on Pd(211) is different from the preferred binding configuration of CHCl*; instead of the preferred b1 site on the step edge, the species is adsorbed on a b2 site adjacent to the step edge which is 0.17 eV less stable. As this reaction step proceeds on Pd(211), the C-Cl bond elongates, and the CH* species moves back to the step edge until it sits on the b1 site. In the final state, the Cl* atom broken away from CHCl* binds on a b3 site on the terrace. At the transition-state on Pd(211), the C-Cl bond length is 2.06 Å. The activation energy barriers for this step are 0.16 eV, 0.07 eV, and 0.24 eV on Pd(111), Pd(100), and Pd(211), respectively.

A.3.2.4 $CH^* + H^* \rightarrow CH_2^* + *$

The hydrogenation of CH* to CH_2* is endothermic by 0.69 eV, 0.54 eV, and 0.30 eV on Pd(111), Pd(100), and Pd(211), respectively. On Pd(111), the activation energy barrier for this step is 0.96 eV. In the initial state, the CH* and H* species are adsorbed on two adjacent fcc sites. As the

reaction step proceeds, the H* atom moves closer to CH*. The transition-state distance of the C-H bond being formed is 1.37 Å on Pd(111). The CH_2* species formed binds on a bridge site in the final state. On Pd(100), this elementary step is associated with an activation energy barrier of 0.79 eV. The step initiates with CH* and H* on two adjacent hollow sites. The H* atom starts to diffuse towards the CH* species until the C-H bond reaches a length of 1.47 Å at the transition state. After the CH_2* species is formed, it binds to its preferred bridge site in the final state on Pd(100). The activation energy barrier of this step on Pd(211) is 0.86 eV. Unlike most of the other steps that occur over the step edge, this hydrogenation step occurs on the terrace of the Pd(211) surface. In the initial state, CH* binds on the h1 site right next to the step edge while H* bind on the and h3 sites on the terrace, respectively. Similar to the other two Pd facets, the reaction step proceeds with H* moving closer to the CH* species. At the transition state, the C-H bond length is 1.37 Å. The CH_2* species formed on Pd(211) binds on a b2 site, instead of its preferred b1 site on the step edge, in the final state.

A.3.2.5 $CH_2^* + H^* \rightarrow CH_3^* + *$

The hydrogenation of CH_2* to CH_3* is almost thermoneutral on all three Pd facets, with reaction energies of 0.07 eV, -0.10 eV, and 0.01 eV on Pd(111), Pd(100), and Pd(211), respectively. In the initial state of this elementary step on Pd(111), the CH_2* species is adsorbed on a bridge site in its preferred tilted configuration, and the H* atom sits on a nearby fcc site. The H* atom diffuses towards the hydrocarbon fragment as the reaction step proceeds. At the transition state, H* is located near a top site, and the length of the C-H bond being formed is 1.71 Å. Once the CH_3* species is formed, it is adsorbed on its preferred top site in the final state on Pd(111). On Pd(100) and Pd(211), the initial states for this elementary step are similar in structure; both involve CH*

and H* on two adjacent bridge sites (on Pd(211), both species bind on adjacent b1 sites on the step edge). The C-H bond is formed as the H* atom moves towards the CH_2* species. At the transition-state, the C-H distances for the bond being formed are 1.75 Å and 1.79 Å on Pd(100) and Pd(211), respectively. In the final state on Pd(100), the CH_3* species binds on its preferred top site, while on Pd(211), it binds on the preferred b1 site on the step edge. The calculated activation energy barriers for this hydrogenation step are: 0.88 eV on Pd(111), 0.60 eV on Pd(100), and 0.67 eV on Pd(211).

A.3.2.6 $CH_3* + H* \rightarrow CH_4 + 2*$

The formation of gas-phase methane from the hydrogenation of CH_3* is almost thermoneutral on Pd(111) and Pd(211) with reaction energies of -0.03 eV and -0.02 eV, respectively; the same elementary step is mildly exothermic on Pd(100) by 0.26 eV. This step occurs through similar paths on all three Pd facets. In the initial state, CH_3* is adsorbed on a top site (t1 site on Pd(211)), and the H* atom sits on a hollow site right next to the CH_3* species (fcc on Pd(111), h5 on the terrace of Pd(211)). The hydrogenation process proceeds with the H* atom moving closer to the CH_3* fragment. The transition-state C-H bond lengths are 1.60 Å, 1.64 Å, and 1.62 Å on Pd(111), Pd(100), and Pd(211), respectively. Once the methane molecule is formed, it immediately moves away from the surfaces. In the final states on all three Pd facets, methane is physisorbed with negligible interaction energy. The activation energy barriers of this hydrogenation step are 0.76 eV, 0.42 eV, and 0.56 eV on Pd(111), Pd(100), and Pd(211), respectively.

A.3.2.7 $CHCl_2* + H* \rightarrow CH_2Cl_2* + *$

The hydrogenation of $CHCl_2$* to the partially dechlorinated product, CH_2Cl_2*, is mildly endothermic by 0.23 eV, 0.11 eV, and 0.12 eV on Pd(111), Pd(100), and Pd(211), respectively.

The activation energy barriers of this hydrogenation step on the three Pd facets are 1.35 eV for Pd(111), 1.06 eV for Pd(100), and 1.14 eV for Pd(211). On all three Pd facets, this step initiates with similar co-adsorption configurations of the $CHCl_2$* and H* species: $CHCl_2$* binds on its preferred top site (t1 on the step edge of Pd(211)), and H* binds on a nearby hollow site (fcc on Pd(111), f2 on the terrace of Pd(211)). As the reaction step proceeds, the H* atom diffuses towards the $CHCl_2$* species, and the entire reaction complex moves away from the surface. At the transition state, the length of the C-H bond being formed is 1.46 Å, 1.45 Å, and 1.54 Å on Pd(111), Pd(100), and Pd(211), respectively. On Pd(111), the CH_2Cl_2* species is adsorbed to the surface through its preferred binding structure, as shown in Table A.1 and Figure A.3, in the final state, while on Pd(100) and Pd(211), it binds through slightly different, yet almost isoenergetic, adsorption structure from the preferred ones.

A.3.2.8 CH_2Cl_2* + * → CH_2Cl* + Cl*

The dechlorination of CH_2Cl_2* to CH_2Cl* is exothermic by 1.21 eV, 1.32 eV, and 1.34 eV on Pd(111), Pd(100), and Pd(211), respectively. The reaction paths for this elementary step are similar on all three Pd facets. The CH_2Cl_2* and CH_2Cl* species bind on their preferred adsorption sites in the initial and final states, respectively. During the reaction, one of the C-Cl bonds is elongated. In the final states, the Cl* atom broken off of the chlorocarbon sits on the fcc, bridge, and f2 sites on Pd(111), Pd(100), and Pd(211), respectively. On Pd(111), the transition-state C-Cl bond length is 2.61 Å, and the activation energy barrier for this step is 0.70 eV. The transition state on Pd(100) is associated with an activation energy barrier of 0.70 eV, and the C-Cl bond distance at this transition state is 2.66 Å. On Pd(211), the C-Cl bond length is 2.72 Å at the transition state; the associated activation energy barrier is 0.39 eV.

A.3.2.9 $CHCl^* + H^* \rightarrow CH_2Cl^* + *$

The hydrogenation of CHCl* to CH_2Cl^* is almost thermoneutral on all three Pd facets studied; the reaction energies for this elementary step are 0.10 eV, 0.04 eV, and -0.06 eV on Pd(111), Pd(100), and Pd(211), respectively. The activation energy barriers are 1.07 eV, 0.83 eV, and 0.83 eV on Pd(111), Pd(100), and Pd(211), respectively. In the initial states, the CHCl* species always prefers to bind on its preferred bridge site (b1 on Pd(211)) regardless of the surface facet. The H* atom in the initial state binds on a nearby fcc site on Pd(111), while it binds on the bridge and h1 sites on Pd(100) and Pd(211), respectively. The reaction step proceeds with the migration of the H* atom towards the CHCl* fragment. The transition-state C-H bond lengths are 1.64 Å, 1.65 Å, and 1.65 Å on Pd(111), Pd(100), and Pd(211), respectively. The CH_2Cl^* species formed in this elementary step binds through its preferred adsorption structure on a top site in the final states on all the Pd facets (t1 on Pd(211)).

A.3.2.10 $CH_2Cl^* + * \rightarrow CH_2^* + Cl^*$

The dechlorination of CH_2Cl^* is exothermic on all three Pd facets with reaction energies of -0.78 eV, -0.87 eV, and -0.85 eV on Pd(111), Pd(100), and Pd(211), respectively. Similar reaction paths were observed on all three Pd facets. The reaction step starts with the CH_2Cl^* species on its preferred top site (t1 on Pd(211)), and finishes with the CH_2^* on its preferred bridge site (b1 on Pd(211)) and Cl* on a nearby hollow site (fcc on Pd(111), h1 on Pd(211)). On Pd(111), stretching of the C-Cl bond leads to a bond length of 2.76 Å at the transition state, which is associated with an activation energy barrier of 0.67 eV. The activation energy barrier of this step on Pd(100) is 0.46 eV, and the transition-state C-Cl bond length is 1.88 Å. On Pd(211), the activation energy

barrier for this dechlorination step is 0.38 eV; at the transition state, the C-Cl bond is stretched to a length of 1.89 Å.

A.3.2.11 $CH_2Cl^* + H^* \rightarrow CH_3Cl^* + *$

The hydrogenation of CH_2Cl^* to CH_3Cl^* is mildly endothermic by 0.13 eV and 0.09 eV on Pd(111) and Pd(211), respectively, whereas it is slightly exothermic by 0.05 eV on Pd(100). On Pd(111), this hydrogenation step initiates with the CH_2Cl^* species on its preferred top site and the H* atom on an adjacent fcc site. The H* atom starts to move towards CH_2Cl^* until it reaches a transition-state C-H bond length of 1.50 Å. Once the C-H bond is formed, the CH_3Cl^* species binds to the surface through one Cl atom and two H atoms (its preferred binding structure). The activation energy barrier for this step on Pd(111) is 1.04 eV. On Pd(100), the reaction starts with CH_2Cl^* on its preferred top site and H* on a nearby bridge site. As the H* atom moves closer to CH_2Cl^*, the transition-state is reached at a C-H distance of 1.53 Å. In the final state, the CH_3Cl^* species formed binds through the Cl atom and one H atom, a binding structure almost isoenergetic as the preferred one on Pd(100); see Table A.1 and Figure A.3 for details. The activation energy barrier for this step on Pd(100) is 0.73 eV. In the initial state on Pd(211), the CH_2Cl^* binds on its preferred t1 site on the step edge, and H* sits on the f2 site right next to the step. The H* atom starts to move towards the CH_2Cl^* fragment and the transition-state is reached at a C-H bond length of 1.54 Å. In the final state, the CH_3Cl^* species binds to the t1 site on the step edge through its Cl atom. This hydrogenation step is associated with an activation energy barrier of 0.97 eV on Pd(211).

A.3.2.12 $CH_3Cl^* + * \rightarrow CH_3^* + Cl^*$

The dechlorination of CH_3Cl^* to CH_3^* is exothermic by 0.84 eV, 0.92 eV, and 0.93 eV on Pd(111), Pd(100), and Pd(211), respectively. The activation energy barriers for this step on the three Pd facets are 1.38 eV on Pd(111), 0.91 eV on Pd(100), and 0.76 eV on Pd(211). On Pd(111) and Pd(211), the reaction initiates and completes with the CH_3Cl^* and CH_3^* species on their preferred binding sites in the initial and final states, respectively. The Cl* atom removed from CH_3Cl^* binds on an fcc site in the final state on Pd(111); it binds on an h1 site right next to the step edge on Pd(211). On Pd(100), this elementary step initiates with CH_3Cl^* adsorbed on the surface through the Cl atom and one H atom, a binding structure almost isoenergetic as the preferred one. Once the Cl atom is broken off, CH_3^* binds on a top site, and Cl* binds on a nearby hollow site in the final state on Pd(100). The transition-state C-Cl bond lengths of this step are 2.58 Å, 2.24 Å, and 2.13 Å on Pd(111), Pd(100), and Pd(211), respectively.

A.3.2.13 $CH^* + * \rightarrow C^* + H^*$

The formation of atomic C* and H* through CH* dissociation is endothermic on Pd(111) by 0.41 eV, whereas exothermic on Pd(100) and Pd(211) by 0.55 eV and 0.59 eV, respectively. The activation energy barriers of this step are 1.38 eV, 0.51 eV, and 0.50 eV on Pd(111), Pd(100), and Pd(211), respectively, which suggests that the dissociation of CH* is much more difficult on Pd(111) compared to the other two less-coordinated facets. Despite the drastically different energetics, the reaction paths share similar structural characteristics on all three Pd facets. In the initial state, CH* always binds through the C atom to its preferred binding site with the C-H bond pointing vertically upwards (see Table A.1 and Figure A.3). Throughout the reaction, the C atom stays on the same binding site, while the C-H bond is elongated and bent towards the surface. Once

the C-H bond is fully broken, H* migrates to a nearby three- or four-fold hollow site. The C-H bond lengths at the transition state are 1.44 Å, 1.50 Å, and 1.49 Å on Pd(111), Pd(100), and Pd(211), respectively. Although the product of this step, C*, is a 'dead end' in the reaction network and does not contribute to the reaction flux for any product, it is a potential route towards coke formation, a well-known catalyst poison.

A.3.2.14 H removal steps from $CHCl_3$, $CHCl_2$, and CHCl

The last set of elementary steps discussed in this section are the following dehydrogenation steps: $CHCl_3^* + * \rightarrow CCl_3^* + H^*$, $CHCl_2^* + * \rightarrow CCl_2^* + H^*$, and $CHCl^* + * \rightarrow CCl^* + H^*$ (indicated by the pink dashed arrows in Figure A.4**).** Here, we demonstrate that, for each of these three elementary steps, either we were unable to determine any feasible reaction path from NEB calculations, or the activation energy barrier is much higher than its competing dechlorination step. Therefore, we exclude these three dehydrogenation steps from further analysis of the reaction network. The detailed reaction energetics and paths are discussed below and compared with those for the competing dechlorination steps.

A.3.2.15 $CHCl_3^* + * \rightarrow CCl_3^* + H^*$ (competing dechlorination step: $CHCl_3^* + * \rightarrow CHCl_2^* + Cl^*$)

On Pd(111), this dehydrogenation step initiates with the chloroform molecule in its preferred adsorption configuration, characterized by one H and one Cl atoms binding to two adjacent top sites. The C-H bond is stretched until it reaches a bond length of 1.48 Å in the transition state; meanwhile, the center of the entire molecule also moves closer to the surface. Once the H atom is completely broken away from $CHCl_3^*$, it binds to a nearby hcp site. The remaining CCl_3^* fragment is adsorbed on its preferred top site in the final state. This step is exothermic by 0.25 eV and

associated with an activation energy barrier of 1.16 eV on Pd(111), which is 0.72 eV higher than the barrier of the competing dechlorination step.

On Pd(100), the initial state of this step involves the adsorption of $CHCl_3$* through two Cl and one H atoms. This adsorption configuration is merely 0.01 eV less stable than the preferred structure through all three Cl atoms. Similar to the reaction path on Pd(111), this step proceeds with the elongation of the C-H bond as well as the movement of the entire molecule towards the surface. The transition-state C-H bond length is 1.42 Å. In the final state, the CCl_3* fragment binds to a top site, its most stable binding site, and the H* atom binds to an adjacent hollow site. The reaction energy of this step is -0.36 eV on Pd(100), and the activation energy barrier is 0.94 eV. On the other hand, the competing dechlorination step of chloroform on Pd(100) is associated with an activation energy barrier of merely 0.19 eV, which is 0.75 eV lower.

The initial state of this dehydrogenation step on Pd(211) is characterized by a titled geometry of the $CHCl_3$* molecule. In this configuration, the molecule binds to the surface through two Cl and one H atoms, and the center of the molecule lies on top of an h1 site, which is a three-fold hollow site right on the edge of the (211) terrace. This initial state is 0.12 eV less stable than the preferred adsorption of $CHCl_3$* on Pd(211) through two Cl atoms on top of the step edge. As the reaction proceeds, the C-H bond is stretched and eventually broken. The transition-state C-H bond length is 1.46 Å. In the final state, the CCl_3* fragment binds to its preferred t1 site on the step edge; the H* atom also binds on the step edge to an adjacent b1 site. This step is exothermic by 0.27 eV and associated with an activation energy barrier of 1.05 eV, 0.70 eV higher than the barrier for the competing dechlorination step on Pd(211).

A.3.2.16 $CHCl_2$ + * → CCl_2* + H* (competing dechlorination step: $CHCl_2$* + * → CHCl* + Cl*)*

On Pd(111), the dehydrogenation of $CHCl_2$* is exothermic by 0.20 eV. This step initiates with the molecular fragment adsorbed in its most-stable top-site configuration. As the reaction proceeds, the entire $CHCl_2$* fragment first shifts slightly towards an adjacent bridge site; then, the C-H bond starts to elongate. In the transition state, the C-H bond length is 1.60 Å. After the C-H bond is fully broken, the H* atom migrates to a nearby fcc site while the remaining CCl_2* fragment binds to its preferred bridge site. The activation barrier for this step is 1.03 eV, 0.75 eV higher than the barrier for the competing dechlorination step $CHCl_2$* + * → CHCl* + Cl*.

On Pd(100), we were unable to determine any feasible reaction path for the dehydrogenation of $CHCl_2$*. One of the C-Cl bond is always broken ($CHCl_2$* + * → CHCl* + Cl*) before the C-H bond scission can occur. We conclude that this step is not possible on Pd(100).

On Pd(211), the reaction energy and activation energy barrier of this dehydrogenation step are -0.23 eV and 0.93 eV, respectively. Despite the different surface geometries, the reaction path is similar to that on Pd(111). Initially, the $CHCl_2$* species binds to its preferred t1 site on the Pd(211) step edge. The reaction starts with the migration of the entire molecular fragment towards an adjacent b1 site on the step edge, followed by the elongation of the C-H bond. The transition-state C-H bond length is 1.60 Å. When the final state of this step is reached, the H* atom binds to an h1 site next to the step edge while the CCl_2* fragment stays on the b1 site, which is also the most stable binding site for this species. The activation energy barrier for the competing dechlorination step on Pd(211) is 0.33 eV, much less activated (by 0.60 eV) than this dehydrogenation step.

A.3.2.17 CHCl + * → CCl* + H* (competing dechlorination step: CHCl* + * → CH* + Cl*)*

The dehydrogenation of CHCl* is exothermic by 0.83 eV on Pd(111). The activation energy barrier for this step is 0.38 eV. In the initial state, the CHCl* species binds through the C atom to its preferred bridge site. In the early stage of the reaction, the entire molecular fragment diffuses towards an adjacent fcc site. After that, the C-H bond is stretched and eventually broken. The transition-state C-H bond length is 1.26 Å. In the final state, the CCl* fragment stays on the fcc site, its most stable binding site, while the H* atom migrates to an adjacent fcc site. Although this dehydrogenation step is associated with a relatively low barrier of 0.38 eV on Pd(111), it is still 0.22 eV higher than that for the competing dechlorination step.

Similar to the case for $CHCl_2$* dehydrogenation, we were unable to determine any possible reaction path for the dehydrogenation of CHCl* on Pd(100). The C-Cl bond is always broken (CHCl* + * → CH* + Cl*) before the C-H bond scission can occur.

On Pd(211), this step initiates with the CHCl* species adsorbed on its preferred b1 site on the step edge. As the reaction proceeds, the entire species moves towards an adjacent h1 site at the top of the (211) step. Then, the C-H bond is stretched and reaches a transition-state bond length of 1.45 Å. Once the C-H bond is fully broken, the H* atom diffuses towards the foot of the (211) step until it reaches an f2 site on the terrace while the remaining CCl* fragment stays on the h1 site. This step is exothermic by 0.57 eV and associated with an activation energy barrier of 0.64 eV, 0.40 eV higher than the barrier for the competing dechlorination step CHCl* + * → CH* + Cl* on Pd(211).

A.3.3 Analysis of Reaction Network and Potential Energy Diagram (PED)

In this section, we first determine the reaction pathways for chloroform hydrodechlorination on all three Pd facets based on the reaction energetics shown in Figure A.4**.** One observation can be made as we examine the activation energy barriers of all the elementary steps: the activation barriers of the hydrogenation steps are much higher than those of the competing dechlorination steps. Therefore, for any partially dechlorinated surface intermediates, the subsequent dechlorination step is energetically favored over the hydrogenation step. For example, after the $CHCl_2$* species is formed from the initial dechlorination step of chloroform, the hydrogenation of $CHCl_2$* to form CH_2Cl_2* is much more activated than the dechlorination step to form CHCl*, by 0.97 eV, 0.65 eV, and 0.81 eV on Pd(111), Pd(100), and Pd(211), respectively. The same observation can be made for the CHCl* species: the activation barrier for its dechlorination step to form CH* is lower than its hydrogenation step to form CH_2Cl* by 0.91 eV, 0.76 eV, and 0.59 eV on Pd(111), Pd(100), and Pd(211), respectively. We thus conclude that the hydrogenation steps should occur after chloroform is fully dechlorinated to the CH* species; the chloroform hydrodechlorination should proceed through the following sequence of elementary steps on all three Pd facets:

$$CHCl_3 \xrightarrow{-Cl} CHCl_2 \xrightarrow{-Cl} CHCl \xrightarrow{-Cl} CH \xrightarrow{+H} CH_2 \xrightarrow{+H} CH_3 \xrightarrow{+H} CH_4$$

The proposed reaction pathway also suggests that the fully dechlorinated product, methane, should be the preferred chloroform hydrodechlorination product on Pd catalysts. The formation of any partially dechlorinated product (CH_2Cl_2 or CH_3Cl) is not energetically favorable. These conclusions agree with the experimental findings by Velázquez and coworkers that methane was produced as the main chloroform hydrodechlorination product on Pd catalysts with over 90% selectivity.[375]

As the reaction pathway for chloroform hydrodechlorination was determined, we constructed the potential energy diagrams along the proposed pathway on all three Pd facets, as shown in Figure A.6. The PEDs allow for direct comparison among the reaction energetics of different Pd facets, thereby elucidating the degree of structure sensitivity of this catalytic reaction. On each of the three PEDs, the transition state of the initial dechlorination step ($CHCl_3^* + * \rightarrow CHCl_2^* + Cl^*$) is the highest-energy transition state. After the initial bond-breaking step, the reaction goes energetically downhill until the fully dechlorinated state ($CH^*|3Cl^*|6H^*$) is reached. Therefore, the initial dechlorination step likely limits the dechlorination activity. Among the three Pd facets, the initial dechlorination barrier is the lowest on Pd(100) with an activation energy barrier of 0.19 eV, followed by Pd(211) (0.35 eV) and Pd(111) (0.44 eV). The inset in Figure A.6 illustrates the competition between the initial dechlorination of chloroform and the desorption of chloroform from the surface. This competition is essential for the activity of a hydrodechlorination catalyst, as the adsorbed chloroform molecule should be dechlorinated readily before it is desorbed from the surface. On Pd(111), the dechlorination barrier (0.44 eV) is 0.24 eV higher than the desorption barrier (0.20 eV), suggesting a higher tendency for a $CHCl_3^*$ molecule to desorb than to proceed with further surface reactions (at room temperature, a difference of every 0.06 eV in activation barriers corresponds to an order of magnitude difference in rates). On both Pd(100) and Pd(211), however, the dechlorination barriers are lower than the desorption barrier, by 0.08 eV and 0.15 eV (which suggests that the dechlorination step is more likely to occur due to approximately 23-fold and 344-fold difference in rates at room temperature), respectively. Therefore, we conclude that the more open facets and the step edges of a Pd particle are more active than its close-packed facet for chloroform hydrodechlorination.

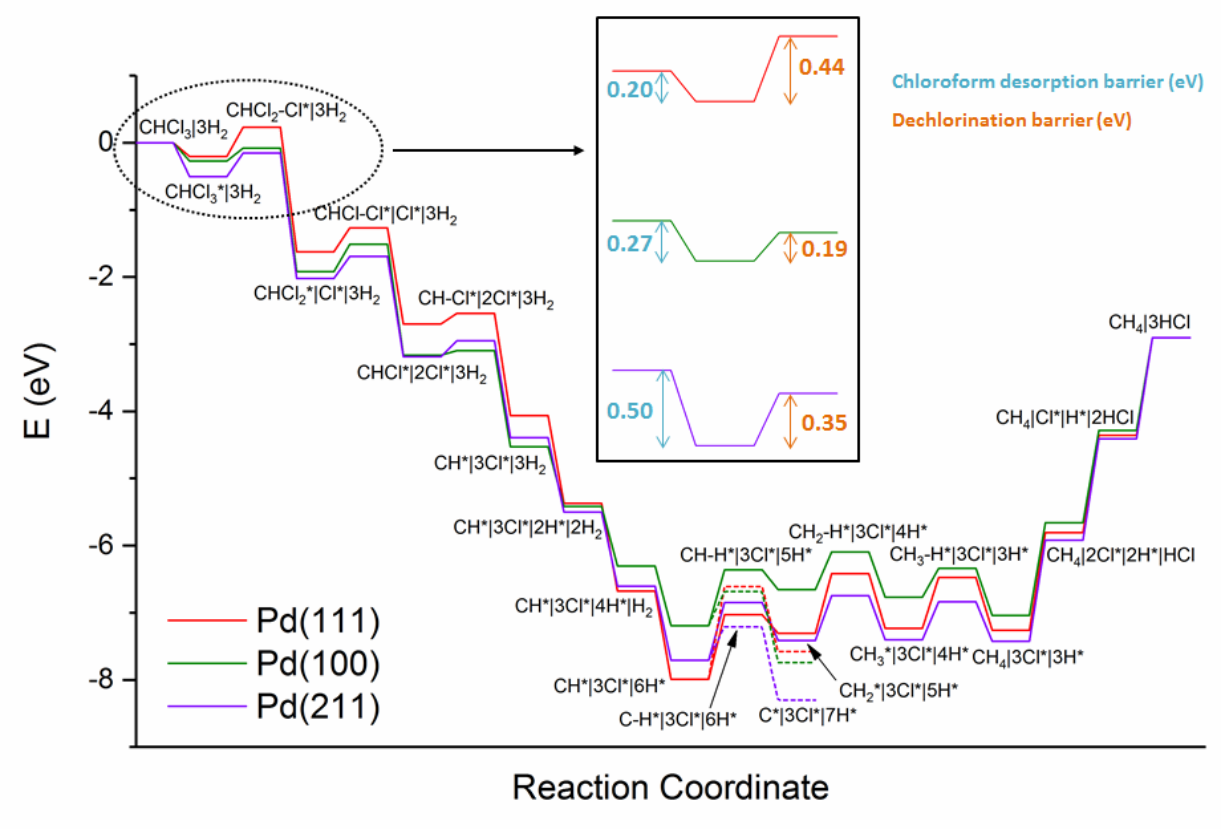


Figure A.6 Potential energy diagram for methane formation from chloroform hydrodechlorination through the proposed reaction pathway on Pd(111) (red lines), Pd(100) (green lines), and Pd(211) (purple lines). Dash lines indicate the formation of C* through CH* dissociation. The inset indicates the comparison between the chloroform first dechlorination barrier and the chloroform desorption barrier. '*' denotes adsorbed species. '|' indicates infinite separation with each surface species at 1/9 ML coverage. '-' denotes the bond made/broken in a transition state.

A.4 Analysis of Site-Blocking Species

We caution readers that our analysis of the reaction energetics in the previous section is based on DFT results obtained on clean surfaces. As shown in Figure A.6**,** the fully dechlorinated state (CH*|3Cl*|6H*) corresponds to a deep energy valley on all three PEDs, which is 7–8 eV more stable than the initial reactants in the gas phase. This strongly indicates that these atoms and molecular fragments (CH*, Cl*, H*) may be present on the surface at a certain coverage,

potentially significant, under realistic reaction conditions. Additionally, Pd(100) and Pd(211) can effectively catalyze the formation of C atoms through CH dissociation. On both surfaces, the activation energy barrier for the CH* dissociation step (CH* + * → C* + H*, E_a = 0.51 eV and 0.50 eV on Pd(100) and Pd(211), respectively) is much lower that that for the CH* hydrogenation step (CH* + H* → CH_2* + *, E_a = 0.79 eV and 0.86 eV on Pd(100) and Pd(211), respectively). As a result, an even more stable atomic state (C*|3Cl*|7H*) can be formed. The presence of strongly bound atomic species raises concerns for the steady state catalytic performance of the under-coordinated sites on Pd(100) and Pd(211), predicted to be more active towards chloroform hydrodechlorination based on the clean-surface DFT results, under realistic conditions.

Based on their respective binding strengths summarized in Table A.1**,** we can make speculations about which species might be responsible for the site blocking on different Pd facets. For example, C* binds significantly stronger on the two under-coordinated facets than on Pd(111) (by 1.02 eV and 0.86 eV for Pd(100) and Pd(211), respectively). Similarly, Cl* binds 0.15 eV and 0.16 eV stronger on Pd(100) and Pd(211), respectively, than on Pd(111). On the other hand, H* binds the strongest to Pd(111) among the three Pd facets, likely due to its preference for three-fold hollow sites. In order to further explore the tendency for Cl* and C* poisoning the under-coordinated sites of Pd(100) and Pd(211), we studied the diffusion of these two atomic species. We observed that, while the diffusion of Cl* is always facile, the diffusion of C* on Pd(100) and Pd(211) is associated with high activation energy barriers of at least 1.1 eV, indicating that C* may become a permanent site-blocking species and hinder the activity of under-coordinated sites on a Pd catalyst particle under steady state conditions. The calculated diffusion barriers and paths on all three Pd facets are

summarized in Table A.2**.** The PEDs for C* and Cl* spillover on Pd(211) from step edge to terrace are shown in Figure A.7 and discussed in details in the following paragraphs.

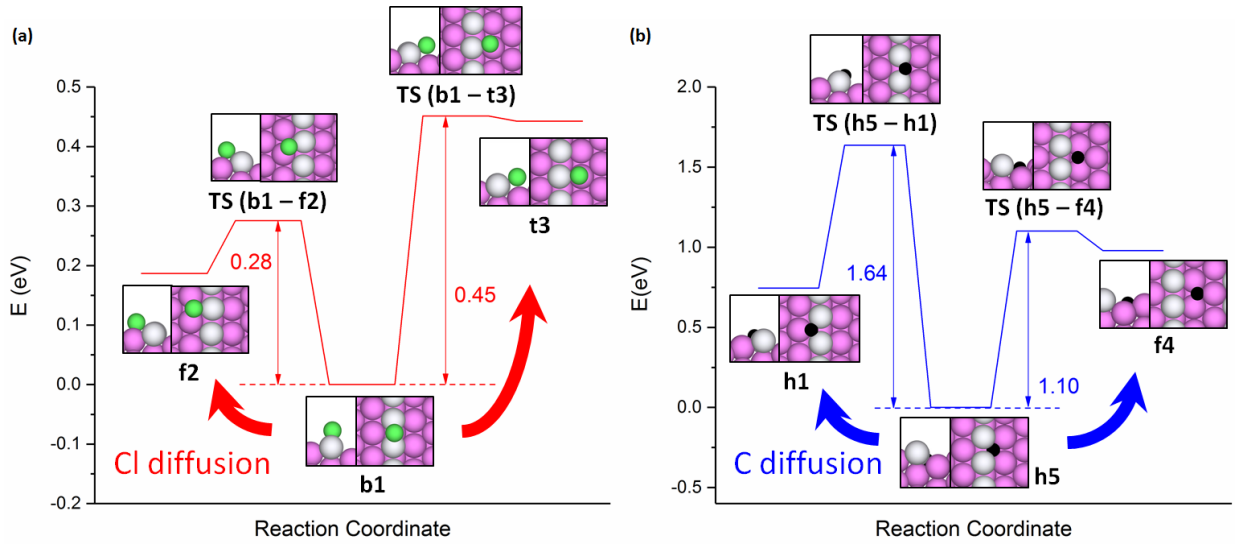


Figure A.7 Potential energy diagram for diffusion of (a) atomic chlorine and (b) atomic carbon on Pd(211). The insets illustrate the side and top views of the stable binding structures and transition states. In each diagram, the energy zero is chosen as the energy of the preferred adsorption structure (b1 and h5 for Cl* and C*, respectively). The arrows and numbers (in eV) denote the activation energy barriers for diffusion from the preferred adsorption structure. Color code: Grey – step-edge Pd; pink – other Pd; black – C; green – Cl.

Table A.2 Diffusion barriers and paths of Cl* and C* on Pd(111), Pd(100), and Pd(211).

Surface	**Diffusion barrier (eV)[a]**		**Diffusion path[b]**	
	Cl*	C*	Cl*	C*
Pd(111)	0.17	0.64	fcc → (bridge) → hcp	fcc → (bridge) → hcp
Pd(100)	0.16	1.13	hollow → (bridge) →hollow	hollow → (bridge) →hollow
Pd(211)[b]	0.28	1.10	b1 → (h1) → f2	h5 → (b5) →f4

[a] Only the lowest diffusion barriers and associated diffusion paths are listed. Parentheses in the diffusion paths denote the transition states.
[b] On Pd(211), we studied the diffusion from step edge to terrace.

The calculated potential energy diagram (PED) for the diffusion of Cl* on Pd(211) is illustrated in Figure A.7 (a). On Pd(211), the most stable binding site for Cl* is the b1 site, which is a bridge site on top of the step edge. The diffusion of Cl* away from its preferred b1 site can occur through two possible paths: the migration over the top of the step edge towards an f2 site, a three-folder hollow site on the terrace; or migration downwards along the (211) step towards a t3 site, a top site at the foot of the step. As shown in Figure A.7 (a), the b1 – f2 path is the energetically favorable diffusion path, which is associated with an activation energy barrier of 0.28 eV. The diffusion barrier for the b1 – t3 path is 0.17 eV higher. Nonetheless, both diffusion processes are associated with moderate barriers comparable to the calculated activation energy barriers of the dechlorination steps (0.07 – 0.44 eV). Therefore, despite the strong binding of Cl* on the Pd(211) step edge, it can readily diffuse away from the step sites under chloroform hydrodechlorination conditions. On Pd(111) and Pd(100), we observed low barriers for Cl* diffusion (0.17 eV and 0.16 eV, respectively, Table A.2), which suggests that Cl* should be a mobile species on Pd regardless of surface facet.

The calculated PED for the diffusion of C* on Pd(211) is shown in Figure A.7 (b)**.** On Pd(211), the preferred binding site for C* is the h5 site, a four-fold hollow site over the (100)-like step. Similar to Cl*, two paths exist for the diffusion of C* away from its preferred h5 site: the C* atom can climb over the top of the step edge and diffuse to an h1 site, a three-fold hollow site on the edge of the (211) terrace; or it can move downwards the foot of the step and reach an f4 site, another three-fold hollow site on the terrace. In this case, both diffusion paths are associated with large activation energy barriers. The h5 – f4 path is the easier one among the two diffusion paths, yet it still needs to overcome a diffusion barrier of 1.10 eV. The barrier of the other path (h5 – h1)

is even higher by 0.54 eV. Unlike Cl*, C* has a strong tendency to stay on its preferred h5 site on Pd(211). On Pd(100), we obtained a similarly high diffusion barrier of 1.13 eV, while the barrier is much lower on Pd(111) (0.64). The highly activated C* diffusion process on the open Pd(100) facet and the Pd(211) step edge is likely caused by the strong affinity of C* to the four-fold hollow sites present on these two surfaces. It is worth noting that the barriers of at least 1.1 eV for C* diffusion on Pd(100) and Pd(211) are well above the activation energy barrier of any elementary step along the preferred reaction pathway $CHCl_3 \rightarrow CHCl_2 \rightarrow CHCl \rightarrow CH \rightarrow CH_2 \rightarrow CH_3 \rightarrow CH_4$ (all below 1 eV, see Figure A.4). Due to the difficult diffusion of C* on Pd(100) and Pd(211), we postulate that the under-coordinated sites on a Pd catalyst might be poisoned by C* under steady state chloroform hydrodechlorination conditions. The accumulation of C* may eventually lead to coking or carbide formation. Pd carbiding has been reported previously during the hydrodechlorination of Dichlorodifluoromethane (CCl_2F_2)[378,379] and tetrachloromethane (CCl_4).[380] Bonarowska and co-workers observed the formation of PdC_x phases on their Pd/C catalysts after CCl_4 hydrodechlorination at reaction temperatures as low as 90ºC.[380] Our results point to the formation of C* on the under-coordinated Pd sites as a possible mechanism towards carbide formation.

In the future, the investigation of the Pd-catalyzed chloroform hydrodechlorination reaction will greatly benefit from the construction of a comprehensive microkinetic model, which has been widely applied in heterogeneous catalysis research for probing reaction kinetics and mechanisms.[41,59,381] For future microkinetic modeling studies, it is potentially desirable to repeat the DFT calculations for chloroform hydrodechlorination on Pd surfaces with suitable coverages of reaction intermediates. Because strongly bound atomic species, particularly C*, were observed

in our clean-surface DFT calculations, it is expected that the surface coverages of these species will build up during the reaction. The presence of site-blocking species has been shown to impact both the reaction thermochemistry and kinetics, and therefore, coverage-dependent microkinetic models are typically required for accurate description of the active sites.[15,382] Nonetheless, the DFT results presented in this work on clean Pd(111), Pd(100), and Pd(211) should serve as a good parameter set for constructing an initial microkinetic model, which, in combination with parameter estimation analyses (i.e., varying DFT parameters to match experimental kinetics results),[12,41] could provide valuable insights towards the nature of the active sites under realistic reaction conditions.

A.5 Conclusions

Plane-wave DFT calculations (GGA-PW91) were performed to examine the reaction energetics for chloroform hydrodechlorination on three Pd facets: Pd(111), Pd(100), Pd(211). The preferred binding structures and energies of all the surface intermediates were identified on these three Pd facets. The binding strength generally increases in the following order: Pd(111) < Pd(100) < Pd(211). Transition states and activation energy barriers were then identified for all the elementary steps in the reaction network. On all three Pd facets, the reaction proceeds through a pathway towards methane formation, where $CHCl_3$* is first fully dechlorinated in successive elementary steps to CH* and then hydrogenated to CH_4. Methane should be the preferred carbon-containing hydrodechlorination product, as the production of any partially dechlorinated chloromethane product is energetically unfavorable. The competition between the desorption of chloroform and its initial dechlorination to form $CHCl_2$* likely determines the hydrodechlorination activity of a

catalyst. The activation energy barrier for the initial chloroform dechlorination step is the lowest on Pd(100) (0.19 eV), followed by Pd(211) (0.35 eV) and Pd(111) (0.44 eV). On Pd(111), the desorption of chloroform is energetically favored over its dechlorination. However, the dechlorination step is easier than desorption on Pd(100) and Pd(211). This observation suggests that the more open facet and the edge sites of a Pd particle, if not poisoned under reaction conditions, can be more active towards chloroform hydrodechlorination than its close-packed facets. The reaction PEDs also indicate that strongly bound surface species (C*, CH*, Cl*, and H*) may be present under realistic reaction conditions. The under-coordinated sites on Pd(100) and Pd(211) are more prone to poisoning by atomic C*. Although beyond the scope of this study, future microkinetic modeling studies to determine the actual surface coverage, as well as DFT studies on high-coverage surfaces, can facilitate further understanding of the chloroform hydrodechlorination mechanism on Pd catalysts.

APPENDIX B

A THERMODYNAMIC PERSPECTIVE ON THE STEPWISE CONVERSION OF METHANE TO METHANOL OVER CU-EXCHANGED SSZ-13

B.1 Introduction

Selective conversion of methane to methanol is an age-old challenge, which has attracted significant attention recently due to the increased availability of natural gas. The major challenge for this reaction is to only activate the first C-H bond in methane and prevent overoxidation to thermodynamically more stable CO/CO_2. Therefore, an indirect industrial process has been developed, where methane is converted to syngas,[383] which is then transformed to longer chain hydrocarbons or methanol.[384] This conversion takes place at high temperatures and pressures, and is economically unfeasible in remote extraction sites, where such technology would be most needed. To achieve on-site conversion of methane to more valuable and easier to transport methanol, it would be desirable to find a direct route for this reaction, operated at mild conditions. In nature, this is achieved by the enzyme methane monooxygenase, where Cu- and Fe-oxo clusters serve as the active sites.[385–387] Inspired by this process, research has recently focused on

reproducing similar active sites in heterogeneous catalysts.[388,389] In particular, Cu-exchanged zeolites have drawn significant attention in this context.[390–398]

Due to strict conversion/selectivity limits in the catalytic conversion of methane to methanol,[399] the stepwise conversion process shows greater promise in comparison with continuous-flow process.[400] Here, the catalyst is activated in an oxidizing atmosphere, followed by exposure to methane. Contact with methane triggers the formation of immobile surface methoxy species (i.e. oxygenates of CH_4 such as methanol), which are subsequently extracted using water vapor.

After the initial discovery of the activity of transition-metal (TM) exchanged zeolites, several oxidants[391,401–403] and zeolite structures have been tested for this reaction.[393,398,401,404] However, despite significant efforts, the nature of the active centers is still under debate. This is best illustrated for Cu-exchanged Mordenite, where different studies report the presence of either Cu dimers[390,392,401,405–407] or trimers[394] as active sites for this chemistry. Further, several studies for different zeolite structures indicate a change in the active sites with the experimental conditions.[396,405,408,409] At the same time, full experimental characterization of a complex system like a zeolite is challenging. These difficulties are rooted in the presence of a distribution of active sites, which show overlapping signals in Raman spectroscopy and UV-vis spectroscopy.[404,410] Even combining information with EXAFS data on coordination environments and bond distances requires a series of assumptions about the active sites.[408,409]

Theoretical modeling can support and extend these experimental assignments by systematically considering an extensive set of potential active site structures and calculating their relative thermodynamic stability.[411,412] This information can then be summarized in phase diagrams, which reveal the most stable phase under various experimental conditions.[413–415] In the conversion of

methane to methanol using Cu-exchanged zeolites, attempts so far have aimed to describe the relative stability of different Cu sites in Mordenite,[416] ZSM-5,[395] or SSZ-13.[404] These studies have, however, considered only few potential active sites, which does not capture the complex distribution of sites expected to be present in such a zeolite system.

The ideal candidate zeolite-framework to study the site-speciation of Cu is SSZ-13 (Cu-SSZ-13). It is a zeolite in the Chabazite framework with a highly symmetrical primitive unit cell, which limits the number of possible Cu configurations.[412] This material has been shown to efficiently convert methane to methanol[391,393,397,404,408,409] and a significant body of work on characterization of the active centers in this material exists.[404,408,409] Lastly, Cu-SSZ-13 has been extensively studied in the context of deNO_x-SCR,[417,418] and it is possible to extend the methodology developed to describe active sites during deNO_x-SCR[414] to gain a comprehensive understanding of Cu-SSZ-13 in the methane to methanol conversion.

In this work, we use theoretical modeling to study the nature of the active centers in Cu-SSZ-13 during the stepwise conversion of methane to methanol. We develop a detailed theoretical model based on the chemical potential of Cu in various monomer, dimer and trimer structures in the zeolite matrix and use phase diagrams to determine the thermodynamically preferred state of Cu. We find that, depending on the local Al distribution, either $Cu_2O_2H_2$ or Cu_2OH, is stabilized during catalyst activation. When methane is introduced, methanol adsorbed to Cu monomers is formed, which desorbs when the water pressure in the system is increased. Our findings are capable of rationalizing experimental EXAFS measurements reported in the literature.[408]

B.2 The Stepwise Conversion of Methane to Methanol

One of the major challenges in converting methane to methanol is to prevent methane overoxidation to thermodynamically preferred CO_2. In catalytic conversion, selectivity/conversion limits have been derived for this reaction and several strategies have been suggested to circumvent these problems.[399] For transition metal exchanged zeolites in particular, the stepwise conversion of methane to methanol using O_2 as oxidant has drawn significant attention.[400] The catalyst is first activated in an O_2 containing atmosphere at high temperature to generate the active sites. In a subsequent step, the system is cooled down and exposed to methane. Interaction with methane triggers the formation of surface methoxy species (i.e. oxygenates of CH_4 such as methanol), which cannot desorb. Since further oxidation requires desorption of methanol and regeneration of the active sites requires oxidative conditions, stably adsorbed surface methoxy species are protected from overoxidation. In a final step, methanol is extracted at lower temperature by introducing water vapor.

For the studies reported in the literature, the fundamental steps remain similar, i.e. activation is followed by methane exposure and methanol extraction. However, the exact experimental conditions can vary between different research groups, which can influence methanol yields.[398] For Cu-SSZ-13, a systematic analysis of the impact of various experimental parameters on the performance at each step of this process has been reported in the literature.[408] Here, we will focus on conditions described as optimal for Cu-SSZ-13 by Pappas et al. (Figure B.1), which are as follows: (1) Initial exposure to 1 bar O_2 at 323 K, (2) Ramping the temperature to 773 K, under 1 bar O_2, (3) Stopping the O_2 flow at 773 K, (4) Cooling the system to 473 K and exposure to 1 bar of CH_4, (5)Stopping the CH_4 flow at 473 K, (6) Exposure to 0.1 bar of H_2O at 473 K;

Typically, at points 1, 3 and 5, conditions change abruptly (Figure B.1), while the system is kept at specific conditions for several hours for points 2, 4, and 6 (Figure B.1). At some points of the process (e.g. after 3, 4, and 5), the system is exposed to inert gases (such as He) to remove excess gas pressures from previous exposure. Inert gases do not influence site speciation and are therefore omitted from our discussion.

While the externally applied gas pressures are known, residual pressures of the other gases, caused by impurities in the supplied gases or small amounts of gases adsorbed in the zeolite nanopores from previous exposure, will also be present. The exact values will depend on the experimental setup and the detailed process protocol. However, since residual gas pressures are impossible to measure experimentally, we use approximate values for them. If not explicitly stated otherwise, we assume a logarithmic O_2 gas pressure $\ln(P^{O_2}/P_0)$=-7, a logarithmic H_2O gas phase pressure $\ln(P^{H_2O}/P_0)$=-7 and after exposure to CH_4, a residual logarithmic CH_4 pressure $\ln(P^{CH_4}/P_0)$=-9. All pressures are calculated with respect to a reference pressure P_0 of 1 bar. The list of all parameters at each point along the stepwise conversion process of methane to methanol is given in the Table B.1. Careful testing revealed that the choice of residual pressures has only a subtle effect on results and wherever variation of the residual pressures affects the results, we explicitly discuss them.

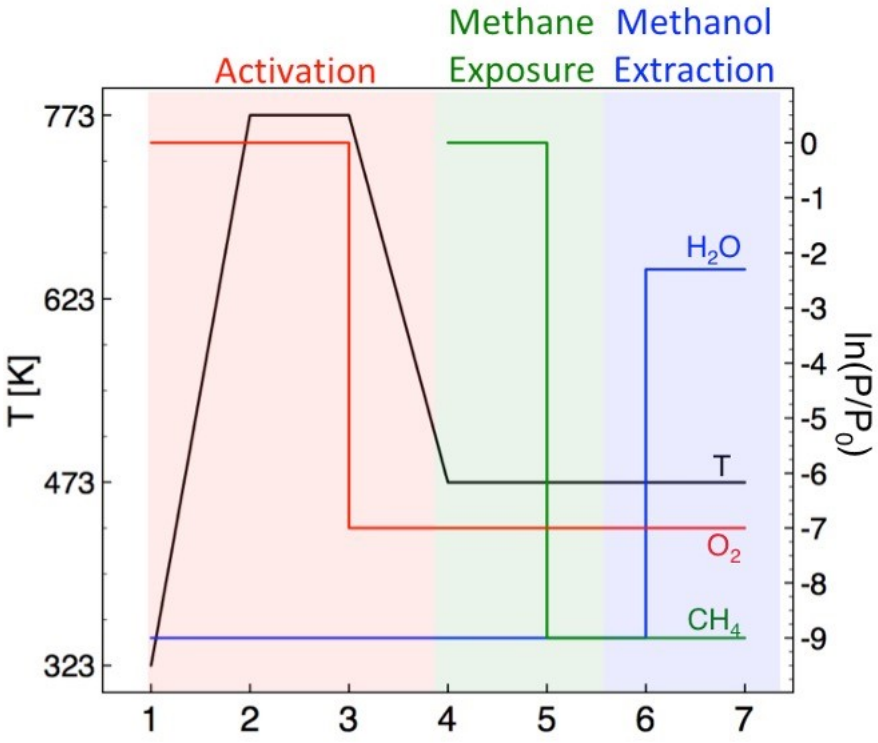


Figure B.1 A representation of the conditions during the stepwise conversion of methane to methanol. The temperature (black line) is given in Kelvin and gas-phase pressure of various participating species (red, green, and blue lines) are given as natural logarithms with respect to a reference pressure P_0 of 1 bar. The temperature and partial pressure profiles of various components correspond to the left and right y-axis, respectively. Shaded regions correspond to catalyst activation (red), methane exposure (green) and methanol extraction (blue), respectively.

B.3 Computational Methods

All calculations were performed using the Vienna Ab-Initio Simulation Package (VASP),[348,419] a plane wave code using PAW pseudo potentials,[123] adapted by Joubert and Kresse.[124] All calculations were performed using an energy cut-off for plane waves of 420 eV and were restricted to the Γ-point. The basic unit cell parameters for periodic calculations are given in the literature[420] and the zeolite volume was set to 830 $Å^3$. All structures were optimized using Density Functional Theory in the parameterization of Perdew, Burke and Ernzerhof[421] and van der Waals interactions

were introduced using the Tkatchenko-Scheffler force field.[422] Prior to optimization a 5 ps molecular dynamics simulation at 500 K using the Andersen thermostat[423] was performed and three different structures from the last 1 ps of this simulation were optimized. In all calculations the spin-states of the different clusters remained fixed and the spin-state leading to the lowest energy was used for further analysis. All minimum spin states are given in Table B.2. For these spin states RPA calculations were performed.[424,425] Here the energy cut-off was increased to 600 eV and the energy cut-off for the response function was set to 250 eV. Furthermore, RPA calculations were restricted to the spin ground state determined in DFT calculations. In a subsequent step, harmonic vibrational frequencies using the frozen phonon approach were calculated at PBE-TS level. Vibrational and translational entropies as well as zero point vibrational corrections for gas phase molecules and zeolite unit cells were calculated using the code thermo.pl,[426] a code provided by the National Institute of Standards and Technology, and only vibrational frequencies above 50 cm^{-1} were considered in the analysis. For computational efficiency we reproduced dimer configurations d-A through d-D, which reach over two adjacent double six O-ring structures, in a single unit cell using periodic boundary conditions, to allow for higher computational efficiency. To confirm the validity of this approach, we compared energies for dimers in the Al configuration C for a single and double primitive unit cell and find that energies per Cu atom calculated at PBE-TS level lie within 6 kJ/mol (see Section B.9.3). Such small energy differences indicate that constructing dimer and trimer structures in a single primitive unit cell can be seen as good approximation. Gas phase molecules were modeled in a 10 Å x 10.1 Å x 12 Å box.

B.4 The Thermodynamic Model

B.4.1 Included Structures

We focus on the Cu exchanged zeolite SSZ-13. SSZ-13 is a material with the chabazite structure, the zeolite framework structure with the smallest primitive unit cell. This feature reduces the complexity of the system, while still retaining all basic features associated with zeolites, which makes this material the ideal test-system for zeolite catalysis. The framework is composed of corner-sharing SiO_4 tetrahedral (T-sites), which form a double six O-ring (6R) building block, containing 12 T-sites representing one-unit cell (see Figure B.2(a)). The unit cells are connected by four O-rings, which leads to a medium-sized pore and the formation of eight O-rings (8R) (see Figure B.2(c)). The framework is activated by replacing Si by Al in some of the T-sites. Compared to Si, Al has one less valence electron and cannot saturate all bonds to the surrounding O atoms. This electron-deficiency is compensated for by the presence of positively charged ions. Most commonly, these are Brønsted protons, but since we are interested in Cu-exchanged zeolites, we choose Cu (monomers) and Cu-clusters (dimers and trimers), which are formed after Cu ion exchange, as compensating ions.

The distribution of Al atoms is controlled during synthesis, but throughout this work, we assume that, similar to defects in solids, a distribution of local Al configurations exists in the zeolite.[411,427] The exact distribution of local Al configurations will most likely vary between different zeolite samples. Typically for this chemistry, SSZ-13 samples in mid to high Si/Al ratio range (>8), have been found to be the most promising in terms of methanol yield per Cu atom.[393] We, therefore, model unit cells containing one (Si/Al=11) and two (Si/Al=5) Al atoms, which, under the assumption of good Al dispersion, most likely represent the majority of the local Al configurations

present in SSZ-13 zeolites used in the literature. Additionally, we assume that the Loewenstein rule is valid,[428] i.e. Al-O-Al bonds are not allowed, and include all possible, symmetrically different Al configurations in the primitive unit cell. This leads to one Al configuration for the 1Al case and five different Al configurations for the 2Al case (2Al-A through 2Al-E),[429] all of which are shown in Figure B.2(b).

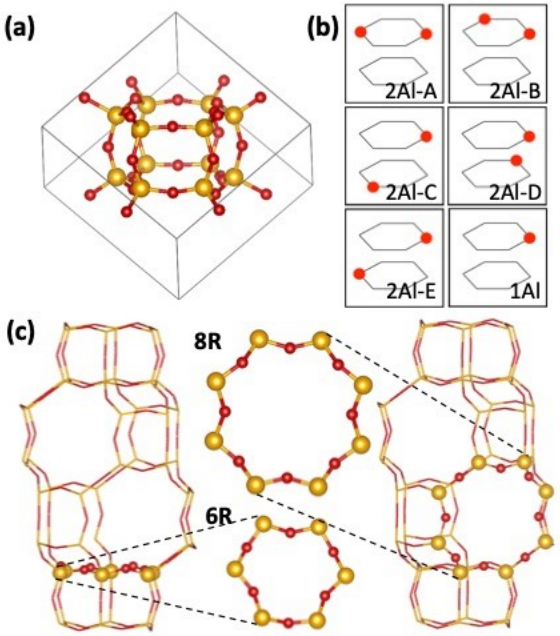
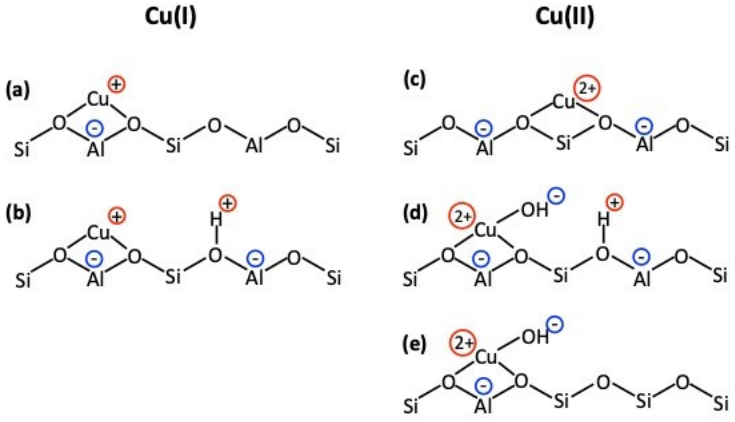


Figure B.2 (a): The primitive unit cell of the purely siliceous SSZ-13 framework. (b): Schematic representation of the various local Al configurations for Cu_1 exchange studied in a single unit cell. Si(Al)-O-Si bonds in the six O-rings are shown as black lines, Al positions are marked by red circles. (c): Extended structure of SSZ-13 zeolite, with highlighted Cu_1 exchange positions in the six O-ring (6R) and eight O-ring (8R). Highlighted structures, displayed using a ball and stick model, while the remaining framework is displayed using a stick representation, are linked to framework models using dashed lines. In the atomistic representation, Si is shown as yellow spheres and O as red spheres.

To study Cu speciation within the SSZ-13 zeolite framework, we consider an extensive set of plausible Cu sites. We start our discussion with mononuclear Cu (Cu_1) sites included in our model, which have been extensively discussed in the literature,[411,413,414,430–432] followed by the dimer and trimer sites.

In zeolites, Cu_1 can exist in two different oxidation states, namely Cu_1(I) and Cu_1(II), which require one and two compensating charges, respectively. In Scheme B.1, several ways to generate Cu_1(I) and Cu_1(II) are shown. When only one Al atom is close to the Cu atom, as is the case for the 1Al configuration, one electron is transferred from Cu to the Al-O bonds and Cu_1(I) will be formed (see Scheme B.1(a)). When two Al atoms are present close to the Cu atom, as is the case in 2Al-A through 2Al-E, Cu_1(I) will require the presence of a proton to compensate for the second negative charge (see Scheme B.1(b)). If the proton is not present, Cu_1(II) will be formed (see Scheme B.1(c)). Additionally, it is possible to form Cu_1(II), if a water molecule is split to form Cu_1(II)-OH and a proton adsorbed to an O atom adjacent to the second Al atom (see Scheme B.1(d)). In a similar way, Cu_1(II)-OH bound to the 1Al configuration forms Cu_1(II) (see Scheme B.1(e)).



Scheme B.1 Schematic representation of different ways to generate Cu_1(I) and Cu_1(II) in zeolites. For Cu_1(I) one uncompensated charge needs to be present, for Cu_1(II) two uncompensated charges are required. Cu_1(I) can either be generated by adding Cu to a 1Al unit cell (a) or by adding a proton and Cu atom to a 2Al unit cell (b). Cu_1(II) can be generated by adding a Cu atom to a 2Al unit cell (c), by adding Cu-OH and a proton to a 2Al unit cell (d) or Cu-OH to a 1Al unit cell (e). In schematic representations black lines show bonds, blue circles represent negative charges and red circles represent positive charges.

Cu_1 species can be stabilized in the 6R or the 8R (exchange sites are shown in Figure B.2(c)), and it has been reported that Cu_1 coordinates with H_2O molecules at lower temperatures.[413,414] We, therefore, explore all the different possibilities to form Cu_1(I) and Cu_1(II) located in a 6R and 8R, for all Al configurations shown in Figure B.2(b), and allow for the coordination of Cu_1 with up to six H_2O molecules, which will allow for the formation of Cu_1-hexaaqua species. A detailed discussion of all Cu_1(II) has been given in the literature and we rely on the published structures[414]. For Cu_1(I), we follow a similar strategy. Only the most stable Cu_1(I) and Cu_1(II) structures for a given number of adsorbed H_2O molecules are included in our thermodynamic model. In phase diagrams, these structures are labeled Cu(I)+nH_2O and Cu(II)+nH_2O for Cu_1(I) and Cu_1(II) sites, respectively, with n adsorbed H_2O molecules.

In the literature, several different Cu dimers and trimers have been suggested to be active in the conversion of methane to methanol.[394,401,404,416] Similar to the Cu_1 case, Cu in dimers and trimers will bind to O atoms adjacent to framework Al, but these structures are generally too large to fit into the double 6R structure of a unit cell. We, therefore, constructed four different local Al configurations reaching over adjacent unit cells, two of which are located in the same 8R (see D-A and D-B in Figure B.3(a) and 8R in Figure B.3(b)).[404,410] The other two Al configurations allow for Cu dimers bridging a 6R and an adjacent 8R (D-C and D-D in Figure B.3(a) and 6R/8R Figure B.3(b)). We construct $Cu_2O_yH_z$ (y=1, 2; z≤y) dimers, for all four Al configurations (D-A though D-D). Additionally, the presence of trimers bound in 8R structures has been suggested for Mordenite.[394] We, therefore, include $Cu_3O_3H_z$ (z≤3) clusters for the D-A and D-B Al configurations. In the subsequent text, the different clusters are denoted by X-$Cu_xO_yH_z$, where X

stands for A through D, which denotes Al configurations D-A through D-D, while x, y and z describe the cluster stoichiometry.

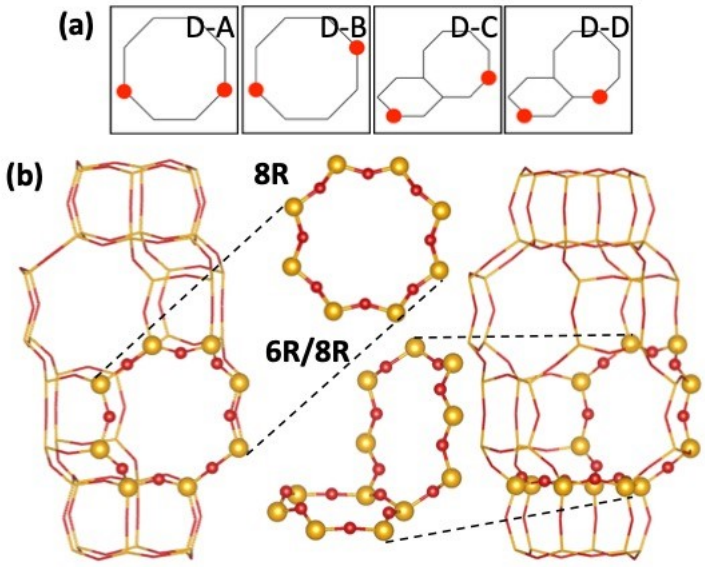


Figure B.3 (a) Schematic representation of local Al configurations for dimer/trimer anchoring. Si(Al)-O-Si bonds are shown as black lines, the Al positions are marked by red circles. (b) Extended structure of SSZ-13 zeolite, with highlighted dimer exchange sites in the eight O-ring (8R) and bridging a six O-ring and an eight O-ring (6R/8R). Highlighted structures, displayed using a ball and stick model, while the remaining framework is displayed using a stick representation, are linked to framework models using dashed lines. In the atomistic representation, Si is shown as yellow spheres and O as red spheres.

All structures were optimized using the PBE-TS[229,422] density functional and periodic boundary conditions as implemented in VASP.[348,419] Several spin states were probed for the different configurations. The spin ground state is used for further analysis and relative energies for the different spin states are given in Section B.9. All optimized structures are shown in Figure B.4.

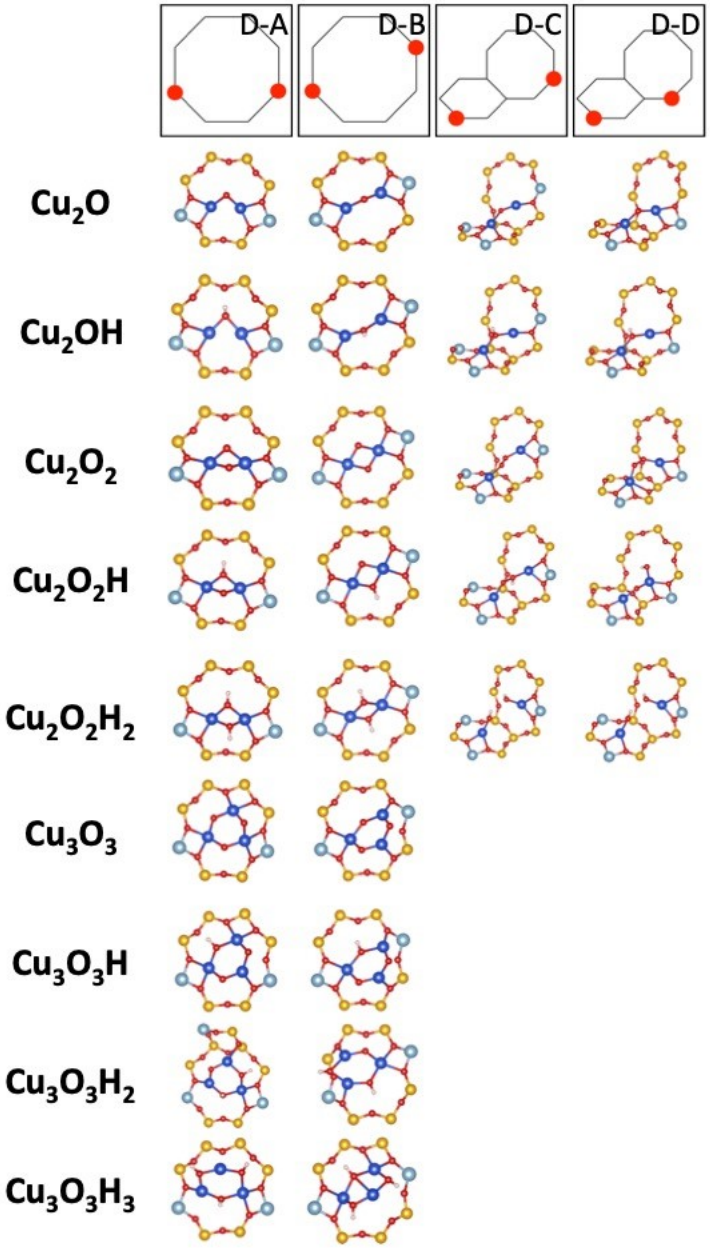


Figure B.4 A graphical representation of dimer and trimer structures included in the thermodynamic model. On top the Al configuration for the studied exchange sites is shown and on the left the studied stoichiometries are given. Atomistic pictures show the optimized structures. In atomistic pictures red atoms correspond to O, yellow atoms to Si, blue atoms to Cu, white atoms to H and blue-grey atoms to Al. As described in the caption of Figure B.2 and Figure B.3, in the schematic representations black lines show Si-O-Si bonds and red circles indicate the position of Al. The presence of a third Al atom in atomistic structures of Al configuration D-C is an artifact of the periodic boundary conditions chosen in this work. A detailed discussion is given in the Section B.9.

B.4.2 Constructing a Model

In our thermodynamic model, we assume that - due to the long activation and reaction times - the system reaches its thermodynamic equilibrium during each step. We, therefore, rely on thermodynamically most stable of all included configurations and neglect potential intermediate states of the system (due to slow reaction steps). In the following, we will explicitly mention situations where the intermediate states might be important to understand the performance of Cu-SSZ-13 in the stepwise conversion of methane to methanol.

To develop a thermodynamic model, we rely on structures obtained from static structural optimization using PBE-TS.[229,422] While functionals using the generalized gradient approximation are known to lead to reasonable structural guesses (i.e. systematic errors of ~1-2% in terms of bond length[433]), comparison with post Hartree Fock/post DFT methods such as MP2[434] or the Adiabatic-Connection Fluctuation-Dissipation Theorem in its Random Phase Approximation (RPA),[424] shows significant errors for reaction energies in the deprotonation of isobutene in ZSM-5 and the conversion of methane to methanol over Fe-oxo sites in SSZ-13.[425,435] Furthermore, RPA has shown excellent performance in describing the adsorption of alkanes in protonated zeolites.[436,437] We, therefore, use RPA to calculate total energies for each configuration. To arrive at the finite temperature Gibbs Free Energies, we incorporate vibrational zero point energies, and entropic corrections from static vibrational corrections calculated using the PBE-TS functional.[414]

Since Cu-SSZ-13 is not connected to an external Cu reservoir, we assume that after ion exchange, the number of Cu atoms in the zeolite matrix is constant. Additionally, only a modest increase in methanol yield with activation time[408] indicates that Cu cations move quickly in the zeolite matrix compared to the time-scales typically associated with the various steps in the experimental

procedure. Therefore, Cu will always be present as the configuration in its thermodynamically preferred position with the lowest chemical potential μ^{Cu} (i.e. the lowest energy per Cu atom). Since we are interested in a reaction environment containing O_2 and H_2O, we calculate μ^{Cu} for sites anchored in unit cells containing 2Al as:

$$\mu^{Cu}_{Cu_xO_yH_z}(T, P^{O_2}, P^{H_2O}) = \frac{G^{Cu_xO_yH_z-zeo}(T) - G^{2H-zeo}(T) - \frac{2y-z+2}{4}\mu^{O_2}(T, P^{O_2}) - \frac{z-2}{2}\mu^{H_2O}(T, P^{H_2O})}{x} \quad (B.1)$$

where, G indicates the Gibbs free energy of the structure in the superscript, where $Cu_xO_yH_z$-zeo indicates $Cu_xO_yH_z$ bound to the zeolite framework and 2H-zeo refers to a zeolite framework passivated by Brønsted protons. The gas phase chemical potentials of O_2 (μ^{O_2}) and H_2O (μ^{H_2O}) are obtained by correcting the energies obtained from static electronic structure calculations using vibrational zero point corrections, translational, vibrational and rotational entropies, and pressures. When only one Al atom is present in the unit cell (for the 1Al Cu_1 case), the formula for μ^{Cu} is adapted accordingly.

Throughout this work, we will use μ^{Cu} to calculate phase diagrams. In a realistic zeolite system, Cu will occupy the most stable Al configuration and as soon as it is filled, the next most stable Al configuration will be occupied,[411,414,438] which we try to account for in our study. The exact nature of the observed Cu species will therefore depend on the distribution of local Al configurations, which is expected to vary based on the synthesis and material parameters across the zeolite samples.[439]

Here, we systematically study the impact of the Al distribution on the observed Cu sites. More specifically, to identify the thermodynamically preferred states for Cu in the zeolite framework, we focus on the influence of two parameters on the phase diagram: (i) the availability of anchoring

points for dimers/trimers (D-A through D-D) and (ii) the availability of the anchoring points for Cu_1 sites (1Al, 2Al-A through 2Al-E). We calculate the phase diagrams for each of the dimer/trimer Al configuration (four possibilities) with every specific monomer Al configuration (six possibilities), which leads to a total of 24 phase diagrams for each set of conditions. This systematic approach allows us to gain insight into the relative stability of Cu at these Al configurations and informs us about the nature of the active sites as a function of the available Al configurations. Here, we discuss phase diagrams for all dimer/trimer sites with Cu_1 monomers in 1Al (the only possible 1Al configuration) and 2Al-A (the most stable 2Al configuration[414] Phase diagrams for Cu_1 in Al configurations 2Al-B through 2Al-E are presented in the Section B.9. Throughout the manuscript, we explicitly mention if other combinations of dimer/trimer Al configurations or monomer Al configurations are used.

B.5 Activation

B.5.1 Phase Diagrams

The first step in the stepwise conversion of methane to methanol is the activation of the catalyst to generate the active sites. Here two variables play a crucial role, namely the O_2 pressure (P^{O_2}) and temperature (T). The T/P^{O_2} phase diagrams are presented in Figure B.5 (for Cu_1 in (a) 1Al and (b) 2Al-A) and Figure B.12 (for Cu_1 in 2Al-B through 2Al-E). We start the analysis by including dimer configurations D-A through D-D, one at a time, with Cu_1 bound to the 1Al configuration (Figure B.5(a)). It is interesting to observe that for Al configurations D-A and D-B, mainly Cu_2OH and $Cu_2O_2H_2$ are found to be stable. At D-A, A-$Cu_2O_2H_2$ is found to be stable at low temperatures, while A-Cu_2OH is stable at higher temperatures, whereas for configuration D-B, B-$Cu_2O_2H_2$ is

almost exclusively preferred. For Al configurations D-C and D-D, which bridge the 6R and 8R, only Cu_2OH is found as dimer site. At lower temperatures, Cu_1(I) with one or two adsorbed H_2O molecules is stabilized.

Next, we repeat the procedure described above considering the scenario where Cu_1 binds to the 2Al-A configuration, instead of the 1Al configuration, and find that the results are quite different (see Figure B.5(b)). While the $Cu_2O_2H_2$ sites are still stabilized in a narrow temperature range for Al configurations D-A and D-B, phase diagrams are otherwise dominated by monoatomic Cu_1(II). At higher temperatures, the Cu atom is located in the 6R, while at lower temperatures Cu_1(II) is coordinated to up to 5 H_2O molecules. The dominance of Cu_1(II) at higher temperatures is intimately linked to its stability in the 6R.[411,414] When Cu_1 binds to 2Al-B through 2Al-E (see Figure B.12(a)-(d)), trends in between the extreme cases of least stable Cu_1 in 1Al and most stable Cu_1 in 2Al-A are observed. At low temperatures, hydrated Cu_1(II) sites are found to be stable. Dehydrated, monoatomic Cu_1(II), on the other hand, is only stabilized for 2Al-B (Figure B.12(a)) and 2Al-D (Figure B.12(c)) in a small region in the phase diagram at high T and P^{O_2}. At the same time Cu dimers are stabilized in a relatively large T/P^{O_2} range.

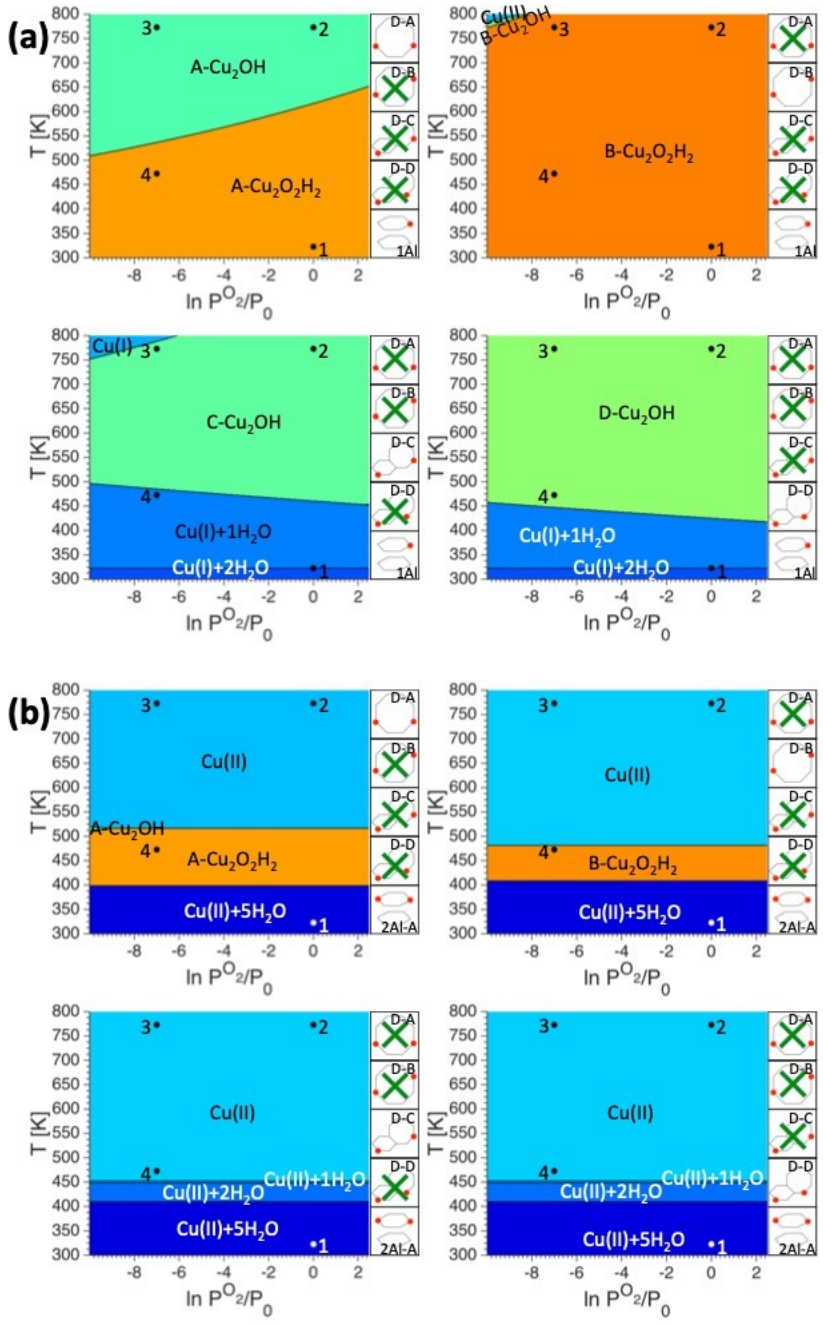


Figure B.5 T/P^{O_2} phase diagrams for different Al configurations (a) Cu_1 anchored in a 1Al configuration or (b) the 2Al-A configuration. The temperature is given in K and P^{O_2} is given with respect to a reference pressure of one bar. The thermodynamically preferred sites are indicated by regions of identical color and the site type is indicated by the labels. The included Al configurations are indicated by schematic representations on the right side of the phase diagrams, which correspond to Figure B.2(b) and Figure B.3(a). Green crosses indicate Al configurations not included in the phase diagrams. Marked points correspond to specific points in the stepwise methane to methanol conversion displayed in Figure B.1. A detailed legend is given in Figure B.11.

So far we have studied phase diagrams where only one possible dimer/trimer Al configuration and one monomer configuration was included. However, in a realistic system, multiple Al configurations will be available. Here, initially Al configurations leading to most stable $Cu_xO_yH_z$ species will be occupied. While extensive discussion about relative stability of Cu_1 in SSZ-13 exists in the literature,[411,413,414,429,438] the relative stability of dimers has been little discussed. We, therefore, study phase diagrams including all four Al configurations for dimer formation (D-A through D-D) and Cu_1 bonded to the 1Al configuration (see Figure B.13) and find that A-Cu_2OH and A-$Cu_2O_2H_2$ are the most stable Cu dimers (Figure B.13) when all dimer exchange sites are available. In a realistic system, only a finite number of Al configurations D-A will exist, therefore, after they are filled with dimers, the next most stable sites will be formed.[412] We remove Al configuration D-A from the phase diagrams and find that B-$Cu_2O_2H_2$ is the second most stable site at low T/high P^{O_2}, while D-Cu_2OH is most stable at high T/low P^{O_2}. When removing either D-B or D-D we find that the other site becomes dominant, which indicates that C-Cu_2OH is the least stable dimer structure and will therefore be formed last.

Using these phase diagrams, we can follow the sites during the first four steps of the stepwise conversion (see Figure B.1, Figure B.5, and Figure B.12). Initially, the system is at 323 K under O_2 pressure of 1 bar. For all 2Al configurations (Figure B.5(b) and Figure B.12(a)-(d)), Cu is found as Cu_1(II) and is coordinated to five or six H_2O molecules. For Cu_1 in 1Al (see Figure B.5(a)), Cu forms $Cu_2O_2H_2$ if the D-A or D-B configuration is available or it is present as Cu_1(I) coordinated to one or two H_2O molecules otherwise. Subsequently, the system is heated to 773 K and now in almost all cases dimers are formed. For Al configurations D-A, D-C, and D-D the preferred configuration is Cu_2OH, while for D-B, $Cu_2O_2H_2$ is preferred. For Cu_1 anchored in Al

configuration 2Al-A (Figure B.5 (b)) and 2Al-D (Figure B.12(c)), however, Cu_1(II) located in the six-ring is found to be stable. In a following step O_2 flow is stopped and P^{O_2} is reduced to e^{-7}. This reduction in pressure leaves most of the sites unchanged, only if 2Al-D (Figure B.12(c)) is included for Cu_1 formation, Cu dimers are now preferred over Cu_1(II). In step four, the system is cooled to 473 K and at this point for Al configurations D-A and D-B, $Cu_2O_2H_2$ is always preferred. For Al configurations D-C and D-D, the situation is somewhat more complex. For these two dimer exchange sites Cu_1 in several 2Al configurations (2Al-A (Figure B.5(b)), 2Al-B, 2Al-C and in part 2Al-D (Figure B.12(a)-(c)) is preferred over dimer formation. However, it cannot be excluded that dimer decomposition is slow compared to the reaction times and therefore dimers might initially still be present during these conditions.

It is interesting to see that at an activation temperature of 773 K several local Al configurations lead to the formation of Cu_1(II). In the literature the activation temperature for zeolites has been a topic of discussion.[391,398,408] To accelerate dimer formation the highest possible temperature that still allows for ideal performance is preferred. However, at some point monomer formation becomes thermodynamically favorable. Typically, an upper limit of 723 K is assumed, but Pappas et al. report an increase in methanol production at 773 K.[408] In our analysis at this temperature the formation of monomers was preferred for two of the 2Al configurations (2Al-A (Figure B.5(b) and 2Al-D (Figure B.12(c))). However, we relied on a residual O_2 pressure (P^{H_2O}) of e^{-9}. When studying the P^{H_2O} dependence during activation for Al configuration D-A and Cu_1 in 2Al-A (see Figure B.14), we find that an increase in P^{H_2O} shifts the transition to Cu_1(II) to higher temperatures, i.e. a slightly higher P^{H_2O} will allow for higher activation temperatures during dimer formation.

B.5.2 Comparison to experimental data

In the literature, the nature of the active sites in Cu-SSZ-13 during catalyst activation has been studied in detail using *in situ* EXAFS measurements,[408] and the following qualitative observations were made: (i) a minority of Cu sites do not form dimers during the activation process and (ii) the coordination number of a fraction of Cu atoms increases from three to four between activation at 773 K and 473 K. As we will show in the following, both observations are well reproduced from the phase diagrams constructed here. As shown in Figure B.5(b) and Figure B.12(c), monoatomic Cu_1 in the 2Al-A and 2Al-D configurations is more stable than dimers or trimers at high T and high P^{O_2}. Therefore, Cu_1 in the 2Al-A and 2Al-D configurations will not form dimers during the high temperature activation process, which supports the experimental observations. Furthermore, for Al configuration D-A, threefold coordinated Cu in the dimer A-Cu_2OH will be formed at 773 K, but fourfold coordinated Cu in A-$Cu_2O_2H_2$ will be most stable for activation at 473 K. Cu in the next most stable dimers B-$Cu_2O_2H_2$ and D-Cu_2OH will not change its coordination number. Therefore, for activation at 773 K, Cu hosted in dimers in Al configuration D-A will be in a three-fold coordinated structure, while after activation at 473 K, Cu in Al configuration D-A will be in a four-fold coordinated structure, which agrees perfectly with experimental observations of an increase in Cu coordination number at lower activation temperatures.

EXAFS measurements contain information about the coordination shells of Cu and distinct coordination peaks at distances of 1.86±0.05 Å, 1.97±0.04 Å, 2.72±0.02 Å and 3.41 Å are observed.[408] To reproduce these values, we studied the structural information of all the dimers and compare them to experimentally measured values (Figure B.6). We split the information into distances between Cu- O in the dimer, Cu-O in the framework, Cu- Cu and Cu-Al atoms. We find

that distances between Cu and the O atom for hydroxyl groups in the dimers, correspond (within errors) to 1.86 Å, while the experimentally measured distance of 1.97 Å corresponds to the distances between Cu and O atoms in the zeolite framework. The distance of 2.72 Å can either be attributed to the Cu-Al distances, the Cu-Cu distance in A-$Cu_2O_2H_2$ or with larger errors to the Cu-Cu distances in B-$Cu_2O_2H_2$ and A-Cu_2OH. The Cu-Cu distances for B-Cu_2OH, C-Cu_2OH and D-Cu_2OH, on the other hand agree well with the experimentally observed length at 3.41 Å. We want to emphasize excellent agreement, in particular with the most stable A-$Cu_2O_2H_2$ with a Cu-OH distances of 1.91 Å and 1.92 Å (experiment 1.86±0.05 Å), Cu and O atoms in the zeolite framework of 1.97 Å and 2.04 Å (experiment 1.97±0.04 Å), Cu-Al distances of 2.72 Å and 2.74 Å and a Cu-Cu distance of 2.73 Å (experiment 2.72±0.02 Å). Thus, we find excellent agreement between experimental measurements and the sites predicted to be stable based on our phase diagrams.

While structural agreement between the stable sites and experiment is encouraging, the presence of other sites such as CuOH, Cu_2O_2, Cu_2O, or Cu trimers, which have been previously suggested in the literature to be the active sites in the methane to methanol conversion,[390,392,394,404,440] is still possible. We therefore discuss bond-lengths for these sites in the Section B.9 and show that the presence of such sites in Cu-SSZ-13 after activation is unlikely.

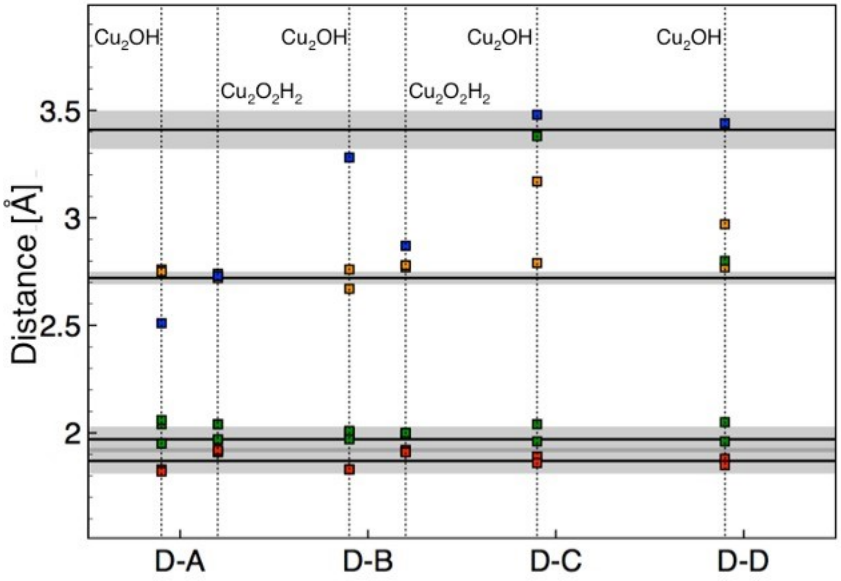


Figure B.6 Bond distances calculated for sites predicted to be stable in Cu-SSZ-13. Red symbols indicate distances between Cu and O in the dimers, green symbols distances between Cu and O in the framework, yellow signals Cu-Al distances and blue symbols shown Cu-Cu distances. X-axis labels correspond to the local Al configurations and columns marked by dashed lines for each Al configurations indicate (from left to right) Cu_2OH (D-A through D-D) and $Cu_2O_2H_2$ (D-A and D-B) (see Figure B.4). Black lines indicate literature values for bond distances measured using EXAFS[408] and grey shaded areas mark the experimentally reported error bars.

B.6 Methane activation and methanol extraction

After the activation of the zeolite, the material is exposed to methane to form methanol adsorbed to Cu sites. To correctly determine the nature of the material under these conditions, we model the adsorbed methanol molecules in the zeolite catalyst. To keep the discussion tractable, we focus on methanol formation at the most stable sites during activation, namely A-$Cu_2O_2H_2$ and B-$Cu_2O_2H_2$ and all Cu_2OH sites. In the following, we assume that each OH group can form one methanol molecule and substitute the OH groups by methanol. To balance the stoichiometries, excess H atoms are included as water molecules in the mathematical description below. A recombination with oxygen could happen by e.g. H diffusing to the zeolite matrix.[403] For Cu_2OH we model the

adsorption of one methanol molecule and for $Cu_2O_2H_2$ we model all possibilities for the adsorption of one methanol molecule (the other OH group remains intact) and two methanol molecules. The most stable structures for a given stoichiometry are displayed in Figure B.7. For Cu_2OH in configurations D-C and D-D and $Cu_2O_2H_2$ dimers in configuration D-A and D-B, formation of methanol leads to the decomposition of the dimer and leaves methanol adsorbed to Cu_1(I). For the adsorption of a single methanol molecule to $Cu_2O_2H_2$, a Cu_2OH dimer remains intact and one methanol molecule is adsorbed to one of the Cu centers, while a dimer containing a methanol molecule is formed for Cu_2OH in Al configurations D-A and D-B.

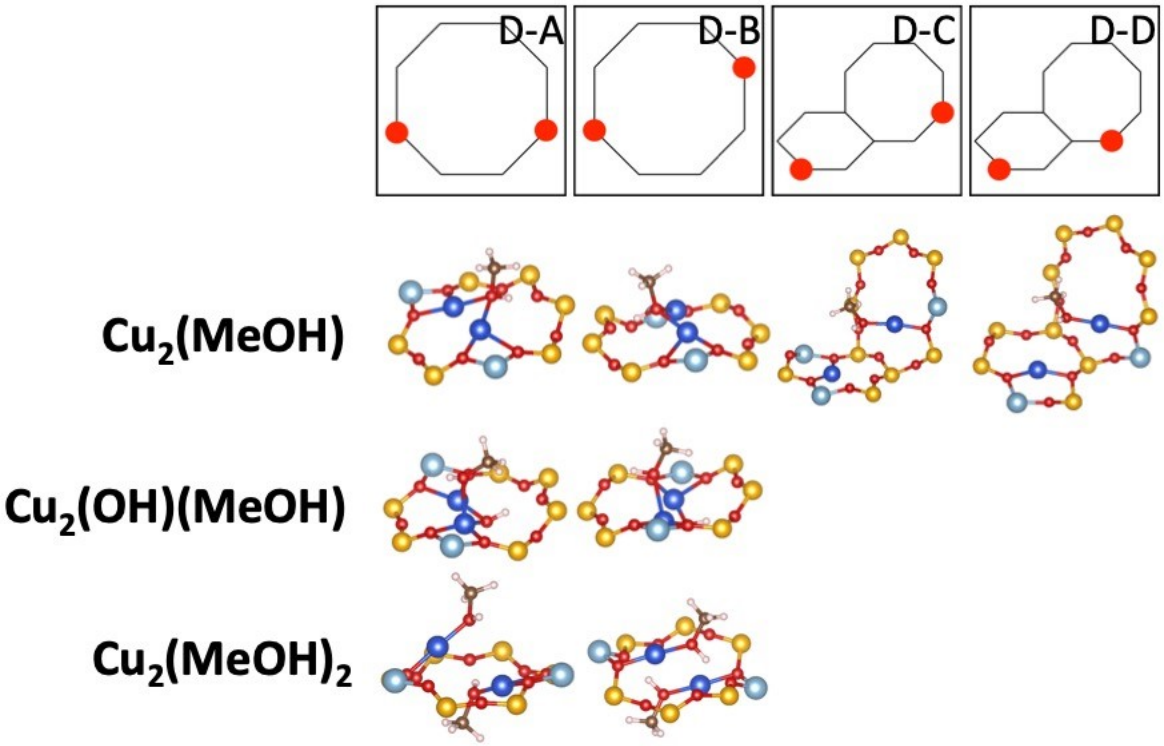


Figure B.7 A graphical representation of all stable sites after exposure to methane and formation of methanol (MeOH). On top the different local Al configurations of the exchange sites are given (see Figure B.3(a)) and on the left the stoichiometries of the different Cu structures are listed. The color code corresponds to Figure B.4 and C atoms are displayed in brown. MeOH is used as shorthand notation for methanol.

Similar to the definition above, we calculate μ^{Cu} for unit cells containing two Al atoms and adsorbed methanol molecules as:

$$\mu^{Cu}_{Cu_xO_yH_z}(T, P^{O_2}, P^{H_2O}, P^{CH_4}) = \frac{G^{Cu_xO_yH_z-zeo}(T) - G^{2H-zeo}(T) - w\mu^{CH_4}(T, P^{CH_4}) - \frac{2y-z+2+w}{4}\mu^{O_2}(T, P^{O_2}) - \frac{z-w-2}{2}\mu^{H_2O}(T, P^{H_2O})}{x} \quad (B.2)$$

where, definitions given above are extended by *w*, the number of CH_3 groups in the system, P^{CH_4}, the CH_4 pressure and μ^{CH_4}, the chemical potential of CH_4 in gas phase. Using this definition, it is now possible to perform an analysis similar to the activation phase.

Similar to the discussion for activation above, we use μ^{Cu} to study the stability of Cu sites with adsorbed methanol molecules. Again, we discuss all possible combinations of dimer exchange sites D-A through D-D and monomer exchange sites (1Al and 2Al-A through 2Al-E). As a first step, we analyze T/P^{CH_4} phase diagrams (see Figure B.8 and Figure B.16). As general trends, we find that the phase diagrams for Al configurations D-A and D-B are dominated by methanol containing structures. For Al configurations D-A and D-B at high pressures, the formation of two methanol molecules is preferred. For Al configuration D-A, the formation of a Cu_2OH dimer with methanol binding to one of the Cu atoms is thermodynamically favored at low P^{CH_4}. For D-C and D-D a structure containing two Cu atoms and one methanol molecule is favorable. Only at high temperatures and low methanol pressures the initial dimers are kept intact and methane is not converted to methanol. When varying the anchoring of Cu_1, a picture similar to the activation conditions emerges. For 1Al Cu_1 is preferred only for Al configurations D-C and D-D at low T and P^{CH_4} (see Figure B.8(a)). For the 2Al-A on the other hand Cu_1 is far more stable and prohibits the formation of methanol for Al configurations D-C and D-D for most of the condition space (see Figure B.8(b)). The other 2Al configurations lie between these extremes (see Figure B.16(a)-(d)).

Similar to Cu_1 anchored in 1Al (see Figure B.8(a)), for Cu_1 in most of the 2Al configurations the formation of one or two methanol molecules is preferred for Cu in dimer Al configurations D-A and D-B (see Figure B.9(b) and Figure B.16(a)-(d)). For D-C and D-D on the other hand a significant portion of the phase diagram is dominated by Cu_1. For 2Al-B (Figure B.16(a)) and to a lesser degree 2Al-C (Figure B.16(b)) this leads to a preference of Cu_1 at reaction temperatures, while for 2Al-D (Figure B.16 (c)) and 2Al-E (Figure B.16 (d)) methanol formation is favorable

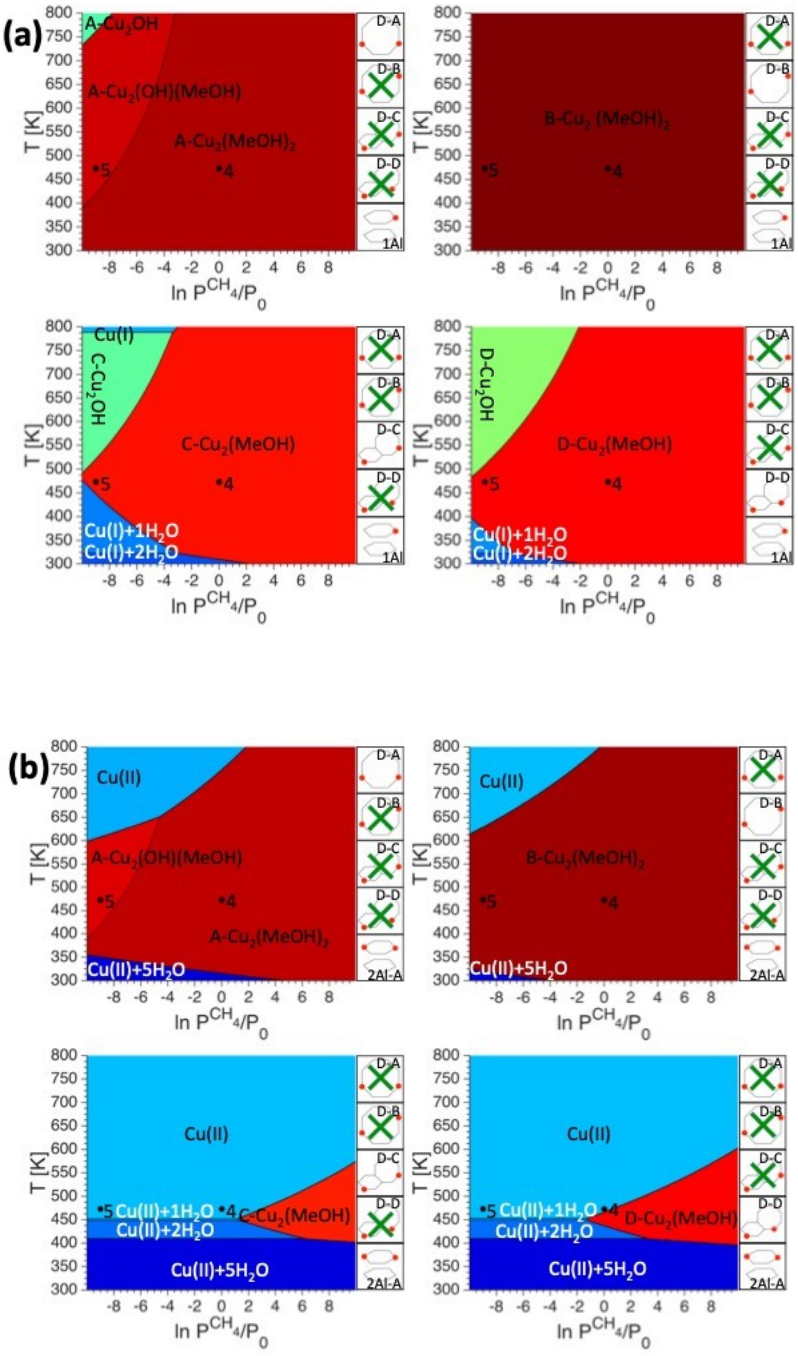


Figure B.8 T/P^{CH_4} phase diagrams for different Al configurations and (a) Cu monomers anchored in a 1Al configuration or (b) the 2Al-A configuration. The temperature is given in K and P^{CH_4} is given with respect to a reference pressure of one bar. Regions of identical color indicate the thermodynamically preferred sites and the site type is indicated by the labels. The included Al configurations are indicated by schematic representations on the right side of the phase diagrams, which correspond to Figure B.2(b) and Figure B.3(a). Green crosses indicate Al configurations not included in the phase diagrams. Marked points correspond to labels in Figure B.1. A detailed legend is given in Figure B.11.

The last step in the stepwise conversion of methane to methanol is the extraction of methanol by introducing water vapor (see Figure B.1). We, therefore, focus on a T/P^{H_2O} phase diagram in the presence of methanol (see Figure B.9 and Figure B.17). We observe that for Cu_1 in the 2Al configurations (see Figure B.9(b) and Figure B.17(a)-(d)) an increase in P^{H_2O} leads to the preference of Cu_1 for D-A and D-B and, therefore, methanol will desorb. For Al configurations D-A and D-B and Cu_1 in 1Al methanol adsorbed to Cu remains stable until higher P^{H_2O}. For Al configurations D-C and D-D methanol is only found when Cu_1 is located in the 1Al, 2Al-D and 2Al-E configurations. This is consistent with T/P^{CH_4} phase diagrams (see Figure B.8 and Figure B.16), where adsorbed methanol was not stabilized for the corresponding Al configurations.

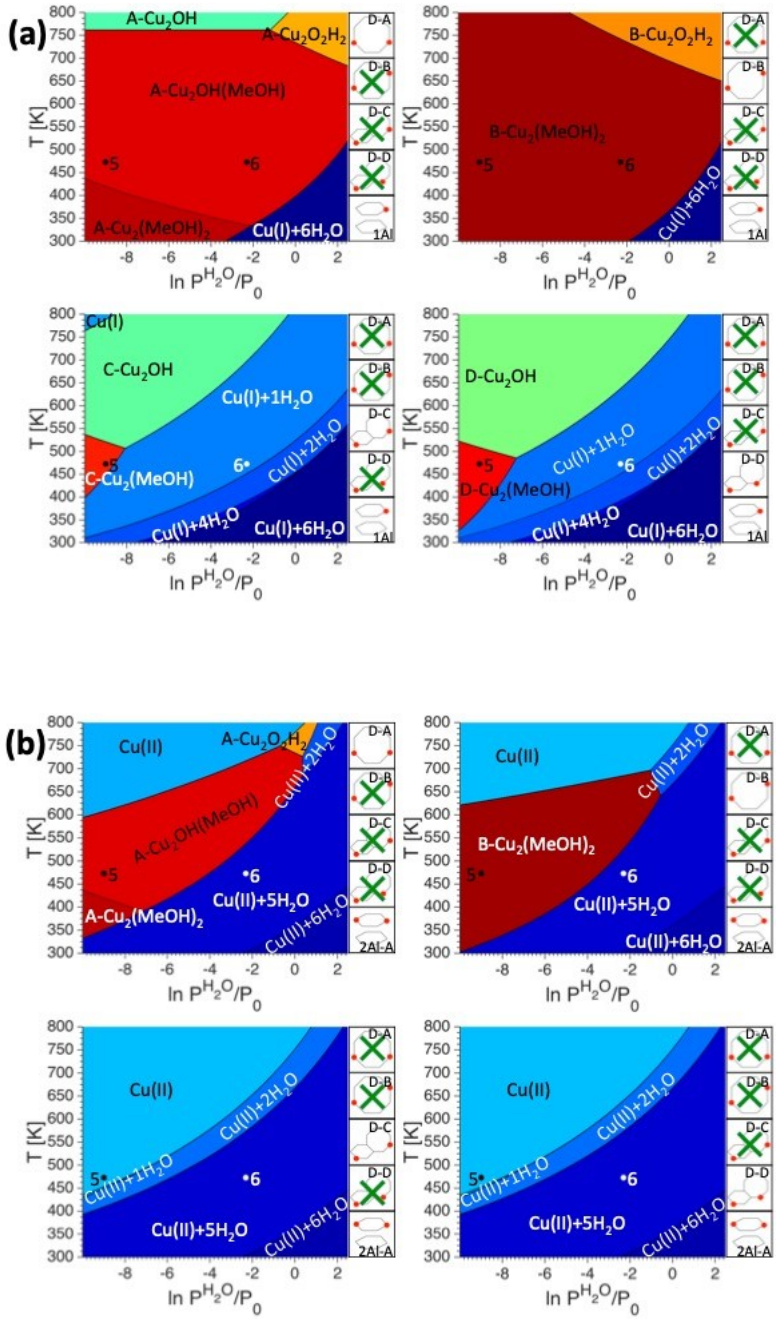


Figure B.9 T/P^{H_2O} phase diagrams for different Al configurations and (a) Cu monomers anchored in a 1Al configuration or (b) the 2Al-A configuration in the presence of CH_4. The temperature is given in K and P^{H_2O} is given with respect to a reference pressure of one bar. The thermodynamically preferred sites are indicated by regions of identical color and the site type is indicated by the labels. The included Al configurations are indicated by schematic representations on the right side of the phase diagrams, which correspond to Figure B.2(b) and Figure B.3(a). Green crosses indicate Al configurations not included in the phase diagrams. Marked points correspond to labels in Figure B.1. A detailed legend is given in Figure B.11.

It is now possible to follow the nature of the active sites through methane activation and extraction. After the introduction of methane at 1 bar almost all sites start to form adsorbed methanol molecules (see Figure B.8 and Figure B.16). Only for C-Cu_2OH and D-Cu_2OH sites and most stable Cu_1 in 2Al-A and 2Al-B no methanol is formed, which might be associated with the absence of hydroxylated dimers during activation in the first place (see Figure B.5(b) and Figure B.12(a)). When P^{CH_4} is reduced, in some cases methanol is directly released. For Al configurations D-A and D-B and for Cu_1 in 2Al-A (see Figure B.9(b)) an increase in P^{H_2O} to 0.1 bar leads to the release of methanol. For perfectly separated Al atoms, as represented by 1Al (see Figure B.9(a)), methanol remains stable and cannot be extracted. For Cu_1 in the other 2Al configurations (2Al-B through 2Al-E, see Figure B.17(a)-(d)) a transition between Cu_1 bonded to methanol and Cu_1 coordinated to water is right at P^{H_2O}=0.1 bar. For these sites potentially a slightly lower temperature (e.g. 408 K) during H_2O treatment would make methanol release more likely.

B.7 Discussion

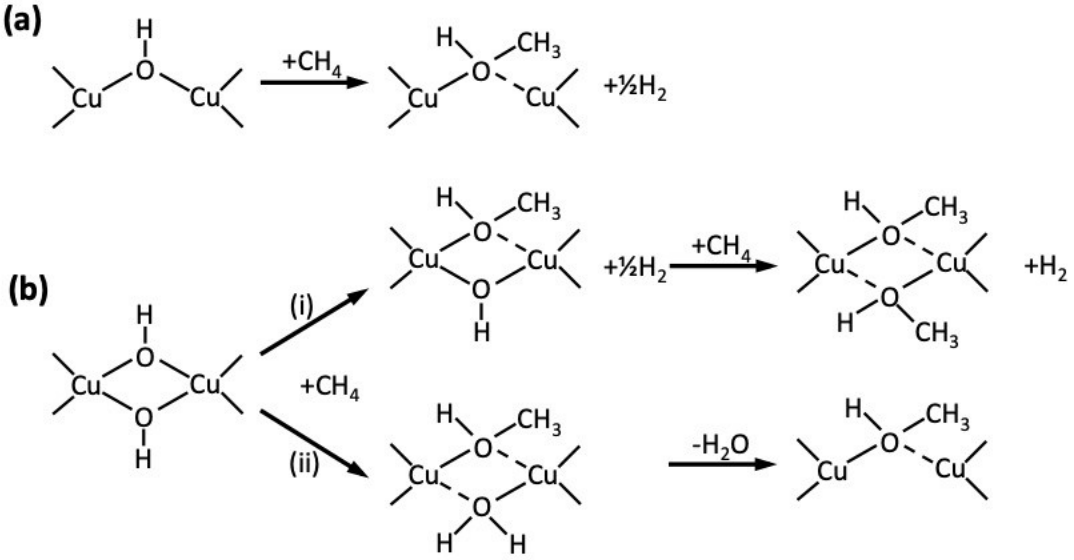
It is encouraging to see that the methodology presented here almost perfectly reproduces experimentally measured bond lengths and coordination numbers reported in the literature[441]. However, contrary to common interpretations the thermodynamic model developed here reveals that hydroxylated dimers ($Cu_2O_2H_2$ or Cu_2OH) are most stable and most likely the sites active in this reaction. In particular Cu-O bond lengths from EXAFS measurements agree perfectly with the most stable $Cu_2O_2H_2$, while oxo sites and Cu-OH underestimate Cu-O bonds by about 10%. At the same time, various parameters, such as the Al distribution and the encountered conditions might determine the exact dimer stoichiometry and geometry. Based on the clear thermodynamic

trends for Cu-SSZ-13, we hypothesize that in different zeolite structures, where other monomer and dimer exchange sites exist, and different local Al configurations will be present, a similar preference of hydroxylated Cu structures might occur when O_2 is used as an oxidant.

The presence of hydroxylated dimers raises significant questions considering the activation of methane. Activation of methane over oxo-sites has been extensively discussed and is often proposed to proceed via an abstraction and rebound step[442,443] or a concerted mechanism.[444] In zeolites only Cu-OH has been discussed as potential hydroxylated active site.[440] However, the site geometries presented in this work imply different mechanisms (see Scheme B.2) and based on our results we hypothesize the following: For $Cu_2(OH)$ stoichiometric arguments point towards H_2 formation during the activation of CH_4 (Scheme B.2(a)). Indeed, experimental measurements indicate the formation of small quantities of H_2 during methane exposure.[403,408] On the other hand, for the $Cu_2O_2H_2$ sites a similar mechanism activating two CH_4 molecules and forming two methanol molecules is possible (see Scheme B.2(b)-(i)) and leads to thermodynamically preferred structures for D-A and D-B (see Figure B.10 and Figure B.14). For such a mechanism formation of H_2/H_2O is necessary, which might require to overcome significant activation energy barriers. In the future careful measurements of the molar ratios of H_2 produced during methane exposure and methanol could help to support this reaction mechanism.

At the same time, a more simple mechanism is possible for $Cu_2O_2H_2$ sites (see Scheme B.2(b)-(ii)). Here, methane gets activated at one OH group and the abstracted H atom combines with OH and forms water, while the methyl group forms methanol at the other OH group. This mechanism, would therefore, after the desorption of H_2O, favor the formation of $Cu_2(MeOH)$, which is not always found to be most stable in the phase diagrams presented in Figure B.8, Figure B.9, Figure

B.16, and Figure B.17, but might be the only site accessible after methane activation. Such a mechanism (Scheme B.2(b)-(ii)) is supported by the highest methanol yields per Cu atom reported in the literature, which is limited to ~0.5 methanol/Cu atom,[406] i.e. the production of one methanol per dimer.



Scheme B.2 Suggested reaction pathways for the activation of methane over (a) Cu_2OH and (b) $Cu_2O_2H_2$. For (a) and (b)-(i), methane gets activated at the OH group and forms methanol. Excess H diffuses away from the Cu active site[403] and recombines as H_2 or H_2O. For (b)-(ii) on the other hand methane forms methanol and H_2O at one $Cu_2O_2H_2$ site. Strong chemical bonds are displayed as black lines, dashed lines represent weak bonds (~2.5 Å or longer) that, depending on the exact active site geometry can easily be broken. Open ended bonds at Cu represent bonds to framework O atoms.

One of the most surprising observations made in this work is that at no point Cu-OH, a site that is believed to be active in the selective catalytic reduction of NO_x[413,418] and has been suggested to be active in the conversion of methane to methanol,[440] is stabilized. It will be interesting to see whether the presence of NH_3 as encountered in deNO_x-SCR can stabilize Cu-OH over hydroxylated dimers.

B.8 Conclusions

We have explored the nature of the active sites in the zeolite SSZ-13 during the stepwise conversion of methane to methanol. We generated a model that includes a series of different Cu dimers and trimers, as well as hydrated Cu_1(I) and Cu_1(II) sites, stabilized in different local Al configurations. We used a combination of static DFT calculations and post-DFT calculations to construct phase diagrams and follow the nature of the active sites during catalyst activation, methane exposure and methanol extraction. We find that in the initial catalyst activation phase, depending on the local Al configurations and the exact conditions, $Cu_2O_2H_2$ or Cu_2OH dimers are formed. When methane is introduced to the system, methanol molecules bound to Cu sites in the zeolite are generated and an increase in the water pressure leads to their desorption. We closely compare the prediction from our thermodynamic model to experimental measurements in the literature and find excellent agreement.

In particular, the prediction that hydroxylated dimers are thermodynamically preferred, contradicts common assumptions about the nature of active Cu centers in zeolites and also enzymes active in the conversion of methane to methanol. In the future, it will be interesting to see to what degree these observations can be utilized to arrive at a closer understanding of this reaction and how the theoretical insights here will allow to optimize the process of methane to methanol conversion.

B.9 Supporting Information

B.9.1 Reaction Conditions Along the Stepwise Conversion of Methane to Methanol

Table B.1 Numerical values for the reaction conditions at each point during the stepwise conversion of methane to methanol. The temperature is given in K and the pressures are given with respect to a reference pressure P_0 of 1 bar.

Step number	T [K]	$\ln(P^{O_2}/P_0)$	$\ln(P^{H_2O}/P_0)$	$\ln(P^{CH_4}/P_0)$
1	323	0	-9	-
2	773	-7	-9	-
3	473	-7	-9	-
4	473	-7	-9	0
5	473	-7	-9	-9
6	473	-7	-2.3	-9
7	473	-7	-2.3	-9

B.9.2 Spin States of Cu Dimers and Trimers

Table B.2 Modeled spin states and their relative stability of all dimers and trimers included in this study. Energy differences (ΔE) are given in kJ/mol and with respect to the most stable spin state for each dimer/trimer.

ΔE [kJ/mol]	**spin**	**A**	**B**	**C**	**D**
Cu_2O	singlet	2.5	0	15.4	16.3
	triplet	0	7.0	0	0
Cu_2OH	doublet	0	0	0	0
	quadruplet	338.3	304.3	335.3	323.3
Cu_2O_2	singlet	0	0	7.4	13.9
	triplet	39.6	62.2	0	0
Cu_2O_2H	doublet	7.2	0	0	6.5
	quadruplet	0	3.9	28.9	0
$Cu_2O_2H_2$	singlet	2.8	3.2	0.3	0.4
	triplet	0	0	0	0
Cu_3O_3	doublet	0	9.9		
	quadruplet	3.3	0		
Cu_3O_3H	singlet	11.3	20.1		
	triplet	0	0		
$Cu_3O_3H_2$	doublet	1.8	7.3		
	quadruplet	0	0		
$Cu_3O_3H_3$	singlet	0	0		
	triplet	7.9	4.7		

B.9.3 The Impact of Unit-Cell Size on Dimer Stability

As mentioned earlier in the Chapter, dimer and trimer structures are hosted in Al configurations that reach beyond the double six O-ring structure of a single primitive unit cell. However, using periodic boundary conditions the Al configurations can be constructed in a single primitive unit cell. In particular for Al configuration C, which reaches over a six O-ring and an eight O-ring structure, this leads to the presence of an additional Al atom in the six O-ring. It is not clear to what degree such an artifact of periodic boundary conditions in particular and the choice of a single unit cell (compared to e.g. a double unit cell) in general will influence the stability of Cu dimers and trimers. We therefore compare the stability of all studied Cu dimers in Al configuration C (i.e. C-Cu_2O, C-Cu_2OH, C-Cu_2O_2, C-Cu_2O_2H, C-$Cu_2O_2H_2$) modeled in a single and double primitive unit cell. In Figure B.10, the structures of C-Cu_2O for modeled in a single primitive unit cell and a double primitive unit cell are displayed.

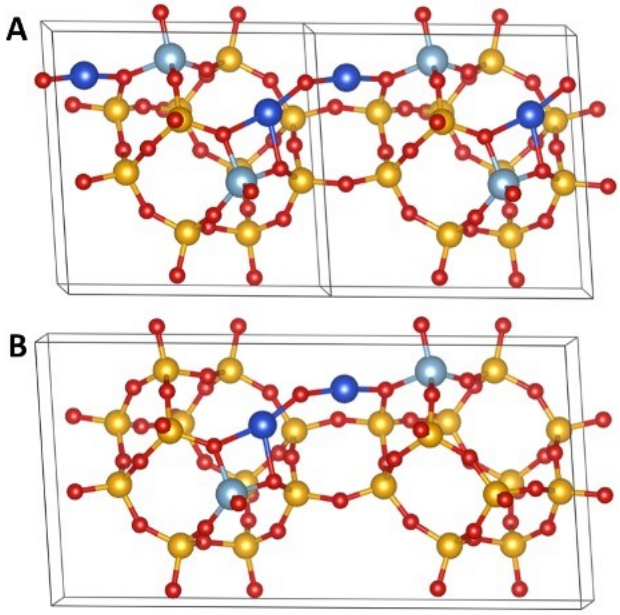


Figure B.10 Structures of C-Cu_2O modeled in a single (A) and a double (B) primitive unit cell. Structures are very similar, but for the single unit cell twice as many Cu atoms are present and a second Al atom is located in the six O-ring. The color code in atomistic pictures corresponds to Figure B.4.

In a next step we compare the stability of all dimers in the two modeled unit cells and find that preferred spin states agree. Subsequently we compare the stability of the different dimers for the single and double primitive unit cell and results are shown in Table B.3. The largest deviations are found for C-Cu_2O with a difference in stabilization of 10.6 kJ/mol between the single and doubled unit cell and 5.3 kJ/mol in terms of μ^{Cu}. These energy differences are small compared to the range of $\Delta\mu^{Cu}$ encountered in the construction of phase diagrams and leave the relative stability of sites unchanged. Based on these results we conclude that the choice of a single unit cell to host dimer and trimer structures is justified.

Table B.3 Energy difference (ΔE) and difference in chemical potential ($\Delta\mu^{Cu}$) for Cu dimers anchored in Al-configuration C modeled in a single primitive unit cell (single u.c.) or double primitive unit cell (double u.c.). Numerical values are given in kJ/mol.

	ΔE [kJ/mol]		$\Delta\mu^{Cu}$ [kJ/mol]	
	single u.c.	double u.c.	single u.c.	double u.c.
C-Cu_2O	10.6	0	5.3	0
C-Cu_2OH	6.2	0	3.1	0
C-Cu_2O_2	0	0.4	0	0.2
C-Cu_2O_2H	0	7.2	0	3.6
C-$Cu_2O_2H_2$	0	0.2	0	0.1

B.9.4 Legend for the Phase Diagrams

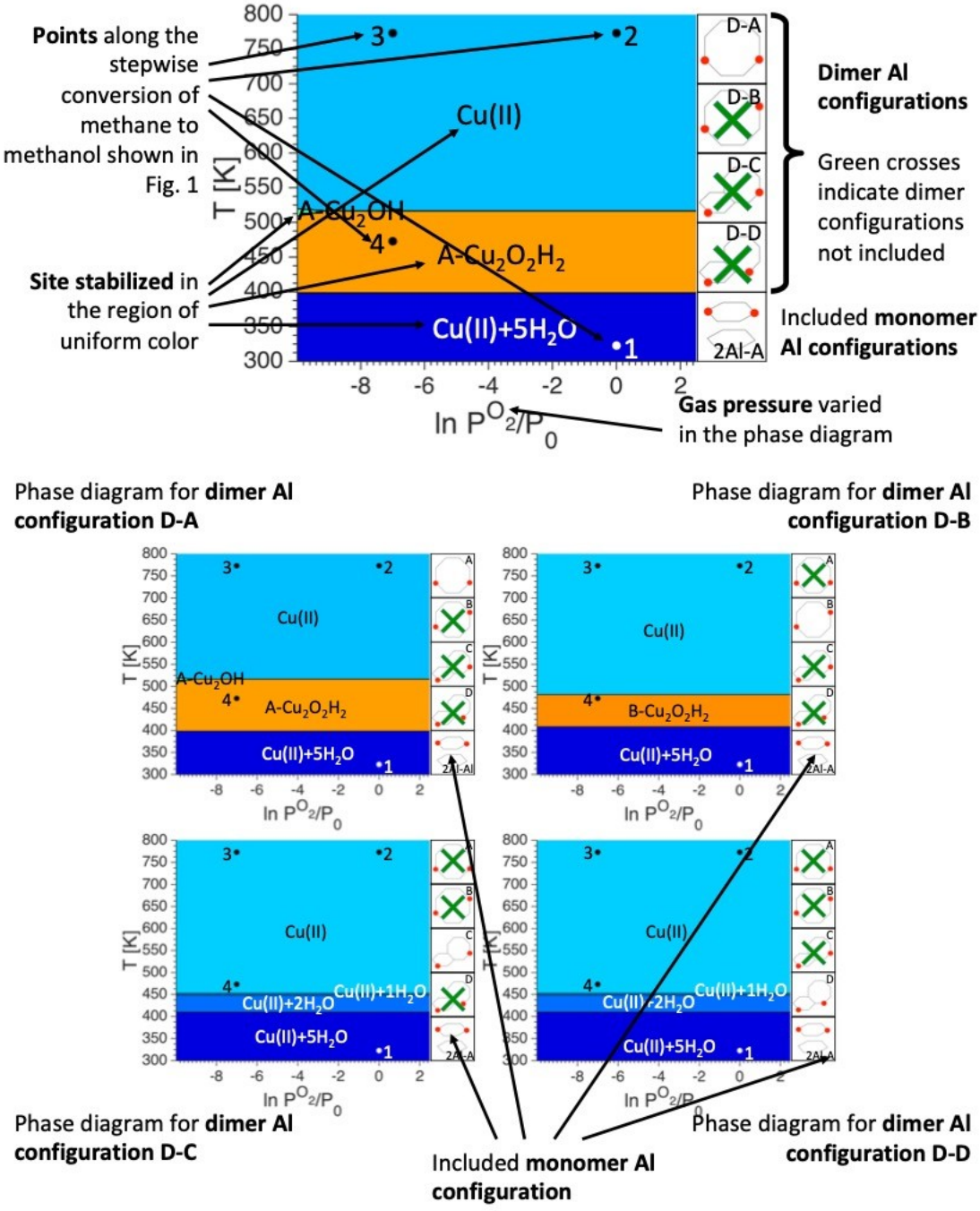
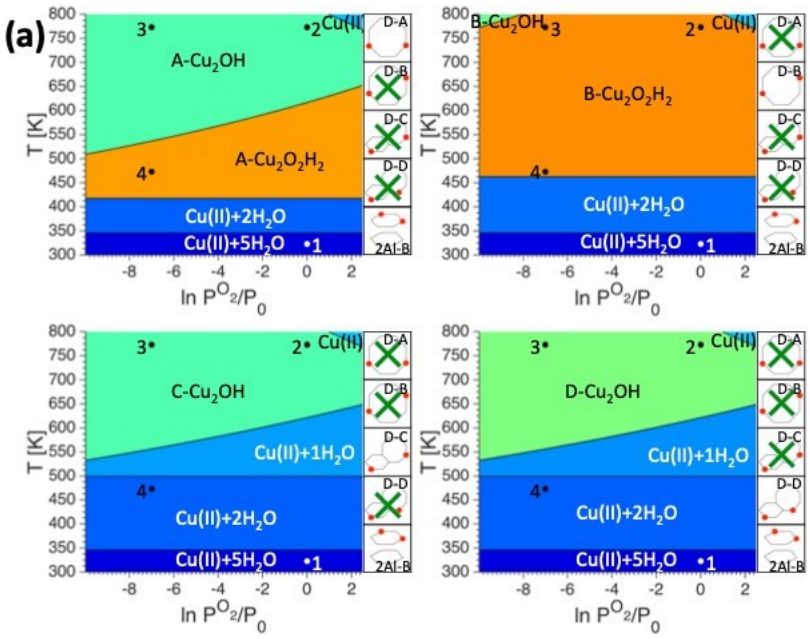
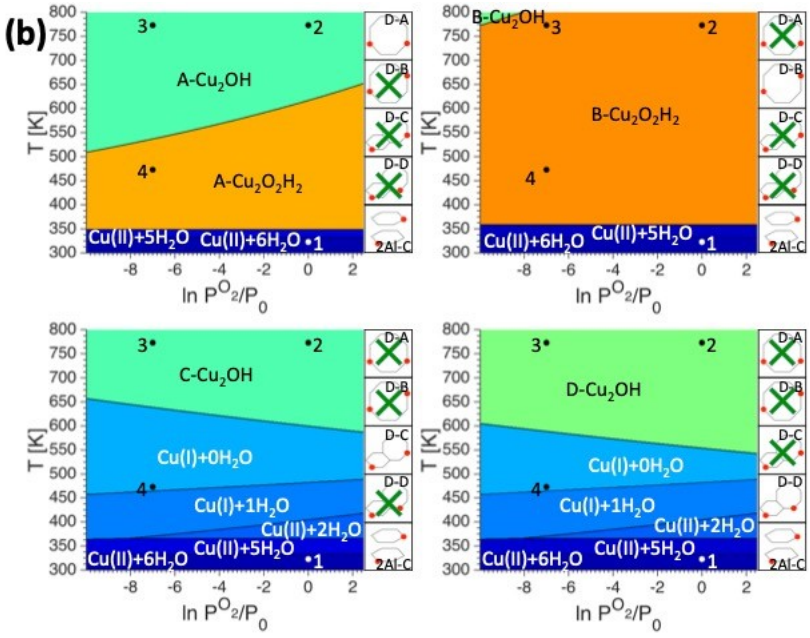


Figure B.11 Detailed legend for the phase diagrams shown in Figure B.5, Figure B.8, Figure B.9, Figure B.12, Figure B.13, Figure B.14, Figure B.16, and Figure B.17. On the top the legend for each individual phase diagram is shown and on the bottom the arrangement of panels for the figures noted above.

B.9.5 T/P(O_2) phase diagrams for 2Al-B through 2Al-E





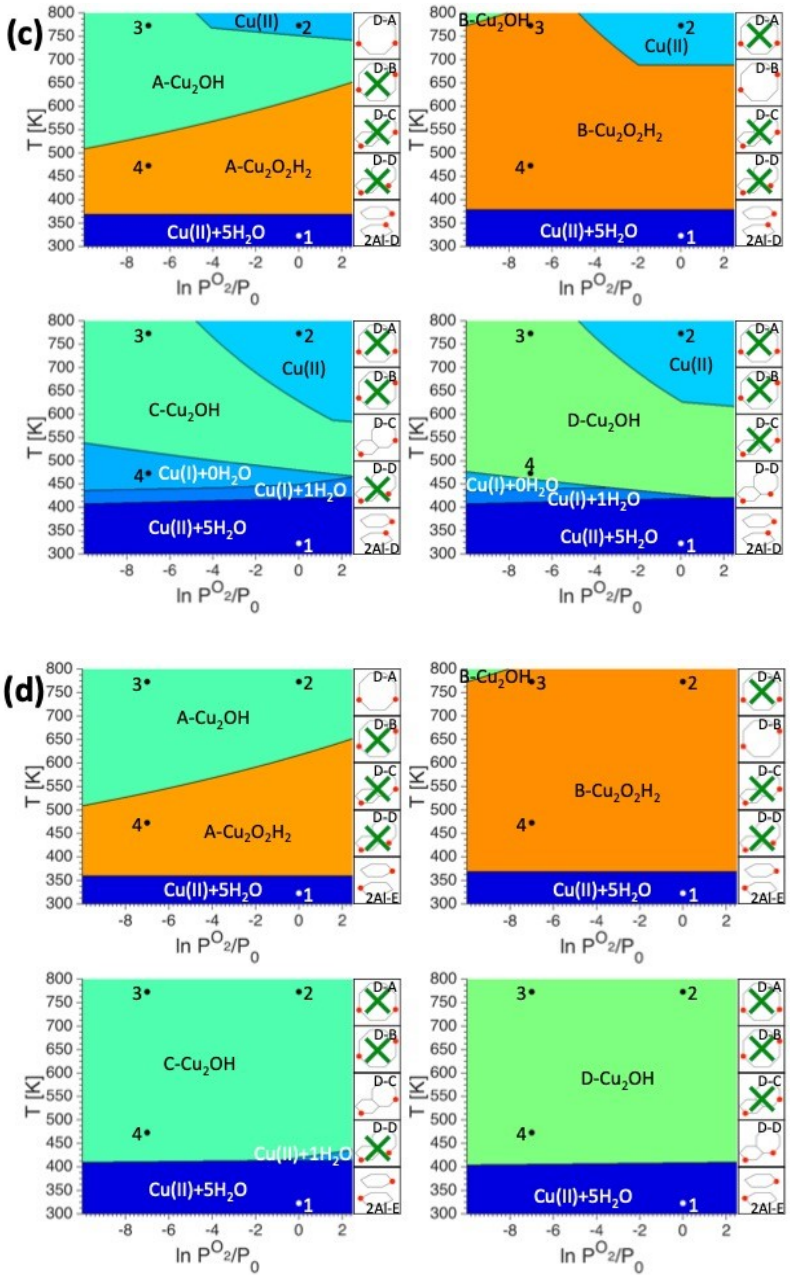


Figure B.12 T/P^{O_2} phase diagrams for different Al configurations and (a) Cu monomers anchored in a 2Al-B configuration or (b) the 2Al-C configuration, (c) the 2Al-D configuration and (d) the 2Al-E configuration. The temperature is given in K and P^{O_2} is given with respect to a reference pressure of one bar. The thermodynamically preferred sites are indicated by regions of identical color and the site type is indicated by the labels. The included Al configurations are indicated by schematic representations on the right side of the phase diagrams, which correspond to Figure B.2(b) and Figure B.3(a). Green crosses indicate Al configurations not included in the phase diagrams. Marked points correspond to specific points in the stepwise methane to methanol conversion displayed in Figure B.1. A detailed legend is given in Figure B.11.

B.9.6 Relative Stability of Dimers and Trimers

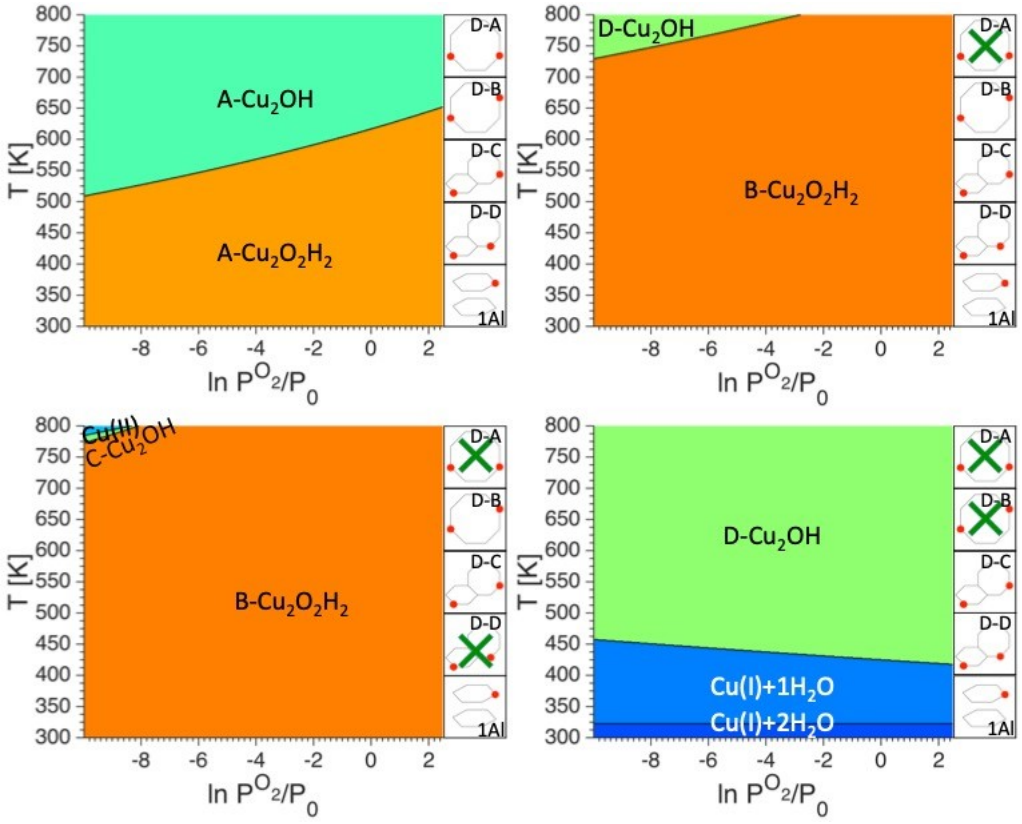


Figure B.13 T/P^{O_2} phase diagrams including multiple Al configurations for dimer sites and Cu_I in the 1Al configuration. Subsequently the most stable sites are removed, which allows to establish an order of thermodynamic stability. The temperature is given in K and P^{O_2} is given with respect to a reference pressure of one bar. The thermodynamically preferred sites are indicated by regions of identical color and the site type is indicated by the labels. The included Al configurations are indicated by schematic representations on the right side of the phase diagrams, which correspond to Figure B.2(b) and Figure B.3(a). Green crosses indicate Al configurations not included in the phase diagrams. A detailed legend is given in Figure B.11.

B.9.7 P(H_2O)/T Phase Diagram for 2Al-A

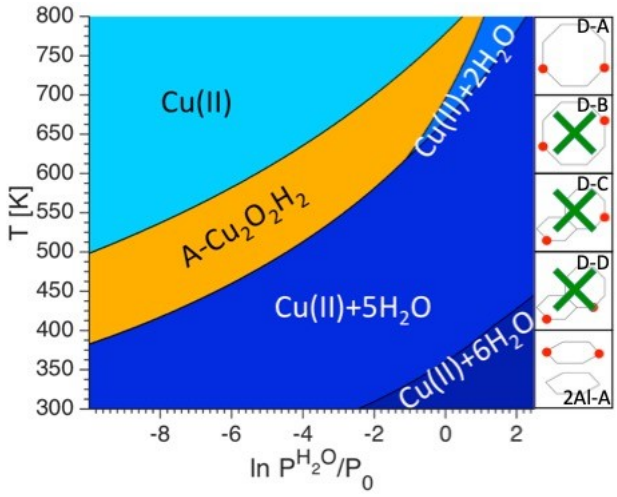


Figure B.14 T/P^{H_2O} phase diagram for Al configuration d-A and Cu_1 stabilized in the 2Al-A Al configuration. The temperature is given in K and P^{H_2O} is given with respect to a reference pressure of one bar. Regions of identical color indicate the thermodynamically preferred sites and the site type is indicated by the labels. The included Al configurations are indicated by schematic representations on the right side of the phase diagrams, which correspond to Figure B.2(b) and Figure B.3(a). Green crosses indicate Al configurations not included in the phase diagrams. A detailed legend is given in Figure B.11.

B.9.8 Cu-X Distances for Non-stabilized Dimers, Trimers and Dehydrated Monomers

In this section we discuss bond distances for sites not stabilized in phase diagrams shown in Figure B.5 and Figure B.13. Bond distances for dimers and trimers are shown in Figure B.15(a)-(b). While agreement between some of the distances can be found, Cu-O distances for most of these configurations lie between 1.70 Å and 1.80 Å, which are too short compared to experimental measurements (experiment 1.86±0.05 Å). Only for A-$Cu_3O_3H_3$ (1.81-1.99 Å), B-$Cu_3O_3H_3$ (1.81-1.98 Å), C-Cu_2O_2 (1.86 Å, 1.88 Å), C-Cu_2O_2H (1.83 Å, 1.92 Å) and D-Cu_2O_2 (1.81 Å, 1.82 Å), Cu-O distances within the Cu clusters agree reasonably well with experimental measurements (1.86±0.05 Å and 1.97±0.04 Å). However, Cu-Al or coordination of Cu to framework O atoms still shows a significant disagreement with experimental measurements, which makes the presence of these sites significantly less likely. Similar arguments hold for the presence of Cu_1 sites such as Cu-OH (see Figure B.14(c)), which indicates that most of them will be converted to larger Cu clusters during catalyst activation.

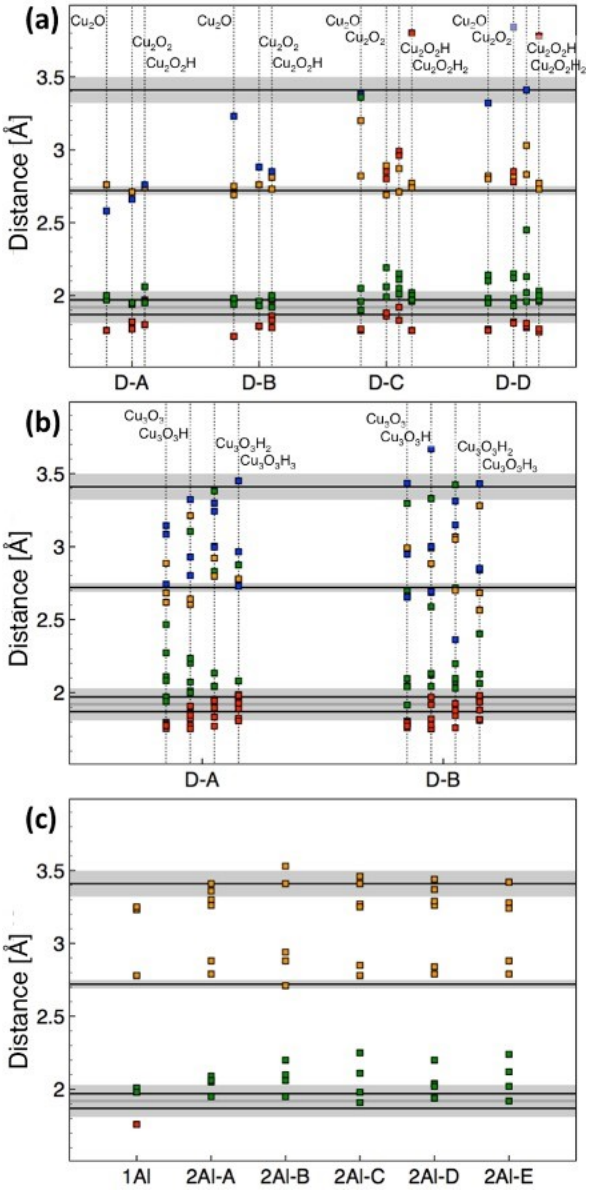
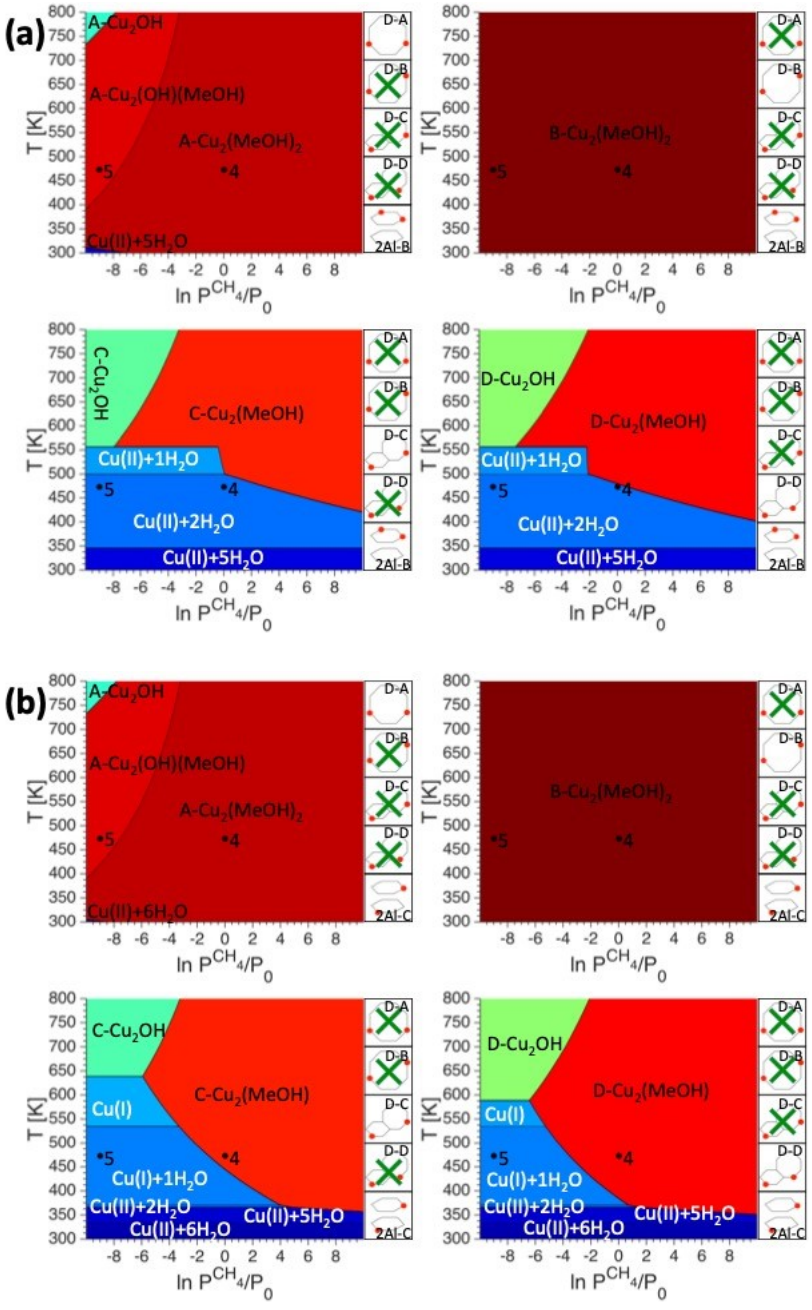


Figure B.15 Bond distances calculated for (a) dimer sites predicted to not be stable in Cu-SSZ13, (b) trimer sites and (c) non-hydrated Cu_1(II) sites. Red symbols indicate distances between Cu and O in the dimers, green symbols distances between Cu and O in the framework, yellow signals Cu-Al distances and blue symbols shown Cu-Cu distances. X-axis labels correspond to the local Al configurations and columns highlighted by dashed lines for each Al configuration indicate (from left to right) in (a) Cu_2O, Cu_2O_2, Cu_2O_2H (Al configurations D-A through D-D) and $Cu_2O_2H_2$ (Al configurations D-C and D-D) and in (b) Cu_3O_3, Cu_3O_3H, $Cu_3O_3H_2$ and $Cu_3O_3H_3$ Black lines indicate literature values for bond distances measured using EXAFS and grey shaded areas mark the experimentally reported error bars.

B.9.9 T/P(CH_4) Phase Diagrams for 2Al-B through 2Al-E



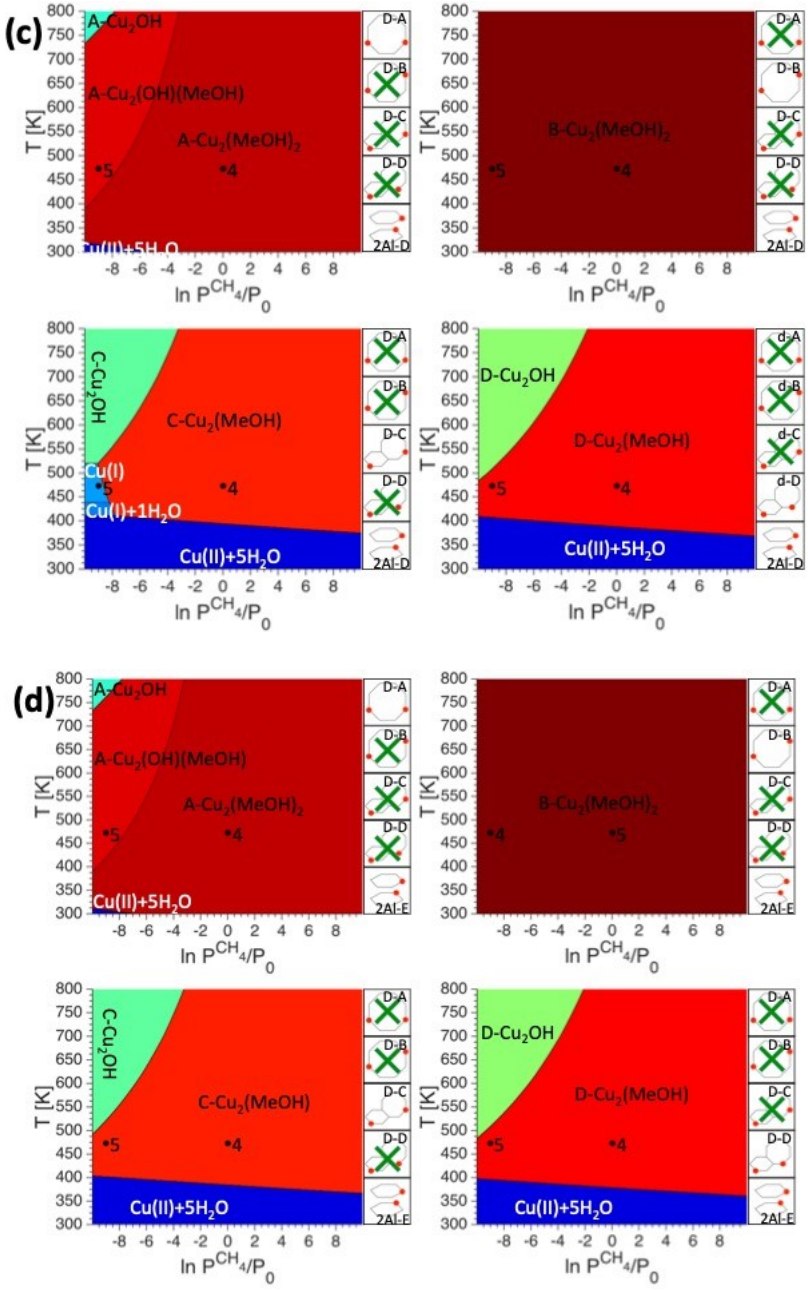
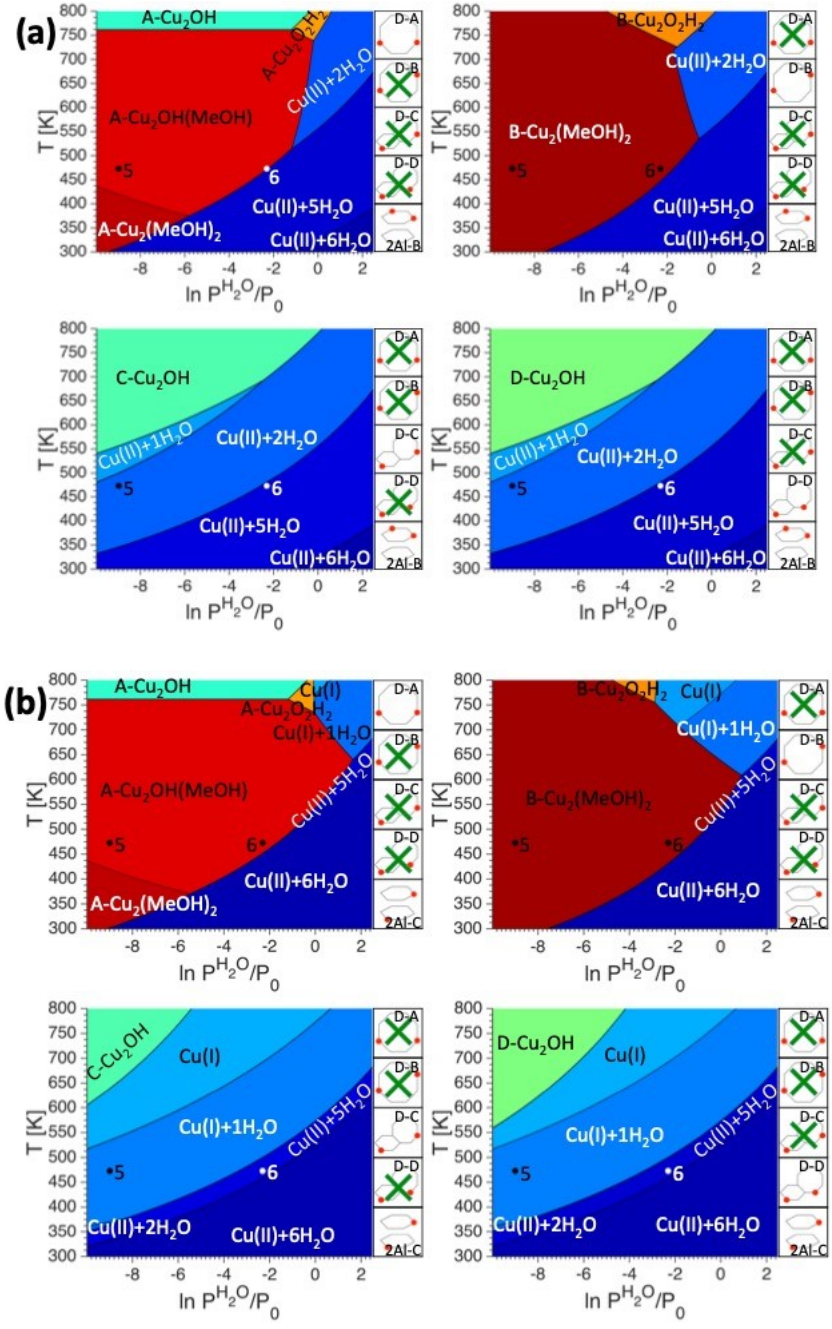


Figure B.16 T/P^{CH_4}phase diagrams for different Al configurations and (a) Cu monomers anchored in a 2Al-B configuration or (b) the 2Al-C configuration, (c) the 2Al-C configuration and (d) the 2Al-E configuration. The temperature is given in K and P^{CH_4} is given with respect to a reference pressure of one bar. The thermodynamically preferred sites are indicated by regions of identical color and the site type is indicated by the labels. The included Al configurations are indicated by schematic representations on the right side of the phase diagrams, which correspond to Figure B.2(b) and Figure B.3(a). Green crosses indicate Al configurations not included in the phase diagrams. Marked points correspond to specific points in the stepwise methane to methanol conversion displayed in Figure B.1. A detailed legend is given in Figure B.11.

S10: T/P(H_2O) Phase Diagrams for 2Al-B through 2Al-E



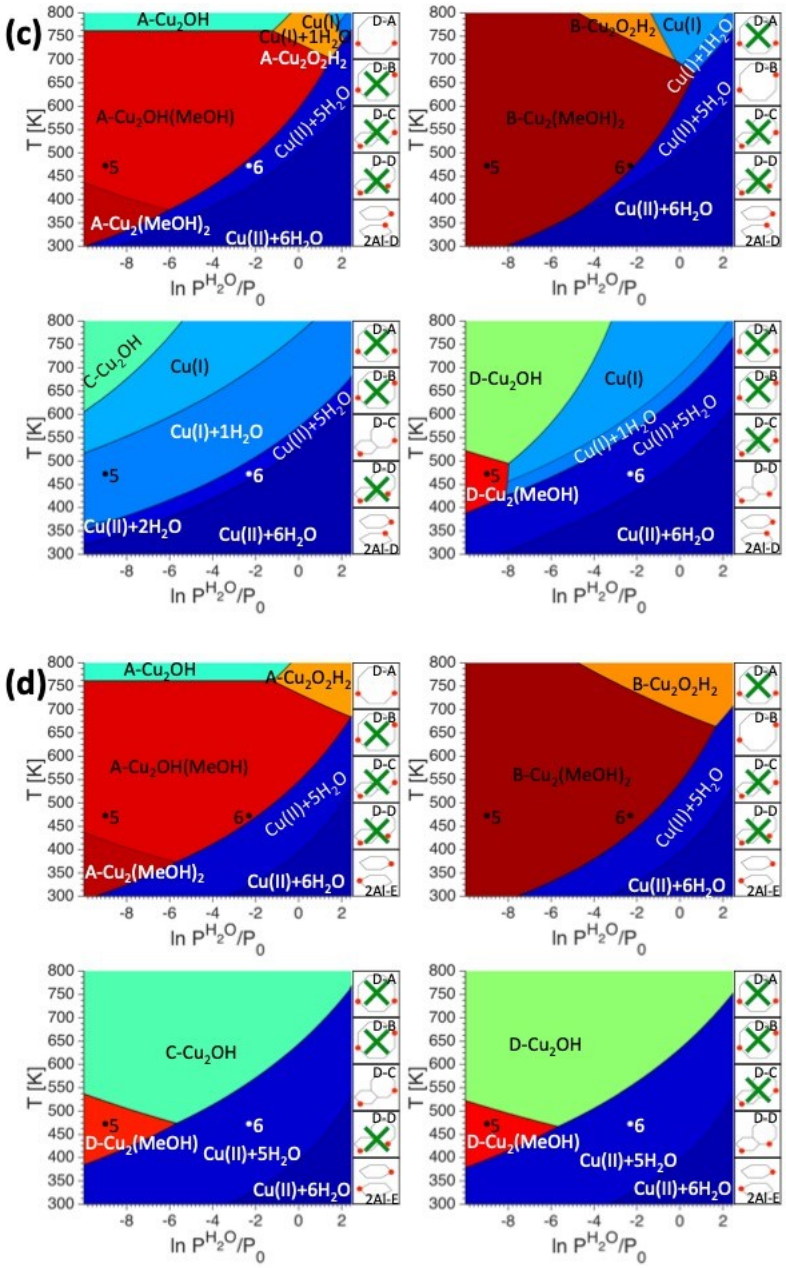


Figure B.17 T/P^{H_2O}phase diagrams for different Al configurations and (a) Cu monomers anchored in a 2Al-B configuration or (b) the 2Al-C configuration, (c) the 2Al-D configuration and (d) the 2Al-E configuration in the presence of CH_4. The temperature is given in K and P^{H_2O} is given with respect to a reference pressure of one bar. The thermodynamically preferred sites are indicated by regions of identical color and the site type is indicated by the labels. The included Al configurations are indicated by schematic representations on the right side of the phase diagrams, which correspond to Figure B.2(b) and Figure B.3(a). Green crosses indicate Al configurations not included in the phase diagrams. Marked points correspond to specific points in the stepwise methane to methanol conversion displayed in Figure B.1. A detailed legend is given in Figure B.11.

APPENDIX C

SUPPORTING INFORMATION FOR CHAPTER 3:REACTION MECHANISM OF VAPOR-PHASE FORMIC ACID DECOMPOSITION OVER PLATINUM CATALYSTS: DFT, REACTION KINETICS EXPERIMENTS, AND MICROKINETIC MODELING[⊥]

C.1 Supplementary Tables for the 4/9 ML CO*-Covered Pt(111) Model

Shomate equations:

$$H(t)[kJ/mol] = A * t + B * \frac{t^2}{2} + C * \frac{t^3}{3} + D * \frac{t^4}{4} - \frac{E}{t} + F \quad (C.1)$$

$$S(t)[J/mol/K] = A * ln(t) + B * t + C * \frac{t^2}{2} + D * \frac{t^3}{3} - \frac{E}{2 * t^2} + G \quad (C.2)$$

Where, t = T (in K)/1000 and A-H are the Shomate parameters, H(t) and S(t) are the enthalpy and entropy, respectively, of the relevant species and transition-states as a function of temperature.

[⊥]Adapted from – Bhandari, S.; Rangarajan, S.; Maravelias, C.T.; Dumesic, J.A.; Mavrikakis, M. Reaction Mechanism of Vapor-Phase Formic Acid Decomposition over Platinum Catalysts: DFT, Reaction Kinetics Experiments, and Microkinetic Modeling. *ACS Catalysis* **2020**, 10 (7) 4112-4126 – https://doi.org/10.1021/acscatal.9b05424

Table C.1 Optimized Shomate parameters (A to H) for the adsorbate binding energies (in kJ/mol) in reaction network in T-range: 300 – 1200 K evaluated on the 4/9ML CO*-covered Pt(111).

4/9 ML CO* covered Pt(111)	A	B	C	D	E	F	G
HCOOH(g)	30.00	114.15	-80.06	22.92	-0.25	-2804.17	252.92
CO_2(g)	39.23	9.25	1.50	-1.82	-0.39	-2193.56	256.34
CO(g)	37.11	0.97	-1.10	0.42	0.01	-1459.23	242.37
H_2O(g)	27.25	7.15	15.65	-9.00	0.27	-1324.99	220.51
H_2(g)	28.91	0.61	-0.69	0.27	0.01	-633.28	165.56
HCOOH*	18.87	164.52	-116.38	32.58	0.08	-2840.72	74.30
cis-HCOOH*	23.15	156.76	-111.47	31.44	-0.07	-2825.01	62.49
HCOO*	19.47	138.56	-102.47	28.94	-0.16	-2462.40	39.15
COOH*	41.31	82.55	-47.86	9.74	-0.97	-2501.81	70.46
cis-COOH*	42.24	82.49	-50.09	11.06	-0.91	-2501.67	73.91
H_2O*	32.48	46.67	-33.90	11.84	-0.29	-1351.35	68.26
HCO*	29.01	58.40	-30.62	5.93	-0.35	-1805.91	62.67
COH*	34.48	53.21	-30.39	6.51	-0.97	-1851.16	46.54
O*	18.74	17.67	-18.54	6.73	-0.34	-540.00	28.78
OH*	25.73	36.85	-33.32	12.17	-0.29	-909.63	55.72
CO_2*	36.21	61.67	-42.82	11.74	-0.08	-2198.24	152.68
CO*	27.55	37.80	-27.89	8.16	-0.13	-1522.39	56.75
H*	10.56	23.00	-11.52	0.97	-0.68	-336.54	6.31

Table C.2 Optimized Shomate parameters (A to H) for the transition-state energies (in kJ/mol) in the reaction network in T-range: 300 – 1200 K evaluated on the 4/9ML CO*-covered Pt(111)

4/9 ML CO* covered Pt(111)	A	B	C	D	E	F	G
HCOOH* + 2* ↔ HCOO* + H*	19.50	174.65	-132.81	38.15	-0.30	-2755.20	32.12
HCOO* ↔ $HCOO_m$* + *	31.04	82.63	-43.79	7.60	-0.49	-2323.14	75.16
$HCOO_m$* + * ↔ CO_2* + H*	36.35	88.14	-47.89	8.73	-0.46	-2386.20	81.96
HCOOH* ↔ *cis*-HCOOH*	20.96	144.08	-98.49	26.87	-0.12	-2802.59	52.50
cis-HCOOH* ↔ COOH* + H*	29.47	136.05	-93.09	24.85	-0.48	-2753.85	54.20
COOH* + * ↔ CO_2* + H*	40.99	83.17	-53.36	12.12	-0.83	-2400.61	83.84
COOH* ↔ *cis*-COOH*	38.38	75.95	-46.78	10.69	-0.78	-2458.21	69.79
cis-COOH* ↔ CO* + OH*	48.37	63.17	-48.63	15.71	-0.70	-2403.95	90.54
COOH* + O* ↔ CO_2* + OH*	28.49	170.70	-132.43	37.82	-0.41	-2968.92	45.78
HCO* + * ↔ CO* + H*	30.08	56.62	-32.83	6.22	-0.64	-1767.62	51.77
COH* + * ↔ CO* + H*	30.55	55.77	-30.11	4.47	-0.80	-1717.94	42.21
COOH* + CO* ↔ COH* + CO_2*	45.66	157.49	-106.99	27.51	-0.57	-3943.70	84.72
COH* + CO* ↔ HCO* + CO*	53.88	96.50	-55.95	10.74	-0.97	-3267.65	91.90
OH* + CO* ↔ HCO* + O*	40.29	72.05	-37.79	6.29	-0.66	-2320.45	71.63
OH* + CO* ↔ COH* + O*	28.15	122.96	-95.49	27.31	-0.60	-2358.08	35.37
OH* + * ↔ O* + H*	24.42	34.74	-26.66	7.21	-0.70	-786.92	33.48
OH* + H* ↔ H_2O* + *	31.63	47.38	-31.59	8.52	-0.83	-1203.16	46.72
H* +H* ↔ H_2(g) + 2*	24.36	22.34	-21.71	8.82	-0.50	-565.17	37.61
HCOO* + OH* ↔ $HCOO_m$* + OH* + *	26.27	186.87	-130.68	35.36	-0.28	-3275.37	50.73
HCOO* + H_2O* ↔ $HCOO_m$* + H_2O* + *	41.74	177.91	-118.41	32.14	-0.47	-3706.16	93.39

Table C.3 Pre-exponential factors for the adsorption steps on 4/9ML CO*-covered Pt(111), where, per collision theory, rate constant $k = AT^{-0.5}$ (where, k is in s^{-1})

	A (× 10^9)
HCOOH(g) + * ↔ HCOOH*	3.93
CO_2(g) + * ↔ CO_2*	4.02
CO(g) + * ↔ CO*	5.04
H_2O(g) + * ↔ H_2O *	6.28

Table C.4 Coefficients for the polynomial expression (ΔBE (in kJ/mol) = $\alpha_0 + \alpha_1\theta + \alpha_2\theta^2 + \alpha_3\theta^3$) employed to update the binding energy of the adsorbates with surface coverage of CO*, from the values calculated on the 4/9 ML CO*-covered Pt(111) facet, where θ is the surface coverage of CO (in ML) calculated by the mean-field microkinetic model during a forward simulation. Value of α_1 was set to zero to ensure that the energy minimum for each species was at clean surface level (no coadsorbed CO*).The parameters α_0, α_2, and α_3 are fit using unadjusted DFT energies calculated at varying coadsorbed CO*-coverages, as described in the main text.

(111)	α_0	α_1	α_2	α_3
cis-COOH*	-43.3	0.0	-12.4	522.6
CO*	-57.7	0.0	386.4	-184.3
COH*	-47.4	0.0	72.2	403.4
COOH*	-44.0	0.0	-11.5	531.2
H*	-14.7	0.0	-11.2	192.5
HCO*	-39.8	0.0	137.0	182.8
HCOO*	-36.3	0.0	58.9	330.3
HCOOH*	-18.1	0.0	-175.7	601.2
cis-HCOOH*	-18.1	0.0	-175.7	601.2
O*	-51.1	0.0	132.8	348.9
OH*	-29.7	0.0	114.8	85.8

Table C.5 Coefficients for the polynomial expression (ΔE_{TS} (in kJ/mol) = $\alpha_0 + \alpha_1\theta + \alpha_2\theta^2 + \alpha_3\theta^3$) employed to update the transition-state energies for the elementary steps with surface coverage of CO*, from the values calculated on the 4/9 ML CO*-covered Pt(111) facet, where θ is the surface coverage of CO (in ML) calculated by the mean-field microkinetic model during a forward simulation. Value of α_1 was set to zero to ensure that the energy minimum for each transition-state was at clean surface level (no coadsorbed CO*). The parameters α_0, α_2, and α_3 are fit using unadjusted DFT energies calculated at varying coadsorbed CO*-coverages, as described in the main text.

(111)	α_0	α_1	α_2	α_3
HCOOH* + 2* ↔ HCOO* + H*	-49.9	0.0	23.8	515.3
HCOOH* ↔ *cis*-HCOOH*	0.0	0.0	0.0	0.0
cis-HCOOH* + * ↔ COOH* + H*	-76.0	0.0	-74.2	1032.9
HCOO* ↔ CO_2* + H*	-76.8	0.0	-21.7	924.1
COOH* + * ↔ CO_2* + H*	-66.6	0.0	-4.3	767.8
COOH* ↔ *cis*-COOH*	-42.1	0.0	-17.0	517.4
cis-COOH* + * ↔ CO* + OH*	-54.8	0.0	15.6	588.6
HCO* + * ↔ CO* + H*	-33.4	0.0	51.7	263.9
CO* + O* ↔ CO_2* + *	-70.6	0.0	-11.1	829.3
OH* + H* ↔ H_2O* + *	-49.3	0.0	24.8	505.8
2H* ↔ H_2 + 2*	-40.6	0.0	39.5	373.5
COOH* + CO* ↔ COH* + CO_2*	-80.0	0.0	-27.0	972.0
HCO* + CO* ↔ COH* + CO*	-85.4	0.0	-90.0	1174.8
COH* + * ↔ CO* + H*	-48.6	0.0	26.1	494.5

Table C.6 Degree of rate control (X_{RC}) and enthalpies (H), wrt. HCOOH(g), CO(g), and H_2(g), for reaction intermediates and elementary steps in FA dehydrogenation pathway on the CO* coverage-cognizant Pt(111) microkinetic model, at home conditions (2.6% FA, balance He, 373K).

4/9 ML CO-covered Pt(111)*	X_{RC}	*H (298 K) / kJ/mol*
Intermediate		
HCOOH*	-0.01	-39.0
cis-HCOOH*	0.00	-21.8
COOH*	0.00	-10.3
H*	-0.10	-17.8
CO_2*	0.00	-19.5
COH*	-0.08	-50.6
Elementary Step		
HCOOH* ↔ *cis*-HCOOH*	0.00	-0.4
cis-HCOOH* + * ↔ COOH* + H*	0.00	51.8
COOH* + * ↔ CO_2* + H*	0.36	72.4
2H* ↔ H_2(g) + 2*	0.27	69.3
COOH* + CO* ↔ CO_2* + COH*	0.24	45.0
COH* + * ↔ CO* + H*	0.07	81.0

We calculate the degree of rate control wrt. all reaction intermediates and elementary steps for the dehydrogenation pathway (Table C.6). For the species involved in the dehydrogenation pathway, H* and COH* carry the highest rate control of -0.10 and -0.08, respectively. Considering the transition-states, our results suggests that the degree of rate control is largely governed by COOH* dehydrogenation, CO*-assisted COOH decomposition, and recombinative desorption of H_2(g). Using these results we calculate apparent activation energy barrier using the methodology described by Mao and Campbell.[445] For FA dehydrogenation, we determine the apparent activation energy barrier of 71.4 kJ/mol, which compares favorably with the experimentally determined value of 66.1 kJ/mol. We hypothesize that the slight mismatch could potentially be due to the complex nature of our reaction network, specifically, the competing direct and CO*-assisted COOH* mechanisms for FA dehydrogenation, which occur in parallel.

Table C.7 Degree of rate control (X_{RC}) for the relevant elementary steps toward the decomposition of FA, obtained by keeping the (a) direct COOH* dehydrogenation, (b) CO* assisted COOH* mechanisms active, one at a time. The energetics were maintained at the steady-state CO* coverages corresponding to home conditions (2.6% FA, balance He, 373K), by co-feeding appropriate amounts of CO(g) in the feed.

(a) Direct COOH* dehydrogenation	**X_{RC}**
$COOH^* + * \leftrightarrow CO_2^* + H^*$	0.57
$H^* + H^* \leftrightarrow H_2(g) + 2^*$	0.35

(b) CO*-assisted COOH* dehydrogenation	**X_{RC}**
$COOH^* + CO^* \leftrightarrow COH^* + CO_2^*$	0.51
$COH^* + * \leftrightarrow CO^* + H^*$	0.14
$H^* + H^* \leftrightarrow H_2(g) + 2^*$	0.30

C.2 Corrections Predicted by Parameter Estimation vs. DFT Intrinsic Errors

The optimized 4/9 ML CO*-covered Pt(111) model required stabilization to the binding energy of HCOOH and *cis*-HCOOH by 0.26 eV (with gas-phase corrections: -0.32 eV) and 0.20 eV (with gas-phase corrections: -0.26 eV), respectively. These corrections can be attributed to the lack of inclusion of dispersion interactions in our calculations, which may dominate the binding energy of closed-shell stable molecules[143,145]. Benchmarking studies comparing experimental adsorption energies with DFT, on a host of transition metal surfaces, have demonstrated that standard DFT functionals, such as PW91, systematically under-predict the adsorption energy of closed-shell molecules which bind mainly through dispersion interactions.[143]. We find that, with our computational setup (PW91-GGA), DFT under-predicts the binding energy of formic acid by 0.26 eV on Pt(111) (Table C.8), compared with the experimental single crystal adsorption calorimetry (SCAC) energies.[141] This is similar in magnitude to the stabilization predicted by our parameter estimation procedure implemented within the framework of our MKM.

Importantly, PW91-DFT energetics have been known to systematically over-bind chemisorbed species (e.g., CO, NO), and require destabilization to match the experimentally measured SCAC values.[143] Our procedure suggests an overall correction of the CO energetics by 0.38 eV, which accounts for: (1) adjustment of CO* binding energy by +0.10 eV, required by the parameter estimation and (2) correction of the CO gas-phase energy by -0.28 eV, to obtain agreement with NIST values. This compares favorably with the required destabilization in the range of 0.3-0.6 eV, on the (111) facets (Table C.9), at low adsorbate coverages, to match the SCAC values.[115] Reaction energy for H_2 dissociative adsorption on Pt(111) was calculated as -1.00 eV, compared with an experimentally reported value of -0.75 eV[143] for ¼ ML of adsorbed H, which translates

to PW91 over-predicting the binding of H* by 0.12 eV (Table C.10). This value is also in close-agreement with the correction of 0.17 eV required by parameter estimation for H* binding energy. Thus, the corrections predicted by parameter estimation are rationalized by the intrinsic errors associated with PW91-GGA energetics.

Table C.8 Comparison of PW91-evaluated binding energy of formic acid with the enthalpy for adsorption of formic acid obtained from experimental values in the literature.[146] Negative Δ implies under prediction of binding energy by PW91-DFT (at FA coverage of 1/9 ML on clean Pt(111)). All values are in eV.

HCOOH	DFT-PW91	Expt.	Δ = Expt - DFT
Pt(111)	-0.34	-0.63[146]	-0.29

Table C.9 Comparison of PW91-evaluated binding energy of CO with the enthalpy for adsorption of CO obtained from experimental values in the literature.[115] Positive Δ implies over prediction of binding energy by PW91-DFT (at CO* coverage of 1/9 ML on clean Pt(111)). All values are in eV.

CO	DFT-PW91	Expt.	Δ = Expt - DFT
Pt(111)	-1.79	-1.51[115]	0.28

Table C.10 Comparison of PW91-evaluated reaction energy for dissociative adsorption of H_2 with that from experimental values in the literature.[143] Numbers in square brackets ([ ]) represents DFT H* binding energy values (at H* coverage of 1/9 ML on Pt(111)), referenced to atomic H(g) in the gas phase, which were used to calculate the reaction energies. The PW91-gas phase bond energy for H_2 is 4.55 eV, whereas that value is 4.52 eV per experiment. Positive Δ implies over prediction of dissociative adsorption energy by PW91-DFT. The entries in the last column: ΔBE (H*) = Δ/2, indicates over-prediction in the H* binding energy by DFT. All values are in eV.

$H_2(g) \rightarrow 2H^*$	DFT-PW91 Reaction Energy [BE (H*)]	Expt.Reaction Energy[143]	Δ = Expt - DFT	ΔBE (H*)
Pt(111)	-1.00 [-2.78]	-0.75	0.25	0.12

C.3 Catalyst Characterization

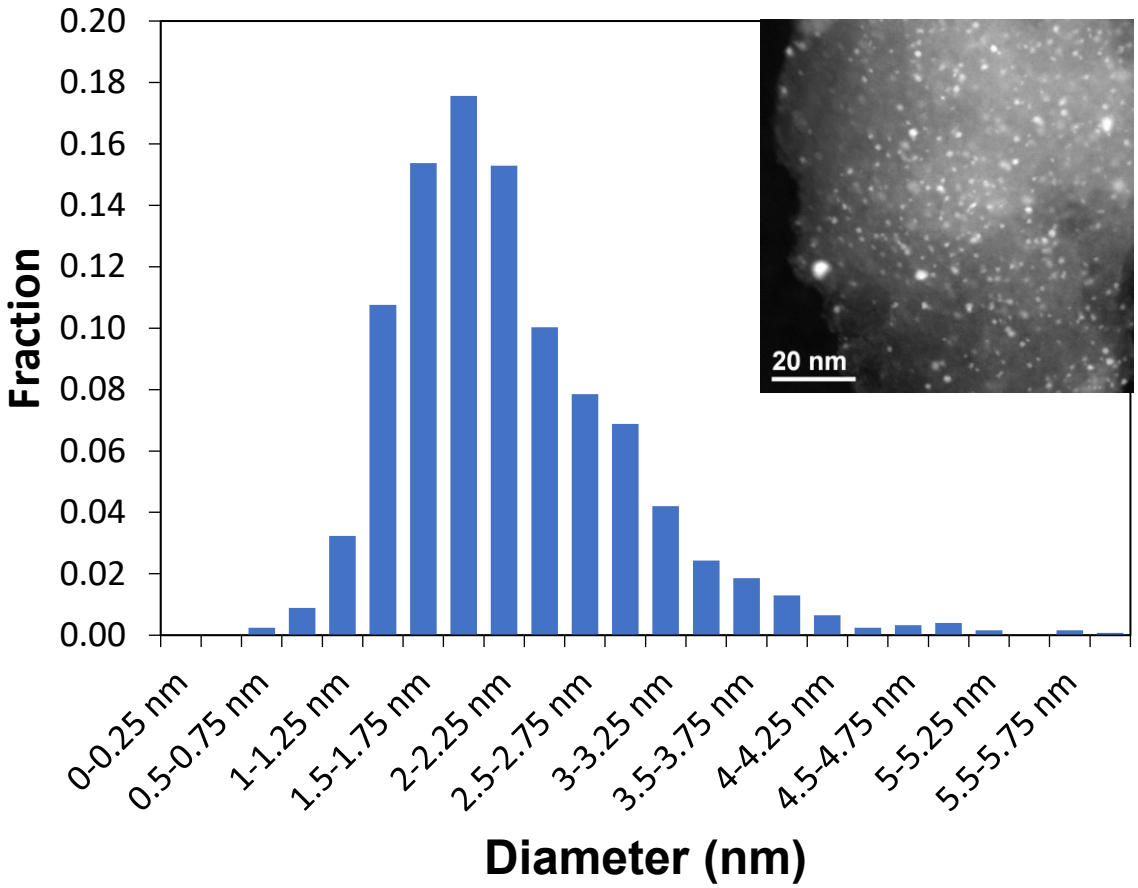


Figure C.1 Particle size distribution of Pt/C catalyst (Average particle size: 2.16 ± 0.65 nm, by analyzing ~2000 particles) as determined by STEM (FEI-Titan). Inset displays an STEM image. The images were collected in high-angle annular dark field (HAADF) mode with a probe current of approximately 25 pA, probe convergence angle of 24.5 mrad, and detector angle ranging from 54 to 270 mrad.

C.4 PFR Simulation: Optimized CO*-coverage Dependent Energetics Pt(111)

Using the optimized CO* coverage dependent energetics we formulated a Plug Flow Reactor (PFR) model to verify the applicability of CSTR model for modeling the kinetics. Since, the energetics of our reaction network is dependent on the MASI - CO*, we specifically investigate the CO* coverage profile along the reactor length (Figure C.2). We find that CO* coverage builds rapidly in the initial portion of the reactor length and converges to within 10% of the CO* coverages predicted by our CSTR model within the initial ~3% of reactor length. The majority of the reactor bed (~97%) experiences CO* coverages similar to that predicted by the CSTR model. Thus, a CSTR should be a good model to use for parameter estimation and modeling the kinetics of this chemistry.

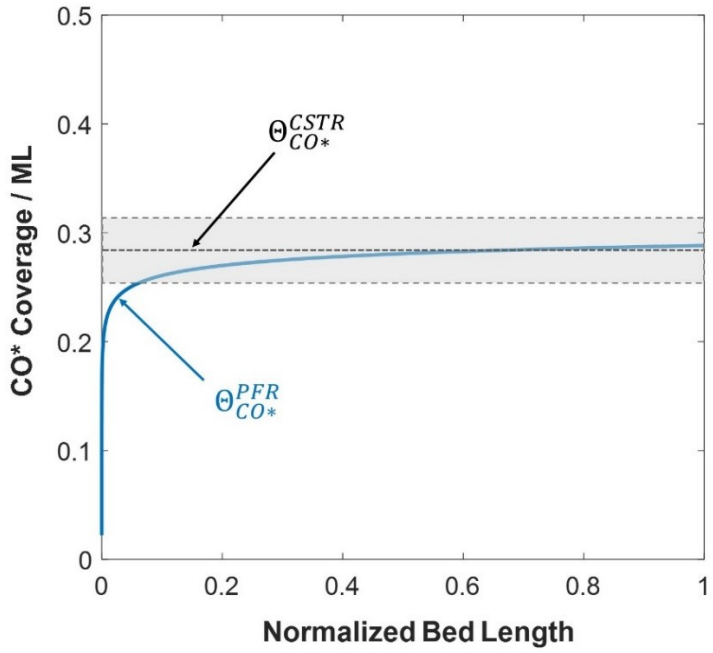


Figure C.2 CO* coverage profile as predicted from a PFR simulation (shown in blue) using the optimized CO* coverage dependent energetics, at the home conditions (2.6% FA, balance He, 373 K). The corresponding CO* coverage predicted by the CSTR model is indicated by the dashed line, along with ±10% error bars.

APPENDIX D

SUPPORTING INFORMATION FOR CHAPTER 4: A COVERAGE SELF-CONSISTENT MICROKINETIC MODEL FOR VAPOR-PHASE FORMIC ACID DECOMPOSITION ON PD/C CATALYSTS

D.1 Experimental

D.1.1 Reaction Kinetics Experiments

Table D.1 Reaction rates obtained from kinetics experiments on Pd/C at 1 atm. The inlet feed flowrates have been normalized by the number of surface sites for Pd/C used in the reactor.

			Inlet Feed (μmol/μmol$_{Pd}$/s)						Experimental Rates	
#	Pressure (atm)	Temperature (K)	FA	CO	CO_2	H_2	H_2O	He	TOF_{CO+H2O} x10^2 (s^{-1})	TOF_{CO2+H2} (s^{-1})
1	1	353	2.21	0.00	0.00	0.00	0.00	82.37	0.03	0.05
2	1	363	2.21	0.00	0.00	0.00	0.00	82.37	0.07	0.09
3	1	373	2.21	0.00	0.00	0.00	0.00	82.37	0.12	0.16
4	1	383	2.21	0.00	0.00	0.00	0.00	82.37	0.26	0.31
5	1	393	2.21	0.00	0.00	0.00	0.00	82.37	0.53	0.58
6	1	373	1.11	0.00	0.00	0.00	0.00	83.47	0.12	0.17
7	1	373	1.67	0.00	0.00	0.00	0.00	82.91	0.12	0.17
8	1	373	2.75	0.00	0.00	0.00	0.00	81.83	0.13	0.16
9	1	373	2.16	0.00	0.00	0.00	0.02	80.51	0.12	0.17
10	1	373	2.16	0.00	0.00	0.00	0.02	80.51	0.13	0.16
11	1	373	2.16	0.00	0.00	0.00	0.03	80.51	0.13	0.16
12	1	373	2.16	0.00	0.00	0.00	0.05	80.51	0.12	0.16
13	1	373	2.17	0.00	0.00	7.90	0.00	73.22	0.15	0.14
14	1	373	2.17	0.00	0.00	11.85	0.00	69.27	0.15	0.11
15	1	373	2.17	0.00	0.00	19.75	0.00	61.37	0.16	0.10
16	1	373	2.06	0.00	2.86	0.00	0.00	74.04	0.13	0.15
17	1	373	2.06	0.00	5.70	0.00	0.00	71.19	0.13	0.16
18	1	373	2.06	0.00	8.51	0.00	0.00	68.38	0.14	0.16
19	1	373	2.06	0.00	11.54	0.00	0.00	65.36	0.15	0.15
20	1	373	2.15	0.02	0.00	0.00	0.00	80.04	-[a]	0.04
21	1	373	2.15	0.04	0.00	0.00	0.00	80.02	-[a]	0.02
22	1	373	2.15	0.08	0.00	0.00	0.00	79.98	-[a]	0.02

[a]The dehydration turnover frequency for the CO co-feed experiments, which correspond to #20-22, could not be accurately measured because of small selectivity of the reaction toward CO formation on Pd/C.

D.1.2 Catalyst Characterization

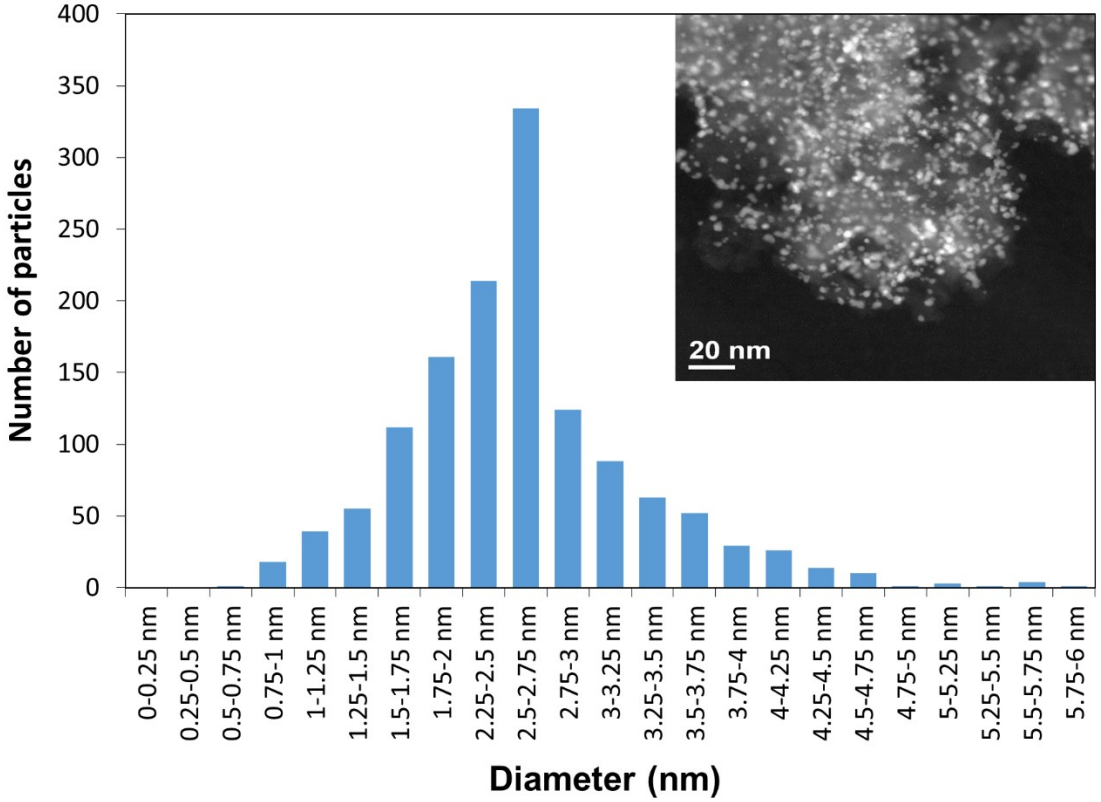


Figure D.1 Particle size distribution of Pd/C catalyst. Average particle size is: 2.47 ± 0.94 nm. Inset displays an STEM image of the catalyst, captured in the high-angle annular dark field (HAADF) mode (probe current: ~25 pA, probe convergence angle: 24.5 mrad, detector angle: 54 to 270 mrad).

D.1.3 Operando FTIR Spectroscopy

Pd/SiO_2 samples were pressed into self-supporting wafers using a 1.1 cm die. Samples were reduced at 573 K (0.6 K min^{-1}, 4h) in flowing 25% H_2/He and cooled down to 403 K under He flow. Fourier transform infrared (FTIR) (Nicolet 6700) spectra of adsorbed CO* were obtained in transmission mode after flowing 10% CO/He for 1h (Figure D.2). The sample was reduced again using the same procedure described above before introducing 1% FA/He. We compare the height of the CO* stretching band from the FA exposure to that obtained during CO/He feed to estimate the CO surface coverage under operating conditions (Table D.2).

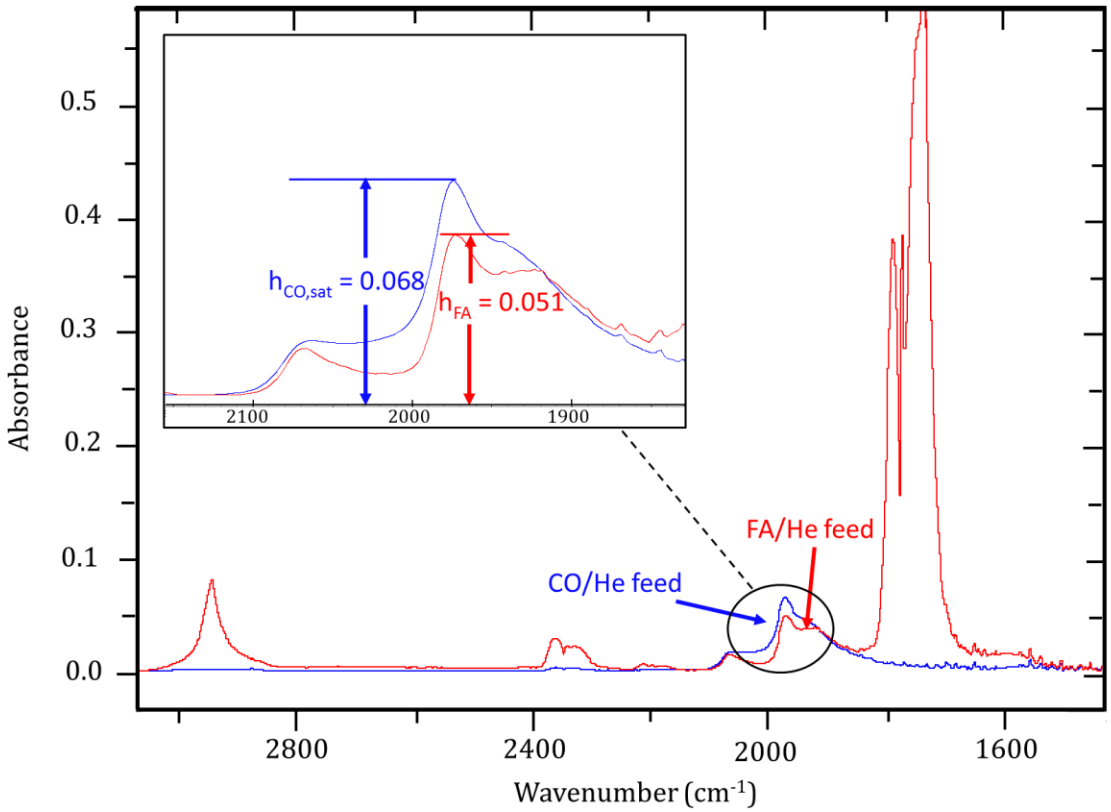


Figure D.2 FTIR spectra comparing the CO* bond-stretching peak under reaction conditions with CO* saturation. The '*h*' values reported in the inset correspond to the peak intensity at respective feed condition.

Table D.2 Comparison of CO coverages on Pd/SiO_2 catalyst through *operando* FTIR. Sample were reduced under 25% H_2/He at 573K for 4h before the first and the second exposure.

#	First Exposure	Second Exposure	% CO saturation (band height)
1	CO/He	HCOOH/He	74.6%
2	CO/He	HCOOH/He	74.4%
3	HCOOH/He	CO/He	75.5%

D.2 Model Formulation

Periodic self-consistent DFT calculations were performed with DACAPO,[56,57] using the PW91-GGA functional.[189] We utilized Ultrasoft Vanderbilt pseudopotentials to describe the core-electrons. The Kohn-Sham valence states were expanded using plane-waves with an energy cut-off value of 25 Ry (340.14 eV). The lattice constant for bulk Pd was determined as 3.99 Å, which was in good agreement with the experimentally determined value of 3.89 Å.[125] The Pd(111) surface was modeled by a (3x3) unit-cell, with three atomic-layers. Our tests revealed negligible changes in binding energy upon relaxing the surface layer, therefore, all three atomic-layers were fixed at their bulk-truncated positions. The Pd(100) surface was modeled by a (3x3) unit-cell with four atomic-layers; the top two surface-layers were allowed to relax. The surface Brillouin zone for Pd(111) was sampled at 6 special Chadi-Cohen k-points[296] and that for Pd(100) was sampled with a 4x4x1 Monkhorst-Pack k-point mesh.[128] The binding energy of reaction intermediates was calculated with respect to the energy of the reaction intermediate in the gas-phase and the energy of the slab (clean or partially covered by CO*, depending on the model under consideration, i.e., clean or partially CO*-covered model, respectively). Convergence of the binding energies for the reaction intermediates with respect to the computational settings, has been verified previously.[108] The transition-state energies were determined using the climbing-image nudged-elastic band (CI-

NEB) method.[129,297,298] The reaction pathways were discretized using 7 intermediate images between the initial and the final state. The structures were optimized until the forces on all images were <0.1 eV/Å. To verify the transition-state, vibrational frequency calculations were performed to identify a single imaginary frequency along the reaction coordinate. In this work, we utilize DFT energetics to obtain initial estimates of the thermodynamic and kinetic rate parameters and formulate microkinetic models.

D.2.1 Coverage Dependent Thermochemical Parameters

Table D.3 Coefficients for the polynomial expression (ΔBE (in kJ/mol) = $\alpha_0 + \alpha_1\theta + \alpha_2\theta^2 + \alpha_3\theta^3$) employed to update the binding energy of the adsorbates with surface coverage of CO*, from the values calculated on 5/9 ML CO*-covered Pd(111), where θ is the surface coverage of CO (in ML) calculated by the mean-field microkinetic model during the simulation. Value of α_1 was set to zero to ensure that the energy minimum for each species was at clean surface level (no coadsorbed CO*). The parameters α_0, α_2, and α_3 are fit using unadjusted DFT energies calculated at varying coadsorbed CO*-coverages, as described in the main text.

(111)	α_0	α_1	α_2	α_3
CO*	-65.2	0.0	95.3	232.7
HCOO*	-85.5	0.0	-302.9	1073.5
H*	-25.9	0.0	141.0	-96.6
COOH*	-87.6	0.0	-42.3	570.0
cis-COOH*	-87.6	0.0	-42.3	570.0
HCOOH*	-10.6	0.0	34.9	0.0
HCOOH*pa**	-10.6	0.0	34.9	0.0
OH*	-45.0	0.0	181.3	0.0
O*	-90.7	0.0	293.8	0.0
HCO*	-70.4	0.0	228.2	0.0
COH*	-70.4	0.0	228.2	0.0
H_2O*	-4.6	0.0	14.8	0.0

Table D.4 Coefficients for the polynomial expression (ΔBE (in kJ/mol) = $\alpha_0 + \alpha_1\theta + \alpha_2\theta^2 + \alpha_3\theta^3$) employed to update the binding energy of the adsorbates with surface coverage of CO*, from the values calculated on the 5/9 ML CO*-covered Pd(100) facet, where θ is the surface coverage of CO (in ML) calculated by the mean-field microkinetic model during the simulation. Value of α_1 was set to zero to ensure that the energy minimum for each species was at clean surface level (no coadsorbed CO*).The parameters α_0, α_2, and α_3 are fit using unadjusted DFT energies calculated at varying coadsorbed CO*-coverages, as described in the main text.

(100)	α_0	α_1	α_2	α_3
CO*	-34.3	-0.0	-171.1	489.9
HCOO*	-84.5	-0.0	-91.9	660.5
COOH*	-103.6	0.0	271.1	86.9
H*	-37.5	0.0	102.6	0.0
cis-COOH*	-103.6	0.0	271.1	86.9
HCOOH*	-29.3	0.0	95.0	0.0
HCOOH*pa**	-30.9	0.0	100.0	0.0
OH*	-55.9	0.0	181.0	0.0
O*	-98.3	0.0	318.5	0.0
HCO*	-88.6	0.0	287.2	0.0
H_2O*	-4.6	0.0	14.8	0.0

D.2.2 Coverage Dependent Kinetic Parameters

Table D.5 Coefficients for the polynomial expression (ΔE_{TS} (in kJ/mol) = $\alpha_0 + \alpha_1\theta + \alpha_2\theta^2 + \alpha_3\theta^3$) employed to update the transition state energies of the elementary steps with surface coverage of CO*, from the values calculated on the 5/9 ML CO*-covered Pd(111) facet, where θ is the surface coverage of CO (in ML) calculated by the mean-field microkinetic model during the simulation. Value of α_1 was set to zero to ensure that the energy minimum for each transition-state was at clean surface level (no coadsorbed CO*).The parameters α_0, α_2, and α_3 are fit using unadjusted DFT energies calculated at varying coadsorbed CO*-coverages, as described in the main text.

(111)	α_0	α_1	α_2	α_3
HCOOH* + 2* → HCOO* + H*	-86.8	0.0	281.3	0.0
HCOOH* → HCOOH*pa**	-10.6	0.0	34.9	0.0
HCOOH*pa** + * → COOH* + H*	-91.7	0.0	297.0	0.0
HCOO* → CO_2* + H*	-156.9	0.0	-71.6	1073.5
COOH* + * → CO_2* + H*	-130.0	0.0	95.2	570.0
COOH* → *cis*-COOH*	-87.6	0.0	-42.3	570.0
cis-COOH* + * → CO* + OH*	-94.3	0.0	-20.4	570.0
HCO* + * → CO* + H*	-99.4	0.0	322.0	0.0
CO* + O* → CO_2* + *	-64.2	0.0	92.1	232.7
OH* + * → O* + H*	-91.3	0.0	331.4	0.0
2OH* → H_2O* + O*	-89.0	0.0	359.5	0.0
OH* + H* → H_2O* + *	-33.2	0.0	200.3	-96.6
2H* → H_2 + 2*	-22.8	0.0	188.1	-193.1
HCOOH* + CO* → COH* + HCOO*	-75.8	0.0	130.1	232.7
HCOO* + CO* → COH* + CO_2*	-150.7	0.0	-207.6	1306.2
COOH* + CO* → COH* + CO_2*	-152.7	0.0	53.0	802.6
HCO* + CO* → COH* + CO*	-135.6	0.0	323.5	232.7
OH* + CO* → COH* + O*	-121.0	0.0	276.2	232.7
OH* + CO* → HCO* + O*	-121.0	0.0	276.2	232.7
COH* + * → CO* + H*	-120.4	0.0	390.2	0.0
COH* + H* → HCOH* + *	-96.3	0.0	369.1	-96.6

Table D.6 Coefficients for the polynomial expression (ΔE_{TS} (in kJ/mol) = $\alpha_0 + \alpha_1\theta + \alpha_2\theta^2 + \alpha_3\theta^3$) employed to update the transition state energies of the elementary steps with surface coverage of CO*, from the values calculated on the 5/9 ML CO*-covered Pd(100) facet, where θ is the surface coverage of CO (in ML) calculated by the mean-field microkinetic model during the simulation. Value of α_1 was set to zero to ensure that the energy minimum for each transition-state was at clean surface level (no coadsorbed CO*).The parameters α_0, α_2, and α_3 are fit using unadjusted DFT energies calculated at varying coadsorbed CO*-coverages, as described in the main text.

(100)	α_0	α_1	α_2	α_3
HCOOH* + 2* → HCOO* + H*	-71.1	0.0	230.2	0.0
HCOOH* + * → *cis*-COOH* + H*	-69.0	0.0	223.7	0.0
HCOO* → CO_2* + H*	-99.0	0.0	-44.9	660.5
COOH* → *cis*-COOH*	-103.6	0.0	271.1	86.9
COOH* + * → CO_2* + H*	-86.3	0.0	215.0	86.9
cis-COOH* + * → CO* + OH*	-143.0	0.0	398.8	86.9
HCO* + * → CO* + H*	-73.5	0.0	238.0	0.0
COH* + * → CO* + H*	-72.0	0.0	-68.5	489.9
CO* + O* → CO_2* + *	-8.6	0.0	147.4	489.9
OH* + * → O* + H*	-98.6	0.0	328.4	0.0
2OH* → H_2O* + O*	-114.7	0.0	389.6	0.0
OH* + H* → H_2O* + *	-87.2	0.0	263.6	0.0
2H* → H_2 + 2*	-45.0	0.0	107.5	0.0
HCO* + CO* → COH* + CO*	-123.1	0.0	116.1	489.9
HCOOHpa* + CO* → COH* + HCOO*	-65.3	0.0	-71.1	489.9
HCOO* + CO* → COH* + CO_2*	-119.0	0.0	-262.9	1150.4
COOH* + CO* → COH* + CO_2*	-138.0	0.0	100.0	576.8

D.2.3 Reaction Energetics on 5/9ML CO*-covered Pd(111) and Pd(100) Facets

Table D.7 Optimized Shomate parameters (A to G) for the gas-phase species and reaction intermediates in reaction network evaluated on 5/9 ML CO* covered Pd(111) facet

5/9ML CO* Pd(111)	A	B	C	D	E	F	G
HCOOH(g)	15.84	143.99	-105.96	31.14	-0.14	-102336.33	231.37
H_2(g)	29.92	-2.35	1.55	0.58	-0.03	-3041.82	171.35
CO_2(g)	27.72	48.61	-28.94	6.74	-0.18	-99321.19	237.82
H_2O(g)	28.06	14.46	-2.99	1.07	0.12	-45237.98	219.56
CO(g)	27.02	0.40	10.80	-5.40	0.11	-57080.80	234.83
HCOOH*	19.95	161.38	-114.08	32.00	0.00	-102401.26	56.94
HCOOH*pa**	19.68	116.45	-67.30	14.89	-0.36	-102352.11	122.26
HCOO*	20.06	135.78	-99.19	27.74	-0.12	-100758.10	42.88
cis-COOH*	44.82	82.49	-56.80	15.37	-0.54	-100760.16	93.79
COOH*	41.56	82.06	-49.07	10.77	-0.83	-100778.52	76.56
CO*	27.73	36.91	-29.44	9.71	0.05	-57128.48	65.58
OH*	26.99	36.26	-34.93	13.23	-0.31	-43602.09	57.92
O*	18.69	17.77	-18.62	6.76	-0.34	-41993.55	28.90
H*	10.91	10.36	10.56	-9.43	-0.92	-1535.29	6.08
HCO*	30.10	57.38	-31.84	7.05	-0.29	-58585.42	67.48
H_2O*	33.20	46.11	-34.99	12.53	-0.30	-45267.35	68.24
CO_2*	31.54	75.91	-59.61	18.44	0.05	-99326.22	113.75
COH*	33.85	53.14	-28.82	5.68	-0.90	-58602.69	47.18
HCOH*	12.86	127.46	-83.99	22.17	-0.20	-60112.02	18.45

Table D.8 Pre-exponential factors for the adsorption steps on 5/9 ML CO* covered Pd(111), where, per collision theory, rate constant $k = AT^{-0.5}$ (where, k is in s^{-1})

5/9ML CO* Pd(111)	A
$HCOOH + * \rightarrow HCOOH*$	3.93E+09
$CO_2* \rightarrow CO_2 + *$	4.02E+09
$CO* \rightarrow CO + *$	5.04E+09
$H_2O* \rightarrow H_2O + *$	6.28E+09

Table D.9 Optimized Shomate parameters (A to G) for the transition-state energies of the elementary steps (in kJ/mol) in reaction network evaluated on the 5/9 ML CO* covered Pd(111) facet

5/9ML CO* Pd(111)	A	B	C	D	E	F	G
HCOOH* + 2* → HCOO* + H*	9.50	216.12	-169.07	49.51	-0.29	-102261.16	6.93
HCOOH* → HCOOH*pa**	0.49	151.57	-107.37	30.31	0.00	-102330.41	70.05
HCOOHpa* + * → COOH* + H*	31.14	142.00	-104.68	29.76	-0.49	-102285.79	54.98
HCOO* → CO_2* + H*	30.81	83.47	-44.70	7.95	-0.44	-100602.48	77.64
HCOO* + H_2O* → CO_2* + H* + H_2O*	41.32	179.69	-119.84	32.38	-0.56	-145969.72	78.71
HCOO* + OH* → CO_2* + H* + OH*	61.28	127.18	-82.50	21.14	-0.91	-144298.04	139.87
COOH* + * → CO_2* + H*	35.40	79.09	-45.62	9.94	-0.19	-100668.93	95.53
COOH* → *cis*-COOH*	38.77	75.66	-48.99	12.26	-0.62	-100741.31	77.73
cis-COOH* + * → CO* + OH*	49.90	62.93	-51.10	17.18	-0.58	-100712.47	95.21
HCO* + * → CO* + H*	20.74	45.69	-17.01	0.23	-0.17	-58549.72	42.05
CO* + O* → CO_2* + *	40.45	47.59	-39.81	13.20	-0.25	-99043.38	79.79
OH* + * → O* + H*	21.80	30.26	-19.17	4.70	-0.16	-43427.79	40.44
2OH* → H_2O* + O*	41.86	70.95	-45.15	10.75	-1.12	-87191.89	62.99
OH* + H* → H_2O* + *	36.55	47.43	-40.04	13.34	-0.93	-45129.36	56.89
2H* → H_2 + 2*	10.41	29.27	-0.38	-5.73	-0.27	-2990.28	14.25
HCOOH* + CO* → COH* + HCOO*	69.84	243.42	-182.55	53.71	-0.57	-159334.52	134.30
HCOO* + CO* → COH* + CO_2*	90.94	166.01	-110.22	28.90	-0.30	-157779.01	214.60
COOH* + CO* → COH* + CO_2*	70.59	214.16	-159.04	45.07	-0.47	-157844.83	147.70
HCO* + CO* → COH* + CO*	79.17	134.53	-84.36	19.82	-0.71	-115598.50	160.80
OH* + CO* → COH* + O*	72.29	104.26	-68.86	18.09	-1.06	-100548.90	129.94
OH* + CO* → HCO* + O*	68.37	111.90	-76.45	21.24	-0.29	-100418.11	158.47
COH* + * → CO* + H*	31.94	54.69	-31.13	5.41	-0.73	-58479.71	46.04
COH* + H* → HCOH* + *	36.39	63.37	-25.55	1.98	-0.92	-60047.44	51.16
HCOH* + * → HCO* + H*	36.15	76.29	-42.01	7.98	-0.86	-60062.44	68.77
HCOH* + 2* → CO* + 2H*	36.15	76.29	-42.01	7.98	-0.86	-59862.37	68.77

Table D.10 Optimized Shomate parameters (A to G) for the gas-phase species and reaction intermediates in reaction network evaluated on 5/9 ML CO* covered Pd(100) facet

5/9ML CO* Pd(100)	A	B	C	D	E	F	G
HCOOH(g)	15.84	143.99	-105.96	31.14	-0.14	-102336.33	231.37
H_2(g)	29.92	-2.35	1.55	0.58	-0.03	-3041.82	171.35
CO_2(g)	27.72	48.61	-28.94	6.74	-0.18	-99321.19	237.82
H_2O(g)	28.06	14.46	-2.99	1.07	0.12	-45237.98	219.56
CO(g)	27.02	0.40	10.80	-5.40	0.11	-57080.80	234.83
HCOOH*	18.54	164.77	-116.82	32.79	0.05	-102365.89	60.88
HCOOH*pa**	39.18	110.09	-61.57	13.02	-0.48	-102339.84	109.17
HCOO*	20.94	134.39	-98.30	27.52	-0.06	-100792.98	46.80
cis-COOH*	41.75	84.14	-53.42	12.82	-0.69	-100793.16	84.29
COOH*	42.31	83.29	-53.18	12.86	-0.74	-100793.34	82.87
CO*	27.98	36.17	-26.89	8.12	-0.09	-57186.46	57.47
OH*	28.55	31.17	-28.94	10.84	-0.65	-43641.08	45.17
O*	18.66	19.34	-21.43	8.10	-0.12	-41997.00	35.75
H*	17.28	18.20	-16.32	5.18	-0.58	-1533.65	20.95
HCO*	32.35	56.72	-31.72	6.63	-0.57	-58610.76	57.16
H_2O*	32.49	52.99	-46.48	17.73	0.28	-45255.10	92.34
CO_2*	15.96	72.81	-56.27	17.20	0.04	-99331.53	110.10
COH*	35.88	55.18	-36.66	9.72	-0.75	-58635.48	56.74
HCOH*	36.23	72.08	-33.52	5.10	-0.98	-60142.16	54.83

Table D.11 Pre-exponential factors for the adsorption steps on 5/9ML CO* covered Pd(100), where, per collision theory, rate constant $k = AT^{-0.5}$ (where, k is in s^{-1})

5/9ML CO* Pd(100)	A
$HCOOH + * \rightarrow HCOOH*$	3.93E+09
$CO_2* \rightarrow CO_2 + *$	4.02E+09
$CO* \rightarrow CO + *$	5.04E+09
$H_2O* \rightarrow H_2O + *$	6.28E+09

Table D.12 Optimized Shomate parameters (A to G) for the transition-state energies of the elementary steps considered in the reaction network evaluated on 5/9ML CO* covered Pd(100) facet

5/9ML CO* Pd(100)	A	B	C	D	E	F	G
HCOOH* + 2* → HCOO* + H*	27.76	157.51	-119.03	34.16	-0.47	-102303.17	52.51
HCOOH* → HCOOH*pa**	8.67	135.05	-93.29	25.97	-0.05	-102306.33	26.2
HCOOH* + * → *cis*-COOH* + H*	29.25	143.14	-103.88	29.11	-0.42	-102273.78	54.18
HCOO* → CO_2* + H*	31.43	80.34	-36.02	3.19	-0.52	-100720.35	64.48
HCOO* + H_2O* → CO_2* + H* + H_2O*	46.94	186.03	-126.21	34.63	-0.71	-145963.01	82.39
HCOO* + OH* → CO_2* + H* + OH*	48.52	161.98	-116.00	32.52	-0.97	-144344.56	74.00
COOH* + * → CO_2* + H*	45.92	79.81	-55.96	14.42	-0.75	-100748.24	89.91
COOH* → *cis*-COOH*	38.12	77.01	-49.97	12.53	-0.56	-100768.82	80.03
cis-COOH* + * → CO* + OH*	48.97	63.37	-49.42	15.99	-0.66	-100704.72	90.11
HCO* + * → CO* + H*	32.7	56.99	-30.93	6.21	-0.25	-58601.76	68.61
CO* + O* → CO_2* + *	46.07	55.66	-47.56	15.7	-0.36	-99095.09	90.33
OH* + * → O* + H*	50.92	72.71	-53.53	14.78	-0.89	-43492.19	87.01
2OH* → H_2O* + O*	28.55	31.17	-28.94	10.84	-0.65	-87229.75	45.17
OH* + H* → H_2O* + *	32.49	52.99	-46.48	17.73	0.28	-45152.17	92.34
2H* → H_2 + 2*	18.23	20.52	-23.53	10.23	-0.03	-2967.40	42.47
COH* + * → CO* + H*	33.34	55.04	-34.09	7.05	-0.76	-58545.06	50.07
COH* + H* → HCOH* + *	36.23	72.08	-33.52	5.1	-0.98	-60091.81	54.83
HCOH* + * → HCO* + H*	36.23	72.08	-33.52	5.1	-0.98	-60099.63	54.83
HCOH* + 2* → CO* + 2H*	36.23	72.08	-33.52	5.1	-0.98	-60021.07	54.83
HCOOH* + CO* → COH* + HCOO*	59.82	284.33	-207.27	57.72	-0.14	-159415.62	130.03
HCOO* + CO* → COH* + CO_2*	48.92	170.56	-125.19	35.64	-0.15	-157671.04	104.27
COOH* + CO* → COH* + CO_2*	87.54	151.93	-91.56	20.86	-0.91	-157850.73	178.86
HCO* + CO* → COH* + CO*	81.22	135.31	-86.29	20.32	-0.85	-115662.72	157.41
OH* + CO* → COH* + O*	56.53	67.34	-55.83	18.96	-0.74	-100586.01	102.64
OH* + CO* → HCO* + O*	56.53	67.34	-55.83	18.96	-0.74	-100585.77	102.64

Table D.13 Degree of rate control (X_{RC}) for the relevant elementary steps toward the decomposition of FA, obtained by keeping the (a) direct COOH* dehydrogenation and (b) CO* assisted COOH* dehydrogenation mechanisms active, one at a time. The energetics were maintained at values corresponding to the steady-state CO* coverage at home conditions (2.6% FA, balance He, 373K), by co-feeding appropriate amounts of CO(g) in the feed.

(a) Direct COOH* dehydrogenation	$\mathbf{X_{RC}}$
$COOH^* + * \leftrightarrow CO_2^* + H^*$	0.63
$H^* + H^* \leftrightarrow H_2(g) + 2^*$	0.25

(b) CO*-assisted COOH* dehydrogenation	$\mathbf{X_{RC}}$
$COH^* + * \leftrightarrow CO^* + H^*$	0.42
$H^* + H^* \leftrightarrow H_2(g) + 2^*$	0.19

D.3 Comparison of PW91-GGA Derived Binding energies with Single Crystal Adsorption Calorimetry (SCAC)

Table D.14 Comparison of PW91-DFT-evaluated binding energy of formic acid (FA) with the enthalpy for adsorption of FA obtained from experimental values in the literature. Negative Δ implies under prediction of binding energy by PW91-DFT (at FA coverage of 1/9 ML on clean Pd(111)). All values are in eV.

HCOOH*	DFT (PW91-GGA)[108]	Expt.	Δ = Expt - DFT
Pt(111)	-0.37	-0.63[146]	-0.26
Ni(111)	-0.32	-0.66[208]	-0.34

Table D.15 Comparison of PW91-DFT-evaluated binding energy of CO* with the reaction enthalpy for adsorption of CO* obtained from experimental values in the literature. Positive Δ implies over prediction of binding energy by PW91-DFT (at CO coverage of 1/9 ML on clean Pd(111)). All values are in eV.

CO*	DFT (PW91-GGA)[108]	Expt.	Δ = Expt - DFT
Pd(111)	-1.95	-1.48[195]	0.47

Table D.16 Comparison of PW91-DFT-evaluated reaction energy for dissociative adsorption of H2 with that from experimental values in the literature. Numbers in the square parentheses ([]) represents the DFT – binding energy for H*, which were used to calculate the reaction energies. The PW91-gas phase bond energy for H_2 is 4.56 eV, whereas that value is 4.52 eV per experiment. Positive Δ implies over prediction of dissociative adsorption energy by PW91-DFT (at H coverage of 1/9 ML on clean Pd(111)). All values are in eV.

H_2(g) → 2H*	DFT (PW91-GGA) Reaction Energy [BE (H*)]	Expt.Reaction Energy[143]s	Δ = Expt - DFT	ΔBE (H*)
Pd(111)	-1.19 [-2.88][446]	-0.91	0.28	0.14

D.4 PFR Simulation: Optimized CO* Coverage-dependent Energetics Pd(111)

To verify the applicability of the CSTR model for modeling the kinetics of FA decomposition on Pd/C, we used to the CO* coverage-dependent energetics of the optimized 5/9 ML CO*-covered Pd(111) model to simulate a plug flow reactor (PFR), which is a more accurate representation of the reactor used in the experiments. Since, the energetics for our reaction network is defined as a function of CO* coverage on the catalyst surface, we examine the CO* coverage profiles along the length of the reactor and compare that with the CO* coverage obtained from the CSTR simulation. Our results (Figure D.3) demonstrate that CO* coverage builds up promptly in the initial portion of the reactor and converges to within 10% of the CO* coverages predicted by the CSTR model (~0.34 ML) in the first ~2% of the reactor length. Thus, ~98% of the reactor bed experiences CO* coverages that are consistent with those predicted in our CSTR simulation. We thus conclude, that a CSTR serves as a good model for modeling the kinetics for the FA decomposition on Pd/C.

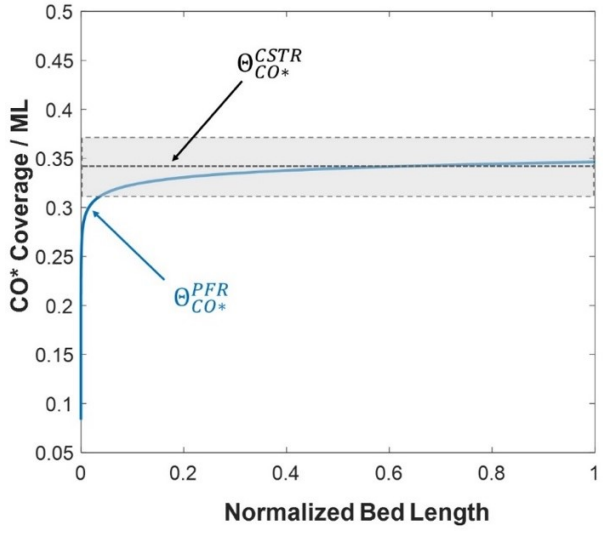


Figure D.3 CO* coverage profile as predicted from a PFR simulation (shown in blue) using the optimized CO* coverage dependent energetics, at the home conditions (2.6% FA, balance He, 373 K). The corresponding CO* coverage predicted by the CSTR model is indicated in black, along with ±10% bars.

APPENDIX E

SUPPORTING INFORMATION FOR CHAPTER 5: ROLE OF HYDROGEN-BONDED BIMOLECULAR FORMIC ACID-FORMATE COMPLEXES FOR FORMIC ACID DECOMPOSITION ON CU(111): A FIRST-PRINCIPLES DFT AND MICROKINETIC MODELING STUDY

E.1 Coverage Self-Consistent Microkinetic Modeling

We present here the intermediate models encountered in our iterative microkinetic modeling process. For all models, we calculate energetics of intermediates and transition states derived from first-principles density functional theory calculations. Temperature effects were accounted for with the use of Shomate parameters fitted from first-principles vibrational frequency calculations.[62] In our models, the denticity of reaction intermediates $HCOO_B$, $HCOO_{MX}$, and $HCOO_{BX}$ were defined as 2, 2, and 3, respectively. The remaining intermediates were defined as monodentate species. Coverages of species reported in this study include their respective denticity. For all the models considered, using parameter estimation[41], we fitted: (1) FA reaction order of zero, in a partial pressure range of 2.5–10% FA (total pressure of 1 atm) at 373 K and (2) apparent activation energy

(E_{app}) of 95 kJ/mol in a temperature range of 368–383 K at 10% FA (total pressure of 1 atm), similar to the experimental conditions studied by Iglesia and Boudart on Cu/Al_2O_3.[223]

E.1.1 Clean Cu(111) Model – Reduced Reaction Network

In the first self-consistent iteration, we parameterize our microkinetic models by considering only a reduced reaction network containing only the uncomplexed decomposition pathway, i.e. $HCOOH \rightarrow HCOO_B + H \rightarrow HCOO_M + H \rightarrow CO_2(g) + 2H \rightarrow CO_2(g) + H_2(g)$, often proposed as the reaction mechanism on Cu catalysts.[105] We initialized our iterative procedure with the hypothesis that a clean Cu(111) surface serves as the active site for FA decomposition on Cu/Al_2O_3. Consequently, we parameterized the microkinetic model using DFT energetics calculated on clean Cu(111). Upon parameter estimation, the optimized model suggested a FA apparent reaction order of 0.04 and E_{app} of 95.5 kJ/mol, which compares favorably with the experimentally reported values.[223] The optimized Shomate parameters for the clean Cu(111) solution, considering the reduced reaction network, are reported in Table E.1.

Table E.1 Optimized Shomate parameters (A to H, temperature range: 300–1200 K) for energies of gas-phase species, reaction intermediates and transition-states (in kJ/mol) for the clean Cu(111) model with the reduced reaction network. For adsorption of HCOOH(g), the rate constant (k) is calculated using collision theory, where $k = AT^{-0.5}$ (where, k is in s^{-1}) and pre-factor (A) is included in the table.

Clean Cu(111) – Reduced Network	*Shomate Parameters*							
	A	B	C	D	E	F	G	H
Species								
HCOOH(g)	31.51	114.78	-82.07	23.77	-0.17	-2813.22	275.32	-2798.85
H_2(g)	30.43	-4.12	3.64	-0.15	-0.04	-624.51	172.27	-615.46
CO_2(g)	38.56	25.21	-12.03	1.82	-0.18	-2199.00	203.87	-2185.89
HCOOH*	21.80	158.19	-108.71	29.58	-0.01	-2855.88	80.94	-33208.43
$HCOO_B$*	19.86	136.52	-99.69	27.83	-0.02	-2566.95	55.29	-32909.40
$HCOO_M$*	21.08	134.44	-94.03	24.72	0.18	-2489.60	84.01	-32829.72
H	-9.79	78.93	-69.07	21.64	-0.21	-336.28	-31.96	-30711.24
Elementary Steps								
HCOOH(g) + * ↔ HCOOH	3.93E+08	-	-	-	-	-	-	-
H +H ↔ H_2(g) + 2*	12.62	48.31	-32.91	8.43	-0.22	-610.96	23.75	-30970.14
HCOOH + 2* ↔ $HCOO_B$ + H	24.39	165.16	-125.27	35.97	-0.31	-2838.31	59.79	-33173.73
$HCOO_B$ ↔ $HCOO_M$ + *	21.94	131.73	-91.71	24.07	0.17	-2470.58	100.87	-32829.32
$HCOO_M$* ↔ CO_2(g) + H*	26.41	125.01	-96.85	27.76	-0.23	-2491.94	69.49	-32831.32

To fit the experimental apparent activation energy barrier and FA reaction order, it was necessary to stabilize $HCOO_B$ and $HCOO_M$, by 0.12 eV and 0.15 eV, respectively (Table E.2). Atomic H required destabilization by 0.15 eV. In addition, the model required the activation energy for the first dehydrogenation of FA to be lowered by 0.15 eV (Table E.2). These corrections are within the DFT error (±0.2 eV). The activation energies for the other elementary steps in the reaction network required no corrections.

Table E.2 Corrections for the DFT-derived binding energies (ΔBE) and activation energy barriers (ΔE_A) for the clean Cu(111) model with the reduced reaction network, as determined from parameter estimation. Negative (positive) corrections denote stabilization (destabilization). Intermediates and elementary steps not listed required no corrections from their initial DFT energetics.

Clean Cu(111) – Reduced Network	*Corrections / eV*
Intermediate	*ΔBE*
HCOOH	-0.12
$HCOO_M$	-0.15
H	0.11
Elementary Step	ΔE_A
$HCOOH + 2^* \leftrightarrow HCOO_B + H$	-0.16

Averaged over all experimental conditions, our solution predicts surface coverage of 0.89 ML $HCOO_B$ and 0.02 ML H, with the remaining 0.09 ML sites vacant. The variation of surface coverages with FA partial pressure and temperature is shown in Figure E.1.

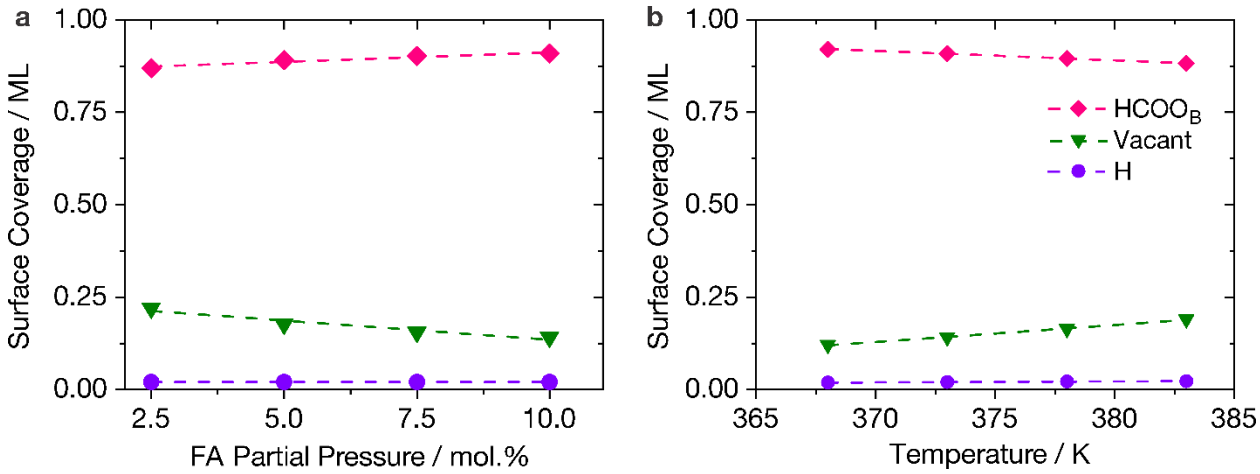


Figure E.1 Surface coverages predicted by the optimized clean Cu(111) model with the reduced reaction network, under varying (a) FA partial pressure (2.5-10%) at 373 K, (b) Temperature (368-383 K) at 10% FA. The reported coverages account for the denticity of the reaction intermediates. Dashed lines are linear trend lines.

In summary, the optimized clean Cu(111) model with the reduced reaction network was able to accurately fit the experimental apparent activation energy and FA reaction order. The necessary

corrections to the DFT energetics for achieving this agreement were within the error bars of our calculations. However, the model predicts that the surface is covered by 0.89 ML $HCOO_B$, which is inconsistent with our assumption of a clean Cu(111) surface on which the DFT energetics were calculated. We therefore conclude that clean Cu(111) with a reduced reaction network fails to accurately represent the nature of the active site for the FA decomposition reaction on Cu/Al_2O_3 catalysts.

E.1.2 0.625 ML $HCOO_B$-covered Cu(111) Model – Reduced Reaction Network

Since the clean Cu(111) model with the reduced reaction network predicted a high coverage of $HCOO_B$, we created a second model using reaction energetics evaluated on a partially $HCOO_B$-covered Cu(111) surface. The clean Cu(111) model suggested 0.89 ML $HCOO_B$, which was unrealistically high. We therefore evaluated the energetics on a 0.625 ML $HCOO_B$ covered Cu(111) surface as a first estimate to evaluate if this model can indeed support such high $HCOO_B$ coverages. The coverage of 0.625 ML $HCOO_B$ corresponds to 5 $HCOO_B$ (bidentate) spectator species in a 4 × 4 unit cell.

These spectator species influence the binding energies of intermediates as well as transition state energies via lateral adsorbate-adsorbate interactions. We explicitly included these energetic influences in our models using polynomial functions (Table E.3) dependent on the coverage of most abundant surface intermediate (MASI, $HCOO_B$ in this model). These functions were fitted to binding and transition state energies computed on clean and 0.625 ML $HCOO_B$ covered Cu(111). The polynomial functions dependent on the coverage of $HCOO_B$ were then self-consistently incorporated in our models to update the energetics (thermochemistry and kinetics) of our reaction network on-the-fly based on the model predicted $HCOO_B$ coverages at each time step.

Table E.3 Coefficients for the quadratic expression employed to update the energies of intermediates and transition states with surface coverage of $HCOO_B$ ($\Delta E(\theta)$ (in kJ/mol) = $\alpha_0 + \alpha_1\theta + \alpha_2\theta^2$), using DFT energetics calculated on clean and 0.625 ML $HCOO_B$ covered Cu(111), where θ is the surface coverage of $HCOO_B$ (in ML) calculated by the mean-field microkinetic model. We set α_1 as zero to ensure zero slope for the functions at clean surface ($\theta = 0$).

0.625 ML $HCOO_B$ covered Cu(111) – Reduced Network	*Polynomial Coefficients*		
Species	α_0	α_1	α_2
HCOOH	-20.02	0.00	51.24
$HCOO_B$	-26.78	0.00	68.54
$HCOO_M$	42.61	0.00	-109.08
H	-12.95	0.00	33.16
Elementary Steps	α_0	α_1	α_2
$H + H \leftrightarrow H_2(g) + 2*$	-13.46	0.00	34.45
$HCOOH + 2* \leftrightarrow HCOO_B + H$	-28.66	0.00	73.37
$HCOO_B \leftrightarrow HCOO_M + *$	27.96	0.00	-71.57
$HCOO_M \leftrightarrow CO_2(g) + H$	-3.52	0.00	9.02

Despite parameter estimation, the model failed to fit the experimentally measured values for the FA reaction order and E_{app}. Our best optimized model predicted a FA reaction order of 0.36 and $\underline{E}_{app}$ of 81.1 kJ/mol, which deviates significantly compared with the experimental values. The optimized Shomate parameters for this solution are reported in Table E.4.

Table E.4 Optimized Shomate parameters (A to H, temperature range: 300–1200 K) for energies of gas-phase species, reaction intermediates and transition-states (in kJ/mol) for the 0.625 ML $HCOO_B$ covered Cu(111) model with the reduced reaction network. For adsorption of HCOOH(g), the rate constant (k) is calculated using collision theory, where $k = AT^{-0.5}$ (where, k is in s^{-1}) and pre-factor (A) is included in the table.

0.625 ML $HCOO_B$ covered Cu(111) – Reduced Network	*Shomate Parameters*							
	A	B	C	D	E	F	G	H
Species								
HCOOH(g)	31.51	114.78	-82.07	23.77	-0.17	-2813.22	275.32	-2798.85
H_2(g)	30.43	-4.11	3.64	-0.15	-0.04	-624.51	172.27	-615.46
CO_2(g)	38.56	25.21	-12.03	1.82	-0.18	-2199.00	203.87	-2185.89
HCOOH	23.26	156.67	-110.50	30.97	-0.13	-2833.20	65.59	-46246.28
$HCOO_B$	19.85	135.87	-98.75	27.47	-0.02	-2581.80	47.21	-45942.39
$HCOO_M$	25.90	122.11	-87.45	24.19	-0.21	-2514.16	51.70	-45926.96
H	-14.75	88.61	-76.49	23.72	-0.07	-329.10	-40.19	-43756.73
Elementary Steps								
HCOOH(g) + * ↔ HCOOH	3.93E+08	-	-	-	-	-	-	-
H + H ↔ H_2(g) + 2*	-4.60	97.52	-80.85	24.33	-0.24	-561.71	-24.58	-44015.40
HCOOH + 2* ↔ $HCOO_B$ + H	19.39	175.81	-134.14	38.64	-0.23	-2802.80	41.87	-46203.85
$HCOO_B$ ↔ $HCOO_M$ + *	15.83	126.34	-90.60	24.98	-0.01	-2498.63	44.47	-45916.02
$HCOO_M$ ↔ CO_2(g) + H	25.27	126.79	-98.00	28.04	-0.23	-2465.24	58.71	-45887.28

For this model, parameter estimation suggested large corrections for the DFT derived energetics. The BE of $HCOO_B$ required a -0.57 eV correction to the DFT derived value (Table E.5). The DFT activation energies for HCOOH → $HCOO_B$ + H and $HCOO_M$ → CO_2(g) + H were corrected by -0.13 eV and +0.09 eV, respectively (Table E.5). Additionally, the activation energy barrier for H + H → H_2(g) required a correction of 0.31 eV, which is outside of the typical DFT error (±0.2 eV).

Table E.5 Corrections for the DFT-derived binding energies (ΔBE) and activation energy barriers (ΔE_A) for the 0.625 ML $HCOO_B$ covered Cu(111) model with the reduced reaction network, as determined from parameter estimation. Negative (positive) corrections denote stabilization (destabilization). Intermediates and elementary steps not listed required no corrections from their initial DFT energetics.

0.625 ML $HCOO_B$ covered Cu(111) – Reduced Network	*Corrections / eV*
Intermediate	*ΔBE*
$HCOO_B$	-0.57
Elementary Step	*ΔE_A*
$HCOOH + 2^* \leftrightarrow HCOO_B + H$	-0.13
$HCOO_M \leftrightarrow CO_2(g) + H$	0.09
$H + H \leftrightarrow H_2(g)$	0.31

Averaged over all experimental conditions, our model predicted surface coverages of 0.67 ML $HCOO_B$, 0.12 ML H, with the remaining 0.21 ML sites vacant. This is consistent with our DFT model, which has a MASI coverage of 0.625 ML $HCOO_B$. The variation of surface coverages with FA partial pressure and temperature is shown in Figure E.2.

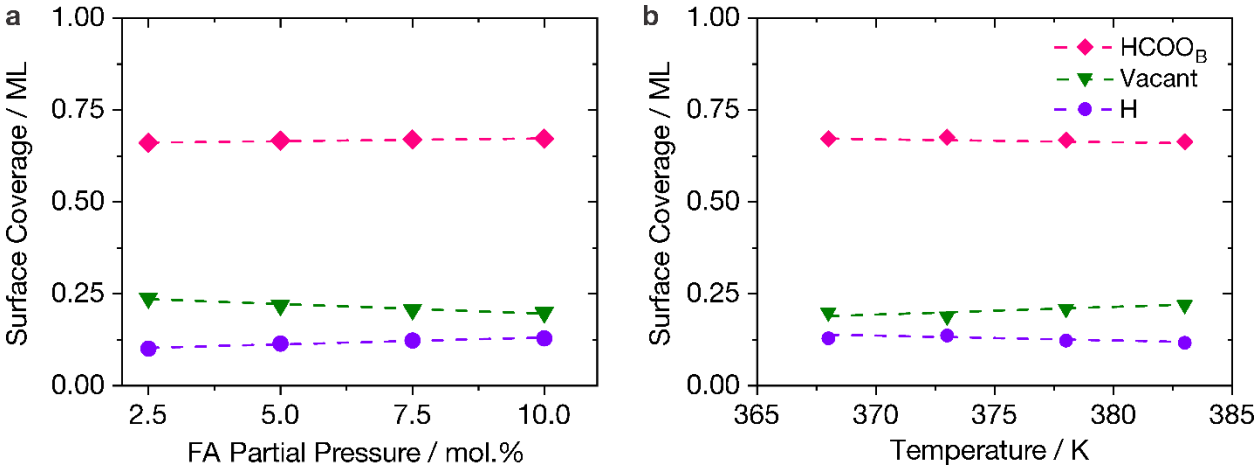


Figure E.2 Surface coverages predicted by the optimized 0.625 ML $HCOO_B$ covered Cu(111) model with the reduced reaction network, under varying (a) FA partial pressure (2.5-10%) at 373 K, (b) Temperature (368-383 K) at 10% FA. The reported coverages account for the denticity of the reaction intermediates. Dashed lines are linear trend lines.

In summary, the 0.625 ML $HCOO_B$ model with the reduced reaction mechanism yielded a coverage self-consistent solution. However, this model was unable to rationalize the experimentally measured FA reaction order and E_{app}. The results suggest the reduced reaction network, which only includes uncomplexed decomposition pathways, is limited in its ability to describe FA decomposition on Cu catalysts. In the next iteration (discussed in the next section), we include the full reaction network, which includes both uncomplexed and complexed decomposition pathways.

E.1.3 Clean Cu(111) Model – Full Reaction Network

In the first self-consistent iteration above, we discovered that the reduced reaction networks (i.e. only the conventionally modeled uncomplexed decomposition pathway) were incapable of accurately fitting the experimental FA reaction order and E_{app}. In this second self-consistent iteration, we therefore formulate microkinetic models considering the full reaction network, which contains both the uncomplexed and complexed decomposition pathways (Figure 5.3, main text). We again begin with DFT energetics on clean Cu(111). The optimized solution predicts a FA reaction order of -0.01 and E_{app} of 97.9 kJ/mol, consistent with the experimentally reported values.[223] The optimized Shomate parameters for the clean Cu(111) solution with the full reaction network are reported in Table E.6.

Table E.6 Optimized Shomate parameters (A to H, temperature range: 300–1200 K) for energies of gas-phase species, reaction intermediates and transition-states (in kJ/mol) for the clean Cu(111) model with the full reaction network. For adsorption of HCOOH(g), the rate constant (k) is calculated using collision theory, where $k = AT^{-0.5}$ (where, k is in s^{-1}) and pre-factor (A) is included in the table.

Clean Cu(111) – Full Network	*Shomate Parameters*							
	A	B	C	D	E	F	G	H
Species								
HCOOH(g)	31.51	114.78	-82.07	23.77	-0.17	-2813.22	275.32	-2798.85
H_2(g)	30.43	-4.12	3.64	-0.15	-0.04	-624.51	172.27	-615.46
CO_2(g)	38.56	25.21	-12.03	1.82	-0.18	-2199.00	203.87	-2185.89
HCOOH	21.80	158.19	-108.71	29.58	-0.01	-2855.66	80.94	-33208.43
$HCOO_B$	19.86	136.52	-99.69	27.83	-0.02	-2559.39	55.29	-32909.40
$HCOO_M$	21.08	134.44	-94.03	24.72	0.18	-2483.67	84.01	-32829.72
$HCOO_{BX}$	25.71	323.58	-225.28	60.40	0.43	-5440.13	106.43	-35773.44
$HCOO_{MX}$	16.49	350.88	-248.79	67.10	0.74	-5382.34	100.81	-35731.55
H	-9.79	78.93	-69.07	21.64	-0.21	-336.39	-31.96	-30711.24
Elementary Steps								
HCOOH(g) + * ↔ HCOOH	3.93E+08	-	-	-	-	-	-	-
H +H ↔ H_2(g) + 2*	12.62	48.31	-32.91	8.43	-0.22	-610.96	23.75	-30970.14
HCOOH + 2* ↔ $HCOO_B$ + H	24.39	165.16	-125.27	35.97	-0.31	-2832.92	59.79	-33173.73
$HCOO_B$ ↔ $HCOO_M$ + *	21.94	131.73	-91.71	24.07	0.17	-2464.03	100.87	-32829.32
$HCOO_M$ ↔ CO_2(g) + H	26.41	125.01	-96.85	27.76	-0.23	-2486.03	69.49	-32831.32
HCOOH(g) + $HCOO_B$ + * ↔ $HCOO_{BX}$	3.93E+08	-	-	-	-	-	-	-
$HCOO_{BX}$ ↔ $HCOO_{MX}$ + *	9.97	345.65	-244.15	65.71	0.75	-5378.44	80.96	-35730.58
$HCOO_{MX}$ ↔ HCOOH + CO_2(g) + H	43.77	290.45	-210.95	58.90	-0.16	-5347.20	148.77	-35692.76
$HCOO_{BX}$ ↔ HCOOH + $HCOO_B$	25.71	323.58	-225.28	60.40	0.43	-5405.00	106.43	-35773.44
$HCOO_{MX}$ ↔ HCOOH + $HCOO_M$	16.49	350.88	-248.79	67.10	0.74	-5322.40	100.81	-35731.55
$HCOO_{MX}$ + $HCOO_B$ ↔ $HCOO_{BX}$ + $HCOO_M$	36.35	487.40	-348.48	94.94	0.72	-7897.81	156.11	-68640.94

The optimized solution suggests that FA decomposition proceeds through the uncomplexed pathway: HCOOH → $HCOO_B$ + H → $HCOO_M$ + H → CO_2(g) + 2H → CO_2(g) + H_2(g). The complexed pathways did not contribute to the reaction flux under the examined experimental conditions. In the parameter estimation process for fitting the experimental observations, we required stabilization of $HCOO_M$ and $HCOO_{BX}$ by 0.09 eV and 0.14 eV, respectively (Table E.7). Atomic H required destabilization by 0.10 eV. The activation energy for HCOOH → $HCOO_B$ + H

required a correction of -0.10 eV (Table E.7), whereas the activation energy for $HCOO_B \rightarrow HCOO_M$ required an increase by 0.16 eV. These corrections are within the ±0.2 eV DFT error bars for our calculations. The activation energies for all the other elementary steps remained unchanged.

Table E.7 Corrections for the DFT-derived binding energies (ΔBE) and activation energy barriers (ΔE_A) for the clean Cu(111) model with the full reaction network, as determined from parameter estimation. Negative (positive) corrections denote stabilization (destabilization). Intermediates and elementary steps not listed required no corrections from their initial DFT energetics.

Clean Cu(111) – Full Network	*Corrections / eV*
Intermediate	*ΔBE*
$HCOO_M$	-0.09
$HCOO_{BX}$	-0.14
H	0.10
Elementary Step	ΔE_A
$HCOOH + 2^* \leftrightarrow HCOO_B + H$	-0.10
$HCOO_B \leftrightarrow HCOO_M + *$	0.16

Averaged over all experimental conditions, the optimized solution predicts surface coverages of 0.65 ML $HCOO_B$, 0.16 ML $HCOO_{BX}$, and 0.02 ML H. The remaining 0.17 ML sites are vacant. The variation of surface coverages with FA partial pressure and temperature is shown in Figure E.3.

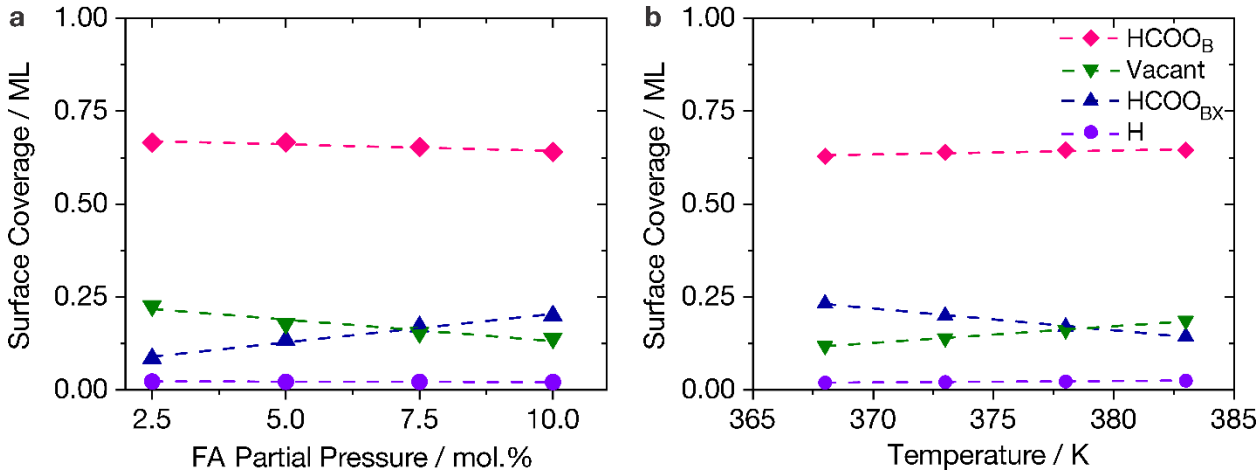


Figure E.3 Surface coverages predicted by the optimized clean Cu(111) model with the full reaction network, under varying (a) FA partial pressure (2.5-10%) at 373 K, (b) Temperature (368-383 K) at 10% FA. The reported coverages account for the denticity of the reaction intermediates. Dashed lines are linear trend lines.

In summary, the clean Cu(111) model together with the full reaction mechanism was able to fit the experimental apparent activation energy barrier and FA reaction order. The corrections to the DFT energetics were within the error bars. Under the examined experimental conditions, this model suggests that the reaction flux goes through the uncomplexed decomposition pathway. However, the model predicted a coverage of 0.65 ML $HCOO_B$, which was inconsistent with our starting assumption of a clean Cu(111) surface, with which we calculate our DFT energetics. We conclude that this clean Cu(111) model fails to accurately represent the nature of the active site for the FA decomposition reaction on Cu/Al_2O_3 catalysts.

E.1.4 0.625 ML $HCOO_B$-covered Cu(111) Model – Full Reaction Network

The results from the above optimized clean Cu(111) model with the full reaction mechanism suggests an average surface coverage of 0.65 ML $HCOO_B$. In this next model, we therefore determined the energetics of the reaction network on 0.625 ML $HCOO_B$ covered Cu(111), which corresponds to 5 $HCOO_B$ (bidentate) spectator species in a 4 × 4 unit cell. The dependence of the thermochemistry and kinetics on $HCOO_B$ coverage was explicitly included in the form of polynomial functions for the binding and transition state energies dependent on the $HCOO_B$ coverage. These polynomial expressions (Table E.8) were fitted from binding and transition state energies computed on clean and 0.625 ML $HCOO_B$ covered Cu(111), and then self-consistently incorporated in our models to update the thermochemistry and kinetics of the reaction network on-the-fly based on the predicted $HCOO_B$ coverages at each time step.

Table E.8 Coefficients for the quadratic expression employed to update the energies of intermediates and transition states with surface coverage of $HCOO_B$ ($\Delta E(\theta)$ (in kJ/mol) = $\alpha_0 + \alpha_1\theta + \alpha_2\theta^2$), using DFT energetics calculated on clean and 0.625 ML $HCOO_B$ covered Cu(111), where θ is the surface coverage of $HCOO_B$ (in ML) calculated by the mean-field microkinetic model. We set α_1 as zero to ensure zero slope for the functions at clean surface ($\theta = 0$).

0.625 ML $HCOO_B$ covered Cu(111)	*Polynomial Coefficients*		
	α_0	α_1	α_2
Species			
HCOOH	-20.02	0.00	51.24
$HCOO_B$	-26.78	0.00	68.54
$HCOO_M$	42.61	0.00	-109.08
$HCOO_{BX}$	-16.54	0.00	42.35
$HCOO_{MX}$	29.44	0.00	-75.37
H	-12.95	0.00	33.16
Elementary Steps			
$H + H \leftrightarrow H_2(g) + 2*$	-13.46	0.00	34.45
$HCOOH + 2* \leftrightarrow HCOO_B + H$	-28.66	0.00	73.37
$HCOO_B \leftrightarrow HCOO_M + *$	27.96	0.00	-71.57
$HCOO_M \leftrightarrow CO_2(g) + H$	-3.52	0.00	9.02
$HCOO_{BX} \leftrightarrow HCOO_{MX} + *$	14.41	0.00	-36.89
$HCOO_{MX} \leftrightarrow HCOOH + CO_2(g) + H$	-6.56	0.00	16.78
$HCOO_{BX} \leftrightarrow HCOOH + HCOO_B$	-16.54	0.00	42.35
$HCOO_{MX} \leftrightarrow HCOOH + HCOO_M$	29.44	0.00	-75.37
$HCOO_{MX} + HCOO_B \leftrightarrow HCOO_{BX} + HCOO_M$	2.67	0.00	-6.83

Upon parameter estimation, our model predicted a FA reaction order of -0.05 and an E_{app} of 93.9 kJ/mol, which is in close agreement with the experimentally measured values.[223] The optimized Shomate parameters for the 0.625 ML $HCOO_B$ covered Cu(111) solution with the full reaction network are reported in Table E.9.

Table E.9 Optimized Shomate parameters (A to H, temperature range: 300–1200 K) for energies of gas-phase species, reaction intermediates and transition-states (in kJ/mol) for the 0.625 ML $HCOO_B$ covered Cu(111) model with the full reaction network. For adsorption of HCOOH(g), the rate constant (k) is calculated using collision theory, where $k = AT^{-0.5}$ (where, k is in s^{-1}) and pre-factor (A) is included in the table.

0.625 ML $HCOO_B$ covered Cu(111) – Full Network	*Shomate Parameters*							
	A	B	C	D	E	F	G	H
Species								
HCOOH(g)	31.51	114.78	-82.07	23.77	-0.17	-2813.22	275.32	-2798.85
H_2(g)	30.43	-4.11	3.64	-0.15	-0.04	-624.51	172.27	-615.46
CO_2(g)	38.56	25.21	-12.03	1.82	-0.18	-2199.00	203.87	-2185.89
HCOOH	23.26	156.67	-110.50	30.97	-0.13	-2836.24	65.59	-46246.28
$HCOO_B$	19.85	135.87	-98.75	27.47	-0.02	-2520.31	47.21	-45942.39
$HCOO_M$	25.90	122.11	-87.45	24.19	-0.21	-2513.39	51.70	-45926.96
$HCOO_{BX}$	22.37	333.04	-233.53	62.80	0.43	-5423.69	70.05	-46230.03
$HCOO_{MX}$	18.44	343.47	-242.97	65.70	0.54	-5406.82	65.17	-46229.28
H	-14.75	88.61	-76.49	23.72	-0.07	-320.13	-40.19	-43756.73
Elementary Steps								
HCOOH(g) + * ↔ HCOOH	3.93E+08	-	-	-	-	-	-	-
H +H ↔ H_2(g) + 2*	-4.60	97.52	-80.85	24.33	-0.24	-591.71	-24.58	-44015.40
HCOOH + 2* ↔ $HCOO_B$ + H	19.39	175.81	-134.14	38.64	-0.23	-2804.44	41.87	-46203.85
$HCOO_B$ ↔ $HCOO_M$ + *	15.83	126.34	-90.60	24.98	-0.01	-2495.88	44.47	-45916.02
$HCOO_M$ ↔ CO_2(g) + H	25.27	126.79	-98.00	28.04	-0.23	-2480.29	58.71	-45887.28
HCOOH(g) + $HCOO_B$ + * ↔ $HCOO_{BX}$	3.93E+08	-	-	-	-	-	-	-
$HCOO_{BX}$ ↔ $HCOO_{MX}$ + *	26.45	324.08	-227.23	61.35	0.46	-5391.24	105.91	-46211.89
$HCOO_{MX}$ ↔ HCOOH + CO_2(g) + H	44.34	289.75	-210.97	59.06	-0.33	-5349.62	107.15	-46158.81
$HCOO_{BX}$ ↔ HCOOH + $HCOO_B$	22.37	333.04	-233.53	62.80	0.43	-5349.62	70.05	-46230.03
$HCOO_{MX}$ ↔ HCOOH + $HCOO_M$	18.44	343.47	-242.97	65.70	0.54	-5335.89	65.17	-46229.28
$HCOO_{MX}$ + $HCOO_B$ ↔ $HCOO_{BX}$ + $HCOO_M$	38.29	479.35	-341.72	93.16	0.52	-7907.54	112.38	-92171.67

The optimized solution suggests that both the uncomplexed and complexed mechanisms contribute to the reaction flux, with the former being dominant across all experimental conditions. Averaged over all experimental conditions, the uncomplexed pathway ($HCOOH \rightarrow HCOO_B + H \rightarrow HCOO_M + H \rightarrow CO_2(g) + 2H \rightarrow CO_2(g) + H_2(g)$) contributes ~85% of the reaction flux. The remaining flux (~15%) first goes through complexed rotation ($HCOO_{BX} \rightarrow HCOO_{MX}$), which then bifurcates into two submechanisms: (1) $HCOO_B$-assisted decomplexation of $HCOO_{MX}$ to release $HCOO_M$

($HCOO_{MX}$ + $HCOO_B$ → $HCOO_M$ + $HCOO_{BX}$), followed by dehydrogenation of $HCOO_M$ to form CO_2(g) + H, and (2) direct dehydrogenation of $HCOO_{MX}$ to form CO_2(g) + H + HCOOH. Averaged over the experimental conditions, the sub-mechanisms (1) and (2) contribute 10% and 5% of the reaction flux, respectively.

Table E.10 Corrections for the DFT-derived binding energies (ΔBE) and activation energy barriers (ΔE_A) for the 0.625 ML $HCOO_B$ covered Cu(111) model with the full reaction network, as determined from parameter estimation. Negative (positive) corrections denote stabilization (destabilization).

0.625 ML $HCOO_B$ covered Cu(111)	*Corrections / eV*
Intermediate	*ΔBE*
$HCOO_B$	0.07
$HCOO_{BX}$	-0.16
H	0.09
Elementary Step	*ΔE_A*
HCOOH + 2* ↔ $HCOO_B$ + H	-0.11
$HCOO_M$ ↔ CO_2(g) + H	-0.07

To fit the experimental E_{app} and FA reaction order, we required stabilization of $HCOO_{BX}$ by 0.16 eV and destabilization of $HCOO_B$ and atomic H by 0.07 eV and 0.09, respectively (Table E.10). The DFT activation energies for HCOOH → $HCOO_B$ + H and $HCOO_M$ → CO_2(g) + H were reduced by 0.11 eV and 0.07 eV, respectively (Table E.10). These corrections are within the ±0.2 eV error bars for DFT calculations. The activation energies for the remaining steps required no corrections.

Averaged over all experimental conditions, our model predicted surface coverages of 0.43 ML $HCOO_{BX}$, 0.13 ML $HCOO_B$, and 0.01 ML H, with the remaining 0.43 ML sites vacant. The variation of surface coverages with FA partial pressure and temperature is shown in Figure E.4.

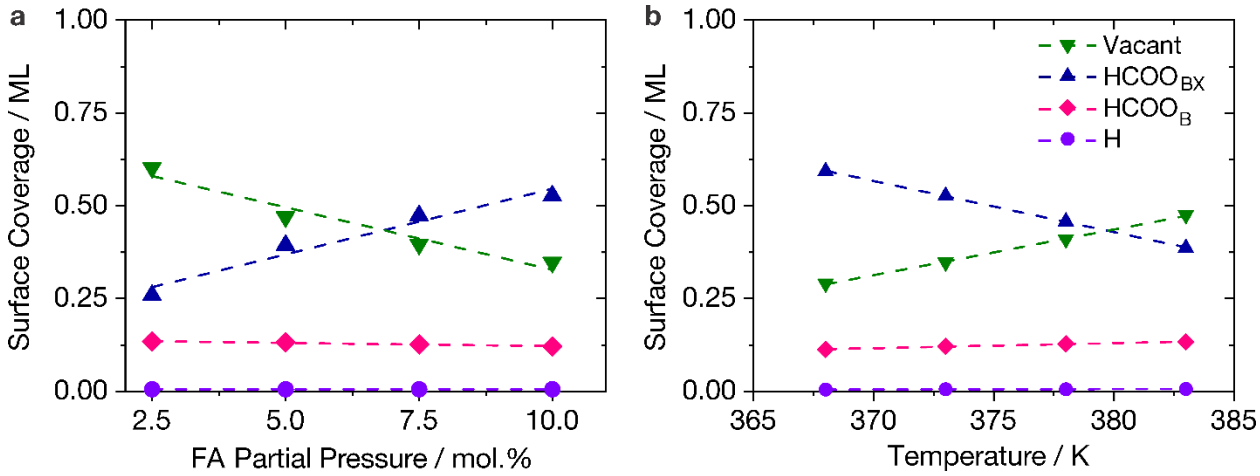


Figure E.4 Surface coverages predicted by the optimized 0.625 ML $HCOO_B$ Cu(111) model with the full reaction network, under varying (a) FA partial pressure (2.5-10%) at 373 K, (b) Temperature (368-383 K) at 10% FA. The reported coverages account for the denticity of the reaction intermediates. Dashed lines are linear trend lines.

In summary, the optimized 0.625 ML $HCOO_B$ covered model was able to fit the experimental E_{app} and FA reaction order. Corrections to the DFT energetics were within error bars. The model suggested both uncomplexed and complexed reaction pathways to contribute toward the FA decomposition flux, with the former being dominant (~85%, averaged over all experimental conditions). However, the optimized model suggests $HCOO_{BX}$ as the MASI (with surface coverage of 0.43 ML, averaged over all experimental conditions), which is inconsistent with the 0.625 ML $HCOO_B$ covered Cu(111) surface on which the DFT calculations were performed. Thus, 0.625 ML $HCOO_B$ covered Cu(111) fails to accurately represent the nature of the active site for FA decomposition on Cu/Al_2O_3 catalysts.

E.1.5 0.375 ML $HCOO_{BX}$-covered Cu(111) Model – Full Reaction Network

The results from our second model in our full reaction network iteration—the optimized 0.625 ML $HCOO_B$ covered Cu(111) model—suggests a surface coverage of 0.43 ML $HCOO_{BX}$ averaged over all experimental conditions. Consequently, we evaluated the energetics of the reaction

network on 0.375 ML $HCOO_{BX}$ covered Cu(111), which corresponds to 2 $HCOO_{BX}$ (tridentate) spectator species in a 4 × 4 unit cell. The dependence of the thermochemistry and kinetics on $HCOO_{BX}$ coverage was explicitly included in the form of polynomial functions for the binding and transition state energies dependent on the coverage of $HCOO_{BX}$. These polynomial expressions (Table E.11) were fitted from binding and transition state energies computed on clean and 0.375 ML $HCOO_{BX}$ covered Cu(111), and then self-consistently incorporated in our models to update the energetics (thermochemistry and kinetics) of the reaction network on-the-fly based on the predicted $HCOO_{BX}$ coverages at each time step.

Table E.11 Coefficients for the quadratic expression employed to update the energies of intermediates and transition states with surface coverage of $HCOO_{BX}$ ($\Delta E(\theta)$ (in kJ/mol) = $\alpha_0 + \alpha_1\theta + \alpha_2\theta^2$), using DFT energetics calculated on clean and 0.375 ML $HCOO_{BX}$ covered Cu(111), where θ is the surface coverage of $HCOO_{BX}$ (in ML) calculated by the mean-field microkinetic model. We fit the coefficients to ensure zero slope for the functions at $HCOO_{BX}$ coverage of 0.375 ML since the interaction energies are stabilizing below 0.375 ML and destabilizing at coverages above 0.375 ML.

0.375 ML $HCOO_{BX}$ covered Cu(111)	*Polynomial Coefficients*		
	α_0	α_1	α_2
Species			
HCOOH	20.55	-109.61	146.14
$HCOO_B$	11.39	-60.72	80.96
$HCOO_M$	39.85	-212.52	283.37
$HCOO_{BX}$	14.38	-76.67	102.23
$HCOO_{MX}$	39.75	-212.01	282.68
H	-1.54	8.23	-10.98
Elementary Steps			
$H + H \leftrightarrow H_2(g) + 2*$	-4.73	25.21	-33.62
$HCOOH + 2* \leftrightarrow HCOO_B + H$	15.15	-80.79	107.72
$HCOO_B \leftrightarrow HCOO_M + *$	58.28	-310.81	414.41
$HCOO_M \leftrightarrow CO_2(g) + H$	29.91	-159.52	212.70
$HCOO_{BX} \leftrightarrow HCOO_{MX} + *$	33.29	-177.53	236.71
$HCOO_{MX} \leftrightarrow HCOOH + CO_2(g) + H$	20.65	-110.12	146.83
$HCOO_{BX} \leftrightarrow HCOOH + HCOO_B$	14.38	-76.67	102.23
$HCOO_{MX} \leftrightarrow HCOOH + HCOO_M$	39.75	-212.01	282.68
$HCOO_{MX} + HCOO_B \leftrightarrow HCOO_{BX} + HCOO_M$	51.14	-272.73	363.64

The results from the parameter estimation are discussed in the main text. The optimized Shomate parameters for the 0.375 $HCOO_{BX}$ model are included in Table E.12. In summary, this model was coverage self-consistent and required corrections to the DFT energetics that were within the DFT error. We thus believe that this model accurately represents the nature of the active site for FA decomposition on Cu/Al_2O_3 catalysts.

Table E.12 Optimized Shomate parameters (A to H, temperature range: 300–1200 K) for energies of *gas-phase species,* reaction intermediates and transition-state*s* (in kJ/mol) for the 0.375 ML $HCOO_{BX}$ covered Cu(111) model with the full reaction network. For adsorption of HCOOH(g), the rate constant (k) is calculated using collision theory, where $k = AT^{-0.5}$ (where, k is in s^{-1}) and pre-factor (A) is included in the table.

0.375 ML $HCOO_{BX}$ covered Cu(111) – Full Network	*Shomate Parameters*							
	A	B	C	D	E	F	G	H
Species								
HCOOH(g)	31.51	114.78	-82.07	23.77	-0.17	-2813.22	275.32	-2798.85
H_2(g)	30.43	-4.12	3.64	-0.15	-0.04	-624.51	172.27	-615.46
CO_2(g)	38.56	25.21	-12.03	1.82	-0.18	-2199.00	203.87	-2185.89
HCOOH	6.11	187.96	-127.08	33.16	0.38	-2878.81	35.04	-44394.68
$HCOO_B$	20.00	135.48	-98.15	27.20	0.02	-2555.18	53.08	-44086.81
$HCOO_M$	23.34	127.22	-90.94	25.00	0.02	-2539.18	62.88	-44064.10
$HCOO_{BX}$	25.34	324.79	-226.84	61.03	0.38	-5452.77	90.73	-46953.36
$HCOO_{MX}$	15.12	360.10	-260.58	71.59	0.54	-5427.38	63.43	-46947.11
H	-9.97	78.86	-68.71	21.46	-0.20	-331.31	-32.07	-41875.41
Elementary Steps								
HCOOH(g) + * ↔ HCOOH	3.93E+08	-	-	-	-	-	-	-
H +H ↔ H_2(g) + 2*	9.43	60.71	-46.16	13.00	-0.26	-606.96	10.63	-42133.69
HCOOH + 2* ↔ $HCOO_B$ + H	24.35	164.40	-123.95	35.39	-0.29	-2838.82	56.20	-44354.26
$HCOO_B$ ↔ $HCOO_M$ + *	14.09	131.00	-94.83	26.30	0.11	-2530.62	50.39	-44054.43
$HCOO_M$* ↔ CO_2(g) + H*	27.57	121.83	-94.00	26.90	-0.28	-2497.22	69.11	-44028.15
HCOOH(g) + $HCOO_B$ + * ↔ $HCOO_{BX}$	3.93E+08	-	-	-	-	-	-	-
$HCOO_{BX}$ ↔ $HCOO_{MX}$ + *	20.99	336.01	-235.04	62.91	0.68	-5411.51	106.40	-46926.86
$HCOO_{MX}$ ↔ HCOOH + CO_2(g) + H	47.79	280.99	-203.17	56.64	-0.25	-5388.58	139.53	-46880.44
$HCOO_{BX}$ ↔ HCOOH + $HCOO_B$	25.34	324.79	-226.84	61.03	0.38	-5433.79	90.73	-46953.36
$HCOO_{MX}$ ↔ HCOOH + $HCOO_M$	15.12	360.10	-260.58	71.59	0.54	-5409.66	63.43	-46947.11
$HCOO_{MX}$ + $HCOO_B$ ↔ $HCOO_{BX}$ + $HCOO_M$	35.12	495.58	-358.73	98.79	0.56	-7979.49	116.51	-91033.92

E.2 Supplementary Figures

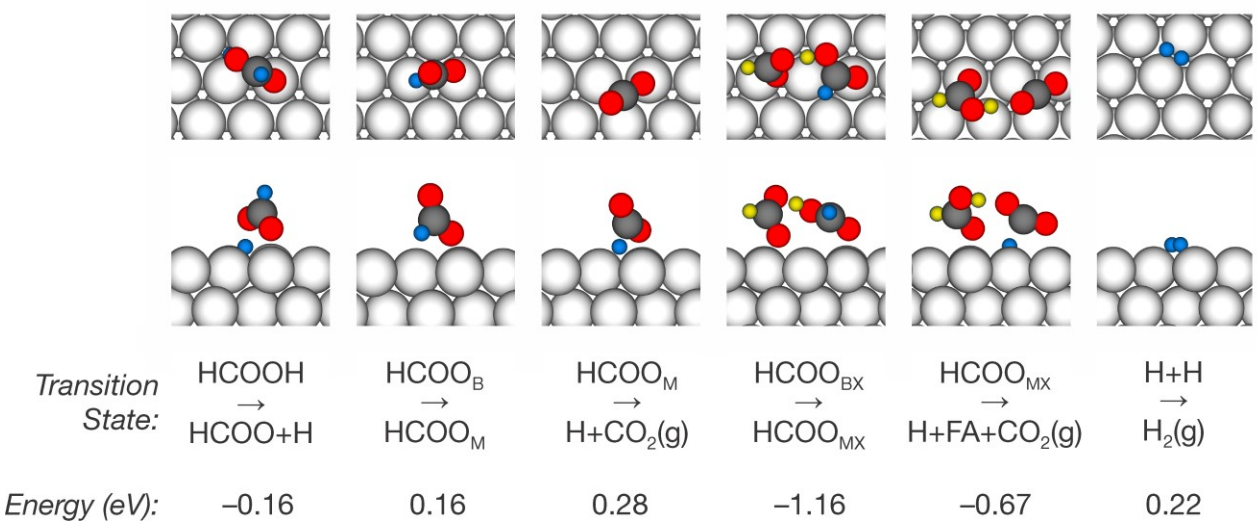


Figure E.5 Optimized structures of transition states involved in formic acid decomposition on clean Cu(111). Panels above and below are top and side views, respectively. Energies are with respect to gas-phase H_2 and CO_2. Color code: light grey – Cu, dark grey – C, red – O, blue – H, yellow – H from complexed HCOOH. Subscripts B and M refer to the bidentate and monodentate configurations of HCOO, respectively. Subscript X refers to complexation of HCOO with HCOOH (i.e. FA-HCOO complexes).

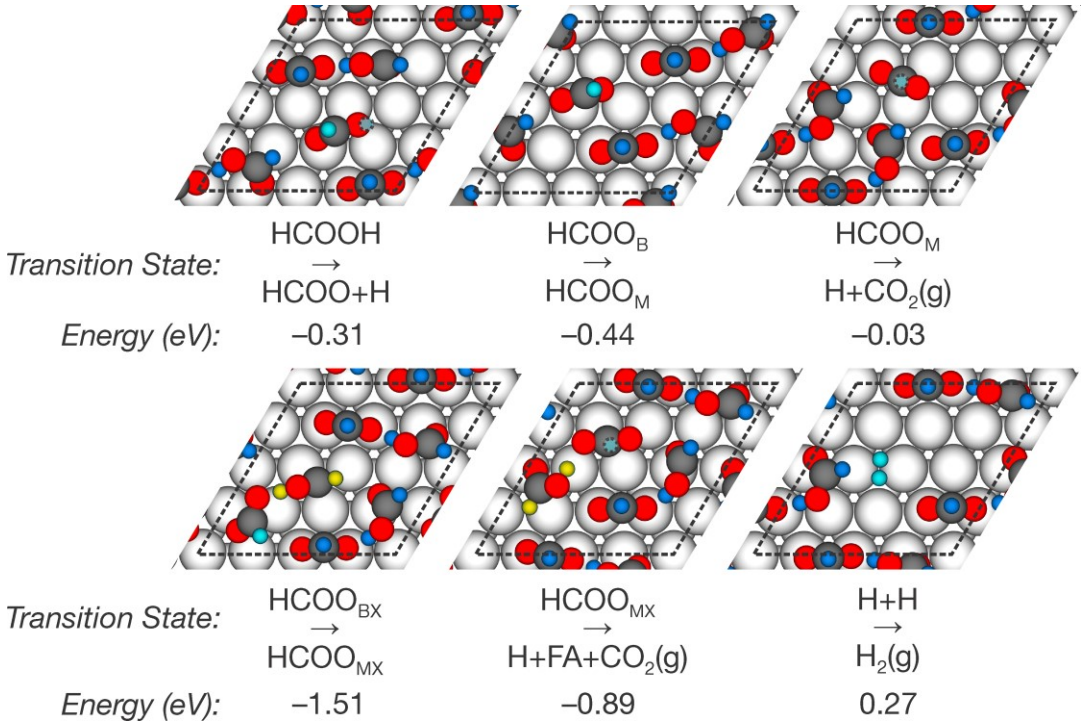


Figure E.6 Optimized structures of transition-states involved in formic acid decomposition on 0.375 ML $HCOO_{BX}$ covered Cu(111). Panels show top views. Black dashed lines mark the unit cell. Energies are with respect to gas-phase H_2 and CO_2. Color code: light grey – Cu, dark grey – C, red – O, blue – H of spectator species, cyan – H of species of interest, yellow – H from complexed HCOOH. Some H atoms are hidden behind other atoms; these atoms are outlined in dotted lines.

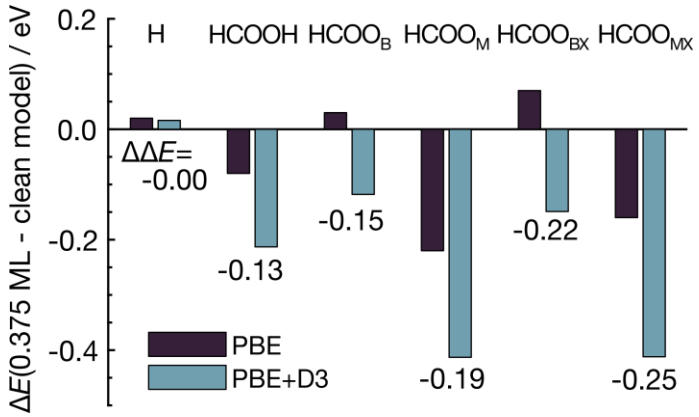


Figure E.7 Effect of coverage (clean Cu(111) vs. 0.375 ML $HCOO_{BX}$ models; Δ*E*) on the energetics of species involved in formic acid decomposition on Cu(111) evaluated with the PBE and PBE+D3 functionals. PBE energies were calculated with single-point calculations on the PBE+D3 geometries; PBE+D3 energies were calculated self-consistently with PBE+D3 geometries. Energies are with respect to gas-phase H_2, CO_2, and the clean slab. Δ*E*s given below the bars denote the differences in coverage effects between the two functionals. Negative ΔE values indicate that PBE+D3 predicts greater stabilization of species higher coverage than PBE.

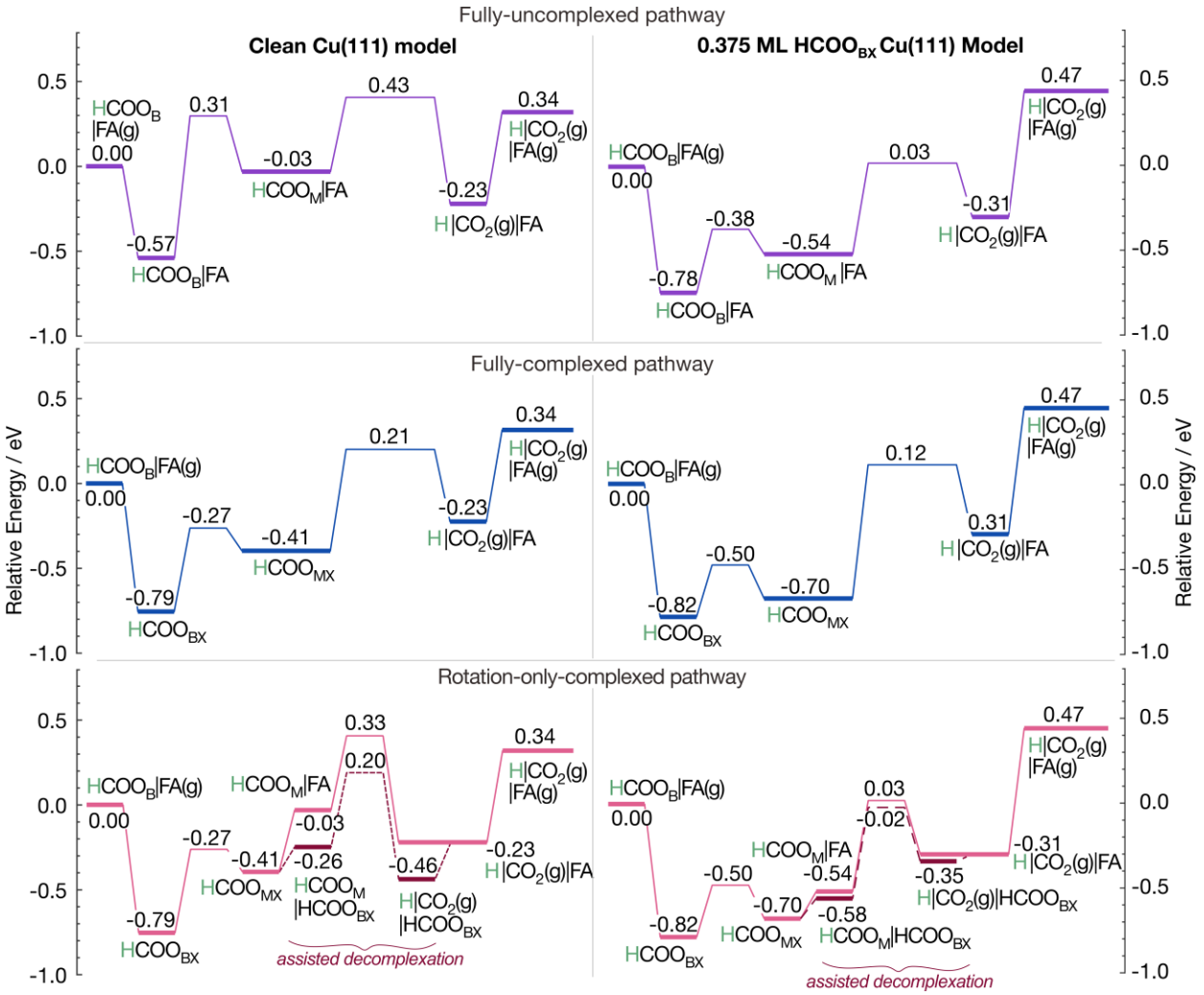


Figure E.8 Side-by-side comparison of potential energy diagrams (PEDs) for $HCOO_B$ decomposition on clean Cu(111) and 0.375 ML $HCOO_{BX}$ covered Cu(111). Bold and thin lines indicate intermediate and transition states respectively. '|' indicates infinite separation. Colors of the pathways are identical to those in Figure 2 in the main text. All states are labeled by their energies, which are with respect to the initial state to compare the pathways on an equal energetic footing; intermediate states are additionally labeled with names of the adsorbates. Teal colored H atoms denote H atoms from the decomposing HCOO species. Subscripts B and M refer to the bidentate and monodentate configurations of HCOO, respectively. Subscript X refers to complexation of HCOO with HCOOH (i.e. FA-HCOO complexes).

APPENDIX F

SUPPORTING INFORMATION FOR CHAPTER 7: TOWARDS EXPERIMENT CALIBRATED COVERAGE-COGNIZANT VOLCANO PLOTS: FORMIC ACID DECOMPOSITION REACTION

F.1 Reaction Thermochemistry

Table F.1 Binding energy of reaction intermediates on close-packed (111) facets of Ag, Au, Cu, Ir, Ni, Pd, Pt, and Rh. The energies are referenced wrt. the corresponding gas-phase energy of the reaction intermediate. All energies are in eV.

(111)	CO	CO_2	COH	COOH	H	H_2O	HCO	HCOO	HCOOH	OH
Ag	-0.23	-0.05	-1.51	-1.16	-2.06	-0.17	-0.86	-2.31	-0.17	-2.28
Au	-0.25	-0.05	-1.93	-1.35	-2.04	-0.15	-1.21	-1.78	-0.16	-1.56
Cu	-0.78	-0.07	-2.48	-1.51	-2.37	-0.19	-1.13	-2.61	-0.23	-2.70
Ir	-1.89	-0.06	-4.50	-2.64	-2.73	-0.38	-2.47	-2.95	-0.43	-2.60
Ni	-1.96	-0.05	-4.29	-2.25	-2.81	-0.27	-2.18	-2.80	-0.32	-2.98
Pd	-1.99	-0.06	-4.22	-2.21	-2.83	-0.30	-2.26	-2.34	-0.41	-2.20
Pt	-1.81	-0.06	-4.47	-2.39	-2.71	-0.29	-2.36	-2.34	-0.40	-2.12
Rh	-1.98	-0.07	-4.58	-2.58	-2.77	-0.39	-2.42	-2.95	-0.48	-2.75

F.2 Unadjusted DFT Energetics on Clean Pd(111)

Table F.2 Shomate parameters (A to H) for gas-phase species and adsorbed reaction intermediates (in kJ/mol) in reaction network in T-range: 300 – 1200 K. The energetics of the reaction intermediates were evaluated on clean Pd(111).

Clean Pd(111)	A	B	C	D	E	F	G
HCOOH(g)	14.23	155.06	-104.97	28.17	-0.02	-102408	52.85
H_2(g)	19.91	135.45	-98.34	27.34	-0.07	-100941	52.18
CO_2(g)	41.6	84.63	-53.78	12.92	-0.73	-100939	84.63
H_2O(g)	27.71	38.42	-29.14	8.75	0.01	-57316.4	59.57
CO(g)	31.22	31.01	-34.46	14.36	-0.18	-43766.6	62.3
HCOOH*	11.86	12.83	4.28	-6.18	-0.92	-1619.52	7.14
HCOO*	31.44	55.65	-48.32	18.21	0.14	-45277.7	95.18
COOH*	15.96	73.15	-56.77	17.41	0.06	-99324.4	111.23
CO*	14.23	155.06	-104.97	28.17	-0.02	-102408	52.85
OH*	19.91	135.45	-98.34	27.34	-0.07	-100941	52.18
H*	41.6	84.63	-53.78	12.92	-0.73	-100939	84.63
H_2O*	27.71	38.42	-29.14	8.75	0.01	-57316.4	59.57
CO_2*	31.22	31.01	-34.46	14.36	-0.18	-43766.6	62.3

Table F.3 Shomate parameters (A to H) for transition-state energies (in kJ/mol) for the elementary steps in reaction network in T-range: 300 – 1200 K evaluated on clean Pd(111).

Clean Pd(111)	A	B	C	D	E	F	G
HCOOH* + 2* → HCOO* + H*	17.87	179.01	-137.03	39.58	-0.3	-102447	36.54
HCOO* → CO_2* + H*	28.15	88.38	-47.49	8.41	-0.34	-100830	84.57
HCOOH* + * → COOH* + H*	24.47	165.96	-130.15	38.62	-0.42	-102407	51.02
COOH* + * → CO_2* + H*	43.19	85.47	-60.22	15.54	-0.7	-100903	97.09
2H* → H_2 + 2*	29.92	-2.35	1.55	0.58	-0.03	-3103.38	171.35
COOH* + * → CO* + OH*	49.4	65.86	-54.36	18.32	-0.52	-100951	99.91
OH* + H* → H_2O* + *	36.4	47.69	-40.06	13.28	-0.99	-45286.3	56.28

Table F.4 Pre-exponential factors for the adsorption steps on clean Pd(111), where, per collision theory, rate constant $k = AT^{-0.5}$ (where, k is in s^{-1})

	A (× 10^9)
HCOOH(g) + * ↔ HCOOH*	3.93
CO_2(g) + * ↔ CO_2*	4.02
CO(g) + * ↔ CO*	5.04
H_2O(g) + * ↔ H_2O *	6.28

F.3 Optimized DFT Energetics for CO*-coverage Cognizant Model on Pd(111)

Table F.5 Shomate parameters (A to H) for gas-phase species and adsorbed reaction intermediates (in kJ/mol) in reaction network in T-range: 300 – 1200 K. The energetics of the reaction intermediates were evaluated on 5/9 ML CO*-covered Pd(111).

5/9ML CO*-covered Pd(111)	A	B	C	D	E	F	G
HCOOH(g)	15.84	143.99	-105.96	31.14	-0.14	-102336.33	231.37
H_2(g)	29.92	-2.35	1.55	0.58	-0.03	-3041.82	171.35
CO_2(g)	27.72	48.61	-28.94	6.74	-0.18	-99321.19	237.82
H_2O(g)	28.06	14.46	-2.99	1.07	0.12	-45237.98	219.56
CO(g)	27.02	0.40	10.80	-5.40	0.11	-57080.80	234.83
HCOOH*	19.95	161.38	-114.08	32.00	0.00	-102401.26	56.94
HCOO*	20.06	135.78	-99.19	27.74	-0.12	-100758.10	42.88
COOH*	41.56	82.06	-49.07	10.77	-0.83	-100778.52	76.56
CO*	27.73	36.91	-29.44	9.71	0.05	-57128.48	65.58
OH*	26.99	36.26	-34.93	13.23	-0.31	-43602.09	57.92
H*	10.91	10.36	10.56	-9.43	-0.92	-1535.29	6.08
HCO*	30.10	57.38	-31.84	7.05	-0.29	-58585.42	67.48
H_2O*	33.20	46.11	-34.99	12.53	-0.30	-45267.35	68.24
CO_2*	31.54	75.91	-59.61	18.44	0.05	-99326.22	113.75
COH*	33.85	53.14	-28.82	5.68	-0.90	-58602.69	47.18

Table F.6 Shomate parameters (A to H) for transition-state energies (in kJ/mol) for the elementary steps in reaction network in T-range: 300 – 1200 K evaluated on 5/9 ML CO*-covered Pd(111).

5/9ML CO*-covered Pd(111)	A	B	C	D	E	F	G
HCOOH* + 2* → HCOO* + H*	9.50	216.12	-169.07	49.51	-0.29	-102261.16	6.93
HCOO* → CO_2* + H*	30.81	83.47	-44.70	7.95	-0.44	-100602.48	77.64
HCOOH* + * → COOH* + H*	31.14	142.00	-104.68	29.76	-0.49	-102285.79	54.98
COOH* + * → CO_2* + H*	35.40	79.09	-45.62	9.94	-0.19	-100668.93	95.53
2H* → H_2 + 2*	10.41	29.27	-0.38	-5.73	-0.27	-2990.28	14.25
COOH* + * → CO* + OH*	49.90	62.93	-51.10	17.18	-0.58	-100712.47	95.21
OH* + H* → H_2O* + *	36.55	47.43	-40.04	13.34	-0.93	-45129.36	56.89
COOH* + CO* → COH* + CO_2*	70.59	214.16	-159.04	45.07	-0.47	-157844.83	147.70
HCO* + CO* → COH* + CO*	79.17	134.53	-84.36	19.82	-0.71	-115598.50	160.80
COH* + * → CO* + H*	31.94	54.69	-31.13	5.41	-0.73	-58479.71	46.04
HCO* + * → CO* + H*	20.74	45.69	-17.01	0.23	-0.17	-58549.72	42.05

F.4 CO and HCOO Coverage-dependent Energetics

Table F.7 Coefficients for the polynomial expression (ΔBE (in kJ/mol) = $\alpha_0 + \alpha_1\theta + \alpha_2\theta^2 + \alpha_3\theta^3$) employed to update the binding energy of the adsorbates with surface coverage of CO*, from the values calculated on 5/9 ML CO*-covered Pd(111), where θ is the surface coverage of CO* (in ML) calculated by the mean-field microkinetic model during a forward simulation. Value of α_1 was set to zero to ensure that the energy minimum for each species was at clean surface level (no coadsorbed CO*).The parameters α_0, α_2, and α_3 are fit using unadjusted DFT energies calculated at varying coadsorbed CO*-coverages.

Pd(111)	α_0	α_1	α_2	α_3
CO*	-65.2	0.0	95.3	232.7
COH*	-70.4	0.0	228.2	0.0
COOH*	-87.6	0.0	-42.3	570.0
H*	-25.9	0.0	141.0	-96.6
HCO*	-70.4	0.0	228.2	0.0
HCOO*	-85.5	0.0	-302.9	1073.5
HCOOH*	-10.6	0.0	34.9	0.0
OH*	-45.0	0.0	181.3	0.0
H_2O*	-4.6	0.0	14.8	0.0

Table F.8 Coefficients for the polynomial expression (ΔBE (in kJ/mol) = $\alpha_0 + \alpha_1\theta + \alpha_2\theta^2 + \alpha_3\theta^3$) employed to update the transition-state energies of the elementary steps with surface coverage of CO*, from the values calculated on 5/9 ML CO*-covered Pd(111), where θ is the surface coverage of CO* (in ML) calculated by the mean-field microkinetic model during a forward simulation. Value of α_1 was set to zero to ensure that the energy minimum for each species was at clean surface level (no coadsorbed CO*).The parameters α_0, α_2, and α_3 are fit using unadjusted DFT energies calculated at varying coadsorbed CO*-coverages.

Pd(111)	α_0	α_1	α_2	α_3
HCOOH* + 2* → HCOO* + H*	-86.8	0.0	281.3	0.0
HCOO* → CO_2* + H*	-156.9	0.0	-71.6	1073.5
HCOOH* + * → COOH* + H*	-91.7	0.0	297.0	0.0
COOH* + * → CO_2* + H*	-130.0	0.0	95.2	570.0
2H* → H_2 + 2*	-22.8	0.0	188.1	-193.1
COOH* + * → CO* + OH*	-94.3	0.0	-20.4	570.0
OH* + H* → H_2O* + *	-33.2	0.0	200.3	-96.6
COOH* + CO* → COH* + CO_2*	-152.7	0.0	53.0	802.6
HCO* + CO* → COH* + CO*	-135.6	0.0	323.5	232.7
COH* + * → CO* + H*	-120.4	0.0	390.2	0.0
HCO* + * → CO* + H*	-99.4	0.0	322.0	0.0

Table F.9 Coefficients for the polynomial expression (ΔBE (in kJ/mol) = $\alpha_0 + \alpha_1\theta + \alpha_2\theta^2$) employed to update the binding energy of the adsorbates with surface coverage of HCOO*, from the values calculated on Cu(111), where θ is the surface coverage of HCOO* (in ML, not accounting for denticity) calculated by the mean-field microkinetic model during a forward simulation. Value of α_0 was set to zero to ensure that the energy minimum for each species was at clean surface level (no coadsorbed HCOO*). The parameters α_0, α_1, and α_2 are fit using unadjusted DFT energies calculated at varying coadsorbed HCOO*-coverages.

Cu(111)	α_0	α_1	α_2
CO*	0.0	-67.5	281.9
COH*	0.0	-200.8	695.8
COOH*	0.0	-662.9	2368.8
H*	0.0	-179.8	695.1
HCO*	0.0	-200.8	695.8
HCOO*	0.0	-355.0	2122.7
HCOOH*	0.0	-419.2	1057.1
OH*	0.0	-221.8	790.7
H_2O*	0.0	-351.6	589.0

Table F.10 Coefficients for the polynomial expression (ΔBE (in kJ/mol) = $\alpha_0 + \alpha_1\theta + \alpha_2\theta^2$) employed to update the transition-state energy of the reaction intermediates with surface coverage of HCOO*, from the values calculated on Cu(111), where θ is the surface coverage of HCOO* (in ML, not accounting for denticity) calculated by the mean-field microkinetic model during a forward simulation. The values are approximated based on the expressions derived for the reaction intermediates assuming the same changes to the transition-state energy as the initial state.

Cu(111)	α_0	α_1	α_2
HCOOH* + 2* → HCOO* + H*	0.0	-419.2	1057.1
HCOO* → CO_2* + H*	0.0	-355.0	2122.7
HCOOH* + * → COOH* + H*	0.0	-419.2	1057.1
COOH* + * → CO_2* + H*	0.0	-662.9	2368.8
2H* → H_2 + 2*	0.0	-359.6	1390.2
COOH* + * → CO* + OH*	0.0	-662.9	2368.8
OH* + H* → H_2O* + *	0.0	-401.6	1485.8
COOH* + CO* → COH* + CO_2*	0.0	-730.4	2650.7
HCO* + CO* → COH* + CO*	0.0	-268.4	977.7
COH* + * → CO* + H*	0.0	-200.8	695.8
HCO* + * → CO* + H*	0.0	-200.8	695.8

F.5 Optimized Structures of the Reaction Intermediates

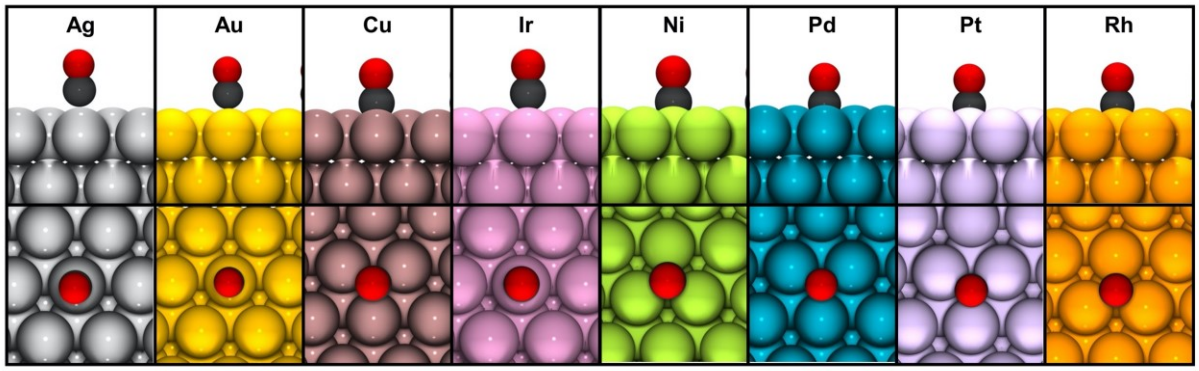


Figure F.1 Side and top views of the most stable structures of CO on clean close-packed (111) facets of: Ag (silver), Au (gold), Cu (brown), Ir (pink), Ni (green), Pd (blue), Pt (purple), and Rh (orange). Carbon and oxygen are shown in gray and red, respectively.

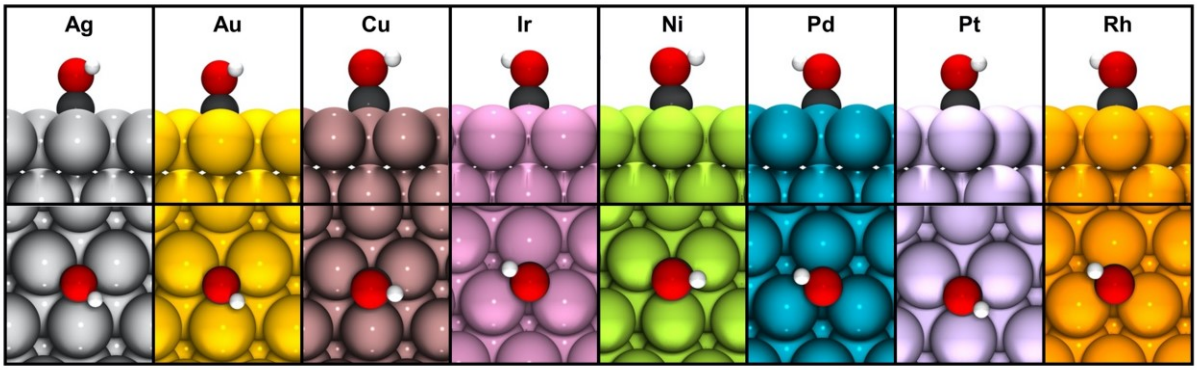


Figure F.2 Side and top views of the most stable structures of COH on clean close-packed (111) facets of: Ag (silver), Au (gold), Cu (brown), Ir (pink), Ni (green), Pd (blue), Pt (purple), and Rh (orange). Carbon, oxygen, and hydrogen are shown in gray, red, and white, respectively.

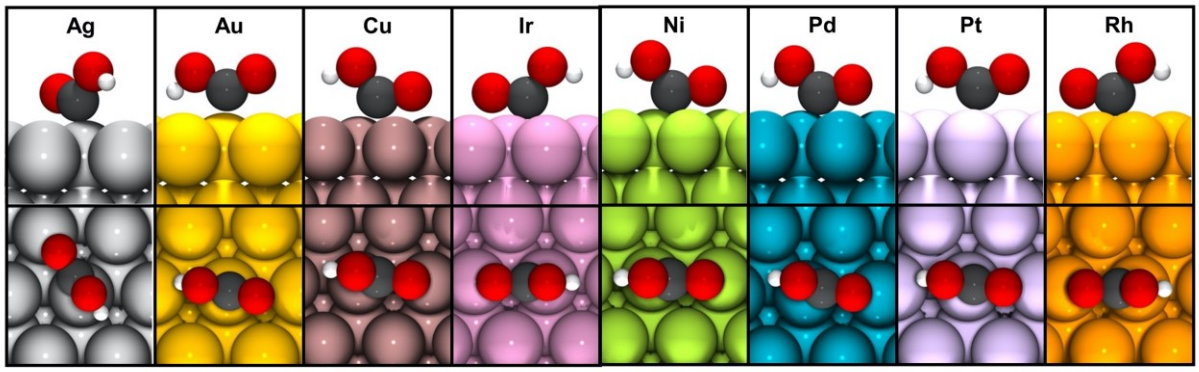


Figure F.3 Side and top views of the most stable structures of COOH on clean close-packed (111) facets of: Ag (silver), Au (gold), Cu (brown), Ir (pink), Ni (green), Pd (blue), Pt (purple), and Rh (orange). Carbon, oxygen, and hydrogen are shown in gray, red, and white, respectively.

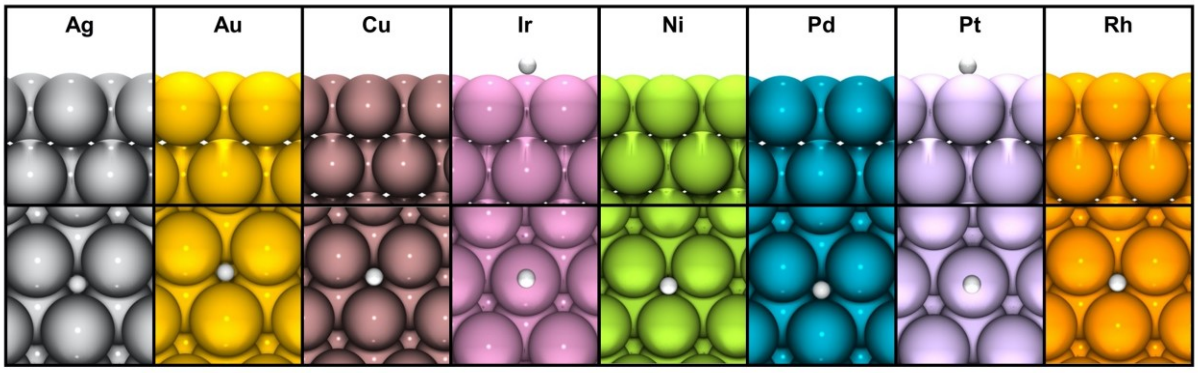


Figure F.4 Side and top views of the most stable structures of H on clean close-packed (111) facets of: Ag (silver), Au (gold), Cu (brown), Ir (pink), Ni (green), Pd (blue), Pt (purple), and Rh (orange). Hydrogen is shown in white.

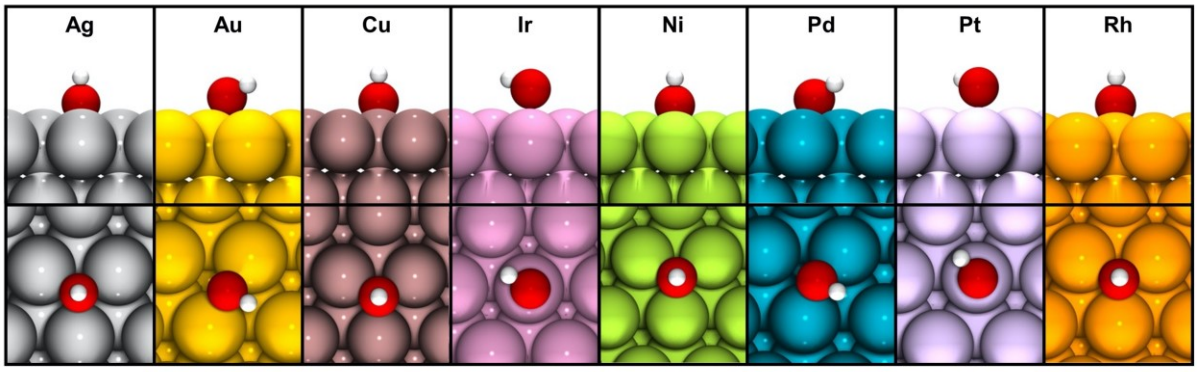


Figure F.5 Side and top views of the most stable structures of OH on clean close-packed (111) facets of: Ag (silver), Au (gold), Cu (brown), Ir (pink), Ni (green), Pd (blue), Pt (purple), and Rh (orange). Oxygen and hydrogen are shown in red, and white, respectively.

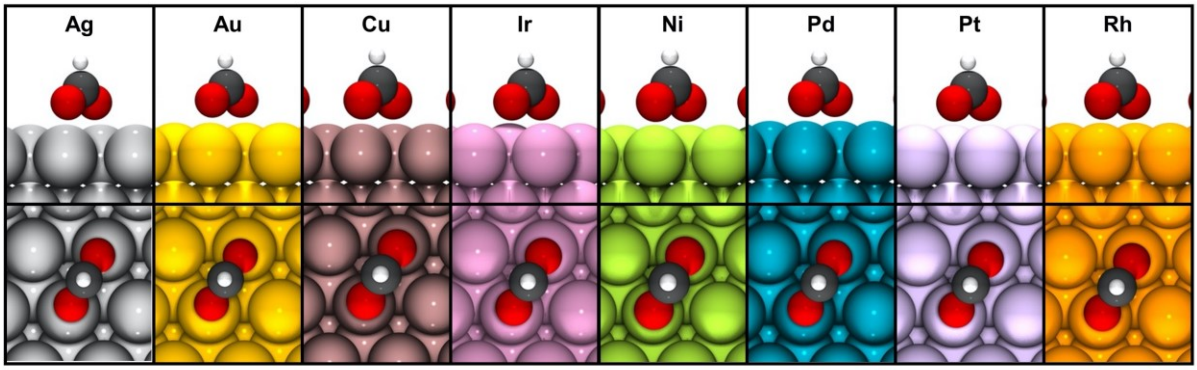


Figure F.6 Side and top views of the most stable structures of HCOO on clean close-packed (111) facets of: Ag (silver), Au (gold), Cu (brown), Ir (pink), Ni (green), Pd (blue), Pt (purple), and Rh (orange). Carbon, oxygen, and hydrogen are shown in gray, red, and white, respectively.

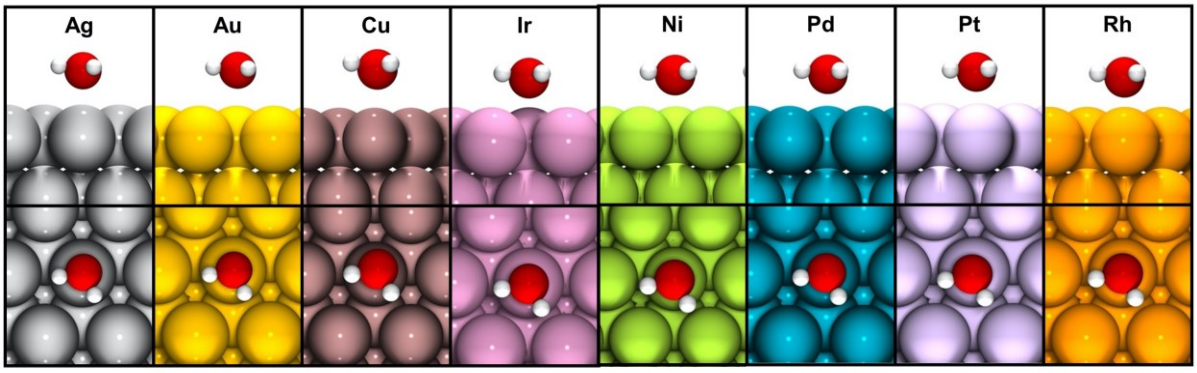


Figure F.7 Side and top views of the most stable structures of H_2O on clean close-packed (111) facets of: Ag (silver), Au (gold), Cu (brown), Ir (pink), Ni (green), Pd (blue), Pt (purple), and Rh (orange). Oxygen and hydrogen are shown in red, and white, respectively.

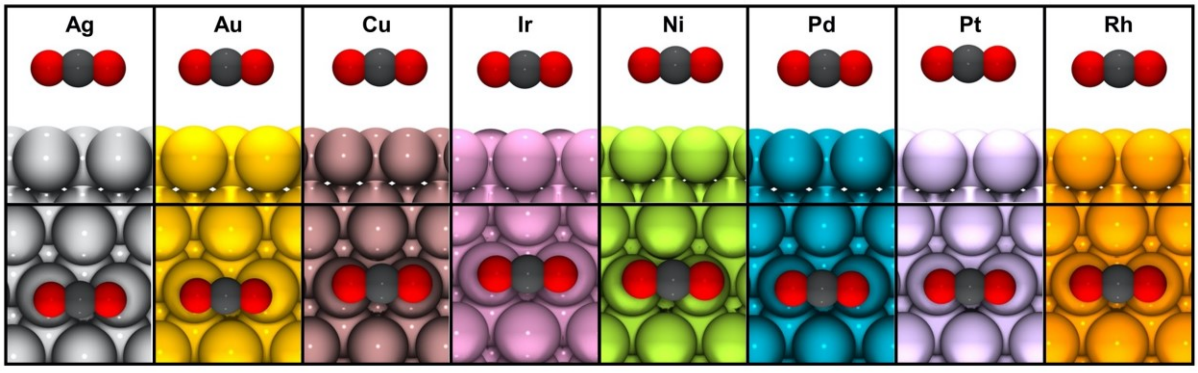


Figure F.8 Side and top views of the most stable structures of CO_2 on clean close-packed (111) facets of: Ag (silver), Au (gold), Cu (brown), Ir (pink), Ni (green), Pd (blue), Pt (purple), and Rh (orange). Carbon and oxygen are shown in gray and red, respectively.

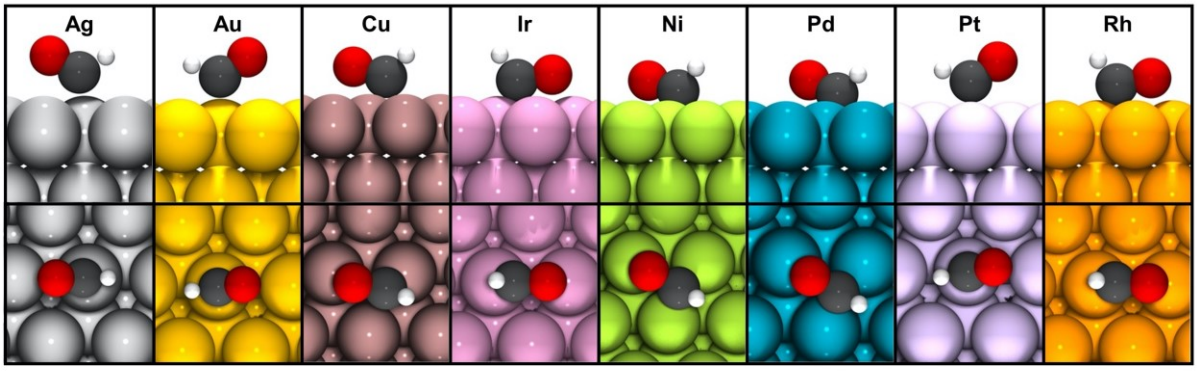


Figure F.9 Side and top views of the most stable structures of HCO on clean close-packed (111) facets of: Ag (silver), Au (gold), Cu (brown), Ir (pink), Ni (green), Pd (blue), Pt (purple), and Rh (orange). Carbon, oxygen, and hydrogen are shown in gray, red, and white, respectively.

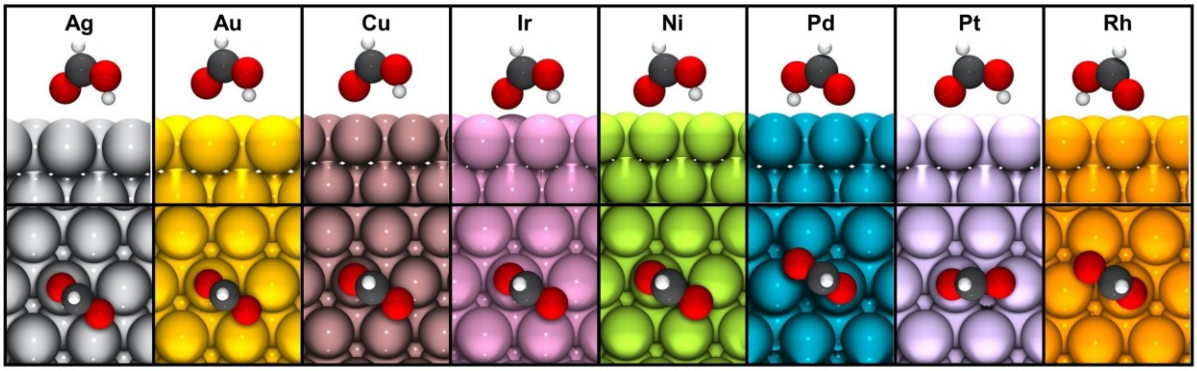


Figure F.10 Side and top views of the most stable structures of HCOOH on clean close-packed (111) facets of: Ag (silver), Au (gold), Cu (brown), Ir (pink), Ni (green), Pd (blue), Pt (purple), and Rh (orange). Carbon, oxygen, and hydrogen are shown in gray, red, and white, respectively.

F.6 Optimized Lattice-constants for Intermetallic Binary Alloys

Table F.11 Optimized lattice-constants for intermetallic binary alloy catalysts with an fcc crystal structure (PW91-GGA, DACAPO).

Composition	Lattice Constant (Å)
Ag_3Pd	4.09
Au_3Cu	4.07
$AuCu_3$	3.81
Cu_3Pd	3.75
Pd_3Pb	4.12
Pd_3Sn	4.06
Au_3Pd	4.12
$AuPd_3$	4.03
Cu_3Pt	3.76
Pt_3Pb	4.15
Pt_3Cd	4.06
Pt_3Sn	4.07
Pt_3Zn	3.95
Pd_3Cd	4.04
Pt_3Rh	3.97
$PtRh_3$	3.87
Pd_3Sc	4.02
Pt_3Sc	4.03
Pd_3Y	4.15
Pt_3Y	4.14
Ni_3Pt	3.67

APPENDIX G

SUPPORTING INFORMATION FOR CHAPTER 8: HOW NON-INNOCENT SPECTATOR SPECIES IMPROVE THE OXYGEN REDUCTION ACTIVITY OF SINGLE-ATOM CATALYSTS: MICROKINETIC MODELS FROM FIRST-PRINCIPLES CALCULATIONS[⊥]

[⊥] Adapted from – Rebarchik, M.†; Bhandari, S.†; Kropp, T.; Mavrikakis, M. († - Equal Contribution) How Non-innocent Spectator Species Improve the Oxygen Reduction Activity of Single-atom Catalysts: Microkinetic Models from First-principles Calculations. *ACS Catalysis* **2020** (*In Press*) – https://doi.org/10.1021/acscatal.0c01642

G.1 Gibbs Free Reaction Energies

Table G.1 Binding energies (BE) of O relative to ½ gas phase O_2 ($r_{O–O}$ = 122 pm) and of water on the single-atom catalysts considered in this work (values in parentheses refer to binding energies in the presence of co-adsorbed water) as well as Gibbs free binding energies for O_mH_n at 298 K and 0.1 MPa relative to gas phase H_2 and O_2; the corresponding atomization energies amount to 2.27 eV (½ H_2 → H) and 3.04 eV (½ O_2 → O). ΔG_{sel} is the decomposition energy of H_2O_2 (H_2O_2 + * → O* + H_2O), which indicates whether the $2e^-$ or $4e^-$ pathway is preferred (positive or negative values, respectively). All values are in eV.

	BE_O	BE_{H2O}	ΔG_{O2}[a]	ΔG_{OOH}[b]	ΔG_O[c]	ΔG_{OH}[d]	ΔG_{sel}
Au	2.13 (2.56)	-0.07	0.14	0.25	2.26	-0.14	0.98
Co	0.16 (0.21)	-0.09	-0.24	-0.46	0.41	-1.21	-0.88
Co–O_2	0.73	-0.03	0.22	-0.09	0.96	-0.55	-0.45
Co–OOH	0.56	-0.05	0.13	-0.18	0.80	-0.97	-0.49
Co=O	0.57	-0.03	0.32	-0.07	0.84	-0.88	-0.33
Co–OH	0.44	-0.05	0.42	-0.21	0.74	-1.03	-0.55
Cr	-2.66 (-2.46)	-0.22	-1.54	-1.45	-2.37	-2.37	-3.66
Cr–O_2	-0.30	-0.03	0.26	0.11	-0.25	-0.78	-1.54
Cr–OOH	-0.94	-0.09	0.02	-0.40	-0.60	-1.25	-1.89
Cr=O	0.46	-0.02	0.58	0.33	0.72	-0.51	-0.57
Cr–OH	-0.83	-0.12	0.05	-0.33	-0.51	-1.21	-1.80
Cu	1.50 (1.41)	-0.05	0.17	0.31	1.71	-0.39	0.42
Fe	-1.21 (-1.05)	-0.20	-0.45	-0.96	-0.94	-1.66	-2.23
Fe–O_2	-0.36	-0.02	0.19	-0.41	-0.17	-1.12	-1.46
Fe–OOH	-0.19	-0.04	0.10	-0.35	0.07	-1.13	-1.22
Fe=O	0.64	-0.05	0.32	0.05	0.92	-0.80	-0.37
Fe–OH	-0.33	-0.04	0.09	-0.43	-0.07	-1.18	-1.36
Ir	-0.22 (-0.22)	-0.21	-0.03	-0.38	0.02	-1.14	-1.26
Mn	-1.48 (-1.29)	-0.22	-0.80	-0.89	-1.20	-1.77	-2.49
Mn–O_2	-0.21	-0.03	0.41	0.05	-0.15	-0.77	-1.44
Mn–OOH	-0.52	-0.10	0.14	-0.37	-0.18	-1.32	-1.47
Mn=O	-0.03	-0.04	0.25	0.14	0.26	-0.71	-1.03
Mn–OH	-0.49	-0.04	0.20	-0.44	-0.15	-1.36	-1.44
Ni	1.72 (1.85)	-0.09	0.20	0.39	1.93	-0.24	0.64
Pd	2.18 (2.12)	-0.10	0.23	0.53	2.38	0.08	1.10
Pt	1.87 (1.85)	-0.13	0.23	0.57	2.08	0.12	0.79
Rh	0.17 (0.21)	-0.20	-0.12	-0.39	0.42	-1.15	-0.87
Ru	-1.75 (-1.72)	-0.12	-1.12	-1.47	-1.49	-2.14	-2.78
Ru–O_2	-0.54	0.03	0.11	-0.38	-0.22	-1.31	-1.51
Ru–OOH	-0.71	-0.06	-0.04	-0.63	-0.37	-1.57	-1.66
Ru=O	-0.51	-0.09	0.15	-0.35	-0.22	-1.26	-1.51
Ru–OH	-0.89	-0.28	-0.28	-0.89	-0.60	-1.58	-1.88

[a] O_2 + * → O_2^*; [b] ½ H_2 + O_2 + * → OOH*; [c] ½ O_2 + * → O*; [d] ½ H_2 + ½ O_2 + * → OH*.

To explore the impact of co-adsorbed water, binding energies were calculated for each intermediate in the presence of water. The reaction energy for the reduction of 0_2^* to OOH* (i.e., the potential-limiting step on less oxophilic metals) changes by less than 0.1 eV, as water affects the binding energies of O_2 and OOH similarly. The reduction energy of OH* (i.e., the potential-limiting step for more oxophilic metals) changes by up to 0.2 eV. These changes are small compared to the impact of co-adsorbed O* and OH*.

Table G.2 Binding energies (BE) of H_2O and O_mH_n intermediates on metal centers of the single-atom catalysts studied in this work relative to gas phase H_2 and O_2; the corresponding atomization energies amount to 2.27 eV (½ H_2 → H) and 3.04 eV (½ O_2 → O). Values in parentheses refer to the presence of co-adsorbed H_2O. All values are in eV.

	BE_{H2O}	BE_{O2}[a]	BE_{OOH}[b]	BE_O[c]	BE_{OH}[d]
Au	-0.07	-0.13 (-0.14)	-0.37 (-0.35)	2.13 (2.56)	-0.58 (-0.52)
Co	-0.09	-0.73 (-0.67)	-1.31 (-1.27)	0.16 (0.21)	-1.77 (-1.73)
Cr	-0.22	-2.06 (-1.88)	-2.25 (-2.12)	-2.66 (-2.46)	-2.93 (-2.83)
Cu	-0.05	-0.11 (-0.09)	-0.45 (-0.37)	1.50 (1.41)	-0.91 (-0.88)
Fe	-0.20	-0.99 (-0.81)	-1.80 (-1.64)	-1.21 (-1.05)	-2.25 (-2.09)
Ir	-0.21	-0.50 (-0.45)	-1.20 (-1.32)	-0.22 (-0.22)	-1.69 (-1.93)
Mn	-0.22	-1.35 (-1.16)	-1.72 (-1.60)	-1.48 (-1.29)	-2.32 (-2.14)
Ni	-0.09	-0.06 (-0.07)	-0.39 (-0.37)	1.72 (1.73)	-0.76 (-0.71)
Pd	-0.10	-0.05 (-0.04)	-0.19 (-0.19)	2.18 (2.12)	-0.40 (-0.39)
Pt	-0.13	-0.06 (-0.05)	-0.14 (-0.14)	1.87 (1.85)	-0.37 (-0.35)
Rh	-0.20	-0.59 (-0.51)	-1.23 (-1.28)	0.17 (0.21)	-1.71 (-1.84)
Ru	-0.12	-1.63 (-1.48)	-2.26 (-2.20)	-1.75 (-1.72)	-2.71 (-2.88)

[a] $O_2 + * \rightarrow 0_2^*$; [b] ½ $H_2 + O_2 + * \rightarrow$ OOH*; [c] ½ $O_2 + * \rightarrow$ O*; [d] ½ H_2 + ½ $O_2 + * \rightarrow$ OH*.

G.2 Scaling Relations

Gibbs free binding energies (298 K, 0.1 MPa) for O_mH_n species on pristine metal sites are shown as a function of the electronic binding energy of atomic oxygen BE_O (Figure G.1). Linear scaling relations were obtained for ΔG_O, ΔG_{OH}, and ΔG_{OOH}. For the adsorption of O_2, Gibbs free reaction energies do not change significantly beyond $BE_O > 0.5$ eV, which is why a quadratic polynomial was used instead. For $BE_O > 1.96$ eV, ΔG_{O2} is assumed to be constant. Figure G.2 shows Gibbs free adsorption energy of co-adsorbed O_2 and OH as a function of BE_O at the pristine metal site.

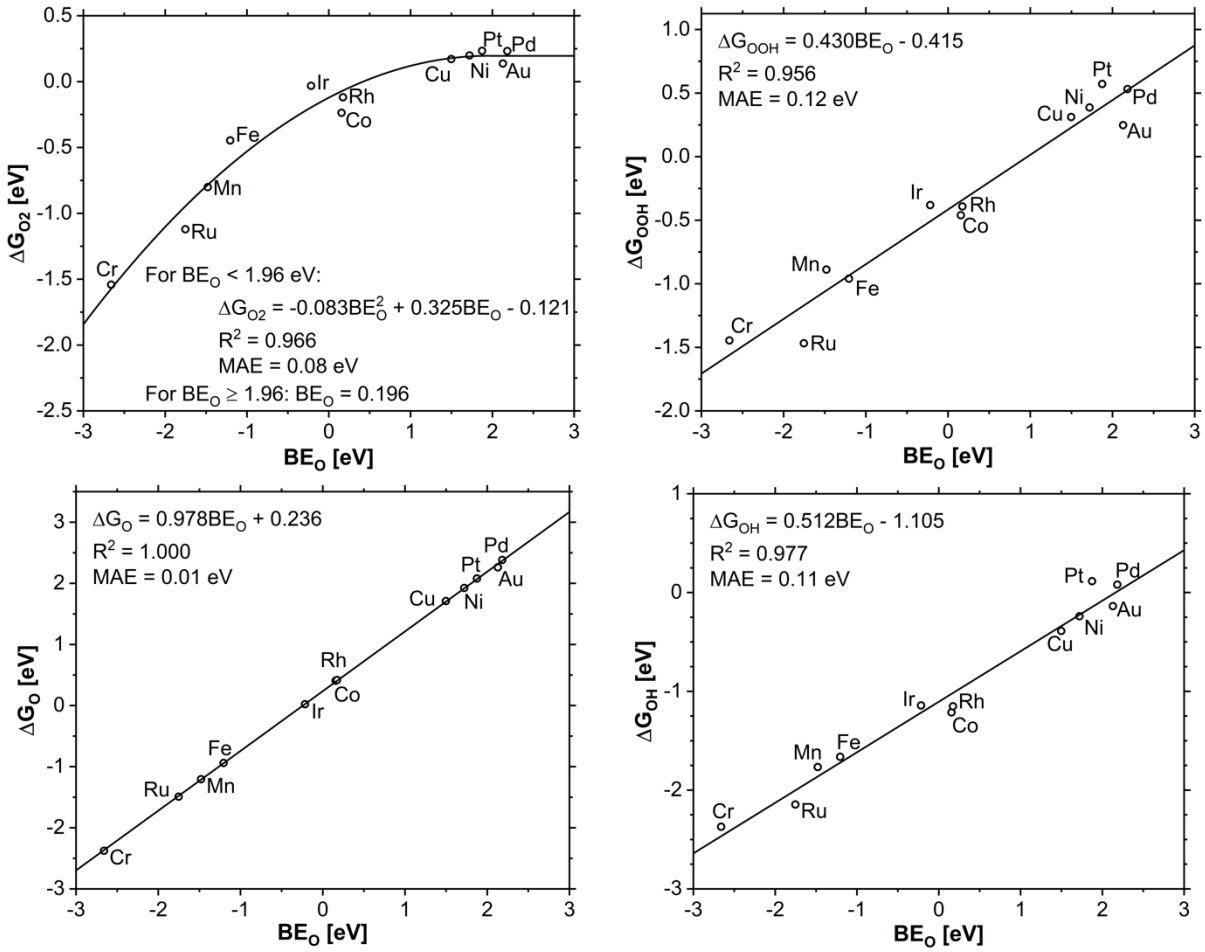


Figure G.1 Gibbs free binding energies of O_mH_n on pristine metal sites (Table G.1) are plotted against BE_O at the same site. R^2 is the coefficient of determination, and MAE denotes the mean absolute error of the fits.

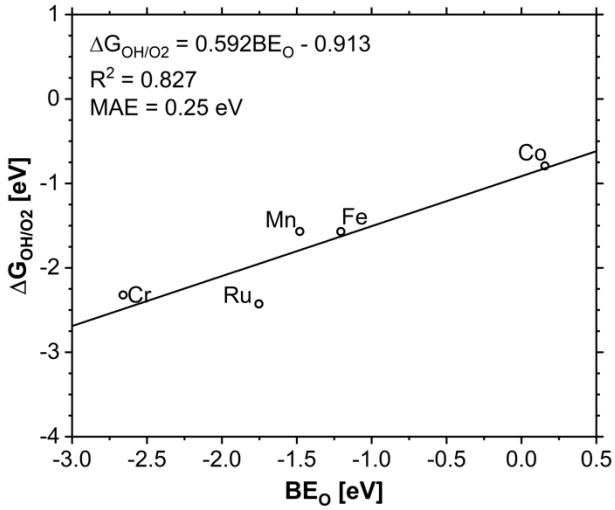


Figure G.2 Gibbs free adsorption energies of co-adsorbed O_2 and OH (i.e., [Me] + 1.5 O_2 + 0.5 H_2 → [Me](OH)-O_2) as a function of BE_O at the pristine metal site. R^2 is the coefficient of determination, and MAE denotes the mean absolute error of the fit.

G.3 Microkinetic Modeling

We formulate a microkinetic model for the oxygen reduction reaction on transition metal atoms embedded in a N-substituted graphene di-vacancy using DFT-derived energetics (Table G.1). The implementation is similar to the model presented by Hansen *et al*.[325] Therein, O_2 molecules diffuse from the bulk to the electrode (step 0). Then, they adsorb on a 'clean' metal site (i.e., a site without co-adsorbed intermediates) and undergo subsequent protonation steps (steps A1-5).

(0) $O_2(aq) \leftrightarrow O_2(dl)$

(A1) $O_2(dl) + * \leftrightarrow O_2^*$

(A2) $(H^+ + e^-) + O_2^* \leftrightarrow OOH^*$

(A3) $(H^+ + e^-) + OOH^* \leftrightarrow H_2O + O^*$

(A4) $(H^+ + e^-) + O^* \leftrightarrow OH^*$

(A5) $(H^+ + e^-) + OH^* \leftrightarrow H_2O + *$

However, O_2 can also adsorb on O_mH_n-decorated sites, which is denoted by $O_2^*/O_mH_n^*$ herein. The corresponding elementary steps in the presence of co-adsorbed OH* are shown in steps B1-5. Similarly, the reaction may occur in the presence of co-adsorbed O* (steps C1-5), OOH* (steps D1-5), or O_2^* (steps E1-5). The inclusion of these steps is the main difference between our microkinetic model and a recently published one,[322] which only considers steps A1-5 and B1-5. In their model, the O_2^*/OH^* intermediate can only be protonated on one side to form OOH*/OH* (step B2 in this work), since the OH* species is considered an innocent spectator. Herein, we allow for adsorption and reduction on both sides of the metal ion. All intermediates are shown in Figure 8.1, and it should be noted that A*/B* and B*/A* are equivalent within our implementation

(B1) $O_2(dl) + OH^* \leftrightarrow O_2^*/OH^*$

(B2) $(H^+ + e^-) + O_2^*/OH^* \leftrightarrow OOH^*/OH^*$

(B3) $(H^+ + e^-) + OOH^*/OH^* \leftrightarrow H_2O + O^*/OH^*$

(B4) $(H^+ + e^-) + O^*/OH^* \leftrightarrow OH^*/OH^*$

(B5) $(H^+ + e^-) + OH^*/OH^* \leftrightarrow H_2O + OH^*$

(C1) $O_2(dl) + O^* \leftrightarrow O_2^*/O^*$

(C2) $(H^+ + e^-) + O_2^*/O^* \leftrightarrow OOH^*/O^*$

(C3) $(H^+ + e^-) + OOH^*/O^* \leftrightarrow H_2O + O^*/O^*$

(C4) $(H^+ + e^-) + O^*/O^* \leftrightarrow O^*/OH^*$

(C5) $(H^+ + e^-) + O^*/OH^* \leftrightarrow H_2O + O^*$

(D1) $O_2(dl) + OOH^* \leftrightarrow O_2^*/OOH^*$

(D2) $(H^+ + e^-) + O_2^*/OOH^* \leftrightarrow OOH^*/OOH^*$

(D3) $(H^+ + e^-) + OOH^*/OOH^* \leftrightarrow H_2O + OOH^*/O^*$

(D4) $(H^+ + e^-) + OOH^*/O^* \leftrightarrow OOH^*/OH^*$

(D5) $(H^+ + e^-) + OOH^*/OH^* \leftrightarrow H_2O + OOH^*$

(E1) $O_2(dl) + O_2^* \leftrightarrow O_2^*/O_2^*$

(E2) $(H^+ + e^-) + O_2^*/O_2^* \leftrightarrow O_2^*/OOH^*$

(E3) $(H^+ + e^-) + O_2^*/OOH^* \leftrightarrow H_2O + O_2^*/O^*$

(E4) $(H^+ + e^-) + O_2^*/O^* \leftrightarrow O_2^*/OH^*$

(E5) $(H^+ + e^-) + O_2^*/OH^* \leftrightarrow H_2O + O_2^*$

(B1)

As derived in previously,[325] the mole fraction of O_2 in the aqueous phase amounts to $x_{aq}(O_2) = 2.34 \cdot 10^{-5}$ (assuming equilibrium with 1 atm O_2 in the gas phase at 298 K), and the diffusion of O_2 (step 0) is assumed to be thermoneutral with a rate constant of $k = 8 \cdot 10^5$ s^{-1}. For O_2 adsorption (steps A1, B1, C1, D1, and E1), a rate constant of $k = 10^8$ s^{-1} is used.

Forward rate constants of electrochemical reduction steps ($k_{f,i}$) are calculated using the approach by Hansen *et al.*,[325] where $G^o_{a,i}$ is the activation free energy at the reversible potential of step *i* at the reversible potential of the step ($U_i^o = -\Delta G_i^o/e$), and *U* is the applied potential. We also define an effective prefactor A_i that is independent of the elementary step to incorporate effects corresponding to solvent reorganization at the electrode.[447] Herein, we use previously published values for effective prefactors ($A_i = 10^9$ s^{-1}), the activation energy at the reversible potential U_i^o ($E^o_{a,i} = 0.26$ eV), and the charge-transfer coefficient ($\beta_i = 0.5$). We do not calculate specific barriers for each reaction, as onset potentials are not significantly affected by variations in the barrier. For example, changing the barrier by ±0.1 eV affects onset potentials on the Fe catalyst by less than 5 mV (Table G.3).

Table G.3 Calculated ORR onset potential for $\mathbf{M_{clean}}$ on [Fe] as a function of the H-transfer barrier.

$E^o_{a,i}$ [eV]	0.16	0.21	0.26	0.31	0.36	0.41
U_{ORR} [V_{RHE}]	0.652	0.652	0.652	0.652	0.646	0.615

$$k_{f,i} = \frac{k_B T}{h} \exp\left(-\frac{G^o_{a,i}}{RT}\right) \exp\left(-\frac{e\beta_i(U - U_i^o)}{k_B T}\right) == A_i \exp\left(-\frac{E^o_{a,i}}{RT}\right) \exp\left(-\frac{e\beta_i(U - U_i^o)}{k_B T}\right) \quad (G.1)$$

Equilibrium constants (K_i), reverse rate constants ($k_{b,i}$), and rates are calculated using:

$$\Delta G_i = \Delta G_i^o + eU \tag{G.2}$$

$$K_i = \exp\left(-\frac{\Delta G_i}{k_B T}\right) \tag{G.3}$$

$$k_{b,i} = \frac{k_{f,i}}{K_i} \tag{G.4}$$

$$\text{rate}_i = k_{f,i}\theta_{\text{reactant}} - k_{b,i}\theta_{\text{product}} \tag{G.5}$$

We then write sets of differential equations for each of the surface-intermediates, subject to the site-balance equation (Equation F.6) and solve the set of ODEs to steady-state. The corresponding current j is calculated from the turnover frequency (Equation F.7), which is calculated by adding the reaction rates for all the steps involving an electron transfer.

$$\theta^* = 1 - \sum_{A,B} \theta^*_{A/B} \tag{G.6}$$

$$j \sim TOF_{e^-} \tag{G.7}$$

Using this approach, we plot the current j (normalized with regard to the maximum current limited by O_2 diffusion in aqueous phase) against the applied potential U for the investigated systems, and define the onset potential as shown in Figure 8.3 of the main text. For the presented volcano plots, we use the scaling correlations derived in the previous section to calculate energetics as a function of the descriptor value (BE_O)

G.4 Electronic Structure of ORR Intermediates

Table G.4 Magnetic moments on the metal ions (μ_B) for each ORR intermediate considered herein.

	Au	**Co**	**Cr**	**Cu**	**Fe**	**Ir**	**Mn**	**Ni**	**Pd**	**Pt**	**Rh**	**Ru**
[Me]	0.00	0.79	3.33	0.55	1.90	0.16	3.03	0.00	0.00	0.00	0.17	1.19
[Me]–O_2	0.00	0.09	1.71	0.56	0.00	0.12	2.26	0.03	0.01	0.01	0.07	0.00
[Me]–OOH	0.00	0.00	2.49	0.63	0.96	0.00	2.20	0.26	0.11	0.12	0.00	0.56
[Me]=O	0.08	0.67	0.36	0.54	1.22	0.43	0.44	0.46	0.04	0.05	0.37	0.01
[Me]–OH	0.02	0.00	2.51	0.65	1.09	0.00	2.27	0.36	0.24	0.28	0.00	0.67
[Me](O_2)–O_2	-	0.04	1.72	-	0.01	-	2.23	-	-	-	-	0.29
[Me](O_2)–OOH	-	0.02	1.71	-	0.70	-	1.97	-	-	-	-	0.00
[Me](O_2)=O	-	0.50	0.00	-	0.44	-	0.44	-	-	-	-	0.00
[Me](O_2)–OH	-	0.00	1.75	-	0.83	-	2.34	-	-	-	-	0.16
[Me](OOH)–OOH	-	0.09	2.18	-	0.65	-	2.25	-	-	-	-	0.27
[Me](OOH)=O	-	0.53	1.19	-	0.02	-	0.00	-	-	-	-	0.51
[Me](OOH)–OH	-	0.11	2.22	-	0.77	-	2.32	-	-	-	-	0.00
[Me](O)=O	-	0.67	1.16	-	0.39	-	0.00	-	-	-	-	0.00
[Me](O)–OH	-	0.58	1.23	-	1.11	-	0.22	-	-	-	-	0.49
[Me](OH)–OH	-	0.00	2.26	-	1.18	-	2.41	-	-	-	-	0.00

Table G.5 Bader charges of metal ions (Q_{Me}) for ORR intermediates on Fe and Ru catalysts.

	Fe	**Ru**
[Me]	1.37	0.98
[Me]–O_2	1.52	1.43
[Me]–OOH	1.54	1.42
[Me]=O	1.58	1.58
[Me]–OH	1.57	1.36
[Me](O_2)–O_2	1.58	1.43
[Me](O_2)–OOH	1.64	1.58
[Me](O_2)=O	1.67	1.64
[Me](O_2)–OH	1.65	1.48
[Me](OOH)–OOH	1.67	1.52
[Me](OOH)=O	1.74	1.65
[Me](OOH)–OH	1.69	1.56
[Me](O)=O	1.81	1.83
[Me](O)–OH	1.75	1.69
[Me](OH)–OH	1.69	1.57

APPENDIX H

SUPPORTING INFORMATION FOR CHAPTER 9: AMMONIA ELECTRO-OXIDATION REACTION ON PT(111): THE EFFECT OF NITROGEN COVERAGE

H.1 Impact of the Functional Choice on the Onset Potential

The accuracy of the PW91 exchange-correlation functional was benchmarked against the RPBE[448] functional. Grimme-D3 semiempirical dispersion corrections[449] were included. The Gibbs free energies for deprotonation and N–N bond making steps calculated with PW91 and RPBE+D3 methods are reported in Figure H.1. Data refer to calculations on a clean surface and at representative N* coverages of 1/12, 1/6, 1/3, and 1/2 ML. The PW91 functional overpredicts the calculated Gibbs free energies by 20%, with respect to RPBE+D3. As a consequence, the onset potentials calculated with PW91 would be higher than the ones calculated through RPBE+D3. However, the identity of the potential-determining step at each N* coverage is the same with both functionals, as well as the observed onset potential vs. N* coverage trend (Figure 9.3).

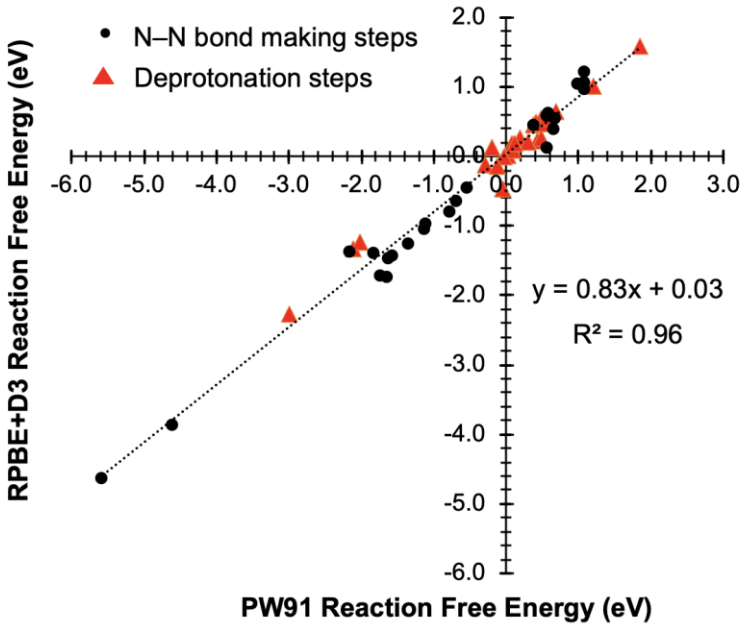


Figure H.1 Parity plot of reaction free energies (in eV) calculated with the PW91 and RPBE functionals. N–N bond formation and deprotonation reaction steps are represented by black circles and red triangles, respectively. Data for 0, 1/12, 1/6, 1/3, and 1/2 ML N* coverages are presented. The dashed line is a linear fit according to the equation shown.

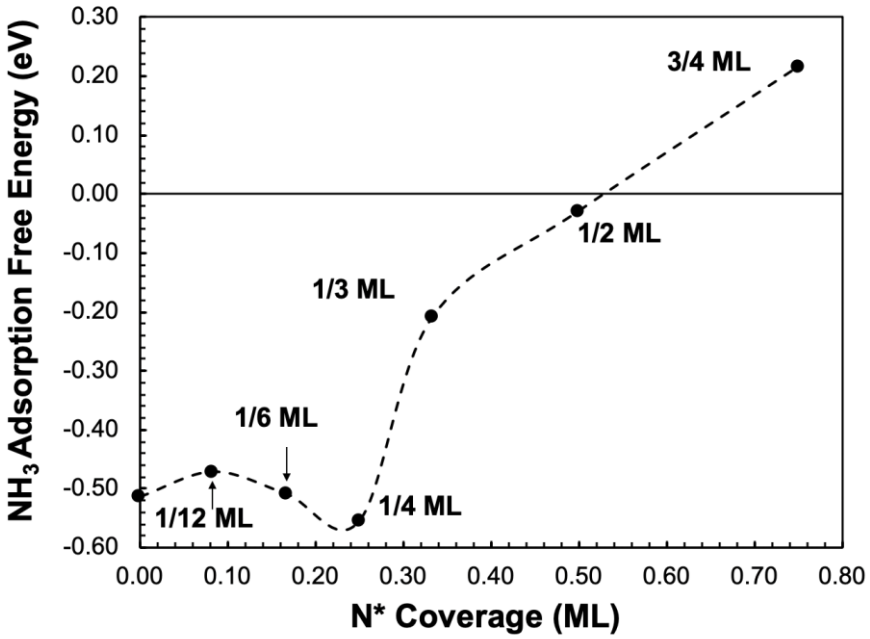


Figure H.2 NH_3 adsorption free energy (PW91-GGA) as function of N* coverage. The dashed line is intended to be a guide for eyes.

Table H.1 Deprotonation free energies (PW91-GGA, in eV) for NHx and HxNNHy species at 0V on Pt(111), at different N* coverages.

Elementary Steps	*Clean*	*1/12 ML*	*1/6 ML*	*1/4 ML*	*1/3 ML*	*1/2 ML*	*3/4 ML*
$NH_3(g) + OH^-(aq) + * \leftrightarrow NH_2* + H_2O(l)$	0.47	0.49	0.59	0.70	1.01	1.63	1.60
$NH_2* + OH^-(aq) \leftrightarrow NH* + H_2O(l)$	0.01	0.08	0.09	0.39	0.52	0.24	2.31
$NH* + OH^-(aq) \leftrightarrow N* + H_2O(l)$	0.46	0.49	0.22	0.27	0.54	0.59	2.32
$H_2NNH_2* + OH^-(aq) \leftrightarrow H_2NNH* + H_2O(l)$	0.47	0.49	0.52	0.69	0.71	0.69	1.61
$H_2NNH* + OH^-(aq) \leftrightarrow HNNH* + H_2O(l)$	0.19	0.18	0.26	0.00	0.00	0.19	-0.88
$H_2NNH* + OH^-(aq) \leftrightarrow H_2NN* + H_2O(l)$	-0.46	-0.07	0.20	0.00	0.00	1.12	-0.81
$HNNH* + OH^-(aq) \leftrightarrow NNH* + H_2O(l)$	-0.14	-0.12	-0.14	0.37	0.47	0.54	0.63
$H_2NN* + OH^-(aq) \leftrightarrow NNH* + H_2O(l)$	0.51	0.13	-0.08	0.06	0.26	0.62	0.56
$NNH* + OH^-(aq) \leftrightarrow N_2(g) + H_2O(l) + *$	-1.24	-1.35	-1.43	-1.83	-2.27	-2.60	-2.77

Table H.2 Free energy of Reaction (PW91-GGA, in eV) for N–N bond making steps, at different N* coverages.

Elementary Steps	*Clean*	*1/12 ML*	*1/6 ML*	*1/4 ML*	*1/3 ML*	*1/2 ML*	*3/4 ML*
$NH_2* + NH_2* \leftrightarrow H_2NNH_2*$	0.55	0.54	-0.09	-0.35	-0.66	-1.73	-1.50
$NH_2* + NH* \leftrightarrow H_2NNH*$	1.02	0.95	0.34	-0.05	-0.47	-1.27	-2.23
$NH_2* + N* \leftrightarrow H_2NN*$	0.10	0.38	0.32	0.00	-0.80	-1.75	-2.04
$NH* + NH* \leftrightarrow HNNH*$	1.20	1.05	0.51	-0.44	-0.99	-1.48	-5.40
$NH* + N* \leftrightarrow HNN*$	0.60	0.43	0.15	-0.34	-1.06	-1.45	-3.80
$N* + N* \leftrightarrow N_2(g)$	-1.09	-1.39	-1.51	-2.44	-3.87	-4.65	-5.60

Table H.3 Activation energy barriers (PW91-GGA, in eV) for N–N bond making steps on a clean and in presence of 1/2 ML of N*.

Elementary Step	*Name*	*Clean*	*1/2 ML*
$NH_2* + NH_2* \leftrightarrow H_2NNH_2*$	TS_1	1.22	0.01
$NH_2* + NH* \leftrightarrow H_2NNH*$	TS_2	1.72	1.14
$NH* + NH* \leftrightarrow HNNH*$	TS_3	2.62	1.35
$NH_2* + N* \leftrightarrow H_2NN*$	TS_4	1.56	0.31
$NH* + N* \leftrightarrow HNN*$	TS_5	2.44	0.80
$N* + N* \leftrightarrow N_2(g)$	TS_{N-N}	2.43	1.42

H.2 N*-coverage Estimation from Previous Experimental Studies

De Vooys et al.[345] performed reductive stripping of the AOR reaction intermediates on a Pt polycristalline electrode. In the interval between 0.65 and 0.85V they determined a constant charge value of 343 μC cm^{-3}, corresponding to 1.63 electrons per surface Pt atom. Although De Vooys et al. did not determine a corresponding N* coverage value, they reported the earlier results of Gootzen et al.,[342] who independently determined a similar charge value of 323 μC cm^{-3} at 0.75 V, and calculated an associated N* coverage of 0.5 ML.

The integrated charge exchanged in the reduction of AOR intermediates is proportional to the coverage of the surface.[342] Assuming that the surface is covered by N* only, we can estimate the charge exchanged in the reductive stripping experiment from the number of electrons exchanged per surface Pt atom reported by De Vooys et al., using 210.4 μC cm^{-3}/n. electron as a conversion factor. Considering that 343 μC cm^{-3} corresponds to 0.5 ML of N*, we can then estimate the N* coverage variation along their reported potential scan. In this way, we estimated that N* coverage could vary from 0.06 ML to 0.36 ML in the 0.4-0.6 V potential range. We emphasize that this qualitative estimation is valid only if N* is considered the only adsorbate on the surface.

H.3 Optimized geometries of AOR reaction intermediates at different N* coverages

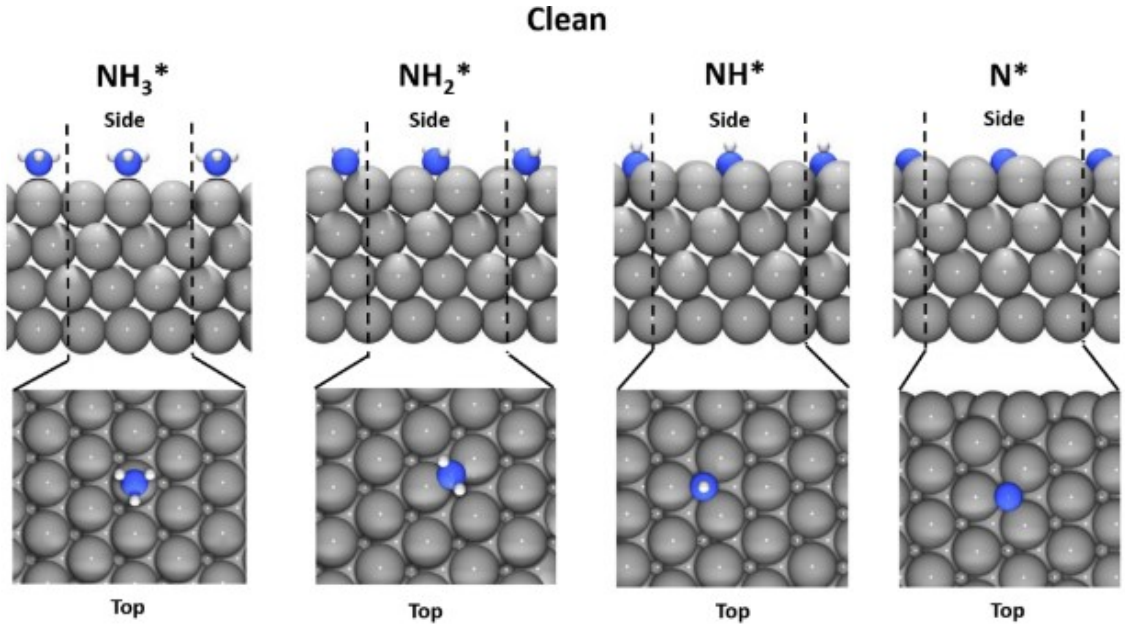


Figure H.3 Optimized structures of the AOR intermediates, with the general formula NHx with x=0−3, on a clean Pt(111) surface. N, H, and Pt are represented with blue, white, and silver spheres, respectively. Top and side views are provided in the bottom and upper panel, respectively. An enlarged prospective of a single unit cell is shown in the top view. Dashed black lines delineate the unit cell lattice vectors.

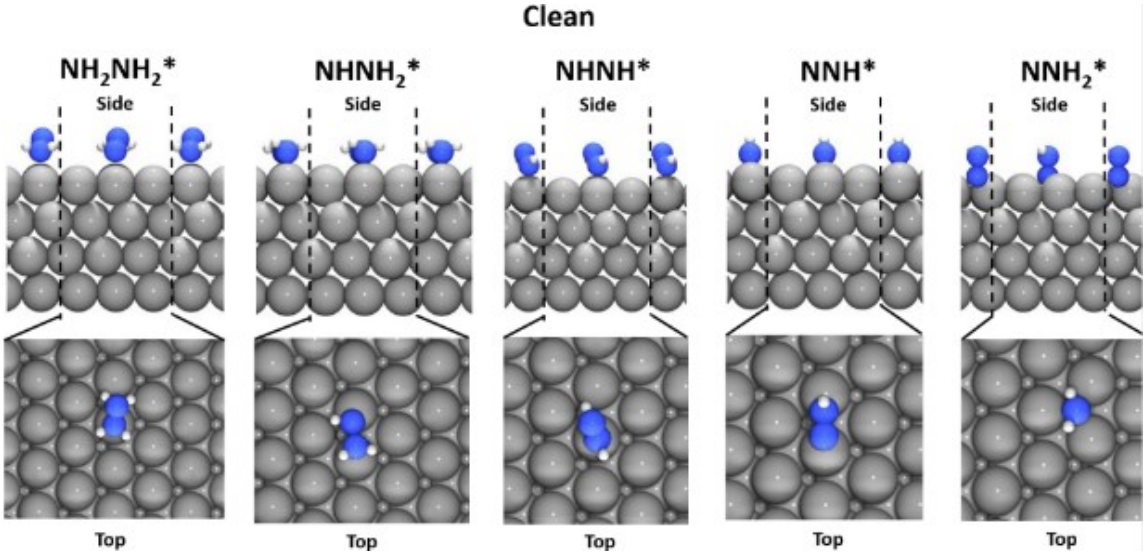


Figure H.4 Optimized structures of the AOR intermediates, with the general formula NHxNHy with x, y =0−2, on a clean Pt(111) surface. N, H, and Pt are represented with blue, white, and silver spheres, respectively. Top and side views are provided in the bottom and upper panel, respectively. An enlarged prospective of a single unit cell is shown in the top view. Dashed black lines delineate the unit cell lattice vectors.

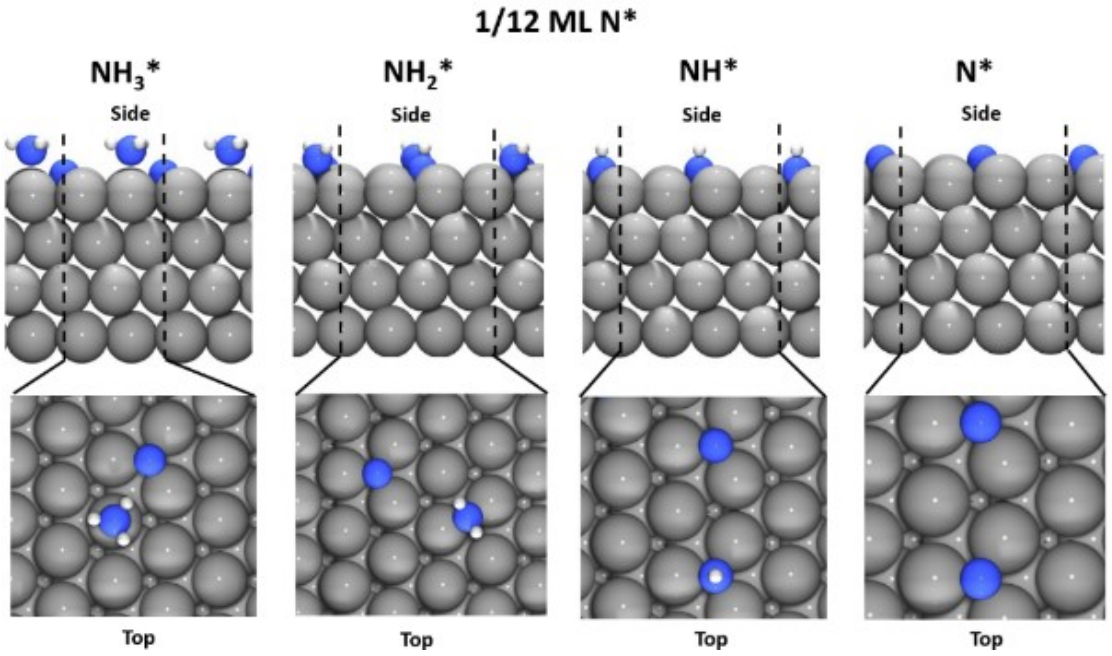


Figure H.5 Optimized structures of the AOR intermediates, with the general formula NHx with x=0−3, on a Pt(111) surface covered by 1/12 ML of spectator N* adatoms. N, H, and Pt are represented with blue, white, and silver spheres, respectively. Top and side views are provided in the bottom and upper panel, respectively. An enlarged prospective of a single unit cell is shown in the top view. Dashed black lines delineate the unit cell lattice vectors.

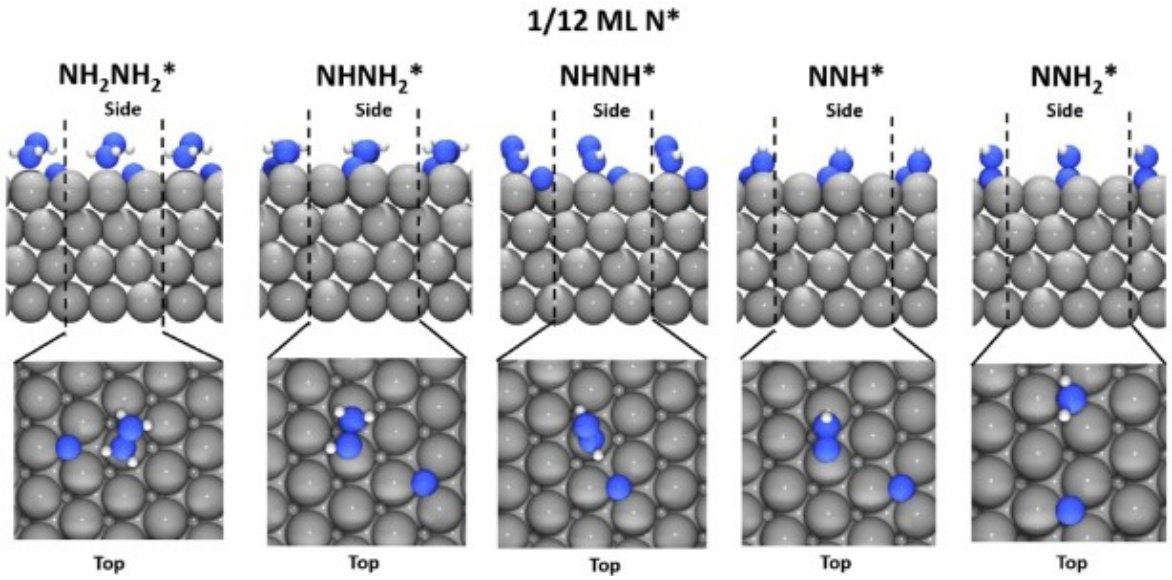


Figure H.6 Optimized structures of the AOR intermediates, with the general formula NH_xNH_y with x, y =0−2, on a Pt(111) surface covered by 1/12 ML of spectator N* adatoms. N, H, and Pt are represented with blue, white, and silver spheres, respectively. Top and side views are provided in the bottom and upper panel, respectively. An enlarged prospective of a single unit cell is shown in the top view. Dashed black lines delineate the unit cell lattice vectors.

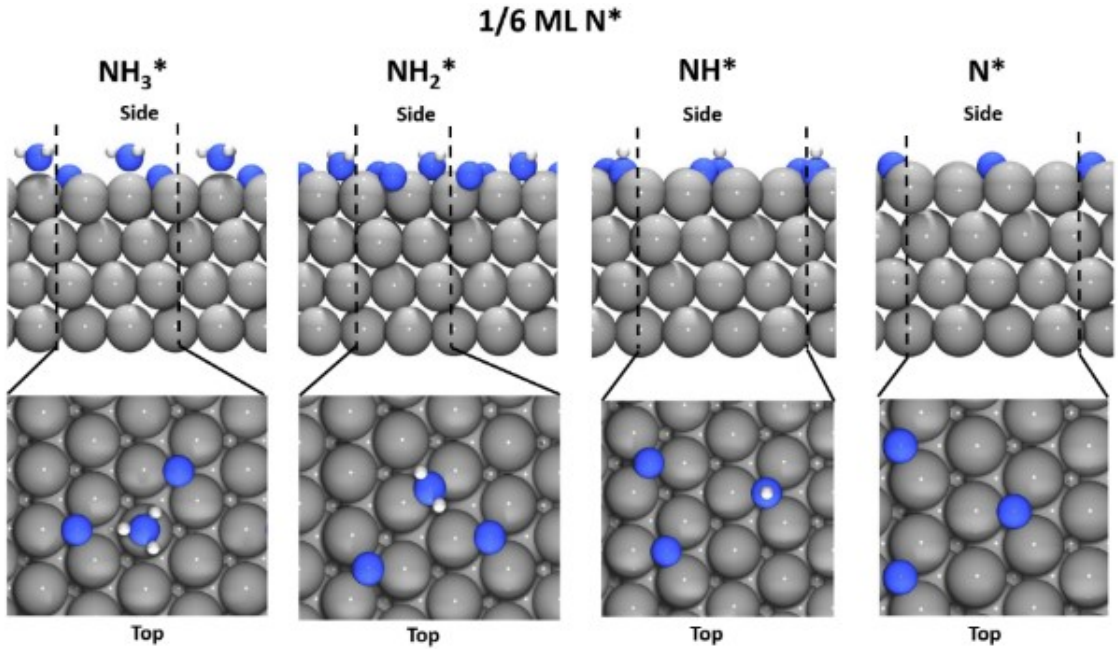


Figure H.7 Optimized structures of the AOR intermediates, with the general formula NH_x with x=0−3, on a Pt(111) surface covered by 1/6 ML N* of spectator adatoms. N, H, and Pt are represented with blue, white, and silver spheres, respectively. Top and side views are provided in the bottom and upper panel, respectively. An enlarged prospective of a single unit cell is shown in the top view. Dashed black lines delineate the unit cell lattice vectors.

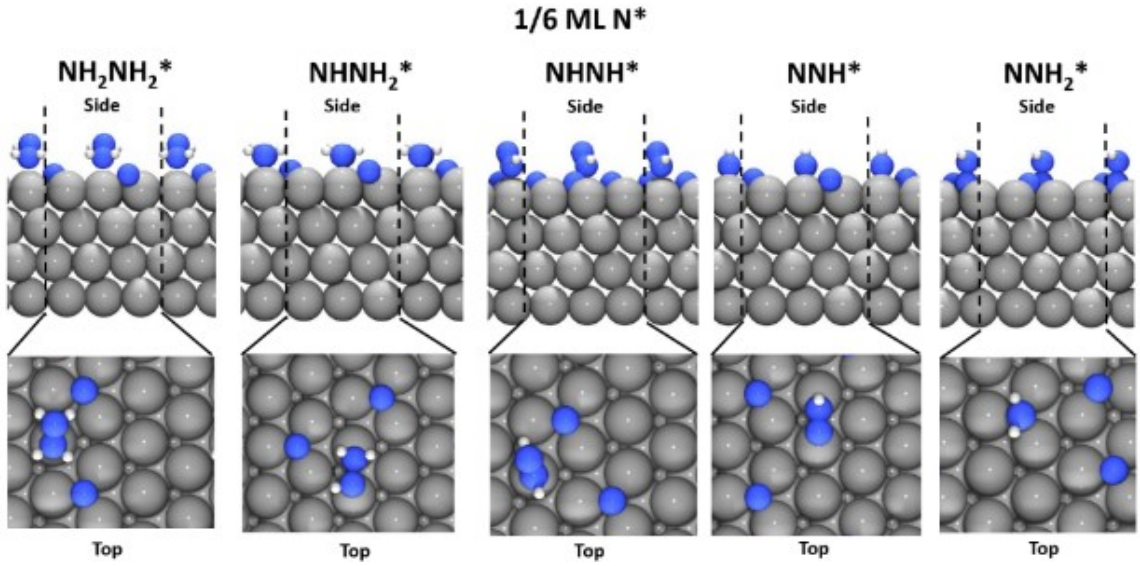


Figure H.8 Optimized structures of the AOR intermediates, with the general formula NH_xNH_y with x, y =0−2, on a Pt(111) surface covered by 1/6 ML of spectator N* adatoms. N, H, and Pt are represented with blue, white, and silver spheres, respectively. Top and side views are provided in the bottom and upper panel, respectively. An enlarged prospective of a single unit cell is shown in the top view. Dashed black lines delineate the unit cell lattice vectors.

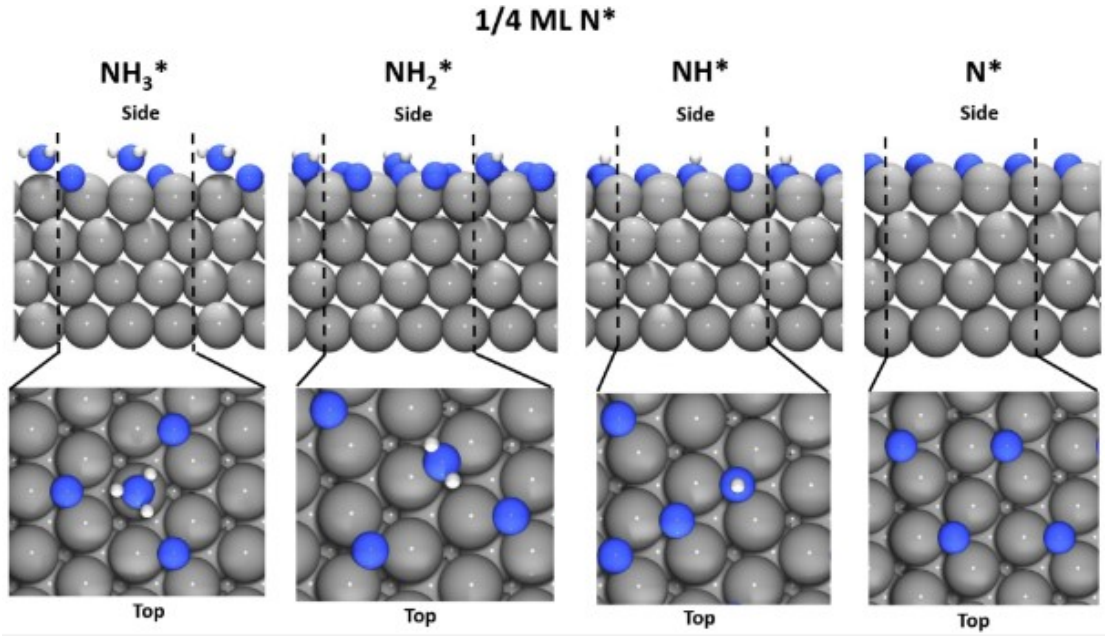


Figure H.9 Optimized structures of the AOR intermediates, with the general formula NH_x with x=0−3, on a Pt(111) surface covered by 1/4 ML of spectator N* adatoms. N, H, and Pt are represented with blue, white, and silver spheres, respectively. Top and side views are provided in the bottom and upper panel, respectively. An enlarged prospective of a single unit cell is shown in the top view. Dashed black lines delineate the unit cell lattice vectors.

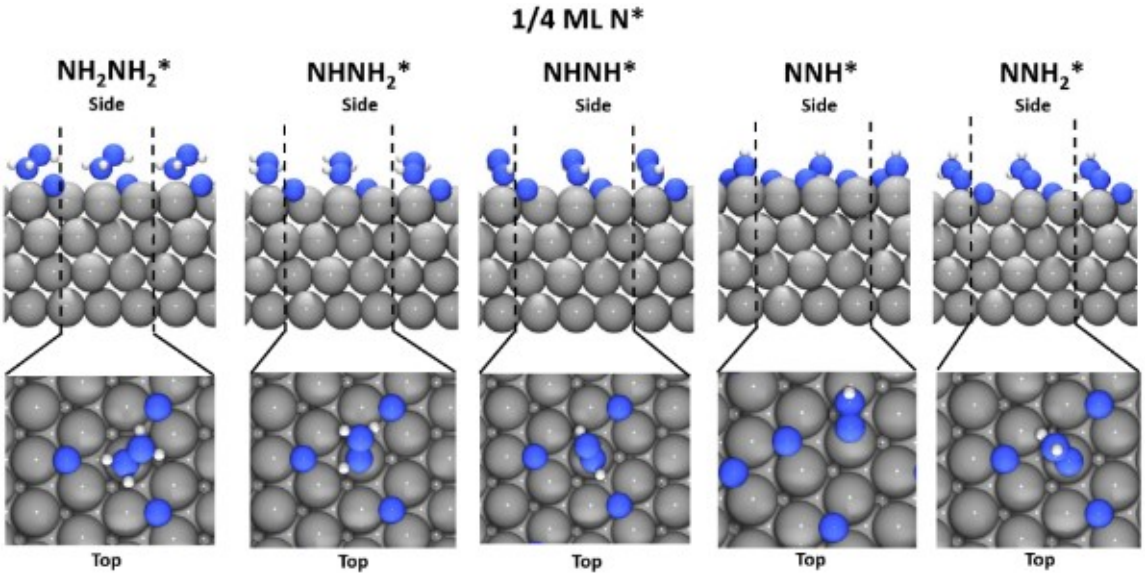


Figure H.10 Optimized structures of the AOR intermediates, with the general formula NH_xNH_y with x, y =0−2, on a Pt(111) surface covered by 1/4 ML of spectator N* adatoms. N, H, and Pt are represented with blue, white, and silver spheres, respectively. Top and side views are provided in the bottom and upper panel, respectively. An enlarged prospective of a single unit cell is shown in the top view. Dashed black lines delineate the unit cell lattice vectors.

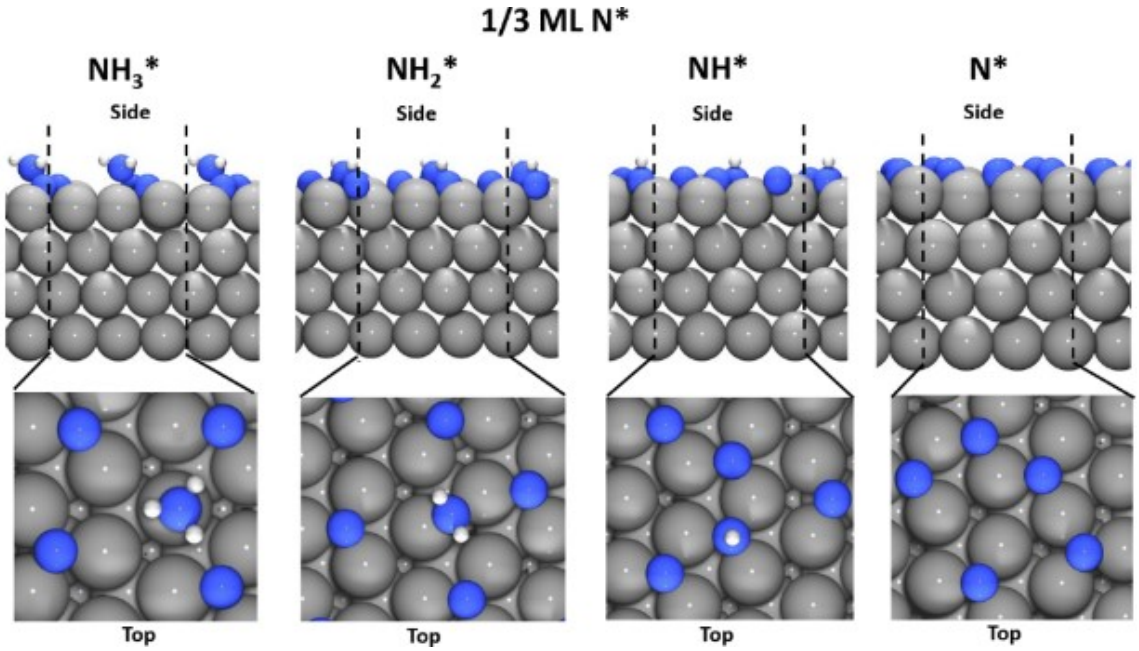


Figure H.11 Optimized structures of the AOR intermediates, with the general formula NH_x with x=0−3, on a Pt(111) surface covered by 1/3 ML of spectator N* adatoms. N, H, and Pt are represented with blue, white, and silver spheres, respectively. Top and side views are provided in the bottom and upper panel, respectively. An enlarged prospective of a single unit cell is shown in the top view. Dashed black lines delineate the unit cell lattice vectors.

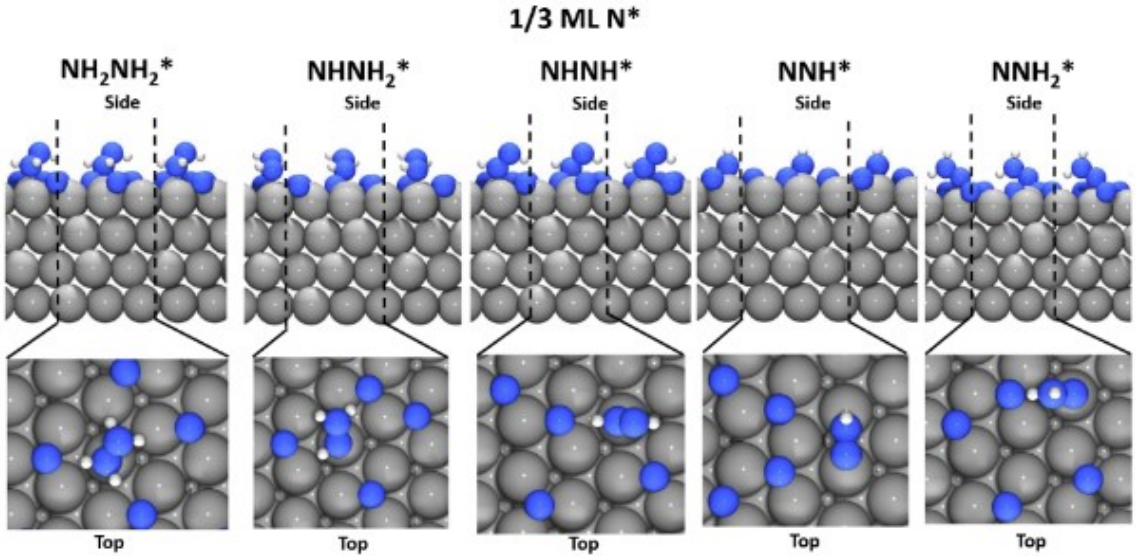


Figure H.12 Optimized structures of the AOR intermediates, with the general formula NH_xNH_y with x, y =0−2, on a Pt(111) surface covered by 1/3 ML of spectator N* adatoms. N, H, and Pt are represented with blue, white, and silver spheres, respectively. Top and side views are provided in the bottom and upper panel, respectively. An enlarged prospective of a single unit cell is shown in the top view. Dashed black lines delineate the unit cell lattice vectors.

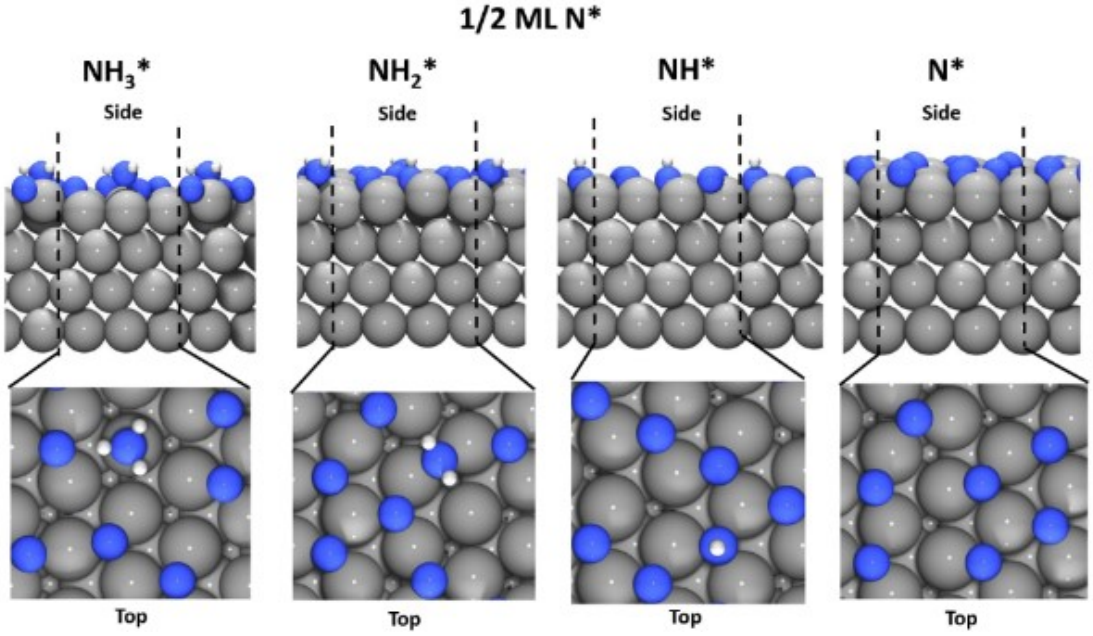


Figure H.13 Optimized structures of the AOR intermediates, with the general formula NH_x with x=0−3, on a Pt(111) surface covered by 1/2 ML of spectator N* adatoms. N, H, and Pt are represented with blue, white, and silver spheres, respectively. Top and side views are provided in the bottom and upper panel, respectively. An enlarged prospective of a single unit cell is shown in the top view. Dashed black lines delineate the unit cell lattice vectors.

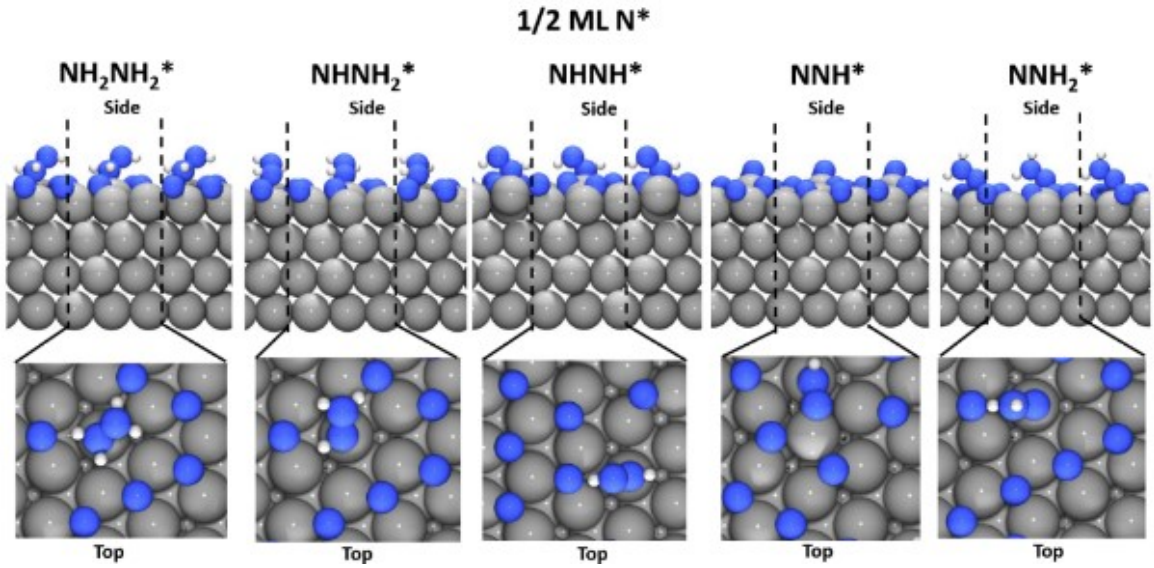


Figure H.14 Optimized structures of the AOR intermediates, with the general formula NH_xNH_y with x, y =0−2, on a Pt(111) surface covered by 1/2 ML of spectator N* adatoms. N, H, and Pt are represented with blue, white, and silver spheres, respectively. Top and side views are provided in the bottom and upper panel, respectively. An enlarged prospective of a single unit cell is shown in the top view. Dashed black lines delineate the unit cell lattice vectors.

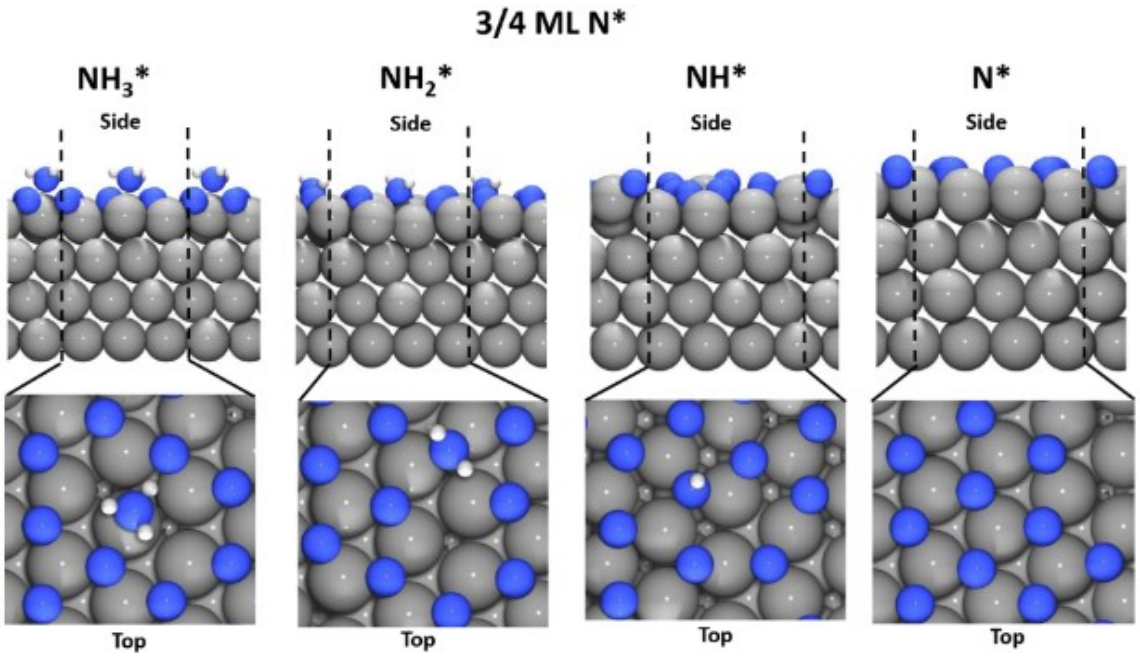


Figure H.15 Optimized structures of the AOR intermediates, with the general formula NH_x with x=0−3, on a Pt(111) surface covered by 3/4 ML N* of spectator adatoms. N, H, and Pt are represented with blue, white, and silver spheres, respectively. Top and side views are provided in the bottom and upper panel, respectively. An enlarged prospective of a single unit cell is shown in the top view. Dashed black lines delineate the unit cell lattice vectors.

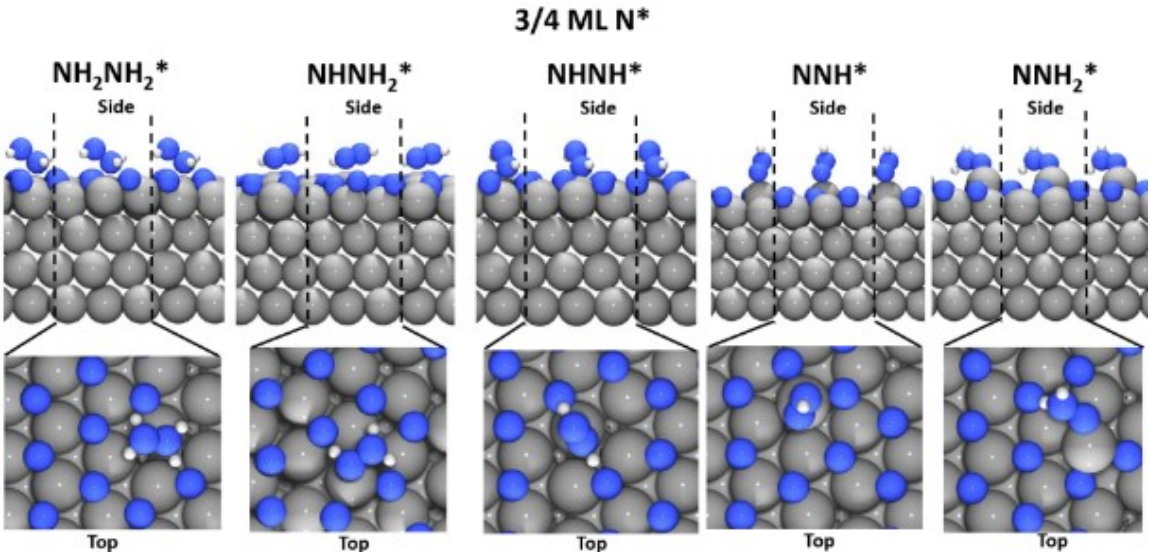


Figure H.16 Optimized structures of the AOR intermediates, with the general formula NH_xNH_y with x, y =0−2, on a Pt(111) surface covered by 3/4 ML of spectator N* adatoms. N, H, and Pt are represented with blue, white, and silver spheres, respectively. Top and side views are provided in the bottom and upper panel, respectively. An enlarged prospective of a single unit cell is shown in the top view. Dashed black lines delineate the unit cell lattice vectors.

APPENDIX I

BIBLIOGRAPHY

(1) Zhang, J.; Vukmirovic, M. B.; Xu, Y.; Mavrikakis, M.; Adzic, R. R. Controlling the Catalytic Activity of Platinum-Monolayer Electrocatalysts for Oxygen Reduction with Different Substrates. *Angew. Chemie - Int. Ed.* **2005**, *44*, 2132–2135.

(2) Zhang, J.; Vukmirovic, M. B.; Sasaki, K.; Nilekar, A. U.; Mavrikakis, M.; Adzic, R. R. Mixed-Metal Pt Monolayer Electrocatalysts for Enhanced Oxygen Reduction Kinetics. *J. Am. Chem. Soc.* **2005**, *127*, 12480–12481.

(3) Greeley, J.; Nørskov, J. K. Combinatorial Density Functional Theory-Based Screening of Surface Alloys for the Oxygen Reduction Reaction. *J. Phys. Chem. C* **2009**, *113*, 4932–4939.

(4) Greeley, J.; Stephens, I. E. L.; Bondarenko, A. S.; Johansson, T. P.; Hansen, H. A.; Jaramillo, T. F.; Rossmeisl, J.; Chorkendorff, I.; Nørskov, J. K. Alloys of Platinum and Early Transition Metals as Oxygen Reduction Electrocatalysts. *Nat. Chem.* **2009**, *1*, 552–556.

(5) Stamenkovic, V.; Mun, B. S.; Mayrhofer, K. J. J.; Ross, P. N.; Markovic, N. M.; Rossmeisl, J.; Greeley, J.; Nørskov, J. K. Changing the Activity of Electrocatalysts for Oxygen Reduction by Tuning the Surface Electronic Structure. *Angew. Chemie - Int. Ed.* **2006**, *45*, 2897–2901.

(6) García-Mota, M.; Bajdich, M.; Viswanathan, V.; Vojvodic, A.; Bell, A. T.; Nørskov, J. K. Importance of Correlation in Determining Electrocatalytic Oxygen Evolution Activity on Cobalt Oxides. *J. Phys. Chem. C* **2012**, *116*, 21077–21082.

(7) Gokhale, A. A.; Dumesic, J. A.; Mavrikakis, M. Article On the Mechanism of Low-Temperature Water Gas Shift Reaction on Copper On the Mechanism of Low-Temperature Water Gas Shift Reaction on Copper. *J. Am. Chem. Soc.* **2008**, *130*, 1402–1414.

(8) Grabow, L. C.; Gokhale, A. A.; Evans, S. T.; Dumesic, J. A.; Mavrikakis, M. Mechanism of the Water Gas Shift Reaction on Pt: First Principles, Experiments, and Microkinetic Modeling. *J. Phys. Chem. C* **2008**, *112*, 4608–4617.

(9) Madon, R. J.; Braden, D.; Kandoi, S.; Nagel, P.; Mavrikakis, M.; Dumesic, J. A. Microkinetic Analysis and Mechanism of the Water Gas Shift Reaction over Copper

Catalysts. *J. Catal.* **2011**, *281*, 1–11.
(10) Honkala, K.; Hellman, A.; Remediakis, I. N.; Logadottir, A.; Carlsson, A.; Dahl, S.; Christensen, C. H.; Nørskov, J. K. Ammonia Synthesis from First-Principles Calculations. *Science (80-.).* **2005**.
(11) Hellman, A.; Baerends, E. J.; Biczysko, M.; Bligaard, T.; Christensen, C. H.; Clary, D. C.; Dahl, S.; Van Harrevelt, R.; Honkala, K.; Jonsson, H.; et al. Predicting Catalysis: Understanding Ammonia Synthesis from First-Principles Calculations. *J. Phys. Chem. B* **2006**, *110*, 17719–17735.
(12) Grabow, L. C.; Mavrikakis, M. Mechanism of Methanol Synthesis on Cu through CO2 and CO Hydrogenation. *ACS Catal.* **2011**, *1*, 365–384.
(13) Studt, F.; Abild-Pedersen, F.; Wu, Q.; Jensen, A. D.; Temel, B.; Grunwaldt, J. D.; Norskov, J. K. CO Hydrogenation to Methanol on Cu-Ni Catalysts: Theory and Experiment. *J. Catal.* **2012**, *293*, 51–60.
(14) Studt, F.; Abild-Pedersen, F.; Varley, J. B.; Nørskov, J. K. CO and CO2 Hydrogenation to Methanol Calculated Using the BEEF-VdW Functional. *Catal. Letters* **2013**, *143*, 71–73.
(15) Ojeda, M.; Nabar, R.; Nilekar, A. U.; Ishikawa, A.; Mavrikakis, M.; Iglesia, E. CO Activation Pathways and the Mechanism of Fischer-Tropsch Synthesis. *J. Catal.* **2010**, *272*, 287–297.
(16) Cheng, J.; Hu, P.; Ellis, P.; French, S.; Kellys, G.; Lok, C. M. Chain Growth Mechanism in Fischer-Tropsch Synthesis: A DFT Study of C-C Coupling over Ru, Fe, Rh, and Re Surfaces. *J. Phys. Chem. C* **2008**, *112*, 6082–6086.
(17) Medford, A. J.; Lausche, A. C.; Abild-Pedersen, F.; Temel, B.; Schjødt, N. C.; Nørskov, J. K.; Studt, F. Activity and Selectivity Trends in Synthesis Gas Conversion to Higher Alcohols. *Top. Catal.* **2014**, *57*, 135–142.
(18) Greeley, J.; Nørskov, J. K.; Kibler, L. A.; El-Aziz, A. M.; Kolb, D. M. Hydrogen Evolution over Bimetallic Systems: Understanding the Trends. *ChemPhysChem* **2006**.
(19) Greeley, J.; Jaramillo, T. F.; Bonde, J.; Chorkendorff, I.; Nørskov, J. K. Computational High-Throughput Screening of Electrocatalytic Materials for Hydrogen Evolution. *Nat. Mater.* **2006**, *5*, 909–913.
(20) Chen, Y.; Vlachos, D. G. Hydrogenation of Ethylene and Dehydrogenation and Hydrogenolysis of Ethane on Pt(111) and Pt(211): A Density Functional Theory Study. *J. Phys. Chem. C* **2010**, *114*, 4973–4982.
(21) Yang, M. L.; Zhu, Y. A.; Fan, C.; Sui, Z. J.; Chen, D.; Zhou, X. G. DFT Study of Propane Dehydrogenation on Pt Catalyst: Effects of Step Sites. *Phys. Chem. Chem. Phys.* **2011**, *13*, 3257–3267.
(22) Peng, G.; Gerceker, D.; Kumbhalkar, M.; Dumesic, J. A.; Mavrikakis, M. Ethane Dehydrogenation on Pristine and AlO: X Decorated Pt Stepped Surfaces. *Catal. Sci. Technol.* **2018**, *8*, 2159–2174.
(23) Alayoglu, S.; Nilekar, A. U.; Mavrikakis, M.; Eichhorn, B. Ru-Pt Core-Shell Nanoparticles for Preferential Oxidation of Carbon Monoxide in Hydrogen. *Nat. Mater.* **2008**, *7*, 333–338.
(24) Nilekar, A. U.; Alayoglu, S.; Eichhorn, B.; Mavrikakis, M. Preferential CO Oxidation in Hydrogen: Reactivity of Core-Shell Nanoparticles. *J. Am. Chem. Soc.* **2010**, *132*, 7418–7428.
(25) Norskov, J. K.; Bligaard, T.; Rossmeisl, J.; Christensen, C. H. Towards the Computational

Design of Solid Catalysts. *Nat Chem* **2009**, *1*, 37–46.
(26) Studt, F.; Abild-Pedersen, F.; Bligaard, T.; Sørensen, R. Z.; Christensen, C. H.; Nørskov, J. K. Identification of Non-Precious Metal Alloy Catalysts for Selective Hydrogenation of Acetylene. *Science (80-.).* **2008**.
(27) Hansgen, D. A.; Vlachos, D. G.; Chen, J. G. Using First Principles to Predict Bimetallic Catalysts for the Ammonia Decomposition Reaction. *Nat. Chem.* **2010**, *2*, 484–489.
(28) Studt, F.; Abild-Pedersen, F.; Hansen, H. A.; Man, I. C.; Rossmeisl, J.; Bligaard, T. Volcano Relation for the Deacon Process over Transition-Metal Oxides. *ChemCatChem* **2010**, *2*, 98–102.
(29) Greeley, J.; Mavrikakis, M. Alloy Catalysts Designed from First Principles. *Nat. Mater.* **2004**, *3*, 810–815.
(30) Stephens, I. E. L.; Bondarenko, A. S.; Perez-Alonso, F. J.; Calle-Vallejo, F.; Bech, L.; Johansson, T. P.; Jepsen, A. K.; Frydendal, R.; Knudsen, B. P.; Rossmeisl, J.; et al. Tuning the Activity of Pt(111) for Oxygen Electroreduction by Subsurface Alloying. *J. Am. Chem. Soc.* **2011**, *133*, 5485–5491.
(31) Ferrin, P.; Nilekar, A. U.; Greeley, J.; Mavrikakis, M.; Rossmeisl, J. Reactivity Descriptors for Direct Methanol Fuel Cell Anode Catalysts. *Surf. Sci.* **2008**, *602*, 3424–3431.
(32) Andersson, M. P.; Bligaard, T.; Kustov, A.; Larsen, K. E.; Greeley, J.; Johannessen, T.; Christensen, C. H.; Nørskov, J. K. Toward Computational Screening in Heterogeneous Catalysis: Pareto-Optimal Methanation Catalysts. *J. Catal.* **2006**, *239*, 501–506.
(33) Dumesic, J. A. The Microkinetics of Heterogeneous Catalysis. *ACS Prof. Ref. B.* **1993**.
(34) Grabow, L. C.; Hvolbæk, B.; Nørskov, J. K. Understanding Trends in Catalytic Activity: The Effect of Adsorbate–Adsorbate Interactions for CO Oxidation Over Transition Metals. *Top. Catal.* **2010**, *53*, 298–310.
(35) Jørgensen, M.; Grönbeck, H. First-Principles Microkinetic Modeling of Methane Oxidation over Pd(100) and Pd(111). *ACS Catal.* **2016**.
(36) Greeley, J. Theoretical Heterogeneous Catalysis: Scaling Relationships and Computational Catalyst Design. *Annu. Rev. Chem. Biomol. Eng.* **2016**, *7*, 605–635.
(37) Nilsson, A.; Pettersson, L. G. M.; Hammer, B.; Bligaard, T.; Christensen, C. H.; Nørskov, J. K. The Electronic Structure Effect in Heterogeneous Catalysis. *Catal. Letters* **2005**, *100*, 111–114.
(38) Cao, L.; Liu, W.; Luo, Q.; Yin, R.; Wang, B.; Weissenrieder, J.; Soldemo, M.; Yan, H.; Lin, Y.; Sun, Z.; et al. Atomically Dispersed Iron Hydroxide Anchored on Pt for Preferential Oxidation of CO in H2. *Nature*. 2019.
(39) Grabow, L. C.; Mavrikakis, M. Mechanism of Methanol Synthesis on Cu through CO2 and CO Hydrogenation. *ACS Catal.* **2011**, *1*, 365–384.
(40) Bhan, A.; Hsu, S. H.; Blau, G.; Caruthers, J. M.; Venkatasubramanian, V.; Delgass, W. N. Microkinetic Modeling of Propane Aromatization over HZSM-5. *J. Catal.* **2005**, *235*, 35–51.
(41) Rangarajan, S.; Maravelias, C. T.; Mavrikakis, M. Sequential-Optimization-Based Framework for Robust Modeling and Design of Heterogeneous Catalytic Systems. *J. Phys. Chem. C* **2017**, *121*, 25847–25863.
(42) Singh, S.; Li, S.; Carrasquillo-Flores, R.; Alba-Rubio, A. C.; Dumesic, J. A.; Mavrikakis, M. Formic Acid Decomposition on Au Catalysts: DFT, Microkinetic Modeling, and

Reaction Kinetics Experiments. *AIChE J.* **2014**, *60*, 1303–1319.
(43) Li, S.; Singh, S.; Dumesic, J. A.; Mavrikakis, M. On the Nature of Active Sites for Formic Acid Decomposition on Gold Catalysts. *Catal. Sci. Technol.* **2019**, *9*, 2836–2848.
(44) Chen, B. W. J.; Stamatakis, M.; Mavrikakis, M. Kinetic Isolation between Turnovers on Au18 Nanoclusters: Formic Acid Decomposition One Molecule at a Time. *ACS Catal.* **2019**, *9*, 9446–9457.
(45) Bhandari, S.; Rangarajan, S.; Maravelias, C. T.; Dumesic, J. A.; Mavrikakis, M. Reaction Mechanism of Vapor-Phase Formic Acid Decomposition over Platinum Catalysts: DFT, Reaction Kinetics Experiments, and Microkinetic Modeling. *ACS Catal.* **2020**, *10*, 4112–4126.
(46) Abild-Pedersen, F.; Greeley, J.; Studt, F.; Rossmeisl, J.; Munter, T. R.; Moses, P. G.; Skúlason, E.; Bligaard, T.; Nørskov, J. K. Scaling Properties of Adsorption Energies for Hydrogen-Containing Molecules on Transition-Metal Surfaces. *Phys. Rev. Lett.* **2007**, *99*, 4–7.
(47) Nørskov, J. K.; Bligaard, T.; Logadottir, A.; Bahn, S.; Hansen, L. B.; Bollinger, M.; Bengaard, H.; Hammer, B.; Sljivancanin, Z.; Mavrikakis, M.; et al. Universality in Heterogeneous Catalysis. *J. Catal.* **2002**, *209*, 275–278.
(48) Sholl, D. S.; Steckel, J. A. *Density Functional Theory: A Practical Introduction*; 2009.
(49) Vosko, S. H.; Wilk, L.; Nusair, M. Accurate Spin-Dependent Electron Liquid Correlation Energies for Local Spin Density Calculations: A Critical Analysis. *Can. J. Phys.* **1980**, *58*, 1200–1211.
(50) Perdew, J. P.; Zunger, A. Self-Interaction Correction to Density-Functional Approximations for Many-Electron Systems. *Phys. Rev. B* **1981**, *23*, 5048–5079.
(51) White, J. A.; Bird, D. M.; Payne, M. C.; Stich, I. Surface Corrugation in the Dissociative Adsorption of H2 on Cu(100). *Phys. Rev. Lett.* **1994**, *73*, 1404–1407.
(52) Perdew, J. P.; Wang, Y. Accurate and Simple Analytic Representation of the Electron-Gas Correlation Energy. *Phys. Rev. B* **1992**, *45*, 13244–13249.
(53) Perdew, J. P.; Burke, K.; Ernzerhof, M. Generalized Gradient Approximation Made Simple. *Phys. Rev. Lett.* **1996**, *77*, 3865–3868.
(54) Kresse, G.; Furthmüller, J. Efficient Iterative Schemes for Ab Initio Total-Energy Calculations Using a Plane-Wave Basis Set. *Phys. Rev. B - Condens. Matter Mater. Phys.* **1996**, *54*, 11169–11186.
(55) Kresse, G.; Furthmüller, J. Efficiency of Ab-Initio Total Energy Calculations for Metals and Semiconductors Using a Plane-Wave Basis Set. *Comput. Mater. Sci.* **1996**, *6*, 15–50.
(56) Hammer, B.; Hansen, L. B.; Nørskov, J. K. Improved Adsorption Energetics within Density-Functional Theory Using Revised Perdew-Burke-Ernzerhof Functionals. *Phys. Rev. B - Condens. Matter Mater. Phys.* **1999**, *59*, 7413–7421.
(57) Greeley, J.; Nørskov, J. K.; Mavrikakis, M. Electronic Structure and Catalysis on Metal Surfaces. *Annu. Rev. Phys. Chem.* **2002**, *53*, 319–348.
(58) Henkelman, G.; Uberuaga, B. P.; Jónsson, H. Climbing Image Nudged Elastic Band Method for Finding Saddle Points and Minimum Energy Paths. *J. Chem. Phys.* **2000**, *113*, 9901–9904.
(59) Gokhale, A. A.; Kandoi, S.; Greeley, J. P.; Mavrikakis, M.; Dumesic, J. A. Molecular-Level Descriptions of Surface Chemistry in Kinetic Models Using Density Functional Theory.

Chem. Eng. Sci. **2004**, *59*, 4679–4691.
(60) Campbell, C. T. Finding the Rate-Determining Step in a Mechanism: Comparing DeDonder Relations with the "Degree of Rate Control." *J. Catal.* **2001**, *204*, 520–524.
(61) Campbell, C. T. The Degree of Rate Control: A Powerful Tool for Catalysis Research. *ACS Catal.* **2017**, *7*, 2770–2779.
(62) Grabow, L. C.; Mavrikakis, M. Mechanism of Methanol Synthesis on Cu through CO_2 and CO Hydrogenation. *ACS Catal.* **2011**, *1*, 365–384.
(63) Acar, C.; Dincer, I. Review and Evaluation of Hydrogen Production Options for Better Environment. *J. Clean. Prod.* **2019**, *218*, 835–849.
(64) Bozell, J. J.; Petersen, G. R. Technology Development for the Production of Biobased Products from Biorefinery Carbohydrates—the US Department of Energy's "Top 10" Revisited. *Green Chem.* **2010**, *12*, 539–554.
(65) Alonso, D. M.; Bond, J. Q.; Dumesic, J. A. Catalytic Conversion of Biomass to Biofuels. *Green Chem.* **2010**, *12*, 1493–1513.
(66) Deng, L.; Li, J.; Lai, D. M.; Fu, Y.; Guo, Q. X. Catalytic Conversion of Biomass-Derived Carbohydrates into γ-Valerolactone without Using an External H2 Supply. *Angew. Chemie - Int. Ed.* **2009**, *48*, 6529–6532.
(67) Yun, J.; Jin, F.; Kishita, A.; Tohji, K.; Enomoto, H. Formic Acid Production from Carbohydrates Biomass by Hydrothermal Reaction. *J. Phys. Conf. Ser.* **2010**, *215*, 012126:1-4.
(68) Reichert, J.; Brunner, B.; Jess, A.; Wasserscheid, P.; Albert, J. Biomass Oxidation to Formic Acid in Aqueous Media Using Polyoxometalate Catalysts - Boosting FA Selectivity by in-Situ Extraction. *Energy Environ. Sci.* **2015**, *8*, 2985–2990.
(69) Zhang, J.; Sun, M.; Liu, X.; Han, Y. Catalytic Oxidative Conversion of Cellulosic Biomass to Formic Acid and Acetic Acid with Exceptionally High Yields. *Catal. Today* **2014**, *233*, 77–82.
(70) van Putten, R.; Wissink, T.; Swinkels, T.; Pidko, E. A. Fuelling the Hydrogen Economy: Scale-up of an Integrated Formic Acid-to-Power System. *Int. J. Hydrogen Energy* **2019**, *44*, 28533–28541.
(71) Ertas, I. E.; Yurderi, M.; Bulut, A.; Agirtas, M. S.; Zahmakiran, M. *Liquid Phase Chemical Hydrogen Storage: From Recent Developments to Future Objectives*; Emerging Materials for Energy Conversion and Storage, Elsevier Inc., 2018.
(72) Loges, B.; Boddien, A.; Junge, H.; Beller, M. Controlled Generation of Hydrogen from Formic Acid Amine Adducts at Room Temperature and Application in H2/O2 Fuel Cells. *Angew. Chemie - Int. Ed.* **2008**, *47*, 3962–3965.
(73) Iguchi, M.; Chatterjee, M.; Onishi, N.; Himeda, Y.; Kawanami, H. Sequential Hydrogen Production System from Formic Acid and H 2 /CO 2 Separation under High-Pressure Conditions . *Sustain. Energy Fuels* **2018**, *2*, 1719–1725.
(74) Sánchez, F.; Motta, D.; Dimitratos, N. Catalytic Decomposition of Carbon-Based Liquid-Phase Chemical Hydrogen Storage Materials for Hydrogen Generation under Mild Conditions. *Appl. Petrochemical Res.* **2016**, *6*, 269–277.
(75) Singh, A. K.; Singh, S.; Kumar, A. Hydrogen Energy Future with Formic Acid: A Renewable Chemical Hydrogen Storage System. *Catal. Sci. Technol.* **2015**, *6*, 12–40.
(76) Laurenczy, G.; Dyson, P. J. Homogeneous Catalytic Dehydrogenation of Formic Acid:

Progress towards a Hydrogen-Based Economy. *J. Braz. Chem. Soc.* **2014**, *25*, 2157–2163.
(77) Johnson, T. C.; Morris, D. J.; Wills, M. Hydrogen Generation from Formic Acid and Alcohols Using Homogeneous Catalysts. *Chem. Soc. Rev.* **2010**, *39*, 81–88.
(78) Grasemann, M.; Laurenczy, G. Formic Acid as a Hydrogen Source – Recent Developments and Future Trends. *Energy Environ. Sci.* **2012**, *5*, 8171–8181.
(79) Czaun, M.; Goeppert, A.; May, R.; Haiges, R.; Prakash, G. K. S.; Olah, G. A. Hydrogen Generation from Formic Acid Decomposition by Ruthenium Carbonyl Complexes. Tetraruthenium Dodecacarbonyl Tetrahydride as an Active Intermediate. *ChemSusChem* **2011**, *4*, 1241–1248.
(80) Zacharska, M.; Chuvilin, A. L.; Kriventsov, V. V.; Beloshapkin, S.; Estrada, M.; Simakov, A.; Bulushev, D. A. Support Effect for Nanosized Au Catalysts in Hydrogen Production from Formic Acid Decomposition. *Catal. Sci. Technol.* **2016**, *6*, 6853–6860.
(81) Yu, W. Y.; Mullen, G. M.; Flaherty, D. W.; Mullins, C. B. Selective Hydrogen Production from Formic Acid Decomposition on Pd-Au Bimetallic Surfaces. *J. Am. Chem. Soc.* **2014**, *136*, 11070–11078.
(82) Tedsree, K.; Li, T.; Jones, S.; Chan, C. W. A.; Yu, K. M. K.; Bagot, P. a J.; Marquis, E. a; Smith, G. D. W.; Tsang, S. C. E. Hydrogen Production from Formic Acid Decomposition at Room Temperature Using a Ag-Pd Core-Shell Nanocatalyst. *Nat. Nanotechnol.* **2011**, *6*, 302–307.
(83) Ojeda, M.; Iglesia, E. Formic Acid Dehydrogenation on Au-Based Catalysts at near-Ambient Temperatures. *Angew. Chemie - Int. Ed.* **2009**, *48*, 4800–4803.
(84) Ai, M. Activities for the Decomposition of Formic Acid and the Acid-Base Properties of Metal Oxide Catalysts. *J. Catal.* **1977**, *50*, 291–300.
(85) Trillo, J. M.; Munuera, G.; Criado, J. M. Catalytic Decomposition of Formic Acid on Metal Oxides. *Catal. Rev.* **1972**, *7*, 51–86.
(86) Peng, X. D.; Barteau, M. A. Dehydration of Carboxylic Acids on the MgO(100) Surface. *Catal. Letters* **1990**, *7*, 395–402.
(87) Senanayake, S. D.; Mullins, D. R. Redox Pathways for HCOOH Decomposition over CeO2 Surfaces. *J. Phys. Chem. C* **2008**, *112*, 9744–9752.
(88) Onishi, H.; Aruga, T.; Iwasawa, Y. Catalytic Reactions on a Metal Oxide Single Crystal: Switchover of the Reaction Paths in Formic Acid Decomposition on TiO2(110). *J. Am. Chem. Soc.* **1993**, *115*, 10460–10461.
(89) Flaherty, D. W.; Berglund, S. P.; Mullins, C. B. Selective Decomposition of Formic Acid on Molybdenum Carbide: A New Reaction Pathway. *J. Catal.* **2010**, *269*, 33–43.
(90) Luo, Q.; Wang, T.; Walther, G.; Beller, M.; Jiao, H. Molybdenum Carbide Catalysed Hydrogen Production from Formic Acid - A Density Functional Theory Study. *J. Power Sources* **2014**, *246*, 548–555.
(91) Wang, J.; Cao, J.; Ma, Y.; Li, X.; Xiaokaiti, P.; Hao, X.; Yu, T.; Abudula, A.; Guan, G. Decomposition of Formic Acid for Hydrogen Production over Metal Doped Nanosheet-like MoC 1−x Catalysts. *Energy Convers. Manag.* **2017**, *147*, 166–173.
(92) Cao, J.; Ma, Y.; Guan, G.; Hao, X.; Ma, X.; Wang, Z.; Kusakabe, K.; Abudula, A. Reaction Intermediate Species during the Steam Reforming of Methanol over Metal Modified Molybdenum Carbide Catalysts. *Appl. Catal. B Environ.* **2016**, *189*, 12–18.
(93) Navlani-García, M.; Martis, M.; Lozano-Castelló, D.; Cazorla-Amorós, D.; Mori, K.;

Yamashita, H. Investigation of Pd Nanoparticles Supported on Zeolites for Hydrogen Production from Formic Acid Dehydrogenation. *Catal. Sci. Technol.* **2015**, *5*, 364–371.
(94) Duncan, T. M.; Vaughan, R. W. The Adsorption of Formic Acid on Y Zeolites: A Multiple-Pulse Nuclear Magnetic Resonance Study. *J. Catal.* **1981**, *67*, 49–70.
(95) Yuan, M.; Long, Y.; Yang, J.; Hu, X.; Xu, D.; Zhu, Y.; Dong, Z. Biomass Sucrose-Derived Cobalt@Nitrogen-Doped Carbon for Catalytic Transfer Hydrogenation of Nitroarenes with Formic Acid. *ChemSusChem* **2018**, *11*, 4156–4165.
(96) Guo, H.; Gao, R.; Sun, M.; Guo, H.; Wang, B.; Chen, L. Cobalt Entrapped in N,S-Codoped Porous Carbon: Catalysts for Transfer Hydrogenation with Formic Acid. *ChemSusChem* **2019**, *12*, 487–494.
(97) Soszka, E.; Reijneveld, H. M.; Jędrzejczyk, M.; Rzeźnicka, I.; Grams, J.; Ruppert, A. M. Chlorine Influence on Palladium Doped Nickel Catalysts in Levulinic Acid Hydrogenation with Formic Acid as Hydrogen Source. *ACS Sustain. Chem. Eng.* **2018**, *6*, 14607–14613.
(98) Tsurusaki, A.; Murata, K.; Onishi, N.; Sordakis, K.; Laurenczy, G.; Himeda, Y. Investigation of Hydrogenation of Formic Acid to Methanol Using H2 or Formic Acid as a Hydrogen Source. *ACS Catal.* **2017**, *7*, 1123–1131.
(99) Sachtler, W. M. .; Fahrenfort, J. The Catalytic Decomposition of Formic Acid Vapour on Metals. In *Proceedings of the 2nd International Congress on Catalysis*; Paris (France), 1960; p 831.
(100) Tang, Y.; Roberts, C. A.; Perkins, R. T.; Wachs, I. E. Revisiting Formic Acid Decomposition on Metallic Powder Catalysts: Exploding the HCOOH Decomposition Volcano Curve. *Surf. Sci.* **2016**, *650*, 103–110.
(101) Solymosi, F.; Koós, Á.; Liliom, N.; Ugrai, I. Production of CO-Free H2 from Formic Acid. A Comparative Study of the Catalytic Behavior of Pt Metals on a Carbon Support. *J. Catal.* **2011**, *279*, 213–219.
(102) Jia, L.; Bulushev, D. A.; Yu, O.; Boronin, A. I.; Kibis, L. S.; Yu, E.; Beloshapkin, S.; Seryak, I. A.; Ismagilov, Z. R.; Ross, J. R. H. Pt Nanoclusters Stabilized by N-Doped Carbon Nanofibers for Hydrogen Production from Formic Acid. *J. Catal.* **2013**, *307*, 94–102.
(103) Yoo, J. S.; Abild-Pedersen, F.; Nørskov, J. K.; Studt, F. A Theoretical Analysis of Transition Metal Catalysts for Formic Acid Decomposition. *ACS Catal.* **2014**, *4*, 1226–1233.
(104) Bulushev, D. a.; Jia, L.; Beloshapkin, S.; Ross, J. R. H. Improved Hydrogen Production from Formic Acid on a Pd/C Catalyst Doped by Potassium. *Chem. Commun.* **2012**, *48*, 4184–4186.
(105) Li, S.; Scaranto, J.; Mavrikakis, M. On the Structure Sensitivity of Formic Acid Decomposition on Cu Catalysts. *Top. Catal.* **2016**, *59*, 1580–1588.
(106) Scaranto, J.; Mavrikakis, M. HCOOH Decomposition on Pt(111) Surface: A DFT Study. *Surf. Sci.* **2015**, *648*, 201–211.
(107) Scaranto, J.; Mavrikakis, M. Density Functional Theory Studies of HCOOH Decomposition on Pd(111). *Surf. Sci.* **2016**, *650*, 111–120.
(108) Herron, A.; Scaranto, J.; Ferrin, P.; Li, S.; Mavrikakis, M. Trends in Formic Acid Decomposition on Model Transition Metal Surfaces : A Density Functional Theory Study. *ACS Catal.* **2014**, *4*, 4434–4445.

(109) Elnabawy, A. O.; Herron, J. A.; Scaranto, J.; Mavrikakis, M. Structure Sensitivity of Formic Acid Electrooxidation on Transition Metal Surfaces: A First-Principles Study. *J. Electrochem. Soc.* **2018**, *165*, J3109–J3121.
(110) Choi, S.; Herron, J. A.; Scaranto, J.; Huang, H.; Wang, Y.; Xia, X.; Lv, T.; Park, J.; Peng, H. C.; Mavrikakis, M.; et al. A Comprehensive Study of Formic Acid Oxidation on Palladium Nanocrystals with Different Types of Facets and Twin Defects. *ChemCatChem* **2015**, *7*, 2077–2084.
(111) Clavilier, J.; Parsons, R.; Durand, R.; Lamy, C.; Leger, J. M. Formic Acid Oxidation on Single Crystal Platinum Electrodes. Comparison with Polycrystalline Platinum. *J. Electroanal. Chem.* **1981**, *124*, 321–326.
(112) Avery, N. R. Reaction of HCOOH with a Pt(111)-O Surface; Identification of Adsorbed Monodentate Formate. *Appl. Surf. Sci.* **1983**, *14*, 149–156.
(113) Columbia, M. R.; Crabtree, A. M.; Thiel, P. A. Effect of CO on Pt-Catalyzed Decomposition of Formic Acid in Ultrahigh Vacuum. *J. Electroanal. Chem.* **1993**, *345*, 93–105.
(114) Columbia, M. R.; Thiel, P. A. The Interaction of Formic Acid with Transition Metal Surfaces, Studied in Ultrahigh Vacuum. *J. Electroanal. Chem.* **1994**, *369*, 1–14.
(115) Campbell, C. T.; Ertl, G.; Kuipers, H.; Segner, J. A Molecular Beam Investigation of the Interactions of CO with a Pt(111) Surface. *Surf. Sci.* **1981**, *107*, 207–219.
(116) Erley, W.; Wagner, H. Absolute CO Coverage: Direct Comparison between the (111) and (110) Faces of Ni, Pd, and Pt at 300 K. *J. Chem. Phys.* **1980**, *72*, 2207–2208.
(117) Ertl, G.; Neumann, M.; Streit, K. M. Chemisorption of CO on the Pt(111) Surface. *Surf. Sci.* **1977**, *64*, 393–410.
(118) McCabe, R. W.; Schmidt, L. D. Binding States of CO on Single Crystal Planes of Pt. *Surf. Sci.* **1977**, *66*, 101–124.
(119) Crossley, A.; A. King, D. Adsorbate Island Dimensions and Interaction Energies from Vibrational Spectra: Co on Pt (001) and Pt (111). *Surf. Sci.* **1980**, *95*, 131–155.
(120) Kneringer, G.; Netzer, F. P. Adsorption Studies of Oxygen and Carbon Monoxide on a Pt (100) Surface. *Surf. Sci.* **1975**, *49*, 125–142.
(121) Norton, P. R.; Davies, J. A.; Jackman, T. E. Absolute Coverages of CO and O on Pt(111); Comparison of Saturation CO Coverages on Pt(100), (110) and (111) Surfaces. *Surf. Sci.* **1982**, *122*, L593–L600.
(122) Plauck, A.; Stangland, E. E.; Dumesic, J. A.; Mavrikakis, M. Active Sites and Mechanisms for H_2O_2 Decomposition over Pd Catalysts. *Proc. Natl. Acad. Sci. U. S. A.* **2016**, *113*, E1973-82.
(123) Blöchl, P. E. Projector Augmented-Wave Method. *Phys. Rev. B* **1994**, *50*, 17953–17979.
(124) Kresse, G.; Joubert, D. From Ultrasoft Pseudopotentials to the Projector Augmented-Wave Method. *Phys. Rev. B - Condens. Matter Mater. Phys.* **1999**, *59*, 1758–1775.
(125) Haynes, W. M. CRC Handbook of Chemistry and Physics (Internet Version). *Taylor Fr. Boca Rat. FL* **2017**.
(126) Neugebauer, J.; Scheffler, M. Adsorbate-Substrate and Adsorbate-Adsorbate Interactions of Na and K Adlayers on Al(111). *Phys. Rev. B* **1992**, *46*, 16067–16080.
(127) Bengtsson, L. Dipole Correction for Surface Supercell Calculations. *Phys. Rev. B - Condens. Matter Mater. Phys.* **1999**, *59*, 12301–12304.
(128) Monkhorst, H. J.; Pack, J. D. Special Points for Brillouin-Zone Integrations. *Phys. Rev. B*

1976, *13*, 5188–5192.
(129) Henkelman, G.; Jónsson, H. Improved Tangent Estimate in the Nudged Elastic Band Method for Finding Minimum Energy Paths and Saddle Points. *J. Chem. Phys.* **2000**, *113*, 9978–9985.
(130) Hickman, D. A.; Degenstein, J. C.; Ribeiro, F. H. Fundamental Principles of Laboratory Fixed Bed Reactor Design. *Current Opinion in Chemical Engineering*. Elsevier Ltd 2016, pp 1–9.
(131) Ro, I.; Sener, C.; Stadelman, T. M.; Ball, M. R.; Venegas, J. M.; Burt, S. P.; Hermans, I.; Dumesic, J. A.; Huber, G. W. Measurement of Intrinsic Catalytic Activity of Pt Monometallic and Pt-MoOxinterfacial Sites over Visible Light Enhanced PtMoOx/SiO2catalyst in Reverse Water Gas Shift Reaction. *J. Catal.* **2016**, *344*, 784–794.
(132) Ro, I.; Aragao, I. B.; Brentzel, Z. J.; Liu, Y.; Rivera-Dones, K. R.; Ball, M. R.; Zanchet, D.; Huber, G. W.; Dumesic, J. A. Intrinsic Activity of Interfacial Sites for Pt-Fe and Pt-Mo Catalysts in the Hydrogenation of Carbonyl Groups. *Appl. Catal. B Environ.* **2018**, *231*, 182–190.
(133) Studt, F.; Behrens, M.; Kunkes, E. L.; Thomas, N.; Zander, S.; Tarasov, A.; Schumann, J.; Frei, E.; Varley, J. B.; Abild-Pedersen, F.; et al. The Mechanism of CO and CO2 Hydrogenation to Methanol over Cu-Based Catalysts. *ChemCatChem* **2015**, *7*, 1105–1111.
(134) Christensen, R.; Hansen, H. A.; Vegge, T. Identifying Systematic DFT Errors in Catalytic Reactions. *Catal. Sci. Technol.* **2015**, *5*, 4946–4949.
(135) Stein, M. Large Sample Properties of Simulations Using Latin Hypercube Sampling. *Technometrics* **1987**, *29*, 143–151.
(136) McKay, M. D.; Beckman, R. J.; Conover, W. J. A Comparison of Three Methods for Selecting Values of Input Variables in the Analysis of Output from a Computer Code. *Technometrics* **1979**, *21*, 239–345.
(137) Sutton, J. E.; Guo, W.; Katsoulakis, M. A.; Vlachos, D. G. Effects of Correlated Parameters and Uncertainty in Electronic-Structure-Based Chemical Kinetic Modelling. *Nat. Chem.* **2016**, *8*, 331–337.
(138) Matera, S.; Schneider, W. F.; Heyden, A.; Savara, A. Progress in Accurate Chemical Kinetic Modeling, Simulations, and Parameter Estimation for Heterogeneous Catalysis. *ACS Catal.* **2019**, *9*, 6624–6647.
(139) Mallikarjun Sharada, S.; Bligaard, T.; Luntz, A. C.; Kroes, G. J.; Nørskov, J. K. SBH10: A Benchmark Database of Barrier Heights on Transition Metal Surfaces. *J. Phys. Chem. C* **2017**, *121*, 19807–19815.
(140) Lykhach, Y.; Happel, M.; Johánek, V.; Skála, T.; Kollhoff, F.; Tsud, N.; Dvořák, F.; Prince, K. C.; Matolín, V.; Libuda, J. Adsorption and Decomposition of Formic Acid on Model Ceria and Pt/Ceria Catalysts. *J. Phys. Chem. C* **2013**, *117*, 12483–12494.
(141) Silbaugh, T. L.; Karp, E. M.; Campbell, C. T. Energetics of Formic Acid Conversion to Adsorbed Formates on Pt(111) by Transient Calorimetry. *J. Am. Chem. Soc.* **2014**, *136*, 3964–3971.
(142) Beden, B.; Bewick, A.; Lamy, C. A Study by Electrochemically Modulated Infrared Reflectance Spectroscopy of the Electrosorption of Formic Acid at a Platinum Electrode. *J. Electroanal. Chem.* **1983**, *148*, 147–160.
(143) Wellendorff, J.; Silbaugh, T. L.; Garcia-Pintos, D.; Nørskov, J. K.; Bligaard, T.; Studt, F.;

Campbell, C. T. A Benchmark Database for Adsorption Bond Energies to Transition Metal Surfaces and Comparison to Selected DFT Functionals. *Surf. Sci.* **2015**, *640*, 36–44.
(144) Sauer, J.; Ugliengo, P.; Garrone, E.; Saunders, V. R. Theoretical Study of van Der Waals Complexes at Surface Sites in Comparison with the Experiment. *Chem. Rev. (Washington, DC, United States)* **1994**, *94*, 2095–2160.
(145) Sauer, J.; Ugliengo, P.; Garrone, E.; Saunders, V. R. Theoretical Study of van Der Waals Complexes at Surface Sites in Comparison with the Experiment. *Chem. Rev.* **1994**, *94*, 2095–2160.
(146) Silbaugh, T. L.; Karp, E. M.; Campbell, C. T. Energetics of Methanol and Formic Acid Oxidation on Pt(111): Mechanistic Insights from Adsorption Calorimetry. *Surf. Sci.* **2016**, *650*, 140–143.
(147) Gao, W.; Keith, J. A.; Anton, J.; Jacob, T. Oxidation of Formic Acid on the Pt(111) Surface in the Gas Phase. *Dalt. Trans.* **2010**, *39*, 8450–8456.
(148) Gao, W.; Keith, J. A.; Anton, J.; Jacob, T. Theoretical Elucidation of the Competitive Electro-Oxidation Mechanisms of Formic Acid on Pt(111). *J. Am. Chem. Soc.* **2010**, *132*, 18377–18385.
(149) Stamatakis, M. Kinetic Modelling of Heterogeneous Catalytic Systems. *J. Phys. Condens. Matter* **2015**, *27*, 013001.
(150) Pineda, M.; Stamatakis, M. Beyond Mean-Field Approximations for Accurate and Computationally Efficient Models of on-Lattice Chemical Kinetics. *J. Chem. Phys.* **2017**, *147*.
(151) Chatterjee, A.; Vlachos, D. G. An Overview of Spatial Microscopic and Accelerated Kinetic Monte Carlo Methods. *J. Comput. Mater. Des.* **2007**, *14*, 253–308.
(152) Salciccioli, M.; Stamatakis, M.; Caratzoulas, S.; Vlachos, D. G. A Review of Multiscale Modeling of Metal-Catalyzed Reactions: Mechanism Development for Complexity and Emergent Behavior. *Chem. Eng. Sci.* **2011**, *66*, 4319–4355.
(153) Prats, H.; Posada-Pérez, S.; Rodriguez, J. A.; Sayós, R.; Illas, F. Kinetic Monte Carlo Simulations Unveil Synergic Effects at Work on Bifunctional Catalysts. *ACS Catal.* **2019**, *9*, 9117–9126.
(154) Prats, H.; Illas, F.; Sayós, R. General Concepts, Assumptions, Drawbacks, and Misuses in Kinetic Monte Carlo and Microkinetic Modeling Simulations Applied to Computational Heterogeneous Catalysis. *International Journal of Quantum Chemistry*. 2018.
(155) Sutton, J. E.; Lorenzi, J. M.; Krogel, J. T.; Xiong, Q.; Pannala, S.; Matera, S.; Savara, A. Electrons to Reactors Multiscale Modeling: Catalytic CO Oxidation over RuO2. *ACS Catal.* **2018**, *8*, 5002–5016.
(156) Frey, K.; Schmidt, D. J.; Wolverton, C.; Schneider, W. F. Implications of Coverage-Dependent O Adsorption for Catalytic NO Oxidation on the Late Transition Metals. *Catal. Sci. Technol.* **2014**, *4*, 4356–4365.
(157) Bajpai, A.; Frey, K.; Schneider, W. F. Comparison of Coverage-Dependent Binding Energy Models for Mean-Field Microkinetic Rate Predictions. *Langmuir* **2020**, *36*, 465–474.
(158) Hess, F.; Over, H. Kinetic Monte Carlo Simulations of Heterogeneously Catalyzed Oxidation Reactions. *Catal. Sci. Technol.* **2014**, *4*, 583–598.
(159) Demir, B.; Kropp, T.; Rivera-Dones, K. R.; Gilcher, E. B.; Huber, G. W.; Mavrikakis, M.; Dumesic, J. A. A Self-Adjusting Platinum Surface for Acetone Hydrogenation. *Proc. Natl.*

Acad. Sci. **2020**, 201917110.
(160) Getman, R. B.; Schneider, W. F. DFT-Based Coverage-Dependent Model of Pt-Catalyzed NO Oxidation. *ChemCatChem* **2010**, *2*, 1450–1460.
(161) Lausche, A. C.; Medford, A. J.; Khan, T. S.; Xu, Y.; Bligaard, T.; Abild-Pedersen, F.; Nørskov, J. K.; Studt, F. On the Effect of Coverage-Dependent Adsorbate-Adsorbate Interactions for CO Methanation on Transition Metal Surfaces. *J. Catal.* **2013**, *307*, 275–282.
(162) Mellmann, D.; Sponholz, P.; Junge, H.; Beller, M. Formic Acid as a Hydrogen Storage Material – Development of Homogeneous Catalysts for Selective Hydrogen Release. *Chem. Soc. Rev.* **2016**, *45*, 3954–3988.
(163) Enthaler, S.; von Langermann, J.; Schmidt, T. Carbon Dioxide and Formic Acid—the Couple for Environmental-Friendly Hydrogen Storage? *Energy Environ. Sci.* **2010**, *3*, 1207.
(164) Yu, X.; Pickup, P. G. Recent Advances in Direct Formic Acid Fuel Cells (DFAFC). *Journal of Power Sources*. 2008, pp 124–132.
(165) El-Nagar, G. A.; Hassan, M. A.; Lauermann, I.; Roth, C. Efficient Direct Formic Acid Fuel Cells (DFAFCs) Anode Derived from Seafood Waste: Migration Mechanism. *Sci. Rep.* **2017**, *7*.
(166) El-Nagar, G. A.; Darweesh, A. F.; Sadiek, I. A Novel Nano-Palladium Complex Anode for Formic Acid Electro-Oxidation. *Electrochim. Acta* **2016**, *215*, 334–338.
(167) Rice, C.; Ha, S.; Masel, R. I.; Waszczuk, P.; Wieckowski, A.; Barnard, T. Direct Formic Acid Fuel Cells. *J. Power Sources* **2002**, *111*, 83–89.
(168) Jiang, K.; Zhang, H.-X.; Zou, S.; Cai, W.-B. Electrocatalysis of Formic Acid on Palladium and Platinum Surfaces: From Fundamental Mechanisms to Fuel Cell Applications. *Phys. Chem. Chem. Phys.* **2014**, *16*, 20360–20376.
(169) Rice, C. A.; Bauskar, A.; Pickup, P. G. *Recent Advances in Electrocatalysis of Formic Acid Oxidation*; 2013; Vol. 9.
(170) Rahimi, A.; Ulbrich, A.; Coon, J. J.; Stahl, S. S. Formic-Acid-Induced Depolymerization of Oxidized Lignin to Aromatics. *Nature* **2014**, *515*, 249–252.
(171) Wang, L.; Zhang, B.; Meng, X.; Su, D. S.; Xiao, F. S. Hydrogenation of Biofuels with Formic Acid over a Palladium-Based Ternary Catalyst with Two Types of Active Sites. *ChemSusChem* **2014**, *7*, 1537–1541.
(172) Gilkey, M. J.; Xu, B. Heterogeneous Catalytic Transfer Hydrogenation as an Effective Pathway in Biomass Upgrading. *ACS Catalysis*. 2016, pp 1420–1436.
(173) Singh, A. K.; Jang, S.; Kim, J. Y.; Sharma, S.; Basavaraju, K. C.; Kim, M. G.; Kim, K. R.; Lee, J. S.; Lee, H. H.; Kim, D. P. One-Pot Defunctionalization of Lignin-Derived Compounds by Dual-Functional Pd50Ag50/Fe3O4/N-RGO Catalyst. *ACS Catal.* **2015**, *5*, 6964–6972.
(174) Feng, J.; Gu, X.; Xue, Y.; Han, Y.; Lu, X. Production of γ-Valerolactone from Levulinic Acid over a Ru/C Catalyst Using Formic Acid as the Sole Hydrogen Source. *Sci. Total Environ.* **2018**, *633*, 426–432.
(175) Gao, Y.; Zhang, H.; Han, A.; Wang, J.; Tan, H. R.; Tok, E. S.; Jaenicke, S.; Chuah, G. K. Ru/ZrO2Catalysts for Transfer Hydrogenation of Levulinic Acid with Formic Acid/Formate Mixtures: Importance of Support Stability. *ChemistrySelect* **2018**, *3*, 1343–1351.

(176) Hu, Z.; Tan, S.; Mi, R.; Li, X.; Bai, J.; Guo, X.; Hu, G.; Hang, P.; Li, J.; Li, D.; et al. Formic Acid or Formate Derivatives as the In Situ Hydrogen Source in Au-Catalyzed Reduction of *Para* -Chloronitrobenzene. *ChemistrySelect* **2018**, *3*, 2850–2853.
(177) Ruppert, A. M.; Jędrzejczyk, M.; Sneka-Płatek, O.; Keller, N.; Dumon, A. S.; Michel, C.; Sautet, P.; Grams, J. Ru Catalysts for Levulinic Acid Hydrogenation with Formic Acid as a Hydrogen Source. *Green Chem.* **2016**, *18*, 2014–2028.
(178) Ashokraju, M.; Mohan, V.; Murali, K.; Rao, M. V.; Raju, B. D.; Rao, K. S. R. Formic Acid Assisted Hydrogenation of Levulinic Acid to γ -Valerolactone over Ordered Mesoporous Cu/Fe2O3catalyst Prepared by Hard Template Method. *J. Chem. Sci.* **2018**, *130*, 1–8.
(179) Lomate, S.; Sultana, A.; Fujitani, T. Vapor Phase Catalytic Transfer Hydrogenation (CTH) of Levulinic Acid to γ-Valerolactone Over Copper Supported Catalysts Using Formic Acid as Hydrogen Source. *Catal. Letters* **2018**, *148*, 348–358.
(180) Bulushev, D. A.; Beloshapkin, S.; Ross, J. R. H. Hydrogen from Formic Acid Decomposition over Pd and Au Catalysts. *Catal. Today* **2010**, *154*, 7–12.
(181) Larsson, R.; Jamróz, M. H.; Borowiak, M. A. On the Catalytic Decomposition of Formic Acid. I. The Activation Energies for Oxide Catalysis. *J. Mol. Catal. A Chem.* **1998**, *129*, 41–51.
(182) Koos, A.; Solymosi, F. Production of CO-Free H2 by Formic Acid Decomposition over Mo2C/Carbon Catalysts. *Catal. Letters* **2010**, *138*, 23–27.
(183) Zacharska, A. M.; Bulusheva, L.; Lisitsyn, A.; Beloshapkin, S.; Guo, Y.; Chuvilin, A.; Podyacheva, O.; Leahy, J.; Bulushev, D.; Zacharska, M.; et al. Factors Influencing the Performance of Pd / C Catalysts in the Green Production of Hydrogen from Formic Acid.
(184) Li, J.; Chen, W.; Zhao, H.; Zheng, X.; Wu, L.; Pan, H.; Zhu, J.; Chen, Y.; Lu, J. Size-Dependent Catalytic Activity over Carbon-Supported Palladium Nanoparticles in Dehydrogenation of Formic Acid. *J. Catal.* **2017**, *352*, 371–381.
(185) Navlani-García, M.; Mori, K.; Wen, M.; Kuwahara, Y.; Yamashita, H. Size Effect of Carbon-Supported Pd Nanoparticles in the Hydrogen Production from Formic Acid. *Bull. Chem. Soc. Jpn.* **2015**, *88*, 1500–1502.
(186) Wang, S.; Vorotnikov, V.; Vlachos, D. G. Coverage-Induced Conformational Effects on Activity and Selectivity: Hydrogenation and Decarbonylation of Furfural on Pd(111). *ACS Catal.* **2015**, *5*, 104–112.
(187) Spiewak, B. E.; Shen, J.; Dumesic, J. A. Microcalorimetric Studies of CO and H2 Adsorption on Nickel Powders Promoted with Potassium and Cesium. *J. Phys. Chem.* **1995**, *99*, 17640–17644.
(188) Zou, W.; Gonzalez, R. D. The Preparation of Silica Supported Pd Catalysts: The Effect of Pretreatment Variables on Particle Size. *Catal. Letters* **1992**, *12*, 73–86.
(189) Perdew, J. P.; Chevary, J. A.; Vosko, S. H.; Jackson, K. A.; Pederson, M. R.; Singh, D. J.; Fiolhais, C. Atoms, Molecules, Solids, and Surfaces: Applications of the Generalized Gradient Approximation for Exchange and Correlation. *Phys. Rev. B* **1992**, *46*, 6671–6687.
(190) Linstrom PJ, Mallard WG (2017) NIST Chemistry WebBook, NIST Standard Reference Database Number 69. Https://Doi.Org/10.18434/T4D303.
(191) Zhou, X.; Huang, Y.; Xing, W.; Liu, C.; Liao, J.; Lu, T. High-Quality Hydrogen from the Catalyzed Decomposition of Formic Acid by Pd-Au/C and Pd-Ag/C. *Chem. Commun. (Camb).* **2008**, No. 30, 3540–3542.

(192) Ruthven, D. M.; Upadhye, R. S. The Catalytic Decomposition of Aqueous Formic Acid over Suspended Palladium Catalysts. *J. Catal.* **1971**, *21*, 39–47.
(193) Conrad, H.; Ertl, G.; Küppers, J. Interactions between Oxygen and Carbon Monoxide on a Pd(111) Surface. *Surf. Sci.* **1978**, *76*, 323–342.
(194) Surnev, S.; Sock, M.; Ramsey, M. G.; Netzer, F. P.; Wiklund, M.; Borg, M.; Andersen, J. N. CO Adsorption on Pd(111): A High-Resolution Core Level Photoemission and Electron Energy Loss Spectroscopy Study. *Surf. Sci.* **2000**, *470*, 171–185.
(195) Conrad, H.; Ertl, G.; Koch, J.; Latta, E. E. Adsorption of CO on Pd Single Crystal Surfaces. *Surf. Sci.* **1974**, *43*, 462–480.
(196) Schauermann, S.; Silbaugh, T. L.; Campbell, C. T. Single-Crystal Adsorption Calorimetry on Well-Defined Surfaces: From Single Crystals to Supported Nanoparticles. *Chem. Rec.* **2014**, *14*, 759–774.
(197) Unterhalt, H.; Rupprechter, G.; Freund, H. J. Vibrational Sum Frequency Spectroscopy on Pd(111) and Supported Pd Nanoparticles: CO Adsorption from Ultrahigh Vacuum to Atmospheric Pressure. *J. Phys. Chem. B* **2002**, *106*, 356–367.
(198) Szanyi, J.; Kuhn, W. K.; Goodman, D. W. CO Adsorption on Pd(111) and Pd(100): Low and High Pressure Correlations. *J. Vac. Sci. Technol. A Vacuum, Surfaces, Film.* **1993**, *11*, 1969–1974.
(199) Bradshaw, A. M.; Hoffmann, F. M. The Chemisorption of Carbon Monoxide on Palladium Single Crystal Surfaces: IR Spectroscopic Evidence for Localised Site Adsorption. *Surf. Sci.* **1978**, *72*, 513–535.
(200) Wachs, I. E.; Madix, R. J. The Kinetics and Mechanism of Catalytic Reactions by Molecular Beam Relaxation Spectroscopy: HCOOH Decomposition. *Surf. Sci.* **1977**, *65*, 287–313.
(201) Cabilla, G.; Bonivardi, A. L.; Baltanás, M. A. Infrared Study of the Adsorption of Formic Acid on Clean and Ca-Promoted Pd/SiO2 Catalysts. *Appl. Catal. A Gen.* **2003**, *255*, 181–195.
(202) Aas, N.; Li, Y.; Bowker, M. The Adsorption and Decomposition of Formic Acid on Clean and Oxygen-Dosed Pd(110). **1991**, *281*.
(203) Zheng, T.; Stacchiola, D.; Saldin, D. K.; James, J.; Sholl, D. S.; Tysoe, W. T. The Structure of Formate Species on Pd(111) Calculated by Density Functional Theory and Determined Using Low Energy Electron Diffraction. *Surf. Sci.* **2005**, *574*, 166–174.
(204) Davis, J. L.; Barteau, M. A. Reactions of Carboxylic Acids on the Pd(111)-(2 × 2)O Surface: Multiple Roles of Surface Oxygen Atoms. *Surf. Sci.* **1991**, *256*, 50–66.
(205) Egawa, C.; Doi, I.; Naito, S.; Tamaru, K. Adsorption of Methanol, Formaldehyde and Formic Acid on Pd(100) Surfaces Modified By A Sodium and Sodium Oxide Overlayer. **1986**, *176*, 491–504.
(206) Jorgensen, S. W.; Madix, R. J. Active Oxygen on Group VIII Metals: Activation of Formic Acid and Formaldehyde on Pd(100). *J. Am. Chem. Soc.* **1988**, *110*, 397–400.
(207) Jeroro, E.; Vohs, J. M. Reaction of Formic Acid on Zn-Modified Pd(111). *Catal. Letters* **2009**, *130*, 271–277.
(208) Zhao, W.; Carey, S. J.; Morgan, S. E.; Campbell, C. T. Energetics of Adsorbed Formate and Formic Acid on Ni(111) by Calorimetry. *J. Catal.* **2017**, *352*, 300–304.
(209) Doyle, A. G.; Jacobsen, E. N. Small-Molecule H-Bond Donors in Asymmetric Catalysis. *Chem. Rev.* **2007**, *107*, 5713–5743.

(210) Wurst, J. M.; Liu, G.; Tan, D. S. Hydrogen-Bonding Catalysis and Inhibition by Simple Solvents in the Stereoselective Kinetic Epoxide-Opening Spirocyclization of Glycal Epoxides to Form Spiroketals. *J. Am. Chem. Soc.* **2011**, *133*, 7916–7925.
(211) Taylor, M. S.; Jacobsen, E. N. Asymmetric Catalysis by Chiral Hydrogen-Bond Donors. *Angew. Chemie - Int. Ed.* **2006**, *45*, 1520–1543.
(212) Farfán, P.; Echeverri, A.; Diaz, E.; Tapia, J. D.; Gómez, S.; Restrepo, A. Dimers of Formic Acid: Structures, Stability, and Double Proton Transfer. *J. Chem. Phys.* **2017**, *147*.
(213) Tedsree, K.; Li, T.; Jones, S.; Chan, C. W. A.; Yu, K. M. K.; Bagot, P. A. J.; Marquis, E. A.; Smith, G. D. W.; Tsang, S. C. E. Hydrogen Production from Formic Acid Decomposition at Room Temperature Using a Ag–Pd Core–Shell Nanocatalyst. *Nat. Nanotechnol.* **2011**, *6*, 302–307.
(214) Bi, Q. Y.; Du, X. L.; Liu, Y. M.; Cao, Y.; He, H. Y.; Fan, K. N. Efficient Subnanometric Gold-Catalyzed Hydrogen Generation via Formic Acid Decomposition under Ambient Conditions. *J. Am. Chem. Soc.* **2012**, *134*, 8926–8933.
(215) Reichert, J.; Brunner, B.; Jess, A.; Wasserscheid, P.; Albert, J. Biomass Oxidation to Formic Acid in Aqueous Media Using Polyoxometalate Catalysts - Boosting FA Selectivity by in-Situ Extraction. *Energy Environ. Sci.* **2015**, *8*, 2985–2990.
(216) Gu, X.; Lu, Z.-H.; Jiang, H.-L.; Akita, T.; Xu, Q. Synergistic Catalysis of Metal–Organic Framework-Immobilized Au–Pd Nanoparticles in Dehydrogenation of Formic Acid for Chemical Hydrogen Storage. *J. Am. Chem. Soc.* **2011**, *133*, 11822–11825.
(217) Wang, H.; Zhou, S.; Gilroy, K. D.; Cai, Z.; Xia, Y. Icosahedral Nanocrystals of Noble Metals: Synthesis and Applications. *Nano Today* **2017**, *15*, 121–144.
(218) Yoo, J. S.; Abild-Pedersen, F.; Nørskov, J. K.; Studt, F. Theoretical Analysis of Transition-Metal Catalysts for Formic Acid Decomposition. *ACS Catal.* **2014**, *4*, 1226–1233.
(219) Elnabawy, A. O.; Herron, J. A.; Scaranto, J.; Mavrikakis, M. Structure Sensitivity of Formic Acid Electrooxidation on Transition Metal Surfaces: A First-Principles Study. *J. Electrochem. Soc.* **2018**, *165*, J3109–J3121.
(220) Eppinger, J.; Huang, K.-W. Formic Acid as a Hydrogen Energy Carrier. *ACS Energy Lett.* **2017**, *2*, 188–195.
(221) Jiang, Z.; Qin, P.; Fang, T. Decomposition Mechanism of Formic Acid on Cu (111) Surface: A Theoretical Study. *Appl. Surf. Sci.* **2017**, *396*, 857–864.
(222) Putra, S. E. M.; Muttaqien, F.; Hamamoto, Y.; Inagaki, K.; Hamada, I.; Morikawa, Y. Van Der Waals Density Functional Study of Formic Acid Adsorption and Decomposition on Cu(111). *J. Chem. Phys.* **2019**, *150*, 154707.
(223) Iglesia, E.; Boudart, M. Unimolecular and Bimolecular Formic Acid Decomposition on Copper. *J. Phys. Chem.* **1986**, *90*, 5272–5274.
(224) Dubois, L. H.; Ellis, T. H.; Zegarski, B. R.; Kevan, S. D. New Insights into the Kinetics of Formic Acid Decomposition on Copper Surfaces. *Surf. Sci.* **1986**, *172*, 385–397.
(225) Sexton, B. A. Observations of Formate Species on Copper(100) Surface by High Resolution Electron Energy Loss Spectroscopy. *Surf. Sci.* **1979**, *88*, 319–330.
(226) Yao, Y.; Zaera, F. Adsorption and Thermal Chemistry of Formic Acid on Clean and Oxygen-Predosed Cu(110) Single-Crystal Surfaces Revisited. *Surf. Sci.* **2016**, *646*, 37–44.
(227) Baber, A. E.; Mudiyanselage, K.; Senanayake, S. D.; Beatriz-Vidal, A.; Luck, K. A.; Charles, E.; Sykes, H.; Liu, P.; Rodriguez, J. A.; Stacchiola, D. J. Assisted Deprotonation

of Formic Acid on Cu(111) and Self-Assembly of 1D Chains. *Phys. Chem. Chem. Phys. Phys. Chem. Chem. Phys* **2013**, *15*, 12291–12298.
(228) Marcinkowski, M. D.; Murphy, C. J.; Liriano, M. L.; Wasio, N. A.; Lucci, F. R.; Sykes, E. C. H. Microscopic View of the Active Sites for Selective Dehydrogenation of Formic Acid on Cu(111). *ACS Catal.* **2015**, *5*, 7371–7378.
(229) Perdew, J. P.; Burke, K.; Ernzerhof, M. Generalized Gradient Approximation Made Simple. *Phys. Rev. Lett.* **1996**, *77*, 3865–3868.
(230) Grimme, S.; Antony, J.; Ehrlich, S.; Krieg, H. A Consistent and Accurate Ab Initio Parametrization of Density Functional Dispersion Correction (DFT-D) for the 94 Elements H-Pu. *J. Chem. Phys.* **2010**, *132*, 154104.
(231) Hansen, P. L. Atom-Resolved Imaging of Dynamic Shape Changes in Supported Copper Nanocrystals. *Science (80-.).* **2002**, *295*, 2053–2055.
(232) Kittel, C. *Introduction to Solid State Physics*, 8th ed.; Johnson, S., Ed.; John Wiley & Sons, Inc.: New York, 2004.
(233) Makov, G.; Payne, M. C. Periodic Boundary Conditions in Ab Initio Calculations. *Phys. Rev. B* **1995**, *51*, 4014–4022.
(234) Methfessel, M.; Paxton, A. T. High-Precision Sampling for Brillouin-Zone Integration in Metals. *Phys. Rev. B* **1989**, *40*, 3616–3621.
(235) Hamada, I.; Morikawa, Y. Density-Functional Analysis of Hydrogen on Pt(111): Electric Field, Solvent, and Coverage Effects. *J. Phys. Chem. C* **2008**, *112*, 10889–10898.
(236) Katsounaros, I.; Figueiredo, M. C.; Chen, X.; Calle-Vallejo, F.; Koper, M. T. M. Structure- and Coverage-Sensitive Mechanism of NO Reduction on Platinum Electrodes. *ACS Catal.* **2017**, *7*, 4660–4667.
(237) Loveless, B. T.; Buda, C.; Neurock, M.; Iglesia, E. CO Chemisorption and Dissociation at High Coverages during CO Hydrogenation on Ru Catalysts. *J. Am. Chem. Soc.* **2013**, *135*, 6107–6121.
(238) Liu, J.; Hibbitts, D.; Iglesia, E. Dense CO Adlayers as Enablers of CO Hydrogenation Turnovers on Ru Surfaces. *J. Am. Chem. Soc.* **2017**, *139*, 11789–11802.
(239) Wu, P.; Yang, B. Significance of Surface Formate Coverage on the Reaction Kinetics of Methanol Synthesis from CO2 Hydrogenation over Cu. *ACS Catal.* **2017**, *7*, 7187–7195.
(240) Yao, Z.; Guo, C.; Mao, Y.; Hu, P. Quantitative Determination of C-C Coupling Mechanisms and Detailed Analyses on the Activity and Selectivity for Fischer-Tropsch Synthesis on Co(0001): Microkinetic Modeling with Coverage Effects. *ACS Catal.* **2019**, *9*, 5957–5973.
(241) Farberow, C. A.; Dumesic, J. A.; Mavrikakis, M. Density Functional Theory Calculations and Analysis of Reaction Pathways for Reduction of Nitric Oxide by Hydrogen on Pt(111). *ACS Catal.* **2014**, *4*, 3307–3319.
(242) Nørskov, J. K.; Bligaard, T.; Rossmeisl, J.; Christensen, C. H. Density Functional Theory in Surface Chemistry and Catalysis. *Nat. Chem.* **2009**, *1*, 37–46.
(243) Tang, Y.; Roberts, C. A.; Perkins, R. T.; Wachs, I. E. Revisiting Formic Acid Decomposition on Metallic Powder Catalysts: Exploding the HCOOH Decomposition Volcano Curve. *Surf. Sci.* **2016**, *650*, 103–110.
(244) Tamaru, K. Adsorption Measurements during Surface Catalysis. The Decomposition of Formic Acid on a Copper Catalyst. *Trans. Faraday Soc.* **1959**, *55*, 1191–1194.
(245) Campbell, C. T. Future Directions and Industrial Perspectives Micro- and Macro-Kinetics:

Their Relationship in Heterogeneous Catalysis. *Top. Catal.* **1994**, *1*, 353–366.
(246) Ying, D. H. S.; Robert, J. M. Thermal Desorption Study of Formic Acid Decomposition on a Clean Cu(110) Surface. *J. Catal.* **1980**, *61*, 48–56.
(247) Hirota, K.; Otaki, T.; Asai, S. Catalytic Dehydrogenation of Formic Acid on Metallic Catalysts. *Zeitschrift fur Phys. Chemie* **1959**, *21*, 438–440.
(248) Sim, W. S.; Gardner, P.; King, D. A. Multiple Bonding Configurations of Adsorbed Formate on Ag{111}. *J. Phys. Chem.* **1996**, *100*, 12509–12516.
(249) Ortiz, A. U.; Freitas, A. P.; Boutin, A.; Fuchs, A. H.; Coudert, F. X. What Makes Zeolitic Imidazolate Frameworks Hydrophobic or Hydrophilic? The Impact of Geometry and Functionalization on Water Adsorption. *Phys. Chem. Chem. Phys.* **2014**, *16*, 9940–9949.
(250) Li, J.-R.; Sculley, J.; Zhou, H.-C. Metal–Organic Frameworks for Separations. *Chem. Rev.* **2012**, *112*, 869–932.
(251) Mavrikakis, M. Computational Methods: A Search Engine for Catalysts. *Nat. Mater.* **2006**, *5*, 847–848.
(252) Medford, A. J.; Vojvodic, A.; Hummelshøj, J. S.; Voss, J.; Abild-Pedersen, F.; Studt, F.; Bligaard, T.; Nilsson, A.; Nørskov, J. K. From the Sabatier Principle to a Predictive Theory of Transition-Metal Heterogeneous Catalysis. *J. Catal.* **2015**, *328*, 36–42.
(253) Cheng, J.; Hu, P. Utilization of the Three-Dimensional Volcano Surface to Understand the Chemistry of Multiphase Systems in Heterogeneous Catalysis. *J. Am. Chem. Soc.* **2008**, *130*, 10868–10869.
(254) Li, H. J.; Lausche, A. C.; Peterson, A. A.; Hansen, H. A.; Studt, F.; Bligaard, T. Using Microkinetic Analysis to Search for Novel Anhydrous Formaldehyde Production Catalysts. *Surf. Sci.* **2015**, *641*, 105–111.
(255) Bruix, A.; Margraf, J. T.; Andersen, M.; Reuter, K. First-Principles-Based Multiscale Modelling of Heterogeneous Catalysis. *Nat. Catal.* **2019**, *2*, 659–670.
(256) Chakarova-Käck, S. D.; Schröder, E.; Lundqvist, B. I.; Langreth, D. C. Application of van Der Waals Density Functional to an Extended System: Adsorption of Benzene and Naphthalene on Graphite. *Phys. Rev. Lett.* **2006**, *96*.
(257) Carrasquillo-Flores, R.; Gallo, J. M. R.; Hahn, K.; Dumesic, J. A.; Mavrikakis, M. Density Functional Theory and Reaction Kinetics Studies of the Water-Gas Shift Reaction on Pt-Re Catalysts. *ChemCatChem* **2013**, *5*, 3690–3699.
(258) Rubert-Nason, P.; Mavrikakis, M.; Maravelias, C. T.; Grabow, L. C.; Biegler, L. T. Advanced Solution Methods for Microkinetic Models of Catalytic Reactions: A Methanol Synthesis Case Study. *AIChE J.* **2014**.
(259) Demir, B.; Kropp, T.; Rivera-dones, K. R.; Gilcher, E. B.; Huber, G. W.; Mavrikakis, M.; Dumesic, J. A. A Self-Adjusting Platinum Surface for Acetone Hydrogenation. **2019**, 1–5.
(260) Linstrom, P. J.; Mallard, W. G. NIST Chemistry WebBook, NIST Standard Reference Database Number 69. *Natl. Inst. Stand. Technol.* **2014**.
(261) Gazsi, A.; Bánsági, T.; Solymosi, F. Decomposition and Reforming of Formic Acid on Supported Au Catalysts: Production of CO-Free H2. *J. Phys. Chem. C* **2011**, *115*, 15459–15466.
(262) Bi, Q. Y.; Lin, J. D.; Liu, Y. M.; He, H. Y.; Huang, F. Q.; Cao, Y. Gold Supported on Zirconia Polymorphs for Hydrogen Generation from Formic Acid in Base-Free Aqueous Medium. *J. Power Sources* **2016**.

(263) Ciftci, A.; Ligthart, D. A. J. M.; Pastorino, P.; Hensen, E. J. M. Nanostructured Ceria Supported Pt and Au Catalysts for the Reactions of Ethanol and Formic Acid. *Appl. Catal. B Environ.* **2013**, *130–131*, 325–335.
(264) Sobolev, V.; Asanov, I.; Koltunov, K. The Role of Support in Formic Acid Decomposition on Gold Catalysts. *Energies* **2019**, *12*, 1–8.
(265) Mavrikakis, M.; Stoltze, P.; Nørskov, J. K. Making Gold Less Noble. *Catal. Letters* **2000**, *64*, 101–106.
(266) Williams, W. D.; Shekhar, M.; Lee, W. S.; Kispersky, V.; Delgass, W. N.; Ribeiro, F. H.; Kim, S. M.; Stach, E. A.; Miller, J. T.; Allard, L. F. Metallic Corner Atoms in Gold Clusters Supported on Rutile Are the Dominant Active Site during Water-Gas Shift Catalysis. *J. Am. Chem. Soc.* **2010**, *132*, 14018–14020.
(267) Shekhar, M.; Wang, J.; Lee, W. S.; Williams, W. D.; Kim, S. M.; Stach, E. A.; Miller, J. T.; Delgass, W. N.; Ribeiro, F. H. Size and Support Effects for the Water-Gas Shift Catalysis over Gold Nanoparticles Supported on Model Al2O3 and TiO2. *J. Am. Chem. Soc.* **2012**, *134*, 4700–4708.
(268) Shekhar, M.; Wang, J.; Lee, W. S.; Cem Akatay, M.; Stach, E. A.; Nicholas Delgass, W.; Ribeiro, F. H. Counting Au Catalytic Sites for the Water-Gas Shift Reaction. *J. Catal.* **2012**, *293*, 94–102.
(269) Häkkinen, H. Electronic Shell Structures in Bare and Protected Metal Nanoclusters. *Advances in Physics: X*. 2016.
(270) Miller, S. D.; Kitchin, J. R. Uncertainty and Figure Selection for DFT Based Cluster Expansions for Oxygen Adsorption on Au and Pt (111) Surfaces. In *Molecular Simulation*; 2009.
(271) Han, B. C.; Van Der Ven, A.; Ceder, G.; Hwang, B. J. Surface Segregation and Ordering of Alloy Surfaces in the Presence of Adsorbates. *Phys. Rev. B - Condens. Matter Mater. Phys.* **2005**.
(272) Stamatakis, M.; Piccinin, S. Rationalizing the Relation between Adlayer Structure and Observed Kinetics in Catalysis. *ACS Catal.* **2016**.
(273) Thirumalai, H.; Kitchin, J. R. The Role of VdW Interactions in Coverage Dependent Adsorption Energies of Atomic Adsorbates on Pt(111) and Pd(111). *Surf. Sci.* **2016**, *650*, 196–202.
(274) Biegler, L. T.; Damiano, J. J.; Blau, G. E. Nonlinear Parameter Estimation: A Case Study Comparison. *AIChE J.* **1986**, *32*, 29–45.
(275) Stewart, W. E.; Caracotsios, M.; Sørensen, J. P. Parameter Estimation from Multiresponse Data. *AIChE Journal*. 1992, pp 641–650.
(276) Biegler, L. T. *Nonlinear Programming: Concepts, Algorithms, and Applications to Chemical Processes*, Volume 10.; Siam, 2010.
(277) Tjoa, I. B.; Biegler, L. T. Simultaneous Solution and Optimization Strategies for Parameter Estimation of Differential-Algebraic Equation Systems. *Ind. Eng. Chem. Res.* **1991**, *30*, 376–385.
(278) Zavala, V. M.; Biegler, L. T. Large-Scale Parameter Estimation in Low-Density Polyethylene Tubular Reactors. *Ind. Eng. Chem. Res.* **2006**, *45*, 7867–7881.
(279) Biegler, L. T. An Overview of Simultaneous Strategies for Dynamic Optimization. *Chem. Eng. Process. Process Intensif.* **2007**, *46*, 1043–1053.

(280) Wächter, A.; Biegler, L. T. *On the Implementation of a Primal-Dual Interior Point Filter Line Search Algorithm for Large-Scale Nonlinear Programming*; 2006; Vol. 106.
(281) Hindmarsh, A. C.; Brown, P. N.; Grant, K. E.; Lee, S. L.; Serban, R.; Shumaker, D. E.; Woodward, C. S. SUNDIALS: Suite of Nonlinear and Differential/Algebraic Equation Solvers. *ACM Trans. Math. Softw.* **2005**, *31*, 363–396.
(282) Biegler, L. T.; Zavala, V. M. Large-Scale Nonlinear Programming Using IPOPT: An Integrating Framework for Enterprise-Wide Dynamic Optimization. *Comput. Chem. Eng.* **2009**, *33*, 575–582.
(283) Sprowl, L. H.; Campbell, C. T.; Árnadóttir, L. Hindered Translator and Hindered Rotor Models for Adsorbates: Partition Functions and Entropies. *J. Phys. Chem. C* **2016**.
(284) Jørgensen, M.; Grönbeck, H. Adsorbate Entropies with Complete Potential Energy Sampling in Microkinetic Modeling. *J. Phys. Chem. C* **2017**.
(285) Tian, H.; Rzepa, C.; Upadhyay, R.; Rangarajan, S. Estimating Vibrational and Thermodynamic Properties of Adsorbates with Uncertainty Using Data Driven Surrogates. *AIChE J.* **2019**.
(286) Zafeiratos, S.; Piccinin, S.; Teschner, D. Alloys in Catalysis: Phase Separation and Surface Segregation Phenomena in Response to the Reactive Environment. *Catal. Sci. Technol.* **2012**, *2*, 1787.
(287) Kang, H. C.; Jachimowski, T. A.; Weinberg, W. H. Role of Local Configurations in a Langmuir-Hinshelwood Surface Reaction: Kinetics and Compensation. *J. Chem. Phys.* **1990**, *93*, 1418–1429.
(288) Bligaard, T.; Honkala, K.; Logadottir, A.; Nørskov, J. K.; Dahl, S.; Jacobsen, C. J. H. On the Compensation Effect in Heterogeneous Catalysis. *J. Phys. Chem. B* **2003**, *107*, 9325–9331.
(289) Walker, E.; Ammal, S. C.; Terejanu, G. A.; Heyden, A. Uncertainty Quantification Framework Applied to the Water-Gas Shift Reaction over Pt-Based Catalysts. *J. Phys. Chem. C* **2016**, *120*, 10328–10339.
(290) Wellendorff, J.; Lundgaard, K. T.; Møgelhøj, A.; Petzold, V.; Landis, D. D.; Nørskov, J. K.; Bligaard, T.; Jacobsen, K. W. Density Functionals for Surface Science: Exchange-Correlation Model Development with Bayesian Error Estimation. *Phys. Rev. B - Condens. Matter Mater. Phys.* **2012**, *85*, 32–34.
(291) Vojvodic, A.; Medford, A. J.; Studt, F.; Abild-Pedersen, F.; Khan, T. S.; Bligaard, T.; Nørskov, J. K. Exploring the Limits: A Low-Pressure, Low-Temperature Haber–Bosch Process. *Chem. Phys. Lett.* **2014**, *598*, 108–112.
(292) Sauer, J. Ab Initio Calculations for Molecule-Surface Interactions with Chemical Accuracy. *Acc. Chem. Res.* **2019**, *52*, 3502–3510.
(293) Ou, Q.; Carter, E. A. Potential Functional Embedding Theory with an Improved Kohn-Sham Inversion Algorithm. *J. Chem. Theory Comput.* **2018**, *14*, 5680–5689.
(294) Yu, K.; Carter, E. A. Extending Density Functional Embedding Theory for Covalently Bonded Systems. *Proc. Natl. Acad. Sci. U. S. A.* **2017**, *114*, E10861–E10870.
(295) Vanderbilt, D. Soft Self-Consistent Pseudopotentials in a Generalized Eigenvalue Formalism. *Phys. Rev. B* **1990**, *41*, 7892–7895.
(296) Chadi, D. J.; Cohen, M. L. Special Points in the Brillouin Zone. *Phys. Rev. B* **1973**, *8*, 5747–5753.

(297) Mills, G.; Jónsson, H.; Schenter, G. K. Reversible Work Transition State Theory: Application to Dissociative Adsorption of Hydrogen. *Surf. Sci.* **1995**, *324*, 305–337.
(298) Ulitsky, a.; Elber, R. A New Technique to Calculate Steepest Descent Paths in Flexible Polyatomic Systems. *J. Chem. Phys.* **1990**, *92*, 1510.
(299) Bhandari, S.; Rangarajan, S.; Li, S.; Singh, S.; Maravelias, C. T. .; Dumesic, J. A. .; Mavrikakis, M. A Coverage Self-Consistent Microkinetic Model for Vapor-Phase Decomposition of Formic Acid on Pd Catalysts. *To Be Submitt.*
(300) Ding, C.; Shen, T.; Yang, Y.; Xu, X. Involvement of the Unoccupied Site Changes the Kinetic Trend Significantly: A Case Study on Formic Acid Decomposition. *ACS Catal.* **2020**, *10*, 5153–5162.
(301) Kim, J.; Kim, H. E.; Lee, H. Single-Atom Catalysts of Precious Metals for Electrochemical Reactions. *ChemSusChem*. 2018, pp 104–113.
(302) Liu, D.; Tao, L.; Yan, D.; Zou, Y.; Wang, S. Recent Advances on Non-Precious Metal Porous Carbon-Based Electrocatalysts for Oxygen Reduction Reaction. *ChemElectroChem* **2018**, *5*, 1775–1785.
(303) Mitchell, S.; Vorobyeva, E.; Pérez-Ramírez, J. The Multifaceted Reactivity of Single-Atom Heterogeneous Catalysts. *Angewandte Chemie - International Edition*. 2018, pp 15316–15329.
(304) Luo, E.; Zhang, H.; Wang, X.; Gao, L.; Gong, L.; Zhao, T.; Jin, Z.; Ge, J.; Jiang, Z.; Liu, C.; et al. Single-Atom Cr−N 4 Sites Designed for Durable Oxygen Reduction Catalysis in Acid Media . *Angew. Chemie Int. Ed.* **2019**, *58*, 12469–12475.
(305) Yin, P.; Yao, T.; Wu, Y.; Zheng, L.; Lin, Y.; Liu, W.; Ju, H.; Zhu, J.; Hong, X.; Deng, Z.; et al. Single Cobalt Atoms with Precise N-Coordination as Superior Oxygen Reduction Reaction Catalysts. *Angew. Chemie - Int. Ed.* **2016**, *55*, 10800–10805.
(306) Wu, J.; Zhou, H.; Li, Q.; Chen, M.; Wan, J.; Zhang, N.; Xiong, L.; Li, S.; Xia, B. Y.; Feng, G.; et al. Densely Populated Isolated Single Co-N Site for Efficient Oxygen Electrocatalysis. *Adv. Energy Mater.* **2019**, *9*.
(307) Jiang, S.; Zhu, C.; Dong, S. Cobalt and Nitrogen-Cofunctionalized Graphene as a Durable Non-Precious Metal Catalyst with Enhanced ORR Activity. *J. Mater. Chem. A* **2013**, *1*, 3593–3599.
(308) Zitolo, A.; Goellner, V.; Armel, V.; Sougrati, M. T.; Mineva, T.; Stievano, L.; Fonda, E.; Jaouen, F. Identification of Catalytic Sites for Oxygen Reduction in Iron- and Nitrogen-Doped Graphene Materials. *Nat. Mater.* **2015**, *14*, 937–942.
(309) Chung, H. T.; Cullen, D. A.; Higgins, D.; Sneed, B. T.; Holby, E. F.; More, K. L.; Zelenay, P. Direct Atomic-Level Insight into the Active Sites of a High-Performance PGM-Free ORR Catalyst. *Science (80-.).* **2017**, *357*, 479–484.
(310) Chen, X.; Yu, L.; Wang, S.; Deng, D.; Bao, X. Highly Active and Stable Single Iron Site Confined in Graphene Nanosheets for Oxygen Reduction Reaction. *Nano Energy* **2017**, *32*, 353–358.
(311) Liu, S.; Li, Z.; Wang, C.; Tao, W.; Huang, M.; Zuo, M.; Yang, Y.; Yang, K.; Zhang, L.; Chen, S.; et al. Turning Main-Group Element Magnesium into a Highly Active Electrocatalyst for Oxygen Reduction Reaction. *Nat. Commun.* **2020**, *11*.
(312) Zhang, C.; Sha, J.; Fei, H.; Liu, M.; Yazdi, S.; Zhang, J.; Zhong, Q.; Zou, X.; Zhao, N.; Yu, H.; et al. Single-Atomic Ruthenium Catalytic Sites on Nitrogen-Doped Graphene for

Oxygen Reduction Reaction in Acidic Medium. *ACS Nano* **2017**, *11*, 6930–6941.
(313) Choi, C. H.; Lim, H. K.; Chung, M. W.; Chon, G.; Ranjbar Sahraie, N.; Altin, A.; Sougrati, M. T.; Stievano, L.; Oh, H. S.; Park, E. S.; et al. The Achilles' Heel of Iron-Based Catalysts during Oxygen Reduction in an Acidic Medium. *Energy Environ. Sci.* **2018**, *11*, 3176–3182.
(314) Wang, G.; He, Y.; Hwang, S.; Cullen, D. A.; Uddin, M. A.; Langhorst, L.; Li, B.; Karakalos, S.; Kropf, A. J.; Wegener, E. C.; et al. Highly Active Atomically Dispersed CoN 4 Fuel Cell Cathode Catalysts Derived from Surfactant-Assisted MOFs: Carbon-Shell Confinement Strategy. *Energy Environ. Sci.* **2019**, *12*, 250–260.
(315) Shao, Y.; Dodelet, J. P.; Wu, G.; Zelenay, P. PGM-Free Cathode Catalysts for PEM Fuel Cells: A Mini-Review on Stability Challenges. *Advanced Materials*. 2019.
(316) Calle-Vallejo, F.; Martínez, J. I.; Rossmeisl, J. Density Functional Studies of Functionalized Graphitic Materials with Late Transition Metals for Oxygen Reduction Reactions. *Phys. Chem. Chem. Phys.* **2011**, *13*, 15639–15643.
(317) Liang, W.; Chen, J.; Liu, Y.; Chen, S. Density-Functional-Theory Calculation Analysis of Active Sites for Four-Electron Reduction of O2 on Fe/N-Doped Graphene. *ACS Catal.* **2014**, *4*, 4170–4177.
(318) Patel, A. M.; Ringe, S.; Siahrostami, S.; Bajdich, M.; Nørskov, J. K.; Kulkarni, A. R. Theoretical Approaches to Describing the Oxygen Reduction Reaction Activity of Single-Atom Catalysts. *J. Phys. Chem. C* **2018**, *122*, 29307–29318.
(319) Back, S.; Kulkarni, A. R.; Siahrostami, S. Single Metal Atoms Anchored in Two-Dimensional Materials: Bifunctional Catalysts for Fuel Cell Applications. *ChemCatChem* **2018**, *10*, 3034–3039.
(320) Hossain, M. D.; Liu, Z.; Zhuang, M.; Yan, X.; Xu, G. L.; Gadre, C. A.; Tyagi, A.; Abidi, I. H.; Sun, C. J.; Wong, H.; et al. Rational Design of Graphene-Supported Single Atom Catalysts for Hydrogen Evolution Reaction. *Adv. Energy Mater.* **2019**, *9*.
(321) Kropp, T.; Rebarchik, M.; Mavrikakis, M. On the Active Site for Electrocatalytic Water Splitting on Late Transition Metals Embedded in Graphene. *Catal. Sci. Technol.* **2019**, *9*, 6793–6799.
(322) Wang, Y.; Tang, Y.-J.; Zhou, K. Self-Adjusting Activity Induced by Intrinsic Reaction Intermediate in Fe–N–C Single-Atom Catalysts. *J. Am. Chem. Soc.* **2019**, *141*, 14115–14119.
(323) Kropp, T.; Mavrikakis, M. Transition Metal Atoms Embedded in Graphene: How Nitrogen Doping Increases CO Oxidation Activity. *ACS Catal.* **2019**, *9*, 6864–6868.
(324) Nørskov, J. K.; Rossmeisl, J.; Logadottir, A.; Lindqvist, L.; Kitchin, J. R.; Bligaard, T.; Jónsson, H. Origin of the Overpotential for Oxygen Reduction at a Fuel-Cell Cathode. *J. Phys. Chem. B* **2004**, *108*, 17886–17892.
(325) Hansen, H. A.; Viswanathan, V.; NØrskov, J. K. Unifying Kinetic and Thermodynamic Analysis of 2 E- and 4 e- Reduction of Oxygen on Metal Surfaces. *J. Phys. Chem. C* **2014**, *118*, 6706–6718.
(326) Tripković, V.; Skúlason, E.; Siahrostami, S.; Nørskov, J. K.; Rossmeisl, J. The Oxygen Reduction Reaction Mechanism on Pt(1 1 1) from Density Functional Theory Calculations. In *Electrochimica Acta*; 2010; Vol. 55, pp 7975–7981.
(327) Dubey, M. K.; Mohrschladt, R.; Donahue, N. M.; Anderson, J. G. Isotope Specific Kinetics of Hydroxyl Radical (OH) with Water (H2O): Testing Models of Reactivity and

Atmospheric Fractionation. *J. Phys. Chem. A* **1997**, *101*, 1494–1500.
(328) Yu, L.; Pan, X.; Cao, X.; Hu, P.; Bao, X. Oxygen Reduction Reaction Mechanism on Nitrogen-Doped Graphene: A Density Functional Theory Study. *J. Catal.* **2011**, *282*, 183–190.
(329) Cui, L.; Cui, L.; Li, Z.; Zhang, J.; Wang, H.; Lu, S.; Xiang, Y. A Copper Single-Atom Catalyst towards Efficient and Durable Oxygen Reduction for Fuel Cells. *J. Mater. Chem. A* **2019**, *7*, 16690–16695.
(330) Liu, J.; Jiao, M.; Mei, B.; Tong, Y.; Li, Y.; Ruan, M.; Song, P.; Sun, G.; Jiang, L.; Wang, Y.; et al. Carbon-Supported Divacancy-Anchored Platinum Single-Atom Electrocatalysts with Superhigh Pt Utilization for the Oxygen Reduction Reaction. *Angew. Chemie - Int. Ed.* **2019**, *58*, 1163–1167.
(331) Li, L.; Liu, Y. Ammonia Removal in Electrochemical Oxidation: Mechanism and Pseudo-Kinetics. *J. Hazard. Mater.* **2009**, *161*, 1010–1016.
(332) Bonnin, E. P.; Biddinger, E. J.; Botte, G. G. Effect of Catalyst on Electrolysis of Ammonia Effluents. *J. Power Sources* **2008**, *182*, 284–290.
(333) Gottesfeld, S.; Dekel, D. R.; Page, M.; Bae, C.; Yan, Y.; Zelenay, P.; Kim, Y. S. Anion Exchange Membrane Fuel Cells: Current Status and Remaining Challenges. *J. Power Sources* **2018**, *375*, 170–184.
(334) Gottesfeld, S. The Direct Ammonia Fuel Cell and a Common Pattern of Electrocatalytic Processes. *J. Electrochem. Soc.* **2018**, *165*, J3405–J3412.
(335) Valera-Medina, A.; Xiao, H.; Owen-Jones, M.; David, W. I. F.; Bowen, P. J. Ammonia for Power. *Progress in Energy and Combustion Science*. Elsevier Ltd November 1, 2018, pp 63–102.
(336) Li, Q.; He, R.; Gao, J. A.; Jensen, J. O.; Bjerrum, N. J. The CO Poisoning Effect in PEMFCs Operational at Temperatures up to 200°C. *J. Electrochem. Soc.* **2003**, *150*, A1599.
(337) Baschuk, J. J.; Li, X. Carbon Monoxide Poisoning of Proton Exchange Membrane Fuel Cells. *Int. J. Energy Res.* **2001**, *25*, 695–713.
(338) Song, L.; Liang, Z.; Ma, Z.; Zhang, Y.; Chen, J.; Adzic, R. R.; Wang, J. X. Temperature-Dependent Kinetics and Reaction Mechanism of Ammonia Oxidation on Pt, Ir, and PTIR Alloy Catalysts. *J. Electrochem. Soc.* **2018**, *165*, J3095–J3100.
(339) Gerischer, H.; Mauerer, A. Untersuchungen Zur Anodischen Oxidation von Ammoniak an Platin-Elektroden. *J. Electroanal. Chem.* **1970**, *25*, 421–433.
(340) Rosca, V.; Koper, M. T. M. Electrocatalytic Oxidation of Ammonia on Pt(111) and Pt(100) Surfaces. *Phys. Chem. Chem. Phys.* **2006**, *8*, 2513–2524.
(341) Matsui, T.; Suzuki, S.; Katayama, Y.; Yamauchi, K.; Okanishi, T.; Muroyama, H.; Eguchi, K. *In Situ* Attenuated Total Reflection Infrared Spectroscopy on Electrochemical Ammonia Oxidation over Pt Electrode in Alkaline Aqueous Solutions. *Langmuir* **2015**, *31*, 11717–11723.
(342) Gootzen, J. F. E.; Wonders, A. H.; Visscher, W.; Van Santen, R. A.; Van Veen, J. A. R. A DEMS and Cyclic Voltammetry Study of NH3 Oxidation on Platinized Platinum. *Electrochim. Acta* **1998**, *43*, 1851–1861.
(343) Herron, J. A.; Ferrin, P.; Mavrikakis, M. Electrocatalytic Oxidation of Ammonia on Transition-Metal Surfaces: A First-Principles Study. *J. Phys. Chem. C* **2015**, *119*, 14692–14701.

(344) Skachkov, D.; Venkateswara Rao, C.; Ishikawa, Y. Combined First-Principles Molecular Dynamics/Density Functional Theory Study of Ammonia Electrooxidation on Pt(100) Electrode. *J. Phys. Chem. C* **2013**, *117*, 25451–25466.
(345) De Vooys, A. C. A.; Koper, M. T. M.; Van Santen, R. A.; Van Veen, J. A. R. The Role of Adsorbates in the Electrochemical Oxidation of Ammonia on Noble and Transition Metal Electrodes. *J. Electroanal. Chem.* **2001**, *506*, 127–137.
(346) Vidal-Iglesias, F. J.; Solla-Gullón, J.; Pérez, J. M.; Aldaz, A. Evidence by SERS of Azide Anion Participation in Ammonia Electrooxidation in Alkaline Medium on Nanostructured Pt Electrodes. *Electrochem. commun.* **2006**, *8*, 102–106.
(347) Oswin, H. G.; Salomon, M. THE ANODIC OXIDATION OF AMMONIA AT PLATINUM BLACK ELECTRODES IN AQUEOUS KOH ELECTROLYTE. *Can. J. Chem.* **1963**, *41*, 1686–1694.
(348) Kresse, G.; Furthmüller, J. Efficiency of Ab-Initio Total Energy Calculations for Metals and Semiconductors Using a Plane-Wave Basis Set. *Comput. Mater. Sci.* **1996**, *6*, 15–50.
(349) Perdew, J. P.; Chevary, J. A.; Vosko, S. H.; Jackson, K. A.; Pederson, M. R.; Singh, D. J.; Fiolhais, C. Atoms, Molecules, Solids, and Surfaces: Applications of the Generalized Gradient Approximation for Exchange and Correlation. *Phys. Rev. B* **1992**, *46*, 6671–6687.
(350) Bhandari, S.; Rangarajan, S.; Maravelias, C. T.; Dumesic, J. A.; Mavrikakis, M. Reaction Mechanism of Vapor-Phase Formic Acid Decomposition over Platinum Catalysts: DFT, Reaction Kinetics Experiments, and Microkinetic Modeling. *ACS Catal.* **2020**.
(351) Davey, W. P. Precision Measurements of the Lattice Constants of Twelve Common Metals. *Phys. Rev.* **1925**, *25*, 753–761.
(352) Heyden, A.; Bell, A. T.; Keil, F. J. Efficient Methods for Finding Transition States in Chemical Reactions: Comparison of Improved Dimer Method and Partitioned Rational Function Optimization Method. *J. Chem. Phys.* **2005**, *123*, 224101.
(353) Henkelman, G.; Jónsson, H. A Dimer Method for Finding Saddle Points on High Dimensional Potential Surfaces Using Only First Derivatives. *J. Chem. Phys.* **1999**, *111*, 7010–7022.
(354) Monkhorst, H. J.; Pack, J. D. Special Points for Brillouin-Zone Integrations. *Phys. Rev. B* **1976**, *13*, 5188–5192.
(355) Wu, K. J.; Kevan, S. D. Isothermal Coverage Dependent Measurements of NH3 and ND 3 Desorption from Cu(001). *J. Chem. Phys.* **1991**, *95*, 5355–5363.
(356) Liang, Z.; Jin Yang, H.; Kim, Y.; Trenary, M. Surface Morphology of Atomic Nitrogen on Pt(111). *J. Chem. Phys.* **2014**, *140*, 114707.
(357) Vidal-Iglesias, F. J.; Solla-Gullón, J.; Montiel, V.; Feliu, J. M.; Aldaz, A. Ammonia Selective Oxidation on Pt(100) Sites in an Alkaline Medium. *J. Phys. Chem. B* **2005**, *109*, 12914–12919.
(358) Katsounaros, I.; Figueiredo, M. C.; Calle-Vallejo, F.; Li, H.; Gewirth, A. A.; Markovic, N. M.; Koper, M. T. M. On the Mechanism of the Electrochemical Conversion of Ammonia to Dinitrogen on Pt(1 0 0) in Alkaline Environment. *J. Catal.* **2018**, *359*, 82–91.
(359) Hess, F.; Over, H. Kinetic Monte Carlo Simulations of Heterogeneously Catalyzed Oxidation Reactions. *Catalysis Science and Technology*. The Royal Society of Chemistry March 1, 2014, pp 583–598.
(360) Grabow, L. C.; Gokhale, A. A.; Evans, S. T.; Dumesic, J. A.; Mavrikakis, M. Mechanism

of the Water Gas Shift Reaction on Pt: First Principles, Experiments, and Microkinetic Modeling. *J. Phys. Chem. C* **2008**, *112*, 4608–4617.
(361) Eigen http://eigen.tuxfamily.org/index.php?title=Main_Page (accessed Jan 1, 2016).
(362) Goldberg, E. D. Halogenated Hydrocarbons: Past, Present and near-Future Problems. *Sci. Total Environ.* **1991**, *100*, 17–28.
(363) Kuhn, T. K.; Hamonts, K.; Dijk, J. A.; Kalka, H.; Stichler, W.; Springael, D.; Dejonghe, W.; Meckenstock, R. U. Assessment of the Intrinsic Bioremediation Capacity of an Eutrophic River Sediment Polluted by Discharging Chlorinated Aliphatic Hydrocarbons: A Compound-Specific Isotope Approach. *Environ. Sci. Technol.* **2009**, *43*, 5263–5269.
(364) Moran, M. J.; Zogorski, J. S.; Squillace, P. J. Chlorinated Solvents in Groundwater of the United States. *Environ. Sci. Technol.* **2007**, *41*, 74–81.
(365) Kovalchuk, V. I.; D'Itri, J. L. Catalytic Chemistry of Chloro- and Chlorofluorocarbon Dehalogenation: From Macroscopic Observations to Molecular Level Understanding. *Appl. Catal. A Gen.* **2004**, *271*, 13–25.
(366) Hsieh, S. H.; Horng, J. J. Deposition of Fe-Ni Nanoparticles on Al2O3 for Dechlorination of Chloroform and Trichloroethylene. *Appl. Surf. Sci.* **2006**, *253*, 1660–1665.
(367) Wang, X.; Chen, C.; Chang, Y.; Liu, H. Dechlorination of Chlorinated Methanes by Pd/Fe Bimetallic Nanoparticles. *J. Hazard. Mater.* **2009**, *161*, 815–823.
(368) Shin, E. J.; Keane, M. A. Gas Phase Catalytic Hydrodechlorination of Chlorophenols Using a Supported Nickel Catalyst. *Appl. Catal. B Environ.* **1998**, *18*, 241–250.
(369) Ordóñez, S.; Sastre, H.; Díez, F. V. Hydrodechlorination of Aliphatic Organochlorinated Compounds over Commercial Hydrogenation Catalysts. *Appl. Catal. B Environ.* **2000**, *25*, 49–58.
(370) Álvarez-Montero, M. A.; Gómez-Sainero, L. M.; Mayoral, A.; Diaz, I.; Baker, R. T.; Rodriguez, J. J. Hydrodechlorination of Chloromethanes with a Highly Stable Pt on Activated Carbon Catalyst. *J. Catal.* **2011**, *279*, 389–396.
(371) Prati, L.; Rossi, M. Reductive Catalytic Dehalogenation of Light Chlorocarbons. *Appl. Catal. B Environ.* **1999**, *23*, 135–142.
(372) Gómez-Sainero, L. M.; Seoane, X. L.; Fierro, J. L. G.; Arcoya, A. Liquid-Phase Hydrodechlorination of CCl4 to CHCl3 on Pd/Carbon Catalysts: Nature and Role of Pd Active Species. *J. Catal.* **2002**, *209*, 279–288.
(373) Mori, T.; Hirose, K.; Kikuchi, T.; Kubo, J.; Morikawa, Y. Formation of Higher Hydrocarbons from Chloromethanes via Hydrodechlorination over Pd/SiO2 Catalyst. *J. Japan Pet. Inst.* **2002**, *45*, 321–324.
(374) Chen, N.; Rioux, R. M.; Barbosa, L. A. M. M.; Ribeiro, F. H. Kinetic and Theoretical Study of the Hydrodechlorination of CH 4- XClx (x = 1-4) Compounds on Palladium. *Langmuir* **2010**, *26*, 16615–16624.
(375) Velázquez, J. C.; Leekumjorn, S.; Nguyen, Q. X.; Fang, Y. L.; Heck, K. N.; Hopkins, G. D.; Reinhard, M.; Wong, M. S. Chloroform Hydrodechlorination Behavior of Alumina-Supported Pd and PdAu Catalysts. *AIChE J.* **2013**, *59*, 4474–4482.
(376) Xu, L.; Yao, X.; Khan, A.; Mavrikakis, M. Chloroform Hydrodechlorination over Palladium-Gold Catalysts: A First-Principles DFT Study. *ChemCatChem* **2016**, *8*, 1739–1746.
(377) Peterson, A. A.; Grabow, L. C.; Brennan, T. P.; Shong, B.; Ooi, C.; Wu, D. M.; Li, C. W.;

Kushwaha, A.; Medford, A. J.; Mbuga, F.; et al. Finite-Size Effects in O and CO Adsorption for the Late Transition Metals. *Top. Catal.* **2012**, *55*, 1276–1282.

(378) Bonarowska, M.; Malinowski, A.; Juszczyk, W.; Karpiński, Z. Hydrodechlorination of CCl2F2 (CFC-12) over Silica-Supported Palladium-Gold Catalysts. *Appl. Catal. B Environ.* **2001**, *30*, 187–193.

(379) Van De Sandt, E. J. A. X.; Wiersma, A.; Makkee, M.; Van Bekkum, H.; Moulijn, J. A. Palladium Black as Model Catalyst in the Hydrogenolysis of CCl2F2 (CFC-12) into CH2F2 (HFC-32). *Appl. Catal. A Gen.* **1997**, *155*, 59–73.

(380) Bonarowska, M.; Kaszkur, Z.; Łomot, D.; Rawski, M.; Karpiński, Z. Effect of Gold on Catalytic Behavior of Palladium Catalysts in Hydrodechlorination of Tetrachloromethane. *Appl. Catal. B Environ.* **2015**, *162*, 45–56.

(381) Cortright, R. D.; Dumesic, J. A. Kinetics of Heterogeneous Catalytic Reactions: Analysis of Reaction Schemes. *Adv. Catal.* **2001**, *46*, 161–264.

(382) Xu, L.; Stangland, E. E.; Mavrikakis, M. A DFT Study of Chlorine Coverage over Late Transition Metals and Its Implication on 1,2-Dichloroethane Hydrodechlorination. *Catal. Sci. Technol.* **2018**, *8*, 1555–1563.

(383) Da Silva, M. J. Synthesis of Methanol from Methane: Challenges and Advances on the Multi-Step (Syngas) and One-Step Routes (DMTM). *Fuel Process. Technol.* **2016**, *145*, 42–61.

(384) Khodakov, A. Y.; Chu, W.; Fongarland, P. Advances in the Development of Novel Cobalt Fischer-Tropsch Catalysts for Synthesis of Long-Chain Hydrocarbons and Clean Fuels. *Chem. Rev.* **2007**, *107*, 1692–1744.

(385) Lieberman, R. L.; Rosenzweig, A. C. Crystal Structure of a Membrane-Bound Metalloenzyme That Catalyses the Biological Oxidation of Methane. *Nature* **2005**, *434*, 177–182.

(386) Balasubramanian, R.; Smith, S. M.; Rawat, S.; Yatsunyk, L. A.; Stemmler, T. L.; Rosenzweig, A. C. Oxidation of Methane by a Biological Dicopper Centre. *Nature* **2010**, *465*, 115–119.

(387) Shu, L.; Nesheim, J. C.; Kauffmann, K.; Münck, E.; Lipscomb, J. D.; Que, L. An Fe2 IV O2 Diamond Core Structure. *Science (80-.).* **1997**, *275*, 515–518.

(388) Nauert, S. L.; Rosen, A. S.; Kim, H.; Snurr, R. Q.; Stair, P. C.; Notestein, J. M. Evidence for Copper Dimers in Low-Loaded CuOx/SiO2 Catalysts for Cyclohexane Oxidative Dehydrogenation. *ACS Catal.* **2018**, *8*, 9775–9789.

(389) Rosen, A. S.; Notestein, J. M.; Snurr, R. Q. Structure–Activity Relationships That Identify Metal–Organic Framework Catalysts for Methane Activation. *ACS Catal.* **2019**, *9*, 3576–3587.

(390) Woertink, J. S.; Smeets, P. J.; Groothaert, M. H.; Vance, M. A.; Sels, B. F.; Schoonheydt, R. A.; Solomon, E. I. A [Cu2O]2+ Core in Cu-ZSM-5, the Active Site in the Oxidation of Methane to Methanol. *Proc. Natl. Acad. Sci. U. S. A.* **2009**, *106*, 18908–18913.

(391) Ipek, B.; Lobo, R. F. Catalytic Conversion of Methane to Methanol on Cu-SSZ-13 Using N2O as Oxidant. *Chem. Commun.* **2016**, *52*, 13401–13404.

(392) Vanelderen, P.; Snyder, B. E. R.; Tsai, M. L.; Hadt, R. G.; Vancauwenbergh, J.; Coussens, O.; Schoonheydt, R. A.; Sels, B. F.; Solomon, E. I. Spectroscopic Definition of the Copper Active Sites in Mordenite: Selective Methane Oxidation. *J. Am. Chem. Soc.* **2015**, *137*,

6383–6392.
(393) Wulfers, M. J.; Teketel, S.; Ipek, B.; Lobo, R. F. Conversion of Methane to Methanol on Copper-Containing Small-Pore Zeolites and Zeotypes. *Chem. Commun.* **2015**, *51*, 4447–4450.
(394) Grundner, S.; Markovits, M. A. C.; Li, G.; Tromp, M.; Pidko, E. A.; Hensen, E. J. M.; Jentys, A.; Sanchez-Sanchez, M.; Lercher, J. A. Single-Site Trinuclear Copper Oxygen Clusters in Mordenite for Selective Conversion of Methane to Methanol. *Nat. Commun.* **2015**, *6*, 7546.
(395) Li, G.; Vassilev, P.; Sanchez-Sanchez, M.; Lercher, J. A.; Hensen, E. J. M.; Pidko, E. A. Stability and Reactivity of Copper Oxo-Clusters in ZSM-5 Zeolite for Selective Methane Oxidation to Methanol. *J. Catal.* **2016**, *338*, 305–312.
(396) Le, H. V.; Parishan, S.; Sagaltchik, A.; Göbel, C.; Schlesiger, C.; Malzer, W.; Trunschke, A.; Schomäcker, R.; Thomas, A. Solid-State Ion-Exchanged Cu/Mordenite Catalysts for the Direct Conversion of Methane to Methanol. *ACS Catal.* **2017**, *7*, 1403–1412.
(397) Narsimhan, K.; Iyoki, K.; Dinh, K.; Román-Leshkov, Y. Catalytic Oxidation of Methane into Methanol over Copper-Exchanged Zeolites with Oxygen at Low Temperature. *ACS Cent. Sci.* **2016**, *2*, 424–429.
(398) Sushkevich, V. L.; Van Bokhoven, J. A. Methane-to-Methanol: Activity Descriptors in Copper-Exchanged Zeolites for the Rational Design of Materials. *ACS Catal.* **2019**, *9*, 6293–6304.
(399) Latimer, A. A.; Kakekhani, A.; Kulkarni, A. R.; Nørskov, J. K. Direct Methane to Methanol: The Selectivity-Conversion Limit and Design Strategies. *ACS Catal.* **2018**, *8*, 6894–6907.
(400) Ravi, M.; Sushkevich, V. L.; Knorpp, A. J.; Newton, M. A.; Palagin, D.; Pinar, A. B.; Ranocchiari, M.; Bokhoven, J. A. Van. Misconceptions and Chellenges in Methane-to-Methanol over Transition-Metal-Exchanged Zeolites. *Nat. Catal.* **2019**, *2*, 485–494.
(401) Groothaert, M. H.; Smeets, P. J.; Sels, B. F.; Jacobs, P. A.; Schoonheydt, R. A. Selective Oxidation of Methane by the Bis(μ-Oxo)Dicopper Core Stabilized on ZSM-5 and Mordenite Zeolites. *J. Am. Chem. Soc.* **2005**, *127*, 1394–1395.
(402) Hammond, C.; Forde, M. M.; Ab Rahim, M. H.; Thetford, A.; He, Q.; Jenkins, R. L.; Dimitratos, N.; Lopez-Sanchez, J. A.; Dummer, N. F.; Murphy, D. M.; et al. Direct Catalytic Conversion of Methane to Methanol in an Aqueous Medium by Using Copper-Promoted Fe-ZSM-5. *Angew. Chemie - Int. Ed.* **2012**, *51*, 5129–5133.
(403) Sushkevich, V. L.; Palagin, D.; Ranocchiari, M.; Bokhoven, J. A. Van. Selective Anaerobic Oxidation of Methane Enables Direct Synthesis of Methanol. *Science (80-.).* **2017**, *356*, 523–527.
(404) Ipek, B.; Wulfers, M. J.; Kim, H.; Göltl, F.; Hermans, I.; Smith, J. P.; Booksh, K. S.; Brown, C. M.; Lobo, R. F. Formation of $[Cu_2O_2]^{2+}$ and $[Cu_2O]^{2+}$ toward C-H Bond Activation in Cu-SSZ-13 and Cu-SSZ-39. *ACS Catal.* **2017**, *7*, 4291–4303.
(405) Pappas, D. K.; Martini, A.; Dyballa, M.; Kvande, K.; Teketel, S.; Lomachenko, K. A.; Baran, R.; Glatzel, P.; Arstad, B.; Berlier, G.; et al. The Nuclearity of the Active Site for Methane to Methanol Conversion in Cu-Mordenite: A Quantitative Assessment. *J. Am. Chem. Soc.* **2018**, *140*, 15270–15278.
(406) Dyballa, M.; Pappas, D. K.; Kvande, K.; Borfecchia, E.; Arstad, B.; Beato, P.; Olsbye, U.; Svelle, S. On How Copper Mordenite Properties Govern the Framework Stability and

Activity in the Methane-to-Methanol Conversion. *ACS Catal.* **2019**, *9*, 365–375.
(407) Brezicki, G.; Kammert, J. D.; Gunnoe, T. B.; Paolucci, C.; Davis, R. J. Insights into the Speciation of Cu in the Cu-H-Mordenite Catalyst for the Oxidation of Methane to Methanol. *ACS Catal.* **2019**, *9*, 5308–5319.
(408) Pappas, D. K.; Borfecchia, E.; Dyballa, M.; Pankin, I. A.; Lomachenko, K. A.; Martini, A.; Signorile, M.; Teketel, S.; Arstad, B.; Berlier, G.; et al. Methane to Methanol: Structure-Activity Relationships for Cu-CHA. *J. Am. Chem. Soc.* **2017**, *139*, 14961–14975.
(409) Borfecchia, E.; Pappas, D. K.; Dyballa, M.; Lomachenko, K. A.; Negri, C.; Signorile, M.; Berlier, G. Evolution of Active Sites during Selective Oxidation of Methane to Methanol over Cu-CHA and Cu-MOR Zeolites as Monitored by Operando XAS. *Catal. Today* **2019**, *333*, 17–27.
(410) Li, H.; Paolucci, C.; Khurana, I.; Wilcox, L. N.; Göltl, F.; Albarracin-Caballero, J. D.; Shih, A. J.; Ribeiro, F. H.; Gounder, R.; Schneider, W. F. Chemical Science Consequences of Exchange-Site Heterogeneity and Dynamics on the UV-Visible Spectrum Of. *Chem. Sci.* **2019**, *10*, 2373–2384.
(411) Göltl, F.; Bulo, R. E.; Hafner, J.; Sautet, P. What Makes Copper-Exchanged SSZ-13 Zeolite Efficient at Cleaning Car Exhaust Gases? *J. Phys. Chem. Lett.* **2013**, *4*, 2244–2249.
(412) Göltl, F.; Müller, P.; Uchupalanun, P.; Sautet, P.; Hermans, I. Developing a Descriptor-Based Approach for CO and NO Adsorption Strength to Transition Metal Sites in Zeolites. *Chem. Mater.* **2017**, *29*, 6434–6444.
(413) Paolucci, C.; Parekh, A. A.; Khurana, I.; Di Iorio, J. R.; Li, H.; Albarracin Caballero, J. D.; Shih, A. J.; Anggara, T.; Delgass, W. N.; Miller, J. T.; et al. Catalysis in a Cage: Condition-Dependent Speciation and Dynamics of Exchanged Cu Cations in Ssz-13 Zeolites. *J. Am. Chem. Soc.* **2016**, *138*, 6028–6048.
(414) Göltl, F.; Love, A. M.; Hermans, I. Developing a Thermodynamic Model for the Interactions between Water and Cu in the Zeolite SSZ-13. *J. Phys. Chem. C* **2017**, *121*, 6160–6169.
(415) Petitjean, H.; Chizallet, C.; Berthomieu, D. Modeling Ammonia and Water Co-Adsorption in CuI-SSZ-13 Zeolite Using DFT Calculations. *Ind. Eng. Chem. Res.* **2018**, *57*, 15982–15990.
(416) Palagin, D.; Knorpp, A. J.; Pinar, A. B.; Ranocchiari, M.; Van Bokhoven, J. A. Assessing the Relative Stability of Copper Oxide Clusters as Active Sites of a CuMOR Zeolite for Methane to Methanol Conversion: Size Matters? *Nanoscale* **2017**, *9*, 1144–1153.
(417) Paolucci, C.; Di Iorio, J. R.; Ribeiro, F. H.; Gounder, R.; Schneider, W. F. Catalysis Science of NOx Selective Catalytic Reduction With Ammonia Over Cu-SSZ-13 and Cu-SAPO-34. In *Advances in Catalysis*; Elsevier Inc., 2016; Vol. 59, pp 1–107.
(418) Beale, A. M.; Gao, F.; Lezcano-Gonzalez, I.; Peden, C. H. F.; Szanyi, J. Recent Advances in Automotive Catalysis for NO_x Emission Control by Small-Pore Microporous Materials. *Chem. Soc. Rev.* **2015**, *44*, 7371–7405.
(419) Kresse, G.; Hafner, J. Ab Initio Molecular Dynamics for Open-Shell Transition Metals. *Phys. Rev. B* **1993**, *48*, 13115–13118.
(420) Göltl, F.; Hafner, J. Structure and Properties of Metal-Exchanged Zeolites Studied Using Gradient-Corrected and Hybrid Functionals. I. Structure and Energetics. *J. Chem. Phys.* **2012**, *136*, 064501.

(421) Perdew, J. P.; Burke, K.; Ernzerhof, M. Generalized Gradient Approximation Made Simple. *Phys. Rev. Lett.* **1996**, *77*, 3865–3868.
(422) Tkatchenko, A.; Scheffler, M. Accurate Molecular van Der Waals Interactions from Ground-State Electron Density and Free-Atom Reference Data. *Phys. Rev. Lett.* **2009**, *102*, 073005.
(423) Andersen, H. C. Molecular Dynamics Simulations at Constant Pressure and/or Temperature. *J. Chem. Phys.* **1980**, *72*, 2384–2393.
(424) Harl, J.; Kresse, G. Cohesive Energy Curves for Noble Gas Solids Calculated by Adiabatic Connection Fluctuation-Dissipation Theory. *Phys. Rev. B - Condens. Matter Mater. Phys.* **2008**, *77*, 1–8.
(425) Göltl, F.; Michel, C.; Andrikopoulos, P. C.; Love, A. M.; Hafner, J.; Hermans, I.; Sautet, P. Computationally Exploring Confinement Effects in the Methane-to-Methanol Conversion over Iron-Oxo Centers in Zeolites. *ACS Catal.* **2016**, *6*, 8404–8409.
(426) Irikura, K. K. Thermo.Pl. *Natl. Inst. Stand. Technol.* **2002**.
(427) Göltl, F.; Love, A. M.; Schuenzel, S. C.; Wolf, P.; Mavrikakis, M.; Hermans, I. Computational Description of Key Spectroscopic Features of Zeolite SSZ-13. *Phys. Chem. Chem. Phys.* **2019**, *21*, 19065–19075.
(428) Loewenstein, W. The Distribution of Aluminum in the Tetrahedra of Silicates and Aluminates. *Am. Mineral.* **1954**, *39*, 92–96.
(429) Göltl, F.; Sautet, P.; Hermans, I. The Impact of Finite Temperature on the Coordination of Cu Cations in the Zeolite SSZ-13. *Catal. Today* **2016**, *267*, 41–46.
(430) Fickel, D. W.; Lobo, R. F. Copper Coordination in Cu-SSZ-13 and Cu-SSZ-16 Investigated by Variable-Temperature XRD. *J. Phys. Chem. C* **2010**, *114*, 1633–1640.
(431) Kwak, J. H.; Zhu, H.; Lee, J. H.; Peden, C. H. F.; Szanyi, J. Two Different Cationic Positions in Cu-SSZ-13? *Chem. Commun.* **2012**, *48*, 4758–4760.
(432) Deka, U.; Juhin, A.; Eilertsen, E. A.; Emerich, H.; Green, M. A.; Korhonen, S. T.; Weckhuysen, B. M.; Beale, A. M. Confirmation of Isolated Cu 2+ Ions in SSZ-13 Zeolite as Active Sites in NH 3-Selective Catalytic Reduction. *J. Phys. Chem. C* **2012**, *116*, 4809–4818.
(433) Göltl, F.; Hafner, J. Structure and Properties of Metal-Exchanged Zeolites Studied Using Gradient-Corrected and Hybrid Functionals. III. Energetics and Vibrational Spectroscopy of Adsorbates. *J. Chem. Phys.* **2012**, *136*, 64501.
(434) Marsman, M.; Grüneis, A.; Paier, J.; Kresse, G. Second-Order Møller-Plesset Perturbation Theory Applied to Extended Systems. I. Within the Projector-Augmented-Wave Formalism Using a Plane Wave Basis Set. *J. Chem. Phys.* **2009**, *130*, 1–10.
(435) Tuma, C.; Kerber, T.; Sauer, J. The Tert-Butyl Cation in h-Zeolites: Deprotonation to Isobutene and Conversion into Surface Alkoxides. *Angew. Chemie - Int. Ed.* **2010**, *49*, 4678–4680.
(436) Göltl, F.; Hafner, J. Alkane Adsorption in Na-Exchanged Chabazite: The Influence of Dispersion Forces. *J. Chem. Phys.* **2011**, *134*, 064102.
(437) Göltl, F.; Grüneis, A.; Bučko, T.; Hafner, J. Van Der Waals Interactions between Hydrocarbon Molecules and Zeolites: Periodic Calculations at Different Levels of Theory, from Density Functional Theory to the Random Phase Approximation and Moller-Plesset Perturbation Theory. *J. Chem. Phys.* **2012**, *137*, 114111.

(438) Göltl, F.; Sautet, P.; Hermans, I. Can Dynamics Be Responsible for the Complex Multipeak Infrared Spectra of NO Adsorbed to Copper(II) Sites in Zeolites? *Angew. Chemie - Int. Ed.* **2015**, *54*, 7799–7804.
(439) Di Iorio, J. R.; Gounder, R. Controlling the Isolation and Pairing of Aluminum in Chabazite Zeolites Using Mixtures of Organic and Inorganic Structure-Directing Agents. *Chem. Mater.* **2016**, *28*, 2236–2247.
(440) Kulkarni, A. R.; Zhao, Z. J.; Siahrostami, S.; Nørskov, J. K.; Studt, F. Monocopper Active Site for Partial Methane Oxidation in Cu-Exchanged 8MR Zeolites. *ACS Catal.* **2016**, *6*, 6531–6536.
(441) Pappas, D. K.; Borfecchia, E.; Dyballa, M.; Pankin, I. A.; Lomachenko, K. A.; Martini, A.; Signorile, M.; Teketel, S.; Arstad, B.; Berlier, G.; et al. Methane to Methanol: Structure-Activity Relationships for Cu-CHA. *J. Am. Chem. Soc.* **2017**, *139*, 14961–14975.
(442) Shaik, S.; Cohen, S.; De Visser, S. P.; Sharma, P. K.; Kumar, D.; Kozuch, S.; Ogliaro, F.; Danovich, D. The "Rebound Controversy": An Overview and Theoretical Modeling of the Rebound Step in C-H Hydroxylation by Cytochrome P450. *Eur. J. Inorg. Chem.* **2004**, No. 2, 207–226.
(443) Ye, S.; Geng, C. Y.; Shaik, S.; Neese, F. Electronic Structure Analysis of Multistate Reactivity in Transition Metal Catalyzed Reactions: The Case of C-H Bond Activation by Non-Heme Iron(Iv)-Oxo Cores. *Phys. Chem. Chem. Phys.* **2013**, *15*, 8017–8030.
(444) Yoshizawa, K.; Shiota, Y.; Yamabe, T. Abstraction of the Hydrogen Atom of Methane by Iron-Oxo Species: The Concerted Reaction Path Is Energetically More Favorable. *Organometallics* **1998**, *17*, 2825–2831.
(445) Mao, Z.; Campbell, C. T. Apparent Activation Energies in Complex Reaction Mechanisms: A Simple Relationship via Degrees of Rate Control. *ACS Catal.* **2019**, *9*, 9465–9473.
(446) Herron, J. A.; Tonelli, S.; Mavrikakis, M. Atomic and Molecular Adsorption on Pd(111). *Surf. Sci.* **2012**, *606*, 1670–1679.
(447) Limmer, D. T.; Willard, A. P.; Madden, P.; Chandler, D. Hydration of Metal Surfaces Can Be Dynamically Heterogeneous and Hydrophobic. *Proc. Natl. Acad. Sci. U. S. A.* **2013**, *110*, 4200–4205.
(448) Hammer, B.; Hansen, L. B.; Nørskov, J. K. Improved Adsorption Energetics within Density-Functional Theory Using Revised Perdew-Burke-Ernzerhof Functionals. *Phys. Rev. B - Condens. Matter Mater. Phys.* **1999**, *59*, 7413–7421.
(449) Grimme, S.; Antony, J.; Ehrlich, S.; Krieg, H. A Consistent and Accurate Ab Initio Parametrization of Density Functional Dispersion Correction ({DFT}-{D}) for the 94 Elements {H}-{Pu}. *J. Chem. Phys.* **2010**, *132*, 154104.